

## ИНСТИТУТ ЗА ФИЗИКУ

ПРИМЉЕНО: 04. 05. 2022			
Рад.јед.	б р о ј	Арх.шифра	Прилог
0801	488/1		

НАУЧНОМ ВЕЋУ  
ИНСТИТУТА ЗА ФИЗИКУ  
У БЕОГРАДУ

Предмет: Молба за покретање поступка за избор у звање виши научни сарадник

### МОЛБА

Молим Научно веће Института за физику у Београду да у складу са Правилником о стицању истраживачких и научних звања Министарства за просвету, науку и технолошки развој покрене поступак за мој избор у звање виши научни сарадник.


У прилогу достављам:

- Мишљење руководиоца са предлогом чланова комисије;
- Биографске податке;
- Преглед научне активности;
- Елементе за квалитативну оцену научног доприноса;
- Елементе за квантитативну оцену научног доприноса;
- Списак објављених научних радова и фотокопије радова објављених након претходног избора у звање;
- Податке о цитираности;
- Копију решења о претходном избору у звање;
- Додатне прилоге са доказима.

У Београду,

04.05.2022.

С поштовањем,



Др Марко Младеновић

**ИНСТИТУТ ЗА ФИЗИКУ**

ПРИМЉЕНО: 04. 05. 2022			
Рад.јед.	б р о ј	Арх.шифра	Прилог
0801	477/1		

**Научном већу Института за физику у Београду**

**Предмет: Мишљење руководиоца лабораторије о избору др Марка Младеновића у звање виши научни сарадник**

Др Марко Младеновић је сарадник Лабораторије за примену рачунара у науци, у оквиру Националног центра изузетних вредности за изучавање комплексних система Института за физику у Београду. У истраживачком раду бави се темама везаним електронске и структурне особине материјала. С обзиром да испуњава све предвиђене услове у складу са Правилником о стицању истраживачких и научних звања МПНТР, сагласан сам са покретањем поступка за избор др Марка Младеновића у звање виши научни сарадник.

За састав комисије за избор др Марка Младеновића у звање виши научни сарадник предлажем:

- (1) др Антун Балаж, научни саветник, Институт за физику у Београду
- (2) др Ненад Вукмировић, научни саветник, Институт за физику у Београду
- (3) др Дарко Танасковић, научни саветник, Институт за физику у Београду
- (4) др Јелена Радовановић, редовни професор Електротехничког факултета Универзитета у Београду

др Антун Балаж  
научни саветник

Руководилац Лабораторије за примену рачунара у науци

## 2. БИОГРАФСКИ ПОДАЦИ КАНДИДАТА

Др Марко Младеновић је рођен 2. септембра 1988. у Зајечару. Завршио је Математичку гимназију у Београду 2007. године као носилац Вукове дипломе. Исте године уписује Електротехнички факултет у Београду. Дипломирао је на Одсеку за физичку електронику као студент генерације 2011. године. Дипломски рад под називом “Монте Карло симулације органских полупроводника” урадио је под менторством др Игора Станковића са Института за физику у Београду. Мастер студије на истом факултету завршио је 2012. године на модулу Наноелектроника, оптоелектроника и ласерска техника. Мастер рад под називом “Атомска и електронска структура граница између кристалних домена у нафталину” урадио је на Институту за физику у Београду под менторством др Ненада Вукмировића. Исте године уписује докторске студије на модулу Наноелектроника и фотоника.

Кандидат је започео истраживачки рад на Институту за физику у Београду у Лабораторији за примену рачунара у науци почетком августа 2011. године, а запослен је од 1. новембра 2012. године. Тема истраживања његове мастер, а потом и докторске дисертације, била је испитивање атомске и електронске структуре органских полупроводника. Током својих докторских студија презентовао је своје резултате на више међународних конференција. На конференцији Европског друштва за материјале (E-MRS Spring Meeting 2014) у Лилу награђен је за најбољег младог истраживача у оквиру секције Компјутерско моделовање органских полупроводника. Докторску дисертацију под називом “Електронска својства органских полупроводника на границама домена”, урађену под руководством др Ненада Вукмировића, одбранио је 19. јануара 2017. на Електротехничком факултету у Београду. За рад на свој докторској дисертацији награђен је Студенском наградом Института за физику, која је додељена 2018. године (за 2017. годину).

Од марта 2017 до марта 2021. године кандидат је боравио на постдокторском усавршавању на Швајцарском федералном технолошком институту у Лозани (EPFL) у групи проф. Урсуле Ротлисбергер. Тема његовог постдокторског истраживања била је испитивање перовскитних материјала за примену у соларним ћелијама. Кандидат је тесно сарађивао са експерименталном групом проф. Мајкла Грецела на истом институту, као и са експерименталном групом проф. Јоакима Мајера са Макс Планк Института за испитивање чврстог стања у Штутгарту. Од марта 2021. године кандидат борави на постдокторском усавршавању на Швајцарском федералном технолошком институту у Цириху (ETHZ) у групи проф. Матјуа Луизијеа. Теме његовог другог постдокторског ангажмана су симулације меморија са променом валенце на бази оксида и испитивање нелинеарног Покелсовог ефекта у оксидима. На првој теми кандидат сарађује са експерименталним групама са ETHZ и са IBM-овог центра са истраживања у Цириху, док на другој теми сарађује са компанијом Lumiphase. Током својих постдокторских ангажмана на EPFL и ETHZ кандидат је учествовао у супервизији једне мастер дисертације и помагао приликом израде једне докторске дисертације.

Др Марко Младеновић је у својој досадашњој каријери објавио 19 радова у међународним часописима. У звање научни сарадник на Институту за физику у Београду изабран је 29.11.2017. године.

### 3. ПРЕГЛЕД НАУЧНЕ АКТИВНОСТИ

Досадашњи научно-истраживачки рад др Марка Младеновића припада области физике кондензоване материје и може се поделити у следеће 4 целине:

- симулације и прорачун електронске структуре органских полупроводника,
- симулације и прорачун електронске структуре перовскита за примену у соларним ћелијама,
- симулације меморија са променом валенце на бази оксида,
- испитивање нелинеарног Покелсовог ефекта у перовскитним оксидима.

Прва целина се односи на рад кандидата на мастер и докторској дисертацији на Институту за физику у Београду и обухвата период пре избора у претходно научно звање. Друга целина се односи на период који обухвата рад кандидата на Институту за физику након одбране докторске дисертације, као и рад током постдокторског истраживања на Швајцарском федералном технолошком институту у Лозани. Последње две целине се односе на рад кандидата на Швајцарском федералном технолошком институту у Цириху, што је започето у периоду од нешто више од годину дана пре писања овог извештаја, те је рад на овим темама још увек у почетној фази.

#### 3.1. Симулације и прорачун електронске структуре органских полупроводника

Кандидат је започео свој научно-истраживачки рад на Институту за физику у Београду у Лабораторији за примену рачунара у науци 2011. године. Током израде свог мастер рада и докторске дисертације бавио се испитивањем атомске и електронске структуре органских полупроводника. Конкретније, бавио се испитивањем различитих типова граница између домена у органским полупроводницима и феномена који се дешавају на границама. Његово истраживање у овој области обухвата 4 теме:

- прорачун електронских стања на границама малих углова у поликристалним органским полупроводницима на бази малих молекула,
- испитивање утицаја термалне неуређености на електронске особине уређених конјугованих полимера,
- прорачун електронских стања на граници кристалног и аморфног домена у конјугованим полимерима и
- рачунање спонтане поларизације индуковане бочним ланцима у уређеном поли (3-хексилтиофену) (РЗНТ).

За добијање атомске структуре испитиваних система кандидат је користио Монте Карло симулације, за које је сам развио кодове. За прорачун електронске структуре користио је методе базиране на теорији функционала густине.

Кандидат се најпре бавио испитивањем електронске структуре границе између кристалних домена у органским полупроводницима на бази малих молекула. Реални органски полупроводници на бази малих молекула су поликристални, тј. садрже кристалне домене различитих оријентација. Експериментално је утврђено да граница између кристалних домена лоше утиче на особине материјала али механизам утицаја није до краја разјашњен. Као пример органских полупроводника на бази малих молекула коришћен је нафталин. На основу прорачуна електронске структуре за мале системе закључено је да на граници долази до формирања локализованих стања замки која се

налазе на паровима молекула између којих је растојање мало. Такође, утврђено је да је енергија стања корелисана са растојањем између молекула. Та корелација је коришћена за прорачун густине стања замки за велике системе.

Познато је да уређени конјуговани полимери исказују значајну неуређеност атомске структуре на собној температури. Кандидат је испитивао утицај термалне неуређености на електронске особине уређеног полимера РЗНТ. Посебно је разматран утицај неуређености бочних ланаца, главних ланаца као и кумулативни ефекат неуређености бочних и главних ланаца. Утицај је квантификован прорачуном укупне локализације носилаца, локализације на различитим ланцима и густине стања. Закључено је да неуређеност главних ланаца доводи до локализације носилаца на неколико, најчешће два ланца. Кандидат је поновио симулације на температури од 100 К, где су добијени слични резултати онима за 300 К.

Реални конјуговани полимери садрже измешане кристалне и аморфне домене. Кандидат је испитивао електронску структуру границе између кристалног и аморфног домена у РЗНТ. Поступак добијања атомске и електронске структуре је био истоветан ономе коришћеном за прорачун ефеката термалне неуређености. Кандидат је разматрао неколико типова границе: (1) оштру границу између домена, (2) границу са неуређеним доменом између кристалног и аморфног домена и (3) границу сачињену од продужених ланаца који припадају и кристалном и аморфном домену. Резултати су показали да независно од типа границе највиша електронска стања у валентној зони припадају кристалном домену и да не долази до формирања стања у енергијском процепу, нити стања која припадају и једном и другом домену.

Коначно, кандидат је испитивао ефекте спонтане поларизације у уређеном РЗНТ. Најпре је извршен прорачун спонтане поларизације у јединичној ћелији РЗНТ помоћу теорије функционала густине. Кандидат је закључио да је узрок значајне вредности спонтане поларизације дуж главног ланца несиметричан распоред бочних ланаца. Потом је кандидат израчунао спонтану поларизацију у ланцу РЗНТ на основу модела границе РЗНТ—вакуум. С обзиром да се овако добијена поларизација слагала са оном добијеном помоћу теорије функционала густине, закључено је да је могуће користити овакав модел за прорачун спонтане поларизације у већим системима. Кандидат је потом израчунао спонтану поларизацију у термално неуређеном РЗНТ на собној температури. На крају, кандидат је израчунао електронску структуру границе између кристалног и аморфног РЗНТ у случају када је граница нормална на правац главних ланаца у кристалном домену. Закључено је да због ефеката спонтане поларизације, највиша стања у валентној зони су конфинирана са једне стране кристалног домена.

На основу резултата ових истраживања кандидат је објавио следеће публикације:

- M. Mladenović, I. E. Stanković: “Monte Carlo Simulations of Crystalline Organic Semiconductors”, *SJEE* **10** (2013) 125-134
- M. Mladenović, N. Vukmirović, I. E. Stanković, “Atomic and Electronic Structure of Grain Boundaries in Crystalline Organic Semiconductors”, *Phys. Scr.* **T 157** (2013) 014061

- M. Mladenović, N. Vukmirović, I. E. Stanković, “Electronic States at Low-Angle Grain Boundaries in Polycrystalline Naphthalene”, *J. Phys. Chem. C*, **117** (2013) 15741
- M. Mladenović, N. Vukmirović, “Effects of Thermal Disorder on the Electronic Properties of Ordered Polymers”, *Phys. Chem. Chem. Phys* **16** (2014) 25950
- M. Mladenović, N. Vukmirović: “Charge Carrier Localization and Transport in Organic Semiconductors: Insights from Atomistic Multiscale Simulations”, *Adv. Funct. Mater* **25** (2015) 1915
- M. Mladenović, N. Vukmirović, “Electronic States at the Interface Between Crystalline and Amorphous Domains in Conjugated Polymers”, *J. Phys. Chem. C*, **119** (2015) 23329
- M. Mladenović, N. Vukmirović, “Spontaneous Polarization Induced by Side Chains in Ordered Poly(3-hexylthiophene)”, *J. Phys. Chem. C*, **120** (2016) 18895

### 3.2. Симулације и прорачун електронске структуре перовскитних једињења за примену у соларним ћелијама

Рад кандидата у овој области се састоји од неколико под-тема:

- симулације и прорачун електронске структуре тродимензионалних перовскитних једињења
- симулације и прорачун електронске структуре дводимензионалних перовскитних једињења
- прорачун електронске структуре границе између домена у соларној ћелији на бази перовскитних једињења.

Истраживања у овој области се односе искључиво на период након избора у претходно звање, а обављена су на Институту за физику у Београду и на Швајцарском федералном технолошком институту у Лозани.

Перовскитни материјали на бази халогених елемената (јод, бром) имају потенцијалну примену у соларним ћелијама, јер измерна ефикасност соларних ћелија на бази ових материјала износи преко 25 %, што је упоредиво са традиционалним соларним ћелијама на бази силицијума. Постоје два основна разлога зашто соларне ћелије на бази халогених перовскита нису још увек доступне на тржишту: (1) њихова нестабилност на собној температури и (2) токсичност олова који је најчешћи метални елемент у перовскитним соларним ћелијама. Да би се умањио недостатак везан за нестабилност перовскита, потребно је детаљно испитати њихово понашање на собној температури. Кандидат је свој рад у овој области започео на Институту за физику у сарадњи са др. Ненадом Вукмировићем. Тема истраживања је била испитивање ефеката термалног неуређења на електронске особине неколико перовскита на бази олова уз помоћ симулација на бази молекулске динамике. Посебно је испитиван ефекат ротације органских катјона, као и ефекат термалног неуређења целе структуре. Закључено је да је ефекат ротације органских катјона мали у поређењу са другим ефектом. Такође, утврђено је да је ефекат термалног неуређења већи у материјалима са мањом константом решетке, уз изузетке

који се могу повезати са степеном слободe ротације и translације органског катјона, као и јачине његовог диполног момента.

Током свог постдокторског истраживања на Швајцарском федералном технолошком институту у Лозани кандидат се подробније бавио проблемом нестабилности перовскита на бази халогених елемената, као и проблемом токсичности олова. У вези са другим проблемом, кандидат је испитивао електронске особне перовскита на бази мешања олова и калаја, уз помоћ теорије функционала густине. Успевши да репродукује резултате експерименталних оптичких мерења, кандидат је идентификовао два ефекта која су присутна приликом мешања олова и калаја: (1) дисторзија кристалне решетке и (2) промена јачине спин-орбитне интеракције, објаснивши тиме нелинеарну зависност енергијског процепа од количине калаја у овим једињењима. Такође, кандидат се бавио испитивањем потенцијалне примене једињења на бази сребра, бизмута и јода у соларним ћелијама, што би било решење за токсично олово. Установљено је, прорачунима на бази теорије функционала густине и апроксимације ефективне масе, да је у овим једињењима, транспорт електрона и шупљина спор у одређеним правцима кристалне решетке, што доводи до локализације носилаца на собној температури и тиме лимитирања ефикасности соларне ћелије. Коначно, у сарадњи са истраживачима из групе проф. Урсуле Ротлисбергер, бавио се и испитивањем утицаја инкорпорације других, нестандартних органских катјона, попут гуанидинијума и диметиламонијума на стабилност перовскитног једињења на бази формаидинијум-олово јодида.

Познато је да дводимензионални перовскити на бази халогених елемента исказују већу стабилност од тродимензионалних. Ипак, њихова структура као и утицај органског молекула на целокупно једињење нису довољно познати. Кандидат је учествовао у креирању оквира за теоријско испитивање ових материјала, који су у том тренутку били потпуно неиспитани. Најпре је извршено поређење теоријских резултата на бази теорије функционала густине и молекулске динамике са експерименталним резултатима у погледу структурних и електронских особина дводимензионалних перовскита. Поређење је показало веома висок степен слагања ова два приступа. Потом је кандидат применио модел на дводимензионалне перовските на бази 5-амино валеричне киселине као органског молекула. Утврђена је зависност између дубине пенетрације органског молекула у неорганску решетку и симетрије неорганске решетке, а самим тим и електронских особине перовскита. Ова зависност је касније потврђена анализом која је укључила и друге молекуле као што су адатамантил-1-метанамонијум, адамантил-амонијум, нафталин-димид и (1,4-фенилен)-диметанамонијум. Поредивши понашање адатамантил-1-метанамонијума и адамантил-амонијума као органских молекула у дводимензионалним перовскитима, кандидат је установио да краћа амино група доводи до неуређености неорганске решетке, што је потврђено експерименталним мерењима. Такође, утврђено је да неки органски молекули попут гуанина и нафталин-димида учествују директно у транспорту електрона, због демонстриране локализације електрона на овим молекулима. У последњој фази свог постдокторског ангажмана на Швајцарском федералном технолошком институту у Лозани, кандидат се бавио и дводимензионалним перовскитима на бази мешавине халогених елемената (јода и брома), показавши нестабилност једињења са 50:50 односом јода и брома, што може бити објашњење за демонстрирано разлагање овог једињења на чиста једињења брома и јода при излагању оптичкој стимулацији. Истраживања дефеката у једињењима са 50:50 односом брома и јода, која се обављају у сарадњи са експерименталном групом проф. Јоакима Мајера, још увек су у току.

Коначно, у склопу свог постдокторског ангажмана на Швајцарском федералном технолошком институту у Лозани, кандидат се бавио и испитивањем границе домена у соларној ћелији, која је често извор радијативне и нерадијативне рекомбинације носилаца. Конкретније, испитивана је граница домена између перовскитног једињења метиламонијум-олово јодида и титанијум диоксида, који служи као транспорти медијум за електроне. Прорачуном електронске структуре границе ова домена утврђено је постојање електронских стања у процепу перовскита, која потичу од хемијских веза јода са титанијум-диоксидом и од међупросторних атома јода, а која потенцијално умањују ефикасност соларне ћелије. Поред тога, испитивана је и улога ваканција атома кисеоника у титанијум-диоксиду, при чему је показана неопходност њиховог укључивања у модел границе, како би се добио реалистичан опис електронске структуре границе ова два домена. Паралелно са овим истраживањем, кандидат је, у сарадњи са експерименталном групом проф. Мајкла Грецела, испитивао дефекте на површини перовскита на бази формаидинијум-олово јодида, као и начине за њихову пасивизацију. Експериментално је показано да се инкорпорацијом комплекса на бази круне етра постиже побољшање карактеристика соларне ћелије. Кандидат је симулацијом интеракције перовскита са молекулом круне етра, уз помоћ теорије функционала густине, демонстрирао интеракцију круне на катјоном формаидинијума, што је значајно утицало на електронску структуру перовскита и делимичну пасивизацију електронских стања у енергијском процепу перовскита, насталих присуством дефекта ваканције јода. Поред улоге пасивизације дефеката на површини, комплекси круне етра и цезијума реагују са површином перовскита, испоручујући катјоне цезијума перовскитном једињењу, који потом мењају електронске особине перовскита, што су експериментална мерења показала. Кандидат је својом прорачунима испитивао утицај распореда атома цезијума у перовскитном једињењу формаидинијум-олово јодида. Такође, утврђено је да ваканције формаидинијума на површини перовскита доводе до појаве стања у енергијском процепу перовскита, што је могуће пасивизирати катјонима цезијума.

На основу резултата из ове области, кандидат је објавио следеће радове:

- M. Mladenović, N. Vukmirović: “Effects of Thermal Disorder on the Electronic Structure of Halide Perovskites: Insights from MD Simulations”, *Phys. Chem. Chem. Phys.* **20** (2018) 25693-25700
- Boziki, M. Mladenović, M. Grätzel, U. Rothlisberger: “Why Choosing the Right Partner is Important: Stabilization of Ternary  $\text{Cs}_y\text{GUA}_x\text{FA}_{(1-y-x)}\text{PbI}_3$  Perovskites”, *Phys. Chem. Chem. Phys.* **22** (2020) 20880-20890
- N. Ashari Astani, F. Jahanbakhshi, M. Mladenović, A. Q. M. Alanazi, I. Ahmadabadi, M. R. Ejtehadi, M. I. Dar, M. Grätzel, U. Rothlisberger: “Ruddlesden-Popper Phases of Methylammonium-based 2D Perovskites with 5-Ammonium Valeric Acid  $\text{AVA}_2\text{MA}_{n-1}\text{Pb}_n\text{I}_{3n+1}$  with  $n=1, 2$  and  $3$ ”, *J. Phys. Chem. Lett* **10** (2019) 3543-3549
- Alanazi, D. J. Kubicki, D. Prochowitz, E. Alharbi, M. Bouduban, F. Jahanbakhshi, M. Mladenović, J. V. Milić, F. Gioradano, D. Ren, et al “Atomic-Level Microstructure of Efficient Formamidinium-Based Perovskite Solar Cells Stabilized by 5-Ammonium Valeric Acid Iodide Revealed by Multi-Nuclear and Two-Dimensional Solid-State NMR”, *J. Amer. Chem. Soc.* **141** (2019) 17659-17669



- L. Hong, J. V. Milić, P. Ahlawat, M. Mladenović, F. Jahanbakhshi, D. J. Kubicki, D. Ren, A. Ummadasingu, Y. Li, C. Tian, et al “Guanine-Stabilized Formamidinium Lead Iodide Perovskites”, *Angewandte Chemie International Edition* **59** (2020), 4691-4697
- M. G.-Rueda, P. Ahlawat, L. Merten, F. Jahanbakhshi, M. Mladenović, A. Hinderhofer, M. I. Dar, Y. Li, A. Dučinskas, B. Carlson, et al “Formamidinium-Based Dion-Jacobson Layered Hybrid Perovskites: Structural Complexity and Optoelectronic Properties”, *Adv. Funct. Mater* (2020), 2003428
- F. Jahanbakhshi, M. Mladenović, L. Merten, M. G.-Rueda, P. Ahlawat, Y. Li, A. Hinderhoffer, M. I. Dar, W. Tress, B. Carlson, et al “Unravelling Structural and Photophysical Properties of Adamantyl-Based Layered Hybrid Perovskites”, *J. Mat. Chem. A* **8** (2020) 17732-17740
- T.-S. Su, H. Zhang, F. T. Eickemeyer, F. Jahanbakhshi, M. Mladenović, J. Li, J. V. Milić, J. H. Yum, K. Sivula, O. Ouellete et al, “Crown Ether Modulation Enables over 23% Efficient Formamidinium-based Perovskite Solar Cells”, *J. Amer. Chem. Soc* **142** (2020) 19980–19991
- M. Hope, T. Nakamura, P. Ahlawat, A. Mishra, M. Cordova, F. Jahanbakhshi, M. Mladenović, R. Runjun, B. Carlsen, D. Kubicki et al, “Nanoscale Phase Segregation in Supramolecular  $\pi$ -Templating for Hybrid Perovskite Photovoltaics from NMR Crystallography”, *J. Amer. Chem. Soc* **143** (2021), 1529–1538
- H. Zhang, F. T. Eickemeyer, Z. Zhou, M. Mladenović, F. Jahanbakhshi, O. Ouellete, A. Hinderhoffer, L. Merten, M. Hope, A. Mishra et al, “Multimodal Host–Guest Complexation for Efficient and Stable Perovskite Photovoltaics”, *Nat. Commun* **12**, (2021) 3383
- Mishra, P. Ahlawat, G. C. Fish, F. Jahanbakhshi, M. Mladenović, M. Almalki, M. A.-R. Preciado, M. C. G.-Rueda, D. J. Kubicki, P. A. Schouwink, V. Dufoulon et al, “Naphthalenediimide/Formamidinium-Based Low-Dimensional Perovskites”, *Chem. Matter* **33** (2021) 6412-6420
- F. Jahanbakhshi, M. Mladenović, M. Dankl, A. Boziki, P. Ahlawat, U. Rothlisberger “Organic Spacers in 2D Perovskites: General Trends and Structure-Property Relationships from Computational Studies”, *Helv. Chim. Acta* **104** (2021), e2000232

### 3.3. Симулације меморија са променом валенце на бази оксида

Централна тема постдокторског истраживања др Марка Младеновића на Швајцарском федералном технолошком институту у Цириху у групу проф. Матјуа Луизијеа јесу симулације меморија са променом валенце на бази оксида. Овај тип меморија је у последње време привукао пажњу истраживача због њихове потенцијалне примене у неуроморфолошким компјутерима. Принцип рада овог типа меморија се заснива на формирању проводног филамента састављеног од ваканција кисеоника у оксиду. Уколико је филамент формиран целом дужином оксида, тада се уређај налази у стању ниске отпорности, док се у случају да је филамент прекинут у једном свом делу, уређај

се налази у стању високе отпорности. Кандидат је развој модел којим се симулирају ови уређаји у 3 корака. Први корак представља рачунање активационих енергија за процесе који се дешавају у уређају, попут дифузије ваканција и јона кисеоника, као и формирања и анихилације ваканција-јон пара. Ови параметри су добијени применом теорије функционала густине. Други корак се састоји у развоју и примени кинетичког Монте Карло метода, који користећи параметре из првог корака, извршава догађаје и даје као излазни податак дистрибуцију ваканција и јона кисеоника на датој температури, при датом примењеном напону и након датог времена. Коначно, у трећем кораку се врши прорачун транспортних особина структуре добијене у другом кораку, помоћу метода неравнотежног метода на бази Гринових функција. Развијени протокол, примењен и тестиран на хафмијум оксиду успешно репродукује експериментална мерења и биће коришћен за испитивање других оксида и типова уређаја на бази промене валенце.

### 3.4. Испитивање нелинеарног Покелсовог ефекта у перовскитним оксидима

Као други правац истраживања у групи проф. Матјуа Луизијеа, др Марко Младеновић се бави испитивањем нелинеарног Покелсовог ефекта у перовскитном оксиду баријум-титан диоксиду. Кандидат је радио на овом пројекту у склопу менторства мастер студента Виржини д' Местрал. У том периоду развијен је модел за прорачун Покелсових коефицијената применом теорије пертурбације функционала густине. Док се у случају електронског дела Покелсових коефицијената добијају добри резултати применом теорије пертурбације функционала густине без укључивања ефекта термалног неуређења, за потребе прорачуна јонског дела Покелсових коефицијената потребно је укључити ефекат термалног неуређења посредством симулација на бази молекулске динамике. Развијени модел даје добре резултате у поређењу са експерименталним мерењима и биће примењен на истраживање ефекта ваканција кисеоника на Покелсове коефицијенте у баријум-титан диоксиду, као и на друге оксиде.

## 4. ЕЛЕМЕНТИ ЗА КВАЛИТАТИВНУ ОЦЕНУ НАУЧНОГ ДОПРИНОСА КАНДИДАТА

### 4.1 Квалитет научних резултата

#### 4.1.1 Научни ниво и значај резултата, утицај научних радова

Др Марко Младеновић је у свом досадашњем раду објавио 19 радова у међународним часописима са ISI листе, од којих 10 у категорији M21a, 6 у категорији M21, 1 у категорији M22, 1 у категорији M23 и 1 у категорији M24. У периоду након одлуке Научног већа о предлогу за стицање претходног научног звања, др Марко Младеновић је објавио 12 радова у међународним часописима са ISI листе од којих 9 у категорији M21a, 2 у категорији M21 и 1 у категорији M22. Као пет најзначајнијих радова током овог периода кандидата могу се узети следећи радови (број цитата на основу базе Scopus):

1. **M. Mladenović**, N. Vukmirović: "Effects of Thermal Disorder on the Electronic Structure of Halide Perovskites: Insights from MD Simulations", *Phys. Chem. Chem. Phys.* **20** (2018) 25693-25700 (DOI: 10.1039/C8CP03726D M21, IF = **4.123**, број цитата: **12**)

2. N. Ashari Astani, F. Jahanbakhshi, **M. Mladenović**, A. Q. M. Alanazi, I. Ahmadabadi, M. R. Ejtehadi, M. I. Dar, M. Grätzel, U. Rothlisberger: "Ruddlesden-Popper Phases of Methylammonium-based 2D Perovskites with 5-Ammonium Valeric Acid  $AVA_2MA_{n-1}Pb_nI_{3n+1}$  with  $n=1, 2$  and  $3$ ", *J. Phys. Chem. Lett* **10** (2019) 3543-3549 (DOI: 10.1021/acs.jpcllett.9b01111 M21a, IF = **8.709**, број цитата: **27**)
3. F. Jahanbakhshi, **M. Mladenović**, L. Merten, M. G.-Rueda, P. Ahlawat, Y. Li, A. Hinderhoffer, M. I. Dar, W. Tress, B. Carlson, et al, "Unravelling Structural and Photophysical Properties of Adamantyl-based Layered Hybrid Perovskites", *J. Mat. Chem. A* **8** (2020) 17732-17740 ( DOI: 10.1039/D0TA05022A M21a, IF = **12.732**, број цитата: **6**)
4. T.-S. Su, H. Zhang, F. T. Eickemeyer, F. Jahanbakhshi, **M. Mladenović**, J. Li, J. V. Milić, J. H. Yum, K. Sivula, O. Ouellete et al, "Crown Ether Modulation Enables over 23% Efficient Formamidiniumbased Perovskite Solar Cells", *J. Amer. Chem. Soc* **142** 47 (2020) 19980–19991 (DOI: 10.1021/jacs.0c08592 M21a, IF = **15.419**, број цитата: **51**)
5. H. Zhang, F. T. Eickemeyer, Z. Zhou, **M. Mladenović**, F. Jahanbakhshi, O. Ouellete, A. Hinderhoffer, L. Merten, M. Hope, A. Mishra et al, "Multimodal Host–Guest Complexation for Efficient and Stable Perovskite Photovoltaics", *Nat. Commun* **12**, (2021) 3383 (DOI: 10.1038/s41467-021-23566-2 M21a, IF = **14.919**, број цитата: **9**)

Први наведени рад је обављен у целости на Институту за физику у Београду. Тема рада је испитивање ефекта термалног неуређења перовскита на његове електронске особине. Кандидат је самостално одабрао метод прорачуна, као и избор једињења која су узета у анализу, извршио симулације на бази молекулске динамике, израчунао стандардну девијацију енергијског процепца у случајевима ротације органског катјона као и неуређења целе структуре. Такође је учествовао у дискусији и интерпретацији резултата заједно са др. Ненадом Вукмировићем. Рад је дао значајан допринос разумевању ефекта термалне неуређености на електронске особине перовскита, издвојивши ефекат неуређености органског катјона, који до тада није био испитан, и устврдивши корелацију између јачине ефекта термалне неуређености и константе решетке перовскита.

Преостали радови су урађени на Швајцарском федералном технолошком институту у Лозани, у групи проф. Урсуле Ротлисбергер, у сарадњи са другим истраживачима из поменуте групе, као и са експерименталним групама. Кандидат је тесно сарађивао са истраживачем на докторским студијама Фарзана Јаханбакши, којој је помагао у изради докторске дисертације. Приликом израде другог наведеног рада, кандидат је имао значајну улогу у одабиру метода, активно је учествовао је у прорачунима, и имао одлучујућу улогу у интерпретацији резултата. Тема овог рада су структурне и електронске особине дводимензионалних перовскита на бази 5-амино валеричне киселине. Наведених рад је један од првих теоријских радова у области дводимензионалних перовскита на бази халогених елемената. Посебно треба издвојити значај резултата који се односи на корелацију дубине пенетрације органског молекула у неорганску решетку и симетрију решетке, који то дата није био довољно истакнут.

У склопу трећег наведеног рада кандидат је имао значајну улогу у одабиру метода, извршио је самостално велики део прорачуна и имао одлучујућу улогу у интерпретацији резултата. Рад се бави испитивањем комплексне структуре дводимензионалних перовскита на бази адамантила као органског молекула. Симулације на бази молекулске

диманике које је кандидат применио дале су значајан допринос разумевању овог феномена, са посебним освртом на резултат којим се показује да дужина амино групе молекула утиче на неуређеност неорганске решетке.

Радови под бројем 4. и 5. дали су велики допринос области соларних ћелија на бази перовскита јер предлажу до тада непознат метод за пасивизирање дефеката на површини перовскита и тиме повећање ефикасности соларне ћелије. У оба случаја кандидат је концептуализовао теоријски део истраживања, извршио већи део прорачуна и имао одлучујућу улогу у интерпретацији резултата. У раду 4. кандидат је својим симулацијама демонстрирао интеракцију круне етра са површином перовскита, што је поткрепљено прорачуном утицаја ове интеракције на електронске особине перовскита. У раду 5. теоријским прорачунима кандидата демонстриран је утицај ваканција формамидинијума на површини перовскита на његову електронску структуру, као и ефекат инкорпорације атома цезијума. Поред тога, дат је значајан допринос разумевању утицаја цезијума на електронске особине перовскита на бази формамидинијум-олово јодида.

#### 4.1.2 Позитивна цитираност научних радова кандидата

Подаци о цитирању свих радова кандидата на дан 01. 05. 2022. су сумирани у наредној табели:

База података	Број цитата	Број цитата без самоцитата	h-index
Scopus	330	298	10
Web of Science	321	289	10

Радови кандидата су цитирани у водећим часописима, попут *Science*, *Nature Chemistry*, *Journal of the Americal Chemical Society* и многим другим.

#### 4.1.3 Параметри квалитета часописа

Процена квалитета часописа у којима је кандидат објављивао се може учинити на основу импакт фактора. Импакт фактор (ИФ) се мења из године у годину, па ниже наводимо најбољу вредност из периода до две године уназад од када је рад објављен. Подвученим се означава број радова након одлуке Научног већа о предлогу за стицање претходног научног звања.

1. 3 рада (0+3) у часопису *Journal of the Americal Chemical Society* (категорија M21a) (ИФ: 1. рад 14.695, 2. рад 15.419, 3. рад 15.419)
2. 2 рада (1+1) у часопису *Advanced Functional Materials* (категорија M21a) (ИФ: 1. рад 11.382, 2. рад 18.808)
3. 1 рад (0+1) у часопису *Journal of Physical Chemistry Letters* (категорија M21a) (ИФ: 1. рад 8.709)
4. 1 рад (0+1) у часопису *Angewandte Chemie International Edition* (категорија M21a) (ИФ: 1. рад 15.336)
5. 1 рад (0+1) у часопису *Journal of Materials Chemistry A* (категорија M21a) (ИФ: 1. рад 12.732)
6. 1 рад (0+1) у часопису *Nature Communications* (категорија M21a) (ИФ: 1. рад 14.919)

7. 1 рад (0+1) у часопису *Chemistry of Materials* (категорија M21a) (ИФ: 1 рад 9.811)
8. 3 рада (3+0) у часопису *Journal of Physical Chemistry C* (категорија M21) (ИФ: 1 рад 4.835, 2. рад 4.509, 3. рад 4.509)
9. 3 рада (1+2) у часопису *Physical Chemistry Chemical Physics* (категорија M21) (ИФ: 1. рад 4.493, 2. рад 4.123, 3. рад 3.676)
10. 1 рад (0+1) у часопису *Helvetica Chimica Acta* (категорија M22) (ИФ: 1 рад 2.309)
11. 1 рад (1+0) у часопису *Physica Scripta* (категорија M23) (ИФ: 1 рад 1.126)
12. 1 рад (1+0) у часопису *Serbian Journal of Electrical Engineering* (категорија M24) (ИФ: -)

Укупан фактор утицаја радова кандидата је 166.810, а у периоду након одлуке Научног већа о предлогу за стицање претходног научног звања тај фактор је 135.956.

Часописи *Journal of American Chemical Society* и *Advanced Functional Materials* су нарочито цењени у области истраживања кандидата.

Додатни библиометријски показатељи у вези са објављеним радовима кандидата након одлуке Научног већа о предлогу за стицање претходног научног звања дати су у доњој табели. Она садржи импакт факторе (ИФ) радова, М бодове радова по српској категоризацији научноистраживачких резултата, као и импакт фактор нормализован по импакту цитирајућег чланка (СНИП) (користимо најбољу вредност из периода до две године уназад од објаве рада). У табели су дате укупне вредности, као и вредности свих фактора усредњених по броју чланака и по броју аутора по чланку, за радове објављене у категоријама

	ИФ	М	СНИП
Укупно	135.956	111	23.27
Усредњено по чланку	11.323	9.25	1.94
Усредњено по аутору	9.899	11.747	1.96

#### 4.1.4 Степен самосталности и степен учешћа у реализацији радова у научним центрима у земљи и иностранству

У току свог досадашњег научно-истраживачког рада кандидат је објавио 8 радова као први аутор и један рад на коме је коаутор са једнаким учешћем као и први аутор. На осталих 10 радова, кандидат је коаутор.

Кандидат је показао висок степен самосталности у току израде свих објављених радова. Све прорачуне везане са радове обављене на Институту за физику у Београду кандидат је извршио самостално, а у великој мери је и допринео и интерпретацији резултата. У току свог рада на Швајцарском федералном технолошком институту у Лозани, кандидат је често предлагао метод и правац истраживања и у великом мери учествовао у прорачунима и интерпретацији добијених резултата.

#### **4.1.5 Награде**

Кандидат је добитник Студентске награде Института за физику у Београду 2018. године (за 2017. годину) за најбољу докторску дисертацију урађену током претходне године.

Прилог: извештај комисије за доделу Студентске награде Института за физику у Београду 2018. год.

#### **4.2 Ангажованост у формирању научних кадрова**

Током свог ангажмана на Швајцарском федералном технолошком институту у Лозани, кандидат је помагао изради докторске дисертације Фарзана Јахамбакши.

Прилог: захвалница докторске тезе Фарзана Јахамбакши.

Током свог ангажмана на Швајцарском федералном технолошком институту у Цириху, кандидат је био ментор мастер рада Виржини д'Местрал.

Напомена: Мастер рад Виржини д'Местрал није јавно доступан, па тренутно није могуће приложити доказ о менторству.

Такође, кандидат је руководио пројектним задацима студената са основних и мастер студија на Швајцарском федералном технолошком институту у Лозани и на Швајцарском федералном технолошком институту у Цириху.

#### **4.3 Нормирање броја коауторских радова, патената и техничких решења**

Након претходног избора у звање, кандидат је објавио укупно 12 радова. Од тога 9 радова је урађено у сарадњи са другим експерименталним групама, па се наведени радови признају са са пуним бројем М бодова до седам коаутора. Преостала 3 рада спадају у категорију радова са нумеричким симулацијама, који се признају са пуним бројем М бодова до пет коаутора.

Број М бодова које је кандидат остварио након одлуке Научног већа о предлогу за стицање претходног научног звања је 111, а након нормализације са бројем коаутора тај број постаје 48.343. Нормирање утиче значајно на број бодова због великог броја аутора на већини радова, а које су последице широке интердисциплинарности истраживања на којима је кандидат радио. Треба напоменути да кандидат и након нормирања има већи број бодова од потребног за сваку категорију.

#### **4.4 Руковођење пројектима, потпројектима и пројектним задацима**

У току свог ангажмана на Институту за физику у Београду, кандидат је учествовао на следећим пројектима:

- пројекат Министарства просвете, науке и технолошког развоја Републике Србије ОН171017 “Моделирање и нумеричке симулације сложених вишечестичних система” (новембар 2012-јун 2017),
- ФП7 пројекат Европске комисије “Електронски транспорт у органским материјалима” (август 2011-јул 2015),

- Пројекат “High-Performance Computing Infrastructure for South East Europe's Research Communities” (HP-SEE), коришћење компјутерских ресурса на суперкомпјутеру у Сегедину (новембар 2013 - јул 2014).

У оквиру ОН171017 пројекта, кандидат је руководио пројектним задатком: ”Испитивање ефекта термалног неуређења на електронске особине перовскита на бази халогених елемената”.

У току свог ангажмана на Швајцарском федералном технолошком институту у Лозани, кандидат је био ангажован на следећим пројектима:

- пројекат Швајцарске националне научне фондације “NCCR MARVEL- Materials’ Revolution: Computational Design and Discovery of Novel Materials” (март 2017-април 2018),
- пројекат Швајцарске националне научне фондације “NCCR MUST - Molecular Ultrafast Science and Technology” (април 2018-јул 2018),
- пројекат Швајцарске националне научне фондације “EPISODE: Engineering of advanced hybrid Perovskite for Integration with Silicon photovoltaic Optoelectronic DEvice ” (јул 2018 - јул 2020).

У току свог ангажмана на Швајцарском федералном технолошком институту у Цириху, кандидат је био ангажован на следећем пројекту:

- пројекат Швајцарске националне научне фондације “Advanced Learning Methods on dedicated nano-Devices” (март 2021 - март 2022).

#### **4.5 Активност у научним и научно-стручним друштвима**

Др Марко Младеновић је био члан Швајцарског хемичарског друштва од марта 2017. до марта 2021. године.

Кандидат је рецензирао један рад у часопису *Physical Chemistry Chemical Physics*.

Прилог: копија позива на рецензију од стране уредништва часописа.

#### **4.6 Утицајност научних резултата**

Утицајност научних резултата кандидата је наведена у одељцима **3** и **4.1** овог документа. Пун списак радова је дат у одељку **6**, а подаци о цитираности са интернет странице базе Scopus и Web of Scienese су дати након списка свих радова кандидата.

#### **4.7 Конкретан допринос кандидата у реализацији радова у научним центрима у земљи и иностранству**

Већина радова објављена након избора у претходно научно звање је уређена на Швајцарском федералном технолошком институту у Лозани у сарадњи са експерименталним групама, углавном из Швајцарске, али и из других земаља. Један рад је урађен на Институту за физику у Београду у сарадњи са др. Ненадом Вукмировићем.

Кандидат је дао значајан допринос свим објављеним радовима. Често је предлагао метод и правац истраживања и учествовао је у прорачунима и интерпретацији резултата. Конкретни доприноси кандидата најистакнутијим радовима након избора у претходно звање дати су у одељку **4.1.1.**

#### 4.8 Уводна предавања на конференцијама и друга предавања

Након покретања поступка за избор у претходно звање на седници Научног већа Института за физику у Београду, др Марко Младеновић је одржао једно предавање по позиву:

- М. Младеновић, Н. Вукмировић, “Electronic Properties of interfaces Between Domains in Organic Semiconductors” *Book of Abstracts, 6<sup>th</sup> International School and Conference on Phononics 28 August – 1 September 2017, p. 43, Belgrade, Serbia (2017)*

Прилог: распоред конференције и позивно писмо организатора

### 5. ЕЛЕМЕНТИ ЗА КВАНТИТАТИВНУ ОЦЕНУ НАУЧНОГ ДОПРИНОСА КАНДИДАТА

**Остварени резултати у периоду након одлуке Научног већа о предлогу за стицање претходног научног звања:**

Категорија	М бодова по раду	Број радова	Укупно М бодова	Нормирани број М бодова
M21a	10	9	90	28.176
M21	8	2	16	16.000
M22	5	1	5	4.167
M32	1.5	1	1.5	1.5
M34	0.5	6	3	3

**Поређење са минималним квантитативним условима за избор у звање виши научни сарадник:**

Минимални број М бодова	Остварено М бодова, без нормирања	Остварено М бодова, са нормирањем
Укупно	50	115.5
M10+M20+M31+M32+M33+M41+M42+M90	40	115.5
M11+M12+M21+M22+M23	30	111

Према бази података Scopus (Web of Science) на дан 01. маја 2022. године, радови кандидата су цитирани укупно 330 (321) пута, односно 298 (289) пута не рачунајући самоцитате. Према обе базе, Хиршов индекс кандидата је 10.

### 6. СПИСАК РАДОВА ДР МАРКА МЛАДЕНОВИЋА

#### 6.1 Радови у међународним часописима изузетних вредности (M21a)

*Радови објављени након претходног избора у звање*



- N. Ashari Astani, F. Jahanbakhshi, M. Mladenović, A. Q. M. Alanazi, I. Ahmadabadi, M. R. Ejtehad, M. I. Dar, M. Grätzel, U. Rothlisberger: “Ruddlesden-Popper Phases of Methylammonium-based 2D Perovskites with 5-Ammonium Valeric Acid  $AVA_2MA_n-1Pb_nI_{3n+1}$  with  $n=1, 2$  and  $3$ ”, *J. Phys. Chem. Lett* **10** (2019) 3543-3549
- Alanazi, D. J. Kubicki, D. Prochowicz, E. Alharbi, M. Bouduban, F. Jahanbakhshi, M. Mladenović, J. V. Milić, F. Gioradano, D. Ren, et al “Atomic-Level Microstructure of Efficient Formamidinium-Based Perovskite Solar Cells Stabilized by 5-Ammonium Valeric Acid Iodide Revealed by Multi-Nuclear and Two-Dimensional Solid-State NMR”, *J. Amer. Chem. Soc.* **141** (2019) 17659-17669
- L. Hong, J. V. Milić, P. Ahlawat, M. Mladenović, F. Jahanbakhshi, D. J. Kubicki, D. Ren, A. Ummadasingu, Y. Li, C. Tian, et al “Guanine-Stabilized Formamidinium Lead Iodide Perovskites”, *Angewandte Chemie International Edition* **59** (2020), 4691-4697
- M. G.-Rueda, P. Ahlawat, L. Merten, F. Jahanbakhshi, M. Mladenović, A. Hinderhofer, M. I. Dar, Y. Li, A. Dučinskas, B. Carlson, et al “Formamidinium-Based Dion-Jacobson Layered Hybrid Perovskites: Structural Complexity and Optoelectronic Properties”, *Adv. Funct. Mater* (2020), 2003428
- F. Jahanbakhshi, M. Mladenović, L. Merten, M. G.-Rueda, P. Ahlawat, Y. Li, A. Hinderhoffer, M. I. Dar, W. Tress, B. Carlson, et al “Unravelling Structural and Photophysical Properties of Adamantyl-Based Layered Hybrid Perovskites”, *J. Mat. Chem. A* **8** (2020) 17732-17740
- T.-S. Su, H. Zhang, F. T. Eickemeyer, F. Jahanbakhshi, M. Mladenović, J. Li, J. V. Milić, J. H. Yum, K. Sivula, O. Ouellete et al, “Crown Ether Modulation Enables over 23% Efficient Formamidinium-based Perovskite Solar Cells”, *J. Amer. Chem. Soc* **142** (2020) 19980–19991
- M. Hope, T. Nakamura, P. Ahlawat, A. Mishra, M. Cordova, F. Jahanbakhshi, M. Mladenović, R. Runjun, B. Carlsen, D. Kubicki et al, “Nanoscale Phase Segregation in Supramolecular  $\pi$ -Templating for Hybrid Perovskite Photovoltaics from NMR Crystallography”, *J. Amer. Chem. Soc* **143** (2021), 1529–1538
- H. Zhang, F. T. Eickemeyer, Z. Zhou, M. Mladenović, F. Jahanbakhshi, O. Ouellete, A. Hinderhoffer, L. Merten, M. Hope, A. Mishra et al, “Multimodal Host–Guest Complexation for Efficient and Stable Perovskite Photovoltaics”, *Nat. Commun* **12**, (2021) 3383
- Mishra, P. Ahlawat, G. C. Fish, F. Jahanbakhshi, M. Mladenović, M. Almalki, M. A.-R. Preciado, M. C. G.-Rueda, D. J. Kubicki, P. A. Schouwink, V. Dufoulon et al, “Naphthalenediimide/Formamidinium-Based Low-Dimensional Perovskites”, *Chem. Matter* **33** (2021) 6412-6420

*Радови објављени пре претходног избора у звање*

- M. Mladenović, N. Vukmirović: “Charge Carrier Localization and Transport in Organic Semiconductors: Insights from Atomistic Multiscale Simulations”, *Adv. Funct. Mater* **25** (2015) 1915

## 6.2 Радови у врхунским међународним часописима (M21)

*Радови објављени након претходног избора у звање*

- M. Mladenović, N. Vukmirović: “Effects of Thermal Disorder on the Electronic Structure of Halide Perovskites: Insights from MD Simulations”, *Phys. Chem. Chem. Phys.* **20** (2018) 25693-25700
- Boziki, M. Mladenović, M. Grätzel, U. Rothlisberger: “Why Choosing the Right Partner is Important: Stabilization of Ternary  $\text{Cs}_y\text{GUA}_x\text{FA}_{(1-y-x)}\text{PbI}_3$  Perovskites”, *Phys. Chem. Chem. Phys.* **22** (2020) 20880-20890

*Радови објављени пре претходног избора у звање*

- M. Mladenović, N. Vukmirović, I. E. Stanković, “Electronic States at Low-Angle Grain Boundaries in Polycrystalline Naphthalene”, *J. Phys. Chem. C*, **117** (2013) 15741
- M. Mladenović, N. Vukmirović, “Effects of Thermal Disorder on the Electronic Properties of Ordered Polymers”, *Phys. Chem. Chem. Phys.* **16** (2014) 25950
- M. Mladenović, N. Vukmirović, “Electronic States at the Interface Between Crystalline and Amorphous Domains in Conjugated Polymers”, *J. Phys. Chem. C*, **119** (2015) 23329
- M. Mladenović, N. Vukmirović, “Spontaneous Polarization Induced by Side Chains in Ordered Poly(3-hexylthiophene)”, *J. Phys. Chem. C*, **120** (2016) 18895

## 6.3 Радови у међународним часописима (M22)

*Радови објављени након претходног избора у звање*

- F. Jahanbakhshi, M. Mladenović, M. Dankl, A. Boziki, P. Ahlawat, U. Rothlisberger “Organic Spacers in 2D Perovskites: General Trends and Structure-Property Relationships from Computational Studies”, *Helv. Chim. Acta* **104** (2021), e2000232

## 6.4 Радови у међународним часописима (M23)

*Радови објављени пре претходног избора у звање*

- M. Mladenović, N. Vukmirović, I. E. Stanković, “Atomic and Electronic Structure of Grain Boundaries in Crystalline Organic Semiconductors”, *Phys. Scr.* **T 157** (2013) 014061

## 6.5 Радови у часописима међународног значаја верификованих посебним одлукама (M24)

*Радови објављени пре претходног избора у звање*

- M. Mladenović, I. E. Stanković: “Monte Carlo Simulations of Crystalline Organic Semiconductors”, *SJEE* **10** (2013) 125-134

## 6.6. Предавање по позиву са међународног скупа штампано у изводу (M32)

*Радови објављени након претходног избора у звање*

- M. Mladenović, N. Vukmirović, “Electronic Properties of interfaces Between Domains in Organic Semiconductors” *Book of Abstracts, 6<sup>th</sup> International School and Conference on Phononics 28 August – 1 September 2017, p. 43, Belgrade, Serbia* (2017)

## 6.7. Саопштења са међународног скупа штампана у изводу (M34)

*Радови објављени након претходног избора у звање*

- M. Mladenović, U Rothlisberger, “First-Principles Calculations of Halide Perovskites”, *10<sup>th</sup> International Conference on Hybrid and Organic Photovoltaics, 28 - 31 May 2018, Benidorm, Spain* (2018) *Session C1*
- F. Jahanbakhshi, M. Mladenović, U Rothlisberger, “Investigating the Interfacial Effects on the Performance of Perovskite Solar Cells”, *10<sup>th</sup> International Conference on Hybrid and Organic Photovoltaics, 28 - 31 May 2018, Benidorm, Spain* (2018) *Poster 277*
- M. Mladenović, U Rothlisberger, “Lead-Free Materials for Solar Cells Applications” *E-MRS 2019 Spring Meeting, 27-31 May 2019, Nice, France* (2019) *Talk G.6.3*
- F. Jahanbakhshi, M. Mladenović, N. Ashari-Astani, U Rothlisberger, “The Role of Spacer Molecules in Designing 2D Ruddlesden-Popper Perovskites”, *E-MRS 2019 Spring Meeting, 27-31 May 2019, Nice, France* (2019) *Talk G.14.5*
- A. Boziki, S. Meloni, M. Mladenović, U Rothlisberger, “Atomistic Origins of the Preferential Stabilization of Perovskite over Non-Perovskite Phases of Mixed Cation Lead Halide Perovskites”, *10th Triennial Congress of the International Society for Theoretical Chemical Physics. July 11-17, 2019. Tromsø, Norway* (2019), *Poster P2-46*
- M. Mladenović, F. Jahanbakhshi, U Rothlisberger, “Ruddlesden-Popper Phases of 2D Halide Perovskites”, *SFKM 2019 7-11 October 2019, Belgrade, Serbia* (2019) *Presentation contributed:62*

*Радови објављени пре претходног избора у звање*

- M. Mladenović, I. E. Stanković, N. Vukmirović, “Atomic and Electronic Structure of Grain Boundaries in Crystalline Organic Semiconductors” *Book of Abstracts, 3rd International conference on optical materials, 3-6 September 2012, p. 90, Belgrade, Serbia (2012)*
- M. Mladenović, N. Vukmirović, I. E. Stanković, “Simulations of Electronic States at Grain Boundaries in Poly-crystalline Naphthalene”, *DPG 2013 Conference, 10-15 March 2013, Regensburg, Germany (2013) Poster HL69.12*
- M. Mladenović, N. Vukmirović, I. E. Stanković, "Electronic Properties of Grain Boundaries in Polycrystalline Naphthalene", *E-MRS Spring Meeting, 27-31 May 2013, Strasbourg, France (2013) Poster PII-15*
- M. Mladenović, N. Vukmirović, I. E. Stanković, "Electronic States at Grain Boundaries in Polycrystalline Naphthalene", *Book of Abstracts, 6th ISFOE, 8-11 July 2013, p.14, Thessaloniki, Greece (2013)*
- M. Mladenović, N. Vukmirović, “Effects of Dynamic Disorder on the Electronic Structure of Crystalline Poly-3-hexylthiophene”, *E-MRS 2014 Spring Meeting, 25-30 May 2014, Lille, France, (2014) Presentation O. 13 5*
- N. Vukmirović, M. Mladenović, “Simulation Insights into Electronic Properties of Disordered Organic Semiconductors”, *Book of Abstracts, ICANS26, 13-18 September 2015, Aachen, Germany, p. 69 (2015)*
- M. Mladenović, N. Vukmirović, “Electronic States at the Interface Between Crystalline and Amorphous Domains in Conjugated Polymers”, *SFKM 2015, 7-11 September 2015, Belgrade, Serbia (2015) Presentation contributed:7*
- M. Mladenović, N. Vukmirović, “Electronic Properties of Interfaces Between Domains in Organic Semiconductors”, *GRC Conference: Electronic Processes in Organic Materials, 6-10 July 2016, Lucca (Barga), Italy (2016) Poster 63*

**Саопштење са скупа националног значаја штампано у целини (M63)**

*Радови објављени пре претходног избора у звање*

- M. Mladenović, I. E. Stanković, “Monte Karlo simulacije kristalnih organskih poluprovodnika”, *Zbornik radova, 56. ETRAN, 11-14 jun 2012, p.48 (2012) Zlatibor, Srbija*



Cite this: *Phys. Chem. Chem. Phys.*,  
2018, 20, 25693

# Effects of thermal disorder on the electronic structure of halide perovskites: insights from MD simulations

Marko Mladenović† and Nenad Vukmirović \*

The effects of thermal disorder on the electronic properties of organic/inorganic halide perovskites were investigated using *ab initio* molecular dynamics simulations. It was generally found that band gap variations due to effects of thermal disorder are the largest in materials with the smallest lattice constant. The factors that may lead to departure from this trend include the degree of rotational and translational motion of the organic cation and the strength of its dipole. It was found that the contribution of the flexible organic part to the band gap variations is considerably smaller than the contribution of the inorganic part of the material. The results of our simulations indicate that band gap variations in halide perovskites fall within the range exhibited in inorganic semiconductors.

Received 12th June 2018,  
Accepted 20th September 2018

DOI: 10.1039/c8cp03726d

rsc.li/pccp

## 1 Introduction

Organic/inorganic halide perovskite materials have attracted enormous attention in the last several years due to their outstanding optoelectronic properties.<sup>1,2</sup> In particular, these materials can be used as low-cost active materials in solar cells<sup>3,4</sup> with power conversion efficiencies larger than 20%.<sup>5</sup> As a consequence, there is a strong interest in understanding their electronic properties and the factors that affect them.

The chemical formula of hybrid perovskites is  $ABX_3$ , where A is the organic cation (for example  $CH_3NH_3^+$ ,  $HC(NH_2)_2^+$ ,  $NH_4^+$ ), B is the metal cation (for example  $Pb^{2+}$ ,  $Sn^{2+}$ ) and X is the halide anion ( $Cl^-$ ,  $Br^-$ ,  $I^-$ ). It is by now well established that the highest states in the valence band and lowest states in the conduction band originate from orbitals of inorganic elements.<sup>6–13</sup> On the other hand, there is a wealth of evidence that organic cations have significant rotational freedom, especially at room temperature or higher temperatures.<sup>14–35</sup> Consequently, a single material combines a flexible organic part with a more inert inorganic part.

The flexibility of organic semiconductors has a profound effect on their electronic properties. Displacements of atoms at room temperature are large enough to lead to variations of the energies of the highest occupied and lowest unoccupied states comparable to the bandwidths. This effect, termed as dynamic

or thermal disorder, often leads to localization of charge carriers, and strongly affects the electrical transport properties.<sup>36–46</sup> While it is a significant challenge to reliably calculate the charge carrier mobility in thermally disordered materials,<sup>47</sup> it is generally understood that stronger thermal disorder leads to smaller charge carrier mobility. On the other hand, in the case of inorganic semiconductors atomic displacements have a weaker effect and can be usually treated perturbatively as electron-phonon interactions.<sup>48,49</sup>

The main goal of this work is to understand the effect of thermal disorder on the electronic properties of several of the most widely used organic/inorganic halide perovskite materials. We investigate these effects using *ab initio* molecular dynamics (MD) simulations at finite temperature by tracking the evolution of the conduction and valence band edge energies as a function of time. Stronger variations of band edge energies produce a more disordered potential for charge carriers and consequently lead to smaller charge carrier mobility. To quantify this effect caused by thermal disorder using a single parameter, we calculate the standard deviation of the band gap during the evolution of the system. It is expected that larger standard deviation of the band gap will lead to slower electrical transport.

We compare the effects of different cations by keeping lead-iodide ( $PbI_3$ ) as the inorganic part and replacing the organic cation methylammonium (MA,  $CH_3NH_3^+$ ) with formamidinium (FA,  $HC(NH_2)_2^+$ ) and ammonium ( $NH_4^+$ ). Additionally, we investigate the effects of metal and halide atom substitution by replacing Pb with Sn and I with Br and Cl while keeping MA as a cation. To isolate the effects of the organic part of the material we perform two sets of simulations – in one set the atoms in the inorganic part are fixed, while in the other set all atoms are allowed to move.

Scientific Computing Laboratory, Center for the Study of Complex Systems,  
Institute of Physics Belgrade, University of Belgrade, Pregrevica 118,  
11080 Belgrade, Serbia. E-mail: nenad.vukmirovic@iph.ac.rs

† Present address: Laboratory of Computational Chemistry and Biochemistry,  
Institute of Chemical Sciences and Engineering, École Polytechnique Fédérale de  
Lausanne, CH-1015 Lausanne, Switzerland.

While *ab initio* molecular dynamics was extensively used in recent years to study the properties of perovskite materials,<sup>14,15,18,20,22–28,30,50</sup> very few of these studies have analyzed the effects of atomic motion on band edge energies and energy gap<sup>14,20,23</sup> and these studies were focused on a single or two perovskite materials. In ref. 14 the authors reported the variations of the HOMO energies of cubic MAPbI<sub>3</sub> at temperatures of 268 K and 319 K (which are below the tetragonal to cubic phase transition and represent hypothetical undercooled cubic structures) and found that the standard deviation of these variations is respectively 54 and 78 meV. In ref. 20 the authors presented the results of band gap variations for MAPbI<sub>3</sub> in three different tetragonal phases and FAPbI<sub>3</sub> in the cubic phase at a temperature of 350 K. They obtained standard deviation of the band gap in the range from 15 to 40 meV. In ref. 23, a tetragonal phase of MAPbI<sub>3</sub> at a temperature of 220 K was analyzed and a band gap standard deviation of 90 meV was obtained. Other *ab initio* MD studies were focused on different effects or properties, such as temporal behavior of the cation orientation and positions,<sup>15,18,24,25,27</sup> the phase transition between the tetragonal and cubic phase,<sup>22,28</sup> (anti)ferroelectric ordering of molecular dipoles,<sup>26,30</sup> and the effects of material degradation by water.<sup>50</sup>

In this work, we analyze the effects of thermal disorder on the electronic structure in detail for a class of organic/inorganic halide perovskite materials and establish and interpret the trends obtained with substitution of a metal atom, halide atom or organic group. We find that the variations of the band gap when all atoms are allowed to move are somewhat smaller than those in inorganic polar semiconductor GaAs and significantly larger than those in Si. Variations in the band gap are highest in perovskites with Br and Cl halide atoms and the smallest in perovskites with ammonium as an organic cation. In the case of a fixed inorganic part, the variations in the band gaps become considerably smaller. We discuss the factors responsible for such trends and the implications for material properties.

## 2 Computational methodology

To investigate the effects of thermal disorder on the electronic structure of halide perovskites, we used *ab initio* Born–Oppenheimer MD simulations. The simulations were performed using the Quantum ESPRESSO package.<sup>51,52</sup> Two sets of MD simulations were carried out: (1) simulations without any constraints for atomic positions and lattice parameters and (2) simulations where only the organic cation is allowed to move freely. Starting geometries for all investigated perovskites were  $2 \times 2 \times 2$  pseudocubic supercells, each containing 8 stoichiometric units, with lattice parameters listed in Table 1. Most of the lattice parameters are taken from ref. 53, which is the database of lattice parameters used in several theoretical studies.<sup>18,54,55</sup> Lattice parameters for the initial structure of MASnI<sub>3</sub> are taken from ref. 56. We note that a single unit cell of perovskites with an organic group is not strictly cubic since orientation of the organic cation defines a preferential direction in space and slightly distorts the cubic shape of the cell. In real materials

Table 1 Pseudocubic unit cell parameters for the initial structure of the perovskites investigated in this work

	<i>a</i> (Å)	<i>b</i> (Å)	<i>c</i> (Å)
MAPbI <sub>3</sub> <sup>53</sup>	6.29	6.27	6.30
MAPbBr <sub>3</sub> <sup>53</sup>	5.92	5.92	5.92
MAPbCl <sub>3</sub> <sup>53</sup>	5.68	5.68	5.68
MASnI <sub>3</sub> <sup>56</sup>	6.23	6.23	6.23
FAPbI <sub>3</sub> <sup>53</sup>	6.41	6.27	6.34
NH <sub>4</sub> PbI <sub>3</sub> <sup>53</sup>	6.21	6.21	6.21

different orientations of organic cations in different cells lead to a cubic structure on average. The distortion of the cubic cell is only slight in most materials, as can be seen in Table 1. Nevertheless, we refer to these cells that are used in our initial structure as pseudocubic. We used norm-conserving pseudopotentials with kinetic energy cut-off 60 Ry,  $2 \times 2 \times 2$   $\Gamma$ -point centered reciprocal points grid and local density approximation (LDA) for exchange–correlation potential. To estimate the accuracy of LDA for quantities of interest in this work, additional calculations using other levels of theory were also performed. In a set of these calculations, we used the hybrid PBE0 functional<sup>57,58</sup> with the effects of spin–orbit interaction taken into account. In another set of calculations, we included the semi-empirical DFT-D dispersion correction<sup>59</sup> in the functional.

The temperature was set to  $T = 350$  K in all simulations and it was controlled *via* velocity rescaling. This temperature was used to enable a fair comparison between the investigated materials since all investigated perovskites with MA as an organic cation exhibit a cubic structure at this temperature.<sup>2,56,60,61</sup> On the other hand, at room temperature, MAPbI<sub>3</sub> adopts a tetragonal phase.<sup>21,62</sup> For FAPbI<sub>3</sub>, both cubic<sup>18</sup> and trigonal<sup>56</sup> structures are reported, whereas for NH<sub>4</sub>PbI<sub>3</sub> there is no experimental evidence of the structure and theoretical studies assume a cubic structure.<sup>54</sup>

MD simulations consisted of a 2 ps long equilibration run followed by an 8 ps long production run. This time is larger than the time necessary for organic cation rotation which was estimated to be on the order of a picosecond.<sup>14,17,19,27,63</sup> Consequently, the organic cation can exhibit a variety of different orientations during this time and it is expected that this timescale is representative enough to reliably estimate the effects of thermal disorder. The simulations without constraints on atomic coordinates were performed at constant temperature and pressure, which implies variable cell dimensions, while simulations with fixed inorganic parts were performed at constant temperature and volume, which implies fixed cell dimensions. The time dependence of the simulated Kohn–Sham band gap of halide perovskite materials investigated in this work is presented in Fig. 1. As can be seen from the figure, for some materials the band gap exhibits strong variations during the first 2 ps of MD simulation due to system equilibration. Consequently, the first 2 ps of each MD simulation were excluded from the analysis.

Next, we discuss possible effects of limited supercell size on the results. Several previous *ab initio* MD simulations of halide perovskites<sup>14,20,64</sup> were performed using the  $2 \times 2 \times 2$  supercell

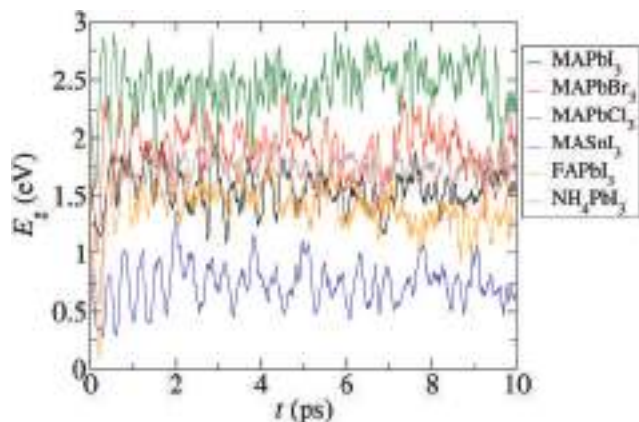


Fig. 1 Time evolution of the simulated Kohn–Sham band gap of halide perovskite materials investigated in this work.

and simulation time on the order of 10 ps, while longer simulation times and larger supercells were employed in more recent studies.<sup>15,24,26,28</sup> It was pointed out in ref. 15 that the limited supercell size may lead to a reduced decay of the dipole autocorrelation function in the case of tetragonal MAPbI<sub>3</sub> at room temperature. On the other hand, in ref. 26 nearly the same distribution of organic cation orientation was obtained in the simulations with a  $2 \times 2 \times 2$  supercell as in the simulations with  $4 \times 4 \times 4$  and  $6 \times 6 \times 6$  supercells, while the dipole autocorrelation functions are largely similar. Nearly the same dipole autocorrelation function was obtained in ref. 24 from  $2 \times 2 \times 2$  and  $4 \times 4 \times 4$  supercells for MAPbI<sub>3</sub> at a temperature of 400 K. Consequently, we choose the  $2 \times 2 \times 2$  supercell as a compromise between computational cost and accuracy. Since the main focus of our study is on comparison between similar materials, we believe that any possible systematic errors arising from limited supercell dimensions would be nearly the same in similar materials.

### 3 Results and discussion

Calculated band gaps and their standard deviations are summarized in Table 2. Band gaps and the corresponding standard deviations were calculated as average of the values obtained at different MD steps. Calculated values for the MAPbI<sub>3</sub> and FAPbI<sub>3</sub> band gaps are within the range of reported experimental values (1.5–1.6 eV for MAPbI<sub>3</sub><sup>22,65</sup> and 1.4–1.5 eV for FAPbI<sub>3</sub><sup>56,66</sup>). In the case of NH<sub>4</sub>PbI<sub>3</sub>, our band gap of 1.75 eV is higher than the

Table 2 Average values of band gaps ( $E_g$ ) and standard deviations of band gaps in MD simulation without constraints ( $\sigma(E_g)$ ) and in MD simulation with a fixed inorganic part ( $\sigma_r(E_g)$ ) for the studied perovskite materials

	$E_g$ (eV)	$\sigma(E_g)$ (eV)	$\sigma_r(E_g)$ (eV)
MAPbI <sub>3</sub>	1.54	0.15	0.079
MAPbBr <sub>3</sub>	1.90	0.19	0.059
MAPbCl <sub>3</sub>	2.47	0.19	0.079
MASnI <sub>3</sub>	0.76	0.16	0.052
FAPbI <sub>3</sub>	1.41	0.15	0.032
NH <sub>4</sub> PbI <sub>3</sub>	1.75	0.088	0.054

reported band gap of 1.13 eV calculated using the LDA functional.<sup>55</sup> This difference originates from the fact that the gap in ref. 55 was calculated for a fixed cubic structure, while in our simulation the structure becomes distorted, which, on average, decreases the antibonding overlap between the Pb and I atoms and increases the band gap. A similar observation related to the structure of NH<sub>4</sub>PbI<sub>3</sub> was reported in ref. 11. However, one should bear in mind that there is no experimental evidence of perovskite phase of NH<sub>4</sub>PbI<sub>3</sub> and we use this compound just for comparison with MAPbI<sub>3</sub> and FAPbI<sub>3</sub>. For other compounds our band gaps are lower than the experimental values (around 2.2 eV for MAPbBr<sub>3</sub>,<sup>65</sup> around 3 eV for MAPbCl<sub>3</sub>,<sup>65</sup> and around 1.3 eV for MASnI<sub>3</sub>,<sup>56</sup>) expressing the well-known problem of LDA band gap underestimation. In the case of PbI<sub>3</sub> perovskites, LDA (and other local functionals such as PBE) gives good estimates for band gaps due to the cancellation of the LDA error and the error of spin–orbit coupling effect neglect.<sup>67</sup> However, the goal of this work is to estimate the effects of thermal disorder on the electronic properties of the material and the focus was not on calculation of correct absolute values of band gaps.

To check the accuracy of LDA in quantifying the degree of variations of the band gap, we have performed electronic structure calculations for 9 snapshots from the MD trajectory, taken at  $t = 2, 3, \dots, 10$  ps, in the case of the MAPbI<sub>3</sub> and MASnI<sub>3</sub> material, using the hybrid PBE0 functional with the effects of spin–orbit interaction (PBE0 + SOC), which we used because it is known to give a rather accurate band structure of halide perovskites.<sup>68</sup> In the case of MAPbI<sub>3</sub>, the standard deviation of the band gap estimated from these snapshots is 158 meV for PBE0 + SOC calculations, while it is 138 meV for LDA calculations. For the MASnI<sub>3</sub> material, the standard deviation calculated from selected snapshots (8 snapshots taken at  $t = 3, 4, \dots, 10$  ps were selected because their standard deviation of the band gap is very similar to full production trajectory) is 174 meV in PBE0 + SOC calculation and 154 meV in LDA calculation. These results suggest that LDA gives rather similar values of standard deviations of the band gap to the more accurate functional.

Another known deficiency of local functionals such as LDA is the inability to treat dispersion interactions.<sup>69</sup> The role of dispersion interactions in organic/inorganic halide perovskites was discussed in some recent studies.<sup>70,71</sup> To assess their role when band gap variations are concerned, we have performed additional MD simulations where dispersion correction<sup>59</sup> was included in the functional. These simulations were performed for MAPbI<sub>3</sub> and FAPbI<sub>3</sub> materials which contain different organic groups and consequently significantly different dispersion interaction between the organic group and the inorganic cage. In such simulations, we find that the standard deviation of the band gap is 152 meV for MAPbI<sub>3</sub> and 167 meV for FAPbI<sub>3</sub>. Therefore, these results only slightly differ from the values obtained in the simulation based on LDA (146 meV for MAPbI<sub>3</sub> and 154 meV for FAPbI<sub>3</sub>, see Table 2), suggesting that dispersion interactions have only a minor effect on the results reported in this work. A similar conclusion was obtained also in ref. 23 where the same band gap variations of tetragonal MAPbI<sub>3</sub> were

obtained in simulations with a local functional and with a dispersion-corrected functional.

Values for standard deviations of band gaps in the case of MD simulations without any constraints are significant. They are all within the range of (0.14–0.20) eV, except for  $\text{NH}_4\text{PbI}_3$  which has a smaller standard deviation. We note that our results yield larger values than previous similar studies of  $\text{MAPbI}_3$ . This is to a large extent expected since the work in ref. 23 considered tetragonal  $\text{MAPbI}_3$  at a low temperature of 220 K, while the simulations in ref. 14 and 20 were performed with fixed Pb atoms and fixed unit cell. To compare the values that we obtained with the corresponding values in inorganic semiconductors, we also performed MD simulations of conventional inorganic semiconductors Si and GaAs. The values that we obtained for perovskites are somewhat smaller than that for inorganic polar semiconductor GaAs that has a standard deviation of the band gap of 0.30 eV, but are significantly larger than those of Si where the standard deviation is only 34 meV.

Next, we also discuss variations of individual conduction band minimum (CBM) and valence band maximum (VBM) energies. In the simulation with a fixed inorganic part (and with fixed supercell), we find for all materials that the standard deviations of the CBM and VBM are rather similar ( $\sigma_f^{\text{CBM}} \approx \sigma_f^{\text{VBM}}$ ) and that these are approximately equal to  $\sigma_f(E_g)/\sqrt{2}$ . Such results suggest that one can consider the total band gap variation  $\sigma_f(E_g)$  to be composed of equal contributions from CBM and VBM satisfying  $(\sigma_f^{\text{CBM}})^2 + (\sigma_f^{\text{VBM}})^2 = \sigma_f(E_g)^2$ . For these reasons, throughout the paper we report only the total band gap variation. On the other hand, within the current simulation setup it is not possible to check if the same relations hold in the simulation without any constraints when supercell dimensions also vary. The reason for this is that the VBM and CBM values obtained from different supercells have different reference energies.

To understand the trends in standard deviations of the band gaps among different perovskite materials, we first discuss different factors that lead to these variations. Since the highest states in the valence band and lowest states in the conduction band originate from the inorganic part, thermal disorder directly influences the band gap by modulating the transfer integrals between relevant orbitals of metal and halide atoms and consequently modulates the band gap of the material. This is the same mechanism as in inorganic semiconductors. On the other hand, organic cations create electrical potential that varies with time and consequently modulates the energies of orbitals of inorganic atoms, leading also to modulation of the band gap. The following factors influence the strength of these variations: (a) lattice constant of the material. For smaller lattice constants, the organic cation is closer to the inorganic atoms leading to stronger variations of the value of electrical potential on the inorganic atoms. (b) The strength of the organic cation dipole. Larger dipole moment of the organic cation leads to larger variations of electrical potential on the inorganic atoms. The MA cation has the largest dipole moment of 2.2 D, and the dipole moment of FA is around 0.2 D, while ammonium cation has no dipole moment.<sup>21</sup> (c) Rotational

flexibility of the organic cations. If the organic cation has more freedom to rotate, its dipole moment can be oriented in many different directions, leading to stronger variations in the potential it creates. (d) Translational motion flexibility of the organic cation. If there is enough space for the organic cation to move as a whole, its charge will create stronger variations of the potential. A quantitative measure of the factor (a) is simply the value of the lattice constant and the measure of the factor (b) is the dipole moment of the organic cation. To quantify the factor (c) we use the conformational entropy defined as

$$s = - \int_0^\pi \sin \theta \, d\theta \int_0^{2\pi} d\phi f(\theta, \phi) \ln \left[ \frac{f(\theta, \phi)}{f_0} \right]. \quad (1)$$

In eqn (1), the variables  $\theta$  and  $\phi$  denote polar and azimuthal angle that represent the direction of the orientation of the cation, while  $f(\theta, \phi)$  is the probability density describing the probability of orientation of the dipole in different directions and  $f_0 = 1 \text{ rad}^{-2}$ .  $f(\theta, \phi)$  is normalized to satisfy  $\int_0^\pi \sin \theta \, d\theta \int_0^{2\pi} d\phi f(\theta, \phi) = 1$ . To quantify the factor (d) we follow the position of the middle of the C–N bond for MA based perovskites, the position of the C atom for FA based perovskites and the position of the N atom for ammonium based materials. Then, we use mean square displacement of this position to quantify the flexibility of organic cation translational motion.

The results obtained for standard deviations of the band gap are presented in Table 2. We first discuss the results of the full simulation when there are no constraints on the lattice parameters or the motion of atoms. The overall trend is that variations tend to decrease with an increase in the lattice constant of the material, as can be seen in Fig. 2. This effect is expected since for a smaller lattice constant the influence of the organic cations on the band gap variations is stronger [the factor (a) discussed in the previous paragraph]. However, effects other than the lattice constant may lead to departures from the main trend. The most pronounced departure occurs in

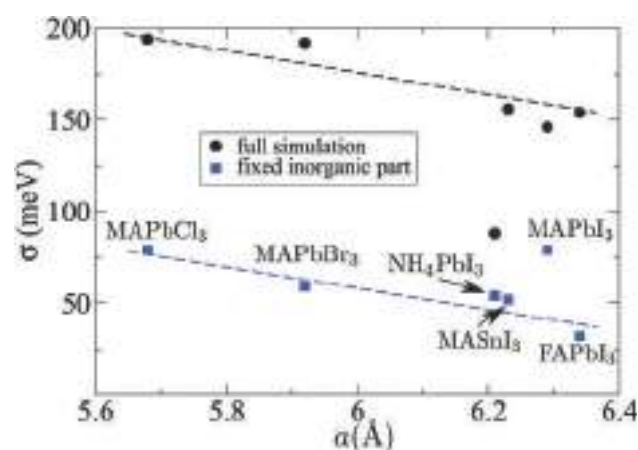
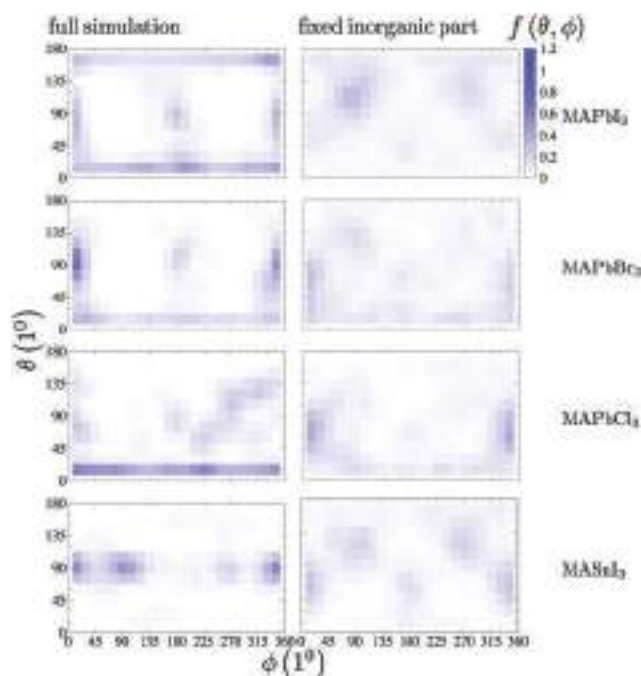


Fig. 2 Dependence of the standard deviation of the band gap on the lattice constant in the case of the simulation without any constraints (circles) and the simulation with a fixed inorganic part (squares). Dashed lines are given only as a guide to the eye.



**Table 3** Rotational entropy and mean square displacement of translational motion in MD simulation without constraints ( $s$  and  $\Delta$ ) and in MD simulation with a fixed inorganic part ( $s_f$  and  $\Delta_f$ ) for the studied perovskite materials

	$s$	$s_f$	$\Delta$ (Å)	$\Delta_f$ (Å)
MAPbI <sub>3</sub>	1.59	2.29	0.52	0.66
MAPbBr <sub>3</sub>	1.37	2.25	0.55	0.58
MAPbCl <sub>3</sub>	1.77	2.03	0.55	0.52
MASnI <sub>3</sub>	1.56	2.17	0.50	0.62
FAPbI <sub>3</sub>	1.78	2.40	0.71	0.65
NH <sub>4</sub> PbI <sub>3</sub>	N/A	N/A	0.48	1.11



**Fig. 3** The distribution of orientations of a CN vector for the studied MA-based perovskite materials in MD simulations without constraints and the simulation with a fixed inorganic part.

the case of NH<sub>4</sub>PbI<sub>3</sub>. This departure occurs due to the fact that a NH<sub>4</sub><sup>+</sup> cation has no dipole moment.

Next, we discuss the trends that arise with substitution of halide anions, metal cations or organic cations. To understand these trends we present in Table 3 the rotational entropy and the mean square displacements that quantify the degree of translational motion. In Fig. 3 we present the function  $f(\theta, \phi)$  that also quantifies the degree of rotational freedom of an MA cation.

### Halide anion substitution

In the sequence MAPbCl<sub>3</sub>, MAPbBr<sub>3</sub>, MAPbI<sub>3</sub> the effects of thermal disorder decrease (see the values of  $\sigma(E_g)$  in Table 2) and are in-line with the trend arising from the change of lattice constant. In addition, the rotational flexibility of MAPbCl<sub>3</sub> is the largest in the sequence (see the values for  $s$  in Table 3), which also suggests that it should have the largest thermal disorder. Translational motion of the organic cations is similar

in all three materials (see the values for  $\Delta$  in Table 3) and does not contribute to the differences in band gap variations.

### Metal cation substitution

MASnI<sub>3</sub> has somewhat larger variations of the band gap than MAPbI<sub>3</sub> (see the values of  $\sigma(E_g)$  in Table 2). This difference may arise from the slightly smaller lattice constant of MASnI<sub>3</sub>. On the other hand, rotational and translational motion is slightly larger in MAPbI<sub>3</sub> ( $s$  and  $\Delta$  in Table 3). Nevertheless, due to small differences in the results for the two materials, it is difficult to reliably explain them.

### Organic cation substitution

In the NH<sub>4</sub>PbI<sub>3</sub>, MAPbI<sub>3</sub>, FAPbI<sub>3</sub> sequence, the smallest effects of thermal disorder arise for NH<sub>4</sub>PbI<sub>3</sub> (see  $\sigma(E_g)$  in Table 2). The reasons for this are that NH<sub>4</sub><sup>+</sup> has no dipole moment and it has the smallest translational freedom (smallest  $\Delta$  in Table 3). On the other hand, FAPbI<sub>3</sub> has slightly larger effects of thermal disorder than MAPbI<sub>3</sub> mainly due to larger translational freedom of the organic cation (compare the values of  $\Delta$  in Table 3).

Our aim is also to understand pure effects of organic cations on the electronic properties of the material quantified by band gap variations. To this end, we performed simulations where the inorganic part is fixed. If the degree of rotational and translational freedom of the organic part in such simulations was the same as in the simulations without any constraints, then such simulations would provide information about the effect of the organic cation on the electronic properties of the material. Interestingly, we find that the conformational rotational entropy of organic cations is larger in simulations with a fixed inorganic part, as can be seen from the fact that  $s_f > s$  in Table 3 and from the more smeared dependence  $f(\theta, \phi)$  in the right part of Fig. 3. Such a result can be rationalized by taking into account that the motion of inorganic atoms can occasionally introduce barriers for organic cation rotation that are otherwise not present when inorganic atoms are fixed. As a consequence of larger rotational freedom of organic cations in simulations with fixed inorganic parts, the results of these simulations overestimate the effect of the organic cation on band gap variations in the real material. Therefore, the standard deviation of the band gap obtained from these simulations, that we discuss next, should be considered as the upper limit for the contribution of the organic cation to the band gap variation in the real material.

The trends obtained in simulations with fixed inorganic atoms can be rationalized as follows.

### Halide anion substitution

We find that in the sequence MAPbCl<sub>3</sub>, MAPbBr<sub>3</sub>, MAPbI<sub>3</sub>, the result for MAPbI<sub>3</sub> departs from the trend expected from values of the lattice constants. MAPbI<sub>3</sub> has the largest translational freedom of the organic cation (largest  $\Delta_f$ ) and somewhat larger rotational freedom (largest  $s_f$ ) than the other two materials, leading to larger band gap variations than those expected simply from the lattice constant trend.

### Metal cation substitution

MAPbI<sub>3</sub> has somewhat larger translational and rotational freedom of the organic cation (larger  $s_f$  and  $\Delta_f$ ) than MASnI<sub>3</sub>, which partially explains the larger band gap variations in MAPbI<sub>3</sub>.

### Organic cation substitution

MAPbI<sub>3</sub> has the largest band gap variations due to the largest dipole moment of the organic cation. Although the organic ammonium cation in NH<sub>4</sub>PbI<sub>3</sub> has no dipole moment, it has by far the largest translational freedom (largest  $\Delta_f$ ), which appears to be the reason for the larger band gap variations in NH<sub>4</sub>PbI<sub>3</sub> compared to FAPbI<sub>3</sub>.

Our results indicate that band gap variations in simulations with fixed inorganic atoms are significantly smaller than in simulations without constraints. Taking into account that these band gap variations actually overestimate the effect of the organic cation in the material, we can conclude that the contribution of the organic cation to thermal disorder in electronic properties is much smaller than the contribution of motion of halide and metal atoms. Consequently, to a good approximation, one can think that these materials have similar properties as inorganic semiconductors, although the effects of the organic part cannot be completely neglected. It is also important to point out that this does not mean that substitution of an organic group will lead only to a small change in band gap variations. Namely, the presence of different organic cations in the two materials leads also to different motion of the inorganic part which may also significantly contribute to differences in band gap variations.

Finally, we make some comments on the implications of the effects of thermal disorder on charge carrier mobility in the material. Relevant energy scales that should be used to compare different materials are the (conduction or valence) bandwidth and standard deviation of the band gap or the (conduction or valence) band edge. Namely, when the standard deviation of the band gap becomes comparable to the bandwidth, (dynamical) localization of carriers takes place which significantly slows down the transport. On the other hand, when the bandwidth is much larger than the standard deviation of the band gap the carriers are delocalized and carrier mobility is high. In this work, we found that standard deviation of the band gap in the investigated perovskites falls within the range exhibited in inorganic semiconductors being larger than in non-polar Si, but smaller than in polar GaAs. Band edge variations in ordered regions in organic semiconductors are also of similar order<sup>36,38</sup> as in perovskites or inorganic semiconductors. However, these three groups of semiconductors exhibit quite different charge carrier mobilities. Inorganic Si or GaAs may have mobilities even larger than  $\sim 1000 \text{ cm}^2 \text{ V}^{-1} \text{ s}^{-1}$ , while organic semiconductors rarely exhibit mobilities beyond  $\sim 1 \text{ cm}^2 \text{ V}^{-1} \text{ s}^{-1}$ . The essential difference between these two groups of materials is that bandwidths in inorganic semiconductors are much larger than band edge variations, while in organic semiconductors band edge variations are comparable to bandwidths, leading to strong effects of thermal disorder and

poor charge carrier transport. Halide perovskites exhibit bandwidths somewhat smaller or comparable to the bandwidths of inorganic semiconductors and we have established in this work that band edge variations in the investigated perovskites are comparable to those in inorganic semiconductors. As a consequence, it is expected that organic/inorganic halide perovskites should exhibit similar or somewhat smaller mobilities than inorganic semiconductors. The fact that mobilities beyond  $\sim 100 \text{ cm}^2 \text{ V}^{-1} \text{ s}^{-1}$  were observed in perovskites<sup>72</sup> is consistent with this expectation.

## 4 Conclusions

In conclusion, we investigated in detail the effects of thermal disorder on the electronic properties of organic/inorganic halide perovskite semiconductors. We find that the trend in the strength of thermal disorder can be largely rationalized by considering only the lattice constant of the material. To understand the departure from the main trend one has to take into account the strength of the dipole of the organic cation or the degree of its rotational or translational flexibility. We find that the contribution of the organic cation to band gap variations is considerably smaller than the contribution of the inorganic part. The strength of these variations, as well as the bandwidths of the material, are similar as in inorganic semiconductors, in agreement with very good charge transport properties of halide perovskites.

## Conflicts of interest

There are no conflicts to declare.

## Acknowledgements

We gratefully acknowledge the support by the Ministry of Education, Science and Technological Development of the Republic of Serbia (Project No. ON171017) and the European Commission under H2020 project VI-SEEM, Grant No. 675121, and contribution of the COST Action MP1406. Numerical computations were performed on the PARADOX supercomputing facility at the Scientific Computing Laboratory of the Institute of Physics Belgrade.

## References

- 1 J.-P. Correa-Baena, M. Saliba, T. Buonassisi, M. Grätzel, A. Abate, W. Tress and A. Hagfeldt, *Science*, 2017, **358**, 739–744.
- 2 Q. Chen, N. D. Marco, Y. M. Yang, T.-B. Song, C.-C. Chen, H. Zhao, Z. Hong, H. Zhou and Y. Yang, *Nano Today*, 2015, **10**, 355–396.
- 3 M. M. Lee, J. Teuscher, T. Miyasaka, T. N. Murakami and H. J. Snaith, *Science*, 2012, **338**, 643–647.
- 4 M. Liu, M. B. Johnston and H. J. Snaith, *Nature*, 2013, **501**, 395–398.

- 5 M. A. Green, Y. Hishikawa, E. D. Dunlop, D. H. Levi, J. Hohl-Ebinger and A. W. Ho-Baillie, *Prog. Photovoltaics*, 2018, **26**, 3–12.
- 6 W.-J. Yin, J.-H. Yang, J. Kand, Y. Yan and S.-H. Wei, *J. Mater. Chem. A*, 2015, **3**, 8926–8942.
- 7 J. Even, L. Pedesseau, C. Katan, M. Kepenekian, J.-S. Lauret, D. Saponi and E. Deleporte, *J. Phys. Chem. C*, 2015, **119**, 10161–10177.
- 8 L. D. Whalley, J. M. Frost, Y.-K. Jung and A. Walsh, *J. Chem. Phys.*, 2017, **146**, 220901.
- 9 W. Geng, L. Zhang, Y.-N. Zhang, W.-M. Lau and L.-M. Liu, *J. Phys. Chem. C*, 2014, **118**, 19565–19571.
- 10 A. Mattoni, A. Filippetti and C. Caddeo, *J. Phys.: Condens. Matter*, 2017, **29**, 043001.
- 11 S. Meloni, G. Palermo, N. Ashari-Astani, M. Grätzel and U. Rothlisberger, *J. Mater. Chem. A*, 2016, **4**, 15997–16002.
- 12 M. R. Filip and F. Giustino, *Phys. Rev. B: Condens. Matter Phys.*, 2014, **90**, 245145.
- 13 S. X. Tao, X. Cao and P. A. Bobbert, *Sci. Rep.*, 2017, **7**, 14386.
- 14 E. Mosconi, C. Quarti, T. Ivanovska, G. Ruani and F. De Angelis, *Phys. Chem. Chem. Phys.*, 2014, **16**, 16137–16144.
- 15 M. A. Carignano, A. Kachmar and J. Hutter, *J. Phys. Chem. C*, 2015, **119**, 8991–8997.
- 16 J. M. Frost, K. T. Butler and A. Walsh, *APL Mater.*, 2014, **2**, 081506.
- 17 A. Mattoni, A. Filippetti, M. I. Saba and P. Delugas, *J. Phys. Chem. C*, 2015, **119**, 17421–17428.
- 18 M. T. Weller, O. J. Weber, J. M. Frost and A. Walsh, *J. Phys. Chem. Lett.*, 2015, **6**, 3209–3212.
- 19 A. A. Bakulin, O. Selig, H. J. Bakker, Y. L. Rezus, C. Müller, T. Glaser, R. Lovrincic, Z. Sun, Z. Chen, A. Walsh, J. M. Frost and T. L. C. Jansen, *J. Phys. Chem. Lett.*, 2015, **6**, 3663–3669.
- 20 C. Quarti, E. Mosconi and F. De Angelis, *Phys. Chem. Chem. Phys.*, 2015, **17**, 9394–9409.
- 21 J. M. Frost and A. Walsh, *Acc. Chem. Res.*, 2016, **49**, 528–535.
- 22 C. Quarti, E. Mosconi, J. M. Ball, V. D’Innocenzo, C. Tao, S. Pathak, H. J. Snaith, A. Petrozza and F. De Angelis, *Energy Environ. Sci.*, 2016, **9**, 155–163.
- 23 A. L. Montero-Alejo, E. Menéndez-Proupin, D. Hidalgo-Rojas, P. Palacios, P. Wahnón and J. C. Conesa, *J. Phys. Chem. C*, 2016, **120**, 7976–7986.
- 24 J. Even, M. Carignano and C. Katan, *Nanoscale*, 2016, **8**, 6222–6236.
- 25 M. A. Carignano, Y. Saeed, S. A. Aravindh, I. S. Roqan, J. Even and C. Katan, *Phys. Chem. Chem. Phys.*, 2016, **18**, 27109–27118.
- 26 J. Lahnsteiner, G. Kresse, A. Kumar, D. D. Sarma, C. Franchini and M. Bokdam, *Phys. Rev. B*, 2016, **94**, 214114.
- 27 O. Selig, A. Sadhanala, C. Müller, R. Lovrincic, Z. Chen, Y. L. A. Rezus, J. M. Frost, T. L. C. Jansen and A. A. Bakulin, *J. Am. Chem. Soc.*, 2017, **139**, 4068–4074.
- 28 M. A. Carignano, S. A. Aravindh, I. S. Roqan, J. Even and C. Katan, *J. Phys. Chem. C*, 2017, **121**, 20729–20738.
- 29 O. Yaffe, Y. Guo, L. Z. Tan, D. A. Egger, T. Hull, C. C. Stoumpos, F. Zheng, T. F. Heinz, L. Kronik, M. G. Kanatzidis, J. S. Owen, A. M. Rappe, M. A. Pimenta and L. E. Brus, *Phys. Rev. Lett.*, 2017, **118**, 136001.
- 30 C. Goehry, G. A. Nemnes and A. Manolescu, *J. Phys. Chem. C*, 2015, **119**, 19674–19680.
- 31 J. Ma and L.-W. Wang, *Nano Lett.*, 2015, **15**, 248–253.
- 32 J. Kang and L.-W. Wang, *J. Phys. Chem. Lett.*, 2017, **8**, 3875–3880.
- 33 S. Kanno, Y. Imamura, A. Saeki and M. Hada, *J. Phys. Chem. C*, 2017, **121**, 14051–14059.
- 34 S. Kanno, Y. Imamura and M. Hada, *J. Phys. Chem. C*, 2017, **121**, 26188–26195.
- 35 T. Chen, B. J. Foley, B. Ipek, M. Tyagi, J. R. D. Copley, C. M. Brown, J. J. Choi and S.-H. Lee, *Phys. Chem. Chem. Phys.*, 2015, **17**, 31278–31286.
- 36 A. Troisi and G. Orlandi, *Phys. Rev. Lett.*, 2006, **96**, 086601.
- 37 S. Fratini and S. Ciuchi, *Phys. Rev. Lett.*, 2009, **103**, 266601.
- 38 M. Mladenović and N. Vukmirović, *Phys. Chem. Chem. Phys.*, 2014, **16**, 25950–25958.
- 39 M. Mladenović and N. Vukmirović, *Adv. Funct. Mater.*, 2015, **25**, 1915–1932.
- 40 T. Vehoff, B. Baumeier, A. Troisi and D. Andrienko, *J. Am. Chem. Soc.*, 2010, **132**, 11702–11708.
- 41 J. Böhlin, M. Linares and S. Stafström, *Phys. Rev. B: Condens. Matter Mater. Phys.*, 2011, **83**, 085209.
- 42 A. Troisi and D. L. Cheung, *J. Chem. Phys.*, 2009, **131**, 014703.
- 43 A. Troisi, *J. Chem. Phys.*, 2011, **134**, 034702.
- 44 Y. Yao, W. Si, X. Hou and C.-Q. Wu, *J. Chem. Phys.*, 2012, **136**, 234106.
- 45 D. L. Cheung, D. P. McMahon and A. Troisi, *J. Am. Chem. Soc.*, 2009, **131**, 11179–11186.
- 46 T. Liu and A. Troisi, *Adv. Funct. Mater.*, 2014, **24**, 925–933.
- 47 S. Fratini, S. Ciuchi, D. Mayou, G. T. de Laissardière and A. Troisi, *Nat. Mater.*, 2017, **16**, 998.
- 48 S. Baroni, S. de Gironcoli, A. Dal Corso and P. Giannozzi, *Rev. Mod. Phys.*, 2001, **73**, 515–562.
- 49 F. Giustino, *Rev. Mod. Phys.*, 2017, **89**, 015003.
- 50 E. Mosconi, J. M. Azpiroz and F. De Angelis, *Chem. Mater.*, 2015, **27**, 4885–4892.
- 51 P. Giannozzi, S. Baroni, N. Bonini, M. Calandra, R. Car, C. Cavazzoni, D. Ceresoli, G. L. Chiarotti, M. Cococcioni, I. Dabo, A. Dal Corso, S. de Gironcoli, S. Fabris, G. Fratesi, R. Gebauer, U. Gerstmann, C. Gougoussis, A. Kokalj, M. Lazzeri, L. Martin-Samos, N. Marzari, F. Mauri, R. Mazzarello, S. Paolini, A. Pasquarello, L. Paulatto, C. Sbraccia, S. Scandolo, G. Sclauzero, A. P. Seitsonen, A. Smogunov, P. Umari and R. M. Wentzcovitch, *J. Phys.: Condens. Matter*, 2009, **21**, 395502.
- 52 P. Giannozzi, O. Andreussi, T. Brumme, O. Bunau, M. B. Nardelli, M. Calandra, R. Car, C. Cavazzoni, D. Ceresoli, M. Cococcioni, N. Colonna, I. Carnimeo, A. D. Corso, S. de Gironcoli, P. Delugas, R. A. D. Jr, A. Ferretti, A. Floris, G. Fratesi, G. Fugallo, R. Gebauer, U. Gerstmann, F. Giustino, T. Gorni, J. Jia, M. Kawamura, H.-Y. Ko, A. Kokalj, E. Kucukbenli, M. Lazzeri, M. Marsili, N. Marzari, F. Mauri, N. L. Nguyen, H.-V. Nguyen, A. O. de-la Roza, L. Paulatto, S. Poncé, D. Rocca, R. Sabatini, B. Santra, M. Schlipf, A. P. Seitsonen, A. Smogunov, I. Timrov, T. Thonhauser, P. Umari, N. Vast, X. Wu and S. Baroni, *J. Phys.: Condens. Matter*, 2017, **29**, 465901.

- 53 <https://github.com/WMD-group/hybrid-perovskites>.
- 54 F. Brivio, A. B. Walker and A. Walsh, *APL Mater.*, 2013, **1**, 042111.
- 55 F. Brivio, K. T. Butler, A. Walsh and M. van Schilfgaarde, *Phys. Rev. B: Condens. Matter Mater. Phys.*, 2014, **89**, 155204.
- 56 C. C. Stoumpos, C. D. Malliakas and M. G. Kanatzidis, *Inorg. Chem.*, 2013, **52**, 9019–9038.
- 57 J. P. Perdew, M. Ernzerhof and K. Burke, *J. Chem. Phys.*, 1996, **105**, 9982–9985.
- 58 C. Adamo and V. Barone, *J. Chem. Phys.*, 1999, **110**, 6158–6170.
- 59 S. Grimme, *J. Comput. Chem.*, 2006, **27**, 1787–1799.
- 60 F. Chen, C. Zhu, C. Xu, P. Fan, F. Qin, A. Gowri Manohari, J. Lu, Z. Shi, Q. Xu and A. Pan, *J. Mater. Chem. C*, 2017, **5**, 7739–7745.
- 61 M. Sendner, P. K. Nayak, D. A. Egger, S. Beck, C. Muller, B. Epding, W. Kowalsky, L. Kronik, H. J. Snaith, A. Pucci and R. Lovrincic, *Mater. Horiz.*, 2016, **3**, 613–620.
- 62 M. T. Weller, O. J. Weber, P. F. Henry, A. M. Di Pumpo and T. C. Hansen, *Chem. Commun.*, 2015, **51**, 4180–4183.
- 63 R. Wasylshen, O. Knop and J. Macdonald, *Solid State Commun.*, 1985, **56**, 581–582.
- 64 G. R. Berdiyorov, A. Kachmar, F. El-Mellouhi, M. A. Carignano and M. E.-A. Madjet, *J. Phys. Chem. C*, 2016, **120**, 16259–16270.
- 65 A. M. A. Leguy, P. Azarhoosh, M. I. Alonso, M. Campoy-Quiles, O. J. Weber, J. Yao, D. Bryant, M. T. Weller, J. Nelson, A. Walsh, M. van Schilfgaarde and P. R. F. Barnes, *Nanoscale*, 2016, **8**, 6317–6327.
- 66 S. Pang, H. Hu, J. Zhang, S. Lv, Y. Yu, F. Wei, T. Qin, H. Xu, Z. Liu and G. Cui, *Chem. Mater.*, 2014, **26**, 1485–1491.
- 67 P. Umari, E. Mosconi and F. De Angelis, *Sci. Rep.*, 2014, **4**, 4467.
- 68 J. Wiktor, U. Rothlisberger and A. Pasquarello, *J. Phys. Chem. Lett.*, 2017, **8**, 5507–5512.
- 69 J. Kohanoff, *Electronic Structure Calculations for Solids and Molecules: Theory and Computational Methods*, Cambridge University Press, 2006.
- 70 C. Motta, F. El-Mellouhi, S. Kais, N. Tabet, F. Alharbi and S. Sanvito, *Nat. Commun.*, 2015, **6**, 7026.
- 71 D. A. Egger and L. Kronik, *J. Phys. Chem. Lett.*, 2014, **5**, 2728–2733.
- 72 L. M. Herz, *ACS Energy Lett.*, 2017, **2**, 1539–1548.

# Ruddlesden–Popper Phases of Methylammonium-Based Two-Dimensional Perovskites with 5-Ammonium Valeric Acid $\text{AVA}_2\text{MA}_{n-1}\text{Pb}_n\text{I}_{3n+1}$ with $n = 1, 2,$ and $3$

Negar Ashari-Astani,<sup>†,‡,§,¶</sup> Farzaneh Jahanbakhshi,<sup>‡,§,¶</sup> Marko Mladenović,<sup>‡,||</sup> Anwar Q. M. Alanazi,<sup>§</sup> Iman Ahmadabadi,<sup>†</sup> Mohammad Reza Ejtehadi,<sup>†</sup> M. Ibrahim Dar,<sup>§,¶</sup> Michael Grätzel,<sup>§,¶</sup> and Ursula Rothlisberger<sup>\*,‡,¶</sup>

<sup>†</sup>Soft Condensed Matter (SCM), Sharif University of Technology, Tehran, Iran

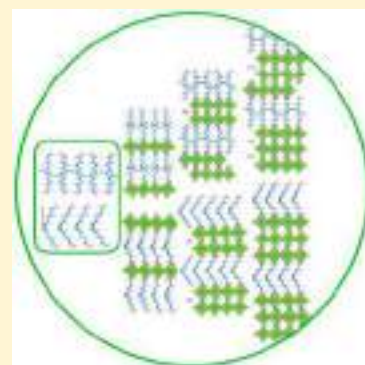
<sup>‡</sup>Laboratory of Computational Chemistry and Biochemistry (LCBC), École Polytechnique Fédérale de Lausanne (EPFL), CH-1015 Lausanne, Switzerland

<sup>§</sup>Laboratory of Photonics and Interfaces (LPI), École Polytechnique Fédérale de Lausanne (EPFL), CH-1015 Lausanne, Switzerland

<sup>||</sup>Scientific Computing Laboratory, Center for the Study of Complex Systems, Institute of Physics Belgrade, University of Belgrade, Pregrevica 118, 11080 Belgrade, Serbia

## S Supporting Information

**ABSTRACT:** 5-Ammonium valeric acid (AVA) is a frequently used additive in the preparation of lead halide perovskites. However, its microscopic role as passivating, cross-linking, or templating agent is far from clear. In this work, we provide density functional theory-based structural models for the Ruddlesden–Popper (RP) phases of  $\text{AVA}_2(\text{CH}_3\text{NH}_3)_{n-1}\text{Pb}_n\text{I}_{3n+1}$  for  $n = 1, 2,$  and  $3$  and validate with experimental data on polycrystalline samples for  $n = 1$ . The structural and electronic properties of the AVA-based RP phases are compared to the ones of other linker families. In contrast to aromatic and aliphatic spacers without additional functional groups, the RP phases of AVA are characterized by the formation of a regular and stable H-bonding network between the carbonyl head groups of adjacent AVA molecules in opposite layers. Because of these additional interactions, the penetration depth of the organic layer into the perovskite sheet is reduced with direct consequences for its crystalline phase. The possibility of forming strong interlinker hydrogen bonds may lead to an enhanced thermal stability.



In view of the rapidly rising photoconversion efficiencies of perovskite solar cells with current record values reaching >23%,<sup>1</sup> it becomes imperative to resolve some of the remaining issues concerning their long-term stability under operating conditions. One promising approach in this respect has been the use of organic additives.<sup>2,3</sup> The microscopic role of these additives is not fully understood, but it has been shown that they can act as passivating surface layers or form fully periodic layered structures (so-called two-dimensional (2D) perovskites) or mixed 2D/3D constructs with enhanced stability. In few cases, it has been possible to prepare and resolve crystals of 2D perovskites showing that they can form Ruddlesden–Popper (RP)<sup>4–6</sup>  $\text{A}_2'\text{A}_{(n-1)}\text{M}_n\text{X}_{3n+1}$  or Dion–Jacobson (DJ)<sup>7</sup>  $\text{A}''\text{A}_{(n-1)}\text{M}_n\text{X}_{3n+1}$  phases where  $\text{A}'$  and  $\text{A}$  are monovalent organic cations and  $\text{A}''$  is a divalent organic cation,  $\text{M}$  a divalent metal cation, and  $\text{X}$  a halide anion. Several RP perovskites with an organic ammonium ion  $\text{A}' = \text{RNH}_3^+$  acting as a spacer between the 3D perovskite layers with  $\text{A} = \text{MA}$  or  $\text{FA}$ ;  $\text{M} = \text{Pb}^{2+}$  or  $\text{Sn}^{2+}$ , and  $\text{X}$  representing a halide anion have been prepared. In particular, butyl ammonium (BA),<sup>8,9</sup> phenylethylammonium (PEA),<sup>10,11</sup> hexylammonium (Hex),<sup>12,13</sup> 4-ammonium butyric acid (ABA),<sup>14</sup> AVA,<sup>15–17</sup> anilinium (Anyl),<sup>18</sup> benzyl ammonium,<sup>19</sup> and a series of

polycyclic aromatic hydrocarbons<sup>20</sup> are some of the organic linkers that have been incorporated thus far. Very recently, also adamantyl-based ammonium linkers have been explored.<sup>21</sup> Despite the general agreement about the beneficial effects on either efficiency<sup>9,11</sup> and/or stability,<sup>22</sup> the molecular origin of these effects is not clear yet. The space of possible linkers is huge and has only just started to be explored. Currently, hardly any structure–function relationships exist that could establish links between the chemical nature of the organic spacers and the resulting structural and electronic properties of the 2D or even 2D/3D perovskite materials. One issue that further complicates an understanding of the microscopic roles of organic linkers is the fact that in many experiments, it is not clear what type of structures are really present. Here, we focus on a systematic investigation of the properties of fully periodic RP phases with AVA as one of the most used additives to detect characteristic signatures that can help in identifying the presence of corresponding 2D RP perovskites experimentally.

Received: April 18, 2019

Accepted: June 10, 2019

Published: June 10, 2019



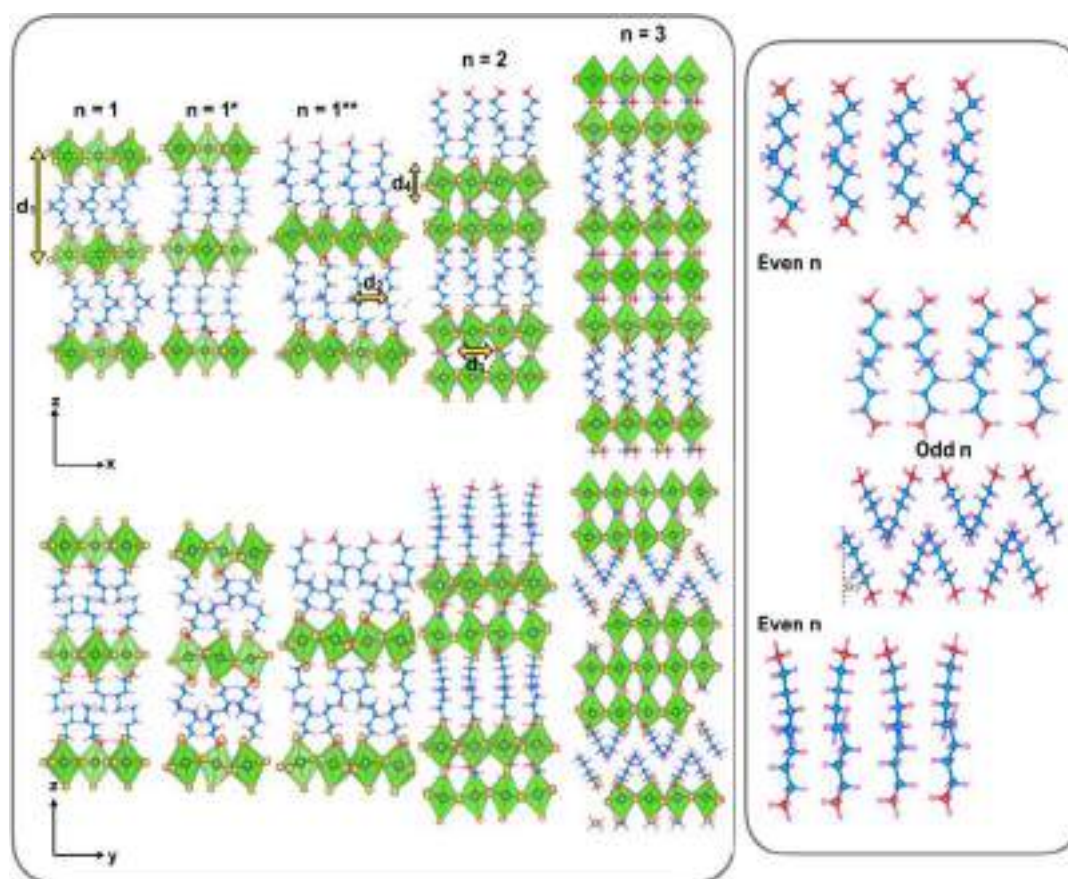


Figure 1. DFT (PBEsol)-optimized structures of  $\text{BA}_2\text{MA}_{n-1}\text{Pb}_n\text{I}_{3n+1}$  for  $n = 1, 2,$  and  $3$  viewed along the  $x$  and  $y$  axes.

Table 1. Characteristic Structural Features of  $\text{BA}_2\text{MA}_{n-1}\text{Pb}_n\text{I}_{3n+1}$  for  $n = 1, 2,$  and  $3$  Defined in the Text and in Figure 1<sup>a</sup>

$n$	$d_1$ (Å)	$d_2$ (Å)	$d_3$ (Å)	$d_4$ (Å)	$\phi_1$ (deg)	$\Theta_1$ (deg), $\Theta_2$ (deg), $\Theta_3$ (deg)	NH...I (Å)	N...Pb (Å)
1	13.2	4.5	6.4	6.3	47	–, 113.9, 113.9	3.61	2.5
	13.1	4.5	6.4	6.3	48	–, 111.1, 111.1	3.69	2.6
1*	14.0	4.3	6.3	6.4	16	–, 120.0, 120.0	3.63	2.6
	13.8	4.3	6.3	6.4	17	–, 114.5, 114.5	3.71	2.6
1**	14.7	4.3	6.3	6.4	24	–, 118.4, 118.4	3.70	2.7
2	14.2	4.4	6.3	6.4	9	$86.4 \pm 4.3, 102.2 \pm 15.1, 104.1 \pm 14.1$	3.75	2.2
	13.2	4.4	6.3	6.3	11	$89.9 \pm 16.0, 90.0 \pm 0.0, 90.0 \pm 0.0$	3.97	2.2
3	12.7	4.5	6.3	6.3	38	$89.9 \pm 1.2, 96.3 \pm 4.8, 95.9 \pm 4.7$	3.86	2.1
	13.1	4.5	6.3	6.4	40	$90.1 \pm 9.9, 90.0 \pm 1.1, 90.0 \pm 1.1$	3.92	2.1
$\infty$	–	–	6.3	6.4	–	$93.4 \pm 2.7, 117.4 \pm 1.3, 116.6 \pm 2.1$	–	–
			6.3	6.3		$91.7 \pm 0.0, 110.1 \pm 0.0, 110.1 \pm 0.0$		

<sup>a</sup>Values are averages over all corresponding distances, angles, and bonds with experimental values given in *italics*.

To this end, we use density functional theory (DFT)-based static calculations as well as molecular dynamics (MD) simulations. In particular, we predict structural models for  $n = 1, 2,$  and  $3$  and validate them with experimental data from X-ray powder diffraction (XRD). The structural and electronic properties of the AVA-based RP phases are compared to the ones of the BA family. Because AVA and BA differ only by the presence/absence of a carboxylic end group, such a comparison can be helpful in trying to establish the direct impact of H-bonding functionalities.

*RP Phases of Butylammonium-methylammonium Lead Iodide.* We first tested the accuracy of our computational approach for a system where single-crystal data on RP phases is available. In the case of  $\text{BA}_2\text{MA}_{n-1}\text{Pb}_n\text{I}_{3n+1}$ , crystal structures have been

resolved for  $n = 1, 2,$  and  $3$ .<sup>23,24</sup> For  $n = 1$ , two different structures have been determined (“1” and “1\*”). As a test, we also generated an RP structure for  $n = 1$  taking the  $n = 2$  and  $n = 3$  structures as the initial template (“1\*\*”). The DFT-optimized systems are shown in Figure 1 (full atomic coordinates and crystal lattice parameters are given in the Supporting Information) and are compared in Table 1 with the corresponding experimental data. To trace the structural changes as a function of  $n$  and compare them to the ones of the full 3D perovskite structure of  $\text{MAPbI}_3$  in the tetragonal room-temperature phase, we define a number of characteristic quantities (indicated in Figure 1). The properties of the organic layer will be characterized by  $d_1$  that measures its thickness,  $d_2$  that indicates the interspacer distance, and the

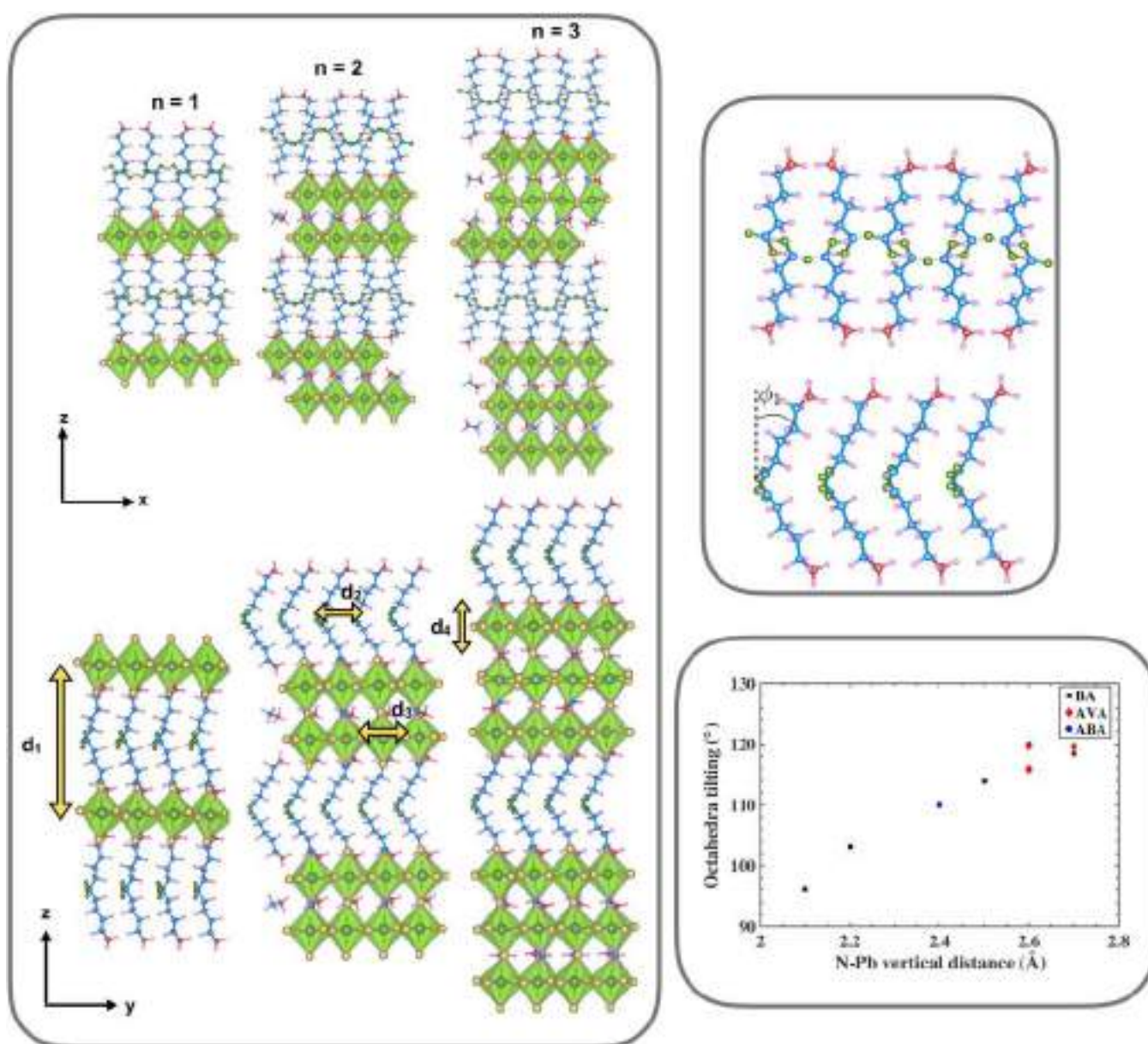


**Figure 2.** DFT (PBESol)-optimized structures for  $\text{AVA}_2 \text{MA}_{n-1} \text{Pb}_n \text{I}_{3n+1}$ , for  $n = 1, 2,$  and  $3$  viewed along the  $x$  and  $y$  axes. Correlation between penetration depth of the spacers (into the inorganic layer) and octahedral tilting is demonstrated in the lower-right inset.

tilting angle  $\phi_1$  formed by the axis defined by the average position of the carbon atoms of the organic spacer and the tetragonal axis ( $z$ ). In addition, we monitor the length of the hydrogen bonds between the hydrogen atoms of the ammonium group and the neighboring iodide ions of the perovskite layer,  $\text{NH}\dots\text{I}$ . The inorganic perovskite part, on the other hand, will be characterized by the parameters  $d_3$  and  $d_4$  (defined as the distance between iodide ions in opposing octahedra corners in the  $xy$  plane and along the tetragonal axis, respectively) as well as the angles  $\Theta_1$ – $\Theta_3$  between adjacent  $\text{PbI}_6^{4-}$  octahedra along the three crystallographic directions that characterize the distortions with respect to a cubic lattice ( $\Theta_1 = \Theta_2 = \Theta_3 = 90^\circ$ ). Table 1 shows that the PBESol-optimized structures are in overall good agreement with the available experimental data. The computationally generated structure ( $1^{**}$ ) for  $n = 1$  deduced from  $n = 2$  and  $n = 3$  shows properties similar to the ones of the crystal structure ( $1^*$ ). As a function of  $n$ , the experimental thickness of the spacer layer is

gradually decreasing from  $13.8 \text{ \AA}$  for  $n = 1^*$  to  $13.1 \text{ \AA}$  for  $n = 3$ ; this trend is even more pronounced in the fully optimized  $0 \text{ K}$  structures where the organic layer changes from  $14$  to  $15 \text{ \AA}$  at  $n = 1$  to  $12.7 \text{ \AA}$  at  $n = 3$ . Surprisingly, the tilting angle is subject to a pronounced even–odd effect (Figure 1). While  $n = 3$  shows a distinct tilting, the structure for  $n = 2$  is characterized by an almost perpendicular orientation of the organic chains with respect to the perovskite layer, and for  $n = 1$ , both structures, one with a smaller tilt around  $20^\circ$  and one with a large tilt of ca.  $50^\circ$ , exist. The rotational angle between neighboring octahedra, on the other hand, starts out with values close to the tetragonal 3D structure of MAPI with rotational angles perpendicular to the tetragonal axis around  $110$ – $120^\circ$  but reaches values resembling a fully cubic structure for  $n = 2$  and  $3$ . Surprisingly, the presence of the organic layer seems to stabilize a higher-symmetry perovskite structure. The electronic structure as a function of  $n$  shows the typical trend expected from a simple particle in a box model with a constant

Table 2. Characteristic Structural Features of  $\text{AVA}_2\text{MA}_{n-1}\text{PbI}_{3n+1}$  for  $n = 1, 2,$  and  $3$  Defined in the Text<sup>a</sup>

$n$	$d_1$ (Å)	$d_2$ (Å)	$d_3$ (Å)	$d_4$ (Å)	$\phi_1$ (deg)	$\Theta_1$ (deg), $\Theta_2$ (deg), $\Theta_3$ (deg)	NH...I (Å)	N..Pb (Å)	H..O (Å)
1	17.5	4.4	6.4	6.4	16	$-119.6 \pm 3.9, 119.6 \pm 3.9$	3.90	2.7	1.5
2	16.7	4.5	6.4	6.4	30	$94.4 \pm 2.2, 119.8 \pm 1.0, 119.7 \pm 1.1$	3.68	2.6	1.6
3	17.1	4.4	6.4	6.4	27	$92.9 \pm 8.9, 115.6 \pm 11.3, 116.2 \pm 10.2$	3.63	2.6	1.6
$\infty$	–	–	6.3	6.4	–	$93.4 \pm 2.7, 117.4 \pm 1.3, 116.6 \pm 2.1$	–	–	–
			6.3	6.3		$91.7 \pm 0.0, 110.1 \pm 0.0, 110.1 \pm 0.0$			

<sup>a</sup>Values are averages over all corresponding distances, angles and bonds with experimental values given in *italics*.

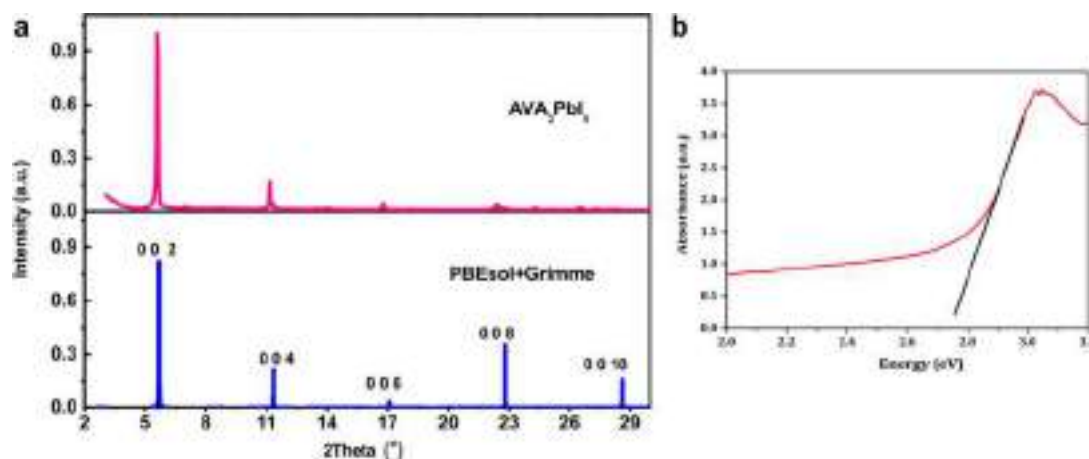


Figure 3. (a) XRD pattern of the experimental (upper panel) versus computationally (PBEsol+Grimme lower panel) predicted structure for  $n = 1$ . (b) Absorption spectrum and corresponding measured band gap of  $\text{AVA}_2\text{PbI}_4$ .

decrease of the calculated band gap from 2.8 eV (for 1 and 1\*\*) and 2.61 eV (for 1\*), 2.17 eV for  $n = 2$ , to 1.93 eV for  $n = 3$  compared to experimental values of 2.43,<sup>23</sup> 2.17,<sup>23</sup> and 2.03 eV<sup>23</sup> for  $n = 1, 2,$  and  $3$ , respectively.

**RP Phases of AVA-methylammonium Lead Iodide.** Figure 2 shows the DFT-optimized structures of  $\text{AVA}_2(\text{MA})_{(n-1)}\text{PbI}_{3n+1}$  RP perovskites for  $n = 1, 2,$  and  $3$ , and Table 2 summarizes characteristic structural features (full atomic coordinates and crystal lattice parameters are given in the Supporting Information).

To trace the structural changes as a function of  $n$  and compare them to the ones of the full 3D perovskite structure of MAPI in the tetragonal room-temperature phase, we are using the same characteristic quantities as in the case of BA (indicated in Figure 1). In addition, we also monitor the length of the interspacer hydrogen bonds (between the O..H atoms of adjacent H-bonded AVA molecules of opposite layers). As expected because of the increased molecular length, the thickness of the spacer layer is larger than in the corresponding BA-based RP phases and decreases from 17.5 Å for  $n = 1$  to 17.1 Å for  $n = 3$ . The compression is mainly caused by an increase in tilting of the organic chains from  $16^\circ$  to  $27\text{--}30^\circ$ . These more continuous trends are in contrast to the pronounced even/odd alteration found in the case of BA. In addition, in contrast to the RP phases of BA, the perovskite layer keeps its tetragonal structure with a gradual diminution of tetragonal distortion as indicated by the average angle between octahedra in the  $xy$  plane that decreases from  $120^\circ$  to  $116^\circ$  at  $n = 3$ , similar to the one observed for tetragonal 3D MAPI of  $117^\circ$ . Thus, while BA spacers seem to have a distinct templating effect forcing the structure of the perovskite layer into a more cubic phase away from the tetragonal room-temperature structure of MAPI, this effect seems entirely absent in the case of AVA. This is somewhat surprising,

because the AVA spacers possess an additional functional group to form strong intermolecular interactions. In search of the origin of this effect, we examined possible correlations between the octahedral tilting in the  $xy$  plane and the penetration depths of the organic layer (defined indirectly by the distance between the ammonium nitrogen atom and the nearest  $\text{PbI}_4$  plane, reported as N..Pb in Tables 1 and 2 for the RP phases of BA and AVA, respectively). As demonstrated in the lower-right inset of Figure 2, a strong correlation is observed between increased penetration depth and a more cubic-like inorganic framework that can be rationalized by the higher spatial demand of deeply penetrating ammonium groups and the maximum of the interoctahedral space reached for a perfectly cubic structure. It is notable that in the case of BA, the absence of interlinker H-bonds allows for a deeper penetration of the spacers into the inorganic layer, which results in a more cubic framework. In the case of AVA, all three structures from  $n = 1\text{--}3$  show a regular network of H-bonds between the carboxylic groups of oppositely oriented AVA molecules (inset Figure 2) and the penetration depth is significantly lower (indicated by an increased N..Pb distance), preserving a tetragonal structure. Each AVA monomer interacts with two other spacer molecules and the H..O bond length experiences a subtle increase from 1.5 Å ( $n = 1$ ) to 1.6 Å ( $n = 3$ ) but indicates a strong acidic hydrogen bond in all cases. Indeed, DFT-based MD simulations at room temperature also indicate that the hydrogen-bond network is well preserved (at least on the 8 ps time scale of the simulations). This strong hydrogen-bond network clearly enhances the cohesion between the two organic layers, increasing thermal stability with respect to the case of BA.

To validate the computationally predicted structural models of the 2D perovskites of AVA, the RP phase for  $n = 1$  was prepared experimentally and structurally characterized via X-



ray powder diffraction (XRD). Figure 3a shows the calculated and the experimental XRD pattern for  $\text{AVA}_2\text{PbI}_4$ . The measured spectrum is in excellent agreement with the computationally predicted structure. The peak at  $2\Theta = 5.67^\circ$  corresponds to the 002 reflection and is a measure of the thickness of the organic layer (15.6 Å) defined by the distance of Pb layers, and the corresponding experimental value (15.8 Å) corresponds to the measured low-angle peak of  $2\Theta = 5.81^\circ$ .

A similar comparison is not possible for the case of  $n = 2$  and 3 because in this case only samples containing coexisting RP phases of  $n = 2$ ,  $n = 3$ , and the 3D phase could be prepared in spite of intense efforts to synthesize pure RP phases. The measured XRD pattern as well as absorption and photoluminescence data corresponding to these mixed samples are dominated by their 3D component (Figures S4–S6) and cannot be used as a validation for the theoretically predicted RP structures. However, the superb agreement for  $n = 1$  provides confidence that the computational models for  $n = 2$  and 3 are equally realistic. Furthermore, the calculated band gap of 2.75 eV for  $\text{AVA}_2\text{PbI}_4$  is also in excellent agreement with the experimentally determined value of 2.75 eV (Figure 3b), while the predicted values for  $n = 2$  and  $n = 3$  are 2.36 and 1.99 eV, respectively, overall similar to the ones observed for BA.<sup>23</sup> Full details on electronic and transport properties are given in the Supporting Information.

In summary, on the basis of DFT calculations, we predict the structure of Ruddlesden–Popper perovskites  $\text{AVA}_2\text{MA}_{n-1}\text{Pb}_n\text{I}_{3n+1}$  with the frequently used additive 5-ammonium valeric acid for  $n = 1, 2$ , and 3 and validate the computational prediction with experimental powder diffraction and absorption data for  $n = 1$ . In contrast to the corresponding RP phases with butylammonium, no even/odd effects and no pronounced templating of the inorganic layer is observed. We demonstrate that there is a direct correlation between the penetration depth of the organic layer and the extent of tetragonal distortion of the perovskite layer; linkers with deep penetration drive structural transitions to more cubic frameworks. In spite of the rather different chemical nature of BA and AVA spacers and the differences in the structures of the RP phases, the overall electronic properties in terms of band gaps and effective masses are similar. However, the strong and persistent interspacer H-bond network may lend additional structural stability to AVA-based RP phases at finite temperatures.

## COMPUTATIONAL METHODS

For the RP phases of AVA, the inorganic frameworks of the initial structures were constructed from the crystal structures of  $(\text{BA})_2(\text{CH}_3\text{NH}_3)_{(n-1)}\text{Pb}_n\text{I}_{3n+1}$ <sup>23</sup> while the initial spacer pattern was inspired by the  $n = 2$  member of the 2D RP ABA family.<sup>14</sup> DFT calculations were carried out using the Quantum Espresso suite of codes.<sup>25</sup> Structural optimizations were performed with the Perdew–Burke–Ernzerhof (PBE)<sup>26</sup> formulation revised for solids (PBEsol).<sup>27</sup> Dispersion interactions were taken into account with the empirical D3 dispersion correction.<sup>28</sup> Band gaps were calculated with PBE<sup>29</sup> and spin–orbit coupling (SOC),<sup>30</sup> which yields values in good agreement with GW.<sup>31</sup> We used ultrasoft pseudopotentials to describe the interaction between valence electrons and ionic cores. Kohn–Sham orbitals were expanded in a plane wave basis set with a kinetic energy cutoff of 40 Ry and a cutoff of 280 Ry for the density. The Brillouin zone was sampled with different grids of  $4 \times 1 \times 4$  and  $5 \times 1 \times 5$  for  $n = 1, 2$ , and 3

tetragonal structures, respectively. These values were chosen by checking the convergence of total energy, band gaps, and atomic forces. Finite temperature simulations were performed for  $n = 3$  using Born–Oppenheimer MD. The system was first equilibrated at room temperature and heated to higher temperatures. The temperature was controlled using the velocity rescaling implemented in Quantum Espresso.<sup>25</sup> Computational XRD patterns and reflection data of our DFT-optimized crystal structures are generated using Mercury package.<sup>32</sup> More details on the computational setup may be found in the Supporting Information.

## EXPERIMENTAL METHODS

**Materials.** All materials were used as received: lead iodide ( $\text{PbI}_2$ ) (>98% purity, Alfa Aesar), methylammonium iodide (MAI) (>99% purity, Dyesol), 5-ammoniumvaleric acid hydroiodide (AVAI) (>99% purity, Dyesol), dimethylformamide (anhydrous, Across), and dimethyl sulfoxide (anhydrous, Across).

**Perovskite Film Preparation.** One molar (M)  $\text{AVA}_2\text{PbI}_4$  precursor solution is prepared by dissolving  $\text{PbI}_2$  and AVAI in a 1:2 molar ratio in a dimethylformamide (DMF) and dimethyl sulfoxide (DMSO) (4:1 v/v) solvent mixture. Similarly, MAI and  $\text{PbI}_2$  (1:1 molar ratio) were dissolved in a DMF and DMSO (4:1 v/v) solvent mixture to prepare 1 M  $\text{MAPbI}_3$  precursor solution. The  $\text{AVA}_2\text{PbI}_4$  and  $\text{MAPbI}_3$  were mixed in different ratios to prepare  $\text{AVA}_2\text{MA}_{n-1}\text{Pb}_n\text{I}_{3n+1}$  ( $n = 1, 2, \dots$ ) precursor solutions. Prior to mixing, both  $\text{AVA}_2\text{PbI}_4$  and  $\text{MAPbI}_3$  precursor solutions were heated at  $65^\circ\text{C}$  for 30 min. Finally,  $\text{MAPbI}_3$  and  $\text{AVA}_2\text{MA}_{n-1}\text{Pb}_n\text{I}_{3n+1}$  perovskite films were obtained by spin coating 50  $\mu\text{L}$  of precursor solution on the precleaned glass substrates at 3000 rpm. The resulting films were annealed at  $100^\circ\text{C}$  for 30 min. The perovskite precursor solutions were prepared inside an argon glovebox, whereas perovskite film deposition was carried out inside a dry air (humidity <2%) glovebox.

**Structural and Absorption Studies.** X-ray diffraction (XRD) data were collected on a Philips X-ray diffractometer with a graphite monochromator, using  $\text{Cu K}\alpha$  radiation. The absorption spectra of perovskite films were recorded with a UV–vis–NIR spectrophotometer (CARY-5) in transmission mode.

## ASSOCIATED CONTENT

### Supporting Information

The Supporting Information is available free of charge on the ACS Publications website at DOI: 10.1021/acs.jpcl.9b01111.

Characteristic structural features, crystal structure parameters, and atomic coordinates of  $\text{BA}_2\text{MA}_{n-1}\text{Pb}_n\text{I}_{3n+1}$  and  $\text{AVA}_2\text{MA}_{n-1}\text{Pb}_n\text{I}_{3n+1}$  for  $n = 1, 2$ , and 3 for PBEsol and PBEsol+Grimme optimized structures; frontier molecular orbitals and band structures of  $\text{AVA}_2\text{MA}_{n-1}\text{Pb}_n\text{I}_{3n+1}$  for  $n = 1, 2$ , and 3; effective masses for  $\text{BA}_2\text{MA}_{n-1}\text{Pb}_n\text{I}_{3n+1}$  and  $\text{AVA}_2\text{MA}_{n-1}\text{Pb}_n\text{I}_{3n+1}$ ; XRD pattern of  $\text{AVA}_2\text{PbI}_4$  with logarithmic scale; experimental XRD pattern and absorption and photoluminescence spectra of  $\text{AVA}_2\text{MA}_{n-1}\text{Pb}_n\text{I}_{3n+1}$  for  $n = 2$  and  $n = 3$  (mixed samples) (PDF)

## AUTHOR INFORMATION

### Corresponding Author

\*E-mail: ursula.roethlisberger@epfl.ch.

### ORCID

Farzaneh Jahanbakhshi: 0000-0001-7113-2746

M. Ibrahim Dar: 0000-0001-9489-8365

Michael Grätzel: 0000-0002-0068-0195

Ursula Rothlisberger: 0000-0002-1704-8591

### Author Contributions

#N.A.-A. and F.J. contributed equally.

### Notes

The authors declare no competing financial interest.

## ACKNOWLEDGMENTS

N.A.-A., M.R.E., and U.R. thank CODEV for two consecutive Seed Money grants. N.A.-A. thanks Iran nanotechnology innovation council (INIC) for funding. U.R. acknowledges Swiss NSF Grant No. 200020-165863, NCCR-MUST, NRP70, and the SINERGIA interdisciplinary research program EPISODE for funding. The authors thank the DIT/EPFL and the CSCS for the computer time. M.G. thanks the King Abdulaziz City for Science and Technology (KACST) for financial support. A.Q.M.A. gratefully acknowledges King Abdulaziz City for Science and Technology (KACST) for the fellowship.

## REFERENCES

- Jeon, N. J.; Na, H.; Jung, E. H.; Yang, T. -y.; Lee, Y. G.; Kim, G.; Shin, H. -w.; Seok, S. I.; Lee, J.; Seo, J. A Fluorene-Terminated Hole-Transporting Material for Highly Efficient and Stable Perovskite Solar Cells. *Nat. Energy* **2018**, *3*, 682.
- Leijtens, T.; Eperon, G. E.; Pathak, S.; Abate, A.; Lee, M. M.; Snaith, H. J. Overcoming Ultraviolet Light Instability of Sensitized TiO<sub>2</sub> with Meso-Superstructured Organometal Tri-Halide Perovskite Solar Cells. *Nat. Commun.* **2013**, *4*, 2885–2885.
- Han, Y.; Meyer, S.; Dkhissi, Y.; Weber, K.; Pringle, J. M.; Bach, U.; Spiccia, L.; Cheng, Y. -b. Degradation Observations of Encapsulated Planar CH<sub>3</sub>NH<sub>3</sub>PbI<sub>3</sub> Perovskite Solar Cells at High Temperatures and Humidity. *J. Mater. Chem. A* **2015**, *3*, 8139–8147.
- Ruddlesden, S. N.; Popper, P. New Compounds of the K<sub>2</sub>NiF<sub>4</sub> Type. *Acta Crystallogr.* **1957**, *10*, 538–539.
- Ruddlesden, S. N.; Popper, P. The Compound Sr<sub>3</sub>Ti<sub>2</sub>O<sub>7</sub> and Its Structure. *Acta Crystallogr.* **1958**, *11*, 54–55.
- Wang, Z.; Shi, Z.; Li, T.; Chen, Y.; Huang, W. Stability of Perovskite Solar Cells: A Prospective on the Substitution of the A Cation and X Anion. *Angew. Chem., Int. Ed.* **2017**, *56*, 1190–1212.
- Mao, L.; Ke, W.; Pedesseau, L.; Wu, Y.; Katan, C.; Even, J.; Wasielewski, M. R.; Stoumpos, C. C.; Kanatzidis, M. G. Hybrid Dion–Jacobson 2D Lead Iodide Perovskites. *J. Am. Chem. Soc.* **2018**, *140* (10), 3775–3783.
- Cao, D. H.; Stoumpos, C. C.; Farha, O. K.; Hupp, J. T.; Kanatzidis, M. G. 2d. Homologous Perovskites as Light-Absorbing Materials for Solar Cell Applications. *J. Am. Chem. Soc.* **2015**, *137*, 7843–7850.
- Zhang, X.; Ren, X.; Liu, B.; Munir, R.; Zhu, X.; Yang, D.; Li, J.; Liu, Y.; Smilgies, D.-m.; Li, R. Stable High Efficiency Two-Dimensional Perovskite Solar Cells via Cesium Doping. *Energy Environ. Sci.* **2017**, *10*, 2095–2102.
- Smith, I. C.; Hoke, E. T.; Solis-Ibarra, D.; McGehee, M. D.; Karunadasa, H. I. A Layered Hybrid Perovskite Solar-Cell Absorber with Enhanced Moisture Stability. *Angew. Chem.* **2014**, *126*, 11414–11417.
- Zhang, X.; Wu, G.; Fu, W.; Qin, M.; Yang, W.; Yan, J.; Zhang, Z.; Lu, X.; Chen, H. Orientation Regulation of Phenylethylammonium Cation Based. *Adv. Energy Mater.* **2018**, *8*, 1702498.

(12) Tanaka, K.; Kondo, T. Bandgap and Exciton Binding Energies in Lead-Iodide-Based Natural Quantum-Well Crystals. *Sci. Technol. Adv. Mater.* **2003**, *4*, 599–604.

(13) Ishihara, T.; Takahashi, J.; Goto, T. Optical Properties Due to Electronic Transitions in Two-Dimensional Semiconductors (C<sub>n</sub>H<sub>2n+1</sub>NH<sub>3</sub>)<sub>2</sub>PbI<sub>4</sub>. *Phys. Rev. B: Condens. Matter Mater. Phys.* **1990**, *42*, 11099–11099.

(14) Mercier, N. (HO<sub>2</sub>C(CH<sub>2</sub>)<sub>3</sub>NH<sub>3</sub>)<sub>2</sub>(CH<sub>3</sub>NH<sub>3</sub>) Pb<sub>2</sub>I<sub>7</sub>: A Predicted Noncentrosymmetrical Structure Built up from Carboxylic Acid Supramolecular Synthons and Bilayer Perovskite Sheets. *CrystEngComm* **2005**, *7*, 429–432.

(15) Mei, A.; Li, X.; Liu, L.; Ku, Z.; Liu, T.; Rong, Y.; Xu, M.; Hu, M.; Chen, J.; Yang, Y.; et al. A Hole-Conductor-Free, Fully Printable Mesoscopic Perovskite Solar Cell with High Stability. *Science* **2014**, *345*, 295–298.

(16) Hoshi, H.; Shigeeda, N.; Dai, T. Improved Oxidation Stability of Tin Iodide Cubic Perovskite Treated by 5-Ammonium Valeric Acid Iodide. *Mater. Lett.* **2016**, *183*, 391–393.

(17) Grancini, G.; Roldán-Carmona, C.; Zimmermann, I.; Mosconi, E.; Lee, X.; Martineau, D.; Narbey, S.; Oswald, F.; De Angelis, F.; Graetzel, M.; et al. One-Year Stable Perovskite Solar Cells. *Nat. Commun.* **2017**, *8*, 15684–15684.

(18) Rodríguez-Romero, J.; Hames, B. C.; Mora-Sero, I.; Barea, E. M. Conjugated Organic Cations to Improve the Optoelectronic Properties of 2D/3D Perovskites. *ACS Energy Letters* **2017**, *2*, 1969–1970.

(19) Iagher, L.; Etgar, L. The Effect of Cs on the Stability and Photovoltaic Performance of 2D/3D Perovskite-Based Solar Cells. *ACS Energy Letters* **2018**, *3*, 366.

(20) Passarelli, J. V.; Fairfield, D. J.; Sather, N. A.; Hendricks, M. P.; Sai, H.; Stern, C. L.; Stupp, S. I. Enhanced Out-of-Plane Conductivity and Photovoltaic Performance in *n* = 1 Layered Perovskites through Organic Cation Design. *J. Am. Chem. Soc.* **2018**, *140*, 7313–7323.

(21) Li, Y.; Milić, J. V.; Ummadisingu, A.; Seo, J.-Y.; Im, J.-H.; Kim, H.-S.; Liu, Y.; Dar, M. I.; Zakeeruddin, S. M.; Wang, P.; et al. Bifunctional Organic Spacers for Formamidinium-Based Hybrid Dion–Jacobson Two-Dimensional Perovskite Solar Cells. *Nano Lett.* **2019**, *19* (1), 150–157.

(22) Chen, Y.; Sun, Y.; Peng, J.; Tang, J.; Zheng, K.; Liang, Z. 2d. Ruddlesden–Popper Perovskites for Optoelectronics. *Adv. Mater.* **2018**, *30*, 1703487.

(23) Stoumpos, C. C.; Cao, D. H.; Clark, D. J.; Young, J.; Rondinelli, J. M.; Jang, J. I.; Hupp, J. T.; Kanatzidis, M. G. Ruddlesden–Popper Hybrid Lead Iodide Perovskite 2D Homologous Semiconductors. *Chem. Mater.* **2016**, *28*, 2852–2867.

(24) Billing, D. G.; Lemmerer, A. Synthesis, Characterization and Phase Transitions in the Inorganic–Organic Layered Perovskite-Type Hybrids [(C<sub>n</sub>H<sub>2n+1</sub>NH<sub>3</sub>)<sub>2</sub>PbI<sub>4</sub>], *n* = 4, 5 and 6. *Acta Crystallogr., Sect. B: Struct. Sci.* **2007**, *63* (5), 735–747.

(25) Giannozzi, P.; Baroni, S.; Bonini, N.; Calandra, M.; Car, R.; Cavazzoni, C.; Ceresoli, D.; Chiarotti, G. L.; Cococcioni, M.; Dabo, I.; et al. A Modular and Open-Source Software Project for Quantum Simulations of Materials. *J. Phys.: Condens. Matter* **2009**, *21*, 395502.

(26) Perdew, J. P.; Burke, K.; Wang, Y. Generalized Gradient Approximation for the Exchange-Correlation Hole of a Many-Electron System. *Phys. Rev. B: Condens. Matter Mater. Phys.* **1996**, *54*, 16533–16533.

(27) Perdew, J. P.; Ruzsinszky, A.; Csonka, G. I.; Vydrov, O. A.; Scuseria, G. E.; Constantin, L. A.; Zhou, X.; Burke, K. Restoring the Density-Gradient Expansion for Exchange in Solids and Surfaces. *Phys. Rev. Lett.* **2008**, *100* (16), 039902.

(28) Grimme, S. Semiempirical GGA-Type Density Functional Constructed with a Long-Range Dispersion Correction. *J. Comput. Chem.* **2006**, *27*, 1787–1799.

(29) Adamo, C.; Barone, V. Toward Reliable Density Functional Methods without Adjustable Parameters: The PBE0Model. *J. Chem. Phys.* **1999**, *110* (13), 6158–6170.

(30) Even, J.; Pedesseau, L.; Jancu, J.-M.; Katan, C. Importance of Spin–Orbit Coupling in Hybrid Organic/Inorganic Perovskites for

Photovoltaic Applications. *J. Phys. Chem. Lett.* **2013**, *4* (17), 2999–3005.

(31) Wiktor, J.; Rothlisberger, U.; Pasquarello, A. Predictive Determination of Band Gaps of Inorganic Halide Perovskites. *J. Phys. Chem. Lett.* **2017**, *8*, 5507–5512.

(32) Macrae, C. F.; Bruno, I. J.; Chisholm, J. A.; Edgington, P. R.; McCabe, P.; Pidcock, E.; Rodriguez-Monge, L.; Taylor, R.; Streek, J. v.; Wood, P. A. Mercury CSD 2.0—New Features for the Visualization and Investigation of Crystal Structures. *J. Appl. Crystallogr.* **2008**, *41*, 466–470.

# Atomic-Level Microstructure of Efficient Formamidinium-Based Perovskite Solar Cells Stabilized by 5-Ammonium Valeric Acid Iodide Revealed by Multinuclear and Two-Dimensional Solid-State NMR

Anwar Q. Alanazi,<sup>†</sup> Dominik J. Kubicki,<sup>\*,†,‡,§,◆</sup> Daniel Prochowicz,<sup>†,§</sup> Essa A. Alharbi,<sup>†</sup> Marine E. F. Bouduban,<sup>⊥</sup> Farzaneh Jahanbakhshi,<sup>∇</sup> Marko Mladenović,<sup>∇,○</sup> Jovana V. Milić,<sup>†</sup> Fabrizio Giordano,<sup>†</sup> Dan Ren,<sup>†</sup> Ahmed Y. Alyamani,<sup>||</sup> Hamad Albrithen,<sup>||,#</sup> Abdulrahman Albadri,<sup>||</sup> Mohammad Hayal Alotaibi,<sup>||</sup> Jacques-E. Moser,<sup>⊥</sup> Shaik M. Zakeeruddin,<sup>†</sup> Ursula Rothlisberger,<sup>∇</sup> Lyndon Emsley,<sup>\*,†,§</sup> and Michael Grätzel<sup>\*,†</sup>

<sup>†</sup>Laboratory of Photonics and Interfaces, Institute of Chemical Sciences and Engineering, School of Basic Sciences, Ecole Polytechnique Fédérale de Lausanne, CH-1015 Lausanne, Switzerland

<sup>‡</sup>Laboratory of Magnetic Resonance, Institute of Chemical Sciences and Engineering, School of Basic Sciences, Ecole Polytechnique Fédérale de Lausanne, CH-1015 Lausanne, Switzerland

<sup>§</sup>Institute of Physical Chemistry, Polish Academy of Sciences, Kasprzaka 44/52, 01-224 Warsaw, Poland

<sup>||</sup>National Center for Nanotechnology, King Abdulaziz City for Science and Technology, P.O. Box 6086, Riyadh 11442, Saudi Arabia

<sup>⊥</sup>Photochemical Dynamics Group, Institute of Chemical Sciences and Engineering, Centre for Ultrafast Science, École Polytechnique Fédérale de Lausanne CH-1015 Lausanne, Switzerland

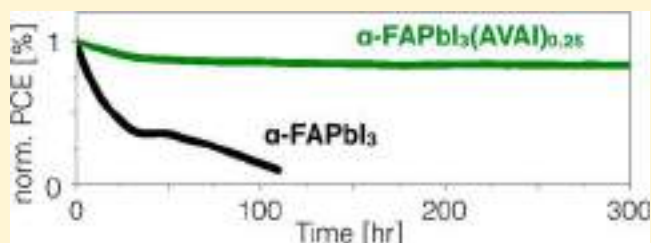
<sup>#</sup>Physics and Astronomy Department-Research Chair for Tribology, Surface and Interface Sciences, College of Science, and King Abdullah Institute for Nanotechnology-Aramco Laboratory for Applied Sensing Research, King Saud University, P.O. Box 2455, Riyadh 11451, Saudi Arabia

<sup>∇</sup>Laboratory of Computational Chemistry and Biochemistry (LCBC), École Polytechnique Fédérale de Lausanne (EPFL), CH-1015 Lausanne, Switzerland

<sup>○</sup>Scientific Computing Laboratory, Center for the Study of Complex Systems, Institute of Physics Belgrade, University of Belgrade, Pregrevaica 118, 11080 Belgrade, Serbia

## Supporting Information

**ABSTRACT:** Chemical doping of inorganic–organic hybrid perovskites is an effective way of improving the performance and operational stability of perovskite solar cells (PSCs). Here we use 5-ammonium valeric acid iodide (AVAI) to chemically stabilize the structure of  $\alpha$ -FAPbI<sub>3</sub>. Using solid-state MAS NMR, we demonstrate the atomic-level interaction between the molecular modulator and the perovskite lattice and propose a structural model of the stabilized three-dimensional structure, further aided by density functional theory (DFT) calculations. We find that one-step deposition of the perovskite in the presence of AVAI produces highly crystalline films with large, micrometer-sized grains and enhanced charge-carrier lifetimes, as probed by transient absorption spectroscopy. As a result, we achieve greatly enhanced solar cell performance for the optimized AVA-based devices with a maximum power conversion efficiency (PCE) of 18.94%. The devices retain 90% of the initial efficiency after 300 h under continuous white light illumination and maximum-power point-tracking measurement.



## INTRODUCTION

Hybrid organic–inorganic lead halide perovskites have received considerable attention since their first application to solar cells in 2009<sup>1</sup> and have recently reached a remarkable power conversion efficiency (PCE) above 24%.<sup>2</sup> These semiconducting materials have emerged as efficient light harvesters due to their easy fabrication process and unique

physicochemical properties such as low band gaps, high extinction coefficients, and high carrier mobilities.<sup>3–6</sup> The most widely used 3D perovskites are methylammonium (MA) lead iodide MAPbI<sub>3</sub> and formamidinium (FA) lead iodide  $\alpha$ -

Received: July 11, 2019

Published: October 8, 2019

FAPbI<sub>3</sub> with band gaps of around 1.5–1.6 and 1.48 eV, respectively.<sup>7,8</sup> This alternation in band gap is very important in view of the Shockley-Queisser efficiency limit,<sup>9</sup> which states that materials with a band gap around 1.4 eV are expected to have optimal light-harvesting ability in solar cell applications. In this respect,  $\alpha$ -FAPbI<sub>3</sub> is a very promising material since it shows a near optimal band gap leading to maximal predicted power conversion efficiency. However, a major disadvantage of  $\alpha$ -FAPbI<sub>3</sub> is its thermodynamic instability; the black perovskite phase of  $\alpha$ -FAPbI<sub>3</sub> is thermodynamically stable only above 150 °C and spontaneously transforms to the wide-band-gap hexagonal, nonperovskite yellow  $\delta$ -phase at room temperature.<sup>10–12</sup> These shortcomings have been tackled by compositional engineering, for example, by mixing FA<sup>+</sup> with smaller A-site cations such as MA<sup>+</sup><sup>13–15</sup> or Cs<sup>+</sup>,<sup>16–18</sup> and through the introducing of mixed halide compositions.<sup>19,20</sup> Another emerging approach to overcome the stability issue consists of applying lower-dimensional perovskites (2D and 2D/3D hybrids) formed by replacing the A-site cation with bulkier molecules such as longer alkylammonium chains.<sup>21,22</sup> This approach is particularly interesting in terms of enhancing the stability of the structure against humidity, as these compounds generally exhibit higher resistance to the incorporation of water into the crystal structure.<sup>23</sup> Therefore, a number of large aliphatic alkylammonium cations, e.g., cyclopropylammonium (CA),<sup>24</sup> poly(ethylenimine) (PEI),<sup>25</sup> phenylethylammonium (PEA),<sup>26–28</sup> or butylammonium (BA)<sup>29–31</sup> have been intercalated into MAPbI<sub>3</sub> crystal lattice forming 2D/3D (also referred to as quasi-3D) hybrid perovskites with improved ambient stability. Alternatively, large-sized organic molecules with bifunctional groups can be utilized as additives to improve the crystallinity and stability of Pb-based perovskites by potentially cross-linking neighboring perovskite grains through strong hydrogen bonding.<sup>32–37</sup> For example, the bifunctional alkylphosphonic acid  $\omega$ -ammonium cation was hypothesized to be a cross-linking agent for facilitating the growth of perovskite crystals and forming high-performance and stable perovskite solar cells (PSCs).<sup>32</sup> The use of bifunctional passivation ligands has also been demonstrated for perovskite nanocrystals.<sup>38,39</sup> In a similar vein, oleate-capped all-inorganic perovskite nanocrystals have been demonstrated as a passivation agent for microcrystalline MAPbI<sub>3</sub> thin films.<sup>40</sup> Recently, the incorporation of a bifunctional salt of 5-ammonium valeric acid iodide (AVAI) has been reported to enhance crystallinity and stability of MAPbBr<sub>3</sub><sup>33</sup> and FASnI<sub>3</sub>.<sup>35</sup> These cations are suggested to cross-link and as such play an important role in reducing the surface energy and passivating surface defects, which subsequently enhances the performance and operational stability of the devices.

Here, we report an effective one-step solution deposition method for the preparation of a high quality and stable  $\alpha$ -FAPbI<sub>3</sub> perovskite active layer using the bifunctional organic molecule AVAI that acts as a structure-directing cross-linking agent between adjacent grains in the perovskite structure. Using solid-state NMR, we reveal that AVAI interacts with  $\alpha$ -FAPbI<sub>3</sub> on the atomic level by binding to the 3D perovskite through hydrogen bonding interaction and stabilizing it against the detrimental  $\alpha$ -to- $\delta$  phase transition. The introduction of AVAI to the perovskite precursor solution leads to the growth of highly crystalline films with large, micrometer-sized grains and enhanced charge-carrier lifetime. As a result, the optimized AVA-based mesoscopic heterojunction PSC yields a high PCE

of 18.94% and high operational stability after 300 h under continuous illumination.

## EXPERIMENTAL SECTION

**Materials.** All materials were purchased from Sigma-Aldrich and used as received, unless stated otherwise. Perovskite powders for solid-state NMR studies were synthesized by grinding precursors in an electric ball mill (Retsch Ball Mill MM-200, agate grinding jar with a volume of 10 mL and 1 agate ball, diameter size 10 mm) for 30 min at 25 Hz. The precursors were packed in a glovebox under an argon atmosphere. After milling, the resulting powders were annealed at 140 °C for 10 min to reproduce the thin-film synthetic procedure. FAPbI<sub>3</sub>: 0.172 g of FAI (1 mmol) and 0.461 g of PbI<sub>2</sub> (1 mmol); FAPbI<sub>3</sub>(AVAI)<sub>0.25</sub>: 0.172 g of FAI (1 mmol), 0.461 g of PbI<sub>2</sub> (1 mmol), and 0.029 g of AVAI (0.25 mmol).

**Solar Cell Preparation.** Fluorine-doped tin oxide (FTO) glass substrates (TCO glass, NSG 10, Nippon sheet glass, Japan) were etched from the edges by using Zn powder and 4 M HCl and then were cleaned by ultrasonication in Hellmanex (2%, deionized water), rinsed thoroughly with deionized water and ethanol, and then treated in oxygen plasma for 15 min. A 30 nm blocking layer (TiO<sub>2</sub>) was deposited on the cleaned FTO by spray pyrolysis at 450 °C using a commercial titanium diisopropoxide bis(acetylacetonate) solution (75% in 2-propanol, Sigma-Aldrich) diluted in anhydrous ethanol (1:9 volume ratio) as precursor and oxygen as a carrier gas. A mesoporous TiO<sub>2</sub> layer was deposited by spin-coating a paste (Dyesol 30NRD) diluted with ethanol (1:6 wt ratio) (4000 rpm, acceleration 2000 rpm for 20 s) onto the substrate containing the TiO<sub>2</sub> compact layer and then sintered at 450 °C for 30 min in dry air.

**Deposition of Perovskite Films.** The perovskite films were deposited using a single-step deposition method from the precursor solution. The precursor solution of FAPbI<sub>3</sub> was prepared in argon atmosphere by dissolving equimolar amounts of PbI<sub>2</sub> and FAI in an anhydrous DMF/DMSO (4:1 (volume ratio)) mixture at a concentration of 1.4 M. Next, we added AVAI into the FAPbI<sub>3</sub> precursor solution using different molar ratios, resulting in several FAPbI<sub>3</sub>(AVAI)<sub>x</sub> compositions ( $x = 0.05, 0.10, 0.25, 0.50$ ). The device fabrication was carried out under controlled atmospheric conditions with humidity < 2%. The precursor solution was spin-coated onto the mesoporous TiO<sub>2</sub> films in a two-step program at 1000 and 6000 rpm for 10 and 30 s, respectively. During the second step, 200  $\mu$ L of chlorobenzene was dropped on the spinning substrate 10 s prior the end of the program. This was followed by annealing the films at 150 °C for 30–40 min. After preparing the initial perovskite layer (control) as described above, the film was cooled down at room temperature. For completing the fabrication of devices, 90 mg of 2,2',7,7'-tetrakis(*N,N*-di-*p*-methoxyphenylamine)-9,9-spirobifluorene (spiro-OMeTAD) was dissolved in 1 mL of chlorobenzene as a hole-transporting material (HTM). The HTM was deposited by spin-coating at 4000 rpm for 20 s. The HTM was doped with bis(trifluoromethylsulfonyl)imide lithium salt (17.8  $\mu$ L prepared by dissolving 520 mg of LiTFSI in 1 mL of acetonitrile) and 28.8  $\mu$ L of 4-*tert*-butylpyridine. Finally, an  $\sim$ 80 nm gold (Au) layer was thermally evaporated.

**Solid-State NMR Measurements.** Room temperature <sup>1</sup>H (900.0 MHz) NMR spectra were recorded on a Bruker Avance Neo 21.1 T spectrometer equipped with a 3.2 mm CPMAS probe. <sup>1</sup>H and <sup>13</sup>C chemical shifts were referenced to solid adamantane ( $\delta_{\text{H}} = 1.91$  ppm and  $\delta_{\text{C}} = 29.45$  (CH) and 38.48 (CH<sub>2</sub>) ppm). <sup>14</sup>N spectra were referenced to solid NH<sub>4</sub>Cl (0 ppm) at 298 K. <sup>2</sup>H spectra were referenced based on the <sup>1</sup>H chemical shift of NH<sub>3</sub><sup>+</sup> in the nondeuterated AVA<sub>2</sub>PbI<sub>4</sub>. Recycle delays of 0.1 s (<sup>14</sup>N), 2.5–25 s (<sup>1</sup>H–<sup>13</sup>C), and 0.25–2 s (<sup>2</sup>H) were used. Longitudinal relaxation times ( $T_1$ ) were measured using a saturation-recovery sequence. <sup>1</sup>H–<sup>1</sup>H spin diffusion measurements at 20 kHz MAS were carried out using a mixing period of 100 ms and a recycle delay of 5 s.

## RESULTS AND DISCUSSION

The hybrid perovskite films were prepared by solution processing. The precursor solution of FAPbI<sub>3</sub> was prepared by dissolving equimolar amounts of PbI<sub>2</sub> and FAI in a DMF/DMSO (4:1 v/v) mixture at a concentration of 1.4 M. Next, we added AVAI into the FAPbI<sub>3</sub> precursor solution using different molar ratios, resulting in several FAPbI<sub>3</sub>(AVAI)<sub>x</sub> compositions ( $x = 0.05, 0.10, 0.25, 0.50$ ). We first evaluated the photovoltaic performance of films fabricated by a one-step antisolvent deposition method (for more details of perovskite film formation, see the [Experimental Section](#)). The solar cells were fabricated using the following architecture: glass/FTO/compact-TiO<sub>2</sub>/mesoporous TiO<sub>2</sub>/perovskite/Spiro-OMeTAD/Au.

The characteristic  $J$ - $V$  curves for the champion FAPbI<sub>3</sub>(AVAI)<sub>x</sub>-based devices measured under reverse voltage scan are shown in [Figure 1a](#). The reference PSCs ( $x = 0$ ) yielded

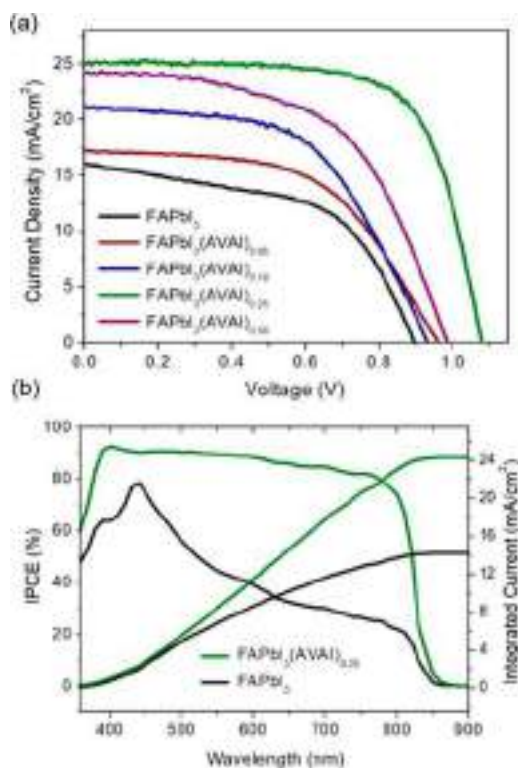


**Figure 1.** Photovoltaic characterization of the devices. (a) Comparison of the  $J$ - $V$  curves for the champion FAPbI<sub>3</sub>(AVAI)<sub>x</sub> ( $x = 0, 0.05, 0.10, 0.25, 0.50$ ) devices. (b) IPCE and integrated  $J_{sc}$  of the  $\alpha$ -FAPbI<sub>3</sub> and FAPbI<sub>3</sub>(AVAI)<sub>0.25</sub> devices.

poor device performance, with a maximum PCE of 7.26%,  $V_{oc}$  of 0.88 V,  $J_{sc}$  of 15 mA cm<sup>-2</sup>, and fill factor (FF) of 55%. We found that the device performance increases monotonically with the amount of added AVAI up to 25% (abbreviated as FAPbI<sub>3</sub>(AVAI)<sub>0.25</sub>), achieving a maximum PCE of 18.94% with a  $V_{oc}$  of 1.07 V,  $J_{sc}$  of 25.1 mA cm<sup>-2</sup>, and FF of 70%. The integrated  $J_{sc}$  calculated from the IPCE spectrum of the FAPbI<sub>3</sub>(AVAI)<sub>0.25</sub> device equals to 24.20 mA cm<sup>-2</sup>, which is within 3% of the  $J_{sc}$  measured under AM 1.5G standard irradiation ([Figure 1b](#)). A further increase in the AVAI content up to 50% deteriorates all figures of merit with PCE declining to 13.22%. [Table 1](#) shows a summary of the photovoltaic parameters for the champion devices with different AVAI

**Table 1.** Comparison of Photovoltaic Parameters for Champion FAPbI<sub>3</sub>(AVAI)<sub>x</sub> Devices ( $x = 0, 0.05, 0.10, 0.25, 0.50$ ) with Backward Scan Direction

perovskite	$V_{oc}$ [V]	$J_{sc}$ [mA/cm <sup>2</sup> ]	FF	PCE [%]
FAPbI <sub>3</sub>	0.88	15.0	0.55	7.26
FAPbI <sub>3</sub> (AVAI) <sub>0.05</sub>	0.89	17.2	0.55	9.15
FAPbI <sub>3</sub> (AVAI) <sub>0.10</sub>	0.89	23.9	0.52	11.67
FAPbI <sub>3</sub> (AVAI) <sub>0.25</sub>	1.08	25.1	0.70	18.94
FAPbI <sub>3</sub> (AVAI) <sub>0.50</sub>	0.98	24.3	0.55	13.22

doping levels. The maximum power point (MPP) of the FAPbI<sub>3</sub>(AVAI)<sub>0.25</sub> device shows the stabilized PCE of 17.70% after 300 s of continuous illumination ([Figure S1](#)). The photovoltaic performance figures of merit are listed in [Figure S2](#) for the control FAPbI<sub>3</sub> and FAPbI<sub>3</sub>(AVAI)<sub>x</sub> ( $x = 0.05, 0.10, 0.25, 0.50$ ) devices. The increase in PCE upon AVAI doping is mainly due to the large improvement of all photovoltaic metrics, i.e.,  $J_{sc}$ ,  $V_{oc}$ ,  $J_{sc}$ , and FF, which can be attributed to improved phase purity, perovskite film morphology, and longer charge carrier lifetimes, as well as reduced defect density (vide infra). Notably, the efficiency of the champion FAPbI<sub>3</sub>(AVAI)<sub>0.25</sub> device is among the highest reported for  $\alpha$ -FAPbI<sub>3</sub>-based solar cells.<sup>41,42</sup>  $J$ - $V$  hysteresis and its suppression have been important subjects of research in the field of PSCs.<sup>43</sup> We have found that both the reference and FAPbI<sub>3</sub>(AVAI)<sub>0.25</sub> PSCs display hysteresis ([Figure S9](#) and [Table S2](#)). We therefore conclude that AVAI does not lead to its suppression.

To investigate the crystallinity of the AVAI-doped perovskite, we measured powder X-ray diffraction (pXRD) of films deposited onto mesoporous-TiO<sub>2</sub>/compact layer TiO<sub>2</sub>/FTO ([Figure 2a](#)). The reference  $\alpha$ -FAPbI<sub>3</sub> and the FAPbI<sub>3</sub>(AVAI)<sub>x</sub> films have a very similar structure, with the peaks at  $\sim 14.0^\circ$  and  $\sim 28.0^\circ$  originating from the (110) and (220) planes of the 3D perovskite phase. The reference  $\alpha$ -FAPbI<sub>3</sub> film also exhibits a strong peak at  $11.6^\circ$  along with a number of low-intensity peaks in the 25–40° region, corresponding to the hexagonal nonperovskite  $\delta$ -FAPbI<sub>3</sub> phase.<sup>10</sup> The  $\delta$ -phase peaks disappear upon AVAI addition and are absent in all the FAPbI<sub>3</sub>(AVAI)<sub>x</sub> films. We note that AVA-rich iodoplumbate phases (yielding peaks below  $2\theta = 10^\circ$ ) are also absent.<sup>34</sup> Furthermore, the overall diffraction intensity is enhanced with increased amounts of AVAI doping, indicative of improved crystallinity. The relative intensity of the two perovskite peaks changes very slightly as the AVAI content increases. This might be related to preferred orientation effects which have been previously observed in other amino acid doped perovskite thin films and ascribed to amino acid-TiO<sub>2</sub> anchoring.<sup>44</sup> We note that there are no diffraction peaks corresponding to the AVA dopant. This is consistent with the pronounced dynamic disorder of AVA evidenced by <sup>2</sup>H MAS NMR (vide infra). This is correlates with the SEM measurements which show that the average grain size in the FAPbI<sub>3</sub>(AVAI)<sub>x</sub> films systematically increases from a few hundred nanometers to about a micrometer with increasing AVAI doping level ([Figure S3](#)). This result suggests that AVAI interacts with  $\alpha$ -FAPbI<sub>3</sub> to facilitate crystal growth during annealing. We note that the largest crystallite size was obtained for the 50% AVAI composition which, however, showed a decrease in the  $J_{sc}$ ,  $V_{oc}$ , and FF. This translated to lower PCE, likely due to an increase in the internal resistance of the devices with an excessive AVAI content, analogous to the result previously

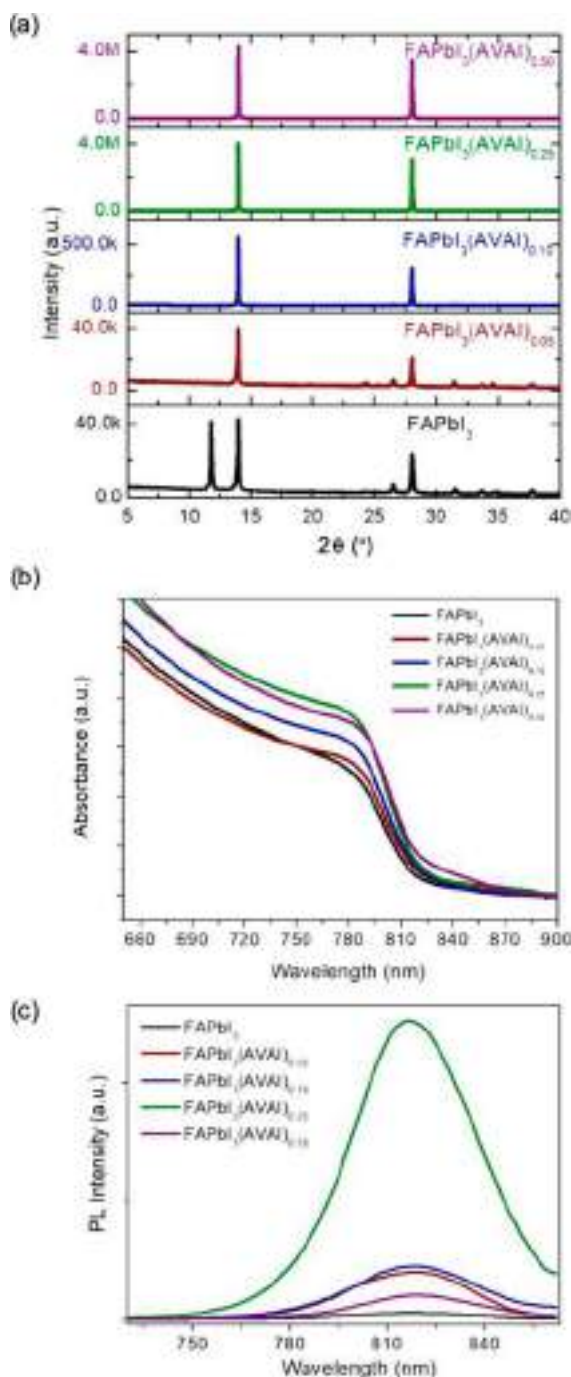


**Figure 2.** Characterization of the  $\text{FAPbI}_3(\text{AVAI})_x$  perovskite films. (a) Powder XRD patterns, (b) UV–vis absorption, and (c) steady-state PL spectra.

observed for PEA.<sup>28</sup> Further, we tested hydrophobicity of the  $\text{FAPbI}_3$  and  $\text{FAPbI}_3(\text{AVAI})_{0.25}$  films by measuring the contact angle of a water droplet (Figure S10). The contact angle increases from  $46.2^\circ$  to  $59.2^\circ$  after AVA doping, indicating higher hydrophobicity of the AVA-doped material.

The effects of the changes in the structural features and morphology on the optoelectronic properties were assessed by means of UV–vis absorption and photoluminescence (PL) absorption spectroscopy. The UV–vis absorption spectra of the  $\text{FAPbI}_3(\text{AVAI})_x$  films deposited on glass are shown in Figure 2b. We find that the band edges of the absorption spectra very slightly red-shift ( $\sim 2$  nm) when the content of

AVAI is increased. In addition, steady-state PL spectra show a correspondingly small red shift for the  $\text{FAPbI}_3(\text{AVAI})_{0.50}$  film with respect to the reference  $\text{FAPbI}_3$  (Figure 2c), consistent with the UV–vis measurements. The red shift in both UV–vis and PL spectra might be caused by the increased crystallinity and larger grain size,<sup>45</sup> consistent with the SEM images, and/or due to the formation of a new chemical compound. These observations are qualitatively different from the previous result, where the absorbance and PL peaks of AVA-doped perovskite films blue-shifted with increasing AVABr amount due to the introduction of Br into the perovskite structure.<sup>33</sup>

To further confirm the beneficial effect of the addition of AVAI to the  $\text{FAPbI}_3$  composition, transient absorption (TA) spectroscopy measurements were performed on both a reference  $\text{FAPbI}_3$  and  $\text{FAPbI}_3(\text{AVAI})_{0.25}$  films deposited on glass slides. Figure 3a shows TA dynamics of the ground-state

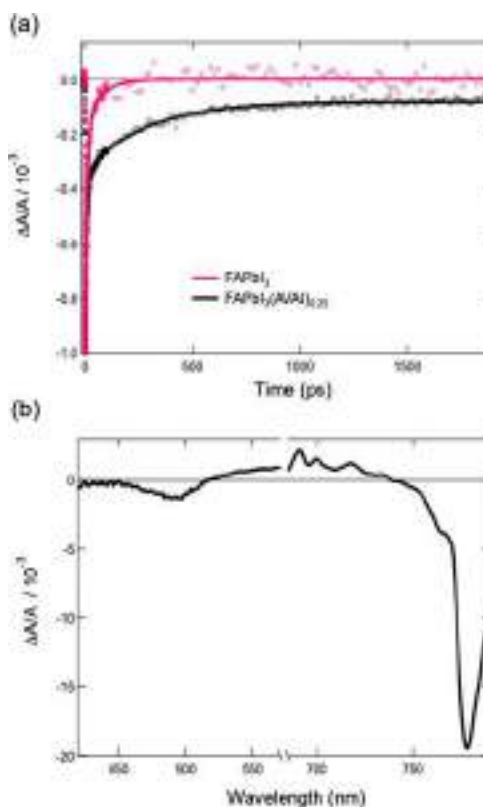


**Figure 3.** (a) Ground-state bleaching (760 nm) and stimulated emission dynamics obtained by transient absorbance with  $I_{\text{ex}} = 390$  nm, at an excitation fluence  $F = 250$  nJ. (b) Transient absorbance spectra of  $\text{FAPbI}_3(\text{AVAI})_{0.25}$  measured under the same conditions as in (a).

bleaching (GSB) and stimulated emission (SE) signals, which closely overlap in the band-edge region (760 nm) for both films (Figure 3b). The GSB signal is related to the filling of the bands due to photoexcitation with its decay corresponding to the depletion of the conduction band and/or the filling of the valence band by electrons. As such, it reflects both charge recombination and charge extraction to a selective contact layer. We note that GB bleaching recovery reflects contributions from both radiative and nonradiative carrier recombination. On the other hand, the dynamics of the SE signal describes only radiative electron–hole recombination. Since the samples were prepared with no extracting layers, it follows

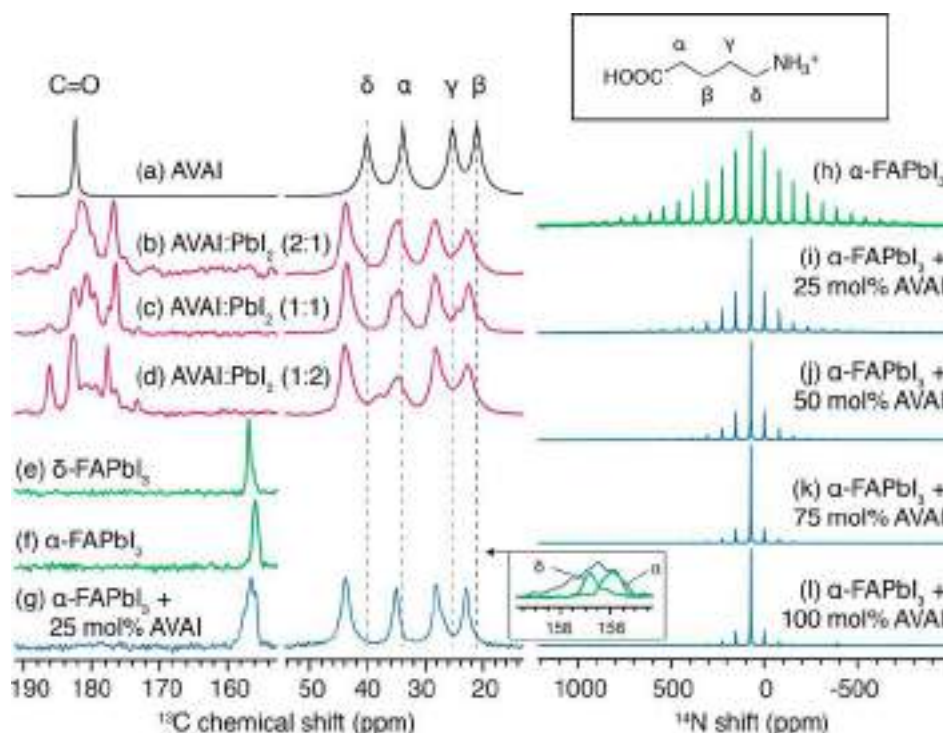


**Figure 4.** Solid-state MAS NMR characterization of the bulk mechanochemical materials.  $^1\text{H}$ - $^{13}\text{C}$  CP spectra at 21.1 T, 298 K, and 20 kHz MAS of (a) neat AVAI (the structure is shown in the inset), (b) AVAI:PbI<sub>2</sub> (2:1 mol/mol), (c) AVAI:PbI<sub>2</sub> (1:1 mol/mol), (d) AVAI:PbI<sub>2</sub> (1:2 mol/mol), (e)  $\delta$ -FAPbI<sub>3</sub>, (f)  $\alpha$ -FAPbI<sub>3</sub>, and (g)  $\alpha$ -FAPbI<sub>3</sub> + 25 mol % AVAI. The inset shows a horizontal zoom of the FA region in panels (e)–(g).  $^{14}\text{N}$  MAS NMR spectra at 21.1 T, 298 K, and 5 kHz MAS of (h)  $\alpha$ -FAPbI<sub>3</sub>, and  $\alpha$ -FAPbI<sub>3</sub> doped with (i) 25 mol % AVAI, (j) 50 mol % AVAI, (k) 75 mol % AVAI, and (l) 100 mol % AVAI.

that comparing the decay rates of the GSB+SE signals for FAPbI<sub>3</sub> versus FAPbI<sub>3</sub>(AVAI)<sub>0.25</sub> is directly related to charge carrier lifetimes in these materials. Clearly, the addition of AVAI results in a significantly slower decay rate and the second decay component is almost four times larger for FAPbI<sub>3</sub>(AVAI)<sub>0.25</sub> than in FAPbI<sub>3</sub> (286 ps vs 76 ps) (Table S1). We note that the long time contribution in the case of FAPbI<sub>3</sub>(AVAI)<sub>0.25</sub> most likely arises from Shockley–Read–Hall pseudo-first-order recombination via charge carrier trapping states.

We employed X-ray photoelectron spectroscopy (XPS) to verify if the surface of the FAPbI<sub>3</sub> film is modified during treatment with AVAI. The comparison of the Pb 4f, C 1s, N 1s, and O 1s XPS peaks for the AVAI, AVAI:PbI<sub>2</sub> (2:1),  $\alpha$ -FAPbI<sub>3</sub>, and FAPbI<sub>3</sub>(AVAI)<sub>0.25</sub> films is shown in Figure S4.

The O 1s spectrum of the AVAI film shows a peak at 532.2 eV, which can be assigned to the binding energy of C–O and C=O in the carboxylate group of AVAI. The O 1s spectrum of the 2:1 AVAI:PbI<sub>2</sub> film shifts toward lower binding energy by 0.41 eV (maximum at 531.82 eV), while the corresponding peak of FAPbI<sub>3</sub>(AVAI)<sub>0.25</sub> shifts to a higher energy by 0.7 eV (maximum at 532.9 eV) compared to the pure AVAI film. This indicates that AVAI is involved in a new chemical interaction with  $\alpha$ -FAPbI<sub>3</sub> rather than exists as a separate AVAI-based iodoplumbate phase on the surface of the perovskite film. A full discussion of the XPS data is given in the Supporting Information.

In order to elucidate the atomic-level microstructure of the AVAI-doped  $\alpha$ -FAPbI<sub>3</sub> compositions, we carried out multinuclear solid-state NMR measurements on materials prepared by mechanochemistry.<sup>15,46,47</sup> We and others have recently shown the broad applicability of solid-state NMR to lead

halide perovskites<sup>48–61</sup> and its utility in assessing the interaction of small organic molecules with the hybrid perovskite phases.<sup>62–64</sup>

Figure 4a shows a  $^{13}\text{C}$  spectrum of neat AVAI which contains five resonances corresponding to the following molecular fragments: C=O (182.4 ppm),  $\delta$ -CH<sub>2</sub> (40.1 ppm),  $\alpha$ -CH<sub>2</sub> (33.8 ppm),  $\gamma$ -CH<sub>2</sub> (25.3 ppm), and  $\beta$ -CH<sub>2</sub> (21.0 ppm). The material formed in a reaction between AVAI and PbI<sub>2</sub> has been hypothesized to be a 2D (AVA)<sub>2</sub>PbI<sub>4</sub> perovskite;<sup>65</sup> however, to the best of our knowledge, its crystal structure has not been solved to date. A perfectly ordered Ruddlesden–Popper (RP) (AVA)<sub>2</sub>PbI<sub>4</sub> structure would be expected to possess exactly one type of carbonyl atom inside the unit cell. Here, we find that, in the reaction between AVAI and PbI<sub>2</sub>, depending on the molar ratio of the two components, up to eight distinct C=O environments are formed (Figure 4b–d for AVAI:PbI<sub>2</sub> ratios of 2:1, 1:1, and 1:2, respectively). In addition, the aliphatic signals of AVAI are shifted with respect to neat AVAI in all three compositions, confirming that AVAI has fully reacted in all three cases. This type of structural complexity is expected in structures capable of forming recombinant analogues (polytypes) with different stacking sequences, with ( $\beta$ -alaninium)<sub>2</sub>SnI<sub>4</sub> being a structurally closely related example.<sup>66</sup> We therefore highlight that the AVAI–PbI<sub>2</sub> phase system cannot be considered as a simple RP phase, and further single crystal studies are necessary to develop its full understanding.

$^{13}\text{C}$  MAS NMR also makes it possible to distinguish between  $\delta$ -FAPbI<sub>3</sub> (156.8 ppm, Figure 4e) and  $\alpha$ -FAPbI<sub>3</sub> (155.9 ppm, Figure 4f).<sup>50</sup> The material formally corresponding to  $\alpha$ -FAPbI<sub>3</sub> mixed with 25 mol % AVAI (Figure 4g) reveals a new broad signal (156.5 ppm) corresponding to a carbon environment in



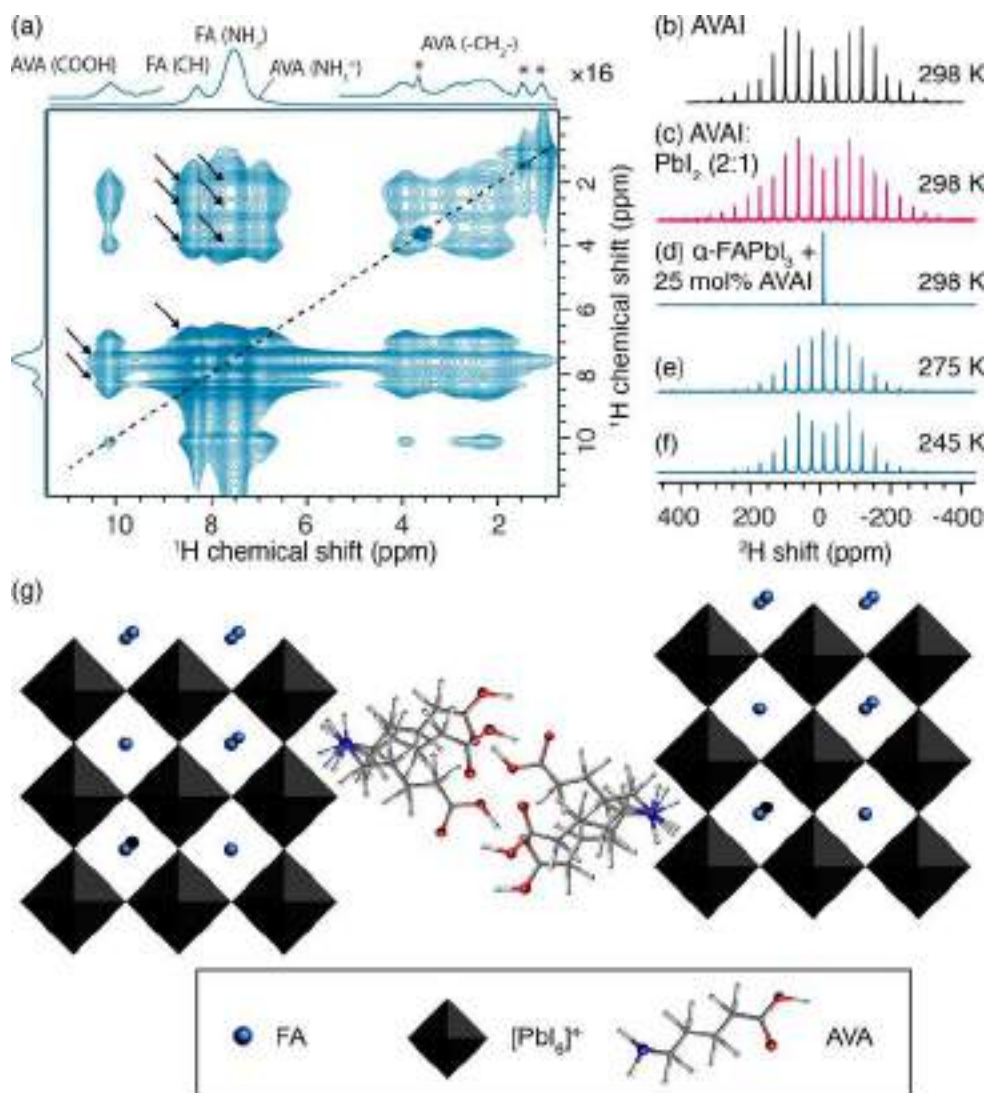


**Figure 5.** Solid-state MAS NMR characterization of the bulk mechanochemical materials. (a)  $^1\text{H}$ – $^1\text{H}$  spin-diffusion measurement at 21.1 T, 298 K, and 20 kHz MAS (mixing time of 100 ms). The aliphatic region has been magnified 16-fold. The asterisks mark trace aliphatic impurities.  $^2\text{H}$  MAS NMR at 21.1 T and 5 kHz MAS of (b) neat AVAI, (c) AVAI: $\text{PbI}_2$  (2:1 mol/mol), and  $\alpha$ -FAPbI<sub>3</sub> + 25 mol % AVAI at (d) 298 K, (e) 275 K, and (f) 245 K. (g) Structural model of the AVAI-modified  $\alpha$ -FAPbI<sub>3</sub> proposed based on the solid-state NMR data.

which FA interacts with AVA on the atomic level. The aliphatic signals of AVA are, again, shifted with respect to neat AVAI, confirming that the precursor has fully reacted to form a new chemical compound. The C=O signals are not visible in this case due to dynamics, as discussed below. We subsequently investigated whether or not the presence of AVAI leads to any changes in the 3D perovskite structure of  $\alpha$ -FAPbI<sub>3</sub>.  $^{14}\text{N}$  MAS NMR is a sensitive probe of cubooctahedral symmetry in 3D perovskites, which determines the breadth of the  $^{14}\text{N}$  spinning sideband (SSB) manifold, with narrower manifolds corresponding to a more symmetric (closer to cubic) environment of the A-site cation reorienting on the picosecond time scale.<sup>50,63</sup> The  $^{14}\text{N}$  MAS NMR spectrum of  $\alpha$ -FAPbI<sub>3</sub> is characterized by a central peak at 75.9 ppm, surrounded by 11 orders of spinning sidebands (Figure 4h).  $\alpha$ -FAPbI<sub>3</sub> doped with 25 mol % AVAI shows no change to the central peak position but the number of visible SSB orders decreases to 7. As the AVAI doping level is increased to 50, 75, and 100 mol % (excess with respect to FAPbI<sub>3</sub>), the number of visible SSB orders decreases to 5, 4, and 3, respectively (Figure 4i–l,

respectively). This narrowing of the  $^{14}\text{N}$  SSB envelope upon AVAI doping suggests that AVAI changes the intrinsic cubooctahedral symmetry of the  $\alpha$ -FAPbI<sub>3</sub> phase so as to make it closer to cubic. We have previously observed similar structure directing effects in the case of 3-(5-mercapto-1H-tetrazol-1-yl)benzenaminium iodide<sup>62</sup> and adamantylammonium iodide.<sup>63</sup> On the other hand, the opposite effect (SSB manifold broadening) is observed upon A-site cation mixing in lead halide perovskites based on MA/FA,<sup>50</sup> Cs/FA,<sup>51</sup> MA/guanidinium,<sup>57</sup> and MA/dimethylammonium<sup>56</sup> mixtures.

In order to corroborate the atomic-level interaction between AVA and FA in AVAI-doped  $\alpha$ -FAPbI<sub>3</sub>, we carried out a two-dimensional  $^1\text{H}$ – $^1\text{H}$  spin diffusion (SD) measurement, which correlates NMR signals based on the atomic-level proximity of the corresponding species for distances on the order of tens of Å through dipole–dipole couplings.<sup>67</sup> Figure 5a shows a  $^1\text{H}$ – $^1\text{H}$  SD spectrum of  $\alpha$ -FAPbI<sub>3</sub> doped with 25 mol % AVAI. The horizontal and vertical projections show a regular 1D  $^1\text{H}$  spectrum with the structural assignments. Each peak in the 1D spectrum has a corresponding diagonal peak lying on the

dashed line. Off-diagonal cross peaks evidence close spatial proximity of the species giving rise to a specific set of diagonal peaks. The spectrum is symmetric around the diagonal. For example, there are cross peaks between the  $-\text{CH}_2-$ ,  $-\text{NH}_3^+$ , and  $-\text{COOH}$  signals of AVA, corresponding to intramolecular contacts. More interestingly, analogous contacts are visible between the CH and  $\text{NH}_2$  groups of FA and all the signals belonging to AVA (indicated by arrows), unambiguously evidencing that *FA and AVA form a mixed phase and are interacting at the atomic level*. We note that AVA is too large to be incorporated as an A-site cation. That said, it could conceivably lead to a hollow perovskite structure characterized by large  $[\text{PbI}_6]^{4-}$  octahedral vacancies.<sup>68,69</sup> However, hollow perovskites exhibit significantly wider band gaps for a comparable amount of dopant while in our case the band gap remains nearly identical up to 50 mol % AVAI doping, excluding the possibility of hollow perovskite formation.

Having investigated the microstructure of the mixed FA/AVA phase, we now turn to the dynamics of AVA in this material. To that end, we use  $^2\text{H}$  MAS NMR which is an excellent probe of dynamics in solids,<sup>70</sup> since the shape of the  $^2\text{H}$  SSB manifold is determined by the available motional degrees of freedom of the reorienting molecular fragment. For example, the  $^2\text{H}$  MAS NMR spectra of AVAI (Figure 5b) and AVAI:PbI<sub>2</sub> (2:1) (Figure 5c) have an SSB manifold characteristic of 3-fold ( $C_3$ ) jumps of the  $-\text{ND}_3^+$  group around the C–N bond, with the backbone of the molecule being rigid. The apparent quadrupolar coupling constant,  $C_Q$ , which can be extracted by fitting the spectra, has a value of 53 and 37 kHz for AVAI and AVAI:PbI<sub>2</sub> (2:1), respectively, and is typical for  $-\text{ND}_3^+$  attached to an otherwise rigid molecular fragment.<sup>71</sup> Structural rigidity in the case of AVA is expected and consistent with the strong intermolecular hydrogen bonding of the COOH groups, analogous to that observed in ( $\beta$ -alaninium)<sub>2</sub>SnI<sub>4</sub>,<sup>66</sup> and further corroborated by molecular dynamics simulations of the  $n = 1$  Ruddlesden–Popper phase (vide infra). In contrast, the  $^2\text{H}$  spectrum of  $\alpha$ -FAPbI<sub>3</sub> doped with 25 mol % AVAI (Figure 5d) consists of a single line (apparent  $C_Q \approx 0$  kHz), which means that in this case the  $-\text{ND}_3^+$  group is reorienting isotropically (in a tetrahedral or lower symmetry) at a rate greater than  $10^5$  jumps per second.<sup>70</sup> This scenario is only possible if the whole AVA backbone has additional degrees of freedom, making it dynamically disordered. We note that this implies that the hydrogen bonding network is also labile and the H-bonds are cleaved and formed at a rate greater than  $10^5$ /s. Rigidity can be gradually reintroduced by cooling the material down to 275 K (Figure 5e) and 245 K (Figure 5f) (apparent  $C_Q$  of 34 and 49 kHz, respectively), at which point the only residual degree of freedom is again the 3-fold  $-\text{ND}_3^+$  jump. Since dynamics partly averages out the  $^1\text{H}$ – $^{13}\text{C}$  dipole–dipole couplings, the cross-polarization efficiency in AVA is expected to be lower.<sup>50</sup> This is indeed the case, as the C=O signal cannot be detected at room temperature (Figure 4g) but is readily detected at lower temperatures when rigidity is reintroduced (Figure 5s). To the best of our knowledge, this is the first demonstration of unrestricted reorientation of a molecular modifier used to stabilize a 3D perovskite. We believe that structural dynamics and lability will become an important design criterium for stable perovskites, once we have gained better understanding of its effects on the resulting photophysics. Based on the above results, we propose that the interaction between the perovskite and AVA is surface-based, as shown in Figure 5g. AVA binds to

the surface of  $\alpha$ -FAPbI<sub>3</sub> through the terminal amino group, while the remaining carboxylate groups are dynamically disordered at room temperature, leading to dynamic formation and breaking of COOH...COOH hydrogen bonds between adjacent AVA molecules. This type of interaction can also conceivably lead to grain cross-linking.

While XRD does not provide insight into the long-range ordering of AVA in the doped FAPbI<sub>3</sub> structure, AVA has been previously reported to form Ruddlesden–Popper (RP) 2D structures with MA,  $\text{AVA}_2(\text{MA})_{n-1}\text{PbI}_{3n+1}$ .<sup>72</sup> We therefore investigated the structural and electronic properties of the analogous RP series,  $\text{AVA}_2(\text{FA})_{n-1}\text{PbI}_{3n+1}$ , for  $n = 1, 2, 3$  and  $\infty$  as a potential structural candidate. For  $n = 2$  and  $n = 3$ , the AVA and FA cations are in atomic-level contact (5–10 Å, similar to the materials studied experimentally by 2D NMR SD measurements) and we use these structures as model, computationally tractable systems, to complement the experimental findings. The initial structures were formed based on the RP structures of  $\text{BA}_2(\text{MA})_{n-1}\text{PbI}_{3n+1}$ .<sup>30</sup> The spacer configuration was taken from the structure of  $\text{ABA}_2(\text{MA})_{n-1}\text{PbI}_{3n+1}$  (ABA = 4-aminobutyric acid)<sup>72</sup> with a hydrogen bonding pattern between carboxylic groups of every two adjacent AVA molecules of opposite layers along the x direction (Figure S6b). Similar to the trend reported for band gaps in  $\text{BA}_2(\text{MA})_{n-1}\text{PbI}_{3n+1}$  RP structure,<sup>30</sup> increasing the inorganic layer thickness (higher  $n$  values) reduces the band gap, which tends to the value of undoped  $\alpha$ -FAPbI<sub>3</sub> as  $n$  increases. Accordingly, the band gap of AVAI-doped  $\alpha$ -FAPbI<sub>3</sub> is essentially identical to that of neat  $\alpha$ -FAPbI<sub>3</sub> (Figure 2b, c), since it can be considered as a high  $n$  representative of the RP  $\text{AVA}_2(\text{FA})_{n-1}\text{PbI}_{3n+1}$  family. To provide additional insight into the experimental observation that AVA-doped  $\alpha$ -FAPbI<sub>3</sub> is more cubic than  $\alpha$ -FAPbI<sub>3</sub> (octahedral tilting angle closer to 90°), we calculated the distribution of octahedral tilting angles of the computationally optimized structure of  $\alpha$ -FAPbI<sub>3</sub> taking also finite temperature effects into account. We performed 2 ps simulations at 300 K and obtained a time-averaged mean value of 89.9° with a standard deviation of 9.1°. Considering the relatively large standard deviation, the subtle templating effect of AVAI observed through  $^{14}\text{N}$  MAS NMR (Figure 4h–l) is likely beyond the accuracy of the DFT MD runs. We in turn addressed the propensity of AVA to form strong intermolecular hydrogen bonds in the iodoplumbate  $\text{AVA}_2\text{PbI}_4$  phase at room temperature, experimentally evidenced by  $^2\text{H}$  MAS NMR (Figure 5c). To that end, we assessed the finite temperature impact on the DFT optimized 0 K structure. We performed a 6 ps Born–Oppenheimer molecular dynamics simulation of the material to investigate the motion of the spacer molecules, as well as the rigidity of the inorganic layers to which the spacers are anchored. We find that, on this time scale, the hydrogen bonding pattern is mostly preserved at 300 K (Figure 6a), consistent with the NMR result. To further understand how the AVA spacers are confined between the inorganic layers, we calculated the vertical penetration depth of AVA into the inorganic sublattice (Figure 6b), as measured by the average Pb–N distance along the normal of the closest PbI<sub>2</sub> plane, since this parameter has been reported to correlate with the octahedral distortion and phase transition temperatures.<sup>73</sup> We find that the penetration depth is mostly below 3.17 Å, which corresponds to the average vertical Pb–I distance, confirming that the spacers penetrate the inorganic sublattice. The rigidity of the spacers was studied by calculating the distribution of polar,  $\theta$ , and azimuthal,  $\varphi$ , angles of the spacers, excluding

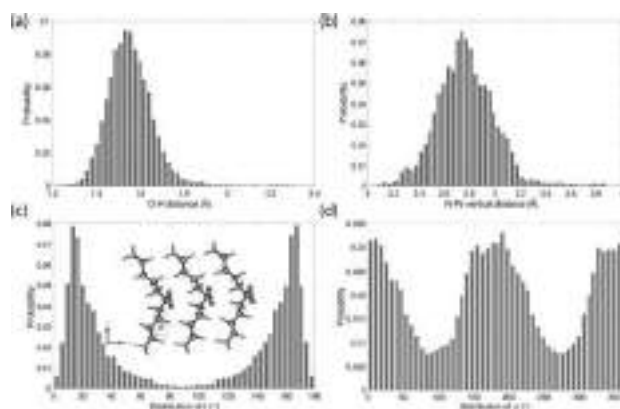


**Figure 6.** Thermal distributions at  $T = 300$  K from 6 ps first-principles MD simulations. (a) Histogram of intermolecular O...H-bond distances between COOH groups of adjacent spacers of opposite layers, (b) Distribution of vertical penetration distances of  $\text{NH}_3^+$  into the inorganic slab (measured as Pb–N distance along the normal of the closest  $\text{PbI}_2$  plane). Distribution of (c) polar,  $\theta$ , and (d) azimuthal,  $\phi$ , angles of AVA in the spacer layers. The polar angle (denoted in the inset) is defined as the inclination of AVA with respect to the vertical  $c$  axis, and the azimuthal angle indicates the inclination of AVA (projection onto the  $ab$  plane) with respect to the  $a$  axis.

translation. The polar angle refers to the inclination of AVA with respect to the vertical axis, while the azimuthal angle is the planar deviation of AVA from the  $x$  axis. The polar angle distribution confirms that the spacers manifest a preferred orientation with respect to the vertical axis (Figure 6c) while showing a certain degree of rotation, yet maintaining their initial H-bond pattern (Figure 6d).

The effects of these structural properties on the long-term stability of the material were investigated by comparing the reference and  $\text{FAPbI}_3(\text{AVAI})_{0.25}$ -based PSC under continuous 1.5 G irradiation ( $100 \text{ mW}\cdot\text{cm}^{-2}$ ) and maximum power point tracking in a nitrogen atmosphere at room temperature. Figure S7 shows that the ambient stability of the  $\text{FAPbI}_3(\text{AVAI})_{0.25}$ -based device is greatly improved as it retains 90% of its initial PCE up to 300 h. On the contrary, the PCE of the undoped  $\alpha$ - $\text{FAPbI}_3$  device decays rapidly and reaches 10% of its initial efficiency within 100 h.

## CONCLUSIONS

In conclusion, we have demonstrated that the bifunctional organic molecule AVAI can act as a molecular modulator that improves the stability of  $\alpha$ - $\text{FAPbI}_3$ . We have elucidated and illustrated the atomic-level interaction between AVAI and the perovskite by applying multinuclear and two-dimensional solid-state NMR spectroscopy. We have found that AVAI displays a structure-directing role by forming hydrogen bonds with the perovskite lattice through its  $\text{NH}_3^+$  group, while its COOH end is involved in dynamic hydrogen bonding with other AVA moieties, as further corroborated by DFT-based molecular dynamics simulations of fully periodic RP phases. These molecular features yield improved morphological and optoelectronic quality of the films. In particular, transient absorption measurements reveal significantly enhanced charge carrier lifetimes in the AVA-doped perovskite. As a result, the mesoscopic heterojunction photovoltaic solar cell demonstrated a high PCE of 18.94% and high operational stability after 300 h under continuous illumination. Our work illustrates that

molecular modulation of 3D perovskites using bifunctional modifiers is an effective way to simultaneously achieve high performing and stable  $\text{FAPbI}_3$ -based PSCs.

## ASSOCIATED CONTENT

### Supporting Information

The Supporting Information is available free of charge on the ACS Publications website at DOI: 10.1021/jacs.9b07381.

Further experimental details, MPP tracking,  $J-V$  statistics, SEM images, XPS spectra, additional NMR spectra, and stability measurements (PDF)

## AUTHOR INFORMATION

### Corresponding Authors

\*[djk47@cam.ac.uk](mailto:djk47@cam.ac.uk)  
 \*[lyndon.emsley@epfl.ch](mailto:lyndon.emsley@epfl.ch)  
 \*[michael.gratzel@epfl.ch](mailto:michael.gratzel@epfl.ch)

### ORCID

Dominik J. Kubicki: 0000-0002-9231-6779  
 Daniel Prochowicz: 0000-0002-5003-5637  
 Farzaneh Jahanbakhshi: 0000-0001-7113-2746  
 Jovana V. Milić: 0000-0002-9965-3460  
 Dan Ren: 0000-0003-3738-6421  
 Abdulrahman Albadri: 0000-0003-1579-0474  
 Mohammad Hayal Alotaibi: 0000-0001-5435-5200  
 Jacques-E. Moser: 0000-0003-0747-4666  
 Ursula Rothlisberger: 0000-0002-1704-8591  
 Lyndon Emsley: 0000-0003-1360-2572  
 Michael Grätzel: 0000-0002-0068-0195

### Present Address

◆D.J.K.: University of Cambridge, Cavendish Laboratory, J J Thomson Avenue, Cambridge CB3 0HE, United Kingdom.

### Notes

The authors declare no competing financial interest.

## ACKNOWLEDGMENTS

A.Q.A and E.A. gratefully acknowledge King Abdulaziz City for Science and Technology (KACST) for the fellowship. M.G. and S.M.Z. thank the King Abdulaziz City for Science and Technology (KACST) for the financial support. D.J.K. and L.E. acknowledge Swiss National Science Foundation Grants No. 200021\_160112 and 200020\_178860. D.P. acknowledges the financial support from the HOMING program of the Foundation for Polish Science cofinanced by the European Union under the European Regional Development Fund (POIR.04.04.00-00-5EE7/18-00). U.R. acknowledges funding from the Swiss National Science Foundation via the NCCR MUST, the Sinergia grant EPISODE and individual grants.

## REFERENCES

- (1) Kojima, A.; Teshima, K.; Shirai, Y.; Miyasaka, T. Organometal Halide Perovskites as Visible-Light Sensitizers for Photovoltaic Cells. *J. Am. Chem. Soc.* **2009**, *131*, 6050–6051.
- (2) Jeon, N. J.; Na, H.; Jung, E. H.; Yang, T.-Y.; Lee, Y. G.; Kim, G.; Shin, H.-W.; Il Seok, S.; Lee, J.; Seo, J. A Fluorene-Terminated Hole-Transporting Material for Highly Efficient and Stable Perovskite Solar Cells. *Nat. Energy* **2018**, *3*, 682–689.
- (3) Stranks, S. D.; Eperon, G. E.; Grancini, G.; Menelaou, C.; Alcocer, M. J. P.; Leijtens, T.; Herz, L. M.; Petrozza, A.; Snaith, H. J. Electron-Hole Diffusion Lengths Exceeding 1 Micrometer in an

Organometal Trihalide Perovskite Absorber. *Science* **2013**, *342*, 341–344.

(4) Wehrenfennig, C.; Eperon, G. E.; Johnston, M. B.; Snaith, H. J.; Herz, L. M. High Charge Carrier Mobilities and Lifetimes in Organolead Trihalide Perovskites. *Adv. Mater.* **2014**, *26*, 1584–1589.

(5) Shi, D.; Adinolfi, V.; Comin, R.; Yuan, M.; Alarousu, E.; Buin, A.; Chen, Y.; Hoogland, S.; Rothenberger, A.; Katsiev, K.; Losovyj, Y.; Zhang, X.; Dowben, P. A.; Mohammed, O. F.; Sargent, E. H.; Bakr, O. M. Low Trap-State Density and Long Carrier Diffusion in Organolead Trihalide Perovskite Single Crystals. *Science* **2015**, *347*, 519–522.

(6) Dong, Q.; Fang, Y.; Shao, Y.; Mulligan, P.; Qiu, J.; Cao, L.; Huang, J. Electron-Hole Diffusion Lengths > 175 nm in Solution-Grown CH<sub>3</sub>NH<sub>3</sub>PbI<sub>3</sub> Single Crystals. *Science* **2015**, *347*, 967–970.

(7) Grätzel, M. The Light and Shade of Perovskite Solar Cells. *Nat. Mater.* **2014**, *13*, 838–842.

(8) Seok, S. I.; Grätzel, M.; Park, N.-G. Methodologies toward Highly Efficient Perovskite Solar Cells. *Small* **2018**, *14*, 1704177.

(9) Shockley, W.; Queisser, H. J. Detailed Balance Limit of Efficiency of *p-n* Junction Solar Cells. *J. Appl. Phys.* **1961**, *32*, 510–519.

(10) Stoumpos, C. C.; Malliakas, C. D.; Kanatzidis, M. G. Semiconducting Tin and Lead Iodide Perovskites with Organic Cations: Phase Transitions, High Mobilities, and Near-Infrared Photoluminescent Properties. *Inorg. Chem.* **2013**, *52*, 9019–9038.

(11) Jeon, N. J.; Noh, J. H.; Kim, Y. C.; Yang, W. S.; Ryu, S.; Seok, S. I. Solvent Engineering for High-Performance Inorganic–Organic Hybrid Perovskite Solar Cells. *Nat. Mater.* **2014**, *13*, 897–903.

(12) Eperon, G. E.; Stranks, S. D.; Menelaou, C.; Johnston, M. B.; Herz, L. M.; Snaith, H. J. Formamidinium Lead Trihalide: A Broadly Tunable Perovskite for Efficient Planar Heterojunction Solar Cells. *Energy Environ. Sci.* **2014**, *7*, 982.

(13) Pellet, N.; Gao, P.; Gregori, G.; Yang, T.-Y.; Nazeeruddin, M. K.; Maier, J.; Grätzel, M. Mixed–Organic–Cation Perovskite Photovoltaics for Enhanced Solar-Light Harvesting. *Angew. Chem., Int. Ed.* **2014**, *53*, 3151–3157.

(14) Ji, F.; Wang, L.; Pang, S.; Gao, P.; Xu, H.; Xie, G.; Zhang, J.; Cui, G. A Balanced Cation Exchange Reaction toward Highly Uniform and Pure Phase FA<sub>1-x</sub>MA<sub>x</sub>PbI<sub>3</sub> Perovskite Films. *J. Mater. Chem. A* **2016**, *4*, 14437–14443.

(15) Prochowicz, D.; Yadav, P.; Saliba, M.; Sasaki, M.; Zakeeruddin, S. M.; Lewiński, J.; Grätzel, M. Mechanochemical Synthesis of Pure Phase Mixed–Cation MA<sub>x</sub>FA<sub>1-x</sub>PbI<sub>3</sub> Hybrid Perovskites: Photovoltaic Performance and Electrochemical Properties. *Sustain. Energy Fuels* **2017**, *1*, 689–693.

(16) Liu, T.; Zong, Y.; Zhou, Y.; Yang, M.; Li, Z.; Game, O. S.; Zhu, K.; Zhu, R.; Gong, Q.; Padture, N. P. High-Performance Formamidinium-Based Perovskite Solar Cells via Microstructure-Mediated  $\delta$ -to- $\alpha$  Phase Transformation. *Chem. Mater.* **2017**, *29*, 3246–3250.

(17) Lee, J.-W.; Kim, D.-H.; Kim, H.-S.; Seo, S.-W.; Cho, S. M.; Park, N.-G. Formamidinium and Cesium Hybridization for Photo- and Moisture-Stable Perovskite Solar Cell. *Adv. Energy Mater.* **2015**, *5*, 1501310.

(18) Yi, C.; Luo, J.; Meloni, S.; Boziki, A.; Ashari-Astani, N.; Grätzel, M.; Zakeeruddin, S. M.; Röthlisberger, U.; Grätzel, M. Entropic Stabilization of Mixed A-Cation ABX<sub>3</sub> Metal Halide Perovskites for High Performance Perovskite Solar Cells. *Energy Environ. Sci.* **2016**, *9*, 656–662.

(19) Yang, Z.; Chueh, C.-C.; Liang, P.-W.; Crump, M.; Lin, F.; Zhu, Z.; Jen, A. K.-Y. Effects of Formamidinium and Bromide Ion Substitution in Methylammonium Lead Triiodide toward High-Performance Perovskite Solar Cells. *Nano Energy* **2016**, *22*, 328–337.

(20) Prochowicz, D.; Yadav, P.; Saliba, M.; Kubicki, D. J.; Tavakoli, M. M.; Zakeeruddin, S. M.; Lewiński, J.; Emsley, L.; Grätzel, M. One-Step Mechanochemical Incorporation of an Insoluble Cesium Additive for High Performance Planar Heterojunction Solar Cells. *Nano Energy* **2018**, *49*, 523–528.

(21) Chen, P.; Bai, Y.; Lyu, M.; Yun, J.-H.; Hao, M.; Wang, L. Progress and Perspective in Low-Dimensional Metal Halide Perovskites for Optoelectronic Applications. *Sol. RRL* **2018**, *2*, 1700186.

(22) Etgar, L. The Merit of Perovskite's Dimensionality; Can This Replace the 3D Halide Perovskite? *Energy Environ. Sci.* **2018**, *11*, 234–242.

(23) Yan, J.; Qiu, W.; Wu, G.; Heremans, P.; Chen, H. Recent Progress in 2D/Quasi-2D Layered Metal Halide Perovskites for Solar Cells. *J. Mater. Chem. A* **2018**, *6*, 11063–11077.

(24) Ma, C.; Leng, C.; Ji, Y.; Wei, X.; Sun, K.; Tang, L.; Yang, J.; Luo, W.; Li, C.; Deng, Y.; Feng, S.; Shen, J.; Lu, S.; Du, C.; Shi, H. 2D/3D Perovskite Hybrids as Moisture-Tolerant and Efficient Light Absorbers for Solar Cells. *Nanoscale* **2016**, *8*, 18309–18314.

(25) Yao, K.; Wang, X.; Xu, Y.; Li, F. A General Fabrication Procedure for Efficient and Stable Planar Perovskite Solar Cells: Morphological and Interfacial Control by in-Situ-Generated Layered Perovskite. *Nano Energy* **2015**, *18*, 165–175.

(26) Smith, I. C.; Hoke, E. T.; Solis-Ibarra, D.; McGehee, M. D.; Karunadasa, H. I. A Layered Hybrid Perovskite Solar-Cell Absorber with Enhanced Moisture Stability. *Angew. Chem.* **2014**, *126*, 11414–11417.

(27) Bai, Y.; Xiao, S.; Hu, C.; Zhang, T.; Meng, X.; Lin, H.; Yang, Y.; Yang, S. Dimensional Engineering of a Graded 3D-2D Halide Perovskite Interface Enables Ultrahigh  $V_{oc}$  Enhanced Stability in the *p-i-n* Photovoltaics. *Adv. Energy Mater.* **2017**, *7*, 1701038.

(28) Chen, P.; Bai, Y.; Wang, S.; Lyu, M.; Yun, J.-H.; Wang, L. In Situ Growth of 2D Perovskite Capping Layer for Stable and Efficient Perovskite Solar Cells. *Adv. Funct. Mater.* **2018**, *28*, 1706923.

(29) Cao, D. H.; Stoumpos, C. C.; Farha, O. K.; Hupp, J. T.; Kanatzidis, M. G. 2D Homologous Perovskites as Light-Absorbing Materials for Solar Cell Applications. *J. Am. Chem. Soc.* **2015**, *137*, 7843–7850.

(30) Stoumpos, C. C.; Cao, D. H.; Clark, D. J.; Young, J.; Rondinelli, J. M.; Jang, J. I.; Hupp, J. T.; Kanatzidis, M. G. Ruddlesden-Popper Hybrid Lead Iodide Perovskite 2D Homologous Semiconductors. *Chem. Mater.* **2016**, *28*, 2852–2867.

(31) Zhang, X.; Munir, R.; Xu, Z.; Liu, Y.; Tsai, H.; Nie, W.; Li, J.; Niu, T.; Smilgies, D.-M.; Kanatzidis, M. G.; Mohite, A. D.; Zhao, K.; Amassian, A.; Liu, S. F. Phase Transition Control for High Performance Ruddlesden-Popper Perovskite Solar Cells. *Adv. Mater.* **2018**, *30*, 1707166.

(32) Li, X.; Ibrahim Dar, M.; Yi, C.; Luo, J.; Tschumi, M.; Zakeeruddin, S. M.; Nazeeruddin, M. K.; Han, H.; Grätzel, M. Improved Performance and Stability of Perovskite Solar Cells by Crystal Crosslinking with Alkylphosphonic Acid  $\omega$ -Ammonium Chlorides. *Nat. Chem.* **2015**, *7*, 703–711.

(33) Zhang, T.; Xie, L.; Chen, L.; Guo, N.; Li, G.; Tian, Z.; Mao, B.; Zhao, Y. In Situ Fabrication of Highly Luminescent Bifunctional Amino Acid Crosslinked 2D/3D NH<sub>3</sub>C<sub>4</sub>H<sub>9</sub>COO(CH<sub>3</sub>NH<sub>3</sub>PbBr<sub>3</sub>)<sub>n</sub> Perovskite Films. *Adv. Funct. Mater.* **2017**, *27*, 1603568.

(34) Grancini, G.; Roldán-Carmona, C.; Zimmermann, I.; Mosconi, E.; Lee, X.; Martineau, D.; Narbey, S.; Oswald, F.; De Angelis, F.; Graetzel, M.; Nazeeruddin, M. K. One-Year Stable Perovskite Solar Cells by 2D/3D Interface Engineering. *Nat. Commun.* **2017**, *8*, 15684.

(35) Kayesh, M. E.; Matsuishi, K.; Kaneko, R.; Kazaoui, S.; Lee, J.-J.; Noda, T.; Islam, A. Coadditive Engineering with 5-Ammonium Valeric Acid Iodide for Efficient and Stable Sn Perovskite Solar Cells. *ACS Energy Lett.* **2019**, *4*, 278–284.

(36) Ye, T.; Bruno, A.; Han, G.; Koh, T. M.; Li, J.; Jamaludin, N. F.; Soci, C.; Mhaisalkar, S. G.; Leong, W. L. Efficient and Ambient-Air-Stable Solar Cell with Highly Oriented 2D@3D Perovskites. *Adv. Funct. Mater.* **2018**, *28*, 1801654.

(37) Hu, Y.; Zhang, Z.; Mei, A.; Jiang, Y.; Hou, X.; Wang, Q.; Du, K.; Rong, Y.; Zhou, Y.; Xu, G.; Han, H. Improved Performance of Printable Perovskite Solar Cells with Bifunctional Conjugated Organic Molecule. *Adv. Mater.* **2018**, *30*, 1705786.

(38) Pan, J.; Shang, Y.; Yin, J.; De Bastiani, M.; Peng, W.; Dursun, I.; Sinatra, L.; El-Zohry, A. M.; Hedhili, M. N.; Emwas, A.-H.; Mohammed, O. F.; Ning, Z.; Bakr, O. M. Bidentate Ligand-Passivated

CsPbI<sub>3</sub> Perovskite Nanocrystals for Stable Near-Unity Photoluminescence Quantum Yield and Efficient Red Light-Emitting Diodes. *J. Am. Chem. Soc.* **2018**, *140*, 562–565.

(39) Krieg, F.; Ochsenbein, S. T.; Yakunin, S.; ten Brinck, S.; Aellen, P.; Süess, A.; Clerc, B.; Guggisberg, D.; Nazarenko, O.; Shynkarenko, Y.; Kumar, S.; Shih, C.-J.; Infante, I.; Kovalenko, M. V. Colloidal CsPbX<sub>3</sub> (X = Cl, Br, I) Nanocrystals 2.0: Zwitterionic Capping Ligands for Improved Durability and Stability. *ACS Energy Lett.* **2018**, *3*, 641–646.

(40) Zheng, X.; Troughton, J.; Gasparini, N.; Lin, Y.; Wei, M.; Hou, Y.; Liu, J.; Song, K.; Chen, Z.; Yang, C.; Turedi, B.; Alsalloum, A. Y.; Pan, J.; Chen, J.; Zhumekenov, A. A.; Anthopoulos, T. D.; Han, Y.; Baran, D.; Mohammed, O. F.; Sargent, E. H.; Bakr, O. M. Quantum Dots Supply Bulk- and Surface-Passivation Agents for Efficient and Stable Perovskite Solar Cells. *Joule* **2019**, *3*, 1963–1976.

(41) Li, G.; Zhang, T.; Xu, F.; Zhao, Y. A Facile Deposition of Large Grain and Phase Pure  $\alpha$ -FAPbI<sub>3</sub> for Perovskite Solar Cells via a Flash Crystallization. *Mater. Today Energy* **2017**, *5*, 293–298.

(42) Niu, T.; Lu, J.; Tang, M.-C.; Barrit, D.; Smilgies, D.-M.; Yang, Z.; Li, J.; Fan, Y.; Luo, T.; McCulloch, I.; Amassian, A.; Liu, S. F.; Zhao, K. High Performance Ambient-Air-Stable FAPbI<sub>3</sub> Perovskite Solar Cells with Molecule-Passivated Ruddlesden-Popper/3D Heterostructured Film. *Energy Environ. Sci.* **2018**, *11*, 3358–3366.

(43) Snaith, H. J.; Abate, A.; Ball, J. M.; Eperon, G. E.; Leijtens, T.; Noel, N. K.; Stranks, S. D.; Wang, J. T.-W.; Wojciechowski, K.; Zhang, W. Anomalous Hysteresis in Perovskite Solar Cells. *J. Phys. Chem. Lett.* **2014**, *5*, 1511–1515.

(44) Shih, Y.-C.; Lan, Y.-B.; Li, C.-S.; Hsieh, H.-C.; Wang, L.; Wu, C.-I.; Lin, K.-F. Amino-Acid-Induced Preferential Orientation of Perovskite Crystals for Enhancing Interfacial Charge Transfer and Photovoltaic Performance. *Small* **2017**, *13*, 1604305.

(45) Kanemitsu, Y. Luminescence Spectroscopy of Lead-Halide Perovskites: Materials Properties and Application as Photovoltaic Devices. *J. Mater. Chem. C* **2017**, *5*, 3427–3437.

(46) Prochowicz, D.; Franckevičius, M.; Cieślak, A. M.; Zakeeruddin, S. M.; Grätzel, M.; Lewiński, J. Mechanochemical Synthesis of the Hybrid Perovskite CH<sub>3</sub>NH<sub>3</sub>PbI<sub>3</sub>: Characterization and the Corresponding Solar Cell Efficiency. *J. Mater. Chem. A* **2015**, *3*, 20772–20777.

(47) Rosales, B. A.; Wei, L.; Vela, J. Synthesis and Mixing of Complex Halide Perovskites by Solvent-Free Solid-State Methods. *J. Solid State Chem.* **2019**, *271*, 206–215.

(48) Rosales, B. A.; Men, L.; Cady, S. D.; Hanrahan, M. P.; Rossini, A. J.; Vela, J. Persistent Dopants and Phase Segregation in Organolead Mixed-Halide Perovskites. *Chem. Mater.* **2016**, *28*, 6848–6859.

(49) Roiland, C.; Trippé-Allard, G.; Jemli, K.; Alonso, B.; Ameline, J.-C.; Gautier, R.; Bataille, T.; Le Pollès, L.; Deleporte, E.; Even, J.; Katan, C. Multinuclear NMR as a Tool for Studying Local Order and Dynamics in CH<sub>3</sub>NH<sub>3</sub>PbX<sub>3</sub> (X = Cl, Br, I) Hybrid Perovskites. *Phys. Chem. Chem. Phys.* **2016**, *18*, 27133–27142.

(50) Kubicki, D. J.; Prochowicz, D.; Hofstetter, A.; Péchy, P.; Zakeeruddin, S. M.; Grätzel, M.; Emsley, L. Cation Dynamics in Mixed-Cation (MA)<sub>x</sub>(FA)<sub>1-x</sub>PbI<sub>3</sub> Hybrid Perovskites from Solid-State NMR. *J. Am. Chem. Soc.* **2017**, *139*, 10055–10061.

(51) Kubicki, D. J.; Prochowicz, D.; Hofstetter, A.; Zakeeruddin, S. M.; Grätzel, M.; Emsley, L. Phase Segregation in Cs-, Rb- and K-Doped Mixed-Cation (MA)<sub>x</sub>(FA)<sub>1-x</sub>PbI<sub>3</sub> Hybrid Perovskites from Solid-State NMR. *J. Am. Chem. Soc.* **2017**, *139*, 14173–14180.

(52) Fabini, D. H.; Siaw, T. A.; Stoumpos, C. C.; Laurita, G.; Olds, D.; Page, K.; Hu, J. G.; Kanatzidis, M. G.; Han, S.; Seshadri, R. Universal Dynamics of Molecular Reorientation in Hybrid Lead Iodide Perovskites. *J. Am. Chem. Soc.* **2017**, *139*, 16875–16884.

(53) Kubicki, D. J.; Prochowicz, D.; Hofstetter, A.; Zakeeruddin, S. M.; Grätzel, M.; Emsley, L. Phase Segregation in Potassium-Doped Lead Halide Perovskites from <sup>39</sup>K Solid-State NMR at 21.1 T. *J. Am. Chem. Soc.* **2018**, *140*, 7232–7238.

(54) Karmakar, A.; Askar, A. M.; Bernard, G. M.; Terskikh, V. V.; Ha, M.; Patel, S.; Shankar, K.; Michaelis, V. K. Mechanochemical Synthesis of Methylammonium Lead Mixed-Halide Perovskites:

Unraveling the Solid-Solution Behavior Using Solid-State NMR. *Chem. Mater.* **2018**, *30*, 2309–2321.

(55) Karmakar, A.; Dodd, M. S.; Agnihotri, S.; Ravera, E.; Michaelis, V. K. Cu(II)-Doped Cs<sub>2</sub>SbAgCl<sub>6</sub> Double Perovskite: A Lead-Free, Low-Bandgap Material. *Chem. Mater.* **2018**, *30*, 8280–8290.

(56) Franssen, W. M. J.; Bruijnaers, B. J.; Portengen, V. H. L.; Kentgens, A. P. M. Dimethylammonium Incorporation in Lead Acetate Based MAPbI<sub>3</sub> Perovskite Solar Cells. *ChemPhysChem* **2018**, *19*, 3107–3115.

(57) Kubicki, D. J.; Prochowicz, D.; Hofstetter, A.; Saski, M.; Yadav, P.; Bi, D.; Pellet, N.; Lewiński, J.; Zakeeruddin, S. M.; Grätzel, M.; Emsley, L. Formation of Stable Mixed Guanidinium-Methylammonium Phases with Exceptionally Long Carrier Lifetimes for High-Efficiency Lead Iodide-Based Perovskite Photovoltaics. *J. Am. Chem. Soc.* **2018**, *140*, 3345–3351.

(58) Askar, A. M.; Karmakar, A.; Bernard, G. M.; Ha, M.; Terskikh, V. V.; Wiltshire, B. D.; Patel, S.; Fleet, J.; Shankar, K.; Michaelis, V. K. Composition-Tunable Formamidinium Lead Mixed Halide Perovskites via Solvent-Free Mechanochemical Synthesis: Decoding the Pb Environments Using Solid-State NMR Spectroscopy. *J. Phys. Chem. Lett.* **2018**, *9*, 2671–2677.

(59) Franssen, W. M. J.; Kentgens, A. P. M. Solid-State NMR of Hybrid Halide Perovskites. *Solid State Nucl. Magn. Reson.* **2019**, *100*, 36–44.

(60) Kubicki, D. J.; Prochowicz, D.; Pinon, A.; Stevanato, G.; Hofstetter, A.; Zakeeruddin, S. M.; Grätzel, M.; Emsley, L. Doping and Phase Segregation in Mn<sup>2+</sup>- and Co<sup>2+</sup>-Doped Lead Halide Perovskites from <sup>133</sup>Cs and <sup>1</sup>H NMR Relaxation Enhancement. *J. Mater. Chem. A* **2019**, *7*, 2326–2333.

(61) Xiang, W.; Wang, Z.; Kubicki, D. J.; Tress, W.; Luo, J.; Prochowicz, D.; Akin, S.; Emsley, L.; Zhou, J.; Dietler, G.; Grätzel, M.; Hagfeldt, A. Europium-Doped CsPbI<sub>2</sub>Br for Stable and Highly Efficient Inorganic Perovskite Solar Cells. *Joule* **2019**, *3*, 205–214.

(62) Bi, D.; Li, X.; Milić, J. V.; Kubicki, D. J.; Pellet, N.; Luo, J.; LaGrange, T.; Mettraux, P.; Emsley, L.; Zakeeruddin, S. M.; Grätzel, M. Multifunctional Molecular Modulators for Perovskite Solar Cells with over 20% Efficiency and High Operational Stability. *Nat. Commun.* **2018**, *9*, 4482.

(63) Tavakoli, M. M.; Tress, W.; Milić, J. V.; Kubicki, D.; Emsley, L.; Grätzel, M. Addition of Adamantylammonium Iodide to Hole Transport Layers Enables Highly Efficient and Electroluminescent Perovskite Solar Cells. *Energy Environ. Sci.* **2018**, *11*, 3310–3320.

(64) Milić, J. V.; Im, J.; Kubicki, D. J.; Ummadisingu, A.; Seo, J.; Li, Y.; Ruiz Preciado, M. A.; Dar, M. I.; Zakeeruddin, S. M.; Emsley, L.; Grätzel, M. Supramolecular Engineering for Formamidinium Based Layered 2D Perovskite Solar Cells: Structural Complexity and Dynamics Revealed by Solid State NMR Spectroscopy. *Adv. Energy Mater.* **2019**, *9*, 1900284.

(65) Chen, J.; Seo, J.-Y.; Park, N.-G. Simultaneous Improvement of Photovoltaic Performance and Stability by In Situ Formation of 2D Perovskite at (FAPbI<sub>3</sub>)<sub>0.88</sub>(CsPbBr<sub>3</sub>)<sub>0.12</sub>/CuSCN Interface. *Adv. Energy Mater.* **2018**, *8*, 1702714.

(66) Willett, R. D.; Maxcy, K. R.; Twamley, B. Polytypism in Columnar Group 14 Halide Salts: Structures of (Et<sub>2</sub>NH<sub>2</sub>)<sub>3</sub>Pb<sub>3</sub>X<sub>9</sub> · nH<sub>2</sub>O (X = Cl, Br) and (β-Alanine)<sub>2</sub>Sn<sub>4</sub>. *Inorg. Chem.* **2002**, *41*, 7024–7030.

(67) Elena, B.; Pintacuda, G.; Mifsud, N.; Emsley, L. Molecular Structure Determination in Powders by NMR Crystallography from Proton Spin Diffusion. *J. Am. Chem. Soc.* **2006**, *128*, 9555–9560.

(68) Ke, W.; Stoumpos, C. C.; Zhu, M.; Mao, L.; Spanopoulos, I.; Liu, J.; Kontsevoi, O. Y.; Chen, M.; Sarma, D.; Zhang, Y.; Wasielewski, M. R.; Kanatzidis, M. G. Enhanced Photovoltaic Performance and Stability with a New Type of Hollow 3D Perovskite {en}FASnI<sub>3</sub>. *Sci. Adv.* **2017**, *3*, No. e1701293.

(69) Spanopoulos, I.; Ke, W.; Stoumpos, C. C.; Schueller, E. C.; Kontsevoi, O. Y.; Seshadri, R.; Kanatzidis, M. G. Unraveling the Chemical Nature of the 3D “Hollow” Hybrid Halide Perovskites. *J. Am. Chem. Soc.* **2018**, *140*, 5728–5742.

(70) *NMR of Quadrupolar Nuclei in Solid Materials*; Wasylshen, R. E., Ashbrook, S. E., Wimperis, S., Eds.; Wiley: Hoboken, NJ, 2012.

(71) Long, J. R.; Sun, B. Q.; Bowen, A.; Griffin, R. G. Molecular Dynamics and Magic Angle Spinning NMR. *J. Am. Chem. Soc.* **1994**, *116*, 11950–11956.

(72) Mercier, N.  $(\text{HO}_2\text{C}(\text{CH}_2)_3\text{NH}_3)_2(\text{CH}_3\text{NH}_3)\text{Pb}_2\text{I}_7$ : A Predicted Non-Centrosymmetrical Structure Built up from Carboxylic Acid Supramolecular Synthons and Bilayer Perovskite Sheets. *CrystEngComm* **2005**, *7*, 429.

(73) Li, T.; Dunlap-Shohl, W. A.; Reinheimer, E. W.; Le Magueres, P.; Mitzi, D. B. Melting Temperature Suppression of Layered Hybrid Lead Halide Perovskites via Organic Ammonium Cation Branching. *Chem. Sci.* **2019**, *10*, 1168–1175.

(74) Fu, Y.; Wu, T.; Wang, J.; Zhai, J.; Shearer, M. J.; Zhao, Y.; Hamers, R. J.; Kan, E.; Deng, K.; Zhu, X.-Y.; Jin, S. Stabilization of the Metastable Lead Iodide Perovskite Phase via Surface Functionalization. *Nano Lett.* **2017**, *17*, 4405–4414.

#### ■ NOTE ADDED IN PROOF

While the article was in press, we became aware of a study using BA, PEA, and 4-fluorophenylethylammonium hydroiodides to stabilize the 3D perovskite structure of FAPbI<sub>3</sub> in nanostructures and thin films, which we have now referenced for completeness.<sup>74</sup>



# Guanine-Stabilized Formamidinium Lead Iodide Perovskites

Li Hong, Jovana V. Milić, Paramvir Ahlawat, Marko Mladenović, Dominik J. Kubicki, Farzaneh Jahanabkshi, Dan Ren, María C. Gélvez-Rueda, Marco A. Ruiz-Preciado, Amita Ummadisingu, Yuhang Liu, Chengbo Tian, Linfeng Pan, Shaik M. Zakeeruddin, Anders Hagfeldt, Ferdinand C. Grozema, Ursula Rothlisberger, Lyndon Emsley, Hongwei Han,\* and Michael Graetzel\*

**Abstract:** Formamidinium (FA) lead iodide perovskite materials feature promising photovoltaic performances and superior thermal stabilities. However, conversion of the perovskite  $\alpha$ -FAPbI<sub>3</sub> phase to the thermodynamically stable yet photovoltaically inactive  $\delta$ -FAPbI<sub>3</sub> phase compromises the photovoltaic performance. A strategy is presented to address this challenge by using low-dimensional hybrid perovskite materials comprising guaninium (G) organic spacer layers that act as stabilizers of the three-dimensional  $\alpha$ -FAPbI<sub>3</sub> phase. The underlying mode of interaction at the atomic level is unraveled by means of solid-state nuclear magnetic resonance spectroscopy, X-ray crystallography, transmission electron microscopy, molecular dynamics simulations, and DFT calculations. Low-dimensional-phase-containing hybrid FAPbI<sub>3</sub> perovskite solar cells are obtained with improved performance and enhanced long-term stability.

## Introduction

Hybrid perovskite solar cells (PSCs) are a new generation of thin-film photovoltaic technologies featuring hybrid organic–inorganic perovskite semiconductors.<sup>[1–4]</sup> They are based on AMX<sub>3</sub> stoichiometry composed of a monovalent cation A (Cs<sup>+</sup>, methylammonium (MA) CH<sub>3</sub>NH<sub>3</sub><sup>+</sup>, formamidinium (FA) CH(NH<sub>2</sub>)<sub>2</sub><sup>+</sup>, or guanidinium (GUA) C(NH<sub>2</sub>)<sub>3</sub><sup>+</sup>), a metal M (Pb<sup>2+</sup>, Sn<sup>2+</sup>), and a halide X (Cl<sup>-</sup>, Br<sup>-</sup>, or I<sup>-</sup>). While hybrid perovskites display remarkable solar-to-electric power conversion efficiencies (PCE), practical applications are still hampered by their instability towards ambient air and

moisture as well as thermal and light stress.<sup>[2,3]</sup> PSCs featuring highly polar MA organic cations (dipole moment of 2.29 D) are more sensitive to moisture and polar solvents, posing the risk of long term instability.<sup>[5]</sup> Alternatively, hybrid perovskite materials based on FA organic cation (dipole moment of 0.21 D) are characterized by a more homogenous distribution of the electron density owing to resonance stabilization that reduces their reactivity, rendering the corresponding material more stable, in particular against thermal stress.<sup>[5,6]</sup> Moreover, the larger FA cation size increases the lattice constant and the degree of space filling,<sup>[7,8]</sup> and its perovskite structure is further stabilized by stronger hydrogen bonding as compared to the MA analogues.<sup>[8]</sup> However, FAPbI<sub>3</sub> exists in two phases, namely the yellow  $\delta$ -FAPbI<sub>3</sub>, which is more thermodynamically stable at room temperature, and the high-temperature black  $\alpha$ -FAPbI<sub>3</sub> perovskite phase that is of interest to photovoltaic applications.<sup>[9,10]</sup> Stabilizing the black  $\alpha$ -FAPbI<sub>3</sub> perovskite phase without significantly altering its optoelectronic properties remains an ongoing challenge that could boost further optoelectronic applications. This has been predominantly achieved by using Cs<sup>+</sup> cations,<sup>[11,12]</sup> which however increase their band gap. It has been recently shown that a number of FA-based layered low-dimensional perovskites can stabilize FAPbI<sub>3</sub> perovskite solar cells via their spacer layer.<sup>[13–15]</sup> However, these early examples mainly employ electronically insulating organic spacers, such as the prototypical butylammonium (BA) and phenylethylammonium (PEA),<sup>[13,14]</sup> as well as more elaborate analogues, such as the 1-adamantanemethylammonium (ADA) and 1,4-phenyl-

[\*] L. Hong, Dr. J. V. Milić, Dr. D. J. Kubicki, Dr. D. Ren, Dr. M. A. Ruiz-Preciado, Dr. A. Ummadisingu, Dr. Y. Liu, Dr. S. M. Zakeeruddin, Prof. M. Graetzel  
Laboratory of Photonics and Interfaces, Institut des Sciences et Ingénierie Chimiques, École Polytechnique Fédérale de Lausanne  
1015 Lausanne (Switzerland)  
E-mail: michael.graetzel@epfl.ch



L. Hong, C. Tian, Prof. H. Han  
Wuhan National Lab for Optoelectronics  
Wuhan, 430074 Hubei (China)  
E-mail: hongwei.han@mail.hust.edu.cn

P. Ahlawat, Dr. M. Mladenović, F. Jahanabkshi,  
Prof. U. Rothlisberger  
Laboratory of Computational Chemistry and Biochemistry, Institut des Sciences et Ingénierie Chimiques, École Polytechnique Fédérale de Lausanne  
1015 Lausanne (Switzerland)

Dr. D. J. Kubicki, Prof. L. Emsley  
Laboratory of Magnetic Resonance, Institut des Sciences et Ingénierie Chimiques, École Polytechnique Fédérale de Lausanne  
1015 Lausanne (Switzerland)

M. C. Gélvez-Rueda, Prof. F. C. Grozema  
Delft University of Technology  
2629 HZ Delft (The Netherlands)

L. Pan, Prof. A. Hagfeldt  
Laboratory of Photomolecular Science, Institut des Sciences et Ingénierie Chimiques, École Polytechnique Fédérale de Lausanne  
1015 Lausanne (Switzerland)

 Supporting information and the ORCID identification number(s) for the author(s) of this article can be found under:  
 <https://doi.org/10.1002/anie.201912051>.

enedimethylammonium (PDMA),<sup>[15,16]</sup> with photovoltaic performances that are inferior to the 3D perovskites. Alternatively, a number of 2D/3D heterostructures have been developed employing the 2D structures as stabilizing layers,<sup>[11,12]</sup> but this effort has been mainly focused on mixed A-cation compositions. Moreover, the contribution of the low dimensional layer to the overall performance is limited, particularly as a result of the insulating character of the organic spacer layers.<sup>[17]</sup> It is therefore instrumental to set the stage for the development of functionalized layered hybrid perovskites comprising electroactive organic spacers that can play a stabilizing role in hybrid perovskite heterostructures while raising the device performance.

Herein, we demonstrate the utility of guaninium (G)-derived low-dimensional perovskites in stabilizing the  $\alpha$ -FAPbI<sub>3</sub> perovskite phase, which is assessed by solid-state NMR spectroscopy, X-ray crystallography, molecular dynamics simulations, and DFT calculations. Guanine is a biologically relevant organic molecule that plays an important role in stabilizing the DNA structure (Figure 1 a), while displaying the propensity for the formation of conductive supramolecular assemblies and functional materials.<sup>[18–21]</sup> We have therefore utilized its functional units to form a novel hybrid perovskite structure based on the low dimensional G<sub>2</sub>PbI<sub>4</sub> composition, which was used to increase the performance and stability of  $\alpha$ -FAPbI<sub>3</sub> perovskite solar cells.

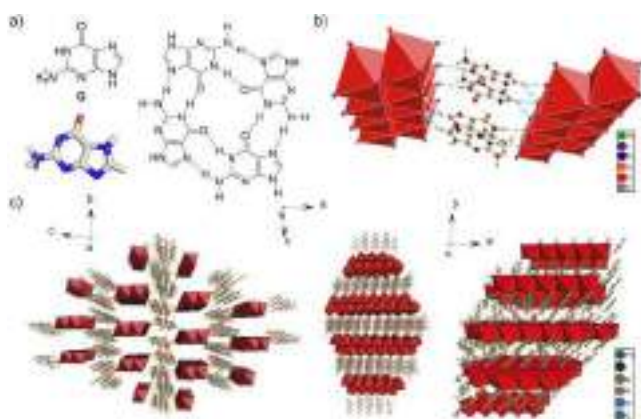


**Figure 1.** a) Structure of guanine (G) with its DFT-optimized (B3LYP/6-31G(d)) geometry (left) and common supramolecular assemblies, such as the G-quadruplex (right). b) The interactions between G and PbI<sub>2</sub> in the G<sub>2</sub>PbI<sub>4</sub> crystal structure. c) Crystal structure of G<sub>2</sub>PbI<sub>4</sub> along *a*, *b*, *c* axis. Solvent molecules are omitted for clarity.

## Results and Discussion

We synthesized G<sub>2</sub>PbI<sub>4</sub> by mixing guaninium iodide (GI; Figure 1 a; Supporting Information, Figure S1) and lead iodide (PbI<sub>2</sub>) in 2:1 molar ratio in  $\gamma$ -butyrolactone (GBL) as a solvent and heating the solution to 70 °C until dissolved. The experimental details are provided in the Supporting Information, Section S1. Hydroiodic acid was added into the turbid solution to fully dissolve the solute at concentration of 0.1M. The crystal structure of the resulting solvated G<sub>2</sub>PbI<sub>4</sub> intermediate reveals intermolecular hydrogen bonding (HB)

between the organic spacer layer and inorganic sheets (Figure 1 b,c). Formation of HB adducts was consistent with the Fourier transform infrared (FTIR) spectra of the thin films of GI, GI·PbI<sub>2</sub>, and GI·PbI<sub>2</sub>·FAI (Supporting Information, Figure S2 a) indicating that –N–H and –NH<sub>3</sub><sup>+</sup> stretching vibrations shift to higher frequencies for GI·PbI<sub>2</sub> and GI·PbI<sub>2</sub>·FAI. Moreover, the differential scanning calorimetry (DSC) and thermal gravimetric analysis (TGA) of GI·PbI<sub>2</sub>, PbI<sub>2</sub>, and GI (Supporting Information, Figure S2 b) show different properties for the three species. During annealing up to 400 °C, there is no weight loss for PbI<sub>2</sub> while GI displays only one exothermic peak at around 290 °C. In the case of GI·PbI<sub>2</sub>, two distinct exothermic peaks are observed at around 257 °C and 327 °C, corresponding to the weight loss in the range of 250–300 °C and 300–350 °C, respectively,

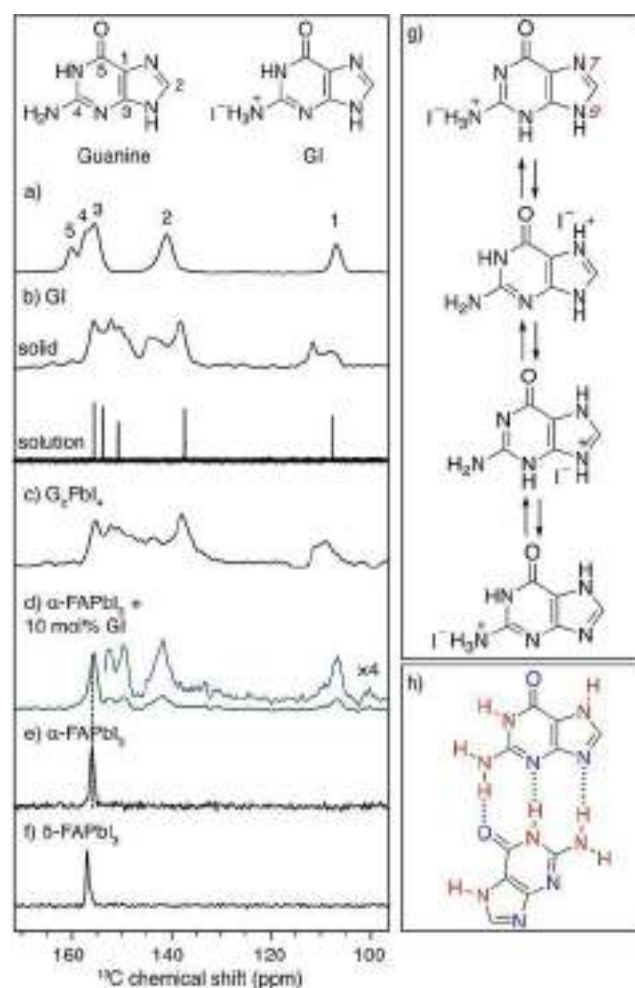


**Figure 2.** <sup>13</sup>C CP MAS spectra at 21.1 T, 298 K, and 20 kHz MAS of a) guanine, b) guaninium hydroiodide (G-HI or GI) in solid-state (upper) and solution of [D<sub>6</sub>]DMSO (lower), and bulk mechanochemical c) G<sub>2</sub>PbI<sub>4</sub>, d)  $\alpha$ -FAPbI<sub>3</sub> with 10 mol% GI, e)  $\alpha$ -FAPbI<sub>3</sub>, and f)  $\delta$ -FAPbI<sub>3</sub>. <sup>15</sup>N solid-state MAS NMR spectra at 21.1 T, 100 K, 12.5 kHz are shown in the Supporting Information, Figure S3. g) Structures of some of the tautomeric forms of GI (atomic numbering is highlighted in red, with alternative protonation sites being N7 and N9) in equilibrium. h) A representative hydrogen-bonded (HB) dimer of two guanine molecules with hydrogen-bond donating (red) and hydrogen-bond accepting (blue) sites.



further suggesting the presence of interactions between GI and  $\text{PbI}_2$  in the  $\text{G}_2\text{PbI}_4$  system.

To characterize these interactions at the atomic level, we have prepared non-solvated  $\text{G}_2\text{PbI}_4$  by mechanochemistry<sup>[22,23]</sup> and used  $^1\text{H}$ ,  $^{13}\text{C}$ , and  $^{15}\text{N}$  solid-state magic-angle-spinning (MAS) NMR at 21.1 T to characterize it (for more details, see Section S2 in the Supporting Information). It has been shown that structural properties of hybrid perovskites<sup>[24–27]</sup> as well as their modulated<sup>[28,29]</sup> and layered low-dimensional analogues<sup>[15]</sup> can be assessed at the atomic level by means of solid-state NMR spectroscopy and that mechanochemically prepared samples correspond well to those fabricated by solution deposition. The  $^{13}\text{C}$  CP MAS spectrum of unprotonated guanine shows five well-resolved resonances, corresponding to the inequivalent sites of the purine ring system (Figure 2a). Protonation of guanine with HI, yielding GI, leads to changes in the chemical shift of all peaks, as well as to the appearance of new peaks, which are most likely due to the protonation of both the primary and secondary amine group of guanine (Figure 2b).<sup>[30,31]</sup> The formation of  $\text{G}_2\text{PbI}_4$  is evidenced by changes in the  $^{13}\text{C}$  NMR spectrum as compared to neat GI (Figure 2c), although peak assignment is difficult due to the high level of disorder. Analogous qualitative changes are visible in  $^{15}\text{N}$  (Supporting Information, Figure S3a,b) and  $^1\text{H}$  (Supporting Information, Figure S3d–f) solid-state NMR spectra. This spectral complexity may be partly associated with guanine adopting several tautomeric forms (Figure 2g).<sup>[30]</sup> Previous reports suggest that G exists in the aqueous phase as a mixture of two tautomers (Figure 2g), the *N9H* (85%) and a *N7H* form (15%). Moreover, *N7H* has been shown to be more stable than *N9H* form in solution, although the latter was found to be the only tautomer in polar solvents or in the solid state.<sup>[30]</sup> Protonation was reported to predominantly occur at position *N7*, which is also suggested by the corresponding *pK<sub>a</sub>* values.<sup>[31]</sup> As a result, hydrogen bonding of protonated G units leads to the formation of regioisomeric dimers (Figure 2h), which further contributes to the broadening of the NMR spectra of GI,  $\text{G}_2\text{PbI}_4$ , and hybrid  $\text{FAPbI}_3$  composites with GI (Figure 2d–f).

For further structural insight, we analyzed the X-ray diffraction (XRD) patterns of  $\text{G}_2\text{PbI}_4$  films on FTO/compact (c-)TiO<sub>2</sub>/mesoporous (mp-)TiO<sub>2</sub> substrates (Figure 3a). The thin films were prepared by the hot-casting method (more details are provided in the Supporting Information, Section S1).<sup>[32]</sup> XRD patterns show two characteristic diffraction peaks at  $2\theta$  of 6.0°, and 7.1°, which are located in the low-angle region, typical for low-dimensional perovskites. The broadening of the XRD signals is consistent with the presence of disorder visible in solid-state NMR spectra. Another unique signature of low-dimensional iodoplumbate phases is the presence of excitonic features in their UV/Vis absorption spectra.<sup>[33]</sup> We have therefore measured the UV/Vis spectra of the corresponding films (Figure 3b), which show two absorp-

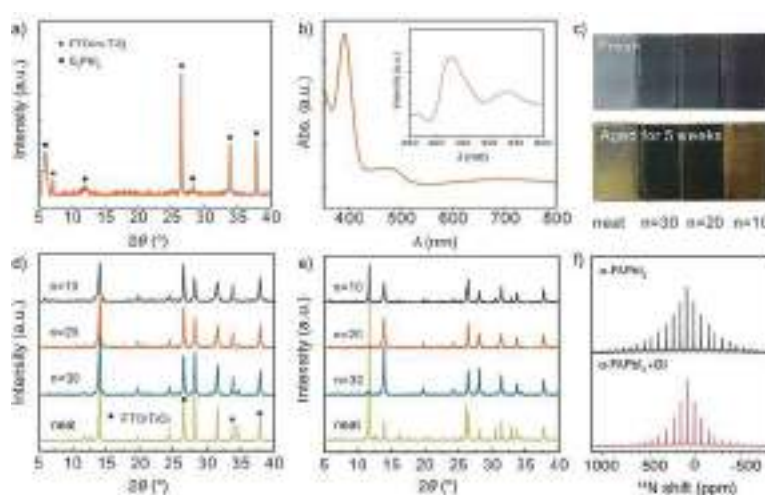


**Figure 3.** a) X-ray diffraction (XRD) patterns and b) UV/Vis spectrum of  $\text{G}_2\text{PbI}_4$  films; inset: corresponding steady photoluminescence (PL) spectrum. c) Pictures of the corresponding perovskite films. d), e) XRD patterns for neat  $\text{FAPbI}_3$  and mixed perovskite films of  $\text{G}_2\text{FA}_{n-1}\text{Pb}_n\text{PbI}_{3n+1}$  composition (formal stoichiometries of  $n = 10, 20$ , and  $30$ ) on FTO/c-TiO<sub>2</sub>/m-TiO<sub>2</sub> substrates d) immediately after preparation and e) upon aging for 5 weeks, respectively. Enlarged XRD patterns are shown in the Figure S2 of the Supporting Information. f)  $^{15}\text{N}$  solid-state magic-angle-spinning NMR spectra at 21.1 T, 298 K, 5 kHz of bulk mechanochemical  $\alpha$ - $\text{FAPbI}_3$  (top) and G-containing  $\alpha$ - $\text{FAPbI}_3$  (10 mol% GI; bottom) powders.

tion band edges at around 425 nm and 525 nm, likely corresponding to the excitonic peaks of the low-dimensional phases. These spectral features are consistent with the results of steady-state photoluminescence (PL; Figure 3b, inset) with Stokes shifts of approximately 25 nm, which is further in accordance with the formation of low-dimensional  $\text{G}_2\text{PbI}_4$  phase.

Having identified the formation of  $\text{G}_2\text{PbI}_4$ , we probed its effect on the stability of  $\alpha$ - $\text{FAPbI}_3$ . The corresponding films and devices were fabricated via a one-step deposition method by spin-coating the precursor solutions without employing an anti-solvent (as detailed in the Supporting Information, Section S1). The mixed G/FA perovskite precursor solutions were prepared based on the  $\text{G}_2\text{FA}_{n-1}\text{Pb}_n\text{I}_{3n+1}$  formula (with  $n$  corresponding to 1, 10, 20, 30, while  $n = \infty$  indicates neat  $\text{FAPbI}_3$ ), which defines the stoichiometry of the precursors without making any assumptions regarding the resulting crystal structure. The changes in color of the thin films deposited on FTO/c-TiO<sub>2</sub>/mp-TiO<sub>2</sub> substrates were indicative of G-induced 3D perovskite stabilization, as films based on G-containing compositions appeared darker and maintained their color for a longer period in ambient conditions (Figure 3c), whereas neat  $\text{FAPbI}_3$  films turned yellow during the same period of time. This suggests that the presence of G may stabilize the black  $\alpha$ - $\text{FAPbI}_3$  phase. To corroborate this effect, we analyzed the XRD patterns of the neat  $\text{FAPbI}_3$  and perovskite films based on the mixed  $\text{G}_2\text{FA}_{n-1}\text{Pb}_n\text{PbI}_{3n+1}$  ( $n = 10, 20$ , and  $30$ ) compositions on FTO/c-TiO<sub>2</sub>/mp-TiO<sub>2</sub> substrates. The XRD patterns immediately after the preparation (Figure 3d) reveal the presence of the hexagonal  $\delta$ - $\text{FAPbI}_3$  phase diffraction peak at 11.8° for neat  $\text{FAPbI}_3$  perovskite films, while this peak is not present in the G-containing compositions. After 5 weeks of storage in the dark at 20–25 °C

in ambient air of relative humidity (RH) of about 40 %, the peak intensity of  $\delta$ -FAPbI<sub>3</sub> sharply increased compared to that of  $\alpha$ -FAPbI<sub>3</sub> for the neat perovskite films (Figure 3 e). On the contrary, the phase transformation was suppressed in the G-containing perovskite films, especially in the films based on the  $n=20$  composition. However, a strong diffraction peak of  $\delta$ -FAPbI<sub>3</sub> was observed in the  $n=10$  composition, which is likely to be the result of poor film morphology owing to the low solubility of GI in organic solvents. In this regard, presence of secondary non-perovskite phases may be detrimental to long-term stability under ambient conditions, facilitating perovskite degradation processes.<sup>[34]</sup> Furthermore, a low angle diffraction peak at 6.0° was observed for both fresh and aged perovskite films of  $n=10$  composition, indicating the presence of a low-dimensional iodoplumbate structure. In the case of  $n=20$ , this peak was not present in the XRD pattern, presumably as a result of the lower concentration of the low-dimensional phase. We have assessed the structural changes by X-ray photoelectron spectroscopy (XPS) of neat and  $n=20$  perovskite films (Supporting Information, Figure S4). The XPS spectra show a peak centered at 399.0 eV in the N 1s spectral domain for the  $n=20$  perovskite films, which can be ascribed to the C=N bond of G. Furthermore, the Pb core level 4f<sub>7/2</sub> and 4f<sub>5/2</sub> peaks of  $n=20$  systems shift to lower binding energies as compared to neat FAPbI<sub>3</sub>, indicating changes in the structure, likely as a result of the interaction with G. This interaction-induced structural change that appears to be more stabilizing at lower concentrations of guanine suggests a structure-directing role,<sup>[28,29]</sup> which was also assessed at the atomic level by solid-state NMR spectroscopy.

We analyzed the microstructure of bulk mechanochemical FAPbI<sub>3</sub> doped with 10 mol % GI by solid-state NMR spectroscopy (Figure 2d–f; Supporting Information, Figure S3). <sup>13</sup>C MAS NMR spectrum of this formulation contains four well-resolved G peaks (Figure 2d–f) corresponding to carbons 1 (107 ppm), 2 (142 ppm), 3 (150 ppm), 4 (153 ppm), which are markedly different from those of neat GI or G<sub>2</sub>PbI<sub>4</sub> and therefore evidence the formation of a new G/FA-based iodoplumbate phase (Figure 2b–d). The peak of carbon 5 overlaps with the FA signal of  $\alpha$ -FAPbI<sub>3</sub> (155 ppm). This change in the underlying atomic-level microstructure allows to rationalize the change in the binding energies of the Pb core levels observed by XPS. Moreover, we have previously shown that <sup>14</sup>N NMR can be used as a sensitive diagnostic tool for structural changes of FAPbI<sub>3</sub>.<sup>[15,28,29]</sup> Specifically, the width of the spinning side band (SSB) pattern of <sup>14</sup>N NMR signals are determined by the local cubooctahedral symmetry of FA, which is tumbling in the ps regime. Consequently, narrower <sup>14</sup>N SSB manifolds indicate higher cubooctahedral symmetry (closer to cubic).  $\alpha$ -FAPbI<sub>3</sub> containing with 10 mol % GI has a narrower <sup>14</sup>N SSB manifold than neat  $\alpha$ -FAPbI<sub>3</sub>, which shows that the crystallographic symmetry of the 3D perovskite is affected by the presence of GI such that it increases the cubooctahedral symmetry (Figure 3 f). We suggest that this may contribute to the improved electronic quality of the thin films. To gain further understanding of this perovskite structure, we analyzed the perovskite films of G<sub>2</sub>FA<sub>*n*-1</sub>Pb<sub>*n*</sub>PbI<sub>3*n*+1</sub> ( $n=20$ ) by transmission electron micros-

copy (TEM; Figure 4). The representative TEM image of the polycrystalline film shows a grain and its boundary (Figure 4 a). A high-resolution (HR) image of the area (indicated by a square in Figure 4 a) and its fast Fourier transform (FFT) analysis reveals an inter-planar spacing of 0.32 nm (Figure 4 c), which

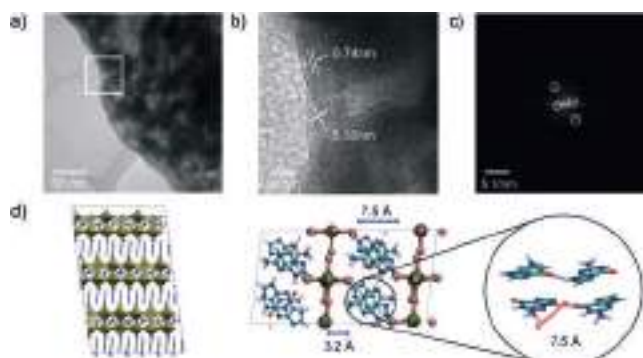


**Figure 4.** TEM images of G<sub>2</sub>FA<sub>*n*-1</sub>Pb<sub>*n*</sub>PbI<sub>3*n*+1</sub> ( $n=20$ ) perovskite compositions: a) A lower magnification image and b) high-resolution image of the marked area in (a) with c) the corresponding Fourier transform (FFT) analysis. d) DFT-optimized structure of G<sub>2</sub>FAPb<sub>2</sub>I<sub>7</sub>. For more details, refer to the Supporting Information, Section S3.

matches the (002) reflection of the cubic  $\alpha$ -FAPbI<sub>3</sub> perovskite phase. Furthermore, an interplanar distance of 0.74 nm is revealed, which corresponds well to the size of the G spacer (7.5 Å) inside the G<sub>2</sub>PbI<sub>4</sub> phase (Figure 1 b). This suggests that the low-dimensional G<sub>2</sub>PbI<sub>4</sub> phase exists along the grain boundaries of the  $\alpha$ -FAPbI<sub>3</sub>, which can account for its stabilization in the hybrid G-containing  $\alpha$ -FAPbI<sub>3</sub> compositions. This result is in line with the NMR analysis, which shows the formation of new G environments modified by the proximity of the 3D perovskite phase in the hybrid G-containing  $\alpha$ -FAPbI<sub>3</sub> system.

A mechanistic model that could explain the formation of such mixed hybrid perovskite structures must consider a number of different tautomeric forms as well as their propensity to dimerization via hydrogen bonding without interfering with the formation of a low-dimensional phase (Figure 2 g,h). Furthermore, the resulting structures should take into consideration the properties of the solvated G<sub>2</sub>PbI<sub>4</sub> intermediate revealed by single crystal XRD (Figure 1 c). We assessed the possible structural models by molecular dynamics (MD) simulations based on both classical and DFT calculations starting from the intermediary G<sub>2</sub>PbI<sub>4</sub> solvated crystal structure (for more details, refer to the Supporting Information, Section S3). We analyzed a number of possible low-dimensional structures based on G<sub>2</sub>PbI<sub>4</sub> and G<sub>2</sub>FAPb<sub>2</sub>I<sub>7</sub> compositions as model systems (Supporting Information, Figures S7, S18), and compared them to the experimental findings. As a result of this analysis, we identified a unique and stable structure composed of alternating hydrogen-bonded G dimers inside the spacer layer, oriented such that both HB of the spacers and their interaction with the perovskite slabs is possible (Figure 4 d; Supporting Information, Figures S11, S12). The structural properties of the resulting system matched well the spacer dimensions revealed

by both the TEM (Figure 4d) and XRD measurements (Supporting Information, Figure S14). Moreover, DFT calculations of the structures suggest that proton transfer occurs between the molecules in the spacer layer, which supports the existence of multiple tautomeric forms (for more details, refer to the Supporting Information, Section S3). This suggests that the formation of G-based low-dimensional structures involves a reorientation of the spacer molecules to form HB within the spacer (Supporting Information, Figure S13), while simultaneously binding to the inorganic slabs. In this fashion, the G-based spacer layer could affect proton transfer along with providing enhanced transport for electronic charge carriers. A more detailed mechanistic insight requires extensive nucleation studies, which are the subject of an ongoing investigation.

To evaluate this model, we analyzed the optoelectronic properties of neat FAPbI<sub>3</sub> and mixed G<sub>2</sub>FA<sub>*n*-1</sub>Pb<sub>*n*</sub>PbI<sub>*3n*+1</sub> (*n* = 10, 20, and 30) perovskite films on FTO/c-TiO<sub>2</sub>/mp-TiO<sub>2</sub> substrates (Figure 5). The UV/Vis absorption spectra suggest that the absorbance of the films of both *n* = 20 and 30 is much higher than that of neat  $\alpha$ -FAPbI<sub>3</sub> films, which is presumably due to improved phase purity and film uniformity (Figure 5a). The films of *n* = 10 show absorbance that is lower than that of *n* = 20 and 30 perovskites, whereas top-view scanning electron microscopy (SEM; Supporting Information, Figure S5) images indicate that the grain sizes do not evidently change with the increasing *n* value. The effect of G<sub>2</sub>PbI<sub>4</sub> perovskite on the optical band gap was probed by analyzing the corresponding Tauc plots (Figure 5b,c). For G<sub>2</sub>FA<sub>*n*-1</sub>Pb<sub>*n*</sub>PbI<sub>*3n*+1</sub> (*n* = 10, 20, 30) compositions, the band gap remained around 1.51 eV, exceeding the value of  $\alpha$ -FAPbI<sub>3</sub> by only 30 meV.<sup>[35,36]</sup> We can thus conclude that the presence of G does not affect the band gap of  $\alpha$ -FAPbI<sub>3</sub> significantly, enabling the G-based perovskite composites to retain the advantages of the low band gap. However, the steady-state PL spectra (Figure 5d) reveal a minor blue-shift with certain asymmetry of the spectrum for *n* = 10, indicating that a higher ratio of low-dimensional phases may affect the optoelectronic properties. The time-resolved photoluminescence (TRPL) spectra of neat  $\alpha$ -FAPbI<sub>3</sub> and mixed G<sub>2</sub>FA<sub>*n*-1</sub>Pb<sub>*n*</sub>PbI<sub>*3n*+1</sub> (*n* = 10, 20, 30) films

on glass microscope slides show a slightly longer charge carrier lifetimes for *n* = 20 as compared to the other compositions, pointing at suppressed charge carrier recombination (Figure 3e). We further measured the TRPL spectra of perovskite/spiro-OMeTAD structure on a glass slide to assess the effect on charge-carrier transport at the interface between the perovskite and spiro-OMeTAD. The mixed G<sub>2</sub>FA<sub>*n*-1</sub>Pb<sub>*n*</sub>PbI<sub>*3n*+1</sub> perovskite materials were found to quench the PL of the 3D perovskite phase faster, with the *n* = 20 system showing the most pronounced effect. This indicates enhanced non-radiative charge carrier recombination at the mixed G<sub>2</sub>FA<sub>*n*-1</sub>Pb<sub>*n*</sub>PbI<sub>*3n*+1</sub> perovskite/spiro-OMeTAD interface, an effect which is important for the photovoltaic performance.

This finding corroborates the calculated electronic properties of the layered G<sub>2</sub>PbI<sub>4</sub> structure (for details, see the Supporting Information, Section S3.5 and Figures S19–S20), which suggest that the conduction band of the low-dimensional structure is delocalized within the spacer layer. This has been previously observed for a very few cases of low-dimensional perovskite structures based on functional organic spacers that can serve as a pathway for charge transport, facilitating charge extraction.<sup>[37,38]</sup> Moreover, the calculated hole effective masses along the three principal axes reveal reduced hole effective masses for in-plane directions coinciding with the  $\pi$ -stacking of the guanine moieties, suggesting a possible pathway for hole transport. To clarify this, the mobility of charge carriers and photoconductivity (product of mobility and concentration of photo-generated charge carriers) were determined by time-resolved microwave conductivity measurements (Supporting Information, Section S4, Figures S21–S23).<sup>[39,40]</sup> The measurements revealed conductivities that increase for *n* = 20 as compared to the *n* = 1 compositions, which is accompanied by charge carrier lifetimes in the order of  $\mu$ s that is of interest to the PV applications. The photovoltaic metrics of neat  $\alpha$ -FAPbI<sub>3</sub> and hybrid G<sub>2</sub>FA<sub>*n*-1</sub>Pb<sub>*n*</sub>PbI<sub>*3n*+1</sub> (*n* = 10, 20, and 30) PSCs with an aperture area of 0.16 cm<sup>2</sup> (Figure 6) show that the *n* = 20 PSCs outperform those of neat  $\alpha$ -FAPbI<sub>3</sub>. The improvement can be

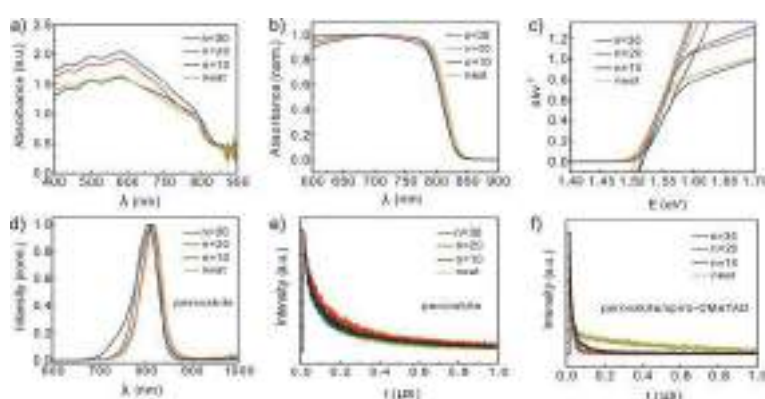


**Figure 5.** Optoelectronic properties of neat FAPbI<sub>3</sub> and mixed-perovskite films of G<sub>2</sub>FA<sub>*n*-1</sub>Pb<sub>*n*</sub>PbI<sub>*3n*+1</sub> (*n* = 10, 20, and 30) compositions. a) UV/Vis absorption spectra, b) normalized absorption spectra and the c) corresponding Tauc plots on FTO/c-TiO<sub>2</sub>/m-TiO<sub>2</sub> substrates; d) steady-state and e), f) time-resolved PL (TRPL) spectra for films on a microscope glass slide. The steady-state PL spectra of G<sub>2</sub>PbI<sub>4</sub> is shown in Figure 3b.

ascribed to the stabilization of the  $\alpha$ -FAPbI<sub>3</sub> in presence of the G-based phase. With the highly increased content of the low-dimensional component, as in the *n* = 10 compositions, however, the PV performance decreases. This is in accordance with the effect on the optoelectronic properties (Figure 5a; Supporting Information, Section S4). The comparatively poorer performance of the *n* = 30 compositions presumably results from the decrease in the film uniformity and optical properties as compared to the neat FAPbI<sub>3</sub> perovskite. This suggests that the optimal concentration thereby lies in the range between the ones defined by the *n* = 10 and *n* = 30 nominal compositions. As a result, we achieved PCEs up to 16.04 % for hybrid G<sub>2</sub>FA<sub>*n*-1</sub>Pb<sub>*n*</sub>PbI<sub>*3n*+1</sub> PSCs based on *n* = 20 compositions with *V*<sub>OC</sub> of 1.08 V, *J*<sub>SC</sub> of 22.08 mA cm<sup>-2</sup>, and FF of 0.67. These parameters are superior to those of neat  $\alpha$ -FAPbI<sub>3</sub>, yielding a PCE of 8.42% with a *V*<sub>OC</sub> of 0.74 V, *J*<sub>SC</sub> of

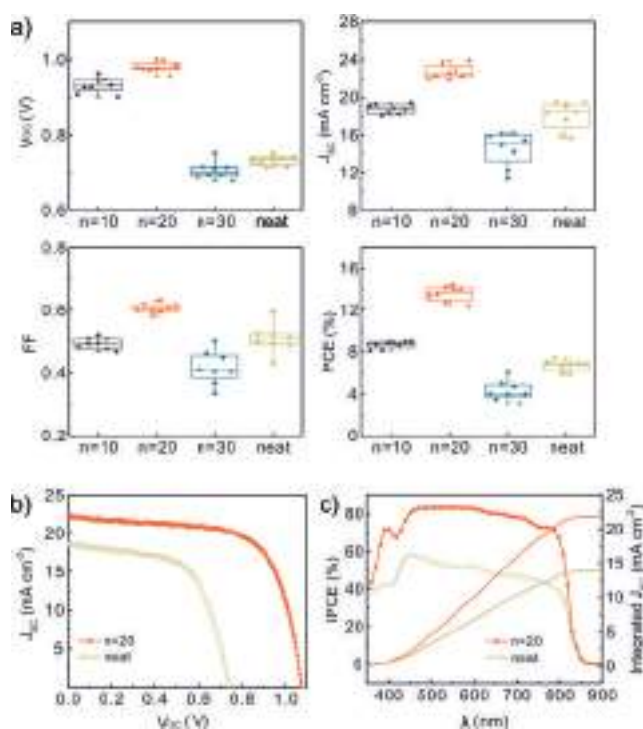


**Figure 6.** a) PV metrics of 32 solar cells based on neat FAPbI<sub>3</sub> and mixed low-dimensional G<sub>2</sub>FA<sub>n-1</sub>Pb<sub>n</sub>PbI<sub>3n+1</sub> ( $n = 10, 20$ , and  $30$ ) perovskite compositions; b)  $J$ - $V$  curves and c) corresponding IPCE spectra with integrated  $J_{SC}$  of the best performed solar cells based on neat FAPbI<sub>3</sub> and perovskites of G<sub>2</sub>FA<sub>n-1</sub>Pb<sub>n</sub>PbI<sub>3n+1</sub> ( $n = 20$ ) composition. The aperture area of the devices is  $0.16 \text{ cm}^2$ .

$18.59 \text{ mA cm}^{-2}$ , and FF of 0.61 based on the reverse scan (Figure 6a). The hysteresis effects however remain apparent in the PSCs (Supporting Information, Figure S6). The corresponding incident photon-to-current conversion efficiency (IPCE) spectra show that the integrated  $J_{SC}$  of  $n = 20$  PSC is  $21.75 \text{ mA cm}^{-2}$ , comparable to the value derived from the  $J$ - $V$  curve, while the integrated  $J_{SC}$  of neat FAPbI<sub>3</sub> PSC is  $13.87 \text{ mA cm}^{-2}$ , lower than the one derived from the  $J$ - $V$  curve. This is ascribed to the instability of untreated  $\alpha$ -FAPbI<sub>3</sub>, leading to its degradation during the measurement (the maximum power point tracking is shown in the Supporting Information, Figure S6), which has been affected by the presence of guanine moieties.

## Conclusion

We introduce guaninium (G) moieties to tune the properties of  $\alpha$ -FAPbI<sub>3</sub>. We used solid-state NMR to establish that G interacts with the perovskite lattice at the atomic level, leading to the formation of mixed G/FAPbI<sub>3</sub> phases. We report the crystal structure of a low-dimensional G-based phase, which evidences the possible binding modes involved in the stabilization of  $\alpha$ -FAPbI<sub>3</sub>. Furthermore, we provide a mechanistic model for the formation of the G-based perovskite phase using molecular dynamics simulations and DFT calculations, which show that the guanine moieties have the propensity to enhance the transport of protons as well as

charge transport through delocalization of the conduction band across the spacer layer. These findings were used to design solar cells based on hybrid G<sub>2</sub>FA<sub>1-n</sub>Pb<sub>n</sub>I<sub>3n+1</sub> composition and obtain PCEs of over 16%, highlighting the prospect of this approach in metal halide perovskite photovoltaics.

## Acknowledgements

J.V.M., S.M.Z., and M.G. are grateful to the European Union's Horizon 2020 research and innovation program under grant agreement No. 826013 (IMPRESSIVE) as well as the GRAPHENE Flagship Core 2 project supported by the European Commission H2020 Program under contract 785219. D.J.K. and L.E. acknowledge support from Swiss National Science Foundation Grant No. 200020\_178860. D.R. acknowledges the SNSF grants IZLCZ2-170294 and IZJSZ2\_180176. U.R. acknowledges SNSF Grant No. 200020-165863, NCCR-MUST, NRP70, and the SINERGIA interdisciplinary research program EPISODE for funding. L.H. and H.H. acknowledge financial support from the National Natural Science Foundation of China (Grant Nos. 21702069, 51502141, 91733301, 91433203 and 61474049), the Ministry of Science and Technology of China (863, 2015AA034601), the Fundamental Research Funds for the Central Universities, the Science and Technology Department of Hubei Province (No. 2017AAA190), the 111 Project (No. B07038), the Program for HUST Academic Frontier Youth Team (2016QYTD06), China Postdoctoral Science Foundation (2017M612452), and the Double first-class research funding of China-EU Institute for Clean and Renewable Energy (No. ICARE-RP-2018- SOLAR-001 and ICARE-RP-2018-SOLAR-002). M.A.R.P. is grateful to CONACyT/SENER Mexico for the financial support granted through the project 291195. The research leading to the results at the Delft University of Technology has received funding from the European Research Council Horizon 2020 ERC Grant Agreement no. 648433. We thank the Analytical and Testing Center of Huazhong University of Science and Technology (HUST) for various measurements. L.H. is grateful to Zaiwei Wang and Péter Péchy (EPFL), as well as Yue Hu and Yaoguang Rong (Wuhan National Lab), for helpful discussions and their support during the study.

## Conflict of interest

The authors declare no conflict of interest. M.M. is also affiliated with the Scientific Computing Laboratory, Center for the Study of Complex Systems, Institute of Physics Belgrade, University of Belgrade, Pregrevice 118, 11080 Belgrade, Serbia.

**Keywords:** guanine · hybrid perovskites · low-dimensional perovskites · perovskite solar cells · solid-state NMR

How to cite: *Angew. Chem. Int. Ed.* **2020**, *59*, 4691–4697  
*Angew. Chem.* **2020**, *132*, 4721–4727

- [1] M. Grätzel, *Nat. Mater.* **2014**, *13*, 838–842.
- [2] Y. Rong, Y. Hu, A. Mei, H. Tan, M. I. Saidaminov, S. I. Seok, M. D. McGehee, E. H. Sargent, H. Han, *Science* **2018**, *361*, eaat8235-9.
- [3] NREL Best Research Cell Efficiency Chart; <https://www.nrel.gov/pv/assets/pdfs/best-research-cell-efficiencies.20190802.pdf> (Accessed in August 2019).
- [4] J. V. Milić, D. J. Kubicki, L. Emsley, M. Grätzel, *Chimia* **2019**, *73*, 317–323.
- [5] N. Arora, M. I. Dar, M. Abdi-Jalebi, F. Giordano, N. Pellet, G. Jacopin, R. H. Friend, S. M. Zakeeruddin, M. Grätzel, *Nano Lett.* **2016**, *16*, 7155–7162.
- [6] N. Pellet, P. Gao, G. Gregori, T.-Y. Yang, M. K. Nazeeruddin, J. Maier, M. Grätzel, *Angew. Chem. Int. Ed.* **2014**, *53*, 3151–3157; *Angew. Chem.* **2014**, *126*, 3215–3221.
- [7] F. C. Hanusch, E. Wiesenmayer, E. Mankel, A. Binek, P. Angloher, C. Fraunhofer, N. Giesbrecht, J. M. Feckl, W. Jaegermann, D. Johrendt, et al., *J. Phys. Chem. Lett.* **2014**, *5*, 2791–2795.
- [8] A. Amat, E. Mosconi, E. Ronca, C. Quarti, P. Umari, M. K. Nazeeruddin, M. Grätzel, F. De Angelis, *Nano Lett.* **2014**, *14*, 3608–3616.
- [9] M. T. Weller, O. J. Weber, J. M. Frost, A. Walsh, *J. Phys. Chem. Lett.* **2015**, *6*, 3209–3212.
- [10] A. Binek, F. C. Hanusch, P. Docampo, T. Bein, *J. Phys. Chem. Lett.* **2015**, *6*, 1249–1253.
- [11] Z. Li, M. Yang, J.-S. Park, S.-H. Wei, J. J. Berry, K. Zhu, *Chem. Mater.* **2016**, *28*, 284–292.
- [12] R. Hamaguchi, M. Yoshizawa-Fujita, T. Miyasaka, H. Kunugita, K. Ema, Y. Takeoka, M. Rikukawa, *Chem. Commun.* **2017**, *53*, 4366–4369.
- [13] G. Li, T. Zhang, N. Guo, F. Xu, X. Qian, Y. Zhao, *Angew. Chem. Int. Ed.* **2016**, *55*, 13460–13464; *Angew. Chem.* **2016**, *128*, 13658–13662.
- [14] J. Yan, W. Fu, X. Zhang, J. Chen, W. Yang, W. Qiu, G. Wu, F. Liu, P. Heremans, H. Chen, *Mater. Chem. Front.* **2018**, *2*, 121–128.
- [15] J. V. Milić, J.-H. Im, D. J. Kubicki, A. Ummadisingu, J.-Y. Seo, Y. Li, M. A. Ruiz Preciado, M. I. Dar, S. M. Zakeeruddin, L. Emsley, M. Grätzel, *Adv. Energy Mater.* **2019**, *131*, 1900284.
- [16] Y. Li, J. V. Milić, A. Ummadisingu, J.-Y. Seo, J.-H. Im, H.-S. Kim, Y. Liu, M. I. Dar, S. M. Zakeeruddin, P. Wang, M. Grätzel, *Nano Lett.* **2019**, *19*, 150–157.
- [17] a) G. Grancini, M. K. Nazeeruddin, *Nat. Rev. Mater.* **2019**, *4*, 4–22; b) L. Mao, C. C. Stoumpos, M. G. Kanatzidis, *J. Am. Chem. Soc.* **2019**, *141*, 1171–1190.
- [18] T. Carell, C. Behrens, J. Gierlich, *Org. Biomol. Chem.* **2003**, *1*, 2221–2228.
- [19] T. Kawakami, T. Taniguchi, T. Hamamoto, Y. Kitagawa, M. Okumura, K. Yamaguchi, *Int. J. Quantum Chem.* **2005**, *105*, 655–671.
- [20] J. C. Genereux, J. K. Barton, *Chem. Rev.* **2010**, *110*, 1642–1662.
- [21] F. D. Lewis, R. M. Young, M. R. Wasielewski, *Acc. Chem. Res.* **2018**, *51*, 1746–1754.
- [22] D. Prochowicz, M. Franckevičius, A. M. Cieślak, S. M. Zakeeruddin, M. Grätzel, J. Lewiński, *J. Mater. Chem. A* **2015**, *3*, 20772–20777.
- [23] D. Prochowicz, P. Yadav, M. Saliba, M. Sasaki, S. M. Zakeeruddin, J. Lewiński, M. Grätzel, *Sustainable Energy Fuels* **2017**, *1*, 689–693.
- [24] D. J. Kubicki, D. Prochowicz, A. Hofstetter, P. Péchy, S. M. Zakeeruddin, M. Grätzel, L. Emsley, *J. Am. Chem. Soc.* **2017**, *139*, 10055–10061.
- [25] D. J. Kubicki, D. Prochowicz, A. Hofstetter, S. M. Zakeeruddin, M. Grätzel, L. Emsley, *J. Am. Chem. Soc.* **2017**, *139*, 14173–14180.
- [26] D. J. Kubicki, D. Prochowicz, A. Hofstetter, M. Sasaki, P. Yadav, D. Bi, N. Pellet, J. Lewiński, S. M. Zakeeruddin, M. Grätzel, L. Emsley, *J. Am. Chem. Soc.* **2018**, *140*, 3345–3351.
- [27] D. J. Kubicki, D. Prochowicz, A. Hofstetter, S. M. Zakeeruddin, M. Grätzel, L. Emsley, *J. Am. Chem. Soc.* **2018**, *140*, 7232–7238.
- [28] D. Bi, X. Li, J. V. Milić, D. J. Kubicki, N. Pellet, J. Luo, T. LaGrange, P. Mettraux, L. Emsley, S. M. Zakeeruddin, M. Grätzel, *Nat. Commun.* **2018**, *9*, 4482.
- [29] M. M. Tavakoli, W. Tress, J. V. Milić, D. Kubicki, L. Emsley, M. Grätzel, *Energy Environ. Sci.* **2018**, *11*, 3310–3320.
- [30] E. E. Bendeif, S. Dahaoui, N. Benali-Cherif, C. Lecomte, *Acta Crystallogr. Sect. B* **2007**, *63*, 448–458.
- [31] K. N. Rogstad, Y. H. Jang, L. C. Sowers, W. A. Goddard, *Chem. Res. Toxicol.* **2003**, *16*, 1455–1462.
- [32] H. Tsai, W. Nie, J.-C. Blancon, C. C. Stoumpos, R. Asadpour, B. Harutyunyan, A. J. Neukirch, R. Verduzco, J. J. Crochet, S. Tretiak, et al., *Nature* **2016**, *536*, 312–316.
- [33] L. Mao, C. C. Stoumpos, M. G. Kanatzidis, *J. Am. Chem. Soc.* **2019**, *141*, 1171–1190.
- [34] Y. Hu, M. F. Aygüler, M. L. Petrus, T. Bein, P. Docampo, *ACS Energy Lett.* **2017**, *2*, 2212–2218.
- [35] E. Smecca, Y. Numata, I. Deretzis, G. Pellegrino, S. Boninelli, T. Miyasaka, A. La Magna, A. Alberti, *Phys. Chem. Chem. Phys.* **2016**, *18*, 13413–13422.
- [36] W. S. Yang, J. H. Noh, N. J. Jeon, Y. C. Kim, S. Ryu, J. Seo, S. I. Seok, *Science* **2015**, *348*, 1230–1234.
- [37] J. V. Passarelli, D. J. Fairfield, N. A. Sather, M. P. Hendricks, H. Sai, C. L. Stern, S. I. Stupp, *J. Am. Chem. Soc.* **2018**, *140*, 7313–7323.
- [38] S. Maheshwari, T. J. Savenije, N. Renaud, F. C. Grozema, *J. Phys. Chem. C* **2018**, *122*, 17118–17122.
- [39] M. C. Gélvez-Rueda, E. M. Hutter, D. H. Cao, N. Renaud, C. C. Stoumpos, J. T. Hupp, T. J. Savenije, M. G. Kanatzidis, F. C. Grozema, *J. Phys. Chem. C* **2017**, *121*, 26566–26574.
- [40] R. Herckens, W. T. M. Van Gompel, W. Song, M. C. Gélvez-Rueda, A. Maufort, B. Ruttens, J. D'Haen, F. C. Grozema, T. Aernouts, L. Lutsen, D. Vanderzande, *J. Mater. Chem. A* **2018**, *6*, 22899–22908.

Manuscript received: September 21, 2019

Revised manuscript received: December 11, 2019

Accepted manuscript online: December 17, 2019

Version of record online: February 3, 2020

# Formamidinium-Based Dion-Jacobson Layered Hybrid Perovskites: Structural Complexity and Optoelectronic Properties


María C. Gélvez-Rueda, Paramvir Ahlawat, Lena Merten, Farzaneh Jahanbakhshi, Marko Mladenović, Alexander Hinderhofer, M. Ibrahim Dar, Yang Li, Algirdas Dučinskas, Brian Carlsen, Wolfgang Tress, Amita Ummadisingu, Shaik M. Zakeeruddin, Frank Schreiber, Anders Hagfeldt, Ursula Rothlisberger,\* Ferdinand C. Grozema,\* Jovana V. Milić,\* and Michael Graetzel\*

Layered hybrid perovskites have emerged as a promising alternative to stabilizing hybrid organic–inorganic perovskite materials, which are predominantly based on Ruddlesden-Popper structures. Formamidinium (FA)-based Dion-Jacobson perovskite analogs are developed that feature bifunctional organic spacers separating the hybrid perovskite slabs by introducing 1,4-phenylenedimethan ammonium (PDMA) organic moieties. While these materials demonstrate competitive performances as compared to other FA-based low-dimensional perovskite solar cells, the underlying mechanisms for this behavior remain elusive. Here, the structural complexity and optoelectronic properties of materials featuring (PDMA)FA<sub>n-1</sub>Pb<sub>n</sub>I<sub>3n+1</sub> ( $n = 1-3$ ) formulations are unraveled using a combination of techniques, including X-ray scattering measurements in conjunction with molecular dynamics simulations and density functional theory calculations. While theoretical calculations suggest that layered Dion-Jacobson perovskite structures are more prominent with the increasing number of inorganic layers ( $n$ ), this is accompanied with an increase in formation energies that render  $n > 2$  compositions difficult to obtain, in accordance with the experimental evidence. Moreover, the underlying intermolecular interactions and their templating effects on the Dion-Jacobson structure are elucidated, defining the optoelectronic properties. Consequently, despite the challenge to obtain phase-pure  $n > 1$  compositions, time-resolved microwave conductivity measurements reveal high photoconductivities and long charge carrier lifetimes. This comprehensive analysis thereby reveals critical features for advancing layered hybrid perovskite optoelectronics.

## 1. Introduction

Hybrid organic–inorganic halide perovskites have taken the leading role in the research on thin film photovoltaics over the past decade.<sup>[1–3]</sup> Their structural versatility enables a wide range of applications in various optoelectronic devices, such as light emitting diodes, photodetectors, photocatalysts, and others.<sup>[1–3]</sup> However, these materials have shown limited stability against oxygen and water,<sup>[4–6]</sup> which has increased the interest in low-dimensional perovskite analogues.<sup>[7–11]</sup> Layered 2D perovskites incorporate hydrophobic organic cations between the hybrid perovskite slabs that are mainly defined by S<sub>2</sub>A<sub>n-1</sub>Pb<sub>n</sub>X<sub>3n+1</sub> and S'A<sub>n-1</sub>Pb<sub>n</sub>X<sub>3n+1</sub> formulations, where S and S' are mono- and bifunctional organic spacers, respectively, A is the organic cation in the perovskite slab (such as methylammonium (MA) or formamidinium (FA)), M is a divalent metal (mostly Pb<sup>2+</sup>), and X is the halide anion (Cl<sup>-</sup>, Br<sup>-</sup>, or I<sup>-</sup>), while  $n$  defines the number of hybrid perovskite slabs.<sup>[9–13]</sup> It is worth noting that, although we refer to these formulations as low-dimensional perovskites in accordance with the conventional nomenclature,<sup>[8,9]</sup> some

Dr. M. C. Gélvez-Rueda, Prof. F. C. Grozema  
 Department of Chemical Engineering  
 Delft University of Technology  
 Delft 2629 HZ, The Netherlands  
 E-mail: f.c.grozema@tudelft.nl

 The ORCID identification number(s) for the author(s) of this article can be found under <https://doi.org/10.1002/adfm.202003428>.

<sup>[†]</sup>Present address: Department of Physics, Cavendish Laboratory, JJ Thomson Avenue, Cambridge CB3 0HE, UK

P. Ahlawat, F. Jahanbakhshi, Dr. M. Mladenović, Prof. U. Rothlisberger  
 Laboratory of Computational Chemistry and Biochemistry  
 Institute of Chemical Sciences and Engineering  
 Ecole Polytechnique Fédérale de Lausanne  
 Lausanne 1015, Switzerland  
 E-mail: ursula.roethlisberger@epfl.ch

L. Merten, Dr. A. Hinderhofer, Prof. F. Schreiber  
 Institut für Angewandte Physik  
 Universität Tuebingen  
 Auf der Morgenstelle 10, Tübingen 72076, Germany

DOI: 10.1002/adfm.202003428

of these materials might not strictly correspond to perovskite structures and they could be more appropriately denoted as perovskite-related structures.<sup>[10]</sup> In addition to their classification by the number of slabs ( $n = 1, 2, 3$ , etc.), two main archetypes of layered perovskites are predominant to date, namely Ruddlesden-Popper (RP) and Dion-Jacobson (DJ) systems.<sup>[9–20]</sup> The RP structural category is defined by the  $S_2A_{n-1}Pb_nX_{3n+1}$  formulation, which comprises an organic double layer between the inorganic layers featuring an offset per unit cell of the perovskite slab.<sup>[9–12]</sup> The DJ systems are based on the  $S'A_{n-1}Pb_nX_{3n+1}$  compositions employing organic layers (S') that stack in an almost perfect alignment between unit cells, featuring smaller interlayer space.<sup>[15–20]</sup> Reducing interlayer distances and tuning their mutual alignment are important parameters for controlling the optoelectronic properties as they strengthen electronic interactions between the inorganic layers and, consequently, facilitate interlayer charge transport, rendering the DJ structures superior to RP phases.<sup>[15–20]</sup> Most of the developments of layered hybrid perovskites are based on RP archetypes and there are very few examples of hybrid DJ architectures to date.<sup>[15–20]</sup> This is particularly the case for FA-containing layered perovskites, which are relatively unexplored despite the superior thermal stabilities of FA-based hybrid perovskite compositions.<sup>[4,14,16,21–25]</sup>

We have recently shown the possibility to form Dion-Jacobson hybrid perovskites with 1,4-phenylenedimethan ammonium (PDMA) spacer moieties (Figure 1).<sup>[16]</sup> This system has been proven effective in forming low compositional ( $n = 1$ ) layered structures, whereas featuring mixed phases for  $n > 1$  representatives.<sup>[16]</sup> Such phase mixtures are commonly observed for 2D hybrid perovskites, where obtaining phase purity is an ongoing challenge.<sup>[16,24,26–29]</sup> Nonetheless, materials based on  $(PDMA)FA_{n-1}Pb_nI_{3n+1}$  compositions ( $n = 1–3$ ) have demonstrated promising photovoltaic performances in conventional mesoscopic (mp) n–i–p device architectures as compared to other FAPbI<sub>3</sub>-based low-dimensional perovskite solar cells with light-to-electric power conversion efficiencies exceeding 7%.<sup>[8,16,22]</sup> This was accompanied by long-term stabilities, which were achieved with thin ( $\approx 200$  nm) films of active materials under room temperature deposition, thus surpassing the performances of FAPbI<sub>3</sub>-based perovskite solar cells with 2D compositions reported to date.<sup>[16,22,24]</sup>

In this work, we unravel the underlying structural complexity and optoelectronic properties of Dion-Jacobson perovskites based on  $(PDMA)FA_{n-1}Pb_nI_{3n+1}$  ( $n = 1–3$ ) compositions. This system was investigated by X-ray scattering measurements in conjunction with molecular dynamics simulations and density functional theory calculations, as well as UV–vis absorption and photoluminescence spectroscopy and microwave conductivity

measurements. We experimentally demonstrate the formation of layered perovskite structures, although obtaining phase-pure  $n > 1$  compositions remains challenging. The latter is rationalized by our computational studies that show that increasingly endothermic formation enthalpies with increasing number of inorganic layers ( $n$ ) obstruct the realization of  $n > 2$  compositions. Combining the experimental and computational results, we elucidate the intermolecular interactions associated with Dion-Jacobson structures and show that subtle templating effects involving both the organic and the inorganic component are responsible for the structural properties. This results in reduced distances and improved alignment between neighboring layers, which directly affects the electronic properties. Accordingly, despite challenges to obtain phase-pure  $n > 1$  compositions, time-resolved microwave conductivity measurements reveal high photoconductivities and long charge carrier lifetimes that highlight the promising use of these materials in optoelectronics.

## 2. Results and Discussion

We have analyzed thin films of  $(PDMA)FA_{n-1}Pb_nI_{3n+1}$  ( $n = 1–3$ ) compositions that are prepared by solution deposition using

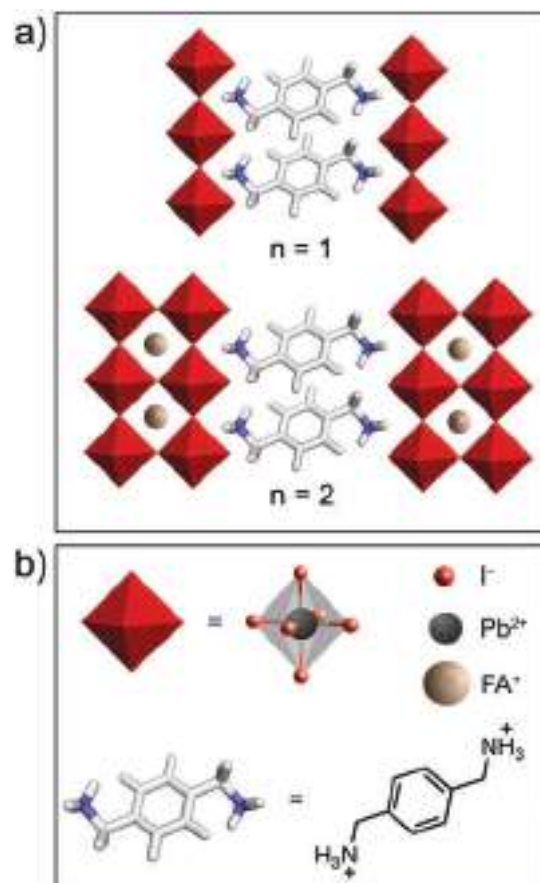


**Figure 1.** Schematic representation of Dion-Jacobson layered hybrid perovskites. a) Envisaged structure of layered perovskites based on  $(PDMA)FA_{n-1}Pb_nI_{3n+1}$  composition incorporating 1,4-phenylenedimethan ammonium cations with b) structural details.

Dr. M. I. Dar, Dr. Y. Li, A. Dučinskas, Dr. A. Ummadisingu,<sup>[\*]</sup>  
Dr. S. M. Zakeeruddin, Dr. J. V. Milić, Prof. M. Graetzel  
Laboratory of Photonics and Interfaces  
Institute of Chemical Sciences and Engineering  
Ecole Polytechnique Fédérale de Lausanne  
Lausanne 1015, Switzerland  
E-mail: jovana.milic@epfl.ch; michael.graetzel@epfl.ch

B. Carlsen, Dr. W. Tress, Prof. A. Hagfeldt  
Laboratory of Photomolecular Science  
Institute of Chemical Sciences and Engineering  
Ecole Polytechnique Fédérale de Lausanne  
Lausanne 1015, Switzerland

stoichiometric amounts of the precursors (PDMAI<sub>2</sub>, FAI, and PbI<sub>2</sub>) in ratios defined by the reported compositions (*n*). The resulting formulations are based on the stoichiometry of the precursors without assumptions regarding the resulting crystal structure. The precursors are dissolved in a mixture of *N,N*-dimethylformamide (DMF) and dimethyl sulfoxide (DMSO) in a 9:1 volume ratio in accordance with the previously optimized procedure.<sup>[16]</sup> The precursor solution was spin-coated at ambient temperature on the corresponding substrate, which was followed by subsequent annealing at 150 °C, as detailed in the Supporting Information. The analysis focused on two substrates, namely fluorine doped tin oxide (FTO) coated with either mp-TiO<sub>2</sub>, which has been previously employed in photovoltaic devices, or mp-Al<sub>2</sub>O<sub>3</sub>, which is used as a nonelectroactive mesoscopic analogue for the analysis of the optoelectronic properties.<sup>[16,24]</sup> Moreover, quartz substrates are used to reliably assess photoconductivities of the materials.<sup>[30,31]</sup>

Structural properties of thin films were investigated by means of X-ray reflectivity (XRR) and grazing incidence X-ray scattering (GIXS) techniques. XRR patterns of the thin films of (PDMA)FA<sub>*n*-1</sub>Pb<sub>*n*</sub>I<sub>3*n*+1</sub> (*n* = 1–3) compositions on FTO/mp-TiO<sub>2</sub> substrates suggest formation of low-dimensional hybrid perovskite structures, which are revealed by the presence of distinct signals in the *q<sub>z</sub>*-range below 1 Å<sup>-1</sup> ( $2\theta < 10^\circ$ ), that are commonly ascribed to the (001) planes (Figure 2a and Figure S1, Supporting Information).<sup>[12,13,15,16]</sup> Films based on *n* = 1 compositions revealed strong signals at *q<sub>z</sub>* = 0.5 Å<sup>-1</sup> and *q<sub>z</sub>* = 1 Å<sup>-1</sup>, indicative for an out-of-plane layered structure. The *n* = 1 structure is characterized by the *d*-spacing of 12.5 Å, that corresponds to the *q*-value of the first maximum, which is in line with the layered phase stacked parallel to the substrate (inset of Figure 2c). This feature is, however, only weakly observed for *n* > 1 compositions (Figure 2 and Figures S1 and S2, Supporting Information). Radial integration of grazing incidence wide-angle X-ray scattering (GIWAXS) patterns (Figure 3d) as well as grazing incidence X-ray diffraction (GIXD) measurements (see Figures S1 and S2 in the Supporting Information) reveal that *n* = 2 compositions feature additional signals at *q<sub>z</sub>* = 0.33 Å<sup>-1</sup> and *q<sub>z</sub>* = 0.67 Å<sup>-1</sup>, indicative of the formation of distinct *n* = 2 layered structures, whereas *n* > 2 compositions were closely comparable to each other irrespective of the stoichiometry of the precursors (Figure 3d and Figures S1 and S2, Supporting Information). Moreover, for *n* = 2 composition, the *n* = 1 structure appears to be present in addition to the newly formed 2D phase, while the sample also features a cubic  $\alpha$ -FAPbI<sub>3</sub> perovskite phase. This is in accordance with the previously reported formation of phase mixtures for *n* > 1 compositions in layered hybrid perovskites.<sup>[16,24,26–29]</sup> The intensity of the cubic  $\alpha$ -FAPbI<sub>3</sub> perovskite phase in the diffraction pattern increases for *n* > 2 compositions, along with the presence of hexagonal  $\delta$ -FAPbI<sub>3</sub> phase. Furthermore, the diffraction patterns for *n* = 3 compositions reveal presence of both *n* = 1 and *n* = 2 phases, along with the 3D  $\alpha$ -FAPbI<sub>3</sub> perovskite phase, possible traces of PbI<sub>2</sub>, as well as  $\delta$ -FAPbI<sub>3</sub> phase, which additionally supports the complexity of the phase mixtures (Figure 3d and Figures S1 and S2, Supporting Information).<sup>[16,24]</sup> However, apart from signals associated with the 3D  $\alpha$ -FAPbI<sub>3</sub> and  $\delta$ -FAPbI<sub>3</sub> phases, the nominal *n* = 3 composition did not reveal presence of any addi-

tional phases that can be directly ascribed to the formation of *n* > 2 representatives (Figures 2 and 3; Figures S1 and S2, Supporting Information).

To understand this absence of the apparent *n* > 2 phases under applied experimental conditions, as well as to further evaluate structural properties of these systems, we conducted a theoretical investigation of their structural and optoelectronic properties. For this purpose, classical molecular dynamics (MD) simulations were performed, followed by density functional theory (DFT) calculations for various perovskite compositions (*n* = 1–3; for computational details refer to the Sections S2 and S3 of the Supporting Information). During the MD simulations for *n* = 1 compositions, a transition from what appears to be a mixed DJ-RP structural intermediate to a pure DJ structure occurs at higher temperatures (>350 K; Figure S5, Supporting Information). Furthermore, the rotation of the spacer is significantly faster for *n* > 1 as compared to the *n* = 1 compositions (Figure S6, Supporting Information). The optimization process further suggests that *n* > 1 compositions do not display any apparent temperature-dependent transition as the system persists in a DJ structure, approaching a near-ideal DJ structure with increasing number of inorganic layers (*n*). This is the result of the complex interplay between the inorganic and organic parts of the material. Unlike the alkyl-based spacer groups that feature weaker van der Waals interactions,<sup>[19]</sup> the intermolecular interactions in the aromatic PDMA spacer layer were found to adopt both T-shaped and parallel-displaced stacking  $\pi$  interactions (Figures S7 and S8, Supporting Information), leading to a more rigid inorganic framework, which was assumed to be associated with the templating effect.<sup>[32]</sup>

To probe possible templating effects of the spacer layer on the inorganic framework, we analyzed the average tilting angle between Pb–I octahedra, as well as the penetration depths of the spacers into the inorganic part by DFT calculations. The latter was assessed by following the distance between the nitrogen atoms of the amino group of the spacer (N) and the nearest inorganic slab Pb positions. We further analyzed the hydrogen bond length between amino group nitrogen atoms of each spacer and the nearest iodide ions of the same inorganic slab (N···I distance), which has previously been used as an indicator of structural stability.<sup>[33]</sup> Based on the DFT-optimized structures, increasing the number of inorganic layers (increasing *n*) leads to an increase in the penetration depth, which corresponds to a decrease of the N···Pb distances. This results in the inorganic layer becoming more cubic, which is indicated by the interoctahedral tilting angles approaching 90°.<sup>[34]</sup> Consequently, the voids between octahedra widen and thus the iodide ions are placed further away from the ammonium groups, leading to an apparent increase of the N···I distances, further suggestive of a templating effect in the inorganic layer.<sup>[34]</sup> To inspect whether this leads in turn to changes in the organic spacer layer, we analyzed its thickness by monitoring the average Pb···Pb distances between opposite layers (*d*<sub>1</sub>) as well as the  $\pi$ – $\pi$  distances between the aromatic rings (*d*<sub>2</sub>) (Figure 2b, Figure S8 and Table S2, Supporting Information). Similar to the behavior of alkyl-based BA and 5-ammonium valeric acid (5-AVA) layered RP perovskite systems,<sup>[34]</sup> the interlayer distance (*d*<sub>1</sub>) was found to decrease upon deeper incorporation of the organic cation into the inorganic layer,



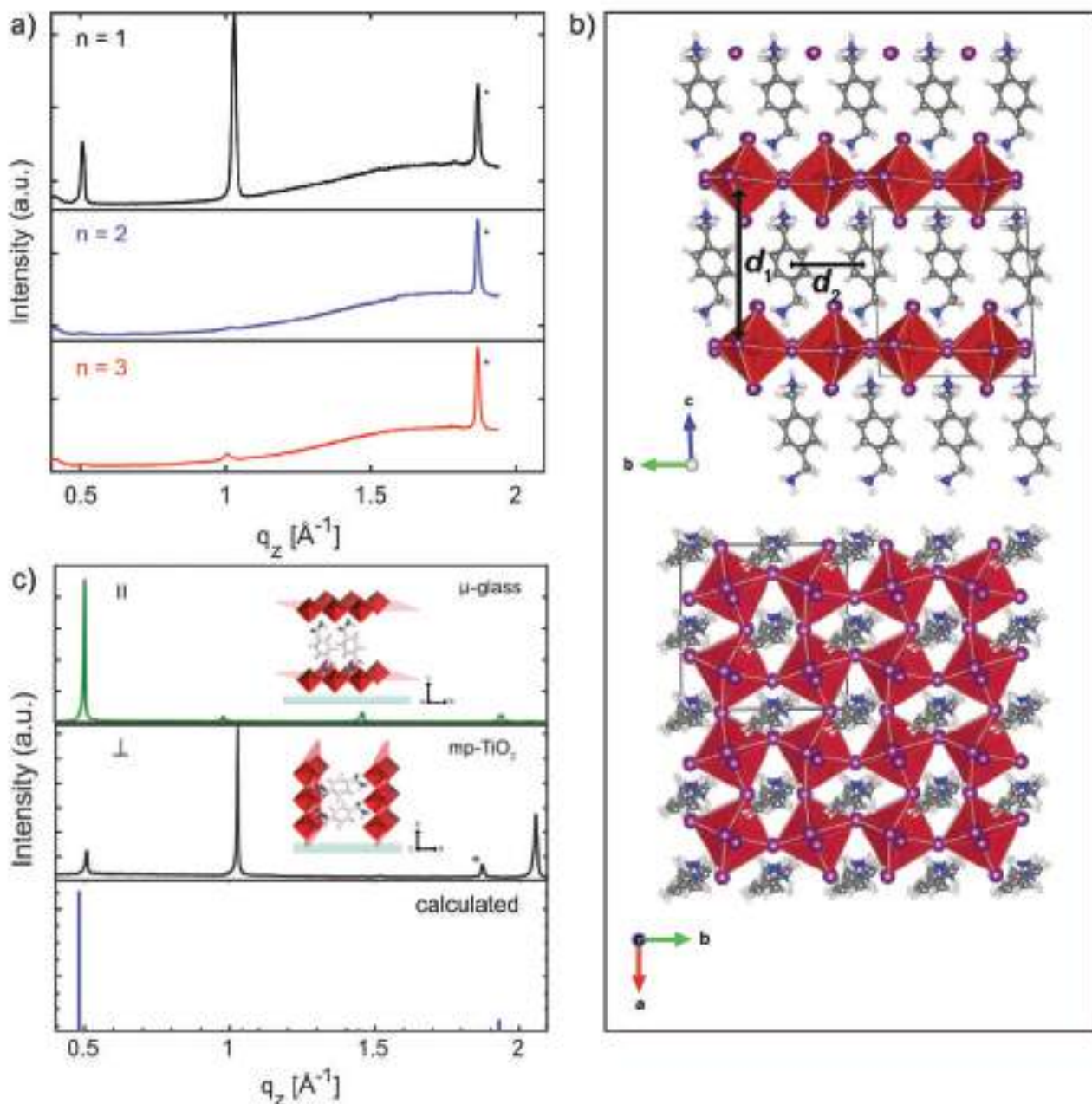


**Figure 2.** Structural properties of thin films based on  $(\text{PDMA})\text{FA}_{n-1}\text{Pb}_n\text{I}_{3n+1}$  composition. a) XRR patterns on FTO/mp-TiO<sub>2</sub> substrates for  $n = 1$  (black),  $n = 2$  (blue) and  $n = 3$  (red) compositions. b) DFT-calculated structure of  $n = 1$  composition ( $d_1$  and  $d_2$  are the characteristic intra and inter-layer distances). More details are shown in Sections S3 and S4 of the Supporting Information. c) Comparison of DFT-simulated (blue) with the experimental XRD patterns of  $(\text{PDMA})\text{PbI}_4$  ( $n = 1$ ) layered structure on either microscopic glass (green) or FTO/mp-TiO<sub>2</sub> (black) substrates. The inset shows schematic representations of parallel ( $\parallel$ ) and perpendicular ( $\perp$ ) orientations of the system with respect to the substrate, commonly associated with  $q_z < 1 \text{ \AA}^{-1}$  ( $2\theta < 10^\circ$ ) and around  $1 \text{ \AA}^{-1}$  ( $2\theta$  around  $14^\circ$ ). Asterisks denote substrate peaks.

which also evidences a templating effect between inorganic slabs and the spacer layer.<sup>[32]</sup> Moreover, the decrease of the inter-layer distances is further pronounced for the DJ phases as compared to the RP ones,<sup>[19]</sup> particularly for spacer groups that feature stronger noncovalent interactions, such as the  $\pi$ -based interactions evidenced for the PDMA spacer. The effect that the organic component has on interlayer distances and alignment of the adjacent layers offers a particularly important approach

to optimize the optoelectronic properties, as these structural parameters are directly related to increasing orbital interactions that facilitate inter-layer charge transport.<sup>[15–20]</sup>

These structural changes are assumed to be apparent in the experimentally obtained thin films. We thereby simulated the XRD patterns for the calculated  $(\text{PDMA})\text{PbI}_4$  structures and compared them to the experimental ones (Figure 2c). The patterns were closely comparable, featuring lowest angle peaks that

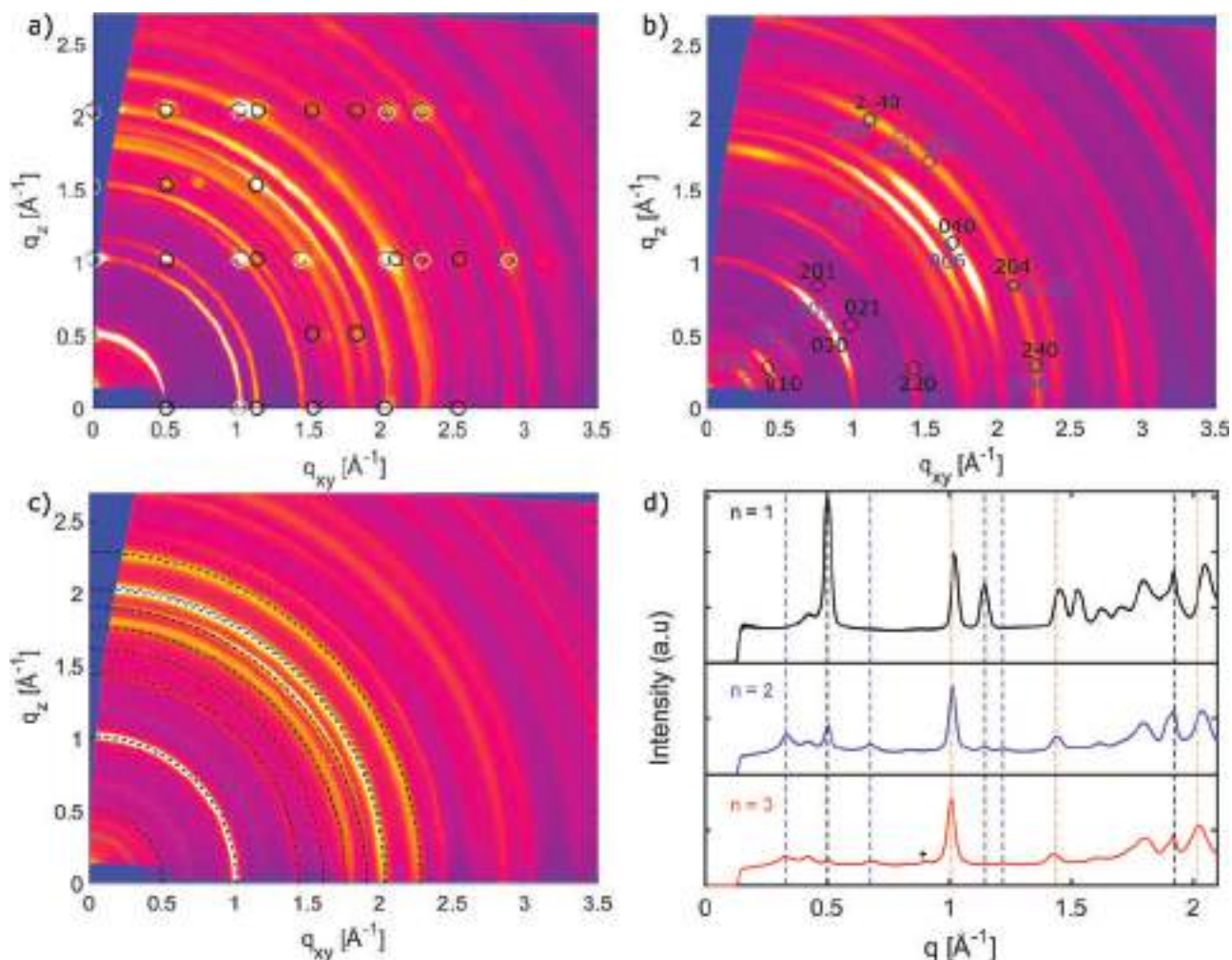


**Figure 3.** Crystal structure analysis and orientation in thin films. a–c) GIWAXS reciprocal space maps ( $\alpha_i = 0.1^\circ$ ) for perovskite thin films based on (PDMA)FA $_{n-1}$ Pb $_n$ I $_{3n+1}$  formulation with a)  $n = 1$ , b)  $n = 2$  and c)  $n = 3$  compositions on FTO/mp-TiO $_2$  substrates. Spot patterns in a) suggest well-defined orientations, while peaks from  $n = 1$  structure oriented perpendicular (parallel) to the substrate are indicated in black (white) circles. Ring-shaped features with angular maxima in b) indicate preferred orientation, while black (blue) circles indicate layered  $n = 1$  ( $n = 2$ ) structure. Uniform angular intensity distribution in c) is in accordance with random orientation of crystallites corresponding to  $n = 1$  and  $n = 2$  structures, which are indicated by black and blue lines, respectively. d) Radially integrated intensities of the  $q$ -maps for nominal  $n = 1$  (black),  $n = 2$  (blue) and  $n = 3$  (red) composition. Signals originating from distinct  $n = 1$  and  $n = 2$  structures are indicated by vertical dashed lines in black and blue, respectively. Yellow vertical dot-dashed lines indicate a cubic perovskite structure, while + marks Pbl $_2$  phase. Angular intensity distributions can be found in Figure S3 (Supporting Information).

correspond to real space interlayer distances of 13 and 12.4  $\text{\AA}$  for calculated and experimental values, respectively. This confirms that the computational models are in good agreement with experimentally obtained systems (Figure 2c).

In the experimental system, however, the anisotropic nature of the layered hybrid perovskite structure enables formation of multiple orientations with respect to the substrate that further affect the properties of these systems. In this regard, two distinct orientations are important, namely the parallel ( $\parallel$ ) and the perpendicular ( $\perp$ ) orientations (Figure 2c, inset). Lower compositional representatives ( $n = 1$ ) are known to feature predominantly  $\parallel$  orientations (Figure 2c), whereas higher compositional representatives ( $n > 1$ ) form  $\perp$  orientations that are more relevant for photovoltaics.<sup>[9,12,14]</sup> The former orientations are commonly revealed through the appearance of (001) plane reflections at  $q_z < 1 \text{ \AA}^{-1}$  ( $2\theta < 10^\circ$ ), while the latter ones

lead to the appearance of the reflections of the (111) plane at  $q_z$  around  $1 \text{ \AA}^{-1}$  ( $2\theta$  of  $\approx 14\text{--}15^\circ$ ). The predominant phase can be further controlled by the experimental conditions (e.g., using additives, hot-casting technique, and other methods).<sup>[9,12]</sup> The orientations with respect to the FTO/mp-TiO $_2$  substrates were analyzed by grazing incidence wide angle X-ray scattering (GIWAXS; Figure 3 and Figures S2–S4, Supporting Information), which indicates well-oriented layered structures for  $n = 1$  compositions with a certain number of disordered domains (Figure 3a, Figures S3a and S4, Supporting Information). Moreover, the  $n = 2$  compositions show ring shaped features with angular maxima, suggesting a preferred orientation (Figure 3b and Figure S3b, Supporting Information). Conversely,  $n > 2$  compositions feature uniform angular intensity distribution that can be associated with a random orientation of crystallites (Figure 3c and Figure S3, Supporting

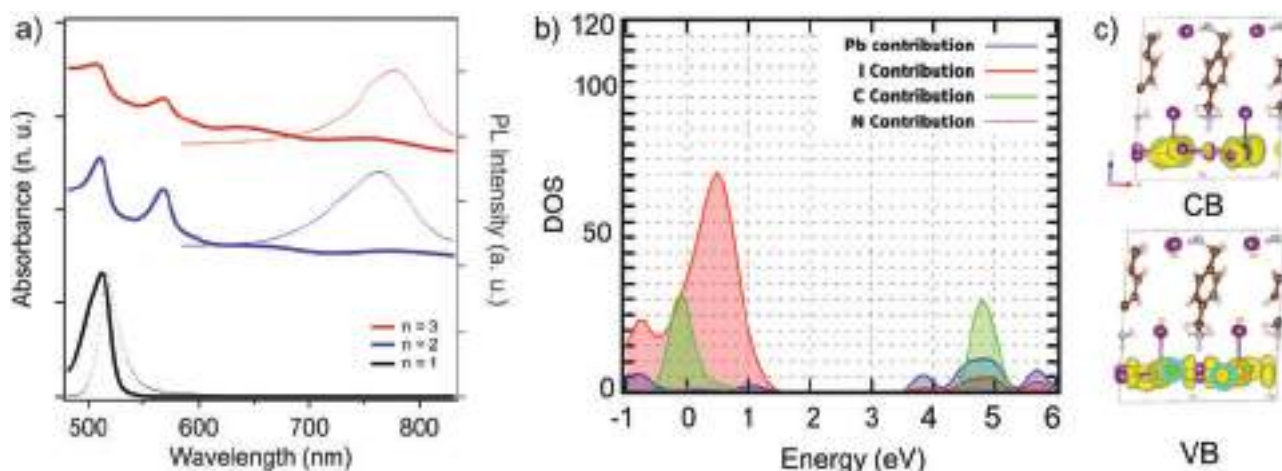


**Figure 4.** Optoelectronic properties of perovskite thin films. a) UV-vis absorption (solid lines, left) and photoluminescence (PL, dashed, right) spectra of thin films based on (PDMA)FA<sub>n-1</sub>Pb<sub>n</sub>I<sub>3n+1</sub> formulation ( $n = 1-3$ ) on FTO/mp-Al<sub>2</sub>O<sub>3</sub> substrates in accordance with the previous report.<sup>[16]</sup> b) Calculated partial density of states and c) Frontier molecular orbitals (top of the valence band (VB, bottom) and bottom of the conduction band (CB, top)) for (PDMA)PbI<sub>4</sub>.

Information), featuring  $n = 1$  and  $n = 2$  compositions. The well-defined orientation of  $n = 1$  compositions enables estimating the unit cell parameters, which were found to match well with the theoretical model, while featuring a minor deviation of the unit cell angles from the ideal cubic structure (Figure S4 and Table S1, Supporting Information). This provides further validation for the theoretical model. However, the challenge lies in the formation of higher compositional ( $n > 2$ ) representatives, which have not been unambiguously evidenced under the applied experimental conditions in this work. To scrutinize the lack of formation of  $n > 2$  phases, we calculated the formation energies by DFT calculations for theoretical models of  $n = 1-3$  systems with respect to the precursors (PbI<sub>2</sub>, FAI, and PDMAI<sub>2</sub>). We found the  $n = 1$  structure exhibits the lowest (essentially thermoneutral) formation energy (-0.00 eV per f.u.), which is higher for  $n > 1$  compositions (0.21 eV per f.u. for  $n = 2$  and 0.30 eV per f.u. for  $n = 3$ ), indicating relative instability of higher ( $n > 1$ ) compositional representatives with respect the  $n = 1$  system and  $\alpha$ -FAPbI<sub>3</sub>, which exhibits the formation energy of 0.08 eV per f.u. (Figure S8, Supporting Information). This could potentially be circumvented by introducing smaller ions in the composition, such as Cs and Br, which can stabilize the perovskite ( $\alpha$ ) FAPbI<sub>3</sub> phase, and consequently, could facilitate the formation of higher compositional ( $n > 2$ ) representatives.<sup>[21,35]</sup>

The resulting structural features directly affect the optoelectronic properties of the system, which were analyzed experimentally by UV-vis absorption and steady-state photoluminescence (PL) emission spectroscopy (Figure 4a). The spectra reveal a trend in optical bandgap energy ( $E_g$ ) that has been previously reported and is typical of low-dimensional perovskites, as it decreases with the increase in the relative number of inorganic slabs ( $n$ , Figure 4a).<sup>[12,14,26,35-37]</sup> Moreover, the UV-vis absorption spectra show characteristic excitonic features, which disappear with an increase in the number of inorganic layers ( $n$ , Figure 4a) and is likely due to the increasing contribution of the 3D perovskite phase.<sup>[13,38]</sup> These features can also serve as a qualitative indicator for the presence of a certain structural phase and, in this regard, the  $n = 1$  compositions show

well-defined optical signatures (Figure 4a, black), whereas  $n > 1$  compositions reveal multiple signals in the UV-vis absorption spectra accompanied by a large Stokes shift in the PL spectra (Figure 4a, red and blue). This is in accordance with the presence of a mixture of phases and the coexistence of 3D FAPbI<sub>3</sub> perovskite phase,<sup>[16,24]</sup> as confirmed by the XRR and GIWAXS measurements. Accordingly, PL spectra of the films based on higher  $n > 1$  compositions display emission around 770 nm whereas those based on lower  $n = 1$  compositions feature the main emission at around 550 nm (Figure 4a), similarly to the other reported DJ phases.<sup>[15,17]</sup> DFT-calculated bandgaps (for details see Section S3, Supporting Information) follow the expected trend as a function of  $n$  and yield a value for (PDMA)PbI<sub>4</sub> of 2.8 eV, which is 0.4 eV larger than the experimental optical gap due to excitonic contributions (Table S3, Supporting Information).<sup>[16]</sup> Indeed, this energy difference is consistent with the reported exciton binding energies for 2D perovskites, which are in the order of 380 meV.<sup>[30,38]</sup> Furthermore, the effective masses in the in-plane directions decrease with increasing  $n$  (Tables S2 and S3, Supporting Information). As expected, significantly higher values of effective masses are observed in the perpendicular direction to the inorganic layer. However, the results of the calculations of the partial density of states (Figure 4b), as well as the frontier molecular orbitals (Figure 4c), exclude a direct contribution of the organic part to the band edges. Nevertheless, the values for effective masses, especially in the perpendicular direction, are smaller than some of the representative RP phases.<sup>[34]</sup> This is likely due to reduced interlayer distances and better alignment of inorganic layers in the DJ structure, which results in improved charge transport and optoelectronics.

The charge carrier dynamics were investigated by time-resolved microwave conductivity (TRMC) measurements. In these measurements, high-frequency microwaves are used to probe the change in the conductivity of materials due to generated mobile charge carriers. Mobile charge carriers absorb a fraction of the incoming microwave power ( $\Delta P$ ), which is proportional to the change in the conductivity of the material

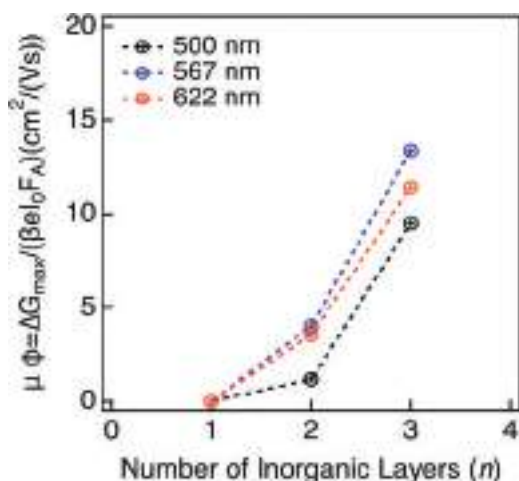


**Figure 5.** Maximum photoconductivity of thin films at 298 K based on (PDMA)FA<sub>n-1</sub>Pb<sub>n</sub>I<sub>3n+1</sub> composition ( $n = 1-3$ ) excited at the respective excitonic wavelengths (500, 567, and 622 nm) of  $n = 1$  (black),  $n = 2$  (blue) and  $n = 3$  (red), respectively.

( $\Delta\sigma$ ). It is possible to generate charge carriers using either a high energy electron pulse (pulse-radiolysis, PR-TRMC) or by laser excitation (photoconductivity TRMC).<sup>[30]</sup> PR-TRMC is used to determine the mobility of charge carriers on materials in crystal form. The high-energy electron pulse assures the generation of free charge carriers (i.e., electrons and holes), independently of the exciton binding energy of the material.<sup>[30]</sup> The mobility of charge carriers was measured on powders of layered hybrid perovskites of different compositions ( $n = 1-3$ ) synthesized mechanochemically. However, the powder samples prepared by this method exhibit a large concentration of defects that obscure the mobility and charge carrier dynamics on these materials (Figures S10 and S11, Supporting Information).<sup>[31]</sup>

In a separate experiment, we used the TRMC technique together with photoexcitation with a nanosecond laser pulse to analyze photoinduced conductivity in thin films based (PDMA) FA<sub>n-1</sub>Pb<sub>n</sub>I<sub>3n+1</sub> ( $n = 1-3$ ) compositions of  $\approx 200$  nm thickness. The photoconductivity signal that is measured is directly influenced by the exciton binding energy of the material.<sup>[30]</sup> As a result, the photoconductivity obtained from the TRMC experiment is the product of charge mobility ( $\mu$ ) and quantum yield of free charge carrier formation ( $\phi$ ) in accordance with the Equation (1).

$$\phi \sum \mu = \frac{\Delta G_{\max}}{I_0 \beta e F_A} \quad (1)$$

Here,  $\Delta G_{\max}$  is the maximum photoconductance,  $I_0$  is the number of photons per unit area per pulse,  $\beta$  is defined by the dimensions of the microwave cavity,  $e$  is the elementary charge, whereas  $F_A$  is the fraction of photons that is absorbed by the sample.

The samples were photoexcited at three different wavelengths that correspond to the excitonic peaks of the different number of inorganic layers (Figure 4a), namely 500 nm ( $n = 1$ ), 560 nm for ( $n = 2$ ) and 622 nm ( $n = 3$ ). The photoconductivity was found to increase with the number of inorganic layers ( $n$ ; Figure 5b), which is in accordance with the reduction of the

effective masses revealed by DFT calculations, as well as a gradual decrease in the exciton binding energy, which will result in an increase of the yield of dissociation of charge carriers ( $\phi$ ).<sup>[30]</sup> The photoconductivity for  $n = 3$  compositions is found to be at the order of magnitude of 3D FAPbI<sub>3</sub> films measured with the same technique (8–60 cm<sup>2</sup> V<sup>-1</sup> s<sup>-1</sup>; Figure 5b and Figure S11, Supporting Information). However, the  $n = 3$  composition contains a mixture of FAPbI<sub>3</sub> with  $n = 2$  and  $n = 1$  layers, hence the high photoconductivity is likely affected by the 3D FAPbI<sub>3</sub> phase. The photoconductivity for the  $n = 2$  composition is around 4 cm<sup>2</sup> V<sup>-1</sup> s<sup>-1</sup>, which is an order of a magnitude higher than 2D Ruddlesden-Popper  $n = 2$  (e.g. BA<sub>2</sub>Pb<sub>2</sub>I<sub>7</sub>) phase<sup>[30]</sup> and a value suitable for photovoltaic applications. The presence of 3D FAPbI<sub>3</sub> is to a large extent responsible for this high, long-lived photoconductivity signal (shown in Figure S11 of the Supporting Information). In the case of the  $n = 1$  material, the photoconductivity is comparable to pure 2D Ruddlesden-Popper layered perovskite systems (0.1–0.3 cm<sup>2</sup> V<sup>-1</sup> s<sup>-1</sup>).<sup>[30]</sup>

We further analyzed the charge carrier dynamics in thin films to find that the height of the photoconductivity and lifetime signal for  $n = 1-3$  compositions decrease as the photon intensity increases, following a second order behavior (Figure S12, Supporting Information). In addition, it is clear that the lifetime increases with the number of inorganic layers, exhibiting a long-lived component for  $n > 1$  compositions in the order of 20  $\mu$ s for  $n = 2$  and 15 ms for  $n = 3$  compositions (Figure 6). This long-lived component is longer than the lifetime observed for 3D FAPbI<sub>3</sub> perovskites (Figure S11, Supporting Information). At these longer time scales, the decay traces for  $n = 2$  compositions seem to show a second order behavior (Figure 6a), whereas for  $n = 3$  composition a first order behavior is apparent, the lifetime of carriers being independent of their initial concentration (Figure 6b).

While the photoconductivity of the films could be improved in pure phases, the corresponding photoconductivity and long-lived component for  $n = 2$  and  $n = 3$  compositions are quite remarkable under these conditions, in line with their promising photovoltaic performance. These performances presently remain inferior to the 3D and 2D/3D perovskite solar cells, which can be ascribed to the challenges associated with the phase purity as well as the lower conductivity of the spacer layer that is particularly detrimental in the parallel orientation of the perovskite phases. Therefore, further control of the corresponding perovskite phase formation and orientation, along with optimizing the device architectures, could lead to improved photovoltaic performances of perovskite solar cells incorporating DJ phases in the future.

### 3. Conclusion

We investigated layered hybrid perovskites based on (PDMA) FA<sub>n-1</sub>Pb<sub>n</sub>I<sub>3n+1</sub> ( $n = 1-3$ ) compositions to unravel the underlying structural and photophysical properties of these unique Dion-Jacobson phases that determine their photovoltaic performances. X-ray scattering measurements confirm presence of a layered structure for  $n = 1$  and  $n = 2$  nominal compositions, whereas mixtures of phases are apparent for  $n = 3$  composition without evidencing the formation of higher  $n > 2$  representatives.

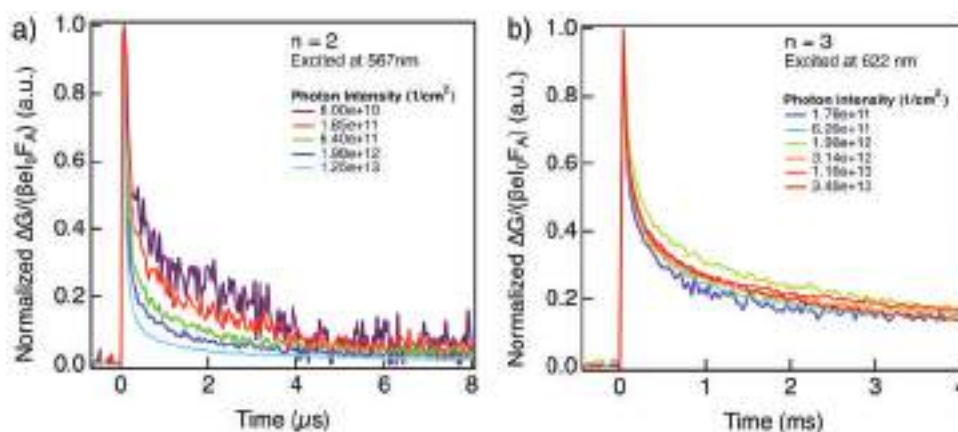


**Figure 6.** Charge carrier dynamics. Normalized photoconductivity as a function of photon intensity of (PDMA)FA<sub>*n*-1</sub>Pb<sub>*n*</sub>I<sub>3*n*+1</sub> thin films on quartz substrates based on a) *n* = 2 and b) *n* = 3 nominal compositions highlighting long lived-component in the order of μs–ms.

Molecular dynamics simulations and density functional theory calculations of Dion-Jacobson structures complement the experimental findings by elucidating intermolecular interactions and revealing less favorable formation enthalpies with increasing number of inorganic layers (*n*). Moreover, the subtle interaction between the organic moieties and hybrid perovskite layers were found to result in smaller interlayer distances and better alignment as compared to the Ruddlesden-Popper phases, resulting in lower effective masses for charge carriers. Consequently, despite the challenges in obtaining pure phases of *n* > 1 compositions, time-resolved microwave conductivity measurements reveal high photoconductivities and long charge carrier lifetimes in the order of hundreds of microseconds for *n* ≥ 2 compositions that can account for the promising photovoltaic performances of these materials. This study thereby provides important new insights for the design of hybrid low-dimensional perovskite materials for optoelectronic applications.

## 4. Experimental Section

Synthesis and characterization of materials, as well as the corresponding methods are provided in the Supporting Information.

## Supporting Information

Supporting Information is available from the Wiley Online Library or from the authors.

## Acknowledgements

J.V.M., S.M.Z., and M.G. are grateful to the European Union's Horizon 2020 research and innovation program under grant agreement No. 826013 (IMPRESSIVE) as well as the King Abdulaziz City for Science and Technology (KACST) for financial support. U.R. acknowledges SNSF Grant No. 200020-185092, NCCR-MUST, NRP70, and the SINERGIA interdisciplinary research program EPISODE for funding. The work at Delft University of Technology (M.C.G.-R. and F.C.G.) is funded by the European Research Council Horizon 2020 ERC Grant Agreement no. 648433. The authors are grateful to the European Synchrotron Radiation Facility (ESRF) for the provision of synchrotron radiation and

they thank Oleg Konovalov for providing assistance in using beamline ID10. The authors are also grateful to Dr. Dominik J. Kubicki (EPFL) for insightful discussions in the course of this project.

## Conflict of Interest

The authors declare no conflict of interest.

## Author Contributions

M.C.G.-R., P.A., and L.M. contributed equally to this work. The manuscript was written by J.V.M., L.M., F.J., P.A., M.M., and M.G.-R. with the support of all authors. The project was conceptualized by J.V.M., who coordinated the investigation. M.C.G.-R. and F.C.G. performed the photoconductivity measurements and analysis of charge carrier dynamics with the support of W.T. while P.A., M.M., F.J., and U.R. performed, analyzed, and interpreted the molecular dynamics simulations and DFT calculations. L.M. and A.H. performed the X-ray scattering measurements and the analysis with the support of M.I.D. and F.S. while Y.L. and A.D. prepared the samples. A.D. analyzed substrate-dependent XRD patterns. A.U. conducted the XRD and PL spectroscopy. B.C., A.H., and S.M.Z. were involved in the discussion and provided support in project coordination, while M.G. directed the project.

## Keywords

2D perovskites, Dion-Jacobson structures, layered hybrid perovskites, perovskite solar cells, photoconductivity

Received: April 18, 2020

Revised: May 15, 2020

Published online: July 19, 2020

- [1] A. K. Jena, A. Kulkarni, T. Miyasaka, *Chem. Rev.* **2019**, *119*, 3036.
- [2] M. Grätzel, *Acc. Chem. Res.* **2017**, *50*, 487.
- [3] S. Kazim, M. K. Nazeeruddin, M. Grätzel, S. Ahmad, *Angew. Chem., Int. Ed.* **2014**, *53*, 2812.
- [4] R. Wang, M. Mujahid, Y. Duan, Z.-K. Wang, J. Xue, Y. Yang, *Adv. Funct. Mater.* **2019**, *29*, 1808843.

- [5] Y. Rong, Y. Hu, A. Mei, H. Tan, M. I. Saidaminov, S. I. Seok, M. D. McGehee, E. H. Sargent, H. Han, *Science* **2018**, *361*, eaat8235.
- [6] J. V. Milić, D. J. Kubicki, L. Emsley, M. Grätzel, *Chim. Int. J. Chem.* **2019**, *73*, 317.
- [7] B. Saparov, D. B. Mitzi, *Chem. Rev.* **2016**, *116*, 4558.
- [8] L. Mao, C. C. Stoumpos, M. G. Kanatzidis, *J. Am. Chem. Soc.* **2019**, *141*, 1171.
- [9] G. Grancini, M. K. Nazeeruddin, *Nat. Rev. Mater.* **2019**, *4*, 4.
- [10] N. Mercier, *Angew. Chem., Int. Ed.* **2019**, *58*, 17912.
- [11] a) G. Liu, H. Zheng, H. Xu, L. Zhang, X. Xu, S. Xu, X. Pan, *Nano Energy* **2020**, *73*, 104753; b) H. Zheng, W. Wu, H. Xu, F. Zheng, G. Liu, X. Pan, Q. Chen, *Adv. Funct. Mater.* **2020**, *30*, 2000034.
- [12] C. C. Stoumpos, D. H. Cao, D. J. Clark, J. Young, J. M. Rondinelli, J. I. Jang, J. T. Hupp, M. G. Kanatzidis, *Chem. Mater.* **2016**, *28*, 2852.
- [13] Y. Chen, Y. Sun, J. Peng, J. Tang, K. Zheng, Z. Liang, *Adv. Mater.* **2017**, *131*, 1703487.
- [14] N. Wang, L. Cheng, R. Ge, S. Zhang, Y. Miao, W. Zou, C. Yi, Y. Sun, Y. Cao, R. Yang, Y. Wei, Q. Guo, Y. Ke, M. Yu, Y. Jin, Y. Liu, Q. Ding, D. Di, Le Yang, G. X., H. Tian, C. Jin, F. Gao, R. H. Friend, J. Wang, W. Huang, *Nat. Photonics* **2016**, *10*, 699.
- [15] L. Mao, W. Ke, L. Pedesseau, Y. Wu, C. Katan, J. Even, M. R. Wasielewski, C. C. Stoumpos, M. G. Kanatzidis, *J. Am. Chem. Soc.* **2018**, *140*, 3775.
- [16] Y. Li, J. V. Milić, A. Ummadisingu, J.-Y. Seo, J.-H. Im, H.-S. Kim, Y. Liu, M. I. Dar, S. M. Zakeeruddin, P. Wang, A. Hagfeldt, M. Grätzel, *Nano Lett.* **2019**, *19*, 150.
- [17] B.-E. Cohen, Y. Li, Q. Meng, L. Etgar, *Nano Lett.* **2019**, *19*, 2588.
- [18] X. Li, W. Ke, B. Traore, P. Guo, I. Hadar, M. Kepenekian, J. Even, C. Katan, C. C. Stoumpos, R. D. Schaller, M. G. Kanatzidis, *J. Am. Chem. Soc.* **2019**, *141*, 12880.
- [19] Z. Xu, M. Chen, S. F. Liu, *J. Phys. Chem. Lett.* **2019**, *10*, 3670.
- [20] Y. Zheng, T. Niu, J. Qiu, L. Chao, B. Li, Y. Yang, Q. Li, C. Lin, X. Gao, C. Zhang, Y. Xia, Y. Chen, W. Huang, *Sol. RRL* **2019**, *3*, 201900090.
- [21] G. Li, T. Zhang, N. Guo, F. Xu, X. Qian, Y. Zhao, *Angew. Chem., Int. Ed.* **2016**, *55*, 13460; *Angew. Chem.* **2016**, *128*, 13658.
- [22] J. Yan, W. Fu, X. Zhang, J. Chen, W. Yang, W. Qiu, G. Wu, F. Liu, P. Heremans, H. Chen, *Mater. Chem. Front.* **2017**, *2*, 121.
- [23] H. Zheng, G. Liu, L. Zhu, J. Ye, X. Zhang, A. Alsaedi, T. Hayat, X. Pan, S. Dai, *Adv. Energy Mater.* **2018**, *8*, 1800051.
- [24] J. V. Milić, J.-H. Im, D. J. Kubicki, A. Ummadisingu, J.-Y. Seo, Y. Li, M. A. Ruiz Preciado, M. I. Dar, S. M. Zakeeruddin, L. Emsley, M. Grätzel, *Adv. Energy Mater.* **2019**, *9*, 1900284.
- [25] A. Q. Alanazi, D. J. Kubicki, D. Prochowicz, E. A. Alharbi, M. E. F. Bouduban, F. Jahanbakhshi, M. Mladenović, J. V. Milić, F. Giordano, D. Ren, A. Y. Alyamani, H. Albrithen, A. Albadri, M. H. Alotaibi, J.-E. Moser, S. M. Zakeeruddin, U. Rothlisberger, L. Emsley, M. Grätzel, *J. Am. Chem. Soc.* **2019**, *141*, 17659.
- [26] D. H. Cao, C. C. Stoumpos, O. K. Farha, J. T. Hupp, M. G. Kanatzidis, *J. Am. Chem. Soc.* **2015**, *137*, 7843.
- [27] L. N. Quan, M. Yuan, R. Comin, O. Voznyy, E. M. Beaugard, S. Hoogland, A. Buin, A. R. Kirmani, K. Zhao, A. Amassian, D. H. Kim, E. H. Sargent, *J. Am. Chem. Soc.* **2016**, *138*, 2649.
- [28] J. Liu, J. Leng, K. Wu, J. Zhang, S. Jin, *J. Am. Chem. Soc.* **2017**, *139*, 1432.
- [29] A. H. Proppe, R. Quintero-Bermudez, H. Tan, O. Voznyy, S. O. Kelley, E. H. Sargent, *J. Am. Chem. Soc.* **2018**, *140*, 2890.
- [30] M. C. Gélvez-Rueda, E. M. Hutter, D. H. Cao, N. Renaud, C. C. Stoumpos, J. T. Hupp, T. J. Savenije, M. G. Kanatzidis, F. C. Grozema, *J. Phys. Chem. C* **2017**, *121*, 26566.
- [31] R. Herckens, W. T. M. Van Gompel, W. Song, M. C. Gélvez-Rueda, A. Maufort, B. Ruttens, J. D'Haen, F. C. Grozema, T. Aernouts, L. Lutsen, D. Vanderzande, *J. Mater. Chem. A* **2018**, *6*, 22899.
- [32] D. B. Mitzi, *J. Chem. Soc., Dalton Trans.* **2001**, 1, <https://doi.org/10.1039/b007070j>.
- [33] S. Ahmad, P. Fu, S. Yu, Q. Yang, X. Liu, X. Wang, X. Wang, X. Guo, C. Li, *Joule* **2019**, *3*, 794.
- [34] N. Ashari-Astani, F. Jahabakhshi, M. Mladenović, A. Q. M. Alanazi, I. Ahmadabadi, M. R. Ejtehadi, M. I. Dar, M. Grätzel, U. Rothlisberger, *J. Phys. Chem. Lett.* **2019**, *10*, 3543.
- [35] a) C. Yi, J. Luo, S. Meloni, A. Boziki, N. Ashari-Astani, C. Grätzel, S. M. Zakeeruddin, U. Rothlisberger, M. Grätzel, *Energy Environ. Sci.* **2016**, *9*, 656; b) Z. Wang, Q. Lin, F. P. Chmiel, N. Sakai, L. M. Herz, H. J. Snaith, *Nat. Energy* **2017**, *2*, 17135.
- [36] H. Tsai, W. Nie, J.-C. Blancon, C. C. Stoumpos, R. Asadpour, B. Harutyunyan, A. J. Neukirch, R. Verduzco, J. J. Crochet, S. Tretiak, L. Pedesseau, J. Even, M. A. Alam, G. Gupta, J. Lou, P. M. Ajayan, M. J. Bedzyk, M. G. Kanatzidis, A. D. Mohite, *Nature* **2016**, *536*, 312.
- [37] L. Gan, J. Li, Z. Fang, H. He, Z. Ye, *J. Phys. Chem. Lett.* **2017**, *8*, 5177.
- [38] J. C. Blancon, H. Tsai, W. Nie, C. C. Stoumpos, L. Pedesseau, C. Katan, M. Kepenekian, C. M. M. Soe, K. Appavoo, M. Y. Sfeir, S. Tretiak, P. M. Ajayan, M. G. Kanatzidis, J. Even, J. J. Crochet, A. D. Mohite, *Science* **2017**, *355*, 1288.

Cite this: *J. Mater. Chem. A*, 2020, **8**, 17732

## Unravelling the structural complexity and photophysical properties of adamantyl-based layered hybrid perovskites†

Farzaneh Jahanbakhshi,<sup>†a</sup> Marko Mladenović,<sup>†§a</sup> Ekaterina Kneschaurek,<sup>†b</sup> Lena Merten,<sup>b</sup> María C. Gélvez-Rueda,<sup>c</sup> Paramvir Ahlawat,<sup>†a</sup> Yang Li,<sup>d</sup> Algirdas Dučinskas,<sup>d</sup> Alexander Hinderhofer,<sup>b</sup> M. Ibrahim Dar,<sup>†d</sup> Wolfgang Tress,<sup>e</sup> Brian Carlsen,<sup>e</sup> Amita Ummadisingu,<sup>†d</sup> Shaik M. Zakeeruddin,<sup>†d</sup> Anders Hagfeldt,<sup>†e</sup> Frank Schreiber,<sup>†\*b</sup> Ferdinand C. Grozema,<sup>†\*c</sup> Ursula Rothlisberger,<sup>\*a</sup> Jovana V. Milić<sup>†\*d</sup> and Michael Graetzel<sup>†\*d</sup>

Layered hybrid perovskites comprising adamantyl spacer (A) cations based on the  $A_2FA_{n-1}Pb_nI_{3n+1}$  ( $n = 1-3$ , FA = formamidinium) compositions have recently been shown to act as promising materials for photovoltaic applications. While the corresponding perovskite solar cells show performances and stabilities that are superior in comparison to other layered two-dimensional formamidinium-based perovskite solar cells, the underlying reasons for their behaviour are not well understood. We provide a comprehensive investigation of the structural and photophysical properties of this unique class of materials, which is complemented by theoretical analysis *via* molecular dynamics simulations and density functional theory calculations. We demonstrate the formation of well-defined structures of lower compositional representatives based on  $n = 1-2$  formulations with (1-adamantyl)methan ammonium spacer moieties, whereas higher compositional representatives ( $n > 2$ ) are shown to consist of mixtures of low-dimensional phases evidenced by grazing incidence X-ray scattering. Furthermore, we reveal high photoconductivities of the corresponding hybrid perovskite materials, which is accompanied by long charge carrier lifetimes. This study thereby unravels features that are relevant for the performance of FA-based low-dimensional hybrid perovskites.

Received 15th May 2020  
Accepted 29th July 2020

DOI: 10.1039/d0ta05022a

rsc.li/materials-a

## Introduction

Hybrid organic–inorganic perovskite materials remain attractive for various optoelectronic applications.<sup>1–3</sup> Their layered two-dimensional (2D) analogues have demonstrated superior

environmental stabilities.<sup>4,5</sup> They are predominantly based on  $S_2Y_{n-1}M_nX_{3n+1}$  compositions, where S represents a monofunctional organic spacer cation, Y stands for the central cation (commonly methylammonium (MA), formamidinium (FA) or  $Cs^+$ ), M for a divalent metal (mainly  $Pb^{2+}$  and  $Sn^{2+}$ ) and X for a halide anion ( $I^-$ ,  $Br^-$ ,  $Cl^-$ ). This development has been particularly important for FA-based hybrid perovskite systems, since their perovskite phase stabilization remains challenging.<sup>6–9</sup> In this regard, there have been very few examples to date that involve low-dimensional perovskite systems incorporating FA as a central cation.<sup>10–13</sup> We have recently shown that this can be achieved by using (1-adamantyl)methan ammonium (ADAM or A) as an organic spacer cation.<sup>13</sup> As a result, performances of the corresponding solar cells that surpass those of the state-of-the-art FA-based two-dimensional (2D) perovskites under ambient preparation conditions were demonstrated, which could not be achieved in absence of the methylene-linker, as in the case of the 1-adamantylammonium (ADA or A') analog.<sup>13</sup> However, the underlying reasons for this behaviour have not been entirely understood, despite their importance for the structure–property relationships that are critical for guiding advanced molecular design.

<sup>a</sup>Laboratory of Computational Chemistry and Biochemistry, EPFL, Switzerland. E-mail: ursula.roethlisberger@epfl.ch

<sup>b</sup>Soft Matter Physics, University of Tuebingen, Germany. E-mail: frank.schreiber@uni-tuebingen.de

<sup>c</sup>Delft University of Technology, The Netherlands. E-mail: f.c.grozema@tudelft.nl

<sup>d</sup>Laboratory of Photonics and Interfaces, EPFL, Lausanne, Switzerland. E-mail: jovana.milic@epfl.ch; michael.graetzel@epfl.ch

<sup>e</sup>Laboratory of Photomolecular Science, EPFL, Lausanne, Switzerland

† Electronic supplementary information (ESI) available. See DOI: 10.1039/d0ta05022a

‡ These authors contributed equally.

§ M. I. D. are currently affiliated with the Cavendish Laboratory at the University of Cambridge, United Kingdom. M. M. is also affiliated with the Scientific Computing Laboratory, Center for the Study of Complex Systems, Institute of Physics Belgrade, University of Belgrade, Pregrevica 118, 11080 Belgrade, Serbia. A. U. is currently a Swiss National Science Foundation Fellow at the Cavendish Laboratory, University of Cambridge, 19 J J Thomson Avenue, Cambridge CB3 0HE, United Kingdom.



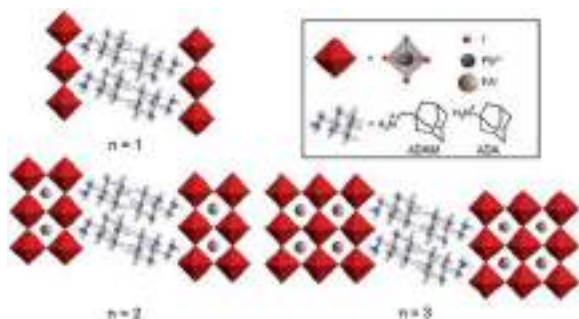


Fig. 1 Schematic representation of adamantyl-based layered hybrid perovskites based on the  $S_2FA_{n-1}Pb_nI_{3n+1}$  ( $n = 1-3$ ;  $S = ADAM$  or  $A$ ,  $ADA$  or  $A'$ ) composition.  $ADAM = (1\text{-adamantyl})\text{methan ammonium}$ ;  $ADA = 1\text{-adamantyl ammonium}$ .

Herein, we investigate the structural and photophysical properties of layered hybrid perovskites based on the  $A_2FA_{n-1}Pb_nI_{3n+1}$  ( $A = ADAM$ ) and  $A'_2FA_{n-1}Pb_nI_{3n+1}$  ( $A' = ADA$ ) compositions (Fig. 1) by a combined methodological approach including grazing incidence wide angle X-ray scattering (GIWAXS) and time-resolved microwave photoconductivity measurements, which are complemented by molecular dynamics (MD) simulations and density functional theory (DFT) calculations. As a result, we scrutinize the phase purity of different compositional representatives and their preferred orientation, as well as the corresponding photoconductivity and charge carrier dynamics, which provide important insights for the advanced design of layered hybrid perovskite materials and their applications.

## Results and discussion

We investigated thin films of  $A_2FA_{n-1}Pb_nI_{3n+1}$  and  $A'_2FA_{n-1}Pb_nI_{3n+1}$  ( $n = 1-3$ ) compositions. The materials were prepared by solution deposition methods of stoichiometric amounts of the corresponding precursors (AI, A'I, FAI, and  $PbI_2$ ) in accordance with the previously reported procedures.<sup>13</sup> The precursors were dissolved in a (4 : 1 v/v) solvent mixture of *N,N*-dimethylformamide (DMF) and dimethyl sulfoxide (DMSO). The precursor solution was spin-coated on the substrates at ambient temperature, which was followed by subsequent annealing at 150 °C for 15 min. The reported compositions ( $n$ ) are based on the stoichiometry of the precursors, without making assumptions about the resulting structure, and are thus referred to as nominal. We employed two different substrates in the study, either microscopic glass or fluorine doped tin oxide (FTO) coated with mp-TiO<sub>2</sub>, which has been previously employed in photovoltaic devices.<sup>13</sup> In addition, we used quartz substrates to assess the photoconductivities of materials in thin films and powders.<sup>14,15</sup> The powders of the perovskite materials were accessed mechanochemically by grinding the precursors in a ball mill based on previously reported procedures.<sup>13,16-18</sup> The methods are detailed in the Experimental section, as well as the ESI†

### Structural properties

Thin films based on  $A_2FA_{n-1}Pb_nI_{3n+1}$  and  $A'_2FA_{n-1}Pb_nI_{3n+1}$  ( $n = 1-3$ ) compositions were investigated by using X-ray diffraction

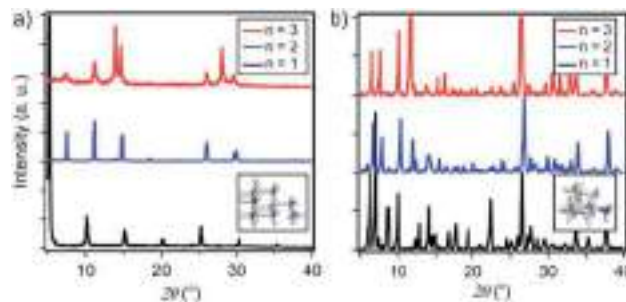


Fig. 2 Structural properties of thin films. XRD patterns of (a)  $A_2FA_{n-1}Pb_nI_{3n+1}$  and (b)  $A'_2FA_{n-1}Pb_nI_{3n+1}$  on FTO/mp-TiO<sub>2</sub> substrates for  $n = 1$  (black),  $n = 2$  (blue) and  $n = 3$  (red) compositions in accordance with the previous report.<sup>13</sup> Inset shows DFT-optimised (B3LYP/6-31G(d)) structures of the spacers (a)  $A$  and (b)  $A'$ .

(XRD; Fig. 2) and GIWAXS (Fig. 3 and S1–S3, ESI†) for the purpose of understanding their structural properties. Their structure was previously assessed at the atomic-level by solid-state nuclear magnetic resonance (NMR) spectroscopy, suggesting the formation of new iodoplumbate phases that are likely to be associated with layered perovskites.<sup>13</sup> As reported earlier, XRD patterns of  $A_2FA_{n-1}Pb_nI_{3n+1}$  on FTO/mp-TiO<sub>2</sub> substrates reveal the appearance of signals in the  $2\theta$  range below 10°, which is indicative of the formation of low-dimensional hybrid perovskite structures (Fig. 2a).<sup>19-22</sup> This is particularly the case for films based on  $n = 1$  compositions, showing periodic patterns that are typical for layered 2D structures (Fig. 2a).<sup>19-22</sup> However,  $A'_2FA_{n-1}Pb_nI_{3n+1}$  analogues feature a number of signals in the  $2\theta < 10^\circ$  range irrespective of their composition ( $n = 1-3$ ) as a result of the formation of complex mixtures of various phases (Fig. 2b), which could correspond to intermediate phases or other low-dimensional polymorphs.<sup>13</sup> Additional high resolution X-ray reflectivity (XRR) for the layered structures of  $A_2FA_{n-1}Pb_nI_{3n+1}$  systems are shown in the ESI (Fig. S1†). XRR was used to complement the GIWAXS analysis in order to investigate the out-of-plane structure of the samples at  $q_{xy} = 0$  since GIWAXS cannot access the true specular (out-of-plane) scattering due to a non-negligible  $q_x$ -component. All compositions show out-of-plane peaks that correspond to low-dimensional perovskite structures. The  $n = 1$  nominal composition features a signal at  $q_z = 0.35 \text{ \AA}^{-1}$  that corresponds to the two-dimensional  $n = 1$  layered perovskite structure (Fig. S1, ESI†), whereas the  $n = 2$  nominal composition reveals the formation of distinct structures characteristic for this composition. However, the XRR patterns for  $n > 2$  nominal compositions show no clear indications of the formation of distinct phases with  $n = 3$  or  $n = 4$  layered perovskites. Instead, the  $n = 2$  layered structure is still present, in addition to 3D perovskite phase and the hexagonal  $FAPbI_3$  polytype. Intensities of the peaks corresponding to the 2D layered phase gradually decrease with the increase of the nominal concentration of the inorganic component ( $n$ ) (Fig. S1, ESI†). For the  $n = 4$  nominal composition, the  $n = 1$  phase and the non-perovskite hexagonal phase of  $FAPbI_3$  could be identified (Fig. S1 and Table S2, ESI†). Based on the  $q$ -value of the first





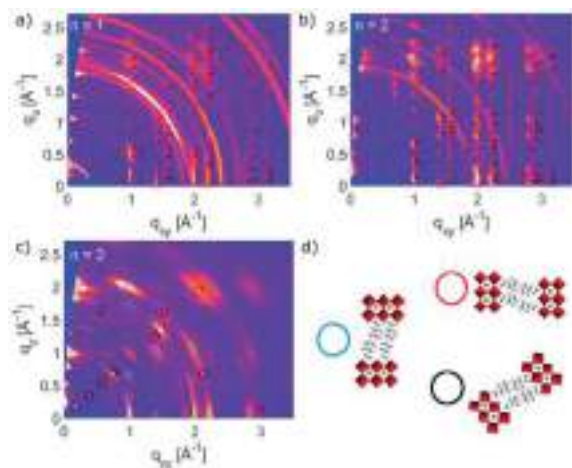


Fig. 3 Orientation of thin films with respect to the substrate. GIWAXS reciprocal space maps for perovskite thin films at angle of incidence  $0.12^\circ$ , based on  $A_2FA_{n-1}Pb_nI_{3n+1}$  formulations with nominal (a)  $n = 1$ , (b)  $n = 2$  and (c)  $n = 3$  compositions on FTO/mp-TiO<sub>2</sub> substrates. Markers denote calculated peak positions based on the structures obtained *via* optimizing unit cell parameters, using DFT calculations as starting values. Ring-shaped features at  $q$ -values of 1.88, 2.36 and 2.65  $\text{\AA}^{-1}$  in the reciprocal space maps originate from the substrate (TiO<sub>2</sub>). (d) Schematic representation of face-on/parallel (blue circle), side-on/perpendicular (red) and tilted ( $\sim 49^\circ$ ) (black) orientations. Markers in (c) correspond to the respective  $n = 2$  structures depicted in (d), which were found for the sample with nominal  $n = 3$  composition. Specific  $n = 3$  structures could not be observed under these conditions.

strong maximum, we estimate that the  $n = 1$  layered structure can be characterized by an interlayer spacing of  $d = 18.0 \text{ \AA}$  that corresponds to the long unit cell axis of the 2D structure and is in line with the layered phase stacked with perovskite slabs oriented mostly parallel to the substrate ('face-on'; Fig. 3d, blue circle). In the sample with  $n = 1$  nominal composition a second co-existing  $n = 1$  polymorph phase was observed, featuring a weak, but resolvable signal at  $q_z = 0.38 \text{ \AA}^{-1}$  as well as higher order reflections (Fig. S1 and Table S2, ESI<sup>†</sup>), that correspond to an interlayer spacing of 16.5  $\text{\AA}$ . This might be ascribed to another  $n = 1$  layered polymorph featuring a slightly different orientation of the organic spacer molecule. By analysis of the dependence on the angle of incidence (*i.e.* penetration depth) of our GIWAXS data (Fig. S3, ESI<sup>†</sup>), we find that the second  $n = 1$  polymorph is located predominantly close to the substrate. For  $n = 2$  composition, GIWAXS measurements reveal that the long unit cell axis is extended, whereas the short unit cell dimensions remain similar for both  $n = 1$  and  $n = 2$  phases (Table S1, ESI<sup>†</sup>). This is consistent with insertion of another perovskite sheet into the unit cell of the layered structure.

The structural complexity was further analysed by considering the presence of various orientations for different compositions with respect to the substrate, which were evaluated by GIWAXS (Fig. 3a–c and S2, ESI<sup>†</sup>).<sup>4,5,26</sup> The GIWAXS data for  $n = 1$  composition show the presence of Bragg reflections that indicate a well oriented layered structure mostly parallel to the substrate ('face-on'), as well as weak rings that correspond to randomly oriented layered structures (Fig. 3a). The system

based on  $n = 2$  composition is also well oriented 'face-on', as suggested by the defined spot pattern (Fig. 3b), which shows no rings that would indicate randomly oriented domains. The nominal  $n = 3$  composition, however, shows presence of the  $n = 2$  structure with three different preferred orientations (Fig. 3c and d).<sup>13,20,22–25</sup> This complexity has been previously indicated by solid-state nuclear magnetic resonance (NMR) spectroscopy, without the capacity to clearly distinguish between the  $n = 2$  and  $n > 2$  structures at the atomic level by means of <sup>13</sup>C, <sup>14</sup>N or <sup>15</sup>N NMR spectra.<sup>13</sup> Moreover,  $n > 2$  compositions also feature additional signals associated with the 3D perovskite  $\alpha$ -FAPbI<sub>3</sub> and  $\delta$ -FAPbI<sub>3</sub> phases.

To further analyse the orientation complexity of the layered structures quantitatively, we have calculated Herman's orientation parameter based on the GIWAXS angular maps, which agrees well with the qualitative description (Fig. S4, ESI<sup>†</sup>). Complex phase mixtures were also obtained for  $A'_2FA_{n-1}Pb_nI_{3n+1}$  ( $n = 1-3$ ) compositions (Fig. S2c, ESI<sup>†</sup>), which supports the previous reports.<sup>13</sup> However, the additional phases cannot be directly associated with new (*e.g.*  $n = 3$ ) structural forms. This apparent absence of the  $n > 2$  structures under experimental conditions, which was observed for both A and A' spacers, was evaluated by the theoretical analysis of their structural and optoelectronic properties.

### Theoretical insights

Towards better understanding of the properties of  $A_2FA_{n-1}Pb_nI_{3n+1}$  and  $A'_2FA_{n-1}Pb_nI_{3n+1}$  ( $n = 1-3$ ) perovskites, classical molecular dynamics (MD) simulations were performed in conjunction with density functional theory (DFT) calculations for different compositions ( $n = 1-3$ ; for computational details refer to the Sections S3 and S4 of the ESI<sup>†</sup>). The initial structures for DFT calculations were extracted from the classical MD simulations (Fig. S5–S8, ESI<sup>†</sup>), which suggest that perovskite materials based on A and A' spacers adopt a Ruddlesden–Popper structure at ambient temperature (298 K). Classical MD simulations at higher temperatures ( $>400 \text{ K}$ ) also provided some information about the thermal stability of the systems. In case of spacer A', we find that the corner-sharing network of Pb–I octahedra slowly transforms into edge-sharing configurations upon increasing the temperature, which does not occur in the case of spacer A. This suggests that the experimentally observed structures for hybrid perovskites based on spacer A' might be a mixture of corner and edge-sharing octahedra, which could lead to phase mixtures and unfavourable optoelectronic properties in comparison to those based on spacer A. This behaviour could be the result of the steric effects of the bulky carbocyclic backbones in the spacer layer and their interaction with the inorganic framework. Specifically, presence of the flexible methylene linker results in higher structural adaptability of the spacer A, as well as higher penetration depth into the inorganic framework, which was assumed to potentially result in templating effects.<sup>13,16,17,27</sup>

To probe the templating role of the spacer, the structures obtained by MD simulations were subsequently optimized by performing DFT calculations, which show that a layered



Ruddlesden–Popper structure is maintained, with ordered stacking of the spacers along the out-of-plane  $a$ -axis in optimized structures, whereas two different alignments with respect to  $c$ -axis occur (denoted as  $\alpha$ ; Fig. 4 and S9, ESI†). Furthermore, we compared the penetration depths of the spacers into the inorganic slabs, which were estimated by the N⋯Pb distance between the nitrogen atom of the amino group of the spacer (N) and the nearest inorganic slab (PbI<sub>4</sub> plane). The penetration depth into the inorganic slabs was shown to be strongly correlated with the average tilting angle between Pb–I octahedra, which in turn determines the overall structural and optoelectronic properties.<sup>16,28,29</sup> For A<sub>2</sub>FA<sub>*n*-1</sub>Pb<sub>*n*I<sub>3*n*+1</sub></sub> ( $n = 1-3$ ) the structure gradually becomes more cubic for higher  $n$  values. This is accompanied by larger penetration depths as reflected by the N⋯Pb distances (Table S3, ESI†). On the contrary, the A'<sub>2</sub>FA<sub>*n*-1</sub>Pb<sub>*n*I<sub>3*n*+1</sub></sub> system (Table S4, ESI†) shows pronounced out-of-plane octahedral distortions (Fig. S9, ESI†), as higher penetration of the ammonium termini is counteracted by the steric requirements of the bulky adamantyl core, preventing the formation of a cubic structure. To evaluate the structural stability of the resulting layered perovskites, we also analysed the hydrogen bond lengths between amino group nitrogens of each spacer (N) and iodide ions (I) of the same inorganic slab (N⋯I distance), which were shown to be important indicators of structural stability.<sup>16,29,30</sup> In principle, a more cubic inorganic slab with intra-octahedral tilting angles approaching 90° provides a larger inter-octahedral space, and consequently larger NH⋯I distances. The DFT calculations suggest that A and A' spacers show a subtle interplay between the interactions in the organic and inorganic layers with a less pronounced templating effect of the inorganic framework towards a cubic phase as compared to spacers featuring longer alkyl-chain-anchoring groups.<sup>16,29</sup> This is in accordance with their bulky shape interfering with the penetration into the perovskite slabs. In this regard, the absence of the methylene group in A' could be attributed to considerably more distorted structures of A'<sub>2</sub>(FA)<sub>*n*-1</sub>Pb<sub>*n*I<sub>3*n*+1</sub></sub> systems, even for  $n = 1$  composition. To assess the effect of these structural features on the spacer layer, we compared the thickness of the organic spacer layer defined by

the Pb⋯Pb distances between the consecutive inorganic layers ( $d_1$ ) as well as the distance between the adjacent spacers ( $d_2$ ) (Fig. 4b, Tables S3 and S4, ESI†). The parameters ( $d_1$ ,  $d_2$ ) were not found to exhibit a clear trend upon incorporating the organic spacer cation into the inorganic layer. This indicates a less pronounced templating effect of the inorganic slabs as compared to other long-alkyl-chain-containing spacers, such as 5-ammonium valeric acid (5-AVA) and  $n$ -butylammonium (BA) cations.<sup>16,27,29</sup>

The dynamics of the spacer molecules is further affected by the interactions with the inorganic slabs as evidenced by the 5 ps long DFT-based Born–Oppenheimer molecular dynamics simulations of A<sub>2</sub>PbI<sub>4</sub> and A'<sub>2</sub>PbI<sub>4</sub> as model systems, where we monitored the changes of N⋯Pb distances and out-of-plane tilting angles (Fig. S10 and S11, ESI†). Both A and A' spacers were found to rotate freely around their central axes, with a preferred molecular orientation for the spacer A. The penetration depth is preserved throughout the finite temperature trajectory of A<sub>2</sub>PbI<sub>4</sub> (Fig. S10, ESI†), which is in agreement with the higher thermal stability of this system. In contrast, for the A'-based system, a broader distribution of N⋯Pb distances is observed, in accordance with the pronounced structural distortion (Fig. S10, ESI†). Similarly, the out-of-plane octahedral angles (Fig. 4b) for A<sub>2</sub>PbI<sub>4</sub> and A'<sub>2</sub>PbI<sub>4</sub> compositions reveal a much broader distribution for the latter (Fig. S11, ESI†).

To validate the DFT-predicted structures, the XRD pattern was simulated for A<sub>2</sub>PbI<sub>4</sub> (Fig. 4a; details are provided in the Section S4 of the ESI†). The patterns of the theoretically predicted structure for the  $n = 1$  composition are in good agreement with the experimentally observed data, with a minor shift that can be ascribed to the different conditions under which the experiment and the simulation are performed, *e.g.* finite temperature effects and dispersion effects.<sup>31</sup> In particular, the lowest angle peaks were found to correspond to 18.0 Å and 18.4 Å (Table S1, ESI†) inter-spacer distances in the experimental samples and the DFT-optimized fully periodic structures, respectively. This evidences that the models are in a very good agreement with experimentally obtained structures.

The absence of higher compositional representatives ( $n > 2$ ) under the applied experimental conditions can be rationalized by calculating the enthalpies of formation ( $\Delta H$ ) for the obtained structures,<sup>21</sup> which slightly increase with the increasing number of inorganic layers ( $n$ ) in A<sub>2</sub>FA<sub>*n*-1</sub>Pb<sub>*n*I<sub>3*n*+1</sub></sub> systems (for details see Section S4, ESI†). Similarly, positive values of formation enthalpies for A'<sub>2</sub>FA<sub>*n*-1</sub>Pb<sub>*n*I<sub>3*n*+1</sub></sub> systems suggest low stability of their RP phases, in accordance with the experimental evidence. This could potentially be circumvented for A<sub>2</sub>FA<sub>*n*-1</sub>Pb<sub>*n*I<sub>3*n*+1</sub></sub> phases by employing smaller ions in the composition, such as Cs and Br,<sup>10,11,32</sup> which can stabilize the perovskite ( $\alpha$ ) phase over the non-perovskite ( $\delta$ ) FAPbI<sub>3</sub> phase, and consequently, might facilitate the observation of higher compositional representatives.<sup>6,13</sup>

### Optoelectronic properties

The effect of the structure on the electronic properties of the system was analysed by UV-vis absorption spectroscopy (Fig. 5a).<sup>13</sup> UV-vis absorption spectra of A<sub>2</sub>FA<sub>*n*-1</sub>Pb<sub>*n*I<sub>3*n*+1</sub></sub> systems

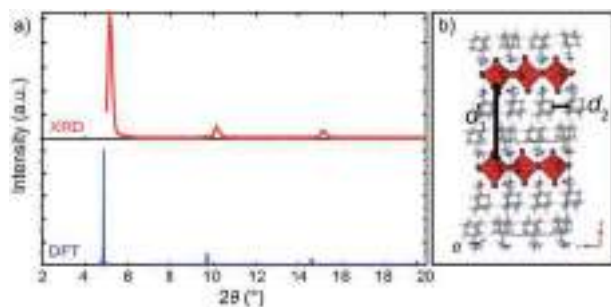


Fig. 4 Structural properties of A<sub>2</sub>PbI<sub>4</sub>. (a) Comparison of the XRD patterns of the DFT-predicted structure (blue) of A<sub>2</sub>PbI<sub>4</sub> ( $n = 1$ ) with the corresponding experimental data on microscopic glass (red). (b) DFT-calculated structure indicating two characteristic distances,  $d_1$  (inter-layer distance measured by the average Pb⋯Pb distance between the adjacent inorganic slabs) and  $d_2$  (distance between the organic spacers in the layer). For more details, refer to the ESI Section S3.†



suggest a gradual decrease in the optical band gap ( $E_g$ ) with increasing number of inorganic slabs ( $n$ ),<sup>22,26,33</sup> along with the presence of typical excitonic features (Fig. 5a).<sup>33–35</sup> Moreover, the  $n = 1–2$  compositions show well-defined spectral signals (Fig. 5a, black and blue), whereas  $n > 2$  compositions feature multiple signals that appear to be in line with the previously reported structural complexity (Fig. 5a, red).<sup>13,20,33</sup> Similarly, the A'-based  $A'_2FA_{n-1}Pb_nI_{3n+1}$  systems show higher spectral complexity for  $n > 1$  compositions (Fig. 5b).

The electronic properties were calculated at PBE0 level<sup>36</sup> including spin-orbit coupling (SOC) effects for the  $n = 1–3$  compositions of  $A_2FA_{n-1}Pb_nI_{3n+1}$  and  $A'_2FA_{n-1}Pb_nI_{3n+1}$  (Tables S5 and S6, ESI†). Following the expected trend, increasing the inorganic layer thickness ( $n$ ) results in decreased band gaps (Table S5, ESI†). The calculated band gap of 2.83 eV for  $A_2PbI_4$  system, in the absence of excitonic effects, exceeds the measured optical band gap by 0.43 eV, which is in accordance with the reported exciton binding energies of around 400 meV for Ruddlesden–Popper phases (Fig. 5c and Table S5, ESI†).<sup>33</sup> The calculated A'-based structures, however, exhibit larger band gaps as compared to their A-based counterparts, presumably as a result of the disruption of the corner-sharing Pb–I network inducing a notable gap opening (Fig. 5b and Table S6, ESI†).

To characterize the transport properties, we calculated the effective masses in the in-plane and out-of-plane directions for both A and A'-based systems (Tables S5 and S6, ESI†). Similar to the

previously studied layered hybrid perovskites,<sup>16,28,29</sup> effective masses in the in-plane direction decrease with the increasing thickness of the inorganic perovskite layer, indicating better charge transfer consistent with lower band gaps for higher compositional representatives ( $n$ ). However, large effective masses in the out-of-plane direction imply a breakdown of the band transport model, similar to other layered perovskite systems that were previously investigated, such as those based on BA and 5-AVA.<sup>29</sup> The partial density of states, as well as the frontier molecular orbitals, show no contribution from the organic part to the band edges for either A- and A'-based systems (Fig. 5c–f). In general, however, the effective masses for A'-based systems are larger than those of A-based systems in all directions, which can also be rationalized by the severely distorted structure that has been evidenced experimentally. These electronic properties directly affect the charge-carrier dynamics that is thereby hereafter investigated exclusively for the  $A_2FA_{n-1}Pb_nI_{3n+1}$  systems.

### Charge carrier dynamics

The charge carrier dynamics were studied by time-resolved microwave conductivity (TRMC) measurements using high frequency microwaves upon excitation.<sup>14,15</sup> Under these conditions, the change in conductivity due to generated free charge carriers is probed with high frequency microwaves. If the charge carriers are mobile, they absorb part of the incoming microwave power ( $\Delta G_{\max}$ ) which is proportional to the change in conductivity of the material ( $\Delta\sigma$ ).

The charge carriers in the material can be generated with either a high energy electron pulse (pulse-radiolysis TRMC) or by laser excitation (photoconductivity-TRMC). Generation by irradiation with high energy electrons allows to determine the mobility of charge carriers ( $\mu$ ) directly in the material prepared mechanosynthetically without considering the effect of orientation or being influenced by the exciton binding energy of the material (as is the case of photoexcited experiments).<sup>14,15</sup> The mobility of charge carriers was probed in layered hybrid perovskites of different  $A_2FA_{n-1}Pb_nI_{3n+1}$  ( $n = 1–3$ ) compositions, which is expected to increase with the number of inorganic layers ( $n$ ).<sup>14</sup> The mobility appears to be higher for  $n = 1$  as compared to  $n = 2–3$  compositions of the corresponding perovskite powders, and it is not substantially affected by temperature in the range between 180–300 K (Fig. 6a), which suggests presence of a large concentration of trap states across compositions under these conditions. The dynamics of charge carrier decays supports this hypothesis as featuring a rather fast recombination at the ns timescale (Fig. S13, ESI†). The recombination of charge carriers is not influenced by the initial charge carrier concentration ( $10^{14}$  to  $10^{16}$  cm<sup>-3</sup>) at room temperature (Fig. S13, ESI†). At lower temperatures, this behaviour is consistent for  $n = 1$  composition (Fig. 6a and S14, ESI†). However, for  $n = 2$  and  $n = 3$  compositions, the conductivity slightly increases after the pulse (Fig. S14 and S15, ESI†), which suggests the existence of phases with higher conductivity within the material. This agrees with the formation of different phases in  $n > 1$  compositions. The lifetime of charge carriers increases with the number of inorganic layers from the order of hundreds

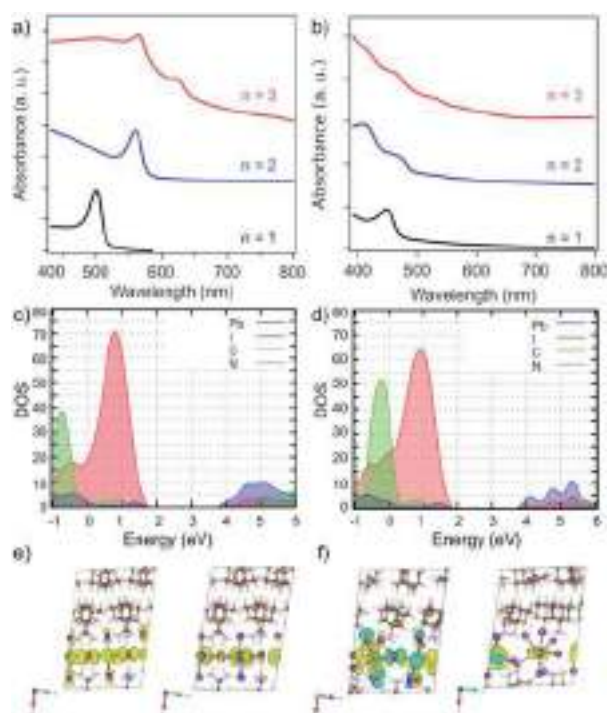


Fig. 5 Optoelectronic properties of perovskite thin films. UV-vis absorption spectra of perovskite thin films based on (a)  $A_2FA_{n-1}Pb_nI_{3n+1}$  and (b)  $A'_2FA_{n-1}Pb_nI_{3n+1}$  ( $n = 1–3$ ) compositions on FTO/mp-TiO<sub>2</sub> substrates in accordance with the previous report.<sup>13</sup> Calculated partial density of states for (c)  $A_2PbI_4$  and (d)  $A'_2PbI_4$  with (e and f) the corresponding frontier molecular orbitals (top of the valence band (left) and bottom of the conduction band (right)).



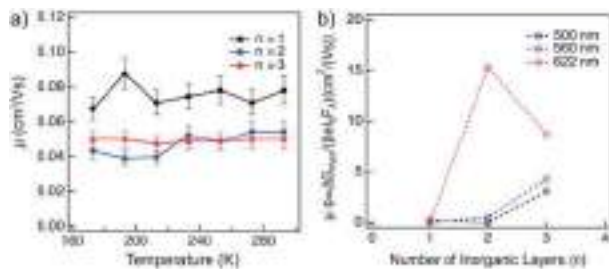


Fig. 6 Conductivities in layered hybrid perovskite powders and thin films based on  $A_2FA_{n-1}Pb_nI_{3n+1}$  perovskite with different compositions ( $n = 1-3$ ). (a) Evolution of mobilities in powders at various temperatures and (b) conductivities in thin films deposited on quartz substrates at ambient temperature (298 K). The initial charge carrier concentration was estimated to be  $10^{14}$  to  $10^{16}$   $\text{cm}^{-3}$  at 298 K.

of ns for  $n = 1$  to hundreds of  $\mu\text{s}$  for  $n = 2$  and  $n = 3$  compositions (Fig. S14, ESI<sup>†</sup>), with further increase at lower temperatures (Fig. S16, ESI<sup>†</sup>).

The photoconductivity determined on thin films after laser excitation is by definition the product of charge mobility ( $\mu$ ) and quantum yield of free charge carrier formation ( $\varphi$ ), based on the following eqn (1)

$$\varphi \sum \mu = \frac{\Delta G_{\max}}{I_0 \beta e F_A}, \quad (1)$$

where  $I_0$  is the number of photons per unit area,  $\beta$  is based on the dimensions of the microwave cavity,  $e$  is the elementary charge, and  $F_A$  is the fraction of the absorbed light. As discussed, these measurements are influenced by the exciton binding energy in the material which is usually large ( $\sim 350$  meV) in layered hybrid perovskites.<sup>14,15,33</sup>

Thin films of  $A_2FA_{n-1}Pb_nI_{3n+1}$  ( $n = 1-3$ ) were photoexcited at three different wavelengths corresponding to the excitonic peaks of the different number of inorganic layers (Fig. 5a), namely 500 nm for  $n = 1$ , 560 nm for  $n = 2$  and 622 nm for  $n = 3$  compositions (Fig. 6b). The photoconductivity was found to increase with the number of inorganic layers, which is in agreement with reports on layered 2D perovskites in which the exciton binding energy decreases with the number of inorganic layers, increasing the yield of dissociation of charge carriers

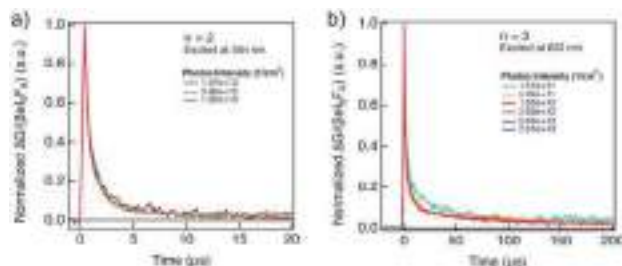


Fig. 7 Evolution of photoconductivities in hybrid perovskite thin films based on  $A_2FA_{n-1}Pb_nI_{3n+1}$  formulation with (a)  $n = 2$  and (b)  $n = 3$  nominal compositions as a function of photon intensity, highlighting long charge carrier lifetimes in the order of  $\mu\text{s}$ . Photoconductivity is defined by the eqn (1) as a product of charge mobility ( $\mu$ ) and quantum yield of free charge carrier formation ( $\varphi$ ).

( $\varphi$ ).<sup>14</sup> However, upon excitation at 622 nm, we can observe that the photoconductivity is higher for the  $n = 2$  than for  $n = 3$  compositions, which is likely the result of higher phase purity and better orientation of the  $n = 2$  representatives.

Notwithstanding, the photoconductivity values for  $n = 3$  are in the order of magnitude of FAPbI<sub>3</sub> films measured with the same technique ( $8-60$   $\text{cm}^2 \text{V}^{-1} \text{s}^{-1}$ ; Fig. S17, ESI<sup>†</sup>), which is likely the result of the presence of the 3D perovskite phase in the composition. For  $n = 1$  composition, the conductivities are comparable to other layered perovskite films measured with the same technique ( $0.1-0.3$   $\text{cm}^2 \text{V}^{-1} \text{s}^{-1}$ ),<sup>14</sup> whereas the values for  $n = 2$  composition are in the  $0.5-5$   $\text{cm}^2 \text{V}^{-1} \text{s}^{-1}$  range that is relevant for optoelectronics. The charge carrier dynamics in the films suggests that the recombination kinetics follows a second order behaviour (Fig. S18, ESI<sup>†</sup>). However, the lifetime gets longer as the number of inorganic layers increases.

The lifetime of the decay for  $n = 1$  compositions is around 400 ns, which is longer than for *n*-butylammonium or phenylethylammonium systems that decay at  $\sim 100-200$  ns.<sup>14</sup> The longer components of the decay for  $n = 2$  and  $n = 3$  compositions are in the order of 40  $\mu\text{s}$  and 400  $\mu\text{s}$ , respectively (Fig. 7), which is longer than the lifetime for FAPbI<sub>3</sub> of about 2  $\mu\text{s}$  (Fig. S17, ESI<sup>†</sup>). At these longer time scales, the decay traces show a first order behaviour, suggesting that there are two decay regimes. This behaviour may potentially also be the result of the transport of carriers in the perpendicular direction that results in improved spatial charge separation, which is relevant for future optoelectronic device applications.

## Conclusions

We have investigated the structural properties of adamantyl-based layered hybrid perovskites of  $A_2FA_{n-1}Pb_nI_{3n+1}$  compositions, which were complemented by molecular dynamics simulations and density functional theory calculations. Our study reveals the formation of well-defined layered hybrid perovskite structures for the representatives based on the (1-adamantyl)methan ammonium spacer in  $n = 1-2$  compositions. On the contrary, higher compositional representatives ( $n > 2$ ) are proven to be based on mixtures of lower-dimensional and 3D perovskite phases, which was evidenced by GIWAXS measurements. This was further in accordance with the decrease in the formation enthalpies for the increasing number of inorganic layers ( $n$ ). Finally, we analysed the photophysical properties to observe high photoconductivities for layered hybrid perovskite structures with (1-adamantyl)methan ammonium-based systems despite their structural complexity, while featuring longer charge carrier lifetimes in the order of tens to hundreds of  $\mu\text{s}$  that can be accounted for their photovoltaic performance. This provides an important incentive for the use of formamidinium-based layered hybrid perovskites in optoelectronics.

## Experimental

### Materials and methods

Perovskite powders were synthesized by grinding the reactants in an electric ball mill (Retsch Ball Mill MM-200) using a grinding jar (10 ml) and a ball ( $\phi 10$  mm) for 30 min at 25 Hz.



The resulting powders were annealed at 150 °C for 15 min to reproduce the thin film synthetic procedure based on the reported conditions.<sup>37</sup> Thin films were fabricated through a step-wise preparation process in accordance with the reported procedure.<sup>13</sup> The quartz substrates were cleaned with oxygen plasma for 15 min. The perovskite film was deposited by spin-coating onto the substrate. The precursor solutions of  $A_2FA_{n-1}Pb_nI_{3n+1}$  and  $A'_2FA_{n-1}Pb_nI_{3n+1}$  perovskite films ( $n = 1, 2, 3$ ) of the concentration of 0.4 M were prepared in a nitrogen-filled glovebox by dissolving the stoichiometric quantities of  $PbI_2$ , FAI, and either ADAMI (AI) or ADAI (A'I) in the solvent mixture comprised of *N,N*-dimethylformamide (DMF) and dimethyl sulfoxide (DMSO) with the volume ratio of DMF/DMSO = 4 : 1. The perovskite film spin-coating procedure was performed in a glovebox under inert nitrogen atmosphere by a consecutive two-step spin-coating process at first 1000 rpm for 10 s with a ramp of 200 rpm  $s^{-1}$  and second 4000 rpm for 20 s with a ramp of 2000 rpm  $s^{-1}$ . Subsequently, the sample was annealed at 150 °C for 15 min. Further experimental details are provided in the ESI.†

### X-ray scattering experiments

X-ray scattering experiments were done at beamline ID10 of the ESRF with a photon energy of 22 keV under nitrogen atmosphere. As a calibrant for the scattering experiments,  $LaB_6$  was used. The sample-detector distance was 295 mm, while the beam size was 20  $\mu m$  in vertical direction and 120  $\mu m$  in horizontal direction. GIXD data was measured under an angle of incidence of 0.12° with a Cyberstar point detector. GIWAXS data was measured with a PILATUS 300k area detector under angles of incidence between 0.02°–0.20°. Powder diffraction data was calculated with Mercury software. Scattering data analysis was performed with self-written Python and Matlab-based software.

### Time-resolved microwave conductivity measurements

Time-resolved microwave conductivity measurements were used to probe changes in conductivity of layered hybrid perovskites by using high frequency microwaves after the excitation by either high energy electron pulse or a laser. The relative mobility of charge carriers was estimated by pulse-radiolysis TRMC. The samples prepared by mechanosynthesis were irradiated with short pulses of 3 MeV electrons from a Van de Graaff accelerator. TRMC upon laser photoexcitation under conditions specified in the corresponding figure captions was used to analyse thin films.

### Molecular dynamics simulations

Molecular dynamics simulations were performed by relying on the methods described in detail in the ESI.† A fixed-point charge interatomic potential was chosen for Pb and I from the literature.<sup>38</sup> The Generalized Amber Force Field (GAFF) was used to parameterize the ligand and formamidinium ions. We have chosen a 1.0 nm cutoff for nonbonded interactions and three-dimensional periodic boundary conditions were applied for each simulation. Long range electrostatic interactions are treated with the particle-particle-mesh Ewald method. We employ the SHAKE

algorithm<sup>39</sup> to constrain the bond length of hydrogen atoms. The time step used in all of the simulations is 2 fs. All simulations are performed with the Large-scale Atomic/Molecular Massively Parallel Simulator (LAMMPS) code (31 Mar 2017).<sup>40</sup> The systems were first minimized with a conjugate gradient algorithm with a tolerance of maximum residual force of  $10^{-3}$  kcal  $mol^{-1}$   $\text{\AA}^{-1}$ . After minimization, the systems were relaxed with an equilibrium run which was carried out in the isothermal-isobaric ensemble. We used a velocity rescaling thermostat<sup>41</sup> with a relaxation time of 0.1 ps. The Parrinello-Rahman barostat was used to keep the pressure equal to the standard atmospheric pressure.<sup>42</sup> The relaxation time of the barostat was set to 10 ps. We used a triclinic variable cell barostat in all of our simulations. With this setup, the temperature was slowly increased from 0 K to  $T$  (temperature) in 10 ns. Then we perform 30 ns simulations at the constant temperature. To calculate the autocorrelation function (ACF), we perform MD simulations for five different temperatures (at 200 K, 250 K, 300 K, 350 K and 400 K). The simulations were run to verify the stability and calculations of the dynamics of the spacers at different temperatures, and for the final structure, they are quenched to 0 K.

### Density functional theory calculations

Density functional theory calculations were performed by relying on the method described in detail in the ESI.† *Ab initio* calculations based on the Generalized Gradient Approximation (GGA) of Density Functional Theory (DFT) for  $A_2FA_{n-1}Pb_nI_{3n+1}$  and  $A'_2FA_{n-1}Pb_nI_{3n+1}$  ( $n = 1, 2$  and 3) were performed using the Quantum Espresso package.<sup>43</sup> The Perdew-Burke-Ernzerhof functional revised for solids (PBEsol)<sup>44</sup> was selected, which has shown to well reproduce measured electronic and structural properties of Ruddlesden-Popper (RP) phases, such as the recently reported  $AVA_2MA_{n-1}Pb_nI_{3n+1}$  systems.<sup>16,29</sup> Dispersion interactions were considered by applying the empirical D2 dispersion correction.<sup>31</sup> To calculate the band gaps, we employed a higher level of theory by applying the PBE0 functional<sup>36</sup> together with incorporating spin-orbit coupling (SOC) effects.<sup>45</sup> Valence-core electron interactions were modelled *via* ultrasoft pseudopotentials with a plane wave basis set of 40 Ry kinetic energy cutoff for the wavefunction and 280 Ry for the density. For band gap calculations, norm-conserving pseudopotentials with 80 Ry wavefunction cutoff and 320 Ry density cutoff were employed. The Brillouin zone was sampled by a  $2 \times 2 \times 1$   $k$ -point grid for all cases. A finite temperature (FT) analysis was carried out by performing 5 ps of constant volume (NVT) Born-Oppenheimer MD for  $A_2PbI_4$  and  $A'_2PbI_4$ , excluding the first 1 ps of equilibration. The initial temperature was set to 300 K and was controlled by the velocity rescaling thermostat implemented in Quantum Espresso.<sup>42</sup> The same Brillouin zone sampling as in the static calculations was adopted for MD simulations. Charge carrier effective masses were calculated using our in-house code.<sup>28</sup>

### Author contribution

The manuscript was written by J. V. M., F. J., M. M., E. K., L. M., and M. C. G.-R. with the support of all authors. The project was conceptualized by J. V. M., who coordinated the



investigation. M. C. G.-R. and F. C. G. performed the photo-conductivity measurements and analysis of charge carrier dynamics with the support of W. T. in the interpretation. Y. L. and A. D. prepared the samples for the analysis and performed basic structural characterization. F. J., M. M., P. A., and U. R. performed, analyzed and interpreted the molecular dynamics simulations and DFT calculations. A. H., E. K. and L. M. performed the X-ray scattering measurements and the analysis with the support of M. I. D. and F. S., while A. U. conducted the XRD measurements. S. M. Z., B. C., and A. H. were involved in the discussion and provided support in project coordination, while M. G. directed the project.

## Conflicts of interest

There are no conflicts to declare.

## Acknowledgements

J. V. M., S. M. Z., and M. G. are grateful to the European Union's Horizon 2020 research and innovation program under grant agreement No. 826013 (IMPRESSIVE) as well as the King Abdulaziz City for Science and Technology (KACST) for financial support. U. R. acknowledges SNSF Grant No. 200020-165863, NCCR-MUST, NRP70, and the SINERGIA interdisciplinary research program EPISODE for funding. The work at Delft University of Technology (M. C. G.-R. and F. C. G) is funded by the European Research Council Horizon 2020 ERC Grant Agreement No. 648433. We are grateful to the DFG for funding and the European Synchrotron Radiation Facility (ESRF) for the provision of synchrotron radiation and Oleg Konovalov for assistance in using beamline ID10.

## References

- 1 M. Grätzel, *Nat. Mater.*, 2014, **13**, 838–842.
- 2 Y. Rong, Y. Hu, A. Mei, H. Tan, M. I. Saidaminov, S. I. Seok, M. D. McGehee, E. H. Sargent and H. Han, *Science*, 2018, **361**, eaat8235.
- 3 A. K. Jena, A. Kulkarni and T. Miyasaka, *Chem. Rev.*, 2019, **119**, 3036–3103.
- 4 G. Grancini and M. K. Nazeeruddin, *Nat. Rev. Mater.*, 2018, **4**, 4–22.
- 5 L. Mao, C. C. Stoumpos and M. G. Kanatzidis, *J. Am. Chem. Soc.*, 2019, **141**, 1171–1190.
- 6 G. E. Eperon, S. D. Stranks, C. Menelaou, M. B. Johnston, L. M. Herz and H. J. Snaith, *Energy Environ. Sci.*, 2014, **7**, 982–988.
- 7 N. Pellet, P. Gao, G. Gregori, T.-Y. Yang, M. K. Nazeeruddin, J. Maier and M. Grätzel, *Angew. Chem., Int. Ed.*, 2014, **53**, 3151–3157.
- 8 Z. Yang, C.-C. Chueh, P.-W. Liang, M. Crump, F. Lin, Z. Zhu and A. K. Y. Jen, *Nano Energy*, 2016, **22**, 328–337.
- 9 W. S. Yang, B.-W. Park, E. H. Jung, N. J. Jeon, Y. C. Kim, D. U. Lee, S. S. Shin, J. Seo, E. K. Kim, J. H. Noh and S. I. Seok, *Science*, 2017, **356**, 1376–1379.
- 10 G. Li, T. Zhang, N. Guo, F. Xu, X. Qian and Y. Zhao, *Angew. Chem., Int. Ed.*, 2016, **55**, 13460–13464.
- 11 R. Hamaguchi, M. Yoshizawa-Fujita, T. Miyasaka, H. Kunugita, K. Ema, Y. Takeoka and M. Rikukawa, *Chem. Commun.*, 2017, **53**, 4366–4369.
- 12 J. Yan, W. Fu, X. Zhang, J. Chen, W. Yang, W. Qiu, G. Wu, F. Liu, P. Heremans and H. Chen, *Mater. Chem. Front.*, 2017, **2**, 121–128.
- 13 J. V. Milić, J.-H. Im, D. J. Kubicki, A. Ummadisingu, J.-Y. Seo, Y. Li, M. A. Ruiz Preciado, M. I. Dar, S. M. Zakeeruddin, L. Emsley and M. Grätzel, *Adv. Energy Mater.*, 2019, **131**, 1900284.
- 14 M. C. Gélvez-Rueda, E. M. Hutter, D. H. Cao, N. Renaud, C. C. Stoumpos, J. T. Hupp, T. J. Savenije, M. G. Kanatzidis and F. C. Grozema, *J. Phys. Chem. C*, 2017, **121**, 26566–26574.
- 15 R. Herckens, W. T. M. Van Gompel, W. Song, M. C. Gélvez-Rueda, A. Maufort, B. Ruttens, J. D'Haen, F. C. Grozema, T. Aernouts, L. Lutsen and D. Vanderzande, *J. Mater. Chem. A*, 2018, **6**, 22899–22908.
- 16 A. Q. Alanazi, D. J. Kubicki, D. Prochowicz, E. A. Alharbi, M. E. F. Bouduban, F. Jahanbakhshi, M. Mladenović, J. V. Milić, F. Giordano, D. Ren, A. Y. Alyamani, H. Albrithen, A. Albadri, M. H. Alotaibi, J.-E. Moser, S. M. Zakeeruddin, U. Rothlisberger, L. Emsley and M. Grätzel, *J. Am. Chem. Soc.*, 2019, **141**, 17659–17669.
- 17 J. V. Milić, D. J. Kubicki, L. Emsley and M. Grätzel, *Chimia*, 2019, **73**, 317–323.
- 18 D. Prochowicz, M. Sasaki, P. Yadav, M. Grätzel and J. Lewiński, *Acc. Chem. Res.*, 2019, **52**, 3233–3243.
- 19 L. Mao, W. Ke, L. Pedesseau, Y. Wu, C. Katan, J. Even, M. R. Wasielewski, C. C. Stoumpos and M. G. Kanatzidis, *J. Am. Chem. Soc.*, 2018, **140**, 3775–3783.
- 20 Y. Li, J. V. Milić, A. Ummadisingu, J.-Y. Seo, J.-H. Im, H.-S. Kim, Y. Liu, M. I. Dar, S. M. Zakeeruddin, P. Wang, A. Hagfeldt and M. Grätzel, *Nano Lett.*, 2019, **19**, 150–157.
- 21 C. M. M. Soe, G. P. Nagabhushana, R. Shivaramaiah, H. Tsai, W. Nie, J.-C. Blancon, F. Melkonyan, D. H. Cao, B. Traoré, L. Pedesseau, M. Kepenekian, C. Katan, J. Even, T. J. Marks, A. Navrotsky, A. D. Mohite, C. C. Stoumpos and M. G. Kanatzidis, *Proc. Natl. Acad. Sci. U. S. A.*, 2019, **116**, 58–66.
- 22 D. H. Cao, C. C. Stoumpos, O. K. Farha, J. T. Hupp and M. G. Kanatzidis, *J. Am. Chem. Soc.*, 2015, **137**, 7843–7850.
- 23 L. N. Quan, M. Yuan, R. Comin, O. Voznyy, E. M. Beauregard, S. Hoogland, A. Buin, A. R. Kirmani, K. Zhao, A. Amassian, D. H. Kim and E. H. Sargent, *J. Am. Chem. Soc.*, 2016, **138**, 2649–2655.
- 24 J. Liu, J. Leng, K. Wu, J. Zhang and S. Jin, *J. Am. Chem. Soc.*, 2017, **139**, 1432–1435.
- 25 A. H. Proppe, R. Quintero-Bermudez, H. Tan, O. Voznyy, S. O. Kelley and E. H. Sargent, *J. Am. Chem. Soc.*, 2018, **140**, 2890–2896.
- 26 C. C. Stoumpos, D. H. Cao, D. J. Clark, J. Young, J. M. Rondinelli, J. I. Jang, J. T. Hupp and M. G. Kanatzidis, *Chem. Mater.*, 2016, **28**, 2852–2867.
- 27 D. B. Mitzi, *J. Chem. Soc., Dalton Trans.*, 2001, 1–12.



- 28 N. Ashari-Astani, S. Meloni, A. H. Salavati, G. Palermo, M. Grätzel and U. Rothlisberger, *J. Phys. Chem. C*, 2017, **121**, 23886–23895.
- 29 N. Ashari-Astani, F. Jahanbakhshi, M. Mladenović, A. Q. M. Alanazi, I. Ahmadabadi, M. R. Ejtehadi, M. I. Dar, M. Grätzel and U. Rothlisberger, *J. Phys. Chem. Lett.*, 2019, **10**, 3543–3549.
- 30 S. Ahmad, P. Fu, S. Yu, Q. Yang, X. Liu, X. Wang, X. Wang, X. Guo and C. Li, *Joule*, 2019, **3**, 794–806.
- 31 S. Grimme, *J. Comput. Chem.*, 2006, **27**, 1787–1799.
- 32 Z. Wang, Q. Lin, F. P. Chmiel, N. Sakai, L. M. Herz and H. J. Snaith, *Nat. Energy*, 2017, **2**, 17135.
- 33 J. C. Blancon, H. Tsai, W. Nie, C. C. Stoumpos, L. Pedesseau, C. Katan, M. Kepenekian, C. M. M. Soe, K. Appavoo, M. Y. Sfeir, S. Tretiak, P. M. Ajayan, M. G. Kanatzidis, J. Even, J. J. Crochet and A. D. Mohite, *Science*, 2017, **355**, 1288–1292.
- 34 Y. Chen, Y. Sun, J. Peng, J. Tang, K. Zheng and Z. Liang, *Adv. Mater.*, 2017, **131**, 1703487.
- 35 L. Gan, J. Li, Z. Fang, H. He and Z. Ye, *J. Phys. Chem. Lett.*, 2017, **8**, 5177–5183.
- 36 C. Adamo and V. Barone, *J. Chem. Phys.*, 1999, **110**, 6158–6170.
- 37 D. J. Kubicki, D. Prochowicz, A. Hofstetter, P. Péchy, S. M. Zakeeruddin, M. Grätzel and L. Emsley, *J. Am. Chem. Soc.*, 2017, **139**, 10055–10061.
- 38 C. Caddeo, M. I. Saba, S. Meloni, A. Filippetti and A. Mattoni, *ACS Nano*, 2017, **11**, 9183–9190.
- 39 J.-P. Ryckaert, G. Ciccotti and H. J. C. Berendsen, *J. Comput. Phys.*, 1977, **23**, 327–341.
- 40 S. Plimpton, *J. Comput. Phys.*, 1995, **117**, 1–19.
- 41 G. Bussi, D. Donadio and M. Parrinello, *J. Chem. Phys.*, 2007, **126**, 014101.
- 42 M. Parrinello and A. Rahman, *J. Appl. Phys.*, 1981, **52**, 7182–7190.
- 43 P. Giannozzi, S. Baroni, N. Bonini, M. Calandra, R. Car, C. Cavazzoni, D. Ceresoli, G. L. Chiarotti, M. Cococcioni, I. Dabo, A. Dal Corso, S. de Gironcoli, S. Fabris, G. Fratesi, R. Gebauer, U. Gerstmann, C. Gougoussis, A. Kokalj, M. Lazzeri, L. Martin-Samos, N. Marzari, F. Mauri, R. Mazzarello, S. Paolini, A. Pasquarello, L. Paulatto, C. Sbraccia, S. Scandolo, G. Sclauzero, A. P. Seitsonen, A. Smogunov, P. Umari and R. M. Wentzcovitch, *J. Phys.: Condens. Matter*, 2009, **21**, 395502.
- 44 J. P. Perdew, A. Ruzsinszky, G. I. Csonka, O. A. Vydrov, G. E. Scuseria, L. A. Constantin, X. Zhou and K. Burke, *Phys. Rev. Lett.*, 2008, **100**, 136406.
- 45 P. Umari, E. Mosconi and F. De Angelis, *Sci. Rep.*, 2014, **4**, 4467.





Cite this: *Phys. Chem. Chem. Phys.*,  
2020, 22, 20880

# Why choosing the right partner is important: stabilization of ternary $\text{Cs}_y\text{GUA}_x\text{FA}_{(1-y-x)}\text{PbI}_3$ perovskites†

Ariadni Boziki,<sup>a</sup> Marko Mladenović,<sup>‡</sup> Michael Grätzel<sup>b</sup> and Ursula Rothlisberger\*<sup>a</sup>

Lead halide perovskites with mixtures of monovalent cations have attracted wide attention due to the possibility of preferentially stabilizing the perovskite phase with respect to photovoltaically less suitable competing phases. Here, we present a theoretical analysis and interpretation of the phase stability of binary  $(\text{CH}_3\text{NH}_3)_x[\text{HC}(\text{NH}_2)_2]_{(1-x)}\text{PbI}_3 = \text{GUA}_x\text{FA}_{(1-x)}\text{PbI}_3$  and ternary  $\text{Cs}_y\text{GUA}_x\text{FA}_{(1-y-x)}\text{PbI}_3$  mixtures. We first estimate if such mixtures are stable and if they lead to a stabilization of the perovskite phase based on static Density Functional Theory (DFT) calculations. In order to investigate the finite temperature stability of the phases, we also employ first-principles molecular dynamics (MD) simulations. It turns out that in contrast to the  $\text{FA}^+$ -rich case of  $\text{FA}/\text{Cs}$  mixtures, although mixing of  $\text{FA}/\text{GUA}$  is possible, it is not sufficient to stabilize the perovskite phase at room temperature. In contrast, stable ternary mixtures that contain 17% of  $\text{Cs}^+$  can be formed that lead to a preferential stabilization of the perovskite phase. In such a way, the enthalpic destabilization due to the introduction of a too large/too small cation that lies outside the Goldschmidt tolerance range can be (partially) compensated through the introduction of a third cation with complementary size. This allows to suggest a new design principle for the preparation of stable perovskite structures at room temperature with cations that lie outside the Goldschmidt range through mixtures with size-complementary cations in such a way that the effective average cation radius of the mixture lies within the stability range.

Received 21st July 2020,  
Accepted 7th September 2020

DOI: 10.1039/d0cp03882b

rsc.li/pccp

## 1 Introduction

Solar cells based on organic–inorganic lead halide perovskites<sup>1–7</sup> are achieving nowadays power conversion efficiencies (PCEs) exceeding 25%.<sup>8</sup> The unique properties of this kind of materials, including high absorption coefficients,<sup>9</sup> small exciton binding energies,<sup>10</sup> large charge-carrier diffusion lengths,<sup>11</sup> low-trap densities<sup>12</sup> and the low production costs when produced by low-temperature solution processes,<sup>13</sup> make them commercially attractive for photovoltaic technologies. Nevertheless, in spite of their exceptional performance, perovskite solar cells still face some unresolved issues, one of them being their limited long-term stability.

Indeed,  $\text{CH}_3\text{NH}_3\text{PbI}_3$  ( $\text{MAPbI}_3$ ),  $\text{CsPbI}_3$  and  $[\text{HC}(\text{NH}_2)_2]\text{PbI}_3$  ( $\text{FAPbI}_3$ ), the three most widely studied perovskite materials exhibit limited stability for different reasons. More specifically,  $\text{MAPbI}_3$  films, with a band gap of 1.5 eV,<sup>3</sup> which is close to the single-junction optimum, (1.34 eV according to Shockley and Queisser's detailed balance considerations, for air mass coefficient (AM) 1.5 G illumination and  $T = 298.15$  K),<sup>14,15</sup> decompose rapidly at 423 K, due to the high volatility of MAI which is prone to be attacked by polar solvents, in particular water.<sup>7</sup> The perovskite phase of  $\text{FAPbI}_3$ , has a band gap that according to different experimental measurements lies within the range of 1.43–1.48 eV,<sup>7,16,17</sup> which is even closer to the single-junction optimum, however at room temperature it adopts a non-perovskite hexagonal  $\delta$ -phase (yellow phase) that is unsuitable for photovoltaic applications due to the large band gap.<sup>18</sup> This  $\delta$ -phase only undergoes a phase transition to a black perovskite  $\alpha$ -phase at 333 K,<sup>18</sup> but a metastable  $\beta$ - $\text{FAPbI}_3$  phase ( $P3$  trigonal space group) that  $\text{FAPbI}_3$  adopts at 150 K has also been reported.<sup>18</sup> The  $\gamma$ -phase of the purely inorganic  $\text{CsPbI}_3$ , on the other hand, has a band gap of 1.73 eV,<sup>19–22</sup> which is close to the optimum top cell band gap for tandem solar cells of 1.7–1.8 eV.<sup>23</sup> However, as in case of  $\text{FAPbI}_3$ , it crystallizes in a non-perovskite insulating hexagonal  $\delta$ -phase (yellow phase) at room temperature.<sup>18</sup>

<sup>a</sup> Laboratory of Computational Chemistry and Biochemistry, Institute of Chemical Sciences and Engineering, École Polytechnique Fédérale de Lausanne, CH-1015 Lausanne, Switzerland. E-mail: ursula.rothlisberger@epfl.ch; Fax: +41 (0)21 693 03 20; Tel: +41 (0)21 693 03 21

<sup>b</sup> Laboratory of Photonics and Interfaces, École Polytechnique Fédérale de Lausanne, CH-1015 Lausanne, Switzerland

† Electronic supplementary information (ESI) available. See DOI: 10.1039/d0cp03882b

‡ Scientific Computing Laboratory, Center for the Study of Complex Systems, Institute of Physics Belgrade, University of Belgrade, Pregrevica 118, 11080 Belgrade, Serbia.



Consequently, to overcome the problems of limited thermal, structural and phase stabilities, different strategies have been proposed. Indeed, it has been shown that mixing two different monovalent cations can result in a preferential stabilization of the perovskite phase at room temperature.<sup>24–26</sup> Many of the devices that have achieved high PCEs include mixtures of monovalent cations.<sup>24,25,27</sup> Pellet *et al.*,<sup>24</sup> successfully added MAPbI<sub>3</sub> in order to stabilize the perovskite phase of FAPbI<sub>3</sub> at room temperature, however at higher temperatures the compound is prone to decomposition due to the presence of MA<sup>+</sup>. Additionally, Lee *et al.*,<sup>26</sup> prepared mixtures of cesium and formamidinium with enhanced thermal and humidity stability achieving a PCE of 16.5% and in one of our previous works, we have shown that Cs<sub>0.2</sub>FA<sub>0.8</sub>PbI<sub>2.84</sub>Br<sub>0.16</sub> solar cells yield a PCE of over 17% exhibiting excellent long term stability in ambient air.<sup>25</sup> This design protocol of using mixed cations has been further extended. Saliba *et al.*,<sup>28</sup> proposed that the incorporation of Cs<sup>+</sup> into mixtures of MAPbI<sub>3</sub> and FAPbI<sub>3</sub> results in an improved thermal stability achieving a PCE of 18%.

As a rule of thumb, ions that are within the range of the Goldschmidt tolerance factor,  $t^{29}$  ( $(R_A + R_X) = t\sqrt{2}(R_B + R_X)$ , where  $R_A$ ,  $R_X$  and  $R_B$  are the ionic radii, of the monovalent cation (A), anion (X) and divalent cation (B), respectively); ( $t \approx 0.8–1.0$ ), are potential candidates for forming a stable perovskite structure. In the case of lead/iodide systems, this allows for a selection of monovalent cations with radii that are roughly 164 to 259 pm.<sup>30</sup> This rule has been extended by Kieslich *et al.*,<sup>31,32</sup> to organic (molecular) cations assuming a rigid sphere model and full freedom for rotation around the center of mass leading to a set of effective ionic radii for mixtures of monovalent cations.<sup>27,33</sup> CH<sub>6</sub>N<sub>3</sub><sup>+</sup> (guanidinium–GUA<sup>+</sup>) for example is an organic cation with a zero dipole moment and a Goldschmidt tolerance factor which is slightly above the upper limit for forming a stable lead iodide perovskite structure.<sup>31,34</sup> Indeed, no perovskite phase formation has been reported so far for pure CH<sub>6</sub>N<sub>3</sub>PbI<sub>3</sub> (GUAPbI<sub>3</sub>); a tetraiodide GUA<sub>2</sub>PbI<sub>4</sub> is formed instead for which a continuous phase transition at 307 K takes place and a low-dimensional (1D) triiodide GUAPbI<sub>3</sub> that undergoes two phase transitions at 255 and 432 K has also been reported.<sup>35,36</sup>

Following the design protocol of mixing two different monovalent cations in order to form a stable perovskite phase at room temperature, GUA<sup>+</sup> has been mixed with MAPbI<sub>3</sub>.<sup>37,38</sup> The devices based on this mixed GUA<sub>x</sub>MA<sub>(1-x)</sub>PbI<sub>3</sub> solar cells resulted in an average PCE of 19.2% and enhanced stability, breaking in that way new ground in the exploration of cations with radii beyond the tolerance factor limit.<sup>38</sup> Originally, it has been proposed that upon mixing, GUA<sup>+</sup> is not directly incorporated into the perovskite structure but acts as a passivating agent,<sup>37</sup> however, a later study demonstrated an increased micro-strain and distortions of the lattice upon GUA<sup>+</sup> doping of MAPbI<sub>3</sub> providing evidence for direct incorporation.<sup>38</sup> This was further confirmed by recent solid-state nuclear magnetic resonance (NMR) measurements that supplied atomic-level evidence that GUA<sup>+</sup> is directly incorporated into the MAPbI<sub>3</sub> lattice.<sup>39</sup>

Nevertheless, in spite of the formation of stable room temperature perovskite phases in the case of MA/FA, FA<sup>+</sup>-rich

FA/Cs and GUA/MA mixtures, GUA/FA mixtures follow another trend. Kubicki *et al.*,<sup>39</sup> through solid-state NMR studies revealed that although black GUA<sub>x</sub>FA<sub>(1-x)</sub>PbI<sub>3</sub> is initially formed, it is thermodynamically unstable, turning yellow within hours after annealing. Furthermore, mixtures of guanidinium with cesium, in different stoichiometries, are adopting layered crystal structures (CsGUAPbI<sub>4</sub>, CsGUAPbBr<sub>4</sub> and Cs<sub>2</sub>GUAPb<sub>2</sub>Br<sub>7</sub>) that are thermally stable and do not decompose up to 573 K.<sup>40</sup> In addition to this, a 2D perovskite structure of a mixture of formamidinium and guanidinium (FAGUAPbI<sub>4</sub>), is thermally stable up to 528 K, exhibiting photoluminescence at room temperature and pronounced photoconductivity.<sup>41</sup> In an attempt to stabilize GUA/FA mixtures in the perovskite phase, compositions of triple cation mixtures have been proposed.<sup>42,43</sup> For instance FA<sub>0.33</sub>GUA<sub>0.19</sub>Cs<sub>0.47</sub>Pb(I<sub>0.66</sub>Br<sub>0.34</sub>)<sub>3</sub> and FA<sub>0.58</sub>GUA<sub>0.10</sub>Cs<sub>0.32</sub>Pb(I<sub>0.73</sub>Br<sub>0.27</sub>)<sub>3</sub> have been proposed as possible candidates for tandem multijunction devices, since they have band gaps of 1.84 eV and 1.75 eV, respectively.<sup>42</sup> In addition, the incorporation of 2% of GUA<sup>+</sup> into FA<sub>0.83</sub>Cs<sub>0.17</sub>PbI<sub>3</sub> resulted in an increase of the device efficiency from 14% to 17% under one sun illumination.<sup>43</sup> Thermal stability tests performed in the same study, predicted an enhanced stability for 5% to 10% GUA<sup>+</sup> doping. However, for concentrations higher than 20% of GUA<sup>+</sup> doping, secondary  $\delta$ -like phases are formed.<sup>43</sup>

In this work, through a theoretical analysis, we investigated the relative stability of binary GUA<sub>x</sub>FA<sub>(1-x)</sub>PbI<sub>3</sub> mixtures with GUA<sup>+</sup> up to 50% and ternary Cs<sub>y</sub>GUA<sub>x</sub>FA<sub>(1-y-x)</sub>PbI<sub>3</sub> mixtures with Cs<sup>+</sup> up to 17%. The relative stability of the mixtures with respect to the pure FAPbI<sub>3</sub>, GUAPbI<sub>3</sub> and CsPbI<sub>3</sub> phases was calculated by estimating the free energy of mixing. In addition to this, we estimated the phase stability of the mixtures by calculating the relative energetics between the different phases. Our approach differs from the one followed by Giorgi *et al.*,<sup>34</sup> where the stability was calculated through the relative substitution energies suggesting that the binary GUA/FA mixtures are not stable with respect to demixing while our approach that takes the mixing entropy into account predicts stable mixtures. Furthermore, we also consider the  $\delta$ -phase and we observe that there is a preferential stabilization of the  $\delta$ -phase over the perovskite phase for the binary GUA/FA mixtures, in agreement with experimental studies that do not only show that  $\delta$ -phase is more stable but also that the mixture is not demixing (in contrast to Giorgi *et al.*, suggestions).<sup>39</sup> For all mixed compounds the structural characteristics as well as the electronic properties have been determined.

## 2 Results and discussion

### 2.1 Stability

DFT<sup>44,45</sup> calculations using the Perdew–Burke–Ernzerhof (PBE)<sup>46</sup> functional have been employed to determine the relative stability at 0 K of the perovskite over the non-perovskite phase for GUA<sub>x</sub>FA<sub>(1-x)</sub>PbI<sub>3</sub> mixtures with up to 50% of FA<sup>+</sup> substituted by GUA<sup>+</sup>. In addition, we investigated triple cation mixtures Cs<sub>y</sub>GUA<sub>x</sub>FA<sub>(1-y-x)</sub>PbI<sub>3</sub> with 8% or 17% Cs<sup>+</sup> when up to 50% of the FA<sup>+</sup> cations in the FAPbI<sub>3</sub> lattice were substituted by GUA<sup>+</sup>.

The DFT-optimized structures of the pure compounds are shown in Fig. 1.

The small energy difference among various substitution pattern that is of the order of 0.005 eV for the  $\beta$  and 0.006 eV for the  $\delta$ -phase, respectively, justifies the use of the analytical formula for ideal alloys for the estimation of the mixing entropy contribution to the free energy as given by eqn (1).<sup>47</sup>

$$T\Delta S_{\text{mix}} = -k_B T \sum_{i=1}^N c_i \ln c_i \quad (1)$$

where  $k_B$  is the Boltzmann constant,  $T$  is the temperature,  $N$  is the number of components and  $c_i$  is the atomic fraction of component  $i$ . Eqn (1) leads to eqn (2) in case of the triple  $\text{Cs}_y\text{GUA}_x\text{FA}_{(1-y-x)}\text{PbI}_3$  cation mixture.

$$T\Delta S_{\text{phase}}(\text{Cs}_y\text{GUA}_x\text{FA}_{(1-y-x)}\text{PbI}_3) = -k_B T [y \ln y + x \ln x + (1 - y - x) \ln(1 - y - x)] \quad (2)$$

where  $y$  is the concentration of  $\text{Cs}^+$ , and  $x$  is the concentration of  $\text{GUA}^+$  incorporated in the  $\text{FAPbI}_3$  structure. On the other hand, the relative energetics of the mixtures with respect to the

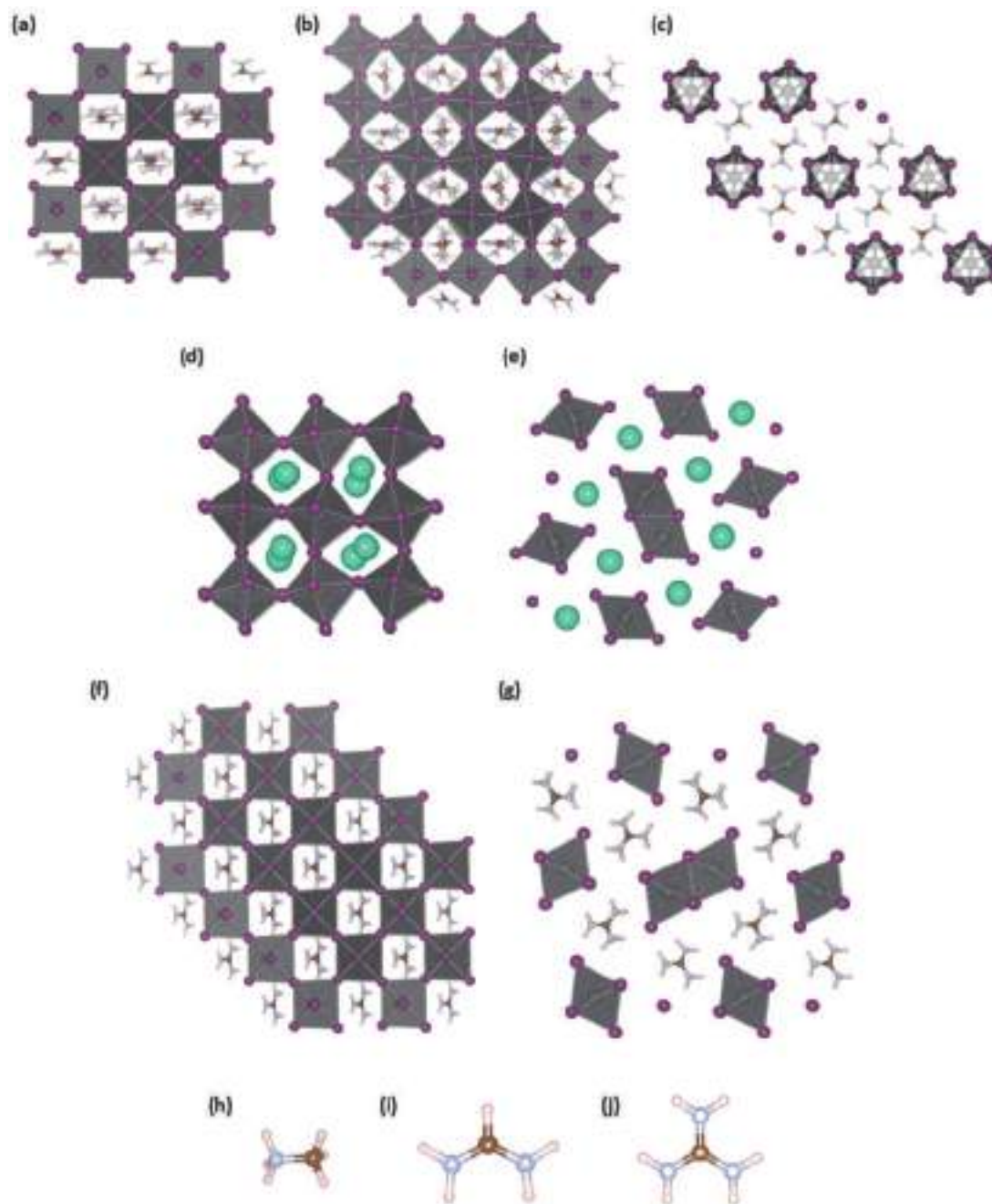


Fig. 1 DFT-optimized structures. (a)  $\alpha$ -FAPbI<sub>3</sub>, (b)  $\beta$ -FAPbI<sub>3</sub>, (c)  $\delta$ -FAPbI<sub>3</sub>, (d)  $\gamma$ -CsPbI<sub>3</sub>, (e)  $\delta$ -CsPbI<sub>3</sub>, (f) 3D perovskite structure of GUAPbI<sub>3</sub> that has been constructed by substituting  $\text{FA}^+$  by  $\text{GUA}^+$  in the  $\alpha$ -FAPbI<sub>3</sub>, (g)  $\delta$ -GUAPbI<sub>3</sub>, (h) MA cation, (i) FA cation, (j) GUA cation.

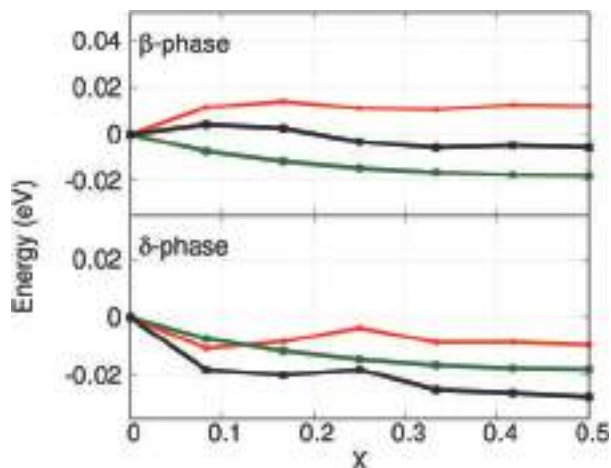


Fig. 2 Variation of the free energy of mixing, which is expressed as  $\Delta F = \Delta E - T\Delta S$  (black line), the internal energy,  $\Delta E$  (red line), and the mixing entropy contribution,  $-T\Delta S$  (green line), as a function of  $x$  GUA<sup>+</sup> ratio in GUA<sub>x</sub>FA<sub>(1-x)</sub>PbI<sub>3</sub> mixtures, for the  $\beta$  and  $\delta$  phases, respectively.

pure FAPbI<sub>3</sub>, GUAPbI<sub>3</sub> and CsPbI<sub>3</sub> compounds is computed by eqn (3). In both eqn (2) and (3), the subscript phase corresponds to one of the two,  $\beta$  or  $\delta$  phases.

$$\Delta E_{\text{phase}}(\text{Cs}_y\text{GUA}_x\text{FA}_{(1-y-x)}\text{PbI}_3) = E_{\text{phase}}(\text{Cs}_y\text{GUA}_x\text{FA}_{(1-y-x)}\text{PbI}_3) - [yE_{\text{phase}}(\text{CsPbI}_3) + xE_{\text{phase}}(\text{CsPbI}_3) + (1-y-x)E_{\text{phase}}(\text{FAPbI}_3)]. \quad (3)$$

As one can see in Fig. 2 where the energetic and entropic contributions to the free energy of mixing are plotted as a function of  $x$  for the two phases, the replacement of FA<sup>+</sup> with GUA<sup>+</sup> cations leads to an energetic destabilization in the  $\beta$ -phase for all GUA<sub>x</sub>FA<sub>(1-x)</sub>PbI<sub>3</sub> compositions. However, the overall mixing free energies are essentially zero (certainly when considering the accuracy of the calculations and the variations due to different substitution pattern that are of the order of 0.005 eV). On the other hand, the  $\delta$ -phase is energetically stabilized and the mixing entropy further favors the stabilization of the mixtures, leading overall to negative mixing free energies. These observations are in contrast to FA<sup>+</sup>-rich FA/Cs mixtures where mixing leads to a preferential stabilization of the perovskite phase and a distinct destabilization of the  $\delta$ -phase.<sup>25</sup>

To estimate the relative stability of perovskite *versus* non-perovskite phases, the 0 K relative energetics per stoichiometric unit between the  $\delta$  and the  $\beta$  phases are shown for binary GUA<sub>x</sub>FA<sub>(1-x)</sub>PbI<sub>3</sub> mixtures (Table 1). Mixing is affecting the relative stability of the two phases in the direction of further stabilization of the  $\delta$ -phase.

We next investigated how the 0 K stabilities are changing at finite temperature, especially due to the inclusion of vibrational entropy. However, in the case of lead halide perovskites the calculation of such corrections is not trivial. Indeed, the initial calculations of harmonic and quasi-harmonic phonons led to imaginary modes.<sup>48</sup> This contradiction seemed to be resolved in the case of double perovskites, by calculating the finite-temperature

Table 1 Relative energetic stability expressed by  $\Delta E_{\beta\delta} = E_{\beta} - E_{\delta}$  per stoichiometric unit of the  $\beta$ -phase with respect to the  $\delta$ -phase upon substitution of FA<sup>+</sup> by GUA<sup>+</sup> in the FAPbI<sub>3</sub> structure

Fraction of FA <sup>+</sup> substituted by GUA <sup>+</sup> in the FAPbI <sub>3</sub> structure (%)	Energy difference at 0 K with respect to $\delta$ -phase (eV)
0	0.12
8	0.15
17	0.16
25	0.16
33	0.17
42	0.18
50	0.19

phonon-spectrum, including the anharmonic phonon-phonon interaction, showing that phonon entropy at finite temperatures plays a critical role in phonon spectrum renormalization.<sup>49,50</sup> However it has been shown that for all-inorganic lead halide perovskites vibrational instabilities are present and are associated with octahedral tilting in the high-temperature and symmetry phase.<sup>51</sup> Finding the actual minimum and using frozen phonon calculations, Marronnier *et al.*,<sup>52</sup> abolished the soft modes at the  $\Gamma$  point of the highly symmetric high-temperature cubic phase of CsPbI<sub>3</sub>, however the remaining phonon instabilities at the M and R points at the edge of the Brillouin zone did not disappear.

Therefore, to assess the relative phase stability at finite temperature, we opted for another approach and performed instead MD simulations at 300 K for both  $\beta$  and  $\delta$  GUA<sub>0.17</sub>FA<sub>0.83</sub>PbI<sub>3</sub> phases. As shown in Fig. 3 where the potential energy for both the  $\beta$  and the  $\delta$  phases is shown, we observe that at 300 K the mixture is more stable in the  $\delta$ -phase. This is consistent with the observations from solid state NMR measurements, where although black mixed-cation GUA<sub>x</sub>FA<sub>(1-x)</sub>PbI<sub>3</sub> phases do form temporarily, they are thermodynamically unstable and become yellow within hours from annealing.<sup>39</sup>

In contrast to FA<sup>+</sup>-rich FA/Cs mixtures, where mixing leads to a stabilization of the perovskite phase at room temperature,<sup>25</sup> we conclude that the addition of GUA<sup>+</sup> into FAPbI<sub>3</sub> does not lead to a sufficient stabilization of the perovskite phase and the  $\delta$ -phase

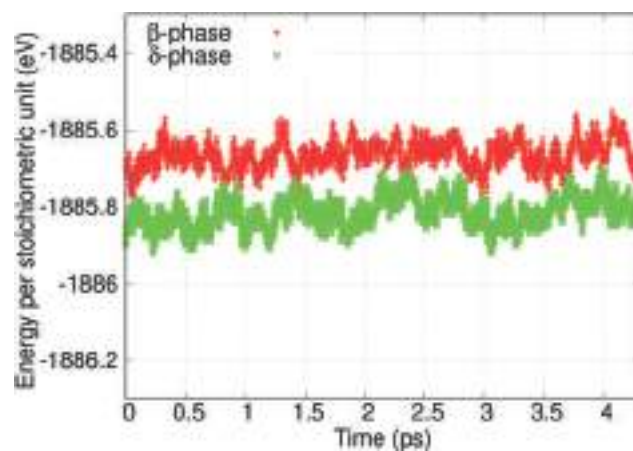


Fig. 3 Potential energy per stoichiometric unit for both  $\beta$  and  $\delta$  phases from first-principles based MD simulations in the NVT ensemble at 300 K. The  $\delta$ -phase is always lower in energy.

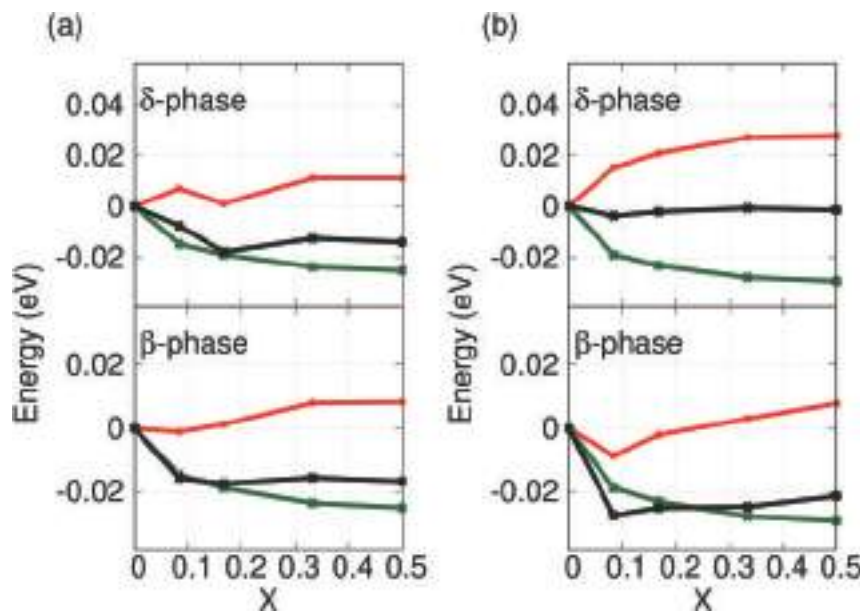


Fig. 4 Variation of the free energy of mixing expressed as  $\Delta F = \Delta E - T\Delta S$  (black line), the internal energy,  $\Delta E$  (red line), and the mixing entropy contribution,  $-T\Delta S$  (green line), as a function of  $x$  GUA<sup>+</sup> ratio in Cs<sub>*y*</sub>GUA<sub>*x*</sub>FA<sub>*(1-y-x)*</sub>PbI<sub>3</sub> mixtures, for the  $\beta$  and  $\delta$  phases, respectively. (a) The concentration of Cs<sup>+</sup> is 8% ( $y = 0.08$ ). (b) The concentration of Cs<sup>+</sup> is 17% ( $y = 0.17$ ).

remains the thermodynamically most stable form. We also explored if this trend can be reversed through the addition of a third cation. In particular, we tested the hypothesis if the energetic penalties induced by substitution of a large cation such as GUA<sup>+</sup> could possibly be balanced through addition of a small cation such as Cs<sup>+</sup>. For this reason, we probed the possible stabilization of the perovskite phase in ternary Cs<sub>*y*</sub>GUA<sub>*x*</sub>FA<sub>*(1-y-x)*</sub>PbI<sub>3</sub> mixtures, where we expect the permutational entropy to induce a further stabilization due to the addition of an additional species, helping to stabilize the mixtures over wider concentration ranges albeit not directly affecting the relative phase stability.

Fig. 4(a), shows that in the  $\delta$ -phase, addition of 8% Cs<sup>+</sup> to GUA<sub>*x*</sub>FA<sub>*(1-x)*</sub>PbI<sub>3</sub> mixtures with different GUA<sup>+</sup> content leads to an energetic destabilization over all the GUA<sup>+</sup> range, but for 17% of GUA<sup>+</sup> where the calculated mixing energy is so small that the value is below the variations due to different substitution pattern that are of the order of 0.006 eV. However the energetic destabilization is compensated by the mixing entropy contribution. For the  $\beta$ -phase, on the other hand, mixing is energetically unfavorable for  $x > 0.17$ , and for lower GUA<sup>+</sup> concentrations the mixing energy is below the variations due to different substitution pattern that are of the order of 0.005 eV for the  $\beta$ -phase. However, permutational entropy induces a further stabilization, leading to an overall negative mixing free energies for the  $\beta$ -phase. In contrast to the binary GUA/FA mixtures the stabilization in the perovskite phase is similar to the  $\delta$ -phase counterpart and is thus not able to induce a reversal in the relative stability order. The trends are further enhanced by adding 17% Cs (Fig. 4(b)). For the  $\delta$ -phase, mixing leads to an energetic destabilization that the mixing entropy contribution can no longer compensate, in the sense that the mixing free energy is essentially zero. In contrast, in the  $\beta$ -phase, mixing leads even to an energetic stabilization for the

lower GUA<sup>+</sup> concentration range (up to 17%) and adding the mixing entropy contributions leads to a free energy that has negative values for all  $\beta$ -Cs<sub>0.17</sub>GUA<sub>*x*</sub>FA<sub>*(0.83-x)*</sub>PbI<sub>3</sub> mixtures. It is worth mentioning that the pronounced stability of the ternary Cs<sub>*y*</sub>GUA<sub>*x*</sub>FA<sub>*(1-y-x)*</sub>PbI<sub>3</sub> mixtures in the perovskite phase is consistent with recent experiments on GUA<sup>+</sup> doping into FA<sub>0.83</sub>Cs<sub>0.17</sub>PbI<sub>3</sub>. According to these measurements, a remarkable enhanced thermal stability of the perovskite phase is observed for 5% and 10% GUA<sup>+</sup> doping content. For higher concentrations than 20% GUA<sup>+</sup> doping, X-ray diffraction (XRD), Ultraviolet-visible spectroscopy (UV-VIS) and scanning electron microscope (SEM) measurements show the formation of secondary  $\delta$ -like phases, that due to lack of structural information have not been considered in this study.<sup>43</sup>

## 2.2 Structural characteristics

In FA<sup>+</sup>-rich FA/Cs mixtures,<sup>25</sup> the preferred stabilization of the perovskite phase upon mixing has been rationalized in terms of the structural similarity or dissimilarity of the perovskite and the  $\delta$  phases of the pure compounds, respectively. Here, we employed a similar analysis and traced the evolution of the volume per stoichiometric unit and average Pb–I–Pb angles upon mixing for different binary and ternary GUA/FA mixtures plotted in Fig. 5, 7, 8 and 9, respectively.

As a function of  $x$ , the volume is increasing for the  $\beta$ -phase, while it is oscillating for the  $\delta$ -phase, leading to an overall volume increase when 50% of FA<sup>+</sup> is substituted by GUA<sup>+</sup>. The overall volume increase is consistent with the incorporation of a larger cation into the lattice. Especially, in the case of the non-perovskite phase, the crystal structure consists of edge-sharing octahedra that are surrounded by monovalent cations. For low GUA<sup>+</sup> concentrations, the volume hardly changes due to the available space between the rods and expands to a new value

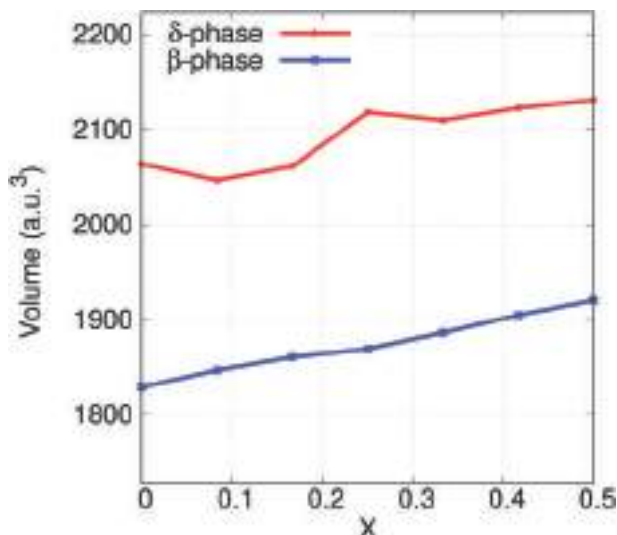


Fig. 5 Volume evolution of  $\text{GUA}_x\text{FA}_{(1-x)}\text{PbI}_3$  mixtures, when  $\text{FA}^+$  is substituted by  $\text{GUA}^+$  in the  $\text{FAPbI}_3$  lattice.

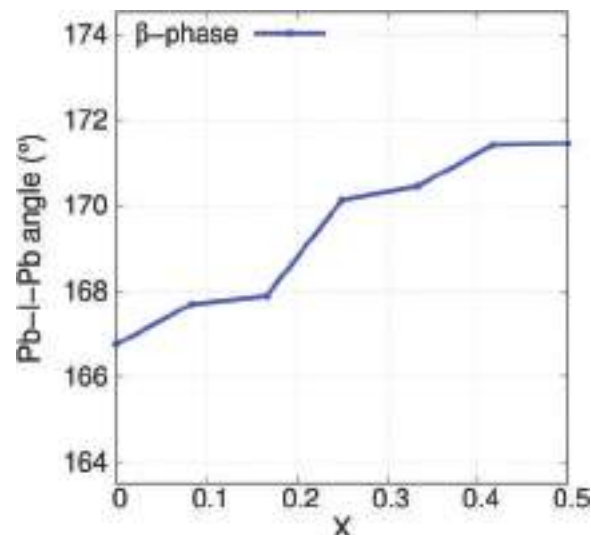


Fig. 7 Average of Pb–I–Pb angle of  $\beta\text{-GUA}_x\text{FA}_{(1-x)}\text{PbI}_3$  mixtures, when  $\text{FA}^+$  is substituted by  $\text{GUA}^+$  in the  $\text{FAPbI}_3$  lattice.

when a critical concentration is reached. In the case of the perovskite phase on the other hand, the lattice expands isotropically. In Fig. 6, the DFT optimized structures of pure  $\text{FAPbI}_3$  and mixed  $\text{GUA}_{0.5}\text{FA}_{0.5}\text{PbI}_3$  in the  $\beta$ -phase are shown. Upon mixing, the space between Pb–I octahedra of the  $\beta$ -phase which is originally characteristic for an orthorhombic phase, tends towards a more cubic like behavior (Fig. 6). This is consistent with the trend of the volume evolution in the orthorhombic like phases, where the incorporation of a larger cation leads to an expansion of the lattice and an increased population at  $\sim 0$  tilting angle.<sup>53</sup> This observation is also supported by the average Pb–I–Pb angles. Fig. 7 shows that for the  $\beta$ -phase, the average Pb–I–Pb angles tend to a more cubic like behavior with increasing  $\text{GUA}^+$  content. The projected density of states (PDOS) of several systems shown in Fig. S1–S6 (ESI<sup>†</sup>) reveals that the valence band maximum (VBM) consists of an antibonding overlap between the I 5p and Pb 6s orbitals and the conduction and minimum (CBM) of an antibonding overlap between the Pb 6p and I 5s orbitals. We also observe that the character of the band edges is preserved for a wide range of different chemical and crystallographic variations.<sup>22,53</sup> Because of the antibonding character of the VBM, the reduction of the lattice distortion leads to an increase

of the antibonding overlap between the I p and Pb s orbitals which in turn leads to an energy increase (destabilization) of the mixed perovskite phases.

For the ternary  $\text{Cs}_y\text{GUA}_x\text{FA}_{(1-y-x)}\text{PbI}_3$  mixtures, the volume evolution upon substitution of  $\text{FA}^+$  by  $\text{Cs}^+$  and  $\text{GUA}^+$  in the  $\text{FAPbI}_3$  lattice for both  $\text{Cs}^+$  concentrations also leads to an overall increase of the lattice volume, as shown in Fig. 8. This is consistent with the incorporation of a larger cation, however, it is important to note that the incorporation of both  $\text{Cs}^+$  and  $\text{GUA}^+$  counterbalances the overall volume increase to some degree, since the space required for the larger  $\text{GUA}^+$  is compensated by the smaller space required by  $\text{Cs}^+$ . This seems to be only effective when the concentrations of  $\text{GUA}^+$  and  $\text{Cs}^+$  are in a similar range. For  $\text{GUA}^+$  concentrations that are higher than the ones of  $\text{Cs}^+$ , the change of the volume as a function of concentration is dominated by the incorporation of the much larger  $\text{GUA}^+$ .

The volume increase is accompanied by a widening of the average Pb–I–Pb angles, as shown in Fig. 9 proposing again that the substitution of  $\text{FA}^+$  by  $\text{Cs}^+$  and  $\text{GUA}^+$  leads to a more cubic-like structure at high  $\text{GUA}^+$  concentrations. However, in contrast to the binary  $\text{GUA}/\text{FA}$  mixtures, for a concentration range which is similar for both cations (low  $\text{GUA}^+$  concentration) the

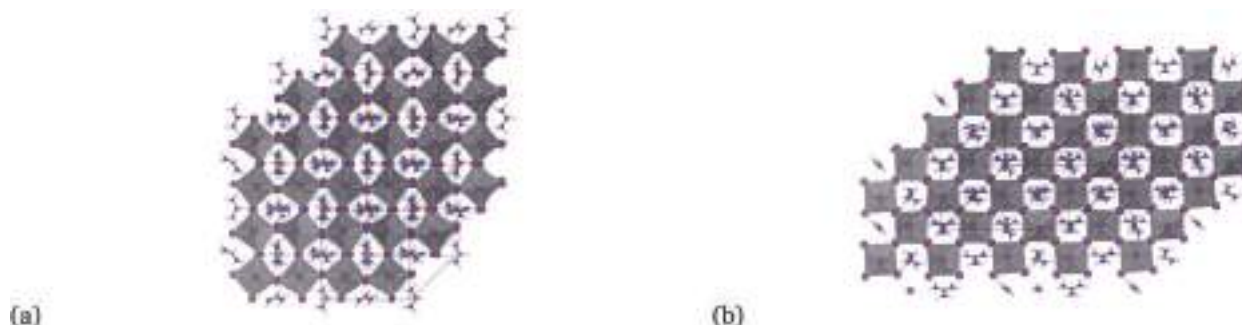


Fig. 6 DFT optimized (a)  $\beta\text{-FAPbI}_3$  and (b)  $\beta\text{-GUA}_{0.5}\text{FA}_{0.5}\text{PbI}_3$  structures, illustrating that the structure becomes more cubic upon mixing.

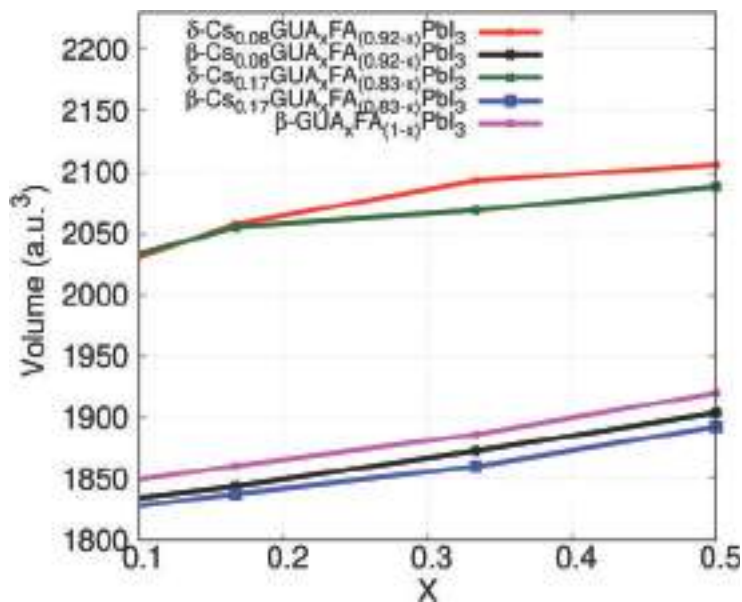


Fig. 8 Volume evolution of  $\text{Cs}_y\text{GUA}_x\text{FA}_{(1-y-x)}\text{PbI}_3$  mixtures for  $\text{Cs}^+$  concentrations of 8% and 17%. The volume evolution of the binary  $\beta\text{-GUA}_x\text{FA}_{(1-x)}\text{PbI}_3$  mixture is replotted for the sake of comparison.

average Pb–I–Pb angle is lower for  $\text{Cs}_y\text{GUA}_x\text{FA}_{(1-y-x)}\text{PbI}_3$  mixtures, (this behavior is more pronounced for 17% of  $\text{Cs}^+$ ) indicating that the incorporation of a smaller cation such as  $\text{Cs}^+$  leads the system to adopt a more orthorhombic-like structure. In this case because of the antibonding character of the VBM, the increase of lattice distortion leads to a decrease of the antibonding overlap between the I p and Pb s orbitals which in turn leads to an energy decrease (stabilization) of the mixed perovskite phases.

### 2.3 Optical properties

Although the perovskite phase of some of the mixtures might only be metastable, it is of interest to understand how mixing

affects the optical properties. The use of the hybrid functional PBE0 in combination with explicit spin orbit coupling (SOC) effects<sup>54</sup> calculated for PBESol optimized geometries,<sup>55</sup> has been shown to be a successful protocol for an accurate description of the band gaps of halide perovskites.<sup>56,57</sup> In addition, our benchmarks shown in Table S1 (ESI<sup>†</sup>), demonstrate that the above mentioned protocol is indeed superior for an accurate description of the band gaps compared to other schemes and functionals. The results using this protocol are summarized in Table 2. The band structures of a few systems are shown in Fig. S7 and S8 (ESI<sup>†</sup>).

The calculated band gap for pure  $\text{FAPbI}_3$  is in good agreement with the experimental results, that according to different experimental measurements lies within the range of 1.43–1.48 eV.<sup>7,16,17</sup> In case of  $\beta\text{-GUA}_x\text{FA}_{(1-x)}\text{PbI}_3$  mixtures, the band gap remains almost unaffected upon mixing and stays very close to the single-junction optimum. However, as shown above, mixtures in the  $\beta$ -phase are thermodynamically unstable with respect to the  $\delta$ -phase, and thus of limited practical interest.

We also calculated the band gaps of the triple cation  $\text{Cs}_y\text{GUA}_x\text{FA}_{(1-y-x)}\text{PbI}_3$  mixtures. As can be seen in Table 3, as for the binary mixtures, the band gaps are close to the single-

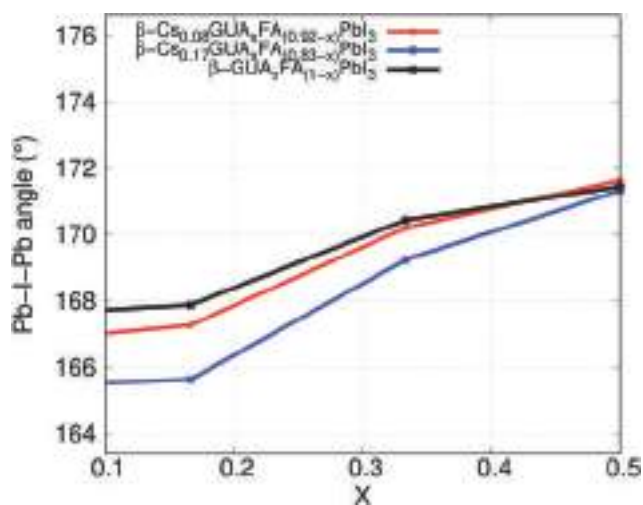


Fig. 9 Average of Pb–I–Pb angles as a function of  $x$  for  $\text{Cs}_y\text{GUA}_x\text{FA}_{(1-y-x)}\text{PbI}_3$  mixtures, upon substitution of  $\text{FA}^+$  by  $\text{Cs}^+$  and  $\text{GUA}^+$  in the  $\text{FAPbI}_3$  lattice. The corresponding values of the binary  $\beta\text{-GUA}_x\text{FA}_{(1-x)}\text{PbI}_3$  mixtures are replotted for the sake of comparison.

Table 2 Band gaps of binary  $\text{GUA}_x\text{FA}_{(1-x)}\text{PbI}_3$  mixtures

Fraction ( $x$ ) of $\text{FA}^+$ substituted by $\text{GUA}^+$ in the $\text{FAPbI}_3$ structure (%)	$\beta\text{-GUA}_x\text{FA}_{(1-x)}\text{PbI}_3$ Band gap (eV) (PBE0 + SOC)
0	1.47
8	1.46
17	1.48
25	1.43
33	1.44
42	1.44
50	1.45

**Table 3** Band gaps of ternary  $\beta$ -Cs<sub>y</sub>GUA<sub>x</sub>FA<sub>(1-y-x)</sub>PbI<sub>3</sub> compounds in the  $\beta$ -phase for  $y = 0.08$  and  $0.17$

Fraction ( $x$ ) of FA <sup>+</sup> substituted by GUA <sup>+</sup> in the FAPbI <sub>3</sub> lattice (%)	$\beta$ -Cs <sub>0.08</sub> GUA <sub>x</sub> FA <sub>(0.92-x)</sub> PbI <sub>3</sub> Band gap (eV) (PBE0 + SOC)	$\beta$ -Cs <sub>0.17</sub> GUA <sub>x</sub> FA <sub>(0.83-x)</sub> PbI <sub>3</sub> Band gap (eV) (PBE0 + SOC)
0	1.47	1.41
8	1.48	1.47
17	1.48	1.47
33	1.44	1.43
50	1.46	1.44

junction optimum and are essentially unaffected upon substitution of FA<sup>+</sup> by GUA<sup>+</sup> for both Cs<sup>+</sup> concentrations considered. Given that for  $\beta$ -Cs<sub>0.17</sub>GUA<sub>x</sub>FA<sub>(0.83-x)</sub>PbI<sub>3</sub> systems, mixing in the perovskite phase seems favorable for low GUA<sup>+</sup> concentrations, these compounds could be potential candidates for efficient solar cell applications. Recent experiments on GUA<sup>+</sup> doping into FA<sub>0.83</sub>Cs<sub>0.17</sub>PbI<sub>3</sub>, showed that the incorporation of less than 10% of GUA<sup>+</sup> into FA<sub>0.83</sub>Cs<sub>0.17</sub>PbI<sub>3</sub> resulted in a band gap around 1.54 eV, which is suitable for single-junction solar cells and especially the incorporation of 2% of GUA<sup>+</sup> resulted in an increase of device efficiency from 14% to 17% under one sun illumination.<sup>43</sup> However, for concentrations of GUA<sup>+</sup> higher than 20%, an additional absorption peak at  $\approx 600$  nm has been observed due to the formation of secondary  $\delta$  phases.<sup>43</sup> If under certain preparation condition Cs<sub>y</sub>GUA<sub>x</sub>FA<sub>(1-y-x)</sub>PbI<sub>3</sub> mixtures can be stabilized, their optical properties are very interesting and these materials should be further investigated as candidates for solar cell applications.

### 3 Conclusions

We have demonstrated that in contrast to FA<sup>+</sup>-rich FA/Cs mixtures,<sup>25</sup> in binary GUA<sub>x</sub>FA<sub>(1-x)</sub>PbI<sub>3</sub> mixtures, the addition of GUA<sup>+</sup> alone into FAPbI<sub>3</sub> does not lead to a sufficient stabilization of the perovskite phase and on the contrary, a further stabilization of the  $\delta$ -phase is observed. Consistently, MD simulations performed at room temperature revealed that the binary mixtures are more stable in the  $\delta$ -phase, in agreement with experimental results.<sup>39</sup> At difference to MA/FA, FA<sup>+</sup>-rich FA/Cs, and GUA/MA mixtures, mixing with one additional monovalent cation is not sufficient for stabilising the perovskite phase, for this reason we also examined the phase stability of triple cation Cs<sub>y</sub>GUA<sub>x</sub>FA<sub>(1-y-x)</sub>PbI<sub>3</sub> mixtures for both 8% and 17% of Cs<sup>+</sup>. It turns out that for 8% of Cs<sup>+</sup>, mixing is favorable in both  $\beta$  and  $\delta$  phases. However, for 17% of Cs<sup>+</sup>, mixing only favors the perovskite phase, suggesting that the inclusion of a third cation into an unstable or metastable binary mixture could pave the way for materials that are thermodynamically stable in the perovskite phase at room temperature at least for a concentration range which is similar for both substituted cations.

Analyzing the resulting structural characteristics upon mixing (volume and average Pb–I–Pb angle evolution), we concluded that the inclusion of a larger cation leads to a volume

increase and structures with cubic-like characteristics. However, in the case of ternary mixtures and for a concentration range which is similar for Cs<sup>+</sup> and GUA<sup>+</sup>, the incorporation of Cs<sup>+</sup> leads to a distortion of the lattice towards a more orthorhombic structure, which in turn lowers the antibonding overlap of the I p-orbitals with the s-orbitals of Pb of the VBM and thus leads to a lower energy and an overall stabilization. This observation allows us to propose a design principle for the preparation of stable mixed cation lead halide perovskites at room temperature according to which mixing monovalent cations that would be outside the stability range with cations that can compensate the size, so that the average radii of the mixed cations lies within the suitable Goldschmidt tolerance range can lead to ternary perovskite mixtures with enhanced stability.

Calculations of the band gaps showed that for both binary and ternary mixtures, the band gap remains unaffected upon mixing and close to the single-junction optimum. Taking into account the pronounced stabilization of the perovskite phase for mixtures with 17% of Cs<sup>+</sup>, solar cells based on these materials can constitute possible candidates for single-junction solar devices as also demonstrated in recent experiments.<sup>43</sup>

### 4 Computational details

DFT calculations<sup>44,45</sup> have been performed using the Quantum Espresso suite of codes.<sup>58,59</sup> The generalized gradient approximation (GGA) to DFT in the PBE<sup>46</sup> formulation has been used for geometry and cell relaxations. The Kohn–Sham orbitals have been expanded in a plane wave basis set with a kinetic energy cutoff of 40 Ry and a density cutoff of 240 Ry. The Brillouin zone has been sampled with a Monkhorst Pack  $k$ -points grid<sup>60</sup> that varied from  $2 \times 2 \times 2$  points for the  $\beta$ -phase to  $2 \times 2 \times 1$  for the  $\delta$ -phase, respectively. All these values have been chosen after performing convergence tests for the total energy, the band gap, the pressure, the stresses and the atomic forces. Ultrasoft pseudopotentials have been used for the interactions between valence electrons, core electrons and nuclei.<sup>61</sup> To compare the absolute energy of Kohn–Sham orbitals and total energies, we followed the protocol suggested by Meloni *et al.*, in which the energies were aligned with respect to the energy of the Pb<sub>5d</sub> semicore state.<sup>53</sup> For an accurate description of the band gaps, the band gaps of the pure phases and binary and ternary perovskite mixtures were calculated using the hybrid functional PBE0<sup>54</sup> on the PBEsol<sup>55</sup> geometries, taking SOC effects (PBE0 + SOC) into account. In this case, fully relativistic norm-conserving pseudopotentials<sup>61</sup> have been used and the Kohn–Sham orbitals have been expanded in a plane wave basis set with a kinetic energy cutoff of 80 Ry and a density cutoff of 320 Ry.

For the pure perovskite phase of FAPbI<sub>3</sub> our 0 K static DFT calculations revealed that among the  $\alpha$  and  $\beta$  FAPbI<sub>3</sub> phases,  $\beta$ -FAPbI<sub>3</sub> has a lower energy, for this reason, the  $\beta$ -phase was considered in our analysis. For the preparation of the mixtures, FA<sup>+</sup> has been successively replaced by GUA<sup>+</sup>. In particular, for

each concentration when allowed by the composition in both the  $\beta$  and the  $\delta$  phases, we considered 10 different possible replacements for the substituted cations, starting from the best configuration at the energetically most favored previous next lower GUA<sup>+</sup> content, in order to find the structure with the lowest energy. The maximum standard deviation of the difference in energy per stoichiometric unit for different substitution pattern for each composition is of the order of 0.005 eV for the  $\beta$  and 0.006 eV for the  $\delta$  phase, respectively. We also performed calculations with different GUA<sup>+</sup> and FA<sup>+</sup> orientations, where the maximum standard deviation of the difference in energy per stoichiometric unit was of the order of 0.007 eV. Once the lowest-energy  $\beta$ -GUA<sub>x</sub>FA<sub>(1-x)</sub>PbI<sub>3</sub> and  $\delta$ -GUA<sub>x</sub>FA<sub>(1-x)</sub>PbI<sub>3</sub> structures were found, FA<sup>+</sup> was replaced by Cs<sup>+</sup>, for the construction of ternary Cs<sub>y</sub>GUA<sub>x</sub>FA<sub>(1-y-x)</sub>PbI<sub>3</sub> mixtures. One should mention here that to estimate the relative energetics of the different phases at 0 K, the alignment procedure requires an identical number of stoichiometric units. For this reason, the  $\delta$  and the  $\beta$  phase superlattices contain 12 stoichiometric units since the crystal structure of  $\beta$ -phase consists of 12 stoichiometric units (144 atoms). To this end, it was not possible to employ the experimental  $\delta$ -GUAPbI<sub>3</sub> structure<sup>35,36,62</sup> in order to compare the mixed compounds with the corresponding pure ones in our calculations since there is no way to create supercells that could have the same number of stoichiometric units with the  $\beta$ -phase. For this reason, we prepared  $\delta$ -GUAPbI<sub>3</sub> structures starting from the known  $\delta$ -FAPbI<sub>3</sub> and  $\delta$ -CsPbI<sub>3</sub> structures by substituting FA<sup>+</sup> or Cs<sup>+</sup> by GUA<sup>+</sup>. We have concluded that the pure  $\delta$ -GUAPbI<sub>3</sub> structure, constructed from  $\delta$ -CsPbI<sub>3</sub> by substituting Cs<sup>+</sup> with GUA<sup>+</sup> is the lowest energy structure and in turn the structure that was used in our calculations. One should also mention here that both experimental  $\delta$ -GUAPbI<sub>3</sub> and  $\delta$ -CsPbI<sub>3</sub> structures are similar since they consist of edge-sharing octahedra that are surrounded by cations. Finally, to compare the mixed perovskite compounds with the corresponding pure ones, we considered different 3D perovskite GUAPbI<sub>3</sub> phases that we constructed by substituting FA<sup>+</sup> by GUA<sup>+</sup> in the  $\alpha$  and  $\beta$  FAPbI<sub>3</sub> phases, considering also different orientations of the cations. We concluded that the structure with the lowest energy and thus the most stable one at 0 K is arising from the  $\alpha$ -FAPbI<sub>3</sub>, with each GUA<sup>+</sup> molecule having the same orientation.

Car-Parrinello MD simulations for a trajectory of 6 ps in the NVT ensemble at 300 K were performed using the CPMD code<sup>63</sup> for systems of 150 atoms. The wavefunction cutoff was set to 90 Ry and Goedecker normconserving pseudopotentials were used.<sup>64–66</sup> A time step of 3 a.u. was used with a fictitious mass parameter of 550 a.u. The temperature was controlled by five different Nosé–Hoover thermostats, one for each species, with a coupling frequency of 1500 cm<sup>-1</sup>.<sup>67–69</sup> The analysis of the relative energetics has been performed for an equilibrated trajectory of 4.3 ps.

## Conflicts of interest

There are no conflicts to declare.

## Acknowledgements

U. R. gratefully acknowledges funding from the Swiss National Science Foundation via the individual grant no. 200020-185092, the NCCR MUST and the Sinergia grant EPISODE. The authors thank the Swiss National Supercomputing Centre (CSCS) for the computer time.

## Notes and references

- 1 A. Kojima, K. Teshima, Y. Shirai and T. Miyasaka, *J. Am. Chem. Soc.*, 2009, **131**, 6050–6051.
- 2 J.-H. Im, C.-R. Lee, J.-W. Lee, S.-W. Park and N.-G. Park, *Nanoscale*, 2011, **3**, 4088–4093.
- 3 H.-S. Kim, C.-R. Lee, J.-H. Im, K.-B. Lee, T. Moehl, A. Marchioro, S.-J. Moon, R. Humphry-Baker, J.-H. Yum, J. E. Moser, M. Grätzel and N.-G. Park, *Sci. Rep.*, 2012, **2**, 591.
- 4 M. M. Lee, J. Teuscher, T. Miyasaka, T. N. Murakami and H. J. Snaith, *Science*, 2012, **338**, 643–647.
- 5 L. Etgar, P. Gao, Z. Xue, Q. Peng, A. K. Chandiran, B. Liu, M. K. Nazeeruddin and M. Grätzel, *J. Am. Chem. Soc.*, 2012, **134**, 17396–17399.
- 6 A. Mei, X. Li, L. Liu, Z. Ku, T. Liu, Y. Rong, M. Xu, M. Hu, J. Chen, Y. Yang, M. Grätzel and H. Han, *Science*, 2014, **345**, 295–298.
- 7 G. E. Eperon, S. D. Stranks, C. Menelaou, M. B. Johnston, L. M. Herz and H. J. Snaith, *Energy Environ. Sci.*, 2014, **7**, 982–988.
- 8 NREL, Best Research-Cell Efficiency Chart Online; accessed 18 September 2019, <http://www.nrel.gov/pv/assets/pdfs/pv-efficiencies-07-17-2018.pdf>, 1976.
- 9 S. De Wolf, J. Holovsky, S.-J. Moon, P. Löper, B. Niesen, M. Ledinsky, F.-J. Haug, J.-H. Yum and C. Ballif, *J. Phys. Chem. Lett.*, 2014, **5**, 1035–1039.
- 10 G. Xing, N. Mathews, S. Sun, S. S. Lim, Y. M. Lam, M. Grätzel, S. Mhaisalkar and T. C. Sum, *Science*, 2013, **342**, 344–347.
- 11 S. D. Stranks, G. E. Eperon, G. Grancini, C. Menelaou, M. J. P. Alcocer, T. Leijtens, L. M. Herz, A. Petrozza and H. J. Snaith, *Science*, 2013, **342**, 341–344.
- 12 D. Shi, V. Adinolfi, R. Comin, M. Yuan, E. Alarousu, A. Buin, Y. Chen, S. Hoogland, A. Rothenberger, K. Katsiev, Y. Losovyj, X. Zhang, P. A. Dowben, O. F. Mohammed, E. H. Sargent and O. M. Bakr, *Science*, 2015, **347**, 519–522.
- 13 M. Grätzel, *Nat. Mater.*, 2014, **13**, 838.
- 14 W. Shockley and H. J. Queisser, *J. Appl. Phys.*, 1961, **32**, 510–519.
- 15 S. Rühle, *Sol. Energy*, 2016, **130**, 139–147.
- 16 S. Pang, H. Hu, J. Zhang, S. Lv, Y. Yu, F. Wei, T. Qin, H. Xu, Z. Liu and G. Cui, *Chem. Mater.*, 2014, **26**, 1485–1491.
- 17 T. M. Koh, K. Fu, Y. Fang, S. Chen, T. C. Sum, N. Mathews, S. G. Mhaisalkar, P. P. Boix and T. Baikie, *J. Phys. Chem. C*, 2014, **118**, 16458–16462.
- 18 C. C. Stoumpos, C. D. Malliakas and M. G. Kanatzidis, *Inorg. Chem.*, 2013, **52**, 9019–9038.
- 19 C. K. Moller, *Nature*, 1958, **182**, 1436.



- 20 G. E. Eperon, G. M. Paternò, R. J. Sutton, A. Zampetti, A. A. Haghighirad, F. Cacialli and H. J. Snaith, *J. Mater. Chem. A*, 2015, **3**, 19688–19695.
- 21 Y. Wang, M. I. Dar, L. K. Ono, T. Zhang, M. Kan, Y. Li, L. Zhang, X. Wang, Y. Yang, X. Gao, Y. Qi, M. Grätzel and Y. Zhao, *Science*, 2019, **365**, 591–595.
- 22 A. Boziki, D. J. Kubicki, A. Mishra, S. Meloni, L. Emsley, M. Grätzel and U. Rothlisberger, *Chem. Mater.*, 2020, **32**, 2605–2614.
- 23 T. J. Coutts, K. A. Emery and J. Scott Ward, *Prog. Photovoltaics*, 2002, **10**, 195–203.
- 24 N. Pellet, P. Gao, G. Gregori, T.-Y. Yang, M. K. Nazeeruddin, J. Maier and M. Grätzel, *Angew. Chem.*, 2014, **53**, 3151–3157.
- 25 C. Yi, J. Luo, S. Meloni, A. Boziki, N. Ashari-Astani, C. Grätzel, S. M. Zakeeruddin, U. Rothlisberger and M. Grätzel, *Energy Environ. Sci.*, 2016, **9**, 656–662.
- 26 J.-W. Lee, D.-H. Kim, H.-S. Kim, S.-W. Seo, S. M. Cho and N.-G. Park, *Adv. Energy Mater.*, 2015, **5**, 1501310.
- 27 M. Saliba, T. Matsui, K. Domanski, J.-Y. Seo, A. Ummadisingu, S. M. Zakeeruddin, J.-P. Correa-Baena, W. R. Tress, A. Abate, A. Hagfeldt and M. Grätzel, *Science*, 2016, **354**, 206–209.
- 28 M. Saliba, T. Matsui, J.-Y. Seo, K. Domanski, J.-P. Correa-Baena, M. K. Nazeeruddin, S. M. Zakeeruddin, W. Tress, A. Abate, A. Hagfeldt and M. Grätzel, *Energy Environ. Sci.*, 2016, **9**, 1989–1997.
- 29 V. M. Goldschmidt, *Naturwissenschaften*, 1926, **14**, 477–485.
- 30 D. B. Mitzi, *J. Chem. Soc., Dalton Trans.*, 2001, 1–12.
- 31 G. Kieslich, S. Sun and A. K. Cheetham, *Chem. Sci.*, 2014, **5**, 4712–4715.
- 32 G. Kieslich, S. Sun and A. K. Cheetham, *Chem. Sci.*, 2015, **6**, 3430–3433.
- 33 D. J. Kubicki, D. Prochowicz, A. Hofstetter, S. M. Zakeeruddin, M. Grätzel and L. Emsley, *J. Am. Chem. Soc.*, 2017, **139**, 14173–14180.
- 34 G. Giorgi, J.-I. Fujisawa, H. Segawa and K. Yamashita, *J. Phys. Chem. C*, 2015, **119**, 4694–4701.
- 35 M. Szafranski, *Thermochim. Acta*, 1997, **307**, 177–183.
- 36 A. D. Jodlowski, A. Yépez, R. Luque, L. Camacho and G. De Miguel, *Angew. Chem.*, 2016, **55**, 14972–14977.
- 37 N. De Marco, H. Zhou, Q. Chen, P. Sun, Z. Liu, L. Meng, E.-P. Yao, Y. Liu, A. Schiffer and Y. Yang, *Nano Lett.*, 2016, **16**, 1009–1016.
- 38 A. D. Jodlowski, C. Roldán-Carmona, G. Grancini, M. Salado, M. Ralaiarisoa, S. Ahmad, N. Koch, L. Camacho, G. De Miguel and M. K. Nazeeruddin, *Nat. Energy*, 2017, **2**, 972.
- 39 D. J. Kubicki, D. Prochowicz, A. Hofstetter, M. Sasaki, P. Yadav, D. Bi, N. Pellet, J. Lewiński, S. M. Zakeeruddin, M. Grätzel and L. Emsley, *J. Am. Chem. Soc.*, 2018, **140**, 3345–3351.
- 40 O. Nazarenko, M. R. Kotyrba, M. Würle, E. Cuervo-Reyes, S. Yakunin and M. V. Kovalenko, *Inorg. Chem.*, 2017, **56**, 11552–11564.
- 41 O. Nazarenko, M. R. Kotyrba, S. Yakunin, M. Aebli, G. Rainò, B. M. Benin, M. Würle and M. V. Kovalenko, *J. Am. Chem. Soc.*, 2018, **140**, 3850–3853.
- 42 R. J. Stoddard, A. Rajagopal, R. L. Palmer, I. L. Braly, A. K.-Y. Jen and H. W. Hillhouse, *ACS Energy Lett.*, 2018, **3**, 1261–1268.
- 43 N. D. Pham, C. Zhang, V. T. Tjong, S. Zhang, G. Will, A. Bou, J. Bisquert, P. E. Shaw, A. Du, G. J. Wilson and H. Wang, *Adv. Funct. Mater.*, 2019, **29**, 1806479.
- 44 P. Hohenberg and W. Kohn, *Phys. Rev.*, 1964, **136**, B864–B871.
- 45 W. Kohn and L. J. Sham, *Phys. Rev.*, 1965, **140**, A1133–A1138.
- 46 J. P. Perdew, K. Burke and M. Ernzerhof, *Phys. Rev. Lett.*, 1996, **77**, 3865–3868.
- 47 B. Fultz, *Prog. Mater. Sci.*, 2010, **55**, 247–352.
- 48 F. Brivio, J. M. Frost, J. M. Skelton, A. J. Jackson, O. J. Weber, M. T. Weller, A. R. Goñi, A. M. A. Leguy, P. R. F. Barnes and A. Walsh, *Phys. Rev. B: Condens. Matter Mater. Phys.*, 2015, **92**, 144308.
- 49 X.-G. Zhao, J.-H. Yang, Y. Fu, D. Yang, Q. Xu, L. Yu, S.-H. Wei and L. Zhang, *J. Am. Chem. Soc.*, 2017, **139**, 2630–2638.
- 50 X.-G. Zhao, D. Yang, Y. Sun, T. Li, L. Zhang, L. Yu and A. Zunger, *J. Am. Chem. Soc.*, 2017, **139**, 6718–6725.
- 51 R. X. Yang, J. M. Skelton, E. L. da Silva, J. M. Frost and A. Walsh, *J. Phys. Chem. Lett.*, 2017, **8**, 4720–4726.
- 52 A. Marronnier, H. Lee, B. Geffroy, J. Even, Y. Bonnassieux and G. Roma, *J. Phys. Chem. Lett.*, 2017, **8**, 2659–2665.
- 53 S. Meloni, G. Palermo, N. Ashari-Astani, M. Grätzel and U. Rothlisberger, *J. Mater. Chem. A*, 2016, **4**, 15997–16002.
- 54 J. P. Perdew, M. Ernzerhof and K. Burke, *J. Chem. Phys.*, 1996, **105**, 9982–9985.
- 55 J. P. Perdew, A. Ruzsinszky, G. I. Csonka, O. A. Vydrov, G. E. Scuseria, L. A. Constantin, X. Zhou and K. Burke, *Phys. Rev. Lett.*, 2008, **100**, 136406.
- 56 N. Ashari-Astani, F. Jahanbakhshi, M. Mladenović, A. Q. M. Alanazi, I. Ahmadabadi, M. R. Ejtehadi, M. I. Dar, M. Grätzel and U. Rothlisberger, *J. Phys. Chem. Lett.*, 2019, **10**, 3543–3549.
- 57 H. Q. Pham, R. J. Holmes, E. S. Aydil and L. Gagliardi, *Nanoscale*, 2019, **11**, 11173–11182.
- 58 P. Giannozzi, S. Baroni, N. Bonini, M. Calandra, R. Car, C. Cavazzoni, D. Ceresoli, G. L. Chiarotti, M. Cococcioni, I. Dabo, A. D. Corso, S. de Gironcoli, S. Fabris, G. Fratesi, R. Gebauer, U. Gerstmann, C. Gougoussis, A. Kokalj, M. Lazzeri, L. Martin-Samos, N. Marzari, F. Mauri, R. Mazzarello, S. Paolini, A. Pasquarello, L. Paulatto, C. Sbraccia, S. Scandolo, G. Sclauzero, A. P. Seitsonen, A. Smogunov, P. Umari and R. M. Wentzcovitch, *J. Phys.: Condens. Matter*, 2009, **21**, 395502.
- 59 P. Giannozzi, O. Andreussi, T. Brumme, O. Bunau, M. B. Nardelli, M. Calandra, R. Car, C. Cavazzoni, D. Ceresoli, M. Cococcioni, N. Colonna, I. Carnimeo, A. D. Corso, S. de Gironcoli, P. Delugas, R. A. D. Jr, A. Ferretti, A. Floris, G. Fratesi, G. Fugallo, R. Gebauer, U. Gerstmann, F. Giustino, T. Gorni, J. Jia, M. Kawamura, H.-Y. Ko, A. Kokalj, E. Küçükbenli, M. Lazzeri, M. Marsili, N. Marzari, F. Mauri, N. L. Nguyen, H.-V. Nguyen, A. O. de-la Roza, L. Paulatto, S. Poncé, D. Rocca, R. Sabatini, B. Santra, M. Schlipf, A. P. Seitsonen, A. Smogunov, I. Timrov, T. Thonhauser, P. Umari, N. Vast, X. Wu and S. Baroni, *J. Phys.: Condens. Matter*, 2017, **29**, 465901.
- 60 H. J. Monkhorst and J. D. Pack, *Phys. Rev. B: Condens. Matter Mater. Phys.*, 1976, **13**, 5188–5192.
- 61 A. D. Corso, *Comput. Mater. Sci.*, 2014, **95**, 337–350.

- 62 L. Dimesso, A. Quintilla, Y.-M. Kim, U. Lemmer and W. Jaegermann, *Mater. Sci. Eng., B*, 2016, **204**, 27–33.
- 63 CPMD, Copyright IBM Corp 1990-2015, Copyright MPI für Festkörperforschung Stuttgart 1997-2001. Online; accessed 1 July 2019, <http://www.cpmc.org/>, 1990.
- 64 S. Goedecker, M. Teter and J. Hutter, *Phys. Rev. B: Condens. Matter Mater. Phys.*, 1996, **54**, 1703–1710.
- 65 C. Hartwigsen, S. Goedecker and J. Hutter, *Phys. Rev. B: Condens. Matter Mater. Phys.*, 1998, **58**, 3641–3662.
- 66 M. Krack, *Theor. Chem. Acc.*, 2005, **114**, 145–152.
- 67 S. Nosé, *Mol. Phys.*, 1984, **52**, 255–268.
- 68 S. Nosé, *J. Chem. Phys.*, 1984, **81**, 511–519.
- 69 W. G. Hoover, *Phys. Rev. A: At., Mol., Opt. Phys.*, 1985, **31**, 1695–1697.

# Crown Ether Modulation Enables over 23% Efficient Formamidinium-Based Perovskite Solar Cells

Tzu-Sen Su,<sup>¶</sup> Felix Thomas Eickemeyer,<sup>¶</sup> Michael A. Hope,<sup>¶</sup> Farzaneh Jahanbakhshi,<sup>¶</sup> Marko Mladenović, Jun Li, Zhiwen Zhou, Aditya Mishra, Jun-Ho Yum, Dan Ren, Anurag Krishna, Olivier Ouellette, Tzu-Chien Wei, Hua Zhou, Hsin-Hsiang Huang, Mounir Driss Mensi, Kevin Sivula, Shaik M. Zakeeruddin, Jovana V. Milić, Anders Hagfeldt, Ursula Rothlisberger, Lyndon Emsley, Hong Zhang,\* and Michael Grätzel\*



Cite This: *J. Am. Chem. Soc.* 2020, 142, 19980–19991



Read Online

ACCESS |



Metrics & More

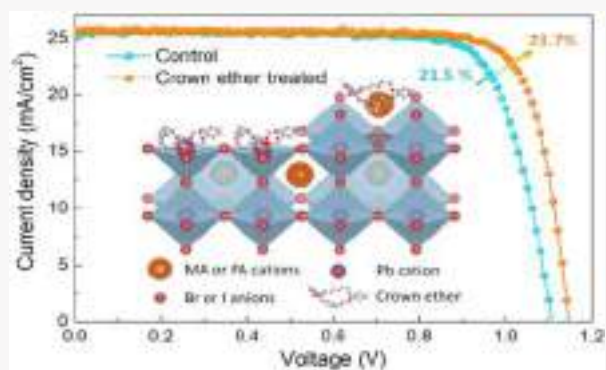


Article Recommendations



Supporting Information

**ABSTRACT:** The use of molecular modulators to reduce the defect density at the surface and grain boundaries of perovskite materials has been demonstrated to be an effective approach to enhance the photovoltaic performance and device stability of perovskite solar cells. Herein, we employ crown ethers to modulate perovskite films, affording passivation of undercoordinated surface defects. This interaction has been elucidated by solid-state nuclear magnetic resonance and density functional theory calculations. The crown ether hosts induce the formation of host–guest complexes on the surface of the perovskite films, which reduces the concentration of surface electronic defects and suppresses nonradiative recombination by 40%, while minimizing moisture permeation. As a result, we achieved substantially improved photovoltaic performance with power conversion efficiencies exceeding 23%, accompanied by enhanced stability under ambient and operational conditions. This work opens a new avenue to improve the performance and stability of perovskite-based optoelectronic devices through supramolecular chemistry.



## INTRODUCTION

Metal halide perovskites have attracted tremendous attention mainly because of their excellent optoelectronic properties.<sup>1–3</sup> The power conversion efficiency (PCE) of solution processed perovskite solar cell (PSCs) has increased from an initial 3.8% to a certified 25.2%, which renders them promising candidates for next-generation photovoltaic devices. However, numerous crystal defects including anion vacancies and undercoordinated lead cations, formed mostly at the surface and grain boundaries of the perovskite layer,<sup>4,5</sup> impair the stability and performance of PSCs.<sup>6,7</sup> The vacancy defects provide a pathway for ion migration, which results in fast degradation of PSCs under operational conditions.<sup>8</sup> Furthermore, several studies have indicated that surface defects and grain boundaries can serve as carrier recombination sites and thus result in PCE loss.<sup>9,10</sup> Some organic molecules are capable of passivating the defect sites at the surface and grain boundaries via coordinate bonding or ionic bonding.<sup>11</sup> For example, a tailored organohalide molecule (i.e., 1,2,4,5-tetrafluoro-3,6-diiodobenzene<sup>12</sup>) has been proposed to coordinate with under-coordinated halide anions on the perovskite surface, passivating them and thus significantly increasing the PSC performances. The uncoordi-

nated metal cations on the surface of perovskite films can be passivated by Lewis bases containing lone pairs of electrons on oxygen, nitrogen, or sulfur (e.g., pyridine,<sup>10</sup> thiophene,<sup>10</sup> benzoquinone<sup>13</sup>). In addition, some electronic trap states can be passivated by Lewis acid molecules, such as bis-phenyl-C<sub>61</sub>-butyric acid methyl ester (PCBM) mixed isomers, which accept electrons from the Lewis base type defects on the perovskite surface.<sup>14</sup> The charged surface sites can also be neutralized by molecular or atomic ions, such as phenethylammonium cations<sup>15</sup> or chloride anions;<sup>16</sup> in some cases, both the cation and anion have been shown to be active (e.g., choline chloride<sup>17</sup>). Based on these previous results, molecular modulators are an effective strategy for perovskite defect passivation; nevertheless, designing new and more effective modulators is required to further improve the efficiency of PSCs

Received: August 12, 2020

Published: November 10, 2020



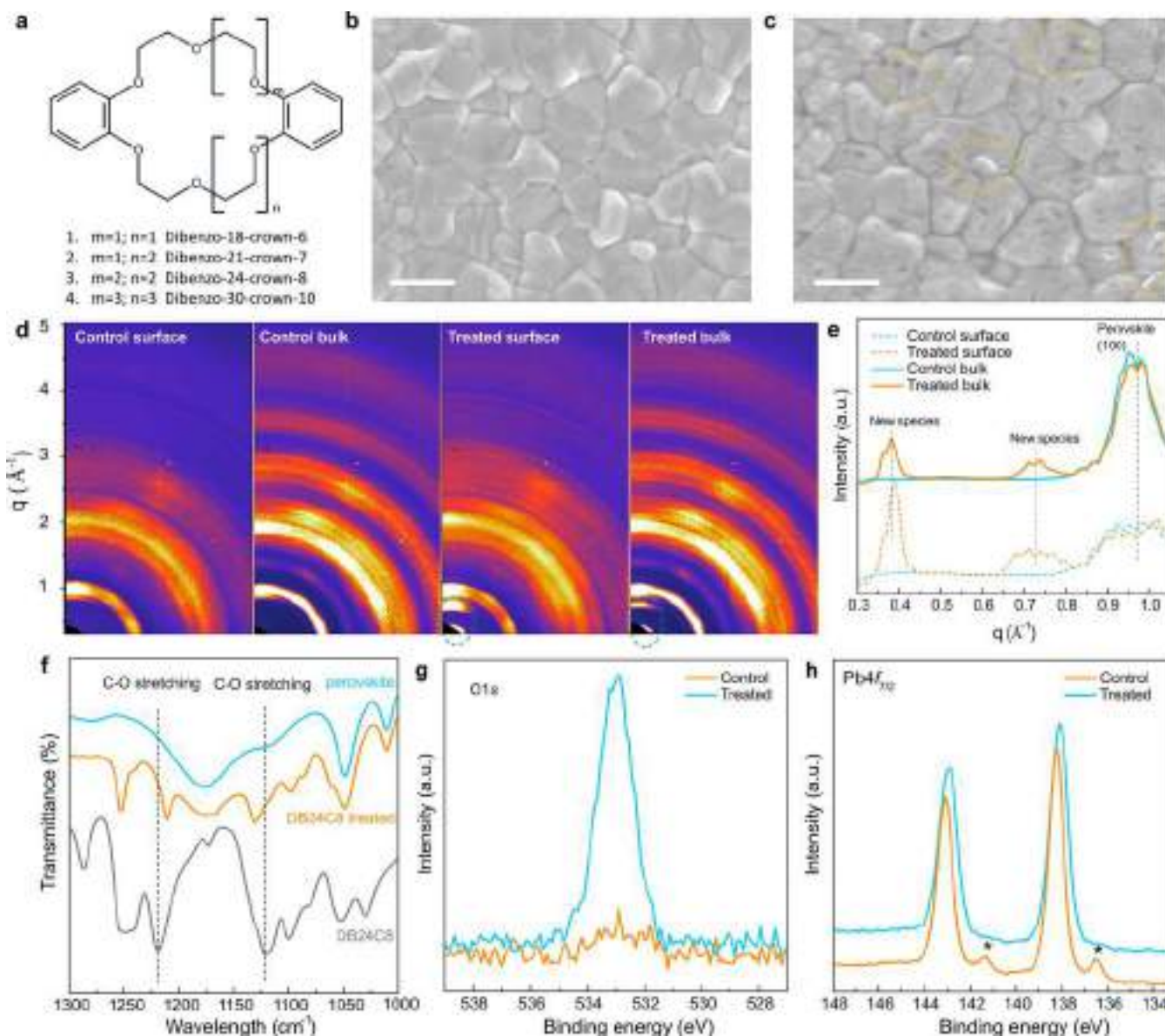


**Figure 1.** Morphology and structural characterizations. (a) Molecular structure of benzannulated crown ethers used in this study. Top-view high-resolution SEM images of (b) control and (c) crown-ether-treated perovskite films (some of the possible new species are highlighted). The scale bar represents 1  $\mu\text{m}$ . (d) GIWAXS two-dimensional reciprocal space maps of control sample and treated sample at incidence angles of  $\alpha_i = 0.1^\circ$  (more surface sensitive) and  $\alpha_i = 0.30^\circ$  (more bulk sensitive). (e) Radially integrated intensity of GIWAXS data in (b) and (c). (f) Attenuated total reflection Fourier transform infrared (ATR-FTIR) spectra of pristine perovskite film, crown-ether-treated perovskite film, and crown ether (DB24C8) powder. X-ray photoelectron spectroscopy (XPS) core-level spectra of pristine perovskite film and crown-ether-treated perovskite film for O 1s (g) and Pb 4f (h). The asterisk (\*) indicates metallic Pb species.

toward their efficiency limit ( $\sim 31\%$ ),<sup>18</sup> as well as to enhance their operational stability.

Crown ethers are well-known cyclic molecules containing ether groups. This results in a highly electronegative cavity, which can selectively complex different cations, whereby the selectivity is based on the size of the ring structure.<sup>19</sup> As a result, crown ethers are widely used as complexation reagents and phase-transfer catalysts.<sup>20</sup>

Herein, we employ crown ethers to modulate hybrid perovskites, affording passivation of undercoordinated metal or organic cation defects. This interaction has been elucidated by solid-state nuclear magnetic resonance spectroscopy (NMR), attenuated total reflection Fourier-transform infrared spectroscopy (ATR-FTIR), X-ray photoelectron spectroscopy (XPS),

and density functional theory (DFT) calculations. We show that the crown ether modulation reduces the trap state density at the interface with the hole conductor and grain boundaries of the perovskite film, thus greatly suppressing nonradiative recombination. As a result, the crown-ether-modulated PSCs exhibit improved PCE exceeding 23%, accompanied by enhanced stability under ambient and operational conditions.

## RESULTS AND DISCUSSION

Double cation, double halide,  $\text{FA}_{0.97}\text{MA}_{0.03}\text{PbI}_{2.97}\text{Br}_{0.03}$  perovskite layers ( $\text{FA}^+$  = formamidinium =  $\text{CH}(\text{NH}_2)_2^+$ ;  $\text{MA}^+$  = methylammonium =  $\text{CH}_3\text{NH}_3^+$ ) were prepared and deposited onto the mesoporous  $\text{TiO}_2$  (mp- $\text{TiO}_2$ ) layer by a one-step method using chlorobenzene as an antisolvent (see Exper-

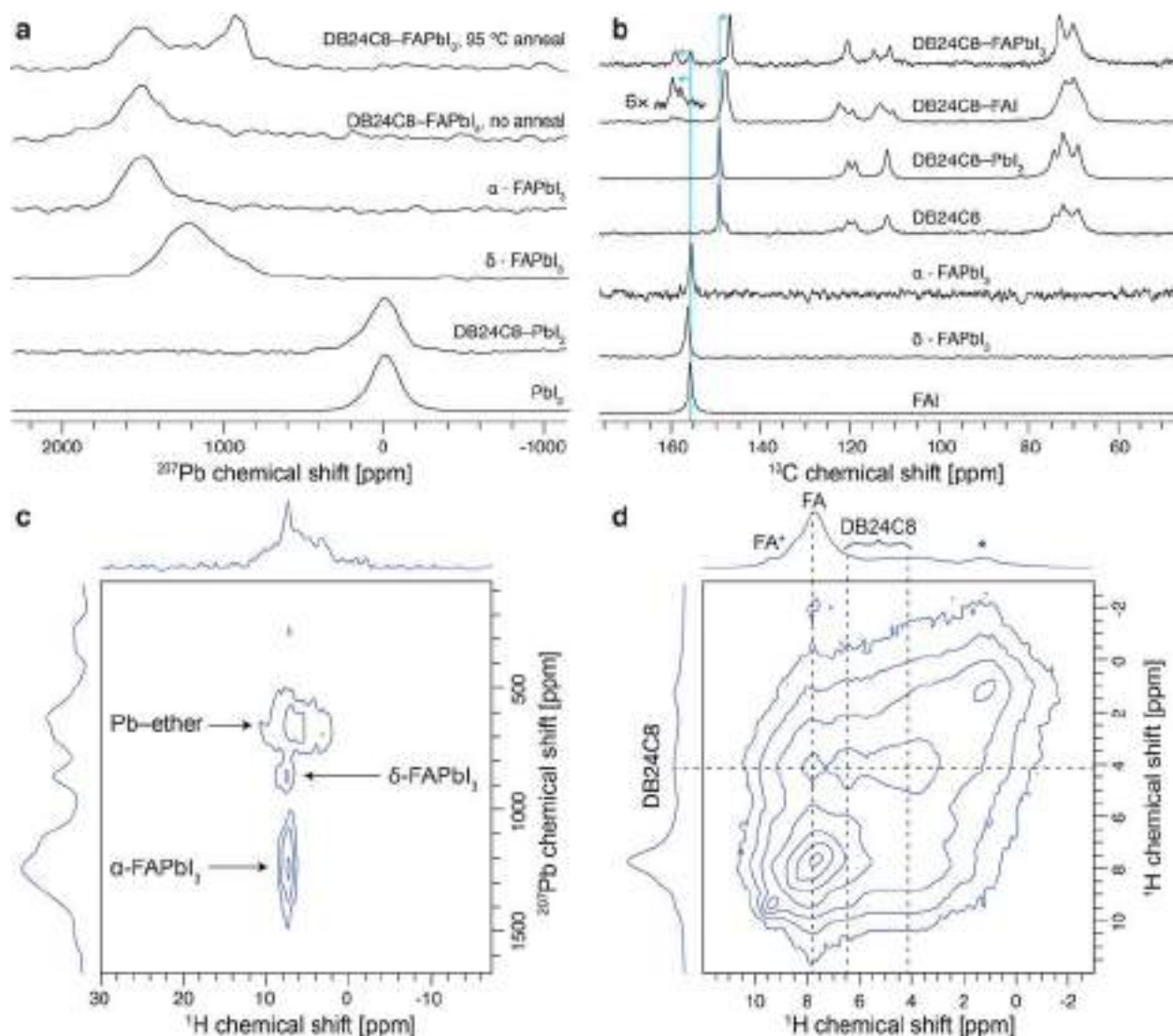


**Figure 2.** Atomic-level insights into the crown ether modulation by NMR. (a)  $^{207}\text{Pb}$  echo and (b)  $^1\text{H} \rightarrow ^{13}\text{C}$  CP NMR spectra of FAI,  $\text{PbI}_2$ , and  $\text{FAPbI}_3$ , with and without ball-milling with DB24C8 crown ether, recorded at 15 kHz MAS. (c)  $^{207}\text{Pb} \rightarrow ^1\text{H}$  HETCOR spectrum of DB24C8- $\text{FAPbI}_3$  recorded at 113 K and 30 kHz MAS. (d)  $^1\text{H} \rightarrow ^1\text{H}$  spin diffusion spectrum of DB24C8- $\text{FAPbI}_3$ , recorded at 40 kHz MAS with a mixing time of 10 ms. The asterisk (\*) indicates polypropylene from the ball-milling jar.

imental Section in the Supporting Information). In a preliminary study, two crown ethers were examined with comparable cavities that were either aliphatic or benzannulated, i.e., 18-crown-6 ether, 18C6, and dibenzo-18-crown-6, DB18C6, respectively. The devices with DB18C6 treatment were found to exhibit better photovoltaic performance than those with 18C6 (Figure S1 and Table S1). Moreover, DB18C6 has a higher reported hydrophobicity than 18C6,<sup>21</sup> which might enhance the moisture tolerance of the perovskite materials in air. Based on the prospect of increased device efficiency and hydrophobicity, benzannulated crown ethers were selected for the second round of screening: DB18C6; dibenzo-21-crown-7, DB21C7; dibenzo-24-crown-8, DB24C8; and dibenzo-30-crown-10, DB30C10 (Figure 1a). The ring size of the crown ether was optimized with respect to the overall photovoltaic performance. The open circuit voltage ( $V_{\text{OC}}$ ) and power conversion efficiency (PCE) of PSCs modulated by the benzannulated crown ethers augmented substantially with increasing the size of the macrocycle from DB18C6 to DB24C8 (Figure S2 and Table S2). Further increasing the size of the macrocycle (e.g., DB30C10) leads to a

reduction of  $V_{\text{OC}}$ , with DB24C8-modulated PSCs showing the best overall photovoltaic performance. We therefore used DB24C8 for further studies.

**Morphology and Structural Characterization.** The morphology of the perovskite surface was analyzed for control and crown-ether-treated perovskite films by scanning electron microscopy (SEM; Figure 1b,c). Both control and treated perovskite films are uniform and highly crystalline with similar compact textures and grain sizes in the range of hundreds of nanometers. Excess  $\text{PbI}_2$  (located at the grain boundaries<sup>7</sup>) disappeared upon crown ether treatment in the films. We further analyzed the structural properties of the perovskite films by grazing incidence wide-angle X-ray scattering (GIWAXS; Figure 1d) at two different angles of incidence, i.e.,  $0.1^\circ$  (more surface sensitive) and  $0.3^\circ$  (more bulk sensitive). Both the control and treated perovskite films show identical Bragg reflections and a preferred orientation for the perovskite phase (100). Compared to the control films, two additional low- $q$  signals ( $\sim 0.39$  and  $\sim 0.73 \text{ \AA}^{-1}$ ) appear in the treated films; the relative Bragg peak intensities decrease with increasing penetration depth (Figure

1e), implying that the new species are located predominantly at the surface of perovskite film, consistent with the species observed in the SEM image (Figure 1b). These species could be formed by the host–guest complexation of the crown ether with cations on the perovskite surface.<sup>22</sup>

The effects of crown ether treatment on the perovskite surface were further investigated by ATR-FTIR and XPS. The FTIR spectrum of pristine crown ether (DB24C8) powder reveals two characteristic peaks of the C–O stretching vibration at  $\sim 1121$  and  $\sim 1219$   $\text{cm}^{-1}$  (Figure 1f), while the control perovskite film does not exhibit these peaks. For the crown-ether-treated perovskite film, these C–O stretching vibrations are still present, but slightly shifted to 1131 and 1211  $\text{cm}^{-1}$ , respectively, indicating an interaction between the functional groups of the crown ether (i.e., the oxygen atoms in the ring) and the perovskite film. Changes in the XPS spectra of the perovskite are also observed upon crown ether treatment (Figure 1g, h). First, a new peak in the O 1s level range at 533.0 eV (Figure 1g) that is associated with the C–O bond suggests that the crown ether is adsorbed on the surface of the treated perovskite film. Furthermore, the two peaks related to Pb  $4f_{7/2}$  and Pb  $4f_{5/2}$  shift to lower energies of 138.1 and 142.8 eV, respectively. Finally, the metallic Pb peaks located at 136.4 and 141.4 eV vanish in the crown-ether-treated films. These results suggest that the crown ether is not just adsorbed but reacts with the perovskite film, presumably through coordination between the oxygen atoms of the crown ether and cations on the perovskite surface.

**Mechanistic Study of Crown Ether Modulation.** Further insight into the mechanism of crown ether modulation was gained by studying bulk mechanosynthesized samples<sup>23</sup> with solid state NMR. As an element-specific probe of local structure, NMR is a powerful tool to determine dopant incorporation and surface modification in perovskite systems.<sup>24–27</sup> In particular,  $^{13}\text{C}$  NMR<sup>28</sup> and  $^{207}\text{Pb}$  NMR<sup>29,30</sup> are sensitive to the local environment of the organic and inorganic cations, respectively, while  $^1\text{H}$ – $^1\text{H}$  spin diffusion experiments can be used to demonstrate atomic-scale proximity (up to  $\sim 10$  Å).<sup>26</sup>

To investigate the possibility of complexation of  $\text{FA}^+$  and  $\text{Pb}^{2+}$  by DB24C8, bulk samples of 1:1 molar ratio  $\text{FAI}:\text{DB24C8}$  and  $\text{PbI}_2:\text{DB24C8}$  were investigated. For  $\text{DB24C8}-\text{PbI}_2$ , there is no change observed either in the  $\text{PbI}_2$  structure as measured by the  $^{207}\text{Pb}$  spectrum (Figure 2a) or in the DB24C8 as probed by the  $^{13}\text{C}$  spectrum (Figure 2b), and no additional reflections are seen in the XRD pattern (Figure S3). This shows that the crown ether cannot form a complex with  $\text{PbI}_2$  under these conditions, most likely due to the high lattice energy of the  $\text{PbI}_2$  salt. In contrast, for  $\text{DB24C8}-\text{FAI}$ , clear changes are seen for the  $^{13}\text{C}$  signals of the crown ether (Figure 2b), most notably an upfield shift of the phenyl-ether environment from 158.3 to 156.9 ppm. The  $\text{FA}^+$  signal also shifts from  $\delta^{13}\text{C} = 164.8$  ppm for FAI to  $\sim 168$  ppm in  $\text{DB24C8}-\text{FAI}$ , concomitantly with a shift in the  $\text{FA}^+$   $^1\text{H}$  signal from  $\delta^1\text{H} \approx 8.1$  ppm in FAI to 8.5–9.0 ppm in  $\text{DB24C8}-\text{FAI}$ , depending on the recycle delay used (Figure S4); these shifted  $\text{FA}^+$   $^{13}\text{C}$  and  $^1\text{H}$  signals are correlated in the  $^1\text{H} \rightarrow ^{13}\text{C}$  HETCOR spectrum (Figure S5). Finally, atomic scale proximity between the crown ether and  $\text{FA}^+$  is demonstrated by cross peaks in the  $^1\text{H}$ – $^1\text{H}$  spin diffusion spectrum (Figure S6). Together, these results indicate the formation of a  $\text{DB24C8}-\text{FAI}$  complex. In the XRD pattern (Figure S3), additional low angle reflections are seen including a low angle reflection at  $2\theta = 7.1^\circ$  ( $q = 0.51$   $\text{\AA}^{-1}$ ), supporting the formation of a complex; notably, this

reflection was not observed for the treated films, indicating that the major species formed there is not the same as this  $\text{DB24C8}-\text{FAI}$  complex, although polymorphism cannot be ruled out.

Subsequently, the interaction between  $\text{DB24C8}$  and bulk  $\text{FAPbI}_3$  perovskite was studied, as a model system for the double cation, double halide perovskite, due to the greater spectral resolution.  $\alpha\text{-FAPbI}_3$  was prepared by ball-milling  $\text{PbI}_2$  and FAI and annealing at 150  $^\circ\text{C}$ , before ball-milling with 10 atom %  $\text{DB24C8}$ . Immediately, following ball-milling, the  $\sim 1520$  ppm  $^{207}\text{Pb}$  signal is indistinguishable from that of neat  $\alpha\text{-FAPbI}_3$  (Figure 2a); however, after annealing at 95  $^\circ\text{C}$  for 15 min, a new signal is observed at  $\sim 900$  ppm, which is ascribed to a  $^{207}\text{Pb}$  environment interacting with the crown ether. We note that the relative ratio of the two signals is not quantitative due to fast transverse decay during the echo pulse sequence, and the high intensity of the new signal is most likely due to a longer  $T_2$  relaxation constant (see Figure S7). The  $^{13}\text{C}$  spectrum (Figure 2b) again shows significant changes to the crown ether signals, with an even greater upfield shift of the phenyl-ether environment to 155.9 ppm, confirming a reaction with the ether, as well as the appearance of a shifted  $\text{FA}^+$  signal at 168.2 ppm, similar to  $\text{DB24C8}-\text{FAI}$ , in addition to the  $\alpha\text{-FAPbI}_3$  peak at 164.5 ppm. The atomic-scale proximity of the  $\text{FA}^+$  and the crown ether is confirmed by  $^1\text{H}$ – $^1\text{H}$  spin diffusion (Figure 2d), where the correlation between the aliphatic signal of the crown ether ( $\delta^1\text{H} = 4.2$  ppm) and the perovskite  $\text{FA}^+$  signal ( $\delta^1\text{H} \approx 7.7$  ppm) can be distinguished from correlation with the aromatic ether signal ( $\delta^1\text{H} = 6.5$  ppm). A minor signal can also be observed at  $\delta^1\text{H} = 9.3$  ppm, assigned to  $\text{FA}^+$  interacting with the ether (denoted  $\text{FA}^*$ ), as also observed for  $\text{DB24C8}-\text{FAI}$  (Figure S3); this signal also correlates with the  $\text{DB24C8}$  crown ether, which can most easily be seen by taking the 4.1 ppm row from the 2D (Figure S5). The new  $^{207}\text{Pb}$  environment correlates with the ether and modified  $\text{FA}^+$   $^1\text{H}$  signals between 3–10 ppm in the  $^{207}\text{Pb} \rightarrow ^1\text{H}$  HETCOR spectrum (Figure 2c), whereas the  $\alpha\text{-FAPbI}_3$   $^{207}\text{Pb}$  signal correlates only with the major  $\text{FA}^+$  signal at  $\delta^1\text{H} = 7.5$  ppm. The HETCOR spectrum was recorded at 113 K since only the  $\alpha\text{-FAPbI}_3$  correlation could be observed at room temperature, presumably due to dynamics of the ether; consequently, all the  $^{207}\text{Pb}$  signals are observed at lower frequencies than at room temperature due to the strong temperature dependence of  $^{207}\text{Pb}$  chemical shifts.<sup>30</sup> A minor component of  $\delta\text{-FAPbI}_3$  can also be observed since its  $^{207}\text{Pb}$  signal is significantly sharper than  $\alpha\text{-FAPbI}_3$  at low temperature (Figure S8). Taken together, the NMR results clearly indicate the formation of a mixed perovskite– $\text{DB24C8}$  phase, with atomic proximity between FA, Pb, and the crown ether. The formation of a new phase is also supported by XRD characterization (Figure S3), with additional major low-angle peaks at  $2\theta = 5.6^\circ$  and  $9.3^\circ$  ( $q = 0.40$  and  $0.66$   $\text{\AA}^{-1}$ ), although the low-angle reflections observed for the treated perovskite film at  $2\theta = 5.3^\circ$  and  $10.5^\circ$  ( $q = 0.38$ ,  $0.75$   $\text{\AA}^{-1}$ ) can also be observed, albeit with lower intensity and wider peak width. This suggests that similar species are formed in both cases, perhaps with some polymorphism.

To shed further light on the crown ether modulation effects, DFT calculations were performed on  $\text{DB24C8}$ –cation complexes and treated perovskite surfaces (the procedure is outlined in the Experimental Section in the Supporting Information). The likelihood of formation of the two complexes,  $\text{DB24C8}-\text{FA}^+$  and  $\text{DB24C8}-\text{Pb}^{2+}$ , was determined by calculating the corresponding complexation energies between the gas phase reactants and the complexes. The complexation energies of

DB24C8–Pb<sup>2+</sup> and DB24C8–FA<sup>+</sup> indicate that the formation of both complexes is favorable (Table 1), which suggests that

**Table 1. Complexation Energies of DB24C8–Pb<sup>2+</sup> and DB24C8–FA<sup>+</sup>**

reaction	complexation energy (eV) <sup>a</sup>
DB24C8 + Pb <sup>2+</sup> → DB24C8–Pb <sup>2+</sup>	–8.79
DB24C8 + FA <sup>+</sup> → DB24C8–FA <sup>+</sup>	–1.79

<sup>a</sup>The more negative values indicate the more stable complex.

undercoordinated surface Pb<sup>2+</sup> or FA<sup>+</sup> ionic defects (e.g., FA cations that are in stoichiometric excess, present at interstitial lattice sites or grain boundaries) could be passivated via crown ether complexation. However, the favorable formation of DB24C8–Pb<sup>2+</sup> from the gas phase ion does not imply that the complex would form from crystalline PbI<sub>2</sub>, as discussed above.

To reveal the changes in the interfacial properties of the crown-ether-modulated perovskites, a comparative study was carried out on the electronic properties of pristine FAPbI<sub>3</sub>, FAPbI<sub>3</sub> slabs containing an iodide vacancy, and FAPbI<sub>3</sub> slabs containing an iodide vacancy in the presence of the crown ether

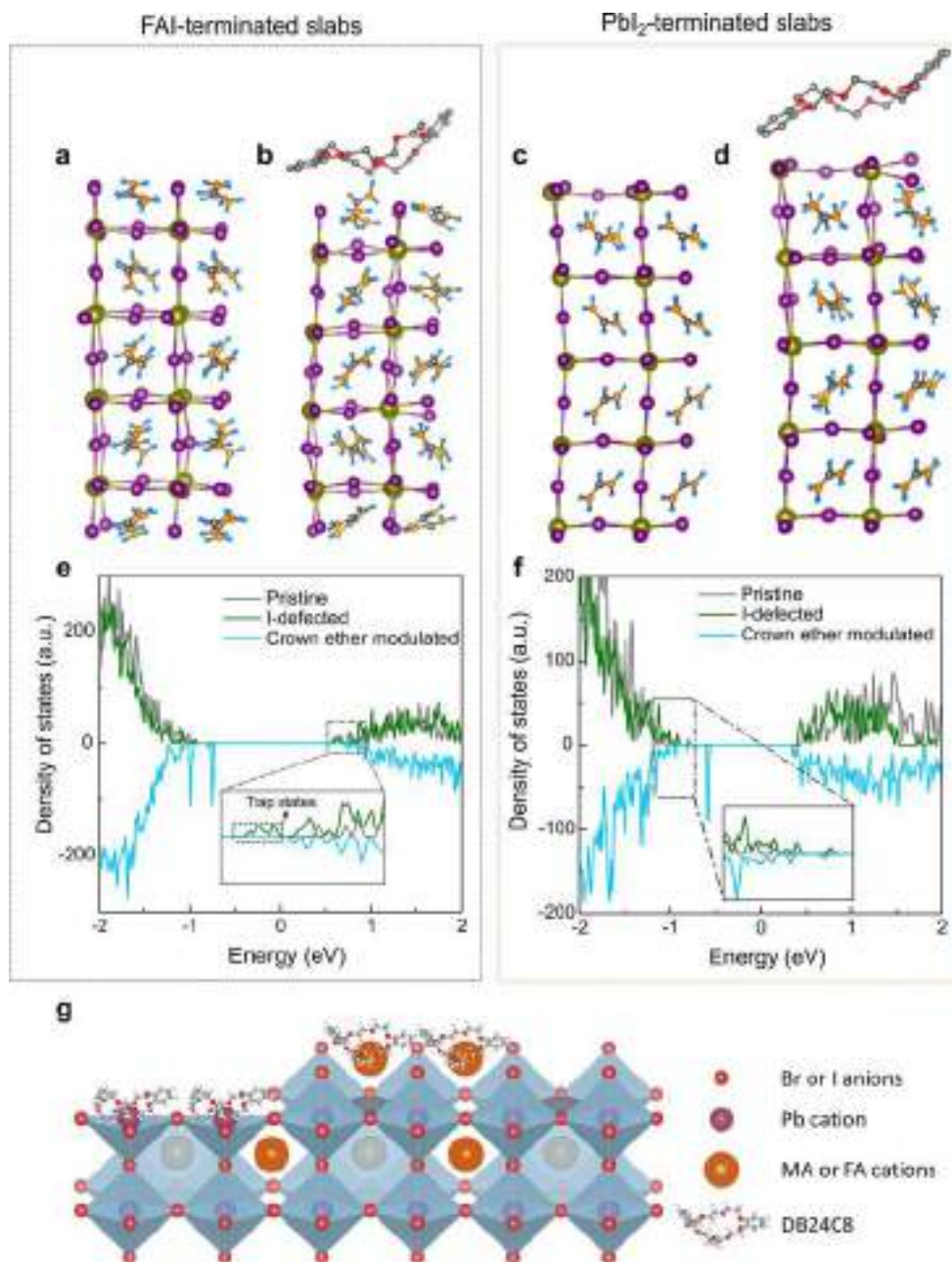


**Figure 3.** DFT calculations. FAI-terminated slabs of FAPbI<sub>3</sub> containing an iodide vacancy without (a) and with (b) crown ether-treatment, where H atoms of the crown are omitted for clarity. The purple, green, orange, red, gray, and blue spheres indicate I, Pb, N, O, C, and H, respectively. PbI<sub>2</sub>-terminated slabs of FAPbI<sub>3</sub> containing an iodide vacancy without (c) and with (d) crown ether-treatment. Density of states of the FAI-terminated (e) and PbI<sub>2</sub>-terminated (f) slabs of pristine FAPbI<sub>3</sub>, FAPbI<sub>3</sub> containing an iodide vacancy, and crown-ether-modulated FAPbI<sub>3</sub> with an iodide vacancy. For readability purposes, the density of states has been mirrored for the modulated systems. (g) Schematic illustration of possible crown ether modulation mechanism and potential interaction sites.

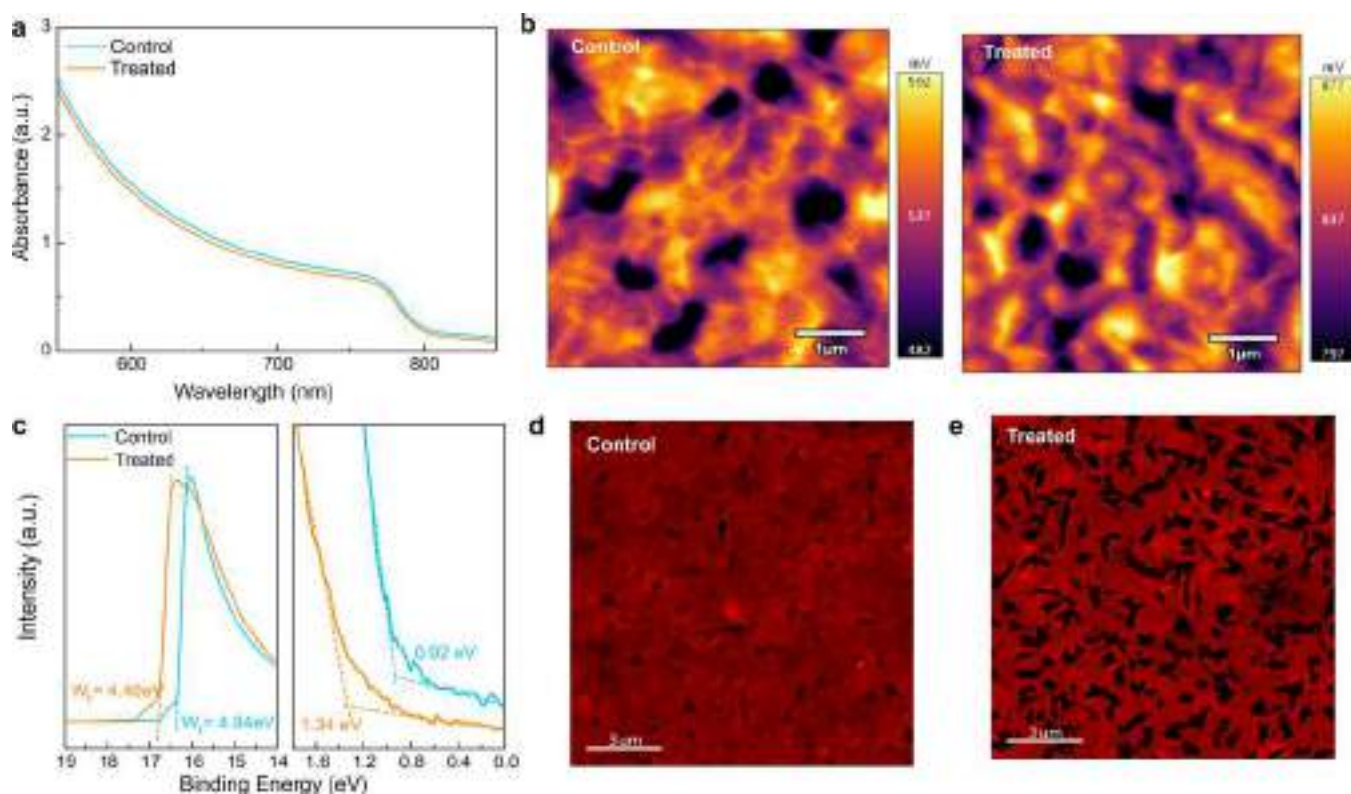


**Figure 4.** Effects of crown ether treatment on optical and electrical properties of perovskite films. (a) UV-vis spectra, (b) Kelvin probe force microscopy (KPFM) images, and (c) ultraviolet photoelectron spectroscopy (UPS) spectra of secondary electron cutoff and valence band (VB) regions, for the control and treated perovskite films. Cathodoluminescence (CL) mapping of the control (d) and treated (e) perovskite films deposited on the FTO (1.1 mm) glass substrates. The spatial distribution of band edge emission intensity was normalized for both samples to the highest intensity in the treated sample, recorded from 800 to 850 nm. The nonemissive dark spots in the treated sample are likely to arise from the crown ether complex.

(DB24C8), for both FAI-terminated (Figure 3a,b) and  $\text{PbI}_2$ -terminated (Figure 3c,d) slabs of  $\text{FAPbI}_3$ . The iodide vacancy defect was selected to study the effect of crown ether modulation, due to its lower formation energy compared to, e.g., Pb vacancies and Pb–I antisite defects.<sup>31</sup> Comparing the FAI-terminated pristine and iodide defected  $\text{FAPbI}_3$  slabs (as observed in Figures 3 and S9), the iodide vacancy introduces localized shallow states at the conduction band minimum of the perovskite. Upon crown-ether treatment of  $\text{FAPbI}_3$ , two sharp peaks belonging to the crown ether molecules at the surface of  $\text{FAPbI}_3$  are predicted close to the valence band edge of the perovskite. This suggests the possibility of the crown ether acting as a barrier for the hole transport. It is however worth noting that the absolute positioning of the energy levels of the crown ether molecule is largely dependent on the electrostatic potential at the surface of the perovskite and the dipole moment imposed by the configuration of the crown ether molecule. Comparing the untreated and treated  $\text{FAPbI}_3$  (as highlighted in the inset of Figure 3e), a shift in the conduction band minimum takes place upon treatment with crown ether. This shift implies the presence of shallower trap states compared to the case of the untreated slab, which is beneficial for obtaining a higher  $V_{\text{OC}}$ . In addition, hydrogen bonding between the H atom of the  $\text{FA}^+$  and the crown ether molecule is observed, which is also reflected in the high binding energy between the  $\text{FAPbI}_3$  slab and the crown of  $-3.03$  eV. In the case of the  $\text{PbI}_2$ -terminated  $\text{FAPbI}_3$  slab, low-density shallow states are now observed in the valence band, instead of the conduction band, upon creating the iodide vacancy (as shown in Figures 3f and S9). Contrary to the FAI-terminated case, a rather insignificant shift in the valence band

maximum takes place upon modulating the surface with the crown ether. Additionally, unlike the FAI-terminated case, a relatively weak crown-slab binding is observed ( $-0.65$  eV); the lower binding energy suggests that the crown ether may preferentially bond to undercoordinated  $\text{FA}^+$  cations at the FAI-terminated perovskite surface, rather than  $\text{Pb}^{2+}$ . Furthermore, crown ether modulation effects on the Pb–I antisite (Pb occupying an I site; Figure S10) were studied where a significant effect on the deep trap states was observed.

In summary, on the basis of the NMR and DFT calculation studies, we propose that the crown ether modulation is via coordinating metal and organic cation interaction sites (illustrated in Figure 3g). The crown ether effectively passivate the uncoordinated  $\text{Pb}^{2+}$  defects and interact with  $\text{FA}^+$  on the perovskite film to modulate its surface properties.

**Optical and Electronic Properties.** We further investigated the optical and electronic properties of perovskite film with and without crown ether modulation. The ultraviolet-visible (UV-vis) absorption spectra (Figure 4a) show that the crown ether treatment did not change the optical properties (i.e., optical band gap) of the perovskite films. Kelvin probe force microscopy (KPFM) of the crown-ether-treated perovskite film (Figure 4b) revealed a higher (+300 mV) and more homogeneous surface potential than that of the untreated film, which indicates fewer grain boundaries upon crown ether treatment (the corresponding atomic force microscopy (AFM) images are presented in Figure S11). Ultraviolet photoelectron spectroscopy (UPS) also shows that the band structure of the perovskite surface has changed upon crown ether treatment (Figure 4c), since the work function decreases by 0.44 eV from



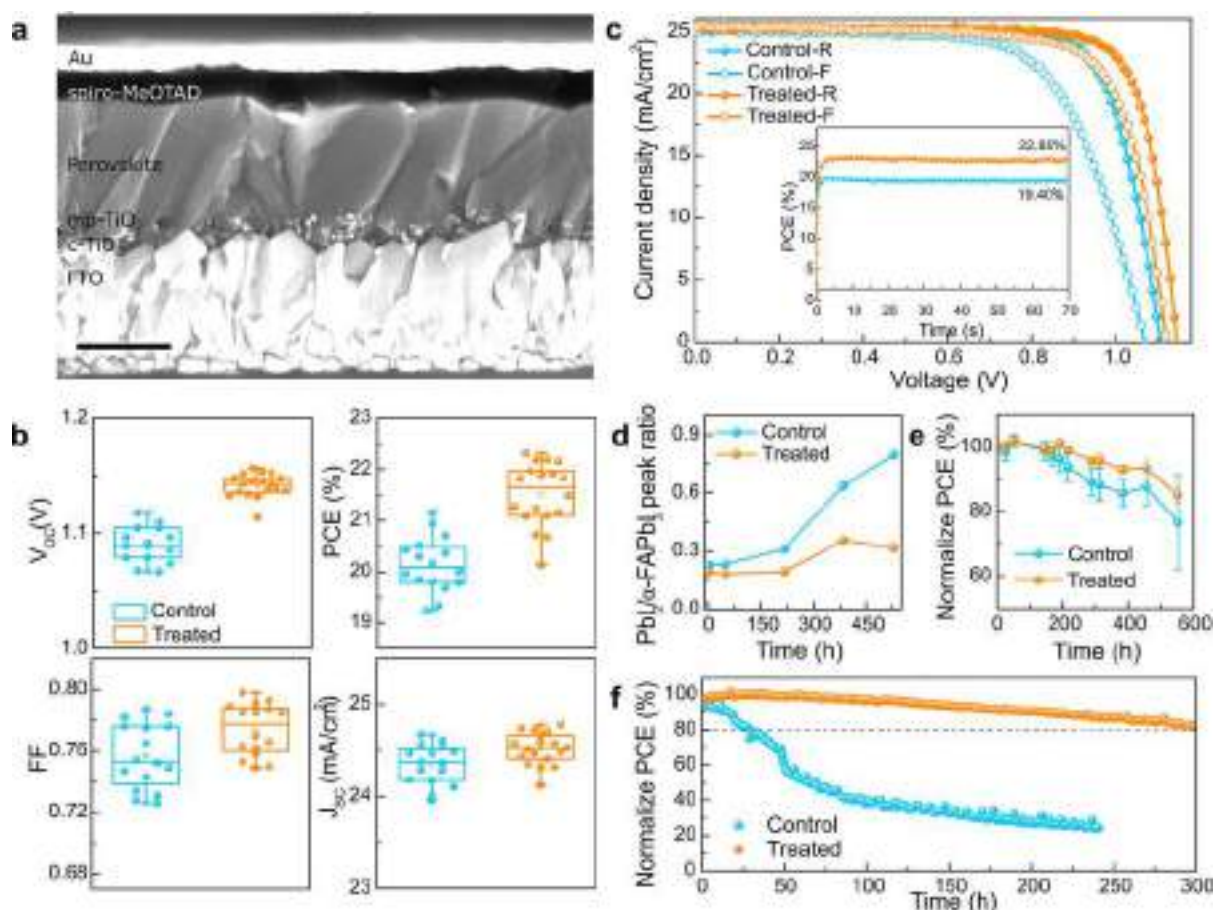


**Figure 5.** Device performance and stability. (a) Cross-sectional SEM image of a typical crown-ether-treated PSC. The scale bar is 500 nm. (b) Photovoltaic metrics with and without treatment. (c)  $J$ - $V$  curves of the champion PSC devices with and without treatment (antireflection film was used). The inset shows the maximum power point tracking data. (d) Plots of the ratio of the  $\text{PbI}_2$   $2\theta = 12.69^\circ$  and  $\alpha$ -FAPbI<sub>3</sub> perovskite  $2\theta = 13.97^\circ$  XRD peaks for perovskite films stored in an ambient environment as a function of time. (e) Ambient stability of PSCs based on the evolution of the average PCE change. The temperature and humidity were  $25 \pm 1^\circ\text{C}$  and  $60 \pm 10\%$ , respectively. (f) Operational stability measured by maximum power point tracking under full solar illumination (AM 1.5 G,  $100\text{ mW}/\text{cm}^2$  in  $\text{N}_2$ ,  $25^\circ\text{C}$ ). F = Forward scan; R = reverse scan.

**Table 2. Summary of the Photovoltaic Parameters for the Best Control and Crown-Ether-Modulated PSCs**

cell	scan direction	$V_{\text{OC}}$ (V)	$J_{\text{SC}}$ ( $\text{mA}/\text{cm}^2$ )	FF	PCE (%)	stabilized PCE (%)	hysteresis index (HI)
control	reverse	1.089	25.50	0.773	21.50	19.40	0.165
	forward	1.069	25.51	0.672	18.33		
crown-ether-treated	reverse	1.154	25.80	0.795	23.70	22.85	0.05
	forward	1.122	25.73	0.753	21.74		

4.84 to 4.40 eV (Figure 4c; left), as schematically represented in the energy-level scheme for the perovskite film with and without passivation (Figure S12). These changes in the band structure of the perovskite surface are in good agreement with the shift of the surface potential probed by KPFM and DFT calculation results (Figure 3e,f).

The lower concentration of defects at the film surface or grain boundary has been reported to reduce the trap state density and charge carrier recombination.<sup>32</sup> This was evaluated via CL mapping of the perovskite deposited on thin (1.1 mm) FTO-coated glass substrates. Before CL characterization, the perovskite films were kept inside a vacuum chamber for a few hours in the dark, to avoid unintended light-induced degradation, and the CL mappings were recorded from regions of the sample that were previously unexposed, except when specifically indicated. The CL intensity for both samples was normalized to the peak value in the treated sample. The treated

perovskite film showed brighter luminescence (higher CL intensity) than that of the control film (Figure 4d,e), which indicates that charge carrier recombination was suppressed via crown ether modulation.<sup>33</sup> The steady-state absolute intensity photoluminescence experiments presented below further confirmed and quantified the suppression of surface defects that enhance nonradiative charge carrier recombination by the crown ether treatment.

**Photovoltaic Performance and Stability.** A cross-sectional SEM image of the employed PSC structure based on fluorine-doped tin oxide (FTO)/compact-TiO<sub>2</sub> (c-TiO<sub>2</sub>)/mesoporous TiO<sub>2</sub> (mp-TiO<sub>2</sub>)/perovskite/2,2',7,7'-tetrakis-[*N,N*-di(4-methoxyphenyl)amino]-9,9'-spirobifluorene (spiro-OMeTAD)/Au (depicted in Figure 5a) shows the thicknesses of the perovskite absorbers is about 700 nm, which is typical for conventional PSCs. It is hard to observe the DB24C8 layer on the cross-sectional SEM image as it is very thin. The

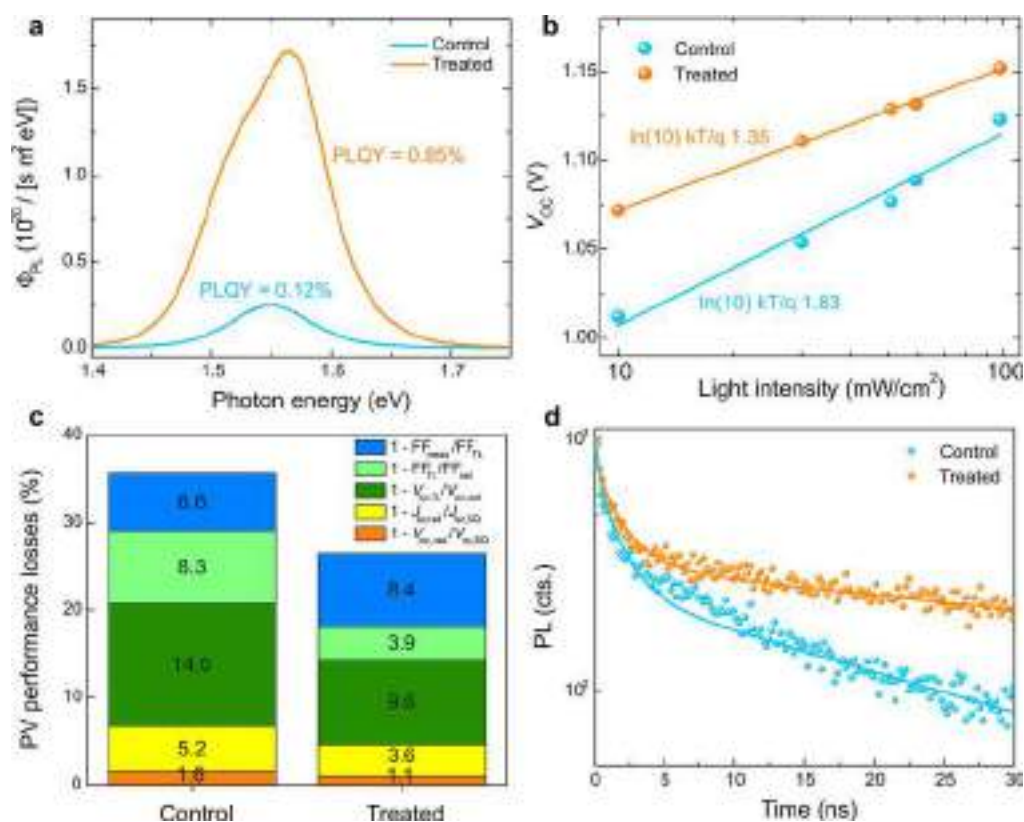


**Figure 6.** Optoelectronic characterization. (a) Absolute photon flux  $\Phi_{\text{PL}}(E)$  measurements of complete devices at 1 sun excitation from which the PLQY is determined. (b) Light intensity dependence of  $V_{\text{OC}}$ . The ideality factor  $n_{\text{id}}$  is calculated from the slope of the linear fit of the semilogarithmic plot. (c) Photovoltaic performance losses due to nonideal absorption (yellow), nonradiative recombination (dark and light green) and charge transport (blue). (d) TRPL measurements of control and treated samples. The layer architecture is FTO glass/c-TiO<sub>2</sub>/mp-TiO<sub>2</sub>/perovskite/spiro-MeOTAD. The solid lines are fit curves according to the model described in the main text. For the latter, an absorption coefficient of  $1 \times 10^5 \text{ cm}^{-1}$  at the laser excitation wavelength (510 nm) and an effective perovskite thickness of 640 nm ( $L_{\text{dense-film}} + 0.5L_{\text{mesoporous-film}}$ ) were used.

concentration of DB24C8 treatment solution was optimized with respect to the photovoltaic performance (see details in Figure S13 and Table S3). The photovoltaic metrics of the PSCs fabricated with optimized DB24C8 treatment and control PSCs (Figure 5b) shows the average PCE values of the PSCs improved from  $20.14 \pm 0.55\%$  (control) to  $21.51 \pm 0.61\%$  for optimized DB24C8 treatment, mainly due to an increase in  $V_{\text{OC}}$  from  $1.090 \pm 0.014 \text{ V}$  to  $1.142 \pm 0.009 \text{ V}$ , while exhibiting slightly higher short-circuit current density ( $J_{\text{SC}}$ ) and fill factor (FF) values. The current density–voltage ( $J$ – $V$ ) curves of champion devices (the front glass was coated with an antireflection film) with and without DB24C8 treatment are shown (Figure 5c), along with the summary of the photovoltaic parameters (Table 2). The control device measured with a reverse scan shows a typical PCE of 21.50% with a  $J_{\text{SC}}$  of  $25.50 \text{ mA cm}^{-2}$ , a  $V_{\text{OC}}$  of 1.089 V, and a FF of 0.773. The treated device exhibited a  $V_{\text{OC}}$  of 1.154 V, a  $J_{\text{SC}}$  of  $25.80 \text{ mA cm}^{-2}$ , a FF of 0.795, and a PCE of 23.70%. The integrated current density derived from the external quantum efficiency (EQE; Figure S14) matches the  $J_{\text{SC}}$  value obtained from the  $J$ – $V$  curve, excluding any significant spectral mismatch between our simulator and the AM1.5G solar source. We further ascertained these values by recording maximum power point tracking tests (Figure 5c, insert) corresponding to PCEs of 19.40% and 22.85% for the control and DB24C8 treated PSCs, respectively. In addition, we quantified the hysteresis effect for different devices by using a modified hysteresis index (HI) given by eq 1:<sup>34</sup>

$$\text{HI} = \frac{J_{\text{R}}(0.8V_{\text{OC}}) - J_{\text{F}}(0.8V_{\text{OC}})}{J_{\text{R}}(0.8V_{\text{OC}})} \quad (1)$$

where  $J_{\text{R}}(0.8V_{\text{OC}})$  and  $J_{\text{F}}(0.8V_{\text{OC}})$  represent the photocurrent density at 80% of the  $V_{\text{OC}}$  for the reverse scan (from open circuit to short circuit) and forward scan (from short circuit to open circuit), respectively. The calculated HI of the DB24C8 treated device (0.05) is much smaller than that of the control device (0.165; Figure 5c and Table 2), which indicates that DB24C8 treatment greatly reduces the hysteresis. The suppression of hysteresis caused by DB24C8 treatment may be attributed to the decrease in the level of electronic surface defects at the perovskite/hole conductor interface,<sup>8</sup> and it may be further reduced by addressing other interfaces present in our PSCs, in particular the contact between the perovskite and the electron conductor.

In addition to the photovoltaic performance, we examined the stability of perovskite films and relevant devices. The composition change of pristine and DB24C8 treated perovskite films was investigated by XRD (Figures 5d and S15). The much slower decomposition of FAPbI<sub>3</sub> to PbI<sub>2</sub> in the DB24C8 treated perovskite films further demonstrates the superior moisture resistance enabled by the crown ether modulation (Figure S16). Furthermore, the shelf-life time measurement for the DB24C8-treated devices shows slower average PCE drop than that of control devices after 23 days kept in the ambient conditions (Figure 5e). The long-term operational stability of the PSCs was also probed by maximum power point (MPP) tracking on

unencapsulated devices under constant simulated AM1.5 illumination ( $100 \text{ mW cm}^{-2}$ ). The DB24C8-treated devices maintain over 80% of their initial PCE after 300 h continuous tests, whereas the control devices degraded to 50% of their initial PCE after 50 h (Figure 5f). The enhanced ambient and operational stability can be attributed to the enhanced hydrophobicity and the decreased surface defect density in the perovskite absorber through crown ether treatment.

**Device Physics and the Origin of the Performance Improvement.** The crown ether treatment is expected to have an impact on the quasi-Fermi level splitting ( $\Delta E_F$ ) which represents the upper limit for the  $V_{OC}$ . We investigated this by measuring steady-state absolute photoluminescence (PL) photon fluxes  $\Phi_{PL}(E)$  of complete devices in an integrating sphere setup (Figure 6a). From this, we could determine the photoluminescence quantum yield (PLQY), which was 0.12% for the control and 0.85% for the treated device. From the PLQY one can determine  $\Delta E_F$  and the radiative limit of  $V_{OC}$  ( $V_{OC,rad}$ ) as explained in detail in the Supporting Information. The results of the  $V_{OC,rad}$  calculation (Table 3 and Figure S17) are similar for

**Table 3. Summary of the Optoelectronic Parameters for the Control and Crown-Ether-Treated Device**

	control	treated
$V_{OC,rad}$ (V)	1.266	1.277
PLQY (%)	0.12	0.85
$\Delta E_F$ (eV)	1.093	1.155
measured $V_{OC}$ (V)	1.089	1.154

the control and the treated films, the small difference being attributed to the statistical compositional batch-to-batch fluctuations. The comparison of the calculated  $\Delta E_F$  with the measured  $V_{OC}$  of the same device (Table 3) also shows that the two values are in excellent agreement, which confirms that the  $V_{OC}$  improvement originates mainly from a  $\Delta E_F$  increase and thus from a reduction in nonradiative recombination.

The origin of the performance improvement is further analyzed in terms of the devices' diode characteristics. First, we evaluated the ideality factor ( $n_{id}$ ) by measuring the dependence of  $V_{OC}$  on the incident light intensity (Figure 6b). Upon crown ether treatment, the  $n_{id}$  decreases from 1.83 to 1.35, indicative of suppressed nonradiative recombination channels.<sup>35</sup> Accordingly, we fit the  $J$ - $V$  curves of the champion control and treated devices to a single-diode equivalent circuit model<sup>36</sup> (Figure S18a,b and Table S4). Following the analysis proposed by Guillemoles et al.<sup>37</sup> and Stolterfoht et al.,<sup>38</sup> the main loss mechanisms can be analyzed (Figure 6c). First, the Shockley–Queisser limit is calculated from the band gap which we determined from the inflection point of the EQE spectrum, as recommended by Krückemeier et al.<sup>39</sup> (Figure S18c,d). For the control device, we obtain a band gap of 1.559 eV and for the treated device, 1.564 eV, which are similar as expected. In the next step, the radiative limit  $J$ - $V$  curve is calculated using  $V_{OC,rad}$  and the measured  $J_{sc}$  of the champion cells, again assuming an ideal diode behavior ( $n = 1$ , with series and shunt resistances of  $R_s = 0$  and  $R_{sh} = \infty$ , respectively). The performance losses related to the radiative limit with respect to the Shockley–Queisser limit account for 1.6% ( $V_{OC}$  loss) + 5.2% ( $J_{sc}$  loss) = 6.8% for the control and 1.1% ( $V_{OC}$  loss) + 3.6% ( $J_{sc}$  loss) = 4.7% for the treated film, mainly stemming from  $J_{sc}$  losses due to nonideal absorption. The contribution of nonradiative recombination in the bulk, at grain boundaries, and at the interfaces is

further evaluated by calculating a  $J$ - $V$  curve using the measured  $J_{sc}$ ,  $V_{OC}$ , and ideality factor while maintaining ideal resistances. Since this  $J$ - $V$  curve does not take into account any losses stemming from nonideal charge transport, it is called the transport limit. Note that this transport limit is similar to the pseudo- $J$ - $V$  curve obtained from the  $J_{sc}$ - $V_{OC}$  method introduced by Wolf and Rauschenbach<sup>40</sup> to evaluate the series resistance of solar cells. In agreement with the previous findings, a significant improvement in nonradiative losses is observed, decreasing from 14.0% ( $V_{OC}$  loss) + 8.3% (FF loss) = 22.3% in the control device to 9.6% ( $V_{OC}$  loss) + 3.9% (FF loss) = 13.5% in the treated device. This shows that solar cell performance losses by nonradiative recombination are reduced by 40%, confirming the role of the reduction of nonradiative recombination as the main driver for performance improvement in our study. Thereafter, the losses due to charge transport characterized by nonideal series and shunt resistances and a further increased ideality factor are obtained from the measured  $J$ - $V$  curve. Transport losses manifest themselves in a further reduction of FF. The transport-related FF losses of the control and treated samples are 6.6% and 8.4%, respectively. Interestingly, the crown ether treatment did slightly impair charge transport which suggests that the DB24C8 complex creates a charge transport (hole transfer) barrier between the perovskite and the HTL.

This loss in transport can also be seen in time-resolved PL (TRPL) measurements on treated and untreated perovskite films with HTL (as shown in Figure 6d). To simulate this data, we used a model which we explain in detail in the Supporting Information. Two regimes can be distinguished: a fast decay within the first 5 ns followed by a significantly slower monoexponential decay. From the simulations, we find that the fast decay is dominated by carrier diffusion which leads to a fast equilibration of the initially narrow exponential carrier concentration profile. The slower decay is mainly due to hole injection into the HTL. We also find that  $k_1$ , with an upper limit of  $10^6 \text{ s}^{-1}$  as determined from TRPL measurements without HTL (Figure S19),<sup>39</sup> has a negligible effect on the TRPL traces of the samples with the interface perovskite/HTL. For the best fits, we obtained a carrier mobility of  $\mu = \frac{q}{kT} D = 4 \text{ cm}^2/(\text{V s})$ , which is in good agreement with literature,<sup>32,41</sup> and a hole transfer velocity for the control and treated samples of  $S_{control} = 1500 \text{ cm/s}$  and  $S_{treated} = 400 \text{ cm/s}$ , respectively. The more than three times lower hole transfer velocity of the treated film indicates an impaired charge transport through the perovskite/HTL interface which is in good agreement with the observed FF losses discussed above. Note that the FF losses referred to here are with respect to the respective transport limits. Overall, due to the improvement in nonradiative recombination losses, the FF of the treated device is higher than that of the control device.

## CONCLUSION

In summary, we employ crown ethers to modulate perovskite films, affording passivation of undercoordinated surface metal or organic cation defects. This interaction has been elucidated by solid-state NMR, ATR-FTIR, XPS, as well as DFT calculations. The crown ether surface modulation reduces the trap state density at the absorber/hole transporting material interface, thus greatly suppressing solar cell performance losses due to nonradiative recombination by 40%, as quantitatively determined by a concerted evaluation of PL, PLQY, and device performance measurements. As a result, the crown-ether-

modulated PSCs exhibit improved operational stability and power conversion efficiency exceeding 23%. Despite this performance improvement, the crown ether treatment creates a small charge transport barrier between the perovskite and the HTL, as analyzed by TRPL measurements, which leaves room for further performance advancements of this interface through improved material design. Consequently, this work opens a new path to enhance the performance and stability of perovskite-based optoelectronic devices.

## ■ ASSOCIATED CONTENT

### Supporting Information

The Supporting Information is available free of charge at <https://pubs.acs.org/doi/10.1021/jacs.0c08592>.

Experimental section, optimization of crown ether structure, powder XRD patterns, solid-state NMR data, DFT calculations, AFM images, device energy band diagram, optimization of crown ether concentrations, IPCE spectra, stability of perovskite films, and device physics data (PDF)

## ■ AUTHOR INFORMATION

### Corresponding Authors

**Hong Zhang** – Laboratory of Photonics and Interfaces, École Polytechnique Fédérale de Lausanne, Lausanne 1015, Switzerland; [orcid.org/0000-0002-5321-0680](https://orcid.org/0000-0002-5321-0680); Email: [hong.zhang@epfl.ch](mailto:hong.zhang@epfl.ch)

**Michael Grätzel** – Laboratory of Photonics and Interfaces, École Polytechnique Fédérale de Lausanne, Lausanne 1015, Switzerland; [orcid.org/0000-0002-0068-0195](https://orcid.org/0000-0002-0068-0195); Email: [michael.gratzel@epfl.ch](mailto:michael.gratzel@epfl.ch)

### Authors

**Tzu-Sen Su** – Laboratory of Photonics and Interfaces, École Polytechnique Fédérale de Lausanne, Lausanne 1015, Switzerland; Department of Chemical Engineering, National Tsing Hua University, Hsinchu 300, Taiwan

**Felix Thomas Eickemeyer** – Laboratory of Photonics and Interfaces and Laboratory of Photomolecular Science, Institute of Chemical Sciences and Engineering, École Polytechnique Fédérale de Lausanne, Lausanne 1015, Switzerland; [orcid.org/0000-0003-0855-9944](https://orcid.org/0000-0003-0855-9944)

**Michael A. Hope** – Laboratory of Magnetic Resonance, Institute of Chemical Sciences and Engineering, École Polytechnique Fédérale de Lausanne, Lausanne 1015, Switzerland; [orcid.org/0000-0002-4742-9336](https://orcid.org/0000-0002-4742-9336)

**Farzaneh Jahanbakhshi** – Laboratory of Computational Chemistry and Biochemistry, École Polytechnique Fédérale de Lausanne, Lausanne 1015, Switzerland; [orcid.org/0000-0001-7113-2746](https://orcid.org/0000-0001-7113-2746)

**Marko Mladenović** – Laboratory of Computational Chemistry and Biochemistry, École Polytechnique Fédérale de Lausanne, Lausanne 1015, Switzerland

**Jun Li** – Laboratory of Photonics and Interfaces, École Polytechnique Fédérale de Lausanne, Lausanne 1015, Switzerland

**Zhiwen Zhou** – Laboratory of Photonics and Interfaces, École Polytechnique Fédérale de Lausanne, Lausanne 1015, Switzerland

**Aditya Mishra** – Laboratory of Magnetic Resonance, Institute of Chemical Sciences and Engineering, École Polytechnique Fédérale de Lausanne, Lausanne 1015, Switzerland

**Jun-Ho Yum** – Laboratory of Molecular Engineering of Optoelectronic Nanomaterials, Institute of Chemical Sciences and Engineering, École Polytechnique Fédérale de Lausanne (EPFL), Lausanne 1015, Switzerland; [orcid.org/0000-0001-8386-2922](https://orcid.org/0000-0001-8386-2922)

**Dan Ren** – Laboratory of Photonics and Interfaces, École Polytechnique Fédérale de Lausanne, Lausanne 1015, Switzerland; [orcid.org/0000-0003-3738-6421](https://orcid.org/0000-0003-3738-6421)

**Anurag Krishna** – Laboratory of Photomolecular Science, Institute of Chemical Sciences and Engineering, École Polytechnique Fédérale de Lausanne, Lausanne 1015, Switzerland

**Olivier Ouellette** – Laboratory of Photonics and Interfaces, École Polytechnique Fédérale de Lausanne, Lausanne 1015, Switzerland

**Tzu-Chien Wei** – Department of Chemical Engineering, National Tsing Hua University, Hsinchu 300, Taiwan; [orcid.org/0000-0002-9608-8275](https://orcid.org/0000-0002-9608-8275)

**Hua Zhou** – Advanced Photon Source, Argonne National Laboratory, Lemont, Illinois 60439, United States; [orcid.org/0000-0001-9642-8674](https://orcid.org/0000-0001-9642-8674)

**Hsin-Hsiang Huang** – Materials Science Division and Center for Molecular Engineering, Argonne National Laboratory, Lemont, Illinois 60439, United States

**Mounir Driss Mensi** – Institute of Chemical Sciences and Engineering, École Polytechnique Fédérale de Lausanne, CH-1951 Sion, Switzerland

**Kevin Sivula** – Laboratory of Molecular Engineering of Optoelectronic Nanomaterials, Institute of Chemical Sciences and Engineering, École Polytechnique Fédérale de Lausanne (EPFL), Lausanne 1015, Switzerland; [orcid.org/0000-0002-8458-0270](https://orcid.org/0000-0002-8458-0270)

**Shaik M. Zakeeruddin** – Laboratory of Photonics and Interfaces, École Polytechnique Fédérale de Lausanne, Lausanne 1015, Switzerland

**Jovana V. Milić** – Laboratory of Photonics and Interfaces, École Polytechnique Fédérale de Lausanne, Lausanne 1015, Switzerland; [orcid.org/0000-0002-9965-3460](https://orcid.org/0000-0002-9965-3460)

**Anders Hagfeldt** – Laboratory of Photomolecular Science, Institute of Chemical Sciences and Engineering, École Polytechnique Fédérale de Lausanne, Lausanne 1015, Switzerland; [orcid.org/0000-0001-6725-8856](https://orcid.org/0000-0001-6725-8856)

**Ursula Rothlisberger** – Laboratory of Computational Chemistry and Biochemistry, École Polytechnique Fédérale de Lausanne, Lausanne 1015, Switzerland; [orcid.org/0000-0002-1704-8591](https://orcid.org/0000-0002-1704-8591)

**Lyndon Emsley** – Laboratory of Magnetic Resonance, Institute of Chemical Sciences and Engineering, École Polytechnique Fédérale de Lausanne, Lausanne 1015, Switzerland; [orcid.org/0000-0003-1360-2572](https://orcid.org/0000-0003-1360-2572)

Complete contact information is available at: <https://pubs.acs.org/doi/10.1021/jacs.0c08592>

### Author Contributions

<sup>†</sup>T.-S.S., F.T.E., M.A.H., and F.J. contributed equally.

### Notes

The authors declare no competing financial interest. M.M. is also affiliated with the Scientific Computing Laboratory, Center for the Study of Complex Systems, Institute of Physics Belgrade, University of Belgrade, Pregrevica 118, 11080 Belgrade, Serbia. H.-H.H. is also affiliated with the Center for Condensed Matter Sciences, Department of Materials Science

and Engineering, National Taiwan University, Taipei 10617, Taiwan. J.V.M. is also affiliated with the Adolphe Merkle Institute of the University of Fribourg, Switzerland.

## ACKNOWLEDGMENTS

This project has received funding from the European Union's Horizon 2020 research and innovation program GRAPHENE Flagship Core 3 Grant Agreement No. 881603 as well as Espresso under Agreement No. 764047. U.R. acknowledges SNSF Grant No. 200020-185092, NCCR-MUST, and the SINERGIA interdisciplinary research program EPISODE for funding. This research used resources of the Advanced Photon Source, a U.S. Department of Energy (DOE) Office of Science User Facility operated for the DOE Office of Science by Argonne National Laboratory under Contract No. DE-AC02-06CH11357. L.E. is grateful for financial support from Swiss National Science Foundation Grant No. 200020-178860. O.O. acknowledges funding from the Natural Sciences and Engineering Research Council of Canada. T.-S.S. acknowledges funding from the Ministry of Science and Technology, Taiwan (MOST 108-2917-I-564-038 and 108-2221-E-007-102-MY3). J.L. and A.K. acknowledge funding from the European Union's Horizon 2020 Research and Innovation program under the Marie Skłodowska-Curie Grant Agreement No. 838686 and No. 843453, respectively. A.H. acknowledges the financial support from the Swiss National Science Foundation R'Equip program under Grant Number 183305. H.-H.H. acknowledges the financial support from 2019 New Partnership Program (108-2911-I-002-561). J.V.M. acknowledges support from the SNSF Grant No. 193174. D.R. acknowledges the financial support from Swiss Nationals Science Foundation (IZLZC2-170294) and Gebert RUF Stiftung under Microbials scheme 'Solar-Bio Fuels' (GRS-080/19). The authors acknowledge the help of Nicolas Tappy for the CL measurement.

## REFERENCES

- (1) Quan, L. N.; Yuan, M.; Comin, R.; Voznyy, O.; Beaugerard, E. M.; Hoogland, S.; Buin, A.; Kirmani, A. R.; Zhao, K.; Amassian, A.; Kim, D. H.; Sargent, E. H. Ligand-Stabilized Reduced-Dimensionality Perovskites. *J. Am. Chem. Soc.* **2016**, *138*, 2649–2655.
- (2) Lin, J.; Lai, M.; Dou, L.; Kley, C. S.; Chen, H.; Peng, F.; Sun, J.; Lu, D.; Hawks, S. A.; Xie, C.; Cui, F.; Alivisatos, A. P.; Limmer, D. T.; Yang, P. Thermochromic Halide Perovskite Solar Cells. *Nat. Mater.* **2018**, *17*, 261–267.
- (3) Ogomi, Y.; Morita, A.; Tsukamoto, S.; Saitho, T.; Fujikawa, N.; Shen, Q.; Toyoda, T.; Yoshino, K.; Pandey, S. S.; Ma, T.; Hayase, S.  $\text{CH}_3\text{NH}_3\text{Sn}_x\text{Pb}_{(1-x)}\text{I}_3$  Perovskite Solar Cells Covering up to 1060 nm. *J. Phys. Chem. Lett.* **2014**, *5*, 1004–1011.
- (4) Wang, F.; Bai, S.; Tress, W.; Hagfeldt, A.; Gao, F. Defects Engineering for High-Performance Perovskite Solar Cells. *npj Flexible Electron.* **2018**, *2*, 22.
- (5) Sum, T. C.; Mathews, N. Advancements in Perovskite Solar Cells: Photophysics behind the Photovoltaics. *Energy Environ. Sci.* **2014**, *7*, 2518–2534.
- (6) Li, B.; Zhang, Y.; Fu, L.; Yu, T.; Zhou, S.; Zhang, L.; Yin, L. Surface Passivation Engineering Strategy to Fully-inorganic Cubic  $\text{CsPbI}_3$  Perovskites for High-Performance Solar Cells. *Nat. Commun.* **2018**, *9*, 1076.
- (7) Bi, D.; Li, X.; Milić, J. V.; Kubicki, D. J.; Pellet, N.; Luo, J.; LaGrange, T.; Mettraux, P.; Emsley, L.; Zakeeruddin, S. M.; Grätzel, M. Multifunctional Molecular Modulators for Perovskite Solar Cells with over 20% Efficiency and High Operational Stability. *Nat. Commun.* **2018**, *9*, 4482.
- (8) Azpiroz, J. M.; Mosconi, E.; Bisquert, J.; De Angelis, F. Defect Migration in Methylammonium Lead Iodide and its Role in Perovskite Solar Cell Operation. *Energy Environ. Sci.* **2015**, *8*, 2118–2127.
- (9) Braly, I. L.; deQuilletes, D. W.; Pazos-Outón, L. M.; Burke, S.; Ziffer, M. E.; Ginger, D. S.; Hillhouse, H. W. Hybrid Perovskite Films Approaching the Radiative Limit with over 90% Photoluminescence Quantum Efficiency. *Nat. Photonics* **2018**, *12*, 355–361.
- (10) Noel, N. K.; Abate, A.; Stranks, S. D.; Parrott, E. S.; Burlakov, V. M.; Goriely, A.; Snaith, H. J. Enhanced Photoluminescence and Solar Cell Performance via Lewis Base Passivation of Organic–Inorganic Lead Halide Perovskites. *ACS Nano* **2014**, *8*, 9815–9821.
- (11) Zhang, H.; Nazeeruddin, M. K.; Choy, W. C. H. Perovskite Photovoltaics: The Significant Role of Ligands in Film Formation, Passivation, and Stability. *Adv. Mater.* **2019**, *31*, 1805702.
- (12) Ruiz-Preciado, M. A.; Kubicki, D. J.; Hofstetter, A.; McGovern, L.; Futscher, M. H.; Ummadisingu, A.; Gershoni-Poranne, R.; Zakeeruddin, S. M.; Ehrler, B.; Emsley, L.; Milić, J. V.; Grätzel, M. Supramolecular Modulation of Hybrid Perovskite Solar Cells via Bifunctional Halogen Bonding Revealed by Two-Dimensional  $^{19}\text{F}$  Solid-State NMR Spectroscopy. *J. Am. Chem. Soc.* **2020**, *142*, 1645–1654.
- (13) Qin, C.; Matsushima, T.; Fujihara, T.; Adachi, C. Multifunctional Benzoquinone Additive for Efficient and Stable Planar Perovskite Solar Cells. *Adv. Mater.* **2017**, *29*, 1603808.
- (14) Zhang, F.; Bi, D.; Pellet, N.; Xiao, C.; Li, Z.; Berry, J. J.; Zakeeruddin, S. M.; Zhu, K.; Grätzel, M. Suppressing Defects through the Synergistic Effect of a Lewis Base and a Lewis Acid for Highly Efficient and Stable Perovskite Solar Cells. *Energy Environ. Sci.* **2018**, *11*, 3480–3490.
- (15) Jiang, Q.; Zhao, Y.; Zhang, X.; Yang, X.; Chen, Y.; Chu, Z.; Ye, Q.; Li, X.; Yin, Z.; You, J. Surface Passivation of Perovskite Film for Efficient Solar Cells. *Nat. Photonics* **2019**, *13*, 460–466.
- (16) Fan, L.; Ding, Y.; Luo, J.; Shi, B.; Yao, X.; Wei, C.; Zhang, D.; Wang, G.; Sheng, Y.; Chen, Y.; Hagfeldt, A.; Zhao, Y.; Zhang, X. Elucidating the Role of Chlorine in Perovskite Solar Cells. *J. Mater. Chem. A* **2017**, *5*, 7423–7432.
- (17) Zheng, X.; Chen, B.; Dai, J.; Fang, Y.; Bai, Y.; Lin, Y.; Wei, H.; Zeng, X. C.; Huang, J. Defect Passivation in Hybrid Perovskite Solar Cells using Quaternary Ammonium Halide Anions and Cations. *Nat. Energy* **2017**, *2*, 17102.
- (18) Sha, W. E. I.; Ren, X.; Chen, L.; Choy, W. C. H. The Efficiency Limit of  $\text{CH}_3\text{NH}_3\text{PbI}_3$  Perovskite Solar Cells. *Appl. Phys. Lett.* **2015**, *106*, 221104.
- (19) Steed, J. W. First- and Second-Sphere Coordination Chemistry of Alkali Metal Crown Ether Complexes. *Coord. Chem. Rev.* **2001**, *215*, 171–221.
- (20) Landini, D.; Maia, A.; Montanari, F.; Pirisi, F. M. Crown Ethers as Phase-transfer Catalysts. A Comparison of Anionic Activation in Aqueous–organic Two-phase Systems and in Low Polarity Anhydrous Solutions by Perhydrodibenzo-18-Crown-6, Lipophilic Quaternary Salts, and Cryptands. *J. Chem. Soc., Perkin Trans. 2* **1980**, *2*, 46–51.
- (21) Vendilo, A. G.; Djigailo, D. I.; Smirnova, S. V.; Torocheshnikova, I. I.; Popov, K. I.; Krasovsky, V. G.; Pletnev, I. V. 18-Crown-6 and Dibenzo-18-Crown-6 Assisted Extraction of Cesium from Water into Room Temperature Ionic Liquids and its Correlation with Stability Constants for Cesium Complexes. *Molecules* **2009**, *14*, 5001–5016.
- (22) Chatterjee, T.; Sarma, M.; Das, S. K. Supramolecular Architectures from Ammonium-Crown Ether Inclusion Complexes in Polyoxometalate Association: Synthesis, Structure, and Spectroscopy. *Cryst. Growth Des.* **2010**, *10*, 3149–3163.
- (23) Prochowicz, D.; Sasaki, M.; Yadav, P.; Grätzel, M.; Lewiński, J. Mechanoperovskites for Photovoltaic Applications: Preparation, Characterization, and Device Fabrication. *Acc. Chem. Res.* **2019**, *52*, 3233–3243.
- (24) Chen, Y.; Smock, S. R.; Flintgruber, A. H.; Perras, F. A.; Brutchey, R. L.; Rossini, A. J. Surface Termination of  $\text{CsPbBr}_3$  Perovskite Quantum Dots Determined by Solid-State NMR Spectroscopy. *J. Am. Chem. Soc.* **2020**, *142*, 6117–6127.

- (25) Franssen, W. M. J.; van Es, S. G. D.; Dervişoğlu, R.; de Wijs, G. A.; Kentgens, A. P. M. Symmetry, Dynamics, and Defects in Methylammonium Lead Halide Perovskites. *J. Phys. Chem. Lett.* **2017**, *8*, 61–66.
- (26) Alharbi, E. A.; Alyamani, A. Y.; Kubicki, D. J.; Uhl, A. R.; Walder, B. J.; Alanazi, A. Q.; Luo, J.; Burgos-Caminal, A.; Albadri, A.; Albrithen, H.; Alotaibi, M. H.; Moser, J.-E.; Zakeeruddin, S. M.; Giordano, F.; Emsley, L.; Grätzel, M. Atomic-Level Passivation Mechanism of Ammonium Salts Enabling Highly Efficient Perovskite Solar Cells. *Nat. Commun.* **2019**, *10*, 3008.
- (27) Zhang, J.; Wang, Z.; Mishra, A.; Yu, M.; Shasti, M.; Tress, W.; Kubicki, D. J.; Avalos, C. E.; Lu, H.; Liu, Y.; Carlsen, B. L.; Agarwalla, A.; Wang, Z.; Xiang, W.; Emsley, L.; Zhang, Z.; Grätzel, M.; Guo, W.; Hagfeldt, A. Intermediate Phase Enhances Inorganic Perovskite and Metal Oxide Interface for Efficient Photovoltaics. *Joule* **2020**, *4*, 222–234.
- (28) Kubicki, D. J.; Prochowicz, D.; Hofstetter, A.; Sasaki, M.; Yadav, P.; Bi, D.; Pellet, N.; Lewiński, J.; Zakeeruddin, S. M.; Grätzel, M.; Emsley, L. Formation of Stable Mixed Guanidinium–Methylammonium Phases with Exceptionally Long Carrier Lifetimes for High-Efficiency Lead Iodide-Based Perovskite Photovoltaics. *J. Am. Chem. Soc.* **2018**, *140*, 3345–3351.
- (29) Hanrahan, M. P.; Men, L.; Rosales, B. A.; Vela, J.; Rossini, A. J. Sensitivity-Enhanced  $^{207}\text{Pb}$  Solid-State NMR Spectroscopy for the Rapid, Non-Destructive Characterization of Organolead Halide Perovskites. *Chem. Mater.* **2018**, *30*, 7005–7015.
- (30) Aebli, M.; Piveteau, L.; Nazarenko, O.; Benin, B. M.; Krieg, F.; Verel, R.; Kovalenko, M. V. Lead-Halide Scalar Couplings in  $^{207}\text{Pb}$  NMR of  $\text{APbX}_3$  Perovskites (A = Cs, Methylammonium, Formamidinium; X = Cl, Br, I). *Sci. Rep.* **2020**, *10*, 8229.
- (31) Wang, R.; Xue, J.; Wang, K.-L.; Wang, Z.-K.; Luo, Y.; Fenning, D.; Xu, G.; Nuryyeva, S.; Huang, T.; Zhao, Y.; Yang, J. L.; Zhu, J.; Wang, M.; Tan, S.; Yavuz, I.; Houk, K. N.; Yang, Y. Constructive Molecular Configurations for Surface-Defect Passivation of Perovskite Photovoltaics. *Science* **2019**, *366*, 1509–1513.
- (32) Sherkar, T. S.; Momblona, C.; Gil-Escrig, L.; Ávila, J.; Sessolo, M.; Bolink, H. J.; Koster, L. J. A. Recombination in Perovskite Solar Cells: Significance of Grain Boundaries, Interface Traps, and Defect Ions. *ACS Energy Lett.* **2017**, *2*, 1214–1222.
- (33) Li, W.; Rothmann, M. U.; Liu, A.; Wang, Z.; Zhang, Y.; Pascoe, A. R.; Lu, J.; Jiang, L.; Chen, Y.; Huang, F.; Peng, Y.; Bao, Q.; Etheridge, J.; Bach, U.; Cheng, Y.-B. Phase Segregation Enhanced Ion Movement in Efficient Inorganic  $\text{CsPbI}_2$  Solar Cells. *Adv. Energy Mater.* **2017**, *7*, 1700946.
- (34) Kim, H.-S.; Park, N.-G. Parameters Affecting I–V Hysteresis of  $\text{CH}_3\text{NH}_3\text{PbI}_3$  Perovskite Solar Cells: Effects of Perovskite Crystal Size and Mesoporous  $\text{TiO}_2$  Layer. *J. Phys. Chem. Lett.* **2014**, *5*, 2927–2934.
- (35) Tress, W.; Yavari, M.; Domanski, K.; Yadav, P.; Niesen, B.; Correa Baena, J. P.; Hagfeldt, A.; Graetzel, M. Interpretation and Evolution of Open-Circuit Voltage, Recombination, Ideality Factor and Subgap Defect States during Reversible Light-Soaking and Irreversible Degradation of Perovskite Solar Cells. *Energy Environ. Sci.* **2018**, *11*, 151–165.
- (36) Zhang, C.; Zhang, J.; Hao, Y.; Lin, Z.; Zhu, C. A Simple and Efficient Solar Cell Parameter Extraction Method from a Single Current-voltage Curve. *J. Appl. Phys.* **2011**, *110*, No. 064504.
- (37) Guillemoles, J.-F.; Kirchartz, T.; Cahen, D.; Rau, U. Guide for the Perplexed to the Shockley–Queisser Model for Solar Cells. *Nat. Photonics* **2019**, *13*, 501–505.
- (38) Stolterfoht, M.; Grischek, M.; Caprioglio, P.; Wolff, C. M.; Gutierrez-Partida, E.; Peña-Camargo, F.; Rothhardt, D.; Zhang, S.; Raoufi, M.; Wolansky, J.; Abdi-Jalebi, M.; Stranks, S. D.; Albrecht, S.; Kirchartz, T.; Neher, D. How To Quantify the Efficiency Potential of Neat Perovskite Films: Perovskite Semiconductors with an Implied Efficiency Exceeding 28%. *Adv. Mater.* **2020**, *32*, 2000080.
- (39) Krückemeier, L.; Rau, U.; Stolterfoht, M.; Kirchartz, T. How to Report Record Open-Circuit Voltages in Lead-Halide Perovskite Solar Cells. *Adv. Energy Mater.* **2020**, *10*, 1902573.
- (40) Wolf, M.; Rauschenbach, H. Series Resistance Effects on Solar Cell Measurements. *Adv. Energy Convers.* **1963**, *3*, 455–479.
- (41) Wenger, B.; Nayak, P. K.; Wen, X.; Kesava, S. V.; Noel, N. K.; Snaith, H. J. Consolidation of the Optoelectronic Properties of  $\text{CH}_3\text{NH}_3\text{PbBr}_3$  Perovskite Single Crystals. *Nat. Commun.* **2017**, *8*, 590.

## Nanoscale Phase Segregation in Supramolecular $\pi$ -Templating for Hybrid Perovskite Photovoltaics from NMR Crystallography

Michael A. Hope,<sup>◇</sup> Toru Nakamura,<sup>◇</sup> Paramvir Ahlawat,<sup>◇</sup> Aditya Mishra,<sup>◇</sup> Manuel Cordova, Farzaneh Jahanbakhshi, Marko Mladenović, Rashmi Runjhun, Lena Merten, Alexander Hinderhofer, Brian I. Carlsen, Dominik J. Kubicki, Renana Gershoni-Poranne, Thomas Schneeberger, Loï C. Carbone, Yuhang Liu, Shaik M. Zakeeruddin, Janusz Lewinski, Anders Hagfeldt, Frank Schreiber, Ursula Rothlisberger,\* Michael Grätzel,\* Jovana V. Milić,\* and Lyndon Emsley\*



Cite This: *J. Am. Chem. Soc.* 2021, 143, 1529–1538



Read Online

ACCESS |



Metrics & More

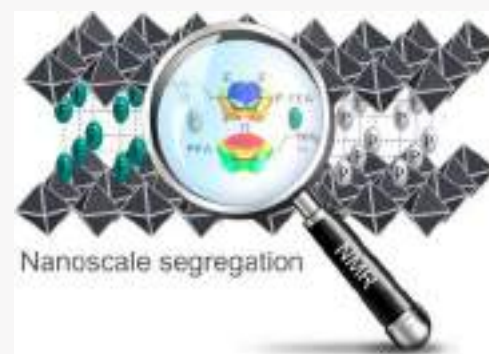


Article Recommendations



Supporting Information

**ABSTRACT:** The use of layered perovskites is an important strategy to improve the stability of hybrid perovskite materials and their optoelectronic devices. However, tailoring their properties requires accurate structure determination at the atomic scale, which is a challenge for conventional diffraction-based techniques. We demonstrate the use of nuclear magnetic resonance (NMR) crystallography in determining the structure of layered hybrid perovskites for a mixed-spacer model composed of 2-phenylethylammonium (PEA<sup>+</sup>) and 2-(perfluorophenyl)ethylammonium (FEA<sup>+</sup>) moieties, revealing nanoscale phase segregation. Moreover, we illustrate the application of this structure in perovskite solar cells with power conversion efficiencies that exceed 21%, accompanied by enhanced operational stability.



### INTRODUCTION

Hybrid perovskite photovoltaics rival other solar cell technologies with their high performance at competitive cost. These systems are based on the AMX<sub>3</sub> composition that defines a corner-sharing crystal structure (such as the cubic lattice shown in Figure 1a) consisting of A cations, mainly Cs<sup>+</sup>, methylammonium (MA<sup>+</sup>, CH<sub>3</sub>NH<sub>3</sub><sup>+</sup>), or formamidinium (FA<sup>+</sup>, CH(NH<sub>2</sub>)<sub>2</sub><sup>+</sup>), as well as their mixtures, along with divalent M cations (such as Pb<sup>2+</sup> and Sn<sup>2+</sup>) and halide anions (I<sup>-</sup>, Br<sup>-</sup>, Cl<sup>-</sup>).<sup>1–3</sup> Their photovoltaic performances and widespread adoption are, however, compromised by limited stability. This can result in degradation due to reactivity with oxygen and water as well as internal ion migration under operating conditions of voltage bias and light irradiation.<sup>1,4,5</sup> One of the emerging strategies to address these instabilities is based on the incorporation of layers of hydrophobic organic cations between the hybrid perovskite slabs to form layered two-dimensional (2D) perovskites. One example of this approach is the Ruddlesden–Popper perovskite phases based on the S<sub>2</sub>A<sub>n-1</sub>M<sub>n</sub>X<sub>3n+1</sub> composition, where S<sup>+</sup> is a spacer cation (Figure 1b).<sup>6–9</sup> These materials have shown greater resilience to degradation, yet their photovoltaic performance is impaired by the poor electronic properties of the spacer layers and by the lack of ordered supramolecular packing, which impedes overall crystallinity.<sup>6,7,10</sup> The interactions between the organic moieties that form the spacer layer directly affect the structure

of the resulting materials and, consequently, their optoelectronic properties.<sup>6,11</sup> While progress has been made in the search for new organic moieties that can form layered perovskites, their assembly can only be controlled by having a thorough understanding of the noncovalent interactions which direct the supramolecular structure, such as hydrogen bonding,<sup>12–15</sup> van der Waals interactions,<sup>9,16</sup> metal coordination,<sup>17</sup> halogen bonding,<sup>18,19</sup> and  $\pi$ -based interactions.<sup>20–23</sup> Furthermore, to unravel these interactions, it is vital to accurately determine the atomic structure. This is a challenge for conventional diffraction techniques, due to polycrystallinity and the presence of heavy atoms.<sup>21</sup>

Solid-state nuclear magnetic resonance (NMR) spectroscopy has previously been used to determine the local structure of hybrid perovskites and their composites with various organic molecules.<sup>24–27</sup> In particular, NMR crystallography, where the structure is determined by comparing the experimental NMR parameters to those calculated for trial structures, is a powerful

Received: November 3, 2020

Published: January 14, 2021



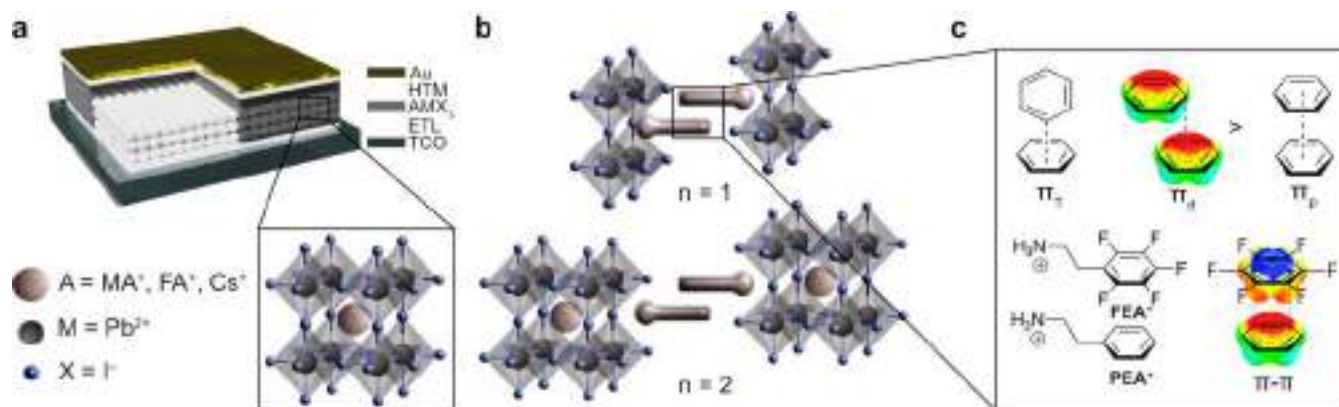


**Figure 1.** Supramolecular material design. (a) Schematic of the perovskite solar cell with the hybrid perovskite absorber material (AMX<sub>3</sub>). HTM = hole transporting material; ETL = electron transporting layer; TCO = transparent conductive oxide. (b) Schematic representation of the structure of Ruddlesden–Popper phases of hybrid 2D perovskites based on the S<sub>2</sub>A<sub>n-1</sub>M<sub>n</sub>X<sub>3n+1</sub> formula ( $n = 1, 2$ , etc.) comprised of an organic spacer (S<sup>+</sup>) bilayer. (c) Top: Overview of possible  $\pi$ – $\pi$  interaction modes between two arenes with comparable electron-density surfaces, with different interaction strengths ( $\pi_T \approx \pi_d > \pi_p$ ). Lower: Arene–fluoroarene  $\pi$ – $\pi$  interaction ( $\pi_p$ ) and the spacer cations used in this study: PEA<sup>+</sup> and FEA<sup>+</sup>. The  $\pi_p$  and  $\pi_d$  interactions of model systems are illustrated by the corresponding ESP maps (also shown in Figure S4 of the SI).

tool for analyzing the organic assemblies and their templating effects in hybrid perovskite materials.<sup>19,28</sup>

One of the most widely employed organic moieties for layered perovskites is 2-phenylethylammonium (PEA<sup>+</sup>; Figure 1c), which interacts with the hybrid perovskite slabs via ion pairing and hydrogen bonding through the ammonium termini (–NH<sub>3</sub><sup>+</sup>).<sup>9,20,21,29</sup> The assembly of the organic layer is directed by weaker van der Waals and  $\pi$ -based interactions between the organic moieties (Figure 1c),<sup>11,20,30</sup> which determine the relative orientation of the aromatic rings according to their quadrupole moments.<sup>31,32</sup> The quadrupole moment of a benzene ring and the corresponding dispersion interactions stabilize two orientations, T-shaped ( $\pi_T$ ) and parallel displaced ( $\pi_d$ ), which are more favorable than the parallel orientation ( $\pi_p$ ; Figure 1c, top).<sup>32</sup> This is due to areas of positive and negative potential of the aromatic core, which can be visualized by the electronic density distribution or electrostatic potential (ESP) maps (Figure 1c and Figure S4, Supporting Information (SI)). Fluoroarenes, such as 2-(perfluorophenyl)ethylammonium (FEA<sup>+</sup>, Figure 1c), feature a reversed quadrupole moment due to the higher electronegativity of fluorine substituents, which favors parallel  $\pi$  interactions ( $\pi_p$ ) in benzene–perfluorobenzene systems (Figure 1c, bottom).<sup>32</sup> Parallel  $\pi$ – $\pi$  stacking of the spacer cations could thus, in principle, be directed by employing alternating arene–fluoroarene moieties.<sup>21,31</sup> In addition, the presence of fluoroarene moieties could further contribute to the hydrophobicity of the material, improving its resilience to moisture, while fluoroarene anion– $\pi$  interactions<sup>33</sup> could reduce halide ion migration, increasing the stability under device operating conditions.<sup>5</sup> Therefore, supramolecular  $\pi$ -assemblies of arenes and fluoroarenes could be used to control the properties of hybrid perovskites and their composites, although they remain underexploited in this context.

Here, we use NMR crystallography in combination with molecular dynamics (MD) simulations, density functional theory (DFT), and X-ray diffraction to elucidate the atomic-level structure of the spacer cations in a model system that consists of PEA<sup>+</sup> and/or FEA<sup>+</sup> spacers (S<sup>+</sup>) in a typical layered 2D perovskite of S<sub>2</sub>PbI<sub>4</sub> ( $n = 1$ ) composition. Contrary to previous reports, we reveal that the arene–fluoroarene interactions of the systems studied here do not lead to

templating of a uniform alternating structure, but instead the spacer layers form nanoscale phase-segregated domains. Furthermore, we find that this nanoscale supramolecular structure with mixed-spacers enhances the performance of perovskite solar cells as compared to either of the components alone, which is accompanied by enhanced operational stability. We suggest that nanoscale segregation provides a new route for the design of layered hybrid perovskite systems. This new understanding is provided by the capacity of NMR crystallography to determine the atomic-level structure of the materials, which thus enables rational structure–activity-based design strategies applicable to other hybrid materials.

## RESULTS AND DISCUSSION

**Hybrid Perovskite Thin Films.** This study focuses on the  $n = 1$  model system with PEA<sup>+</sup> and/or FEA<sup>+</sup> spacers (S<sup>+</sup>) in a S<sub>2</sub>PbI<sub>4</sub> layered 2D perovskite composition. Higher compositional representatives of Ruddlesden–Popper S<sub>2</sub>A<sub>n-1</sub>M<sub>n</sub>X<sub>3n+1</sub> systems ( $n > 1$ ) commonly form mixtures of phases (known as quasi-2D perovskites) and are thus not well-defined.<sup>6,11</sup> Moreover, we assessed 2D/3D composites with overlayers of the organic spacer(s) on the 3D perovskite, which form a thin layer of a 2D phase upon annealing and are relevant for photovoltaic applications.<sup>12,34</sup> For these materials, we have based our investigation on compositions comprising FA<sup>+</sup> as the central A<sup>+</sup> cation due to its higher thermal stability.<sup>35,36</sup>

Thin films of layered perovskites were prepared based on  $n = 1$  S<sub>2</sub>PbI<sub>4</sub> compositions (S<sup>+</sup> = PEA<sup>+</sup>, FEA<sup>+</sup>, and 1:1 PEA<sup>+</sup>:FEA<sup>+</sup> denoted PF) as well as 3D (Cs<sub>0.05</sub>FA<sub>0.95</sub>MA<sub>0.1</sub>)-(PbI<sub>3</sub>)<sub>1.05</sub> perovskite thin films with a spacer overlayer of PEAI, FEAI or 1:1 PEAI:FEAI to form 2D/3D perovskite compositions on the surface, in accordance with the previous reports.<sup>34</sup>

The structural properties of the resulting perovskite films were analyzed by X-ray diffraction (XRD) in the Bragg–Brentano configuration. XRD patterns of S<sub>2</sub>PbI<sub>4</sub> compositions evidence the capacity of all of the spacers to form well-defined layered perovskite structures (Figure 2a). This is revealed by the presence of characteristic periodic patterns and low-angle reflections in the 2 $\theta$  region below 10° that are associated with the basal ( $h00$ ) planes.<sup>6</sup> The (FEA)<sub>2</sub>PbI<sub>4</sub> films also show



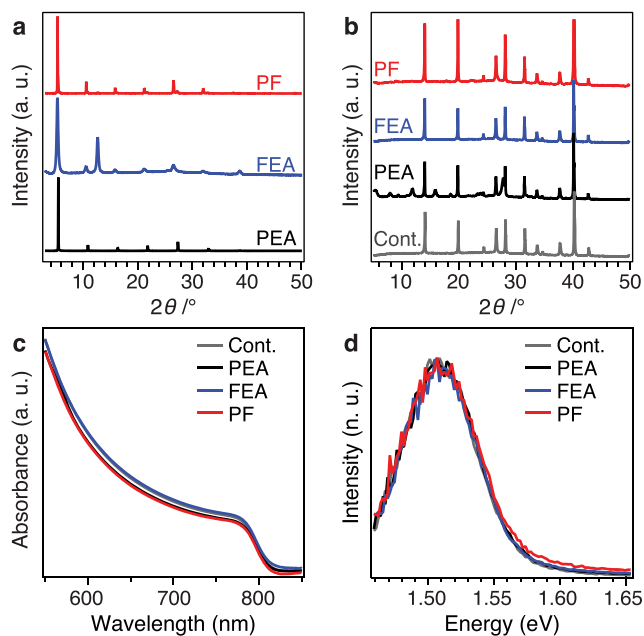


**Figure 2.** Structural and optical properties of the perovskite thin films. XRD patterns of (a) layered 2D perovskite films of  $S_2PbI_4$  composition and (b) 2D/3D perovskites ( $S^+ = PEA^+$ ,  $FEA^+$ , and 1:1  $PEA^+ : FEA^+$  denoted PF) on glass microscope slides. (c) UV–vis absorption spectra and (d) steady-state PL spectra of 2D/3D perovskite films on microscopic glass slide. n.u. = normalized units; cont. = control.

additional reflections (e.g., around  $2\theta$  of  $12.6^\circ$ ) that are associated with residual  $PbI_2$ .

For the 2D/3D perovskites (Figure 2b), the overlayers of organic spacers do not substantially change the crystal structure of the 3D perovskite, as the characteristic signals remain unaltered. The PEA-based system features additional low-angle reflections in the region of  $2\theta$  below  $10^\circ$ , which are indicative of the formation of low-dimensional perovskite phases.<sup>6</sup> These signals were not apparent for FEA- and PF-treated perovskite thin films. The low-angle signals could be seen, however, for both the  $PEA^+$  and  $FEA^+$  treated samples using grazing-incidence wide-angle X-ray scattering (GI-WAXS) and X-ray reflectivity (Figure S5). The assemblies of the  $FEA^+$  and PF spacers on the 3D perovskite surface were also probed by X-ray photoelectron spectroscopy (XPS), which confirms the presence of  $FEA^+$  on the surface of the hybrid perovskite through the appearance of F 1s core level signals (Figure S6 shows XPS data for control and treated samples). The F 1s binding energies for FEA- and PF-treated samples of 686.89 and 688.09 eV, respectively, indicate that the organic moieties engage in different binding modes on the surface of the hybrid perovskite. However, the spacer layers were not found to significantly alter the optical properties of the 3D perovskite, as demonstrated by the UV–vis absorption and photoluminescence (PL) spectroscopy of the corresponding films (Figure 2c,d). This is beneficial for maintaining favorable optoelectronic features relevant to their application.

In summary, the analysis of perovskite films of  $S_2PbI_4$  ( $n = 1$ ) composition indicates that the spacer moieties ( $PEA^+$ ,  $FEA^+$ , and their 1:1 mixture, PF) form layered 2D perovskite structures. Moreover, the presence of the spacer overlayer does not substantially affect the optoelectronic properties of the resulting 2D/3D perovskite films, which is beneficial for their

application. Although XRD determines the layered 2D nature of the inorganic lattice, it is not sensitive to the structure of the organic spacer cation. The atomic-level structure was therefore investigated by solid-state NMR spectroscopy<sup>25,37–39</sup> in conjunction with MD simulations and DFT calculations.

**Elucidating the Supramolecular Structure.** To analyze the bulk properties of the materials, powders of  $S_2PbI_4$  composition ( $n = 1$ ;  $S^+ = PEA^+$ ,  $FEA^+$ , and PF) were prepared mechanochemically.<sup>19</sup> XRD reveals that the crystalline low-dimensional perovskite structure is formed for all compositions, exemplified by the low-angle reflections at around  $2\theta = 5.2^\circ$  (Figure 3). These correspond to layer spacings of 16.5, 17.5, and 16.7 Å for  $(PEA)_2PbI_4$ ,  $(FEA)_2PbI_4$ , and  $(PF)_2PbI_4$ , respectively, consistent with the trend observed for calculated structures (Figure S3). Many more reflections are seen than for the thin-film samples, due to the lack of preferred orientation. The pattern for  $(PEA)_2PbI_4$  is in good agreement with the previously reported crystal structure,<sup>40</sup> and similar patterns are observed for the other samples. The reflections at  $2\theta$  values of  $\sim 14$ – $15^\circ$  are consistent with in-plane Pb–Pb distances of  $\sim 6.1$  Å. The  $(FEA)_2PbI_4$  and  $(PF)_2PbI_4$  samples show an additional reflection at  $2\theta$  of  $12.6^\circ$  which is ascribed to unreacted  $PbI_2$ , as also observed for the thin-film  $(FEA)_2PbI_4$  sample.

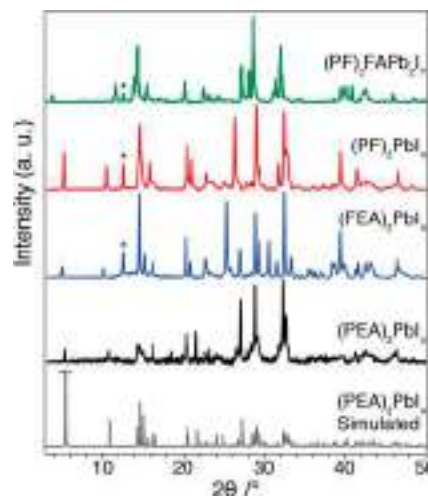


**Figure 3.** PXRD patterns of mechanothesized layered hybrid perovskites of  $S_2FA_{n-1}Pb_nI_4$  composition ( $S^+ = PEA^+$ ,  $FEA^+$  and 1:1  $PEA^+ : FEA^+$  denoted PF). The simulated pattern for  $(PEA)_2PbI_4$  is shown for the previously reported (*twisted*) crystal structure.<sup>40</sup> The major  $PbI_2$  reflection is marked with an asterisk.

Comparison of the  $^1H/^{19}F \rightarrow ^{13}C$  cross-polarization (CP) and direct  $^{19}F$  NMR spectra in the aromatic regions of the spacer cations for the pure PEAI and FEAI precursors and for the layered 2D perovskites (Figure 4) shows that the spacer environment changes upon formation of layered 2D perovskites. The  $^{19}F$  spectra for pentafluorophenyl derivatives are well-known.<sup>41</sup> The assignment of the  $^{13}C$  signals for FEAI was determined by  $^{19}F \rightarrow ^{13}C$  heteronuclear correlation (HETCOR) spectroscopy (Figure S8), whereas the assignment of the  $^{13}C$  signals for  $PEA^+$  was found by comparison with the calculated shifts, *vide infra*. Ball-milling a 1:1 mixture of PEAI and FEAI under comparable conditions to the mechanochemical preparation of the layered perovskite systems causes only relatively minor changes to the NMR spectra (Figure 4, red spectra, bottom panels). This indicates that the sample adopts

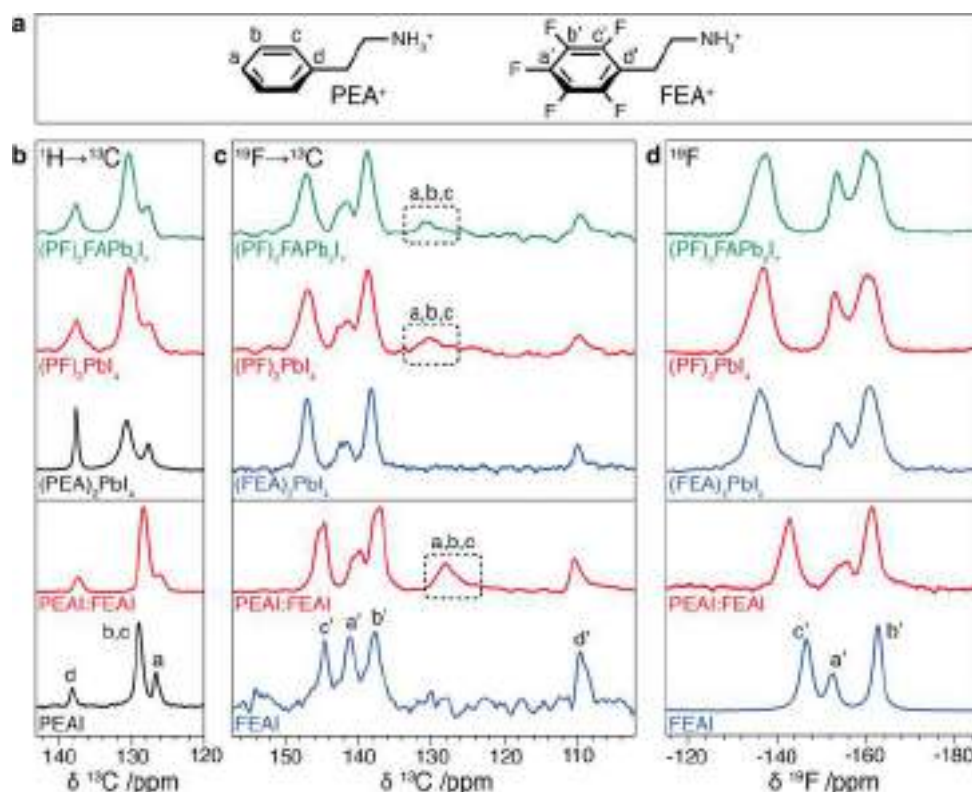


**Figure 4.** Solid-state NMR spectra of the spacer cations. (a) Structure of PEA<sup>+</sup> and FEA<sup>+</sup> cations with the corresponding <sup>13</sup>C and <sup>19</sup>F sites labeled. (b) <sup>1</sup>H→<sup>13</sup>C CP, (c) <sup>19</sup>F→<sup>13</sup>C CP, and (d) direct <sup>19</sup>F MAS NMR spectra. The top half of the panels are spectra from the layered hybrid perovskites, whereas the bottom half are from the neat spacer salts and their 1:1 mixture, following ball-milling. PF = 1:1 PEA<sup>+</sup>:FEA<sup>+</sup>. Signals arising from PEA<sup>+</sup> in the <sup>19</sup>F→<sup>13</sup>C CP spectra are highlighted in dashed boxes. Experimental parameters are given in Table S1. Full <sup>13</sup>C spectra are shown in Figure S7.

a similar structure to the neat spacer precursors. The atomic-level mixing between the phenyl moieties of the two components in the PEAI:FEAI sample is nevertheless clearly evidenced by the signal arising from the PEA<sup>+</sup> carbons (labeled a–c, Figure 4a) in the <sup>19</sup>F→<sup>13</sup>C CP spectrum (Figure 4c, dashed box). The <sup>19</sup>F spectrum for PEAI:FEAI (Figure 4d) exhibits slightly different shifts compared to pure FEAI, due to the sensitivity of the <sup>19</sup>F shifts to the modified structure. For the layered perovskites, clear differences are observed in the NMR spectra of the spacer cations, implying the formation of a new supramolecular structure (Figure 4b–d, top panels). The spectra for (PF)<sub>2</sub>PbI<sub>4</sub> (*n* = 1) and (PF)<sub>2</sub>FAPb<sub>2</sub>I<sub>7</sub> (*n* = 2) compositions are comparable, which implies that the organic structures are also very similar. This is expected, since the presence of a second layer of lead iodide octahedra should not significantly influence the spacer cations. Furthermore, for both systems, the PEA<sup>+</sup> carbons can be observed in the <sup>19</sup>F→<sup>13</sup>C CP spectra (Figure 4c, dashed boxes), indicating atomic-scale mixing of the spacer cations, since CP transfer relies on through-space dipole–dipole interactions at the subnanometer length scale. However, the layered perovskites containing only a single type of spacer cation, namely (PEA)<sub>2</sub>PbI<sub>4</sub> and (FEA)<sub>2</sub>PbI<sub>4</sub>, exhibit very similar spectra to the samples with mixed spacers. These observations can be explained by nanoscale segregation due to self-recognition or “narcissistic” self-sorting,<sup>42</sup> which would result in the local environments remaining similar to the individual spacer structures, while still affording the atomic-level contact observed by <sup>19</sup>F→<sup>13</sup>C CP. The broader signals in the mixed samples may thus correspond to the broader distribution of slightly different possible local

environments experienced within nanodomains of the different spacer cations.

To test whether the results obtained for the bulk mechanosynthesised samples are also applicable to solution-processed thin films, the <sup>1</sup>H→<sup>13</sup>C spectrum was recorded for a thin-film sample of (PF)<sub>2</sub>PbI<sub>4</sub> after scraping off the substrate (Figure S7, top). Although the signal-to-noise ratio is relatively low due to the low sample mass, the aromatic signals for the spacer cations are observed with the same shifts as for the bulk (PF)<sub>2</sub>PbI<sub>4</sub> sample, within a root-mean-squared error (RMSE) of 0.45 ppm. This indicates that the same supramolecular structure is adopted here for both the bulk and thin-film layered perovskites.

To illuminate the atomic-level structure using the NMR data, the predicted chemical shieldings were calculated using DFT for different trial structures. These were then converted to chemical shifts using a regression obtained from a set of reference organic structures containing fluorine and iodine (for details refer to Sections S3–S5). The *n* = 1 structure was used for the comparison, since the structure of the organic layer is shared by higher order 2D/3D homologues. Trial structures were generated by selecting low-energy structures from molecular dynamics simulations (detailed in Section S3), some of which were based on previously reported crystal structures,<sup>9,40,43,44</sup> prior to geometry optimization using DFT. Structures with two different relative orientations of the spacer cation aromatic rings were considered: the “*twisted*” structure (Figure 5a), with a twist between the aromatic rings in the two opposing layers, resulting in predominantly  $\pi_T$  interactions (Figure 1c) and the “*parallel*” structure (Figure 5b), with

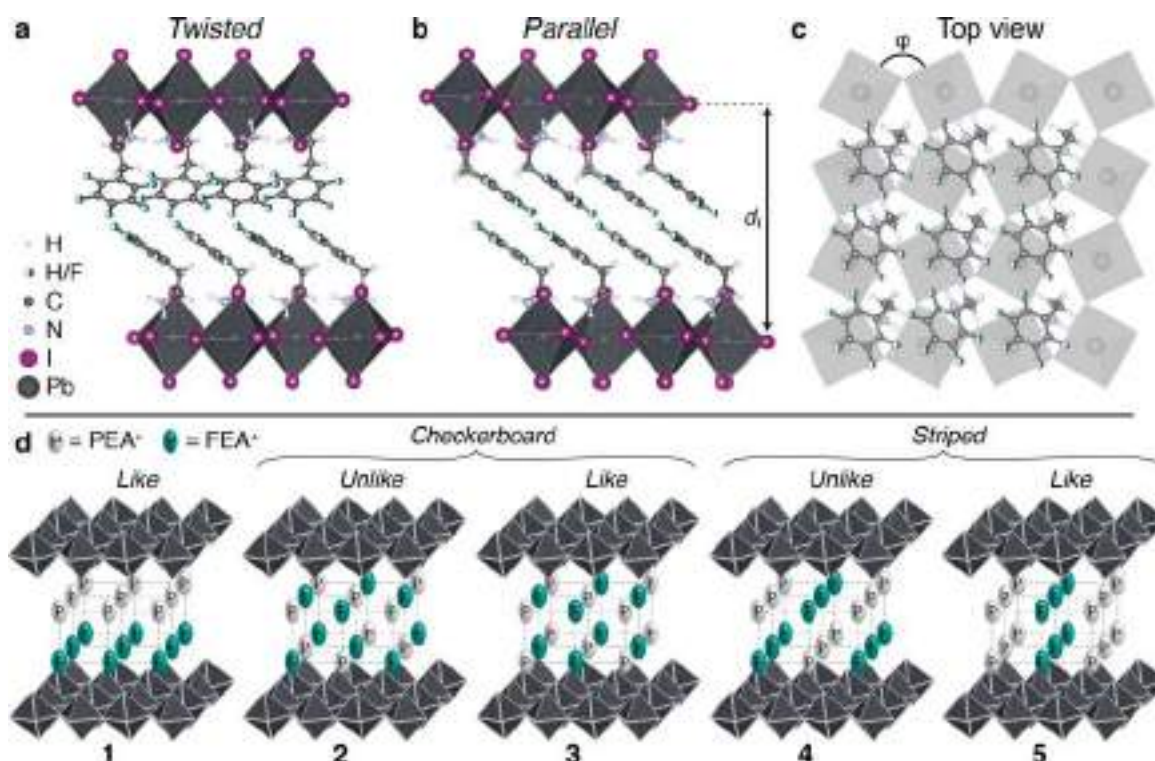


**Figure 5.** Trial structures for DFT calculations and NMR crystallography of  $S_2PbI_4$  layered perovskites. (a, b) *Twisted* and *parallel* relative orientations of the aromatic rings in adjacent layers and (c) top view of the spacer layer, showing the square lattice of interstices in the inorganic layer. The interlayer spacing ( $d_i$ ) and octahedral tilting ( $\varphi$ ) are also indicated. (d) Schematic of different possible arrangements (1–5) of  $PEA^+$  (P) and  $FEA^+$  (F) moieties on the two opposing lattices representing the spacer bilayer within the layered perovskite.

aromatic rings from opposite layers aligned in parallel planes at  $180^\circ$  between the layers, allowing displaced parallel  $\pi_D$  interactions (Figure 1c). For  $(PEA)_2PbI_4$ , the experimental  $^{13}C$  shifts agree with the calculated shifts for the *twisted* structure better than for the *parallel* structure (Table S4). This observation is in agreement with the previously reported single crystal structure (CCDC no. 1542461)<sup>40</sup> and the slightly lower calculated DFT energy (Section S3). For this analysis, only the aromatic carbons in the spacer cations were considered because the aliphatic carbons are close to the heavy Pb and I atoms and may require full relativistic treatment to obtain accurate shieldings. In contrast, for  $(FEA)_2PbI_4$ , the calculated  $^{13}C$  and  $^{19}F$  shifts for the *parallel* structure are in better agreement with experiment (Table S4), in accordance with the fact that the DFT energy is lower for the *parallel* structure (Section S3).

For the mixed  $(PF)_2PbI_4$  layered perovskite, there are many possible arrangements of the  $PEA^+$  and  $FEA^+$  spacers. Each lead iodide layer contains an array of tilted corner-sharing octahedra, resulting in a square lattice of rhombic interstices on each face in which the spacer cations reside (Figure 5c). We have considered the simplest representative examples of tiling the spacer cations over the two opposing lattices to form five trial structures (1–5, Figure 5d). In structure 1, each face comprises only a single type of spacer, while structures 2 and 3 have “checkerboard” arrangements of the cations on each face. In structure 2, the arrangements are offset so that *unlike* spacers are opposite each other (i.e.,  $PEA^+$  is opposite  $FEA^+$ ), while structure 3 has *like* spacers opposing. Finally, structures 4 and 5 have *striped* arrangements of the spacers on each face with *unlike*- and *like*-pairing arrangements of the opposing spacers, respectively. In addition, we also consider a segregated

model, where the shifts are calculated for the separate pure *twisted*  $(PEA)_2PbI_4$  and *parallel*  $(FEA)_2PbI_4$  structures, to imitate the environments in a nanoscale segregated structure that would form as a result of predominantly narcissistic self-sorting.

Figure 6 compares the experimental and calculated  $^{13}C$  and  $^{19}F$  chemical shifts for the five mixed  $(PF)_2PbI_4$  structures and the segregated model with the shifts from the pure  $(PEA)_2PbI_4$  and  $(FEA)_2PbI_4$  structures. The best agreement was found for a segregated model, and this is the only case for which the RMSEs between the calculated and experimental chemical shifts (Figure 6, insets) are less than the expected RMSE in DFT calculated shifts: 2.32 and 1.98 ppm for  $^{13}C$  and  $^{19}F$ , respectively, as estimated by the error in the calculated shifts for the external reference set (Section S5.2). Bayesian analysis of the data with the Bayesian NMR tool<sup>45</sup> indicates that the segregated system matches the experimental data with 99.9% probability, which is also consistent with the experimental shifts for  $(PF)_2PbI_4$  being very similar to those for  $(PEA)_2PbI_4$  and  $(FEA)_2PbI_4$ .

We therefore conclude that the layered hybrid perovskite structure formed by mixed  $PEA^+$  and  $FEA^+$  spacers comprises segregated domains of the two spacer moieties; however, since the  $PEA^+$   $^{13}C$  signals are observed in the  $^{19}F \rightarrow ^{13}C$  CP spectrum (Figure 4c), the domains must be limited to the nanoscale. Although the opposite quadrupolar moments of the aromatic systems were expected to favor  $PEA^+ - FEA^+$   $\pi$  interactions, the segregation may reflect the differing preferences of the two spacer cations to form *twisted* and *parallel* aromatic contacts, respectively (Figure 5a,b). Nevertheless, nanoscale mixing of the two spacers is observed, which may be entropically driven and is further supported by the

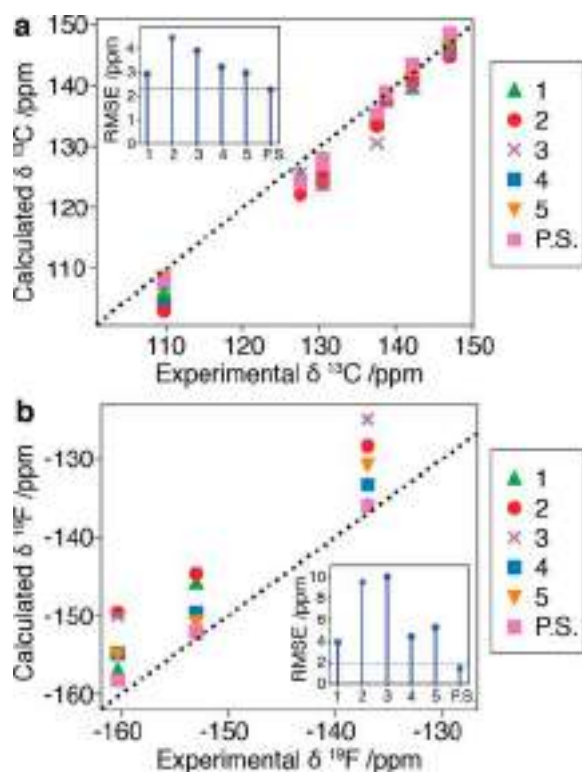


**Figure 6.** NMR shift calculations. Calculated aromatic (a)  $^{13}\text{C}$  and (b)  $^{19}\text{F}$  chemical shifts plotted against the experimental (PF) $_2$ PbI $_4$  chemical shifts for structures 1–5 (Figure Sd) and a phase segregated model (P.S., the calculated shifts for pure (PEA) $_2$ PbI $_4$  and (FEA) $_2$ PbI $_4$ ). The dashed diagonal lines indicate exact agreement. The insets show the RMSE between the calculated and experimental chemical shifts for each structure, and the horizontal lines are the expected error in DFT calculated shifts given by the RMSE in the regression set.

single basal reflection observed by XRD (Figure 3), despite the pure layered 2D perovskites having different layer spacings (*vide supra*). As a result, the photovoltaic performance of the mixed system could be affected as compared to the pure system (*vide infra*) through a synergistic effect

**Photovoltaic Performance and Stability.** The photovoltaic performance of hybrid perovskites with overlayers of layered perovskites with the different spacer cations was investigated using devices with the conventional fluorine-doped tin oxide (FTO)/c-TiO $_2$  (40 nm)/ mp-TiO $_2$  (250 nm)/ perovskite (450 nm)/2,2',7,7'-tetrakis(*N,N*-di-4-methoxyphenylamino)-9,9'-spirobifluorene (Spiro-OMeTAD; 180 nm)/Au (80 nm) configuration to probe their utility (Figure 7a–d). The layer thicknesses were estimated by cross-sectional SEM imaging (Figure 7c and Figure S9), and the photovoltaic (PV) metrics were extracted from the current–voltage (*J*–*V*) characteristics (Figure 7a,d and Figure S10). The differences between the short-circuit currents ( $J_{\text{SC}}$ ) for different compositions were found to be rather small, in the range of approximately 1%. This is in accordance with the minor changes in the optoelectronic properties of the 2D/3D perovskite films (Figure 2c,d). DFT-calculated band gaps of S $_2$ PbI $_4$  systems ( $\text{S}^+ = \text{PEA}^+$ , FEA $^+$ , and PF; Figure S1) revealed that nonfluorinated systems have lower gaps, which coincides with their less pronounced octahedral tilting compared to the fluorinated systems (Figure S2) as well as lower interlayer distances (Figure S3). The current density obtained by

integrating the incident photon-to-current efficiency (IPCE) as a function of wavelength for the champion device, 24.4 mA cm $^{-2}$ , is in good agreement with the values obtained from the *J*–*V* data (24.8 mA cm $^{-2}$ ), excluding any mismatch between the simulator and AM 1.5G light source (Figure 7b and Figure S11). Unlike the  $J_{\text{SC}}$ , the open-circuit voltages ( $V_{\text{OC}}$ ) of treated devices increased on average for PEA $^+$  and PF systems by 30 mV and 45 mV, respectively, which is likely to be associated with the role of the spacer overlayer in passivating the surface defects. The improvement in  $V_{\text{OC}}$  resulting from a low-dimensional overlayer is in agreement with numerous previous studies.<sup>25,46,47</sup> However, while the fill factor (FF) of FEA $^+$ -treated devices decreased relative to the controls, it increased for PF-treated devices. As a result, the mean PCEs of control, PEA $^+$ , FEA $^+$ , and PF-treated devices were 19.6%, 19.6%, 18.7%, and 20.8%, respectively, with the champion device reaching an efficiency of 21.6% for the PF-treated system (Figure 7a and Figure S10).

Notably, the performance of the mixed-spacer treated device, which we have determined to have a nanoscale-segregated structure of the spacer cations, shows a higher power conversion efficiency than with either spacer individually. We note, however, that the photovoltaic performances were not the primary objective of this study and were instead analyzed to illustrate the utility of this class of hybrid perovskites; therefore, further optimization of the corresponding devices can be envisaged. We further examined the effect of the overlayer on the operational stability of unencapsulated devices by monitoring the evolution of their maximum power point (MPP) under continuous irradiation of 1 sun in a nitrogen atmosphere (Figure 7e), which has previously been found to play a role in suppressing the degradation under operational conditions.<sup>48,49</sup> While the initial performance of the control devices dropped to values below 80% after just 20 h of operation, the treated devices showed improved stability during this period of time, maintaining around 90% of their initial performance value after 100 h of operation. These performance and stability improvements indicate the potential of such mixed-spacer layered perovskites in perovskite photovoltaics, which should stimulate further investigations.

## CONCLUSION

In summary, we present a systematic NMR crystallography approach based on solid-state NMR spectroscopy and computational analysis to elucidate the supramolecular structure of the organic spacer layer for layered hybrid perovskites. Specifically, a mixed arene–fluoroarene model system was studied, for which we find that although there is atomic-level contact between the spacers, the structures most closely resemble those of the end-members, implying nanoscale segregation. We illustrate the application of this system in enhancing the performance and stability of perovskite solar cells and demonstrate that the performance is greater than for either of the spacers individually. In general, we envisage that NMR crystallography will play an important role in determining the supramolecular structure of layered hybrid perovskites, facilitating molecular design of spacer systems driven by an understanding of their assemblies, thereby advancing the properties and applications of hybrid materials.

## EXPERIMENTAL SECTION

*Layered perovskite thin films* were deposited on microscope glass slides from a 0.5 M precursor solution by spin-coating, followed by

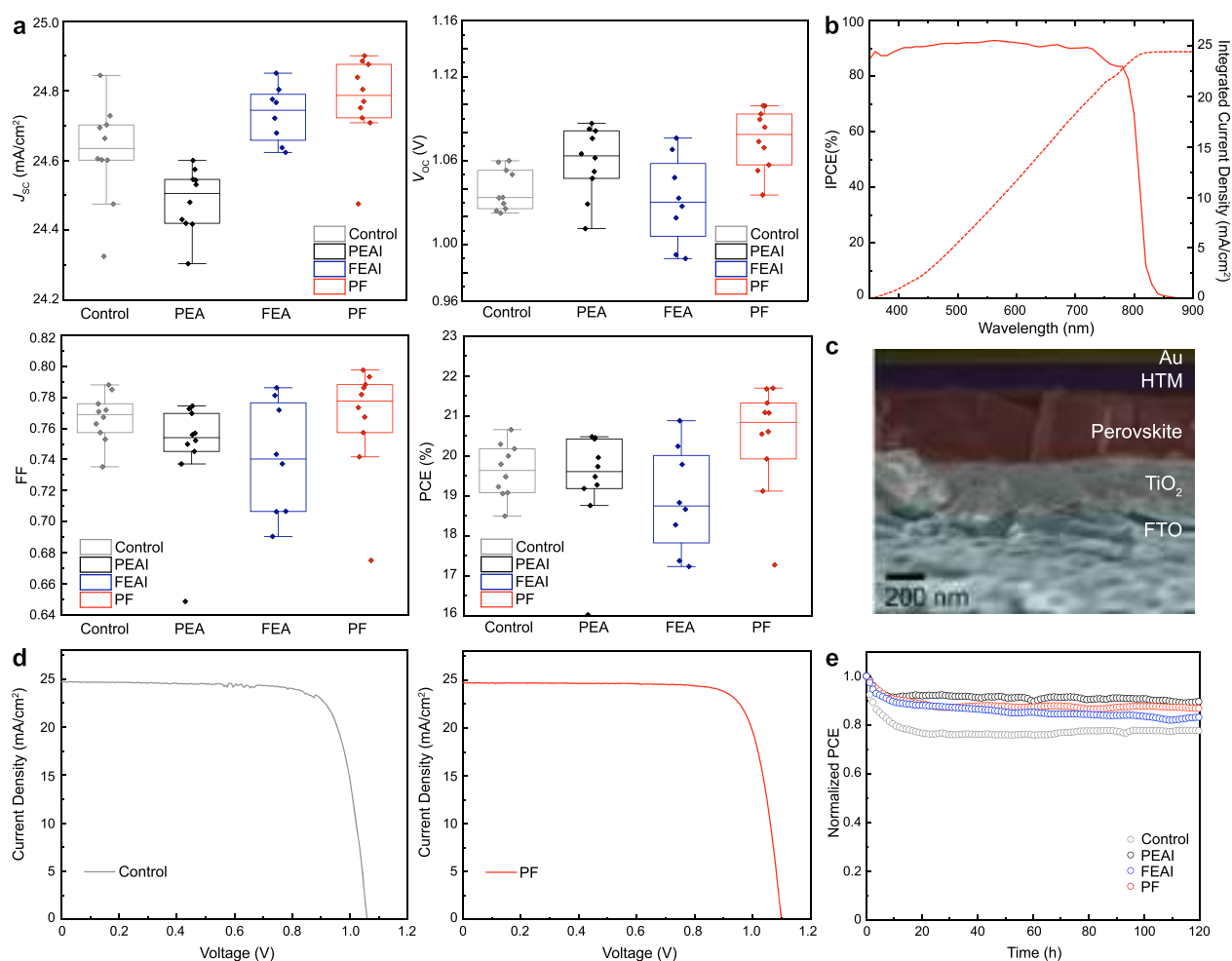


**Figure 7.** Photovoltaic performance and operational stability. (a) PV metrics of representative control and treated devices with aperture areas of 0.16 cm<sup>2</sup> under full solar intensity at ambient temperature in reverse (from  $V_{oc}$  to  $J_{sc}$ ) and forward bias with the PV metrics.  $J-V$  curves were recorded at a scanning rate of 50 mV s<sup>-1</sup> under standard AM 1.5G solar radiation. (b) IPCE spectrum of the champion device with the projected photocurrent derived by integrating the IPCE over the spectral emission. (c) Cross-sectional SEM image of the photovoltaic device of FTO/cp-TiO<sub>2</sub>/mp-TiO<sub>2</sub>/perovskite/Spiro-OMeTAD/Au architecture. (d)  $J-V$  curves of champion control (left) and PF-treated (right) devices. (e) Evolution of the MPP over time upon 1 sun illumination in nitrogen atmosphere at 60 °C.

annealing at 120 °C for 15 min. 2D/3D thin films were similarly prepared by spin-coating with a 1.5 M perovskite precursor solution, followed by annealing at 120 °C for 10 min and 100 °C for 40 min, before spin-coating an overlayer with a 30 mM solution of the spacer precursor in isopropanol at ambient temperature, followed by annealing at 110 °C for 5 min. Full details are provided in Section S1. Details on device characterization are given in Section S2.

Bulk layered perovskite powders were prepared by mechano-synthesis according to previous protocols.<sup>38,50</sup>

Solid-state NMR spectra were recorded at 9.4, 11.7, or 21.1 T. Full details are given in Section S2 and Table S1. Samples were annealed at 150 °C before recording the NMR.

Trial structures for the layered perovskites were determined from MD simulations and DFT calculations following an analogous procedure as previously reported.<sup>51</sup> Details are provided in Section S3 and S4.

NMR crystallography was used to determine the structure of the organic spacers, and the chemical shifts were calculated for the different trial structures using DFT (Section S5).

## ■ ASSOCIATED CONTENT

### SI Supporting Information

The Supporting Information is available free of charge at <https://pubs.acs.org/doi/10.1021/jacs.0c11563>.

Experimental details for device preparation, synthesis, characterization, solid-state NMR, MD and DFT calculations as well as supplementary data (PDF)

The raw data for this work (including NMR data, molecular dynamics data, structure files, photovoltaic data, and additional characterization data) are deposited at DOI: 10.5281/zenodo.4427776

## ■ AUTHOR INFORMATION

### Corresponding Authors

Lyndon Emsley – Laboratory of Magnetic Resonance, École Polytechnique Fédérale de Lausanne, Lausanne CH-1015, Switzerland; [orcid.org/0000-0003-1360-2572](https://orcid.org/0000-0003-1360-2572); Email: [lyndon.emsley@epfl.ch](mailto:lyndon.emsley@epfl.ch)

Jovana V. Milić – Laboratory of Photonics and Interfaces, École Polytechnique Fédérale de Lausanne, Lausanne CH-1015, Switzerland; [orcid.org/0000-0002-9965-3460](https://orcid.org/0000-0002-9965-3460); Email: [jovana.milic@epfl.ch](mailto:jovana.milic@epfl.ch)

Michael Grätzel – Laboratory of Photonics and Interfaces, École Polytechnique Fédérale de Lausanne, Lausanne CH-1015, Switzerland; [orcid.org/0000-0002-0068-0195](https://orcid.org/0000-0002-0068-0195); Email: [michael.gratzel@epfl.ch](mailto:michael.gratzel@epfl.ch)

**Ursula Rothlisberger** – Laboratory of Computational Chemistry and Biochemistry, École Polytechnique Fédérale de Lausanne, Lausanne CH-1015, Switzerland; [orcid.org/0000-0002-1704-8591](https://orcid.org/0000-0002-1704-8591); Email: [ursula.rothlisberger@epfl.ch](mailto:ursula.rothlisberger@epfl.ch)

## Authors

**Michael A. Hope** – Laboratory of Magnetic Resonance, École Polytechnique Fédérale de Lausanne, Lausanne CH-1015, Switzerland; [orcid.org/0000-0002-4742-9336](https://orcid.org/0000-0002-4742-9336)

**Toru Nakamura** – Laboratory of Photonics and Interfaces, École Polytechnique Fédérale de Lausanne, Lausanne CH-1015, Switzerland; Technology Innovation Division, Panasonic Corporation, Osaka 570-8501, Japan; [orcid.org/0000-0002-4290-4695](https://orcid.org/0000-0002-4290-4695)

**Paramvir Ahlawat** – Laboratory of Computational Chemistry and Biochemistry, École Polytechnique Fédérale de Lausanne, Lausanne CH-1015, Switzerland; [orcid.org/0000-0003-2355-3663](https://orcid.org/0000-0003-2355-3663)

**Aditya Mishra** – Laboratory of Magnetic Resonance, École Polytechnique Fédérale de Lausanne, Lausanne CH-1015, Switzerland

**Manuel Cordova** – Laboratory of Magnetic Resonance, École Polytechnique Fédérale de Lausanne, Lausanne CH-1015, Switzerland; [orcid.org/0000-0002-8722-6541](https://orcid.org/0000-0002-8722-6541)

**Farzaneh Jahanbakhshi** – Laboratory of Computational Chemistry and Biochemistry, École Polytechnique Fédérale de Lausanne, Lausanne CH-1015, Switzerland; [orcid.org/0000-0001-7113-2746](https://orcid.org/0000-0001-7113-2746)

**Marko Mladenović** – Laboratory of Computational Chemistry and Biochemistry, École Polytechnique Fédérale de Lausanne, Lausanne CH-1015, Switzerland

**Rashmi Runjhun** – Laboratory of Photonics and Interfaces, École Polytechnique Fédérale de Lausanne, Lausanne CH-1015, Switzerland; Institute of Physical Chemistry, Polish Academy of Sciences, Warsaw 01-224, Poland

**Lena Merten** – Institut für Angewandte Physik, Universität Tübingen, 72076 Tübingen, Germany

**Alexander Hinderhofer** – Institut für Angewandte Physik, Universität Tübingen, 72076 Tübingen, Germany; [orcid.org/0000-0001-8152-6386](https://orcid.org/0000-0001-8152-6386)

**Brian I. Carlsen** – Laboratory of Photomolecular Science, École Polytechnique Fédérale de Lausanne, Lausanne CH-1015, Switzerland

**Dominik J. Kubicki** – Laboratory of Magnetic Resonance, École Polytechnique Fédérale de Lausanne, Lausanne CH-1015, Switzerland; [orcid.org/0000-0002-9231-6779](https://orcid.org/0000-0002-9231-6779)

**Renana Gershoni-Poranne** – Laboratory of Chemistry and Applied Biosciences, ETH Zurich, 8092 Zurich, Switzerland; [orcid.org/0000-0002-2233-6854](https://orcid.org/0000-0002-2233-6854)

**Thomas Schneeberger** – Laboratory of Photonics and Interfaces, École Polytechnique Fédérale de Lausanne, Lausanne CH-1015, Switzerland

**Loïc C. Carbone** – Laboratory of Photonics and Interfaces, École Polytechnique Fédérale de Lausanne, Lausanne CH-1015, Switzerland

**Yuhang Liu** – Laboratory of Photonics and Interfaces, École Polytechnique Fédérale de Lausanne, Lausanne CH-1015, Switzerland

**Shaik M. Zakeeruddin** – Laboratory of Photonics and Interfaces, École Polytechnique Fédérale de Lausanne, Lausanne CH-1015, Switzerland

**Janusz Lewinski** – Institute of Physical Chemistry, Polish Academy of Sciences, Warsaw 01-224, Poland; [orcid.org/0000-0002-3407-0395](https://orcid.org/0000-0002-3407-0395)

**Anders Hagfeldt** – Laboratory of Photomolecular Science, École Polytechnique Fédérale de Lausanne, Lausanne CH-1015, Switzerland; [orcid.org/0000-0001-6725-8856](https://orcid.org/0000-0001-6725-8856)

**Frank Schreiber** – Institut für Angewandte Physik, Universität Tübingen, 72076 Tübingen, Germany

Complete contact information is available at: <https://pubs.acs.org/10.1021/jacs.0c11563>

## Author Contributions

These authors contributed equally.

## Notes

The authors declare no competing financial interest.

<sup>¶</sup>Cavendish Laboratory, University of Cambridge, United Kingdom CB3 0HE

<sup>◆</sup>Scientific Computing Laboratory, Center for the Study of Complex Systems, Institute of Physics Belgrade, University of Belgrade, Pregrevica 118, 11080 Belgrade, Serbia

<sup>●</sup>Soft Matter Physics Group at the Adolphe Merkle Institute of the University of Fribourg, 1700 Fribourg, Switzerland.

## ACKNOWLEDGMENTS

L.E. is grateful for financial support from SNSF grant no. 200020\_178860. J.V.M., S.M.Z., and M.G. are grateful to the European Union's Horizon 2020 research and innovation program under grant agreement no. 826013 (IMPRESSIVE). J.V.M. acknowledges support from the Swiss National Science Foundation (SNSF) grant no. 193174. U.R. acknowledges SNSF grant no. 200020-165863, NCCR-MUST, NRP70, and the SINERGIA interdisciplinary research program EPISODE for funding. R.R. acknowledges funding from the European Union's Horizon 2020 research and innovation program under the Marie Skłodowska Curie grant agreement no. 711859 and the Polish Ministry of Science and Higher Education from the cofunded project, grant agreement no. 3549/H2020/CO-FUND2016/2. We would like to thank several colleagues at EPFL for their support in the course of this study: Dr. Dan Ren for performing a TEM study, Dr. Linfeng Pan for support with the XRD of the films, Dr. Sandy Sanchez for support with the XRD and SEM of the films, Dr. Claudia Avalos for support in performing NMR experiments, and Masaud Almalki and Anwar Alanazi for preparing supplementary samples of films and devices.

## REFERENCES

- (1) Jena, A. K.; Kulkarni, A.; Miyasaka, T. Halide Perovskite Photovoltaics: Background, Status, and Future Prospects. *Chem. Rev.* **2019**, *119*, 3036–3103.
- (2) Kim, H. S.; Lee, C. R.; Im, J. H.; Lee, K. B.; Moehl, T.; Marchioro, A.; Moon, S. J.; Humphry-Baker, R.; Yum, J. H.; Moser, J. E.; Grätzel, M.; Park, N. G. Lead Iodide Perovskite Sensitized All-Solid-State Submicron Thin Film Mesoscopic Solar Cell with Efficiency Exceeding 9%. *Sci. Rep.* **2012**, *2*, 591.
- (3) Eperon, G. E.; Stranks, S. D.; Menelaou, C.; Johnston, M. B.; Herz, L. M.; Snaith, H. J. Formamidinium Lead Trihalide: A Broadly Tunable Perovskite for Efficient Planar Heterojunction Solar Cells. *Energy Environ. Sci.* **2014**, *7*, 982–988.
- (4) Grätzel, M. The Rise of Highly Efficient and Stable Perovskite Solar Cells. *Acc. Chem. Res.* **2017**, *50*, 487–491.
- (5) Wang, R.; Mujahid, M.; Duan, Y.; Wang, Z.-K.; Xue, J.; Yang, Y. A Review of Perovskites Solar Cell Stability. *Adv. Funct. Mater.* **2019**, *29*, 1808843.

- (6) Mao, L.; Stoumpos, C. C.; Kanatzidis, M. G. Two-Dimensional Hybrid Halide Perovskites: Principles and Promises. *J. Am. Chem. Soc.* **2019**, *141*, 1171–1190.
- (7) Mao, L.; Ke, W.; Pedesseau, L.; Wu, Y.; Katan, C.; Even, J.; Wasielewski, M. R.; Stoumpos, C. C.; Kanatzidis, M. G. Hybrid Dion–Jacobson 2D Lead Iodide Perovskites. *J. Am. Chem. Soc.* **2018**, *140*, 3775–3783.
- (8) Tsai, H.; Nie, W.; Blancon, J.-C.; Stoumpos, C. C.; Asadpour, R.; Harutyunyan, B.; Neukirch, A. J.; Verduzco, R.; Crochet, J. J.; Tretiak, S.; Pedesseau, L.; Even, J.; Alam, M. A.; Gupta, G.; Lou, J.; Ajayan, P. M.; Bedzyk, M. J.; Kanatzidis, M. G.; Mohite, A. D. High-Efficiency Two-Dimensional Ruddlesden–Popper Perovskite Solar Cells. *Nature* **2016**, *536*, 312–316.
- (9) Smith, I. C.; Hoke, E. T.; Solis-Ibarra, D.; McGehee, M. D.; Karunadasa, H. I. A Layered Hybrid Perovskite Solar Cell Absorber with Enhanced Moisture Stability. *Angew. Chem., Int. Ed.* **2014**, *53*, 11232–11235.
- (10) Grancini, G.; Nazeeruddin, M. K. Dimensional Tailoring of Hybrid Perovskites for Photovoltaics. *Nat. Rev. Mater.* **2019**, *4*, 4–22.
- (11) Saparov, B.; Mitzi, D. B. Organic–Inorganic Perovskites: Structural Versatility for Functional Materials Design. *Chem. Rev.* **2016**, *116*, 4558–4596.
- (12) Grancini, G.; Roldán-Carmona, C.; Zimmermann, I.; Mosconi, E.; Lee, X.; Martineau, D.; Narbey, S.; Oswald, F.; De Angelis, F.; Nazeeruddin, M. K. One-Year Stable Perovskite Solar Cells by 2D/3D Interface Engineering. *Nat. Commun.* **2017**, *8*, 15684.
- (13) Li, X.; Guo, P.; Kepenekian, M.; Hadar, I.; Katan, C.; Even, J.; Stoumpos, C. C.; Schaller, R. D.; Kanatzidis, M. G. Small Cyclic Diammonium Cation Templated (110)-Oriented 2D Halide (X = I, Br, Cl) Perovskites with White-Light Emission. *Chem. Mater.* **2019**, *31*, 3582–3590.
- (14) Alanazi, A. Q.; Kubicki, D. J.; Prochowicz, D.; Alharbi, E. A.; Bouduban, M. E. F.; Jahanbakhshi, F.; Mladenović, M.; Milić, J. V.; Giordano, F.; Ren, D.; Alyamani, A. Y.; Albrithen, H.; Albadi, A.; Alotaibi, M. H.; Moser, J.-E.; Zakeeruddin, S. M.; Rothlisberger, U.; Emsley, L.; Grätzel, M. Atomic-Level Microstructure of Efficient Formamidinium-Based Perovskite Solar Cells Stabilized by 5-Ammonium Valeric Acid Iodide Revealed by Multinuclear and Two-Dimensional Solid-State NMR. *J. Am. Chem. Soc.* **2019**, *141*, 17659–17669.
- (15) Ashari-Astani, N.; Jahanbakhshi, F.; Mladenović, M.; Alanazi, A. Q. M.; Ahmadabadi, I.; Ejtehadi, M. R.; Dar, M. I.; Grätzel, M.; Rothlisberger, U. Ruddlesden Popper Phases of Methylammonium-Based Two-Dimensional Perovskites with 5-Ammonium Valeric Acid  $\text{AVA}_2\text{MA}_{n-1}\text{Pb}_n\text{I}_{3n+1}$  with  $n = 1, 2$ , and  $3$ . *J. Phys. Chem. Lett.* **2019**, *10*, 3543–3549.
- (16) Jahanbakhshi, F.; Mladenović, M.; Kneschaurek, E.; Merten, L.; Gélvez-Rueda, M. C.; Ahlawat, P.; Li, Y.; Dučinskas, A.; Hinderhofer, A.; Dar, M. I.; Tress, W.; Carlsen, B.; Ummadisingu, A.; Zakeeruddin, S. M.; Hagfeldt, A.; Schreiber, F.; Grozema, F. C.; Rothlisberger, U.; Milić, J. V.; Graetzel, M. Unravelling the Structural Complexity and Photophysical Properties of Adamantyl-Based Layered Hybrid Perovskites. *J. Mater. Chem. A* **2020**, *8*, 17732–17740.
- (17) Bi, D.; Li, X.; Milić, J. V.; Kubicki, D. J.; Pellet, N.; Luo, J.; LaGrange, T.; Mettraux, P.; Emsley, L.; Zakeeruddin, S. M.; Grätzel, M. Multifunctional Molecular Modulators for Perovskite Solar Cells with over 20% Efficiency and High Operational Stability. *Nat. Commun.* **2018**, *9*, 4482.
- (18) Abate, A.; Saliba, M.; Hollman, D. J.; Stranks, S. D.; Wojciechowski, K.; Avolio, R.; Grancini, G.; Petrozza, A.; Snaith, H. J. Supramolecular Halogen Bond Passivation of Organic–Inorganic Halide Perovskite Solar Cells. *Nano Lett.* **2014**, *14*, 3247–3254.
- (19) Ruiz-Preciado, M. A.; Kubicki, D. J.; Hofstetter, A.; McGovern, L.; Futscher, M. H.; Ummadisingu, A.; Gershoni-Poranne, R.; Zakeeruddin, S. M.; Ehrler, B.; Emsley, L.; Milić, J. V.; Grätzel, M. Supramolecular Modulation of Hybrid Perovskite Solar Cells via Bifunctional Halogen Bonding Revealed by Two-Dimensional  $^{19}\text{F}$  Solid-State NMR Spectroscopy. *J. Am. Chem. Soc.* **2020**, *142*, 1645–1654.
- (20) Mitzi, D. B.; Medeiros, D. R.; Malenfant, P. R. L. Intercalated Organic–Inorganic Perovskites Stabilized by Fluoroaryl–Aryl Interactions. *Inorg. Chem.* **2002**, *41*, 2134–2145.
- (21) Hu, J.; Oswald, I. W. H.; Hu, H.; Stuard, S. J.; Nahid, M. M.; Yan, L.; Chen, Z.; Ade, H.; Neilson, J. R.; You, W. Aryl-Perfluoroaryl Interaction in Two-Dimensional Organic–Inorganic Hybrid Perovskites Boosts Stability and Photovoltaic Efficiency. *ACS Mater. Lett.* **2019**, *1*, 171–176.
- (22) Li, Y.; Milić, J. V.; Ummadisingu, A.; Seo, J.-Y.; Im, J.-H.; Kim, H.-S.; Liu, Y.; Dar, M. I.; Zakeeruddin, S. M.; Wang, P.; Hagfeldt, A.; Grätzel, M. Bifunctional Organic Spacers for Formamidinium-Based Hybrid Dion–Jacobson Two-Dimensional Perovskite Solar Cells. *Nano Lett.* **2019**, *19*, 150–157.
- (23) Gélvez-Rueda, M. C.; Ahlawat, P.; Merten, L.; Jahanbakhshi, F.; Mladenović, M.; Hinderhofer, A.; Dar, M. I.; Li, Y.; Dučinskas, A.; Carlsen, B.; Tress, W.; Ummadisingu, A.; Zakeeruddin, S. M.; Schreiber, F.; Hagfeldt, A.; Rothlisberger, U.; Grozema, F. C.; Milić, J. V.; Graetzel, M. Formamidinium-Based Dion–Jacobson Layered Hybrid Perovskites: Structural Complexity and Optoelectronic Properties. *Adv. Funct. Mater.* **2020**, *30*, 2003428.
- (24) Zhang, J.; Wang, Z.; Mishra, A.; Yu, M.; Shasti, M.; Tress, W.; Kubicki, D. J.; Avalos, C. E.; Lu, H.; Liu, Y.; Carlsen, B. I.; Agarwalla, A.; Wang, Z.; Xiang, W.; Emsley, L.; Zhang, Z.; Grätzel, M.; Guo, W.; Hagfeldt, A. Intermediate Phase Enhances Inorganic Perovskite and Metal Oxide Interface for Efficient Photovoltaics. *Joule* **2020**, *4*, 222–234.
- (25) Alharbi, E. A.; Alyamani, A. Y.; Kubicki, D. J.; Uhl, A. R.; Walder, B. J.; Alanazi, A. Q.; Luo, J.; Burgos-Caminal, A.; Albadi, A.; Albrithen, H.; Alotaibi, M. H.; Moser, J.-E.; Zakeeruddin, S. M.; Giordano, F.; Emsley, L.; Grätzel, M. Atomic-Level Passivation Mechanism of Ammonium Salts Enabling Highly Efficient Perovskite Solar Cells. *Nat. Commun.* **2019**, *10*, 3008.
- (26) Karmakar, A.; Dodd, M. S.; Zhang, X.; Oakley, M. S.; Klobukowski, M.; Michaelis, V. K. Mechanochemical Synthesis of 0D and 3D Cesium Lead Mixed Halide Perovskites. *Chem. Commun.* **2019**, *55*, 5079–5082.
- (27) Franssen, W. M. J.; van Es, S. G. D.; Dervişoğlu, R.; de Wijs, G. A.; Kentgens, A. P. M. Symmetry, Dynamics, and Defects in Methylammonium Lead Halide Perovskites. *J. Phys. Chem. Lett.* **2017**, *8*, 61–66.
- (28) Bryce, D. NMR Crystallography: Structure and Properties of Materials from Solid-State Nuclear Magnetic Resonance Observables. *IUCrJ* **2017**, *4*, 350–359.
- (29) Chen, P.; Bai, Y.; Wang, S.; Lyu, M.; Yun, J.-H.; Wang, L. In Situ Growth of 2D Perovskite Capping Layer for Stable and Efficient Perovskite Solar Cells. *Adv. Funct. Mater.* **2018**, *28*, 1706923.
- (30) Xu, Z.; Mitzi, D. B.  $\text{SnI}_4$ -Based Hybrid Perovskites Templated by Multiple Organic Cations: Combining Organic Functionalities through Noncovalent Interactions. *Chem. Mater.* **2003**, *15*, 3632–3637.
- (31) Sutton, C.; Risko, C.; Brédas, J.-L. Noncovalent Intermolecular Interactions in Organic Electronic Materials: Implications for the Molecular Packing vs Electronic Properties of Acenes. *Chem. Mater.* **2016**, *28*, 3–16.
- (32) Kim, K. S.; Tarakeshwar, P.; Lee, J. Y. Molecular Clusters of  $\pi$ -Systems: Theoretical Studies of Structures, Spectra, and Origin of Interaction Energies. *Chem. Rev.* **2000**, *100*, 4145–4186.
- (33) Giese, M.; Albrecht, M.; Rissanen, K. Anion– $\pi$  Interactions with Fluoroarenes. *Chem. Rev.* **2015**, *115*, 8867–8895.
- (34) Liu, Y.; Akin, S.; Pan, L.; Uchida, R.; Arora, N.; Milić, J. V.; Hinderhofer, A.; Schreiber, F.; Uhl, A. R.; Zakeeruddin, S. M.; Hagfeldt, A.; Dar, M. I.; Grätzel, M. Ultrahydrophobic 3D/2D Fluoroarene Bilayer-Based Water-Resistant Perovskite Solar Cells with Efficiencies Exceeding 22%. *Sci. Adv.* **2019**, *5*, eaaw2543.
- (35) Weller, M. T.; Weber, O. J.; Frost, J. M.; Walsh, A. Cubic Perovskite Structure of Black Formamidinium Lead Iodide,  $\alpha$ -[ $\text{HC}(\text{NH}_2)_2$ ]PbI<sub>3</sub>, at 298 K. *J. Phys. Chem. Lett.* **2015**, *6*, 3209–3212.

(36) Binek, A.; Hanusch, F. C.; Docampo, P.; Bein, T. Stabilization of the Trigonal High Temperature Phase of Formamidinium Lead Iodide. *J. Phys. Chem. Lett.* **2015**, *6*, 1249–1253.

(37) Franssen, W. M. J.; Kentgens, A. P. M. Solid-state NMR of Hybrid Halide Perovskites. *Solid State Nucl. Magn. Reson.* **2019**, *100*, 36–44.

(38) Kubicki, D. J.; Prochowicz, D.; Hofstetter, A.; Zakeeruddin, S. M.; Grätzel, M.; Emsley, L. Phase Segregation in Cs-, Rb- and K-Doped Mixed-Cation (MA)<sub>x</sub>(FA)<sub>1-x</sub>PbI<sub>3</sub> Hybrid Perovskites from Solid-State NMR. *J. Am. Chem. Soc.* **2017**, *139*, 14173–14180.

(39) Krishna, A.; Akhavan Kazemi, M. A.; Sliwa, M.; Reddy, G. N. M.; Delevoye, L.; Lafon, O.; Felten, A.; Do, M. T.; Gottis, S.; Sauvage, F. Defect Passivation via the Incorporation of Tetrapropylammonium Cation Leading to Stability Enhancement in Lead Halide Perovskite. *Adv. Funct. Mater.* **2020**, *30*, 1909737.

(40) Du, K.-z.; Tu, Q.; Zhang, X.; Han, Q.; Liu, J.; Zauscher, S.; Mitzi, D. B. Two-Dimensional Lead(II) Halide-Based Hybrid Perovskites Templated by Acene Alkylamines: Crystal Structures, Optical Properties, and Piezoelectricity. *Inorg. Chem.* **2017**, *56*, 9291–9302.

(41) Hogben, M. G.; Graham, W. A. G. Chemical Shifts and Coupling Constants in Pentafluorophenyl Derivatives. I. Correlations of Chemical Shifts, Coupling Constants, and  $\pi$ -electronic Interactions. *J. Am. Chem. Soc.* **1969**, *91*, 283–291.

(42) Safont-Sempere, M. M.; Fernandez, G.; Würthner, F. Self-Sorting Phenomena in Complex Supramolecular Systems. *Chem. Rev.* **2011**, *111*, 5784–5814.

(43) Slavney, A. H.; Smaha, R. W.; Smith, I. C.; Jaffe, A.; Umeyama, D.; Karunadasa, H. I. Chemical Approaches to Addressing the Instability and Toxicity of Lead-Halide Perovskite Absorbers. *Inorg. Chem.* **2017**, *56*, 46–55.

(44) Straus, D. B.; Iotov, N.; Gau, M. R.; Zhao, Q.; Carroll, P. J.; Kagan, C. R. Longer Cations Increase Energetic Disorder in Excitonic 2D Hybrid Perovskites. *J. Phys. Chem. Lett.* **2019**, *10*, 1198–1205.

(45) Engel, E. A.; Anelli, A.; Hofstetter, A.; Paruzzo, F.; Emsley, L.; Ceriotti, M. A Bayesian approach to NMR crystal structure determination. *Phys. Chem. Chem. Phys.* **2019**, *21*, 23385–23400.

(46) Chavan, R. D.; Prochowicz, D.; Tavakoli, M. M.; Yadav, P.; Hong, C. K. Surface Treatment of Perovskite Layer with Guanidinium Iodide Leads to Enhanced Moisture Stability and Improved Efficiency of Perovskite Solar Cells. *Adv. Mater. Interfaces* **2020**, *7*, 2000105.

(47) Hu, Y.; Schlipf, J.; Wussler, M.; Petrus, M. L.; Jaegermann, W.; Bein, T.; Müller-Buschbaum, P.; Docampo, P. Hybrid Perovskite/Perovskite Heterojunction Solar Cells. *ACS Nano* **2016**, *10*, 5999–6007.

(48) Domanski, K.; Roose, B.; Matsui, T.; Saliba, M.; Turren-Cruz, S. H.; Correa-Baena, J. P.; Carmona, C. R.; Richardson, G.; Foster, J. M.; De Angelis, F.; Ball, J. M.; Petrozza, A.; Mine, N.; Nazeeruddin, M. K.; Tress, W.; Grätzel, M.; Steiner, U.; Hagfeldt, A.; Abate, A. Migration of Cations Induces Reversible Performance Losses Over Day/Night Cycling in Perovskite Solar Cells. *Energy Environ. Sci.* **2017**, *10*, 604–613.

(49) Domanski, K.; Alharbi, E. A.; Hagfeldt, A.; Grätzel, M.; Tress, W. Systematic Investigation of the Impact of Operation Conditions on the Degradation Behaviour of Perovskite Solar Cells. *Nat. Energy* **2018**, *3*, 61–67.

(50) Prochowicz, D.; Sasaki, M.; Yadav, P.; Grätzel, M.; Lewiński, J. Mechanoperovskites for Photovoltaic Applications: Preparation, Characterization, and Device Fabrication. *Acc. Chem. Res.* **2019**, *52*, 3233–3243.

(51) Hong, L.; Milić, J. V.; Ahlawat, P.; Mladenović, M.; Kubicki, D. J.; Jahanabkshi, F.; Ren, D.; Gélvez-Rueda, M. C.; Ruiz-Preciado, M. A.; Ummadisingu, A.; Liu, Y.; Tian, C.; Pan, L.; Zakeeruddin, S. M.; Hagfeldt, A.; Grozema, F. C.; Rothlisberger, U.; Emsley, L.; Han, H.; Grätzel, M. Guanine-Stabilized Formamidinium Lead Iodide Perovskites. *Angew. Chem., Int. Ed.* **2020**, *59*, 4691–4697.



# Multimodal host-guest complexation for efficient and stable perovskite photovoltaics

Hong Zhang<sup>1</sup>, Felix Thomas Eickemeyer<sup>1</sup>, Zhiwen Zhou<sup>1</sup>, Marko Mladenović<sup>2</sup>, Farzaneh Jahanbakhshi<sup>2</sup>, Lena Merten<sup>3</sup>, Alexander Hinderhofer<sup>3</sup>, Michael A. Hope<sup>4</sup>, Olivier Ouellette<sup>1</sup>, Aditya Mishra<sup>4</sup>, Paramvir Ahlawat<sup>2</sup>, Dan Ren<sup>1</sup>, Tzu-Sen Su<sup>1</sup>, Anurag Krishna<sup>5</sup>, Zaiwei Wang<sup>5</sup>, Zhaowen Dong<sup>6</sup>, Jinming Guo<sup>7</sup>, Shaik M. Zakeeruddin<sup>1</sup>, Frank Schreiber<sup>3</sup>, Anders Hagfeldt<sup>5,9</sup>, Lyndon Emsley<sup>4</sup>, Ursula Rothlisberger<sup>2</sup>, Jovana V. Milić<sup>1,8</sup>✉ & Michael Grätzel<sup>1</sup>✉

Formamidinium lead iodide perovskites are promising light-harvesting materials, yet stabilizing them under operating conditions without compromising optimal optoelectronic properties remains challenging. We report a multimodal host-guest complexation strategy to overcome this challenge using a crown ether, dibenzo-21-crown-7, which acts as a vehicle that assembles at the interface and delivers Cs<sup>+</sup> ions into the interior while modulating the material. This provides a local gradient of doping at the nanoscale that assists in photo-induced charge separation while passivating surface and bulk defects, stabilizing the perovskite phase through a synergistic effect of the host, guest, and host-guest complex. The resulting solar cells show power conversion efficiencies exceeding 24% and enhanced operational stability, maintaining over 95% of their performance without encapsulation for 500 h under continuous operation. Moreover, the host contributes to binding lead ions, reducing their environmental impact. This supramolecular strategy illustrates the broad implications of host-guest chemistry in photovoltaics.

<sup>1</sup>Laboratory of Photonics and Interfaces, Institute of Chemical Sciences and Engineering, École Polytechnique Fédérale de Lausanne, Lausanne, Switzerland.

<sup>2</sup>Laboratory of Computational Chemistry and Biochemistry, Institute of Chemical Sciences and Engineering, École Polytechnique Fédérale de Lausanne, Lausanne, Switzerland. <sup>3</sup>Institut für Angewandte Physik, Universität Tübingen, Tübingen, Germany. <sup>4</sup>Laboratory of Magnetic Resonance, Institute of Chemical Sciences and Engineering, École Polytechnique Fédérale de Lausanne, Lausanne, Switzerland. <sup>5</sup>Laboratory of Photomolecular Science, Institute of Chemical Sciences and Engineering, École Polytechnique Fédérale de Lausanne, Lausanne, Switzerland. <sup>6</sup>Laboratory of Supramolecular Chemistry, Institute of Chemical Sciences and Engineering, École Polytechnique Fédérale de Lausanne, Lausanne, Switzerland. <sup>7</sup>Laboratory for Biological Geochemistry, École Polytechnique Fédérale de Lausanne, Lausanne, Switzerland. <sup>8</sup>Adolphe Merkle Institute of the University of Fribourg in Switzerland, Fribourg, Switzerland. <sup>9</sup>Present address: Department of Chemistry – Ångström Laboratory, Uppsala University, Uppsala, Sweden. ✉email: [jovana.milic@unifr.ch](mailto:jovana.milic@unifr.ch); [michael.gratzel@epfl.ch](mailto:michael.gratzel@epfl.ch)

Perovskite solar cells (PSCs) presently attain high power conversion efficiencies (PCE) and show the potential for low-cost fabrication, positioning them as one of the leading candidates for the next generation of thin-film photovoltaics<sup>1–6</sup>. They nevertheless still suffer from poor operational stability and degradation under ambient conditions, while presenting a potential negative environmental impact from the toxic lead component<sup>6</sup>. Moreover, the performance is still limited by defects and impurities that enhance non-radiative recombination of photogenerated charge carriers<sup>7–12</sup>. Conventional passivation is an effective strategy to remove defects from the surface of films<sup>8,13–15</sup>, yet a number of defects remain in the bulk and it is vital to mitigate both types of defects. Formamidinium lead iodide (FAPbI<sub>3</sub>) and FAPbI<sub>3</sub>-rich perovskites are particularly preferred for photovoltaic applications due to their superior optoelectronic properties and thermal stability<sup>5</sup>. However, the photoactive black phase (3C,  $\alpha$ ) readily transforms to the undesired wide-bandgap (2H,  $\delta$ ) phase under ambient conditions. Moreover, several polytypes (i.e., 2H, 4H, and 6H) can be formed, as evidenced both experimentally and theoretically<sup>16</sup>, with the  $\delta$  polytype being the most thermodynamically stable at ambient temperature (Supplementary Fig. 1). To address the thermodynamic instability of  $\alpha$ -FAPbI<sub>3</sub>, it has been previously shown that using alkali metal cations could be an effective strategy to stabilize the black phase<sup>17,18</sup>. However, this bulk approach results in homogenous doping that comes at the expense of increasing the bandgap and hampering the formation of high-quality films without addressing the detrimental lead impact<sup>6,16–18</sup>.

Here, we introduce an unprecedented concept of multimodal host–guest-complexation of dopants to simultaneously modulate the surface and bulk composition of perovskite films through a

synergistic effect of the host, guest, and the host–guest complex, which we demonstrate for the case of Cs<sup>+</sup> metal ions. The polar solvents that are commonly used (e.g., water, dimethylformamide, dimethyl sulfoxide, etc.) for dissolving metal halide salts could dissolve or damage the perovskite film<sup>17</sup>. This prevents the use of these solvents to dissolve metal halide salts for the treatment of FAPbI<sub>3</sub>-based perovskites. Crown ethers are known to serve as vehicles for different ions, for example in phase-transfer catalysis<sup>19</sup>, forming host–guest complexes via ion–dipole interactions between the oxygen atoms of the macrocycle and the metal cation, with remarkable selectivity for certain alkali metal ions due to the complementary size<sup>20,21</sup>. We exploit this key property of crown ethers and their molecular assemblies to infuse Cs<sup>+</sup> ions onto the perovskite film without damaging them, by dissolving the complex in an orthogonal non-polar solvent (e.g., chlorobenzene). We have employed dibenzo-21-crown-7 (DB21C7) as a proof of concept due to its strong affinity for Cs<sup>+</sup> ions<sup>20,21</sup>, forming a well-defined host–guest complex (Fig. 1a). This complex is soluble in chlorobenzene, which is compatible with the perovskite solution-processing. This strategy was found to substantially decrease defects and improve the morphology of perovskite films without significant change in the optoelectronic properties, resulting in high performance and stability. The synergistic effect of the host, guest, and their complex enables simultaneous passivation of the surface and bulk defects, while reducing the environmental impact of lead.

## Results and discussion

**Surface modification of perovskite films.** FAPbI<sub>3</sub>-based perovskite films were deposited on mesoporous (mp) TiO<sub>2</sub> substrates

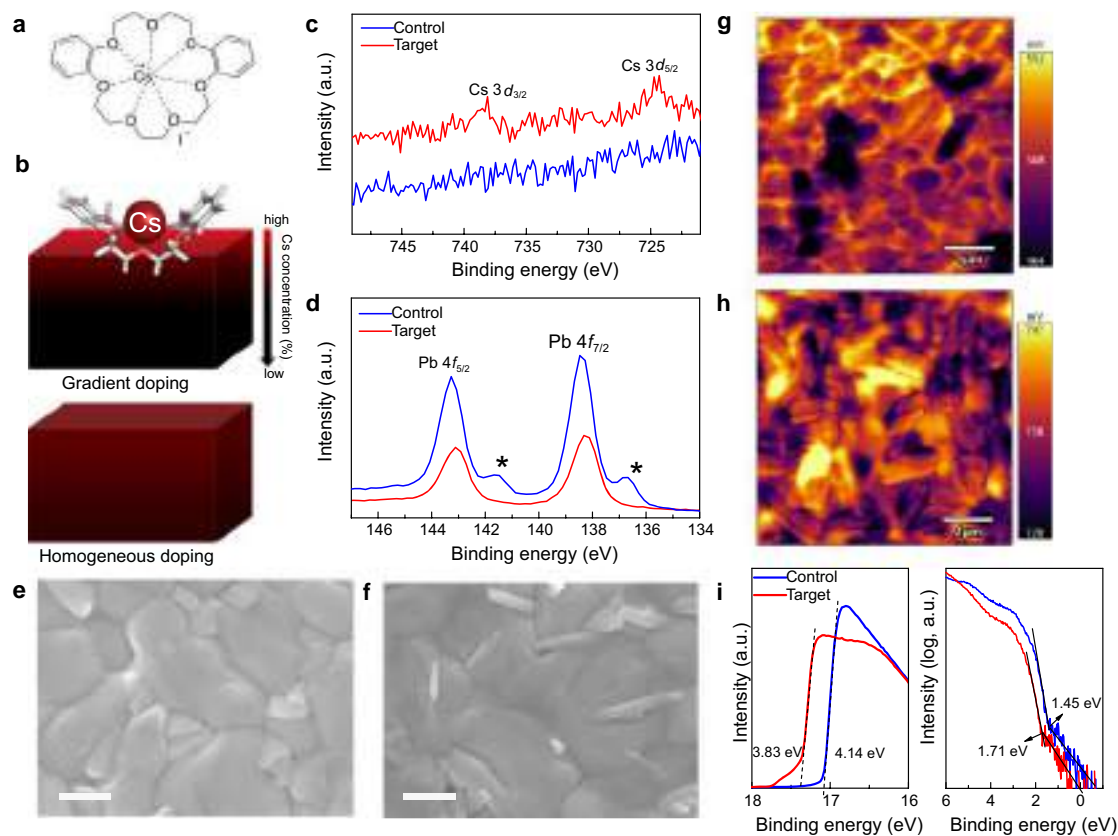


**Fig. 1** Effect of crown-ether-mediated interfacial Cs doping on the properties of perovskite films. **a** Molecular structure of the CsI-DB21C7 complex. **b** Schematic representation of the gradient and homogeneous Cs doping of perovskite films. XPS core-level spectra for Cs 3d (**c**) and Pb 4f (**d**). The asterisk (\*) indicates metallic Pb species. Top-view SEM images of control (**e**) and target (**f**) perovskite films revealing surface nanostructures upon treatment. The scale bar represents 500 nm. KPFM images of control (**g**) and target (**h**) perovskite films. **i** UPS spectra of perovskite films.

via a one-step method using an antisolvent (see the Methods section). After thermal annealing, the perovskite film was treated with a solution of the CsI-DB21C7 complex. The control films were based on FAPbI<sub>3</sub> or a FAPbI<sub>3</sub>-rich composition of (FAPbI<sub>3</sub>)<sub>0.97</sub>(MAPbBr<sub>3</sub>)<sub>0.03</sub> unless otherwise noted. The synthesis of the CsI-DB21C7 complex is detailed in the Methods section and its complexation by cesium cations was subsequently verified by nuclear magnetic resonance (NMR; Supplementary Fig. 2). An additional annealing step was then carried out to promote the infusion of Cs<sup>+</sup> into the bulk of the perovskite film, to form a gradient-doped structure, which increases stability without compromising the optimal optoelectronic properties, unlike homogeneous doping (Fig. 1b). The treatment conditions (i.e., concentration, annealing temperature, annealing duration, and counter ion) were optimized (as detailed in Supplementary Fig. 3) and samples with the optimized condition were studied further, labeled as target below.

The surface composition of the perovskite films was investigated by X-ray photoelectron spectroscopy (XPS). The XPS spectra in the Cs 3*d* level range (Fig. 1c and Supplementary Fig. 4a–d) show two signals in the treated film with binding energies of 739.0 and 725.0 eV that can be ascribed to Cs 3*d*<sub>3/2</sub> and Cs 3*d*<sub>5/2</sub> levels, respectively, whereas no signals are observed in the control perovskite film. This confirms that Cs<sup>+</sup> has been successfully transferred to the target perovskite film. Moreover, the XPS spectra in the Pb 4*f* level range (Fig. 1d) reveal two main peaks associated with Pb 4*f*<sub>7/2</sub> and Pb 4*f*<sub>5/2</sub> at 138.5 and 143.3 eV, respectively, attributed to Pb–I species, along with two smaller peaks located at 136.6 and 141.6 eV that arise from the presence of metallic Pb. The metallic Pb peak vanishes in the treated film, which suggests the host crown binds to the undercoordinated Pb<sup>2+</sup> ions which are responsible for the formation of metallic Pb<sup>22</sup>. This would greatly benefit the operational stability of the PSCs which suffer severely from the presence of elemental Pb<sup>7–12</sup>. Moreover, the peaks in the O 1*s* level range at 533.1 eV and C 1*s* at 286.3 eV (Supplementary Fig. 4a, b) that are associated with C–O binding energies suggest that the crown ether ligands remain on the surface of the film. In the attenuated total reflection Fourier transform infrared (ATR-FTIR) spectra (Supplementary Fig. 5), the shift of the characteristic C–O stretching vibration peaks of DB21C7 after treatment of the perovskite is consistent with the interaction between the crown ether and Pb<sup>2+</sup> in the perovskite phase.

The morphology of the perovskite surface was then analyzed by scanning electron microscopy (SEM; Fig. 1e, f and Supplementary Fig. 6). The target Cs-doped perovskite film shows larger grain sizes compared to the reference, with the appearance of needle-like structures and fewer grain boundaries due to increase of the size of the grains upon treatment<sup>22</sup>. This could be the result of preferential binding of the DB21C7 at the boundaries, similarly to other molecular modulators that contribute to reducing grain boundaries<sup>23</sup>. Elemental mapping of the treated perovskite films by energy-dispersive X-ray spectroscopy (EDS) further suggests that the needle-like structures contain carbon and Cs (Supplementary Fig. 6a), and are thus likely to be the CsI-DB21C7 complex, in accordance with the XPS analysis.

In addition to these structural changes, Kelvin probe force microscopy (KPFM) and ultraviolet photoelectron spectroscopy (UPS) demonstrate that the electronic structure at the surface of the treated perovskite film differs from that of the control samples. The target Cs-doped perovskite surface exhibited a higher and more homogeneous electrochemical potential than that of the control film, in accordance with a decrease in the number of grain boundaries upon treatment (Fig. 1g, h). The UPS results also show that the surface band structure has changed (Fig. 1i), since the work function decreases from 4.14 to 3.83 eV, i.e., by 0.31 eV, as

determined by a linear extrapolation of the secondary electron cutoff (Fig. 1i; left). This change is consistent with the shift of the surface potential probed by KPFM. Moreover, the logarithmic extrapolation of the leading edge (Fig. 1i; right) provides a value of 1.45 eV for the valence band maximum (VBM) of the control perovskite and 1.71 eV for the treated perovskite<sup>24</sup>. The VBM of the treated sample surface is slightly larger than the bulk bandgap of 1.56 eV<sup>24</sup>, which is an indication of a possible bandgap widening at the perovskite surface due to Cs incorporation upon treatment. Such surface bandgap widening can be helpful in suppressing interface recombination, and the corresponding structural origin of these interfacial changes is further investigated below.

**Structural properties of perovskite materials.** The structural properties of the perovskite films were analyzed by grazing incidence wide-angle X-ray scattering (GIWAXS; Fig. 2a–d and Supplementary Fig. 7a, b)<sup>25</sup>. Apart from the perovskite phases, unreacted PbI<sub>2</sub> ( $q = 0.9 \text{ \AA}^{-1}$ ) and, in some cases, even hexagonal phases, can be detected on the surface of the control films (Fig. 2a, Supplementary Fig. 7a). Conversely, in the treated sample, the PbI<sub>2</sub> peaks almost completely disappear while additional low- $q$  signals appear located at  $q = 0.5 \text{ \AA}^{-1}$  and below (Fig. 2b, Supplementary Fig. 7b). These low- $q$  signals might be ascribed to new unknown surface species, the CsI-DB21C7 complex. The new peak at  $q = 0.5 \text{ \AA}^{-1}$  also occurs in the powder X-ray diffraction pattern (pXRD; Supplementary Fig. 7c) of perovskite films after treatment. Since a broad peak around  $q = 0.5 \text{ \AA}^{-1}$  has also been observed in the pXRD pattern of CsI-DB21C7 powder, this peak might therefore arise from the formation of crystals of CsI-DB21C7. To verify this hypothesis, we generated a crystal structure of CsI-DB21C7 based on previously reported crown ether crystal structures<sup>26</sup> (Supplementary Fig. 7d) and optimized it by using density functional theory (DFT) calculations (computational details provided in the Methods). The simulated XRD patterns reveal that the first peak is positioned at  $q = 0.5 \text{ \AA}^{-1}$  (Supplementary Fig. 7c) in good agreement with the experimental observations. Therefore, we propose that the new peak at  $q = 0.5 \text{ \AA}^{-1}$  (Fig. 2b) corresponds to the CsI-DB21C7 complex, while the three peaks below  $q = 0.5 \text{ \AA}^{-1}$  could arise from slightly different polymorphs, i.e., different complexes in the solid state, which are known to occur<sup>20</sup>.

We further analyzed the GIWAXS as a function of the incident angle to assess the structural properties at the surface as well as the bulk (Supplementary Fig. 7a, b). Lower incidence angles imply a smaller probing depth in the material and thus increased surface sensitivity (Supplementary Fig. 7e). For the target Cs-doped film, the intensities of the perovskite peaks increase with the probing depth, indicating that the modified surface has a lower perovskite content than the bulk of the material (Fig. 2c). In contrast, the control sample shows only a slight increase in the perovskite signal with increasing probing depth (Fig. 2c), which is much less pronounced than the target sample, indicating a homogeneous perovskite composition. Moreover, much more PbI<sub>2</sub> is found in the control sample than in the treated sample. In the former, there is more PbI<sub>2</sub> near the surface than in the bulk; however, in the latter, the PbI<sub>2</sub> content increases with incident angle in a similar manner to the perovskite signal, indicating a homogeneous distribution throughout the perovskite film, and the total amount is greatly reduced upon surface modification. This is expected to enhance the stability of the Cs-doped perovskite films<sup>11</sup>. The peak intensity of the surface species associated with the CsI-DB21C7 complex remains approximately the same throughout the probed range of incident angles (Fig. 2c), in accordance with it being located exclusively on the surface of the film. This is not surprising considering that the complex is too

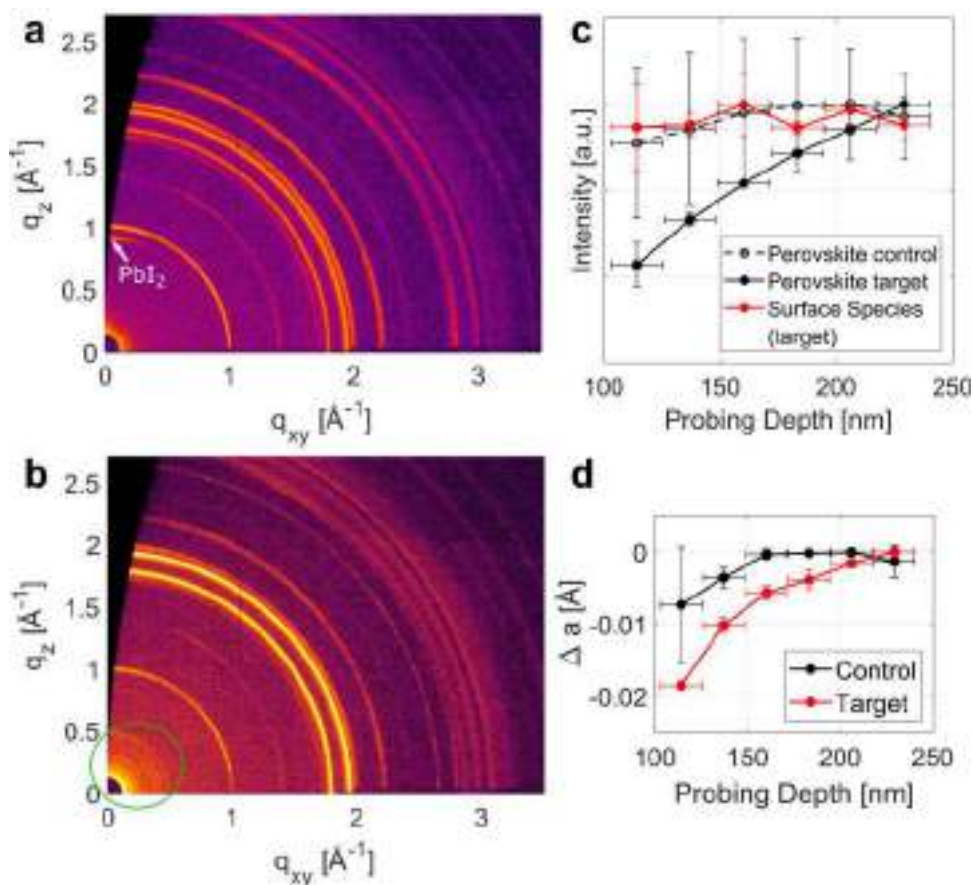


**Fig. 2 Structural characterization of perovskite films.** **a–b** GIWAXS two-dimensional reciprocal space maps of **a** control sample, **b** treated sample at an incidence angle of  $0.12^\circ$ , probing the surface of the material. Low  $q$  signals of the new surface species are marked with a green circle. Measurements were done under vacuum conditions. **c** Peak intensities of different crystal phases as a function of the estimated probing depth, normalized to their respective maximum value for control and treated samples. The intensity of surface species is approximately the same for the probed depth (red). **d** Relative change in pseudo-cubic unit cell parameters as a function of probing depth. Values were calculated from radial profiles of reciprocal space maps and averaged over two sets of samples. GIWAXS probing depth was varied by changing the angle of incidence of the X-ray beam from between  $0.12$  and  $0.3^\circ$ . The error in the probing depth (horizontal error bars) was estimated from the angular error due to the surface roughness of the sample. The vertical error bars were determined from the standard deviation from repeated measurements on two sets of samples.

large to diffuse into the perovskite lattice. The X-ray reflectivity (XRR) scans (Supplementary Fig. 7f) yield an estimated minimum thickness of the surface layer (i.e., crystallite size in the vertical direction) of approximately 15 nm.

The hexagonal 4H phase of FAPbI<sub>3</sub> can also be found near the film surface of some of the control samples, but in none of the target samples (Supplementary Fig. 7a, b). This might originate from incomplete conversion to the perovskite ( $\alpha$ ) phase, since the structure of the 4H phase is a combination of  $\delta$  (face-sharing) and  $\alpha$  (corner-sharing) phases, suggesting that the 4H phase could constitute a possible intermediate during the conversion from  $\delta$  to  $\alpha$  phase. The 4H polytype, however, is converted into the  $\alpha$ -phase perovskite structure at the Cs-rich surface of the treated samples. To understand the effect of Cs<sup>+</sup> incorporation on the 4H polytype, we calculated the relative energies of the 4H polytype and the  $\alpha$  phase as a function of Cs<sup>+</sup> concentration (Supplementary Fig. 8a). The calculation reveals that Cs<sup>+</sup> doping with increasing concentrations significantly decreases the stability of the 4H phase as compared to  $\alpha$ -FAPbI<sub>3</sub>. Therefore, the formation of a Cs-rich surface benefits the stabilization of  $\alpha$ -FAPbI<sub>3</sub>. The formation of a wider-bandgap Cs-substituted perovskite at the interface between the bulk perovskite and the hole transporting material would also be beneficial for the hole extraction and inhibition of charge

recombination. Furthermore, with increasing angle of incidence, i.e., increasing penetration depth, the perovskite unit cell parameter increases (Fig. 2d). This effect is much more pronounced in the target sample, which indicates a smaller unit cell near the surface than in the bulk due to the higher concentration of Cs<sup>+</sup>, which is smaller than FA<sup>+</sup>, corroborating the gradient of incorporation of Cs<sup>+</sup>. The XPS (Supplementary Fig. 4c, d) and time-of-flight secondary ion mass spectrometry (TOF-SIMS; Supplementary Fig. 6c) depth profiles further verify the infusion of Cs<sup>+</sup> ions (as detailed in Supplementary Note 1).

#### Elucidation of the Cs doping and passivation at the atomic level.

To gain atomic-level insight into the effect of Cs<sup>+</sup> ion-complexed crown ether on hybrid perovskite materials, we performed solid-state nuclear magnetic resonance (ssNMR) experiments. Previously, various key phenomena in hybrid perovskite systems have been unraveled using ssNMR, such as halide mixing<sup>27</sup>, phase segregation<sup>28</sup>, cation incorporation<sup>28,29</sup>, as well as the effect of larger organic moieties<sup>30–32</sup> on these complex organic–inorganic photovoltaic materials. In the present case, the chemical shift of <sup>133</sup>Cs NMR can distinguish the incorporation of Cs<sup>+</sup> ions into the perovskite<sup>28</sup> from its association with the crown ether<sup>33</sup>, and the quadrupolar coupling of <sup>14</sup>N in FA cations<sup>34</sup> is

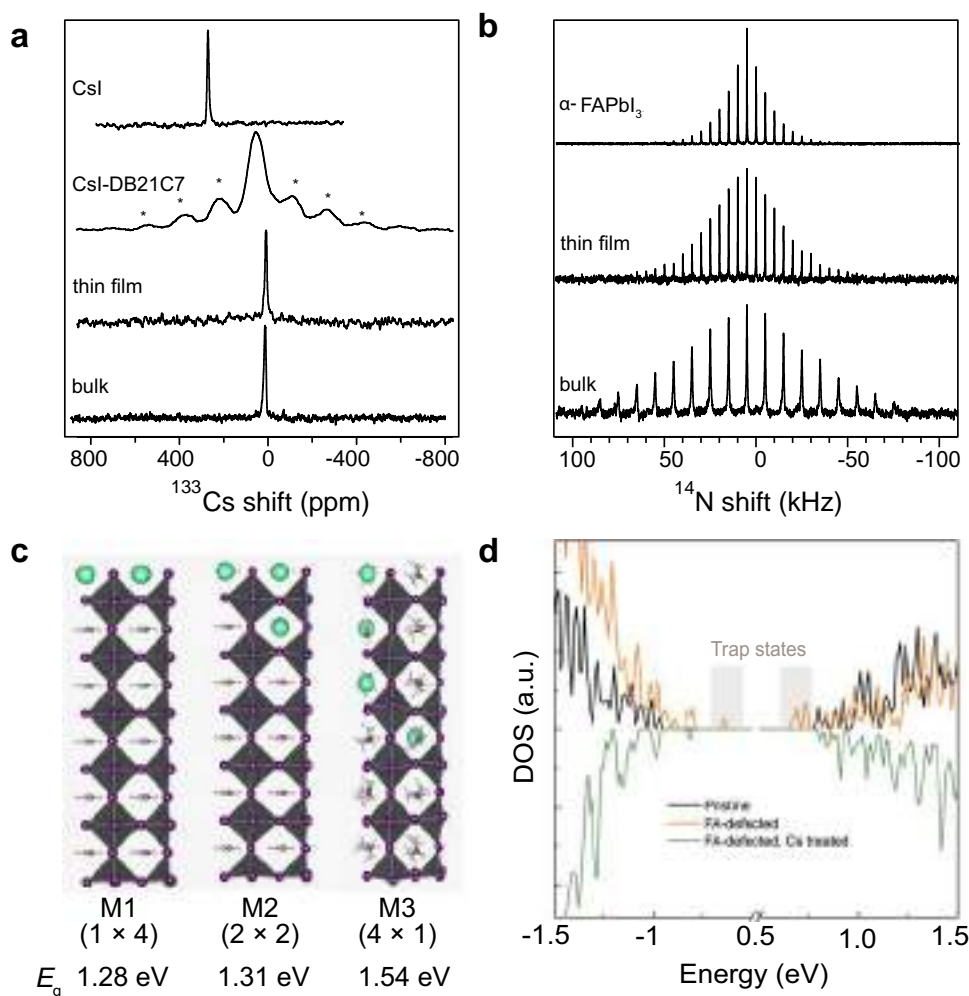


**Fig. 3 Atomic-level effects of Cs doping on the properties of FAPbI<sub>3</sub>.** Solid-state NMR measurements at 21.1 T recorded with a Hahn-echo pulse sequence: **a**  $^{133}\text{Cs}$  spectra at 20 kHz magic angle spinning (MAS) of crystalline CsI, the CsI-DB21C7 powder, the FAPbI<sub>3</sub> thin film treated with CsI-DB21C7 (thin film) and a sample of FAPbI<sub>3</sub> mixed with CsI-DB21C7 complex (bulk). **b**  $^{14}\text{N}$  spectra at 5 or 10 kHz MAS and ambient temperature of the treated samples and powders prepared by mechanochemical synthesis of pure FAPbI<sub>3</sub>. **c** Schematic representation of inhomogeneous (1 × 4 and 2 × 2) and homogeneous (4 × 1) models (M1–M3) of Cs-doped FAPbI<sub>3</sub> structures and their DFT-calculated band gap ( $E_g$ ) values associated with each configuration. The difference in the bandgap between the experimental and theoretical values is mainly due to finite temperature effects (more details provided in the supplementary materials). **d** Density of states of FAI-terminated pristine FAPbI<sub>3</sub>, FAPbI<sub>3</sub> containing a FA<sup>+</sup> vacancy and Cs<sup>+</sup>-treated FAPbI<sub>3</sub> with a FA<sup>+</sup> vacancy. For readability purposes, the density of states has been mirrored for the treated system.

extremely sensitive to the symmetry of tumbling of the organic cation and hence to distortions of the cuboctahedral cavity<sup>30,31</sup>.

The  $^{133}\text{Cs}$  spectrum of CsI shows a single sharp peak at 271 ppm indicating that the Cs<sup>+</sup> ion is in a well-defined cubic environment, whereas upon reaction with DB21C7 a broad  $^{133}\text{Cs}$  resonance is observed with several spinning sidebands (Fig. 3a, CsI and CsI-DB21C7). This is consistent with a distribution of asymmetric local Cs<sup>+</sup> environments arising from coordination by the crown ether. The  $^{133}\text{Cs}$  and  $^{14}\text{N}$  NMR spectra of mechanochemically prepared<sup>35</sup> FAPbI<sub>3</sub> with 10 at% CsI-DB21C7 demonstrate incorporation of Cs<sup>+</sup> into the perovskite. Specifically, a sharp  $^{133}\text{Cs}$  resonance is observed at 15 ppm (Fig. 3a, bulk). Using the linear dependence of the  $^{133}\text{Cs}$  shift on the Cs<sup>+</sup> concentration of  $\delta = 122x + 0.6$  ppm based on the previous data (Supplementary Fig. 9)<sup>28</sup>, a concentration of 12 at% is predicted from the experimental shift. There is no evidence of the signal corresponding to the Cs<sup>+</sup> in the crown ether complex (CsI-DB21C7; Fig. 3a) although, due to its broadness, the intensity of this signal would be far lower. The  $^{14}\text{N}$  spectrum exhibits a spinning sideband manifold with a full width at half

maximum (FWHM) of 76 kHz (Fig. 3b), compared to pure FAPbI<sub>3</sub> which has a FWHM of 19 kHz at room temperature. This indicates that the cuboctahedral cavity is more distorted upon exposure of the FAPbI<sub>3</sub> film to CsI-DB21C7, which is consistent with the incorporation of Cs<sup>+</sup> ions into the perovskite lattice. For the thin-film sample with gradient Cs doping, ssNMR further confirms the incorporation of Cs<sup>+</sup>. Specifically, a sharp  $^{133}\text{Cs}$  signal can be observed at 8 ppm, which would correspond to a lower Cs<sup>+</sup> concentration of 6 at% (Fig. 3b, thin film). The FWHM of the  $^{14}\text{N}$  sideband manifold is 48 kHz; this is intermediate between those of pure FAPbI<sub>3</sub> and the sample mechano-synthesized with CsI-DB21C7, which again is consistent with an intermediate Cs<sup>+</sup> concentration.

The concentration of Cs<sup>+</sup> in the doped layer of FAPbI<sub>3</sub> is further determined by the propensity for release of Cs<sup>+</sup> from CsI-DB21C7 into the perovskite, which was assessed by DFT calculations. The complexation energy of CsI-DB21C7 was calculated and compared to that of FAI-DB21C7 and PbI<sub>2</sub>-DB21C7 (Supplementary Table 1). Complexation energies of DB21C7–Cs<sup>+</sup> (−2.22 eV) and DB21C7–FA<sup>+</sup> (−1.68 eV) show

a higher stability of the  $\text{Cs}^+$  complex with respect to the  $\text{FA}^+$  complex, yet indicate that the formation of a crown ether- $\text{FA}^+$  adduct, DB21C7- $\text{FA}^+$ , is also energetically favorable. In addition, the large complexation energy of DB21C7- $\text{Pb}^{2+}$  ( $-8.93$  eV) strongly suggests that such complexes could form on the surface of  $\text{FAPbI}_3$ , which would be further beneficial for the suppression of uncoordinated Pb defects.

The dissociation of  $\text{Cs}^+$  ions from the crown ether and its incorporation into the perovskite phase are expected to cause changes in the electronic structure of  $\text{FAPbI}_3$ , which are further analyzed via DFT calculations to assess the benefits of the gradient doping. Accordingly, we considered  $2 \times 2 \times 6$  supercells of 16.7% Cs-doped  $\text{FAPbI}_3$  with three distinct distributions of  $\text{Cs}^+$  (models M1–M3) (Fig. 3c, Supplementary Fig. 8b–e), which closely corresponds to the experimental concentrations while enabling a comparison of different distributions and pure  $\text{FAPbI}_3$ . Although the compositions are slightly different and we recognize the limitation of the periodic models, the effect of the different doping distributions can nevertheless be inferred. The M1 ( $1 \times 4$ ) model was constructed by replacing an entire  $2 \times 2$  layer of  $\text{FA}^+$  by  $\text{Cs}^+$ . Similarly, the M2 ( $2 \times 2$ ) model was constructed by replacing 2  $\text{FA}^+$  cations in each of two adjacent layers by  $\text{Cs}^+$  ions. Lastly, the M3 ( $4 \times 1$ ) model was constructed by replacing one  $\text{FA}^+$  cation by  $\text{Cs}^+$  in each of the 4 layers. Models M1 ( $1 \times 4$ ) and M2 ( $2 \times 2$ ) represent inhomogeneous surface treatment of  $\text{FAPbI}_3$ , which do not show a significant difference in the bandgap (1.28 eV and 1.31 eV, respectively, as shown in Fig. 3c and Supplementary Fig. 8e) compared to the pure  $\text{FAPbI}_3$  (1.32 eV), in accordance with the experimental findings. The compositions represented by models M1–M2 feature an FA-rich and a Cs-rich domain. The band edges are found to be dominated by the Pb and I contributions from the FA-rich region, which remains undistorted, hence maintaining the band gap of  $\text{FAPbI}_3$ . However, the bandgap of the Cs-rich region is, as demonstrated by the corresponding projected density of states (Supplementary Fig. 8c, d), larger than that of the FA-rich region, allowing for a more efficient charge extraction and lower recombination. On the contrary, in the case of the more homogeneously Cs-doped model M3 ( $4 \times 1$ ), a significant increase in the bandgap is observed (Fig. 3d) due to considerable structural distortion (octahedral tilting away from  $90^\circ$  to more orthorhombic environments), which leads to shifts of both the VBM and conduction band minimum (CBM; Supplementary Fig. 8e).

To investigate potential benefits of  $\text{Cs}^+$  incorporation for defect passivation at the atomic level, we performed a DFT study of a  $\text{FA}^+$  vacancy-containing surface of  $\text{FAPbI}_3$ . When the  $\text{FA}^+$  vacancy is present at the perovskite surface (Fig. 3d, Supplementary Fig. 8f, g), localized trap states were introduced in the vicinity of both the VBM and the CBM, as a result of strong structural distortions of the surface induced by the vacancy. Upon the vacancy passivation by  $\text{Cs}^+$ , the VBM and the CBM states delocalized and the gap became larger, resulting in a direct passivation effect of the surface defects by  $\text{Cs}^+$ . In a similar fashion, incorporation of  $\text{Cs}^+$  ions in the bulk of the perovskite can passivate defects, thus hindering the recombination and improving the photovoltaic performances. However, the gradient structure enables this without compromising the resulting optoelectronic properties, which is more beneficial for photovoltaic applications.

**Photovoltaic performances and device physics.** The device performance of the corresponding perovskite solar cells was investigated using the conventional configuration of FTO/compact  $\text{TiO}_2$  ( $\sim 60$  nm)/mesoporous  $\text{Li-TiO}_2$ /perovskite composite layer ( $\sim 150$  nm)/perovskite upper layer ( $\sim 650$  nm)/spiro-OMeTAD ( $\sim 150$  nm)/Au ( $\sim 70$  nm)<sup>36</sup>. The perovskite layers were based on both

$\text{FAPbI}_3$  and a more widely used  $\text{FAPbI}_3$ -rich composition of  $(\text{FAPbI}_3)_{0.97}(\text{MAPbBr}_3)_{0.03}$ , to illustrate the generality of the approach. The DB21C7-CsI target treatment is compared with undoped control samples, homogeneously  $\text{Cs}^+$  doped samples and DB21C7 treated samples. Experimental details are provided in the Methods and photovoltaic (PV) performance is illustrated in Fig. 4 and Supplementary Figs. 10–12. The treatment significantly improves the performance of PSCs compared to that of the controls (without doping; Fig. 4a). This is particularly reflected in the  $V_{\text{OC}}$ , which is improved from  $1.08 \pm 0.01$  V to  $1.17 \pm 0.01$  V and the fill factor (FF), which improves from  $75.7 \pm 0.9\%$  to  $79.7 \pm 0.9\%$ , resulting in a significant improvement of the power conversion efficiency (PCE) (average) from  $20.56 \pm 0.21\%$  to  $23.62 \pm 0.43\%$ . Current density–voltage ( $J$ - $V$ ) curves of the champion devices (Fig. 4b and Supplementary Fig. 10) show that the target (gradient-Cs-doped) device exhibited a  $V_{\text{OC}}$  of 1.17 V, a short-circuit current ( $J_{\text{SC}}$ ) of  $25.50$  mA  $\text{cm}^{-2}$ , a fill factor of 81.9%, and a PCE of 24.30% for  $(\text{FAPbI}_3)_{0.97}(\text{MAPbBr}_3)_{0.03}$  composition, while the control device showed an overall PCE of 21.20% with a  $V_{\text{OC}}$  of 1.09 V, a  $J_{\text{SC}}$  of  $25.60$  mA  $\text{cm}^{-2}$ , and a FF of 75.9%. We further ascertained these values by recording scan-speed-independent maximum power point tracking (MPP) measurements (Fig. 4b, insert) corresponding to PCEs of 20.5% and 23.9% for the control and target PSCs, respectively.

The target PSCs show much higher performance than for the homogeneous Cs-doped perovskites<sup>17,18</sup>, which further demonstrates the advantages of the approach (Fig. 4a). Furthermore, after releasing the  $\text{Cs}^+$  ions, the remaining crown ether assemblies also play a passivating role as a modulator of surface defects, further improving the PSC performance (Fig. 4a). This is in accordance with the binding mode previously assessed by solid-state NMR spectroscopy and DFT calculations. Consequently, the synergistic effect of the  $\text{Cs}^+$  gradient structure and crown ether surface modulation contribute to the significant improvement of photovoltaic performances through a multimodal host–guest complexation approach, i.e., beneficially affecting both bulk and surface properties. This strategy could also be employed in the delivery of other alkali metal cations<sup>19,20</sup>, which we demonstrate by using  $\text{Rb}^+$  ions (Supplementary Fig. 11); however, we note that since, unlike  $\text{Cs}^+$ ,  $\text{Rb}^+$  has been shown not to incorporate into bulk perovskites by occupying A cation sites, rather passivation of grain boundary defects by  $\text{Rb}^+$ -rich phases is the most likely mechanism in this case, as previously indicated<sup>28</sup>. Moreover, we further illustrate the generality of the approach by fabricating different perovskite compositions, both Br/MA-based and Br/MA-free  $\text{FAPbI}_3$  (Supplementary Fig. 12a). We note that the perovskite compositions based on excess A-cations (such as FAI) are not the subject of this investigation. The  $J_{\text{SC}}$  value obtained from the  $J$ - $V$  characteristics matches (within 2%) the integrated currents obtained from the external quantum efficiency (EQE; Supplementary Fig. 12b), excluding any significant spectral mismatch between our simulator and the AM1.5 G solar source.

We further investigated the origin of the improved photovoltaic performance by performing time-resolved photoluminescence (TRPL) measurements to study the carrier transport and recombination at the perovskite layer deposited on microscope glass substrates. To evaluate the TRPL data we applied a kinetic model described in our previous study<sup>37</sup>. Assuming a negligible surface recombination rate, we calculate the average monomolecular bulk recombination constant  $k_1$  to be  $2.3 \times 10^5$  s<sup>-1</sup> for the control and  $1.4 \times 10^5$  s<sup>-1</sup> for the target Cs-doped film (the TRPL data and the fit curves are shown in Supplementary Fig. 13). This indicates that the nonradiative recombination channels in perovskite films have been suppressed by the treatment, which was further demonstrated by the increased perovskite emission in

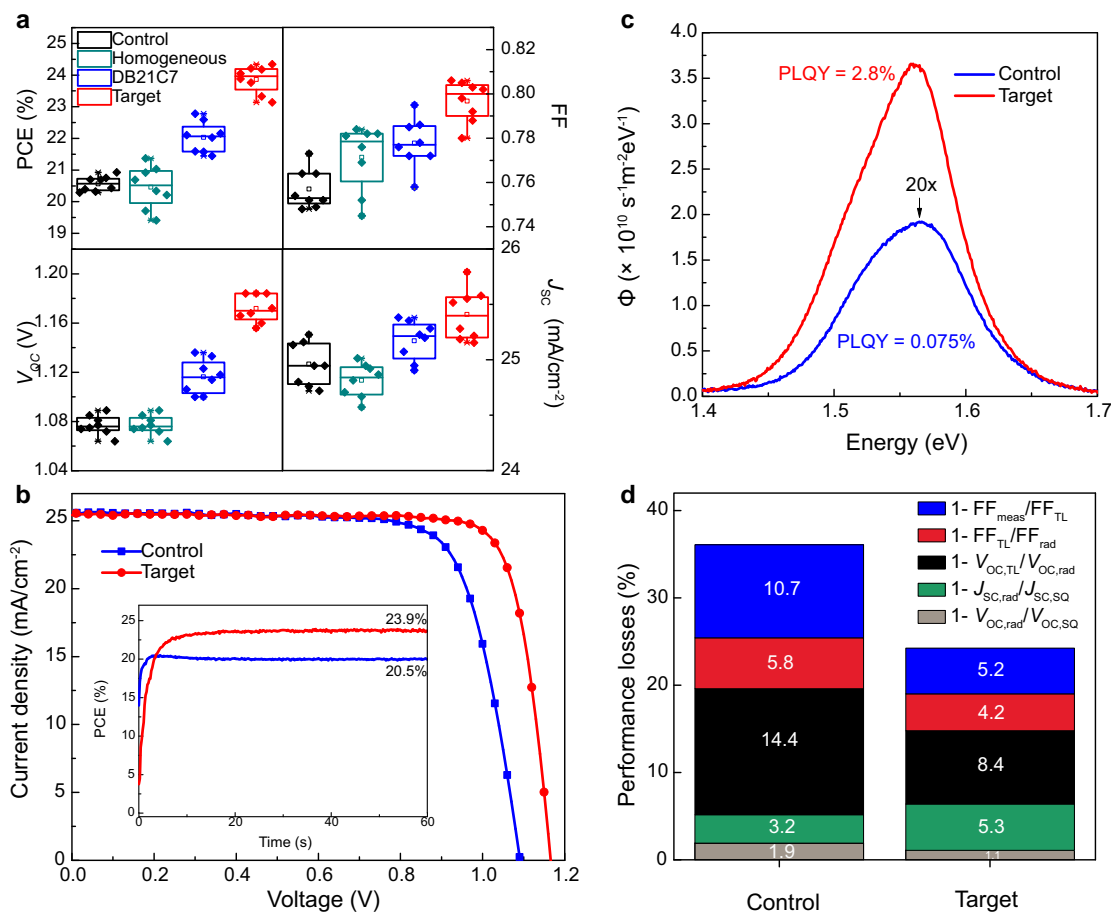


**Fig. 4 Photovoltaic device performance.** **a** Photovoltaic metrics of devices without Cs doping (control), with homogeneous Cs doping, after treatment with DB21C7–CsI (target) and after just crown ether (DB21C7) treatment. **b** J–V curves of the champion control and target PSCs. The inset shows the maximum power point tracking data. An anti-reflection coating was used for the champion devices. **c** Photoluminescence spectral photon flux  $\Phi$  measured on full devices. **d** Breakdown of losses derived from the J–V curves in **b**; radiative  $J_{sc}$  and  $V_{oc}$  losses are shown in green and grey, respectively; non-radiative  $V_{oc}$  and FF losses in black and red; transport losses affecting FF in blue.

the cathodoluminescence (CL) mapping (Supplementary Fig. 14) and decreased ideality factor  $n$  (from 1.51 to 1.41; Supplementary Fig. 15). These changes are expected to be further reflected by the quasi-Fermi level splitting ( $\Delta E_F$ ) which represents the upper limit for the  $V_{oc}$ <sup>38,39</sup>. For this we measured the absolute spectral photon flux  $\Phi$  in an integrating sphere (Fig. 4c) and derived the PL quantum yield (PLQY) according to the method described in de Mello et al.<sup>40</sup>,  $\Delta E_F$  was determined by  $\Delta E_F = q V_{oc,rad} + k_B T \ln(\text{PLQY})$ , where  $q$  is the elementary charge,  $V_{oc,rad}$  the radiative limit of  $V_{oc}$ ,  $k_B$  the Boltzmann constant, and  $T$  the device temperature (25 °C). The determination of  $V_{oc,rad}$  from the absorbance spectrum (Supplementary Fig. 16) is described in detail in our previous work<sup>37</sup> (the values are shown in Supplementary Table 2).  $\Delta E_F$  for the control device is 1.09 eV and for the target device 1.17 eV which is in very good agreement with the measured  $V_{oc}$  (Fig. 4a). This confirms that the  $V_{oc}$  improvement originates mainly from a  $\Delta E_F$  increase, and thus from a reduction in non-radiative recombination. Further analysis of the PL spectra<sup>41</sup> reveal no significant contribution arising from Urbach energy and radiative-recombination  $V_{oc}$  limit differences (Supplementary Fig. 16 and Supplementary Table 2).

The origin of the performance improvement is further analyzed by investigating the devices' diode characteristics (as detailed in Supplementary Note 2, Supplementary Figs. 17 and 18,

and Supplementary Tables 3 and 4). The analysis of performance losses (Fig. 4d) shows that a significant improvement in non-radiative losses is observed, decreasing from 20.2% in the control device to 12.6% in the target device, confirming the role of the reduction of non-radiative recombination as the main driver for the performance improvement observed here. Meanwhile, a notable improvement in transport losses (10.7% to 5.2%) is also observed, arising from decreases in series resistance and ideality factor, which are both traced to the suppression of interfacial defects or barriers<sup>42</sup>. The suppression of interfacial defects is also relevant to the overall stability of the resulting devices.

**Stability and environmental impact.** We investigated the stability (shelf life) of the perovskite films and the corresponding devices by exposing the films to an ambient air environment of  $60 \pm 10\%$  relative humidity and temperature of  $25 \pm 1$  °C, respectively (Fig. 5a–b). The monthly average humidity during the aging test is presented in Fig. 5b. The Cs-complex surface treatment was found to significantly enhance the stability under these conditions, as the target perovskite film was stable in air for more than one year (380 days), while the control film degraded completely within 5 days. In addition, we probed the long-term operational stability of the unencapsulated PSCs under one-sun illumination by maximum power point tracking (Fig. 5c). The target device exhibited very high photostability, maintaining

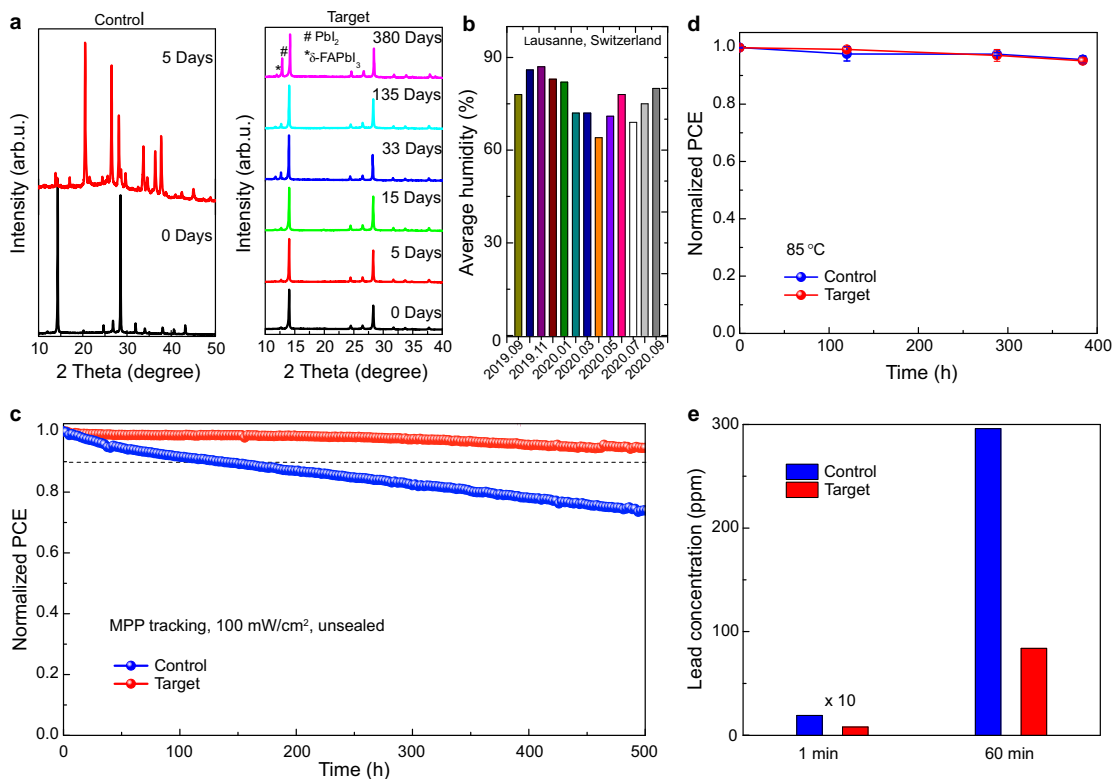


**Fig. 5 Stability and environmental impact.** **a** Ambient stability of the control perovskite film (left) and target perovskite film (right) based on the evolution of the XRD patterns of the perovskite films stored in an ambient environment for various times. **b** The average relative humidity during the aging process in Lausanne, Switzerland. **c** Maximum power point tracking measured with the unencapsulated device under full solar illumination (AM 1.5 G, 100 mW cm<sup>-2</sup> in N<sub>2</sub>, 25 °C). **d** Thermal stability of perovskite devices at an elevated temperature of 85 °C. **e** Assessment of lead leakage upon immersing solar cells into water. The PCE refers to the steady-state efficiency. The concentration of lead in water was determined by inductively coupled plasma optical emission spectroscopy (ICP-OES) measurement.

>95% of its initial PCE over 500 h of illumination, whereas the control device degraded to 80% of initial PCE in the first 300 h. The enhanced ambient and operational stability can be attributed to a lower concentration of defects at the interface between the hole transport material and the perovskite absorber, as well as to fewer impurities (including excess PbI<sub>2</sub><sup>11</sup> and non-perovskite polytypes) on the surface and in the bulk of FAPbI<sub>3</sub>, caused by Cs<sup>+</sup> infusion via the host-guest complexation and the corresponding nanostructures. Finally, the devices maintain >90% of their operational stability over 300 h at elevated temperatures of 85 °C (Fig. 5d). Under these accelerated aging conditions, the stabilities of the control and treated devices are comparable, which is likely due to the bulk becoming more homogeneous, whereas the surface still retains a local Cs-rich gradient structure as indicated by the elemental mapping (Supplementary Fig. 19). Moreover, the capacity for competitive complexation of Pb cations (Supplementary Table 1) enables lead leakage to be suppressed, which has been probed by immersing the solar cells in water and quantifying the lead content, showing that presence of the crown ether hosts mitigates the detrimental environmental impact of lead (Fig. 5e). This has been shown for the optimal concentrations of the crown ether used in the solar cell fabrication, which is rather low, and increasing this content is likely to further suppress the environmental impact of lead. Treatment with Cs-crown ether complexes therefore provides a versatile approach for the enhancement of performance and stability of perovskite-based devices, while reducing their environmental impact by virtue of multimodal host-guest complexation, suggesting wide-ranging applications.

## Methods

**Materials.** Lead iodide (PbI<sub>2</sub>) is purchased from Alfa Aesar. Formamidinium iodide (FAI) and titanium dioxide paste (TiO<sub>2</sub>-30 NRD) are purchased from Greatcell. 2,2',7,7'-Tetrakis[N,N-di(4-methoxyphenyl)amino]-9,9'-spirobifluorene (Spiro-OMeTAD) is purchased from Xi'an Polymer Light Technology Corp. Methylammonium lead tribromide (MAPbBr<sub>3</sub>) purchased from Share Chem. Ultra-dry dimethylformamide (DMF), dimethyl sulfoxide (DMSO), ethanol (EtOH), and chlorobenzene (CB) are purchased from Acros. Dibenzo-21-crown-7 (DB21C7), cesium iodide (CsI), cesium bromide (CsBr), cesium fluoride (CsF), cesium chloride (CsCl), 4-*tert*-butyl pyridine (TBP), lithium bis(trifluorosulfonyl) imide (LiTFSI), acetonitrile (ACN), acetyl acetone, titanium diisopropoxide bis (acetylacetonate) 75 wt.% in isopropanol, and methylammonium chloride (MACl) are purchased from Sigma-Aldrich. Fluorine-doped tin oxide (FTO) (10 Ω/sq) conductive glass is purchased from Nippon Sheet Glass (NSG). All the chemicals are used as received without further purification.

**Synthesis of CsX-DB21C7 complex.** CsX-DB21C7 complex (X = F, Cl, Br, I) is synthesized by mixing DB21C7 and CsX with 1:1.2 mole ratio in 1 mL dry chlorobenzene and stirring at 50 °C for 7 days. The solution was filtered to obtain a nearly quantitative amount of the complex, which was used for device fabrication. The concentration of CsX-DB21C7 solution is controlled by the amount of crown ether.

**Preparation of perovskite precursor solution.** For (FAPbI<sub>3</sub>)<sub>0.97</sub>(MAPbBr<sub>3</sub>)<sub>0.03</sub> precursor solution preparation, a mixture of PbI<sub>2</sub> (735 mg), FAI (252 mg), MAPbBr<sub>3</sub> (21 mg), and MACl (30 mg) is dissolved in 1 mL mixed solution of DMF and DMSO (volume ratio of DMF/DMSO of 4:1). For the homogeneously doped perovskite, 50 μL CsI solution (390 mg/mL in DMSO) is added to the 1.1 mL above (FAPbI<sub>3</sub>)<sub>0.97</sub>(MAPbBr<sub>3</sub>)<sub>0.03</sub> precursor solution to prepare ~4 at% Cs-doped perovskite film. For pure FAPbI<sub>3</sub> precursor solution preparation, a mixture of PbI<sub>2</sub> (755 mg), FAI (252 mg), and MACl (40 mg) is dissolved in 1 mL mixed solution of DMF and DMSO (volume ratio of DMF/DMSO of 4:1).



**Device fabrication.** FTO substrates are cleaned using 2% Hellmanex aqueous solution, deionized water, acetone, and ethanol consecutively by sonicating for 20 min for each solvent. After drying with compressed air, UV-Ozone treatment for 15 min is applied for further cleaning. Compact TiO<sub>2</sub> (c-TiO<sub>2</sub>) is deposited on top of FTO using spray pyrolysis method: the substrates are preheated to 450 °C; a precursor solution of titanium diisopropoxide bis(acetylacetonate), 75 wt.% in isopropanol is diluted with ethanol with a volume ratio of 1:9 and the addition of 4% volume ratio of acetylacetonate. After spray pyrolysis, the FTO/c-TiO<sub>2</sub> substrate is allowed to heat at 450 °C for 30 min before cooling down to room temperature. Mesoscopic TiO<sub>2</sub> (mp-TiO<sub>2</sub>) is applied by spin-coating a diluted solution of 30 NR-D paste (mass ratio of paste:ethanol = 1:10) at 4000 rpm with the acceleration of 2000 rpm/s, followed by sintering at 450 °C for 60 min to obtain mp-TiO<sub>2</sub> substrate. 0.1 M LiTFSI solution is then coated on the mp-TiO<sub>2</sub> according to our previous report<sup>36</sup>. Another sintering process at 450 °C for 30 min is performed. The Li-treated mp-TiO<sub>2</sub> is transferred to dry box for device fabrication intermediately. The perovskite active layer is deposited using antisolvent method. The corresponding perovskite precursor solution is deposited on the freshly prepared FTO/c-TiO<sub>2</sub>/mp-TiO<sub>2</sub> substrate with a two-step spin-coating method at 1000 rpm for 10 s and followed by 5000 rpm for 25 s. 200 µL of diethyl ether is applied at the last 10 s. After spin-coating, the substrate is allowed to anneal at 150 °C for 10 min, then 100 °C for 10 min. The whole procedure is done in a glovebox filled with dry air. The CsX-DB21C7 treatment is conducted by coating the as-prepared perovskite with a solution of CsX-DB21C7 complex solution (100 µL) with various concentration. The solutions are kept on surface of the perovskite film for 2 s, and substantially spin-coated at 4000 rpm for 30 s. The treated perovskite films are annealed at 100 °C for 5 min. The optimized concentration is 8 mg/mL. Later, the perovskite films are washed with 100 µL CB five times (the effects of the antisolvent are excluded by comparison in a control experiment; Supplementary Fig. 20). The doped spiro-OMeTAD solution was spin-casted on the surface of the perovskite at 4000 rpm with acceleration of 2000 rpm/s for 30 s. Spiro-OMeTAD is dissolved in chlorobenzene with a concentration of 90 mg/mL, which is doped by 23 µL LiTFSI (520 mg/mL in CH<sub>3</sub>CN) and 39.5 µL 4-*tert*-butyl pyridine, and 10 µL FK209 (375 mg/mL in ACN). The whole procedure is carried out in a glovebox filled with dry air (temperature < 28 °C; relative humidity < 15%). The device fabrication is completed with deposition of gold electrode (~70 nm) by evaporation.

**Photovoltaic performance measurements.** The prepared perovskite solar cells were measured using a 300 W Xenon light source from Oriel. The spectral mismatch between AM 1.5 G and the solar simulator was calibrated by a Schott K113 Tempax filter (Prasopms G; as & Optik GmbH). Before each measurement, the exact light intensity was determined using a calibrated Si reference diode (certified and calibrated by Newport Corporation PV Lab, Bozeman, MT, USA) equipped with an infrared cut-off filter (KG-3, Schott). Keithley 2400 is used for the current-voltage scan by applying an external voltage bias and measuring the response current with a scan rate of 50 mV/s. The device area was 0.25 cm<sup>2</sup> (0.5 cm × 0.5 cm). The cells were masked with a black metal mask with an area of 0.16 cm<sup>2</sup>. No preconditioning (e.g., bias and light soaking) was used for the photovoltaic measurement. External quantum efficiency (EQE) was recorded with a commercial apparatus (Aegeo-Ariadne, Cicci Research s.r.l.) based on a 300 W Xenon lamp. Stability of the cells was measured under a white light-emitting diode lamp with biologic MPG2 potentiostat and was performed under open air. The device area is masked to around 0.13 cm<sup>2</sup>. The spectral mismatch between AM 1.5 G and the solar simulator was calibrated by a Schott K113 Tempax filter, whose light intensity is calibrated with a silicon diode. The light intensity is around 100 mW cm<sup>-2</sup>, and the actual current is adjusted according to in-time calibration result from the silicon diode. The stability data is acquired from MPP tracking of unencapsulated device under a continuous nitrogen flow at 25 °C.

**GIWAXS and pXRD measurements.** X-ray scattering experiments were done at beamline P08 at PETRA III (DESY) with a photon energy of 18 keV under nitrogen atmosphere. The beam size was 100 µm in vertical direction and 500 µm in horizontal direction. GIWAXS data were measured with a PerkinElmer XRD1621 area detector under various angles of incidence. Powder X-ray diffraction (pXRD) spectra were recorded on an X'Pert MPD PRO (PANalytical) equipped with a ceramic tube providing Ni-filtered (Cu anode,  $\lambda = 1.54060 \text{ \AA}$ ) radiation and a RTMS X'Celerator (PANalytical).

**SEM and EDX measurements.** The morphologies and element mapping of the films were characterized using high-resolution scanning electron microscope (Zeiss Merlin) with an in-lens detector.

**STEM-EDX measurements.** Transmission electron microscopy (TEM) investigations were undertaken to study the microstructure and chemical composition using a Thermo Fisher Tecnai Osiris electron microscope under 200 kV accelerating voltage. Energy dispersive X-ray spectroscopy (EDX) elemental mapping were carried out using the TEM-attached 4 super-detectors, combining with high angle annular dark field (HAADF) images in scanning transmission electron microscopy (STEM) mode with a spot size of 0.5 nm and step size of 1.0 nm. TEM

lamellae are extracted and thinned down using Focused Ion Beam (Gemini NVision 40) at 30 kV and finally polished at 5 kV.

**PL, TRPL, and UV-Vis measurements.** UV-Vis absorptions were measured using Varian Cary 500 spectrometer (Varian USA). Photoluminescence lifetime (TCSPC) was measured using an Edinburgh Instruments lifspec II fluorescence spectrometer; a picosecond pulse diode laser (EPL-510, excitation wavelength 510 nm, pulse width < 60 ps, fluence < 3 nJ/cm<sup>2</sup>) was used. Photoluminescence spectral photon flux was measured using an Andor Kymera 193i spectrograph and a 660 nm continuous-wave laser set at 1-Sun equivalent photon flux (1.1 µm beam full-width half-maximum, 632 µW); photoluminescence was collected at normal incidence using a 0.1 NA, 110 µm-diameter optical fiber.

**XPS measurements.** XPS measurements were performed with a PHI VersaProbe II scanning XPS microprobe using a monochromatic Al K $\alpha$  X-ray of 24.8-W power with a beam size of 100 nm. Core-level signals were obtained at 45° take-off angle. All peaks were calibrated using C 1s peak at 284.8 eV to correct charge shift of binding energies. Curve fitting was performed using the PHI MultiPak software. Depth profiling etching speed was calibrated using Si as standard. The Cs diffusion length is estimated by combing the I 3d level XPS depth profiles and cross-sectional SEM image of treated perovskite film. In detail, the average thickness of treated perovskite film is calculated to be 820 ± 80 nm from the cross-sectional SEM in Supplementary Fig. 4b. The I 3d signal can only be detected at layer 22 in the XPS depth profiles. So, the sputtering thickness for each layer is 37.3 ± 3.7 nm. Considering the Cs 3d signal can only be detected at layer 13, the Cs diffusion length in the treated perovskite is calculated to be 484 ± 49 nm. An ultraviolet photoelectron spectrometer (UPS) equipped with a He-I source ( $h\nu = 21.22 \text{ eV}$ ) (AXIS Nova, Kratos Analytical Ltd, UK) was used to determine the valence band energy and Fermi-level.

**Solid-state NMR measurements.** Room temperature <sup>133</sup>Cs (118.04 MHz) and <sup>14</sup>N (65.37 MHz) NMR spectra were recorded on a Bruker Avance 400 MHz Neo 21.1 T spectrometer equipped with a 3.2 mm low-temperature CPMAS probe. <sup>133</sup>Cs shifts were referenced to 1 M aqueous solution of CsCl, using solid CsI ( $\delta = 271.05 \text{ ppm}$ ) as a secondary reference. <sup>133</sup>Cs spectra were recorded with a Hahn echo and the following recycle delays: CsI, 5 s; CsI-crown ether complex, 1 s; mechanosynthesised and thin film perovskite samples, 15 s. <sup>14</sup>N spectra were acquired with a Hahn echo and a repetition time of 53 ms. <sup>14</sup>N spectra were referenced to solid NH<sub>4</sub>Cl (0 ppm) at 298 K.

**Liquid <sup>1</sup>H NMR measurements.** <sup>1</sup>H NMR spectra of Cs-DB21C7 complex was conducted on a proton nuclear magnetic resonance spectrometer (NMR, Avance 400, Bruker) using dichloromethane-*d*<sub>2</sub> as solvent at ambient temperature (300 K).

**TOF-SIMS measurements.** The TOF-SIMS measurements (Model TOF-SIMS V, ION-TOF GmbH) were performed with the pulsed primary ions from a C<sub>60</sub> (10 keV) for the sputtering and a Bi<sup>+</sup> pulsed primary ion beam for the analysis (25 keV).

**Cathodoluminescence (CL) measurements.** CL spectra were acquired on the Attolight ROSA 4634. CL SEM operating at 2 keV with the sample held at stage temperature of 10 K in a vacuum of < 10<sup>-7</sup> Torr with probe current of a few 100 s pA. CL signal integrated for 1 ms per pixel. The spectrometer centered at 900 nm with spectral range from 622 to 1176 nm. Sample is kept slightly out of focus to even out the dosis distribution in each pixel. Because the sample is very sensitive to beam damage, we ensure to expose each area only once with the electron beam, during acquisition of the CL map. SE images to retrieve morphology are acquired posteriori. Hyperspectral maps were acquired with 128 × 128 pixel resolution, a pixel size of 104 nm, and a pixel dwell (spectrum exposure) time of 1 ms. The average center emission wavelength for each sample type was determined and false colored CL emission maps were reconstructed from deconvoluted CL intensity counts in the pixel spectra by subtracting the background and fitting the center CL emission peak with a Gaussian function.

**Lead leakage test.** A piece of a perovskite solar cell (substrate size: 14 × 17 mm) was immersed into 40 ml deionized water. The concentration of the Pb<sup>2+</sup> were determined using a ICP-OES 5110 (Agilent) instrument.

**Computational methods.** For calculating the relative energies between polytypes, we used supercells of 144 atoms for each poly-type of FAPbI<sub>3</sub>. To understand the effect of Cs on stabilization of cubic phase, we computed the relative energies between the cubic phase and 4H polytype by doping different Cs concentrations into cubic phase and 4H. All the structures are reported in the Supplementary Figs. 21–23. For calculating energies, we performed variable-cell DFT calculations with Perdew–Burke–Ernzerhof (PBE)<sup>43</sup> functional with D3-vdW<sup>44</sup> dispersion corrections. The Quantum Espresso<sup>45</sup> package is used for the DFT calculations with ultra-soft pseudo-potentials for valence-core electron interactions with k-

point sampling ( $3 \times 2 \times 1$  grid for delta phase,  $3 \times 1 \times 2$  grid for 4H,  $3 \times 2 \times 1$  grid for 6H and  $1 \times 1 \times 2$  grid for cubic phase) with a plane wave basis set of 60 Ry kinetic energy cutoff and 420 Ry density cutoff. To obtain DFT-optimized structure of CsI-DB21C7, we have used PBEsol<sup>46</sup> functional with D2-vdW dispersion corrections<sup>44</sup> using the ultra-soft pseudopotentials for valence-core electron interactions and a k-point sampling ( $8 \times 3 \times 4$ ) with a plane wave basis set of 40 Ry kinetic energy cutoff and 280 Ry density cutoff. Complexation energies of DB21C7-Cs<sup>+</sup>, DB21C7-FA<sup>+</sup>, and DB21C7-Pb<sup>2+</sup> were calculated for the gas phases of the reactants and the products, based on Generalized Gradient Approximation (GGA) of density functional theory, employing the PBE functional<sup>44</sup> within the CPMD package<sup>47</sup>. Valence-core electron interactions were modeled via norm-conserving pseudopotentials in a simulation box of  $50 \times 50 \times 50 \text{ \AA}^3$  together with a 100 Ry kinetic energy cutoff. The structures of Cs-doped cubic FAPbI<sub>3</sub> were optimized at DFT level using the PBEsol functional<sup>46</sup> within the Quantum Espresso suite<sup>45</sup>. To study the effect of different doping models,  $2 \times 2 \times 6$  supercells of cubic FAPbI<sub>3</sub> were used. The model  $1 \times 4$  was constructed by replacing an entire  $2 \times 2$  layer of FA<sup>+</sup> by Cs<sup>+</sup>. Similarly, the model  $2 \times 2$  was constructed by replacing 2 FA<sup>+</sup> cations in 2 layers by Cs<sup>+</sup> ions. Lastly, the model  $4 \times 1$  was constructed by replacing one FA<sup>+</sup> cation by Cs<sup>+</sup> in each of the 4 layers. To study the effect of Cs<sup>+</sup> on defects at the perovskite surface, FAI-terminated slabs of cubic FAPbI<sub>3</sub> were employed. FA<sup>+</sup> vacancy-containing slab was created by removing one FA<sup>+</sup> from the surface. Cs<sup>+</sup>-treated slab with a FA<sup>+</sup> vacancy was created by filling the FA<sup>+</sup> vacant site by a Cs<sup>+</sup> ion. A vacuum gap of 25 Å was used for all slab structures to prevent interaction of the slab images. A k-point grid of  $2 \times 2 \times 1$  ( $4 \times 4 \times 1$  for post processing analyses) and ultra-soft pseudopotentials for valence core electron interactions with a plane wave basis set of 60 and 420 Ry kinetic energy cutoff for the expansion of the wavefunction and the density, respectively, were employed for both bulk and slab structures. The hybrid PBE0 functional<sup>48</sup> was utilized to calculate band gaps taking also spin orbit coupling (SOC) effects into account, with norm-conserving pseudopotentials of 80 Ry wavefunction cutoff and 320 Ry density cutoff. To compare valence band maximum and conduction band minimum of different configurations, energy levels were aligned with respect to the energy levels of 5d orbitals of Pb atoms.

**Reporting summary.** Further information on research design is available in the Nature Research Reporting Summary linked to this article.

## Data availability

Data that support the findings of this study are available in Supplementary Data Files in the Supplementary Information section. All relevant data are available at <https://doi.org/10.5281/zenodo.4768098> under the license CC-BY-4.0 (Creative Commons Attribution 4.0 International). Source data are provided with this paper.

Received: 30 November 2020; Accepted: 29 March 2021;

Published online: 07 June 2021

## References

- Saparov, B. & Mitzi, D. B. Organic-inorganic perovskites: structural versatility for functional materials design. *Chem. Rev.* **116**, 4558–4596 (2016).
- Ogomi, Y. et al. CH<sub>3</sub>NH<sub>3</sub>Sn<sub>x</sub>Pb<sub>(1-x)</sub>I<sub>3</sub> perovskite solar cells covering up to 1060 nm. *J. Phys. Chem. Lett.* **5**, 1004–1011 (2014).
- Tsai, H. et al. High-efficiency two-dimensional Ruddlesden-Popper perovskite solar cells. *Nature* **536**, 312–316 (2016).
- Lin, R. et al. Monolithic all-perovskite tandem solar cells with 24.8% efficiency exploiting comproportionation to suppress Sn(II) oxidation in precursor ink. *Nat. Energy* **4**, 864–873 (2019).
- Zhao, Y. & Zhu, K. Organic-inorganic hybrid lead halide perovskites for optoelectronic and electronic applications. *Chem. Soc. Rev.* **45**, 655–689 (2016).
- Bisquert, J. & Jurez-Perez, E. J. The Causes of Degradation of Perovskite Solar Cells. *J. Phys. Chem. Lett.* **10**, 5889–5891 (2019).
- Zhang, H., Nazeeruddin, M. K. & Choy, W. C. H. Perovskite photovoltaics: the significant role of ligands in film formation, passivation, and stability. *Adv. Mater.* **31**, 1805702 (2019).
- Jiang, Q. et al. Surface passivation of perovskite film for efficient solar cells. *Nat. Photonics* **13**, 460–466 (2019).
- Wang, R. et al. Constructive molecular configurations for surface-defect passivation of perovskite photovoltaics. *Science* **366**, 1509–1513 (2019).
- Zheng, X. et al. Managing grains and interfaces via ligand anchoring enables 22.3%-efficiency inverted perovskite solar cells. *Nat. Energy* **5**, 131–140 (2020).
- Tumen-Ulzii, G. et al. Detrimental effect of unreacted PbI<sub>2</sub> on the long-term stability of perovskite solar cells. *Adv. Mater.* **32**, 1905035 (2020).
- Yin, W.-J., Shi, T. & Yan, Y. Unusual defect physics in CH<sub>3</sub>NH<sub>3</sub>PbI<sub>3</sub> perovskite solar cell absorber. *Appl. Phys. Lett.* **104**, 063903 (2014).
- Krishna, A. et al. Defect passivation via the incorporation of tetrapropylammonium cation leading to stability enhancement in lead halide perovskite. *Adv. Func. Mater.* **30**, 1909737 (2020).
- Ruiz-Preciado, M. A. et al. Supramolecular modulation of hybrid perovskite solar cells via bifunctional halogen bonding revealed by two-dimensional <sup>19</sup>F solid-state NMR spectroscopy. *J. Am. Chem. Soc.* **142**, 1645–1654 (2020).
- Zhang, F. et al. Suppressing defects through the synergistic effect of a Lewis base and a Lewis acid for highly efficient and stable perovskite solar cells. *Energy Environ. Sci.* **11**, 3480–3490 (2018).
- Gratia, P. et al. The many faces of mixed ion perovskites: unraveling and understanding the crystallization process. *ACS Energy Lett.* **2**, 2686–2693 (2017).
- Saliba, M. et al. Cesium-containing triple cation perovskite solar cells: improved stability, reproducibility and high efficiency. *Energy Environ. Sci.* **9**, 1989–1997 (2016).
- Park, Y. H. et al. Inorganic rubidium cation as an enhancer for photovoltaic performance and moisture stability of HC(NH<sub>2</sub>)<sub>2</sub>PbI<sub>3</sub> perovskite solar cells. *Adv. Funct. Mater.* **27**, 1605988 (2017).
- Landini, D., Maia, A., Montanari, F. & Pirisi, F. M. Crown ethers as phase-transfer catalysts. A comparison of anionic activation in aqueous-organic two-phase systems and in low polarity anhydrous solutions by perhydrodibenzo-18-crown-6, lipophilic quaternary salts, and cryptands. *J. Chem. Soc., Perkin Trans. 2*, 46–51 (1980).
- Steed, J. W. First- and second-sphere coordination chemistry of alkali metal crown ether complexes. *Coord. Chem. Rev.* **215**, 171–221 (2001).
- A Veldhuis, S. et al. Crown ethers enable room-temperature synthesis of CsPbBr<sub>3</sub> quantum dots for light-emitting diodes. *ACS Energy Lett.* **3**, 526–531 (2018).
- Yang, M. et al. Facile fabrication of large-grain CH<sub>3</sub>NH<sub>3</sub>PbI<sub>3-x</sub>Br<sub>x</sub> films for high-efficiency solar cells via CH<sub>3</sub>NH<sub>3</sub>Br-selective Ostwald ripening. *Nat. Commun.* **7**, 12305 (2016).
- Ono, L. K., Qi, Y. & Liu, S. Progress toward stable lead halide perovskite solar cells. *Joule* **2**, 1961–1990 (2018).
- Zu, F. et al. Constructing the electronic structure of CH<sub>3</sub>NH<sub>3</sub>PbI<sub>3</sub> and CH<sub>3</sub>NH<sub>3</sub>PbBr<sub>3</sub> perovskite thin films from single-crystal band structure measurements. *J. Phys. Chem. Lett.* **10**, 601–609 (2019).
- Greco, A. et al. Kinetics of ion-exchange reactions in hybrid organic-inorganic perovskite thin films studied by in situ real-time X-ray scattering. *J. Phys. Chem. Lett.* **9**, 6750–6754 (2018).
- Wiedemann, D. & Kohl, J. Invariom-model refinement and Hirshfeld surface analysis of well-ordered solvent-free dibenzo-21-crown-7. *Acta Cryst. Sect. C* **73**, 654–659 (2017).
- Hanrahan, M. P., Men, L., Rosales, B. A., Vela, J. & Rossini, A. J. Sensitivity-enhanced <sup>207</sup>Pb solid-state NMR spectroscopy for the rapid, non-destructive characterization of organolead halide perovskites. *Chem. Mater.* **30**, 7005–7015 (2018).
- Kubicki, D. J. et al. Phase segregation in Cs-, Rb- and K-doped mixed-cation (MA)<sub>x</sub>(FA)<sub>1-x</sub>PbI<sub>3</sub> hybrid perovskites from solid-state NMR. *J. Am. Chem. Soc.* **139**, 14173–14180 (2017).
- Zhang, J. et al. Intermediate phase enhances inorganic perovskite and metal oxide interface for efficient photovoltaics. *Joule* **4**, 222–234 (2020).
- Bi, D. et al. Multifunctional molecular modulators for perovskite solar cells with over 20% efficiency and high operational stability. *Nat. Commun.* **9**, 4482 (2018).
- Milić, J. V. et al. Supramolecular engineering for formamidinium-based layered 2D perovskite solar cells: structural complexity and dynamics revealed by solid-state NMR spectroscopy. *Adv. Energy Mater.* **9**, 1900284 (2019).
- Franssen, W. M. J., Bruijnaers, B. J., Portengen, V. H. L. & Kentgens, A. P. M. Dimethylammonium incorporation in lead acetate based MAPbI<sub>3</sub> perovskite solar cells. *ChemPhysChem* **19**, 3107–3115 (2018).
- Soong, L. L., Leroi, G. E. & Popov, A. I. Cesium-133 NMR studies of crown ether-cesium(1+) complexes in high dielectric amide solvents. *Inorg. Chem.* **29**, 1366–1370 (1990).
- Franssen, W. M. J., van Es, S. G. D., Dervişoğlu, R., de Wijs, G. A. & Kentgens, A. P. M. Symmetry, dynamics, and defects in methylammonium lead halide perovskites. *J. Phys. Chem. Lett.* **8**, 61–66 (2017).
- Braga, D. et al. Supramolecular complexation of alkali cations through mechanochemical reactions between crystalline solids. *Chem. Eur. J.* **10**, 3261–3269 (2004).
- Giordano, F. et al. Enhanced electronic properties in mesoporous TiO<sub>2</sub> via lithium doping for high-efficiency perovskite solar cells. *Nat. Commun.* **7**, 10379 (2016).
- Zhu, H. et al. Tailored amphiphilic molecular mitigators for stable perovskite solar cells with 23.5% efficiency. *Adv. Mater.* **32**, 1907757 (2020).
- Jeong, M. et al. Stable perovskite solar cells with efficiency exceeding 24.8% and 0.3-V voltage loss. *Science* **369**, 1615–1620 (2020).
- Wolff, C. M., Caprioglio, P., Stolterfoht, M. & Neher, D. Nonradiative recombination in perovskite solar cells: the role of interfaces. *Adv. Mater.* **31**, 1902762 (2019).

40. de Mello, J. C., Wittmann, H. F. & Friend, R. H. An improved experimental determination of external photoluminescence quantum efficiency. *Adv. Mater.* **9**, 230–232 (1997).
41. Tress, W. et al. Predicting the open-circuit voltage of  $\text{CH}_3\text{NH}_3\text{PbI}_3$  perovskite solar cells using electroluminescence and photovoltaic quantum efficiency spectra: the role of radiative and non-radiative recombination. *Adv. Energy Mater.* **5**, 1400812 (2015).
42. Tress, W. et al. Interpretation and evolution of open-circuit voltage, recombination, ideality factor and subgap defect states during reversible light-soaking and irreversible degradation of perovskite solar cells. *Energy Environ. Sci.* **11**, 151–165 (2018).
43. Perdew, J. P., Burke, K. & Ernzerhof, M. Generalized gradient approximation made simple. *Phys. Rev. Lett.* **77**, 3865–3868 (1996).
44. Grimme, S. Semiempirical GGA-type density functional constructed with a long-range dispersion correction. *J. Comput. Chem.* **27**, 1787–1799 (2006).
45. Giannozzi, P. et al. QUANTUM ESPRESSO: a modular and open-source software project for quantum simulations of materials. *J. Phys.* **21**, 395502 (2009).
46. Perdew, J. P. et al. Restoring the density-gradient expansion for exchange in solids and surfaces. *Phys. Rev. Lett.* **100**, 136406 (2008).
47. CPMD, <http://www.cpmd.org/> Copyright IBM Corp 1990–2015, Copyright MPI für Festkörperforschung Stuttgart 1997–2001.
48. Adamo, C. & Barone, V. Toward reliable density functional methods without adjustable parameters: the PBE0 model. *J. Chem. Phys.* **110**, 6158–6170 (1999).

## Acknowledgements

The project leading to this application has received funding from the European Union's Horizon 2020 research and innovation programme under Grant agreements No. 785219, 881603, and 764047. J.V.M. acknowledges the SNSF PRIMA Grant No. 193174. U.R. acknowledges SNSF Grant No. 200020-185092, NCCR-MUST, and the SINERGIA interdisciplinary research program EPISODE for funding and Swiss National Supercomputing Centre (CSCS) for computing time. L.E. is grateful for financial support from Swiss National Science Foundation Grant No. 200020-178860. L.M., A.H. (Alex), and F.S. acknowledge funding from the DFG. O.O. acknowledges funding from the Natural Sciences and Engineering Research Council of Canada. M.M. acknowledges the affiliation with the Scientific Computing Laboratory, Center for the Study of Complex Systems, Institute of Physics Belgrade, University of Belgrade, Serbia. A.H. (Anders) acknowledges the financial support from the Swiss National Science Foundation R'Equip program under the Grant number 183305. For the PL measurements the authors acknowledge the help of Wolfgang Tress and funding by the Swiss National Science Foundation (Ambizione Energy Grant no. 173617). A.K. acknowledges funding from the European Union's Horizon 2020 Research and Innovation program under the Marie Skłodowska-Curie Grant Agreement No. 843453. Z.D. and J.G. are grateful to Prof. Kay Severin and Prof. Anders Meibom for hosting and supporting his research at EPFL, respectively. The authors acknowledge the help of Mr. Shi Wang, Dr. M. D. Mensi, and Mr. Anand Agarwalla for the assistance in TOF-SIMS, UPS, and stability tests, respectively. We are also grateful to Prof. Kevin Sivula and Dr. Jun Ho Yum for KPFM measurement, Dr. Pierre Mettraux for XPS measurement, Dr. David Bi for XRD measurements, and Prof. Shien-Ping Feng for the assistance in the GIWAXS preliminary studies, respectively. We acknowledge DESY (Hamburg, Germany) for the provision of synchrotron facilities and we would like to thank Florian Bertram for assistance in using beamline P08 (PETRA III).

## Author contributions

M.G. supervised the study. H.Z. conceived the idea, designed the experiments, conducted the device fabrication and characterization. J.V.M. has conceptually contributed to the project while being involved in the mechanistic investigation, analysis, as well as project coordination. F.E. and O.O. performed the PL/TRPL characterizations and the analysis of the optoelectronic loss mechanisms. Z.Z. participated in device optimization and assisted in some sample preparations as well as GIWAXS preliminary studies. A.M., M.H., and L.E. performed the solid-state NMR studies and analysis. M.M., F.J., P.A., and U.R. were responsible for the molecular dynamics simulations and DFT calculations as well as the analysis. T.S.S. optimized the device fabrication. A.H. (Alex), L.M., and F.S. performed the GIWAXS measurements and the analysis. D.R. and Z.W. performed the SEM and EDS. Z.D. synthesized the cesium crown ether complex for ssNMR studies and performed  $^1\text{H}$  NMR characterization. A.K. assisted in device stability test and data analysis. J.G. performed the STEM/EDX measurement and analysis. S.M.Z. and A.H. (Anders) was involved in discussion and project coordination. H.Z. wrote the first manuscript draft, and all the authors contributed to the revision.

## Competing interests

The authors declare no competing interests.

## Additional information

**Supplementary information** The online version contains supplementary material available at <https://doi.org/10.1038/s41467-021-23566-2>.

**Correspondence** and requests for materials should be addressed to J.V.M. or M.G.

**Peer review information** *Nature Communications* thanks the anonymous reviewer(s) for their contribution to the peer review of this work.

**Reprints and permission information** is available at <http://www.nature.com/reprints>

**Publisher's note** Springer Nature remains neutral with regard to jurisdictional claims in published maps and institutional affiliations.



**Open Access** This article is licensed under a Creative Commons Attribution 4.0 International License, which permits use, sharing, adaptation, distribution and reproduction in any medium or format, as long as you give appropriate credit to the original author(s) and the source, provide a link to the Creative Commons license, and indicate if changes were made. The images or other third party material in this article are included in the article's Creative Commons license, unless indicated otherwise in a credit line to the material. If material is not included in the article's Creative Commons license and your intended use is not permitted by statutory regulation or exceeds the permitted use, you will need to obtain permission directly from the copyright holder. To view a copy of this license, visit <http://creativecommons.org/licenses/by/4.0/>.

© The Author(s) 2021

# Organic Spacers in 2D Perovskites: General Trends and Structure-Property Relationships from Computational Studies

Farzaneh Jahanbakhshi,<sup>a</sup> Marko Mladenović,<sup>a</sup> Mathias Dankl,<sup>a</sup> Ariadni Boziki,<sup>a</sup> Paramvir Ahlawat,<sup>a</sup> and Ursula Rothlisberger\*<sup>a</sup>

<sup>a</sup> Laboratory of Computational Chemistry and Biochemistry, École Polytechnique Fédérale de Lausanne, CH-1015 Lausanne, Switzerland, e-mail: ursula.roethlisberger@epfl.ch

Dedicated to Prof. *Michael Grätzel* on the occasion of his 76th birthday.

Addition of large organic molecules to halide perovskites has been shown to provoke dimensionality reduction and formation of two-dimensional phases that demonstrate improved long-term stabilities. Optoelectronic properties of the resulting 2D layered perovskites are strongly influenced by the chemical nature of the additive molecules, which opens immense possibilities for preparation of materials with tailored properties. However, given the huge chemical space of possible organic spacers, a systematic and exhaustive search for optimal compounds is impossible and general structure–property relationships that could guide a rational design are still largely absent. Here, we provide an overview of a series of recent computational studies from our group on different types of spacers. We first develop a simplified universal monovalent cation model to map out approximate structural stability maps as a function of the *van der Waals* radius and the magnitude of dispersion interactions to monitor the possible emergence of 2D phases. We further provide structural and photophysical insights from classical and first-principles molecular dynamics simulations and density functional theory calculations on 2D hybrid perovskites based on a wide range of spacers with different chemical nature and varying conformational properties. Our computational predictions are validated through comparison with powder diffraction, conductivity and optical measurements. Such comparative study allows for providing some general structure–property correlations, which can serve as design guidelines in the search for optimal 2D and mixed 2D/3D perovskite photovoltaic materials.

**Keywords:** 2D hybrid perovskites, *ab initio* calculations, *ab initio* molecular dynamics, compositional engineering, density functional theory, organic additives, perovskite phases.

## Introduction

Hybrid Organic-Inorganic Halide Perovskites (HOIHP) of the general formula  $ABX_3$ , with A being a monovalent cation ( $Cs^+$ , methylammonium ( $MA^+$ )  $CH_3NH_3^+$ , formamidinium ( $FA^+$ )  $CH(NH_2)_2^+$ , or guanidinium ( $GUA^+$ )  $C(NH_2)_3^+$ ), B representing a divalent cation ( $Pb^{2+}$  or  $Sn^{2+}$ ), and X featuring a halide anion ( $I^-$ ,  $Br^-$ , or  $Cl^-$ ), have been known now for nearly a decade as promising candidates for solar cell applications with outstanding electronic and transport properties. Meanwhile, their limited stability presents an unsolved issue that currently prevents their large-scale commercialization.<sup>[1–3]</sup> One of the recently

emerging routes to improve the stability of these materials, is the introduction of 2D layered Hybrid Perovskites (2DHP) that are formed upon addition of cationic organic ligands of larger size and/or bulkier shapes than the commonly used organic cations (*i.e.*,  $MA^+$  and  $FA^+$ ).<sup>[4–7]</sup> This increase in size of the monovalent cation evidently leads to an interesting transition from 3D to 2D semiconductors in two most commonly formed phases of the *Ruddlesden–Popper* (RP)  $(Y)_2(A)_{n-1}B_nX_{3n+1}$  or the *Dion–Jacobson* (DJ)  $Y(A)_{n-1}B_nX_{3n+1}$  type.<sup>[7–11]</sup> RP systems are composed of double layers of organic ligands that anchor to and impose a relative offset of adjacent inorganic slabs consisting of  $n$  layers of Pb–I octahedra (*Figure 1, a*).



Ursula Rothlisberger is a professor of computational chemistry and biochemistry at École Polytechnique Fédérale de Lausanne (EPFL). She is an Associate Editor of the ACS Journal of Chemical Theory and Computations and has served several years as a member of the Research Council of the Swiss National Science Foundation. She has been elected as a member of the International Academy of Quantum Molecular Science,

a board member of the World Association of Computationally Oriented Chemists (WATOC) and a Fellow of the American Association for the Advancement of Science (AAAS). She got numerous awards and honors including the Ron Hides Award, the Doron prize, the EuCheMS Lecture Award, the WATOC Dirac Medal and the Ružička Prize. Her research areas are concentrated on the development of first-principles and multiscale molecular dynamics simulation methods based on density functional theory and their application, adaption and extension to systems of chemical and/or biological interest and materials for energy technologies.



Farzaneh Jahanbakhshi is a doctoral researcher in computational chemistry at École Polytechnique Fédérale de Lausanne (EPFL). She graduated from Sharif University of Technology, Tehran prior to joining the group of Prof. Ursula Rothlisberger. Her research areas include computational materials design and modeling from first principles, molecular dynamics and multiscale methods. She is interested in sustainable energy development and

design of materials for clean energy technologies, including but not limited to photovoltaics.



Marko Mladenović is a soon-to-be postdoctoral research associate at ETHZ. He earned a PhD from University of Belgrade under the supervision of Dr. Nenad Vukmirović and joined the group of Prof. Ursula Rothlisberger at École Polytechnique Fédérale de Lausanne (EPFL) in 2017 as a postdoctoral researcher. He strives to find solutions to a global demand for novel, cheap and environment-friendly sources of energy,

and his research interests include the application of halide perovskites for photovoltaics and novel materials for energy storage and memory devices.



Mathias Dankl is a doctoral researcher holding a master's degree in chemistry and a bachelor's degree in physics. Since his last research internship at Lund University (Sweden) in 2015, his scientific interest is the computational and theoretical modeling of light absorbing materials. Currently, he is pursuing a PhD within the internationally recognized group of Prof. Rothlisberger at École Polytechnique Fédérale de Lausanne

(Switzerland). There, he develops methods for the computational prediction of phase stabilities in 2D/3D hybrid halide perovskites using a combined approach of ab-initio, QM and classical force field based MD methods. For the latter, he is exploiting state-of-the-art supervised machine learning techniques for constructing high quality ab-initio based force fields. He is also involved in multiple projects in close collaboration with Prof. Grätzel's experimental group, in which he investigates the influence of defects and surface additives on the stability and optical performance properties of new perovskite materials. Apart from his research on perovskites, he continues previous collaborations with Prof. Renger's group at Johannes Kepler University Linz related to the modelling of optical properties of chlorophyll based systems.



Ariadni Boziki was born in Athens, Greece in 1991. She received her diploma in Chemical Engineering from the National Technical University of Athens, in 2014. In the same year, she joined the group of Prof. Rothlisberger at Ecole Polytechnique Fédérale de Lausanne in Switzerland and completed her Ph.D. in computational chemistry in 2019. Her research interests are ab-initio and classical molecular dynamics simula-

tions, Monte Carlo simulations and ground and excited-state properties of halide perovskites, polymer/solid interfaces and biomolecules such as proteins.



Paramvir Ahlawat graduated with a M.Sc. degree in Chemical Engineering from KTH Royal Institute of Technology, Sweden. He is currently undertaking his doctoral studies in the Laboratory of Computational Chemistry and Biochemistry at EPFL Lausanne, Switzerland. His focus lies on understanding the atomic level details of the phase transition and crystallization process of halide perovskites from solution.

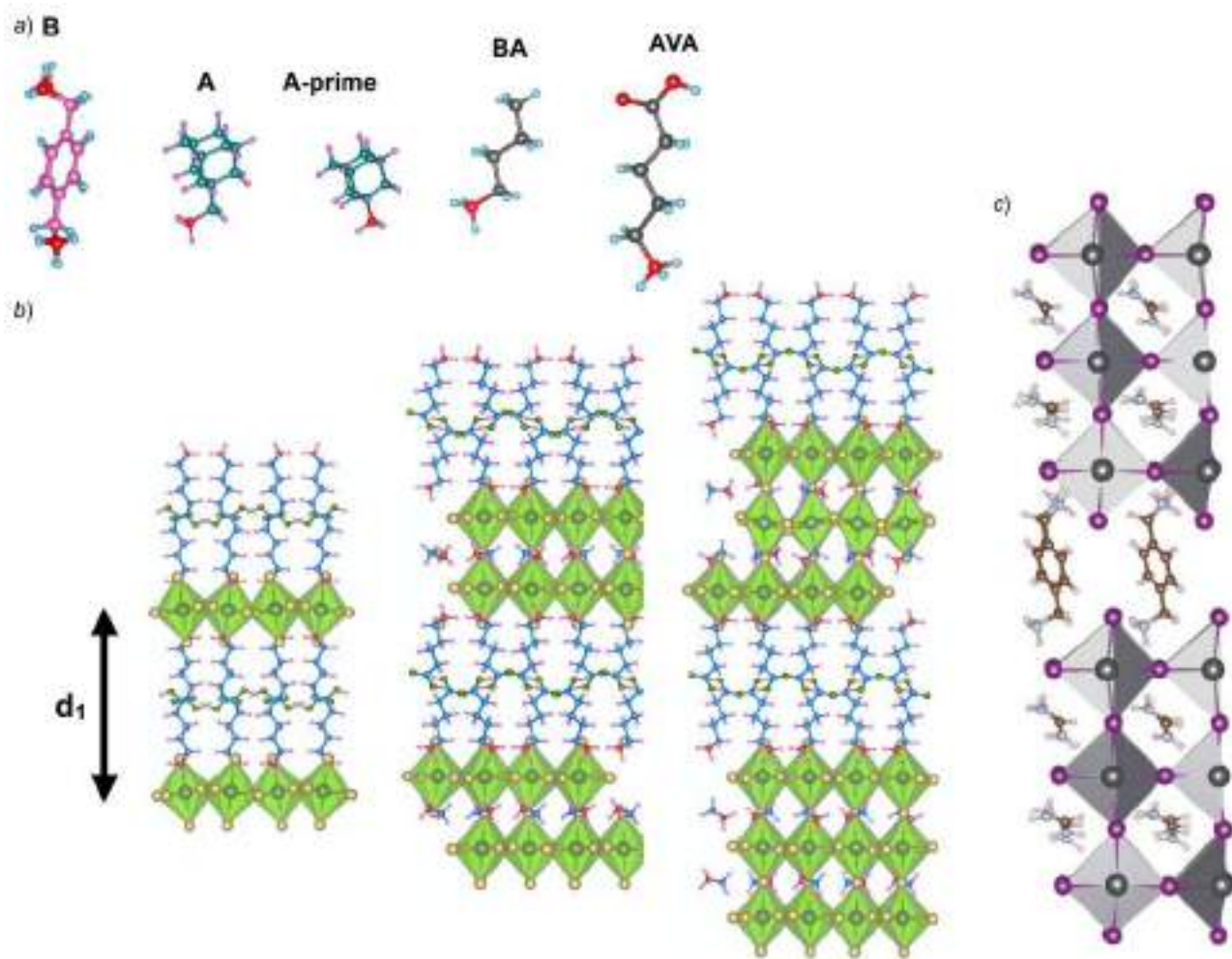


**Figure 1.** Investigated organic spacers (a), and representative examples of an RP of  $\text{AVA}_2(\text{MA})_{n-1}\text{Pb}_n\text{I}_{3n+1}$  for  $n=1-3$  (b) and a DJ phase of  $\text{BFA}_2\text{Pb}_3\text{I}_{10}$  (c).

In DJ phases on the other hand, a single layer of bi-functional ligands (Y) separates two consecutive inorganic frameworks (Figure 1,b) resulting in general in a thinner organic layer, and consequently higher orbital overlap, and improved transport properties compared to their RP counterparts.<sup>[11–15]</sup> 2D layered materials in general present longer carrier lifetimes compared to their pure 3D analogues, as a consequence of spatial confinement and image charge effects as well as higher exciton binding energies (for the lower  $n$  values), which offers possibilities for tailoring the exciton-binding energies (EBE) by playing with the thickness of the inorganic framework and the nature of the organic ligand.<sup>[5,16–18]</sup>

Extensive research has been conducted in an attempt to unravel different characteristics of both RP and DJ phases of 2DHPs ranging from structural to

electronic and finite temperature properties as a function of  $n$ .<sup>[7,8,11–13]</sup> Some of the ligands that have been examined so far include ammonium ions of aliphatic or aromatic hydrocarbon molecules with either linear or more bulky shapes, such as butylammonium (BA),<sup>[8,19]</sup> phenethylammonium (PEA),<sup>[20–22]</sup> hexylammonium (Hex),<sup>[23,24]</sup> anilinium (AnyI),<sup>[25]</sup> benzylammonium,<sup>[26]</sup> (adamantan-1-yl)methan ammonium (A), adamantylammonium (A-prime),<sup>[27,28]</sup> or (1,4-phenylene)dimethan ammonium (PDMA),<sup>[29,30]</sup> as well as functionalized spacers with hydrogen-bonding possibilities such as 4-ammonium butyric acid (4-ABA),<sup>[31]</sup> and 5-ammonium valeric acid (5-AVA),<sup>[32–37]</sup> guanine,<sup>[38]</sup> and naphthalene diimide (NDI).<sup>[39]</sup> It is however worth noting that in many of the cases listed above, pure 2-dimensional perovskites have been observed to form merely in the case of lower  $n$

values, *i.e.*, in a limited range of inorganic layer thickness (or in some cases even only for  $n=1$ ) whereas mixed 2D/3D phases are evidently formed for higher  $n$ .<sup>[8,27–30,40]</sup> This can be rationalized by a direct correlation between the thickness of the inorganic layer and the enthalpies of formation of 2DHP,<sup>[28,30]</sup> that becomes increasingly unfavorable with respect to the 3D counterpart as a function of  $n$ . In addition to the interplay between the inorganic layer thickness and the enthalpies of formation, EBEs of these systems also vary with the inorganic thickness as formerly mentioned (*e.g.* for BA-based systems, EBEs vary between 470 and 125 meV for  $n=1–4$ ).<sup>[41,42]</sup> Increasing  $n$  also leads to a considerable charge mobility increase,<sup>[43]</sup> in agreement with *ab initio* calculated hole and electron effective masses.<sup>[28,30]</sup> In addition, mixing MAPbI<sub>3</sub> with *t*-BA-based 2DHPs has been reported to help mitigate moisture instability.<sup>[44]</sup> A band gap opening accompanied by octahedral distortion away from cubic symmetry was observed in BA-based 2D systems upon fluorination of the spacers,<sup>[45]</sup> as well as in Pb–Sn 2DHP systems.<sup>[46]</sup> Charge transport properties of 2D halide perovskites have been characterized by time-resolved microwave conductivity (TRMC) measurements,<sup>[30,47]</sup> and modeled by calculating the effective masses through the band transport model.<sup>[28,30]</sup> Owing to the mostly insulating nature of the organic spacer layer, charge transport in the direction perpendicular to the inorganic layers (out-of-plane direction) through the organic layer is found to be an order of magnitude slower than within the inorganic sheets (in-plane direction).<sup>[47]</sup> Accordingly, reported effective masses for the out-of-plane direction largely suggest the break-down of the band model of transport. The effective masses in the in-plane directions on the contrary, are comparable to those in 3D halide perovskites and decrease as the thickness of the inorganic layer increases.<sup>[8,28,30]</sup> Notable exceptions to this trend are cases where the organic spacer directly contributes to the band edges, such as in the NDI molecules, some oligothiophenes and pyrene.<sup>[5,39,48]</sup> Despite recent improvements of the performance of 2D layered perovskites, for instance by suitably orienting perovskite crystallites, the power conversion efficiencies of such systems remains in general much lower compared to 3D perovskites, due to shorter diffusion lengths orthogonal to the inorganic plane and consequently, large band gaps.<sup>[19,49,50]</sup> Despite lower efficiencies, 2D systems exhibit substantial stability improvements. In particular, moisture and thermal stability increases

have been reported for lower  $n$  values of FA-based 2DHP.<sup>[6,20,35,49]</sup> In addition to the formation of pure 2D systems, organic ligands can form mixed 2D/3D structures and can also act as surface passivating layers. In this regard, the emergence of one-year stable AVA-based 2D/3D perovskite in 2017 is particularly notable.<sup>[33]</sup>

Organic ligands have also been utilized for anchoring the perovskite material to the electron transporting layer (ETL) as well as cross-linking perovskite grains leading to substantial efficiency improvements from 8.8% to 16.7% that are attributed to a more uniformly crystallized perovskite.<sup>[51]</sup> 5-AVA for which we recently reported structural and optoelectronic properties of MA-based RP phases,<sup>[37]</sup> was early on employed as anchoring component on TiO<sub>2</sub> (ETL) in perovskite devices. An efficiency of 12% due to improved retardation in charge recombination was attained for the HOOC-(CH<sub>2</sub>)<sub>3</sub>-NH<sub>3</sub><sup>+</sup> anchoring ligand.<sup>[36]</sup>

In a nutshell, 2DHPs have opened new avenues towards a next generation of efficient and more stable HOIHPs by providing a tailorable length of the quantum well and a tunable degree of hydrophobicity through an appropriate selection of both size and type of the organic ligands.<sup>[41,42,52,53]</sup> However, despite numerous studies on the efficiency and stability of 2DHPs, general designing guidelines for producing materials with desired properties are mostly lacking. Herein, we summarize computational results on different 2DHP systems (with  $n=1–3$ ), studied previously by our group, composed of both monovalent (BA, 5-AVA, A and A-prime) and bivalent (PDMA) ligands, including aliphatic (BA), aromatic (PDMA) chains, bulky ligands (A and A-prime), as well as ligands containing functional groups (AVA; *Figure 1,c*), that result in different structural and electronic properties. We present a general computational methodology to predict structures of 2DHPs, which can also be used in turn to help resolve the complexity of experimentally observed samples. Eventually, we provide a series of designing principles based on structure–property correlations in 2DHPs.

## Methods

### *Structural and Electronic Properties of 2DHPs*

Classical molecular dynamics (MD) simulations were performed to predict initial structures using the Generalized Amber Force Field (GAFF),<sup>[54,55]</sup> for modeling interactions between the ligands and the

previously reported parameters for Pb and I,<sup>[56,57]</sup> within the LAMMPS suite of codes (31 Mar 2017).<sup>[58]</sup> Trial structures were first optimized with a conjugate gradient (CG) algorithm followed by an equilibrium run in an isothermal-isobaric ensemble at higher temperatures (up to 500 K). After the system reaches the finite temperature, a 30 ns constant temperature run was performed and quenched to 0 K. More details on the MD computational scheme can be found.<sup>[28,30]</sup> To calculate the electronic properties, the Generalized Gradient Approximation (GGA) of Density Functional Theory (DFT) was employed to find the lowest-energy configurations of the structures obtained from classical MD with the Quantum Espresso package.<sup>[59]</sup> To optimize the cell and the coordinates, the *Perdew–Burke–Ernzerhof* functional revised for solids (PBEsol),<sup>[60]</sup> was used. Dispersion corrections, that are influential for systems containing large organic molecules, were treated with the empirical D3 dispersion correction.<sup>[61]</sup> To calculate the electronic band gaps, we employed a higher level of theory in form of the hybrid PBE0 functional with explicit incorporation of spin-orbit coupling (SOC) effects.<sup>[62,63]</sup> For further details of the electronic structure calculations including k-points sampling, pseudopotentials and plane wave wavefunction and charge density cutoffs that vary depending on the specific spacer and the corresponding 2D system, we refer the reader to the detailed studies.<sup>[28,30,37]</sup> Additionally, to evaluate transport properties, charge carrier effective masses for each spacer-based system were calculated using our in-house developed code based on a quadratic fit of the 3D band structure.<sup>[64]</sup>

### Structural Exploration of $\sigma$ - $\epsilon$ Space

Motivated by the fact that the introduction of large monovalent cations triggers the emergence of 2D layered perovskites,<sup>[4–11]</sup> we first performed a purely exploratory study to see what type of structures are induced when the size of the monovalent cation is systematically increased. To this end, we constructed a simplified universal monovalent cation model, in the form of a cationic spherical particle with a constant charge +1 but varying size described by the *Lennard–Jones* parameter  $\sigma$  (defined as the distance where the interatomic *Lennard–Jones* potential is zero) and different strengths of dispersion interactions, typified by the parameter  $\epsilon$  (representing the potential energy well depth for *van der Waals* interactions). Naturally, in this highly simplified model, interactions of the monovalent cation are purely isotropic in contrast to

the anisotropic nature of real cation/spacer systems. The choice of a purely isotropic zero order model can however, at least to a certain extent, be justified by the fact that at room temperature, the anisotropic nature of typical counterions such as MA and FA is averaged out due to almost free rotation.<sup>[65,66]</sup>

To construct a structural map in  $\sigma$ - $\epsilon$  space, *i. e.*, as a function of the *van der Waals* radius and the magnitude of dispersion interactions, a series of MD simulations were performed within the LAMMPS package,<sup>[57]</sup> for discrete combinations of  $\sigma$  and  $\epsilon$ . Initial cell dimensions and coordinates were constructed by replicating unit cells of cubic-CsPbI<sub>3</sub>,  $\delta$ -CsPbI<sub>3</sub> and  $\delta$ -FAPbI<sub>3</sub> to construct fully periodic supercells of 1715, 1280 and 1620 atoms, respectively. To model Pb–I interactions, a fixed-point charge potential initially parametrized for CsPbI<sub>3</sub> was chosen,<sup>[67]</sup> which is reported to well reproduce the corner-sharing Pb–I octahedra of the perovskite phase, the edge-sharing Pb–I octahedra of the  $\delta$ -CsPbI<sub>3</sub> as well as the face-sharing Pb–I octahedra of  $\delta$ -FAPbI<sub>3</sub>. For the discretization of the parameter space, eleven  $\sigma$  values in the range of 1.82–6.84 Å were picked on a linear scale, which covers ionic radii smaller than K<sup>+</sup> and larger than GUA<sup>+</sup>. For the  $\epsilon$  values a set of eleven points in the range of 0.34–70 kcal/mol was scanned on a logarithmic scale. LJ interactions between atoms of different kind were calculated from *Lorentz–Berthelot* mixing rules. Long-range electrostatic interactions were treated through the *Ewald* summation with a real-space cutoff of 6 Å. The cutoff for *van der Waals* interactions, however, was set to 17 Å for supercells of 1715 and 1280 atoms, and 11 Å for the supercell of 1620 atoms. Initial systems were primarily optimized through CG, followed by NPT equilibration and around 10 ns production runs with a time step of 0.1 fs. A *Nosé–Hoover* thermostat that keeps the average temperature equal to 300 K and a *Martyna–Tobias–Klein* (at 1 bar) with relaxation times of 50 fs were employed.

## Results and Discussion

As a preamble, we first discuss some general trends obtained from the simple isotropic cation model. In order to explore potential 3D as well as 1D and possibly 2D phases composed of monovalent cations with different ionic radii and intermolecular interaction strengths, we performed MD simulations based on  $\alpha$ (cubic)-CsPbI<sub>3</sub>,  $\delta$ -CsPbI<sub>3</sub> and  $\delta$ -FAPbI<sub>3</sub> crystal structures as starting points. The results are summarized in



Figure 2. Remarkably, even with this simple model, various experimentally known 3D phases can be reproduced. In an intermediate  $\sigma$  and  $\epsilon$  range, the cubic perovskite structure (dark blue area in Figure 2) is a (meta)stable minimum that transforms into a more distorted orthorhombic phase for either smaller cation sizes (as known experimentally) or stronger dispersion interactions. Furthermore, a large portion of the existence region of the perovskite structures is overlapping with the one of  $\delta$ -phases (green areas in Figure 2), derived from CsPbI<sub>3</sub> for smaller cations, respectively from FAPbI<sub>3</sub> for larger cation sizes. Figure 2 also shows that the  $\delta$ -phases further extend to higher  $\epsilon$  regions than the 3D perovskite structures that have a much more limited stability range. Very interestingly, over the scanned parameter space two distinct overlapping regions of emerging (meta)-stable 2D phases were found, which originate either from  $\delta$ -CsPbI<sub>3</sub> with edge-sharing Pb–I octahedra or from  $\delta$ -FAPbI<sub>3</sub> with face-sharing Pb–I octahedra, respectively. The  $\delta$ -FAPbI<sub>3</sub> analogous 2D phase spans over cation sizes corresponding to K<sup>+</sup> up to FA<sup>+</sup> and for  $\epsilon$  values ranging from 30–45 kcal/mol, whereas the  $\delta$ -CsPbI<sub>3</sub> like 2D phase exists in a smaller range of cation sizes, yet over a larger range for  $\epsilon$ . As shown in the insets of Figure 2, both phases consist of alternating layers of cations and Pb–I networks, a characteristic feature of 2D perovskite phases. Therefore, when designing 2D perovskite structures, the choice of cations with

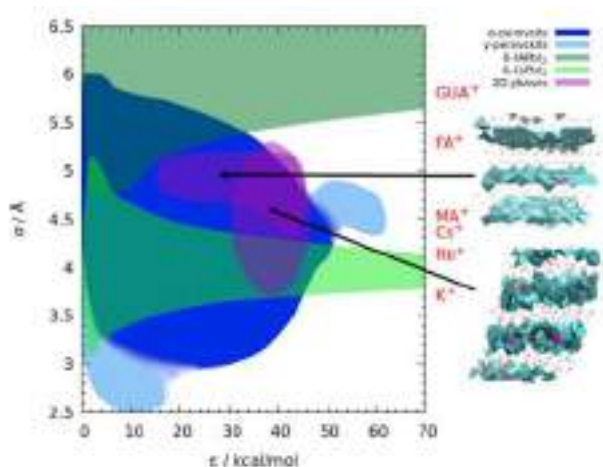


**Figure 2.** (Meta)-stable structures for cations with varying size ( $\sigma$ ) and  $vdW$  interaction strength ( $\epsilon$ ) showing the approximate existence ranges for crystal structures of cubic-CsPbI<sub>3</sub>,  $\delta$ -CsPbI<sub>3</sub> (edge-sharing) and  $\delta$ -FAPbI<sub>3</sub> (face-sharing) as well as the emergence of 2D layered structures. The symbols on the right side indicate the approximate size range of realistic systems from K<sup>+</sup> to GUA<sup>+</sup>.

respect to size and  $vdW$  interaction strength is expected to fall into these regions located at the borders of the stability range of the 3D perovskite structure towards larger cations and/or higher dispersion interactions.

After these general considerations based on the simple universal cation model, we will discuss the properties of 2D perovskites in the case of various realistic spacer molecules shown in Figure 1, a.

The prerequisite for any property calculation is an atomic structure model. Unfortunately, in the case of 2D perovskite systems, only few atomically-resolved crystal structures are available,<sup>[8,68]</sup> and in the majority of the cases reviewed here, the detailed structure is unknown. To search for the most stable structures computationally, we therefore first use classical finite temperature MD simulations based on parameterized force fields. The power of this approach is illustrated in Figure 3 that shows that even starting with a structural model that is not the most stable arrangement, MD simulations of 2D phases with the A spacer are able to predict a transition from the initial DJ-type structure to a lower-energy RP-like arrangement through a gradual annealing process as discussed in the *Methods* section. Thus, starting from different initial trial structures in combination with multiple simulated annealing runs at the force field level, generates likely candidate structures that then can be further validated and refined at the *ab initio* electronic structure (DFT) level. Depending on the chemical nature and possible conformations of the spacers, a variety of prototype configurations may be observed as the lowest-energy 2D phases. In the case of BA-based systems (an example of aliphatic linear spacers and one of the few cases where atomically-resolved crystal structures are available<sup>[8]</sup>), different packing patterns were observed and shown to slightly influence the electronic properties. On the contrary, in the case of functionalized aliphatic spacers, the presence of a carboxyl group results in the formation of an inter-spacer H-bonding pattern that influences the inorganic framework and the electronic properties of the system.<sup>[37]</sup> Aromatic linear spacers on the other hand may exhibit different stacking patterns (e.g.  $\pi$ - $\pi$  sandwich or T-shape) that further allows for tuning the structure and the resulting properties. This feature was however not observed for bulky spacers such as A and A-prime.

To validate our computational methodology for predicting structures of 2DHPs, computationally obtained structural and electronic properties were compared with experimental results including X-ray powder diffraction (XRD), GIWAX, Nuclear Magnetic

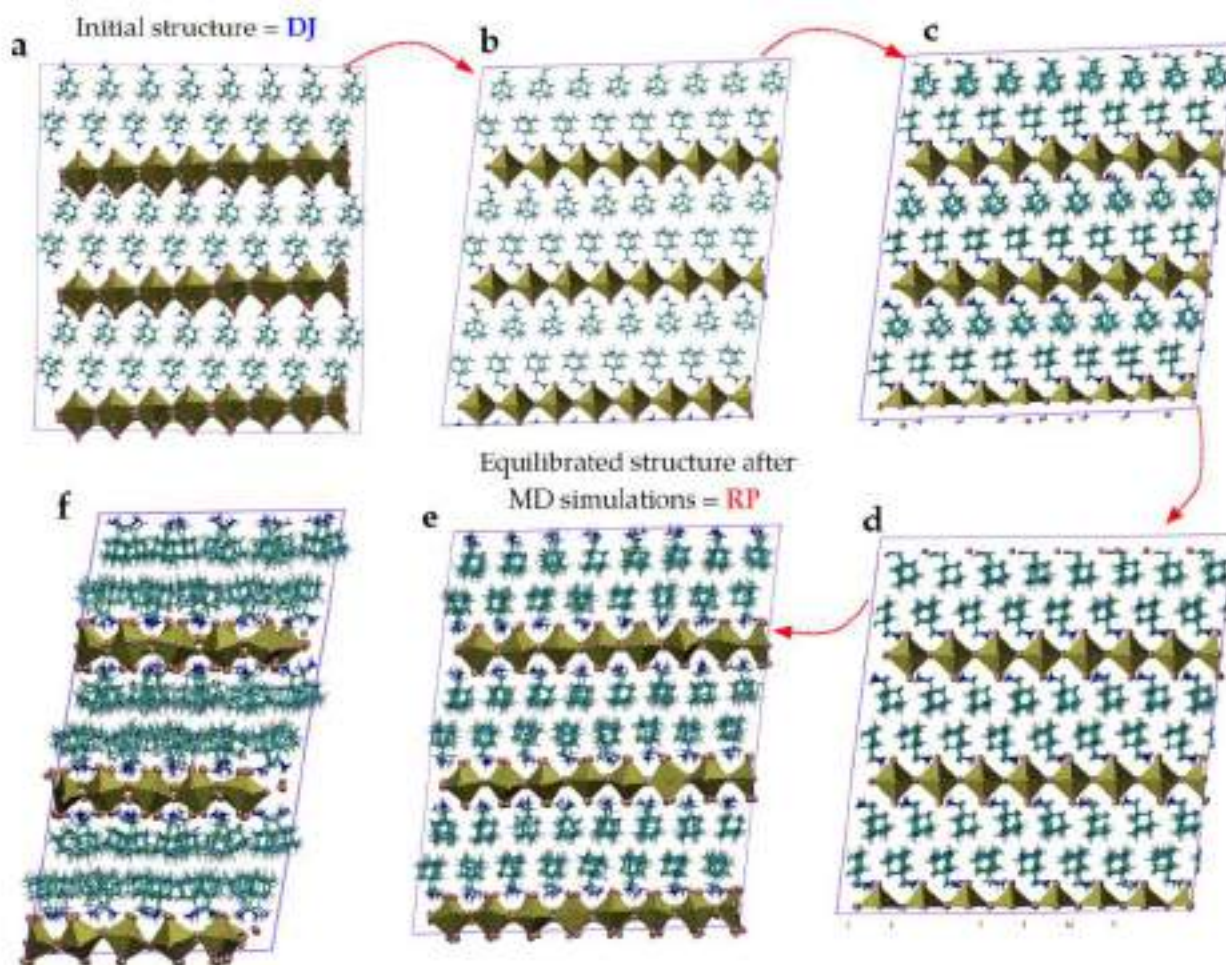


**Figure 3.** Time evolution of the transition of  $A_2PbI_4$  from a DJ-type to an RP-like arrangement from classical MD simulations.

Resonance (NMR) and optical measurements. In addition to excellent agreements between the measured and the calculated XRD pattern, a maximum deviation of only 10% from the GIWAX data was obtained for the calculated cell parameters for B- and A-based 2DHPs.<sup>[28,30]</sup> An example of a perfect match particularly for the low angle peaks, between measured and calculated XRD, obtained for the  $AVA_2(MA)_{n-1}Pb_{n+1}I_{3n+1}$  ( $n=1$ ),<sup>[37]</sup> is illustrated in Figure 4, a. A detailed comparison between experimental and calculated structural properties ( $d_1$ -spacing, penetration depth and octahedral tilting) is given in<sup>[37]</sup>. We further verified the proposed computational methodology by comparing the calculated rotational dynamics of the spacers with NMR findings. To this end, the autocorrelation function (ACF) for the spacer orientation was calculated for the A and B-based systems and found to agree with measured quantities.<sup>[28,30]</sup>

Once validated, the properties of these structural models have been evaluated and classified by a set of unified structural, electronic, and transport parameters that include: in-plane octahedral tilting (|—| angles in two directions within the inorganic layer), thickness of the spacer layer ( $d_1$ ) and penetration depth of the organic layer into the inorganic network (given as distance between the N atom of the ammonium anchoring group and Pb atoms of the inorganic layer), band gaps, and effective masses. Looking for possible correlations between different properties of 2DHPs, we first consider the two structural parameters penetration depth and in-plane octahedral tilting. These two parameters are indeed found to have a strong and essentially linear correlation as demonstrated in Figure 5 that shows the more cubic the structure of the inorganic layer is (with octahedral tilting angles approaching  $90^\circ$ ) the deeper the organic spacer is penetrating into the perovskite layer (*i.e.*, the smaller

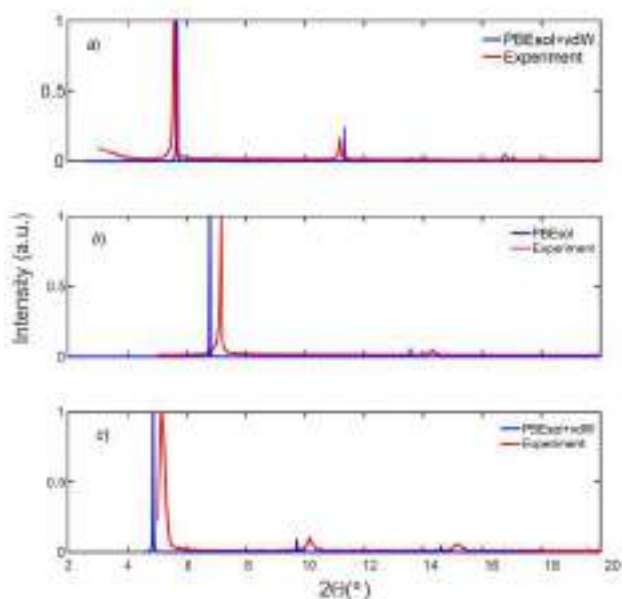


**Figure 4.** Comparison of the experimentally measured<sup>[28,30,37]</sup> (top panel in red) and the calculated XRD spectra of the computationally predicted lowest energy structure (bottom panel in blue) for a) AVA<sub>2</sub>PbI<sub>4</sub>, b) BPbI<sub>4</sub> and c) A<sub>2</sub>PbI<sub>4</sub>.

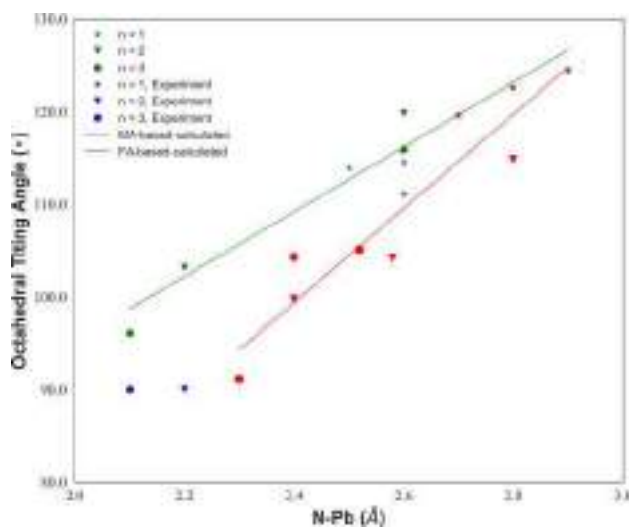


**Figure 5.** Dependence of the in-plane octahedral tilting angles on the N–Pb vertical distance (penetration depth) for MA and FA based 2DHP.

the N–Pb distances are). This can be rationalized by the fact that the interoctahedral space that hosts the ammonium group of the spacer is largest for a perfectly cubic arrangement and allows for a deeper penetration. FA-based systems are more cubic than MA-based 2DHPs as the 3D phase of FAPbI<sub>3</sub> is cubic at room temperature, while MAPbI<sub>3</sub> adopts a tetragonal

structure under ambient conditions. This difference is reflected by the different slope found for MA-compared to FA-based systems and is vanishing for the  $n=1$  structures that do not contain any of these smaller organic cations. A parallel trend is found in the corresponding electronic properties. As discussed below, the band edges of 2DHP systems considered here (that do not contain electroactive spacers<sup>[39,48]</sup>) are in general determined by the inorganic layer and are of similar nature (*i.e.*, the top of the valence made up by antibonding iodide p and lead s orbitals and the bottom of the conduction band consisting of antibonding lead p and iodide s orbitals) as in their 3D analogues.<sup>[69]</sup> Since the antibonding overlap between *e.g.* p-orbitals of iodide and s-orbitals of lead in the TVB is largest in a perfectly cubic structure (perfect alignment) leading to a destabilization of the TVB and thus to smaller band gaps. Therefore, the more cubic the structure, the lower is the band gap. The correlation between the penetration depth of the organic spacer and the resulting phase of the inorganic layer thus also provides an indirect guideline for tuning the electronic properties of 2DHPs. However, specific systems can deviate from the general trend shown in *Figure 5*, such as A-prime systems that exhibit strong structural distortions or electroactive spacers that directly contribute to the band edges.<sup>[39,48]</sup>

2DHPs are usually modeled as a multiple quantum well,<sup>[16–18,41,42,53]</sup> where the number of inorganic layers ( $n$ ) in the out-of-plane direction corresponds to the width of the well and the organic layer represents a barrier of thickness  $d_1$  (shown in *Figure 1,b*) that depends on the spacer.<sup>[70]</sup> It is therefore intuitive to probe a possible correlation between  $d_1$  and the geometric length of the fully extended organic spacer molecule, that could however be obscured by additional factors such as the specific packing of the organic layer, its tilt or the mutual penetration of adjacent spacer layers in RP structures. It turns out that these latter factors seem to be secondary since a nearly linear trend between  $d_1$  and the geometric length can be observed for BA, AVA and PDMA spacers (*Figure 6*) confirming a strong correlation between the geometry of the isolated spacer molecule and the thickness of the resulting organic (double or single) layer. A larger deviation from this general trend is however observed for A and A-prime spacers that can be attributed to their bulky shape that does not allow for close packing resulting in an unexpectedly larger thickness of the organic spacer layer (*Figure 1,b*).

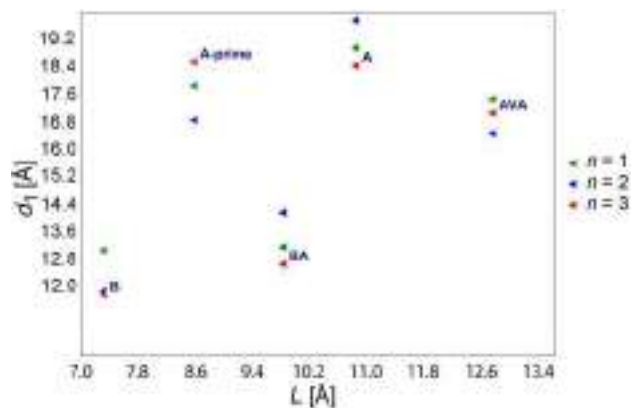


**Figure 6.** Distance  $d_1$  between adjacent inorganic layers as a function of geometric length of the fully extended spacer molecule. To make a fair comparison between RP and DJ structures, the lengths of the monovalent spacers (BA, 5-AVA, A and A-prime) were multiplied by 2 and compared to that of a bifunctional ligand (B).

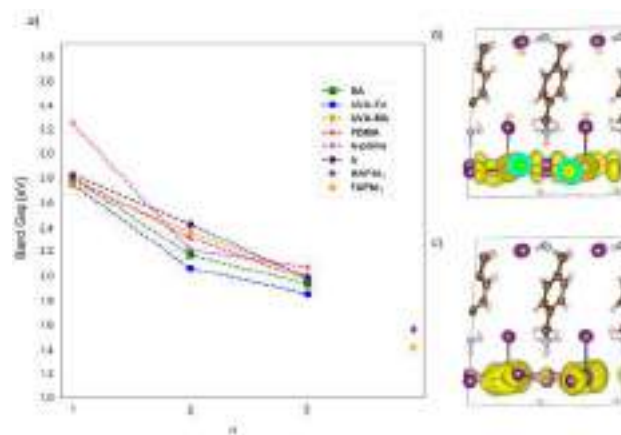


**Figure 7.** a) Calculated band gaps of the investigated 2D halide perovskite systems as a function of  $n$ . Frontier molecular orbitals for  $\text{BPbI}_4$  (top of the valence band (b) and bottom of the conduction band (c)). Iodide, lead, carbon and nitrogen atoms are shown in purple, gray, brown and silver, respectively.

To further investigate the trends in the electronic properties of the different 2D systems, the evolution of the band gaps as a function of  $n$  is calculated and shown in Figure 7,a. All the systems exhibit a trend typical for 2DHPs that is consistent with a simple quantum well model: the band gap decreases upon increasing the thickness of the inorganic layer and converges gradually towards the band gaps of the 3D crystals of  $\text{MAPbI}_3$  respectively,  $\text{FAPbI}_3$ . In accordance with other reported studies,<sup>[8]</sup> for the spacers considered here, we find that the band edges (top of the valence band and bottom of the conduction band) are dominated by the inorganic layers (Figure 7,b and 7,c), while the organic spacers mostly act as indirect modulators that influence the structural properties (e.g. octahedral tilting and  $d_1$ ) that in turn impacts the band gaps. That is reflected in the general finding that the  $n$ -dependence of the gap is more pronounced than variations induced by the specific chemical nature of the different spacers. One exception to this general trend are e.g. NDI-based systems where the bottom of

the conduction band is found to be dominated by the spacer itself.<sup>[39]</sup> In addition, the  $n=1$  member of A-prime-based systems exhibits an unusually large band gap (3.25 eV) which can be explained by the strong structural distortion that disrupts the corner-sharing network of  $\text{Pb-I}$  octahedral.<sup>[27,28]</sup> For all studied systems, the calculated single-particle band gaps are in a good agreement with the experimentally measured gaps showing a maximum deviation of 300–400 meV that can be attributed to the exciton-binding energies that is not included in the calculations.<sup>[41,42]</sup>

To investigate transport properties of 2DHPs, we calculated effective masses for the in-plane directions ( $x$  and  $y$ ) within the inorganic layer, as well as the out-of-plane direction ( $z$ ) as listed in Table 1. Not surprisingly, the 2D nature of the systems is clearly reflected in the anisotropy of the calculated values: while the in-plane effective masses are within the typical range for 3D halide perovskites, large values in the out-of-plane direction demonstrate hindered transport through the spacer layer. Effective masses along  $x$  and  $y$  directions

**Table 1.** Hole ( $m_{h,xx}$ ,  $m_{h,yy}$ ,  $m_{h,zz}$ ) and electron effective masses ( $m_{e,xx}$ ,  $m_{e,yy}$ ,  $m_{e,zz}$ ) for the investigated 2DHP systems along three principal axes ( $x$ ,  $y$  and  $z$ ). Hole effective masses are marked in bold, and effective mass values  $> 10$  are considered out of validity of the band model of transport and are noted as  $> 10$ .

Spacer	$n=1$	$n=2$	$n=3$
PDMA	<b>0.30</b> , <b>0.34</b> , $> 10$ , 0.31, 0.38, $> 10$	<b>0.29</b> , <b>0.32</b> , <b>2.7</b> , 0.12, 0.81, 4.2	<b>0.21</b> , <b>0.24</b> , <b>2.1</b> , 0.12, 1.18, 6.5
A	<b>0.39</b> , <b>0.44</b> , $> 10$ , 0.13, 0.17, $> 10$	<b>0.32</b> , <b>0.33</b> , $> 10$ , 0.12, 6.40, 8.8	<b>0.19</b> , <b>0.19</b> , $> 10$ , 0.10, 0.64, 3.6
A-prime	<b>0.46</b> , <b>6.22</b> , $> 10$ , 0.19, 7.34, $> 10$	<b>0.34</b> , <b>0.52</b> , $> 10$ , 0.14, 0.58, 3.3	<b>0.22</b> , <b>0.23</b> , $> 10$ , 0.10, 0.99, 2.4
AVA-MA	<b>0.32</b> , <b>0.32</b> , $> 10$ , 0.37, 0.37, $> 10$	<b>0.23</b> , <b>0.23</b> , $> 10$ , 0.28, 0.28, $> 10$	<b>0.28</b> , <b>0.28</b> , $> 10$ , 0.15, 0.15, $> 10$
BA	<b>0.08</b> , <b>0.08</b> , $> 10$ , 0.14, 0.14, $> 10$	–	<b>0.09</b> , <b>0.09</b> , $> 10$ , 0.14, 0.14, $> 10$

mostly follow the band gap behavior with the exception of the systems where organic spacers have an active role in charge transport<sup>[39]</sup> for which the hopping transport model would provide a better description. Finally, to quantify the transport in the out-of-plane direction, we estimate charge carrier tunneling probabilities through the spacer layer ( $T$ ) using the following equation:

$$T \sim \exp(-2\alpha L)$$

where  $\alpha$  is a function of energy level difference between the inorganic and the organic layers ( $V_0$ ) through  $\alpha = \frac{\sqrt{2m_0V_0}}{\hbar}$  and  $L$  is equal to  $d_1$ . The probabilities plotted in *Figure 8* were computed for  $d_1$  and  $V_0$  values that correspond respectively to the typical thickness and potential barrier heights of the organic layer in the investigated systems. The rather small probabilities shown in *Figure 8* reflect the rather insulating nature of the organic layer in 2DHPs.

## Conclusions

In this work, we presented a general approach towards modeling 2DHP systems also for the cases where experimental structural data is missing and gave an overview of computational results for a range of prototypical spacers. Specifically, we performed a comprehensive study on 2D systems based on both monovalent (BA, 5-AVA, A and A-prime) and divalent (PDMA) spacers, including aliphatic chain (BA), aliphatic bulky (A and A-prime), aromatic (PDMA) and

functionalized (5-AVA) spacers as characteristic representatives. We validated the structural models by available XRD, absorption and transport measurements. Performing DFT calculations on top of the energy-minimized structures obtained from classical molecular dynamics simulations led to the prediction of lowest energy structures that are in very good agreement with the experimental observables. Some general trends emerged from these studies that also allowed to derive first structure–property relationships as guides for the search of optimal spacers:

- 1) In most cases, the thickness of the organic layer is directly correlated to the geometric length of the spacer.
- 2) The penetration depth of the organic spacers into the inorganic layer determines the octahedral tilting and thus the phase and band gap of the perovskite layer.
- 3) With the exception of systems with electronically active spacer molecules that directly contribute to the band edges, the electronic gaps are mainly a function of the thickness of the inorganic layer ( $n$ ) and can be further fine-tuned by the nature of the organic ligand through indirect structural effects.
- 4) Transport properties are found to be a direct function of the thickness of the inorganic layer and the organic layers with the exception of electronically active spacers with localized orbital contributions to the band edges.

## Acknowledgments

*U. R.* acknowledges SNSF Grant No. 200020–165863, NCCR-MUST and the SINERGIA interdisciplinary research program EPISODE for funding and the Swiss Computing Centre CSCS for computational resources.

## Author Contribution Statement

The manuscript was written by *F. J.* and *M. M.* with the support of all co-authors. *F. J.*, *M. M.*, *P. A.* and *U. R.* performed, analyzed or interpreted the MD and DFT calculations. *M. D.*, *A. B.* and *U. R.* performed, analyzed or interpreted the high-throughput MD calculations for structural analysis of the  $\sigma$ - $\epsilon$  space. *U. R.* conceptualized and supervised the research.

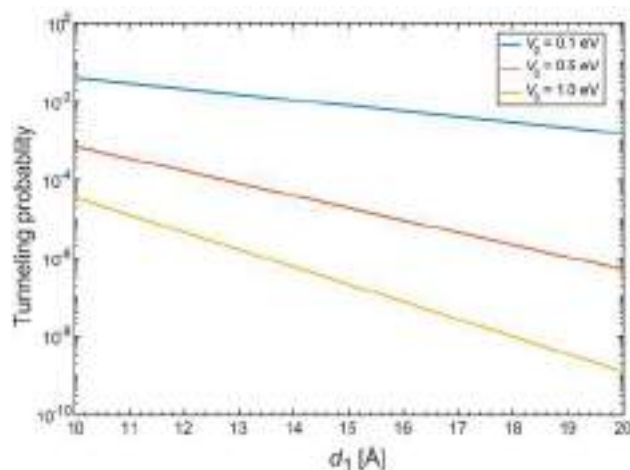


**Figure 8.** Tunneling probabilities for charge carriers through the spacer layer.

## References

- [1] A. K. Jena, A. Kulkarni, T. Miyasaka, 'Halide Perovskite Photovoltaics: Background, Status and Future Prospects', *Chem. Rev.* **2019**, *119*, 3036–3103.
- [2] M. Grätzel, 'The Rise of Highly Efficient and Stable Perovskite Solar Cells', *Acc. Chem. Res.* **2017**, *50*, 487–491.
- [3] S. Kazim, M. K. Nazeeruddin, M. Grätzel, S. Ahmad, 'Perovskite as Light Harvester: A Game Changer in Photovoltaics', *Angew. Chem. Int. Ed.* **2014**, *53*, 2812–2824.
- [4] G. C. Papavassiliou, I. B. Koutselas, A. Terzis, M.-H. Whangbo, 'Structural and Electronic Properties of the Natural Quantum-well System (C<sub>6</sub>H<sub>5</sub>CH<sub>2</sub>CH<sub>2</sub>NH<sub>3</sub>)<sub>2</sub>SnI<sub>4</sub>', *Solid State Commun.* **1994**, *91*, 695–698.
- [5] D. B. Mitzi, K. Chondroudis, C. R. Kagan, 'Design, Structure, and Optical Properties of Organic–Inorganic Perovskites Containing an Oligothiophene Chromophore', *Inorg. Chem.* **1999**, *38*, 6246–6256.
- [6] I. C. Smith, E. T. Hoke, D. Solis-Ibarra, M. D. McGehee, H. I. Karunadasa, 'A Layered Hybrid Perovskite Solar-Cell Absorber with Enhanced Moisture Stability', *Angew. Chem. Int. Ed.* **2014**, *53*, 11232–11235.
- [7] H. Tsai, W. Nie, J.-C. Blancon, C. C. Stoumpos, R. Asadpour, B. Harutyunyan, A. J. Neukirch, R. Verduzco, J. J. Crochet, S. Tretiak, L. Pedesseau, J. Even, M. A. Alam, G. Gupta, J. Lou, P. M. Ajayan, M. J. Bedzyk, M. G. Kanatzidis, A. D. Mohite, 'High-efficiency two-dimensional Ruddlesden–Popper perovskite solar cells', *Nature* **2016**, *536*, 312–316.
- [8] C. C. Stoumpos, D. H. Cao, D. J. Clark, J. Young, J. M. Rondinelli, J. I. Jang, J. T. Hupp, M. G. Kanatzidis, 'Ruddlesden–Popper Hybrid Lead Iodide Perovskite 2D Homologous Semiconductors', *Chem. Mater.* **2016**, *28*, 2852–2867.
- [9] Y. Chen, Y. Sun, J. Peng, J. Tang, K. Zheng, Z. Liang, '2D Ruddlesden–Popper Perovskites for Optoelectronics', *Adv. Mater.* **2018**, *30*, 1703487.
- [10] S. Zeng, S. Shi, S. Wang, Y. Xiao, 'Mixed-ligand Engineering of Quasi-2D Perovskites for Efficient Sky-blue Light-emitting Diodes', *J. Mater. Chem. C* **2020**, *8*, 1319–1325.
- [11] L. Mao, W. Ke, L. Pedesseau, Y. Wu, C. Katan, J. Even, M. R. Wasielewski, C. C. Stoumpos, M. G. Kanatzidis, 'Hybrid Dion–Jacobson 2D Lead Iodide Perovskites', *J. Am. Chem. Soc.* **2018**, *140*, 3775–3783.
- [12] B.-E. Cohen, Y. Li, Q. Meng, L. Etgar, 'Dion–Jacobson Two-Dimensional Perovskite Solar Cells Based on Benzene Dimethan ammonium Cation', *Nano Lett.* **2019**, *19*, 2588–2597.
- [13] X. Li, W. Ke, B. Traoré, P. Guo, I. Hadar, M. Kepenekian, J. Even, C. Katan, C. C. Stoumpos, R. D. Schaller, M. G. Kanatzidis, 'Two-Dimensional Dion–Jacobson Hybrid Lead Iodide Perovskites with Aromatic Diammonium Cations', *J. Am. Chem. Soc.* **2019**, *141*, 12880–12890.
- [14] Z. Xu, M. Chen, S. F. Liu, 'First-Principles Study of Enhanced Out-of-Plane Transport Properties and Stability in Dion–Jacobson Two-Dimensional Perovskite Semiconductors for High-Performance Solar Cell Applications', *J. Phys. Chem. Lett.* **2019**, *10*, 3670–3675.
- [15] Y. Zheng, T. Niu, J. Qiu, L. Chao, B. Li, Y. Yang, Q. Li, C. Lin, X. Gao, C. Zhang, Y. Xia, Y. Chen, W. Huang, 'Oriented and Uniform Distribution of Dion–Jacobson Phase Perovskites Controlled by Quantum Well Barrier Thickness', *Solar RRL* **2019**, *3*, 1900090.
- [16] K. Tanaka, T. Takahashi, T. Kondo, T. Umabayashi, K. Asai, K. Ema, 'Image Charge Effect on Two-dimensional Excitons in an Inorganic–organic Quantum-well Crystal', *Phys. Rev. B.* **2005**, *71*, 045312.
- [17] I. B. Koutselas, L. Ducasse, G. C. Papavassiliou, 'Electronic Properties of Three- and Low-dimensional Semiconducting Materials with Pb Halide and Sn Halide Units', *J. Phys. Condens. Matter* **1996**, *8*, 5953.
- [18] M. K. Jana, S. M. Janke, D. J. Dirkes, S. Dovletgeldi, C. Liu, X. Qin, K. Gundogdu, W. You, V. Blum, D. B. Mitzi, 'Direct-Bandgap 2D Silver–Bismuth Iodide Double Perovskite: The Structure-Directing Influence of an Oligothiophene Spacer Cation', *J. Am. Chem. Soc.* **2019**, *141*, 7955–7964.
- [19] D. H. Cao, C. C. Stoumpos, O. K. Farha, J. T. Hupp, M. G. Kanatzidis, '2D Homologous Perovskites as Light-Absorbing Materials for Solar Cell Applications', *J. Am. Chem. Soc.* **2015**, *137*, 7843–7850.
- [20] L. N. Quan, M. Yuan, R. Comin, O. Voznyy, E. M. Beauregard, S. Hoogland, A. Buin, A. R. Kirmani, K. Zhao, A. Amassian, D. H. Kim, E. H. Sargent, 'Ligand-Stabilized Reduced-Dimensionality Perovskites', *J. Am. Chem. Soc.* **2016**, *138*, 2649–2655.
- [21] X. Zhang, G. Wu, W. Fu, M. Qin, W. Yang, J. Yan, Z. Zhang, X. Lu, H. Chen, 'Orientation Regulation of Phenylethylammonium Cation Based 2D Perovskite Solar Cell with Efficiency Higher Than 11%', *Adv. Energy Mater.* **2018**, *2*, 1702498.
- [22] M. A. Hope, T. Nakamura, P. Ahlawat, A. Mishra, M. Cordova, F. Jahanbakhshi, M. Mladenović, R. Runjhun, L. Merten, A. Hinderhofer, B. I. Carlsen, D. J. Kubicki, R. Gershoni-Poranne, T. Schneeberger, L. C. Carbone, Y. Liu, S. M. Zakeeruddin, J. Lewinski, A. Hagfeldt, F. Schreiber, U. Rothlisberger, M. Grätzel, J. V. Milić, L. Emsley, 'Nanoscale Phase Segregation in Supramolecular  $\pi$ -Templating for Hybrid Perovskite Photovoltaics from NMR Crystallography', *J. Am. Chem. Soc.* **2021**, *143*, 1529–1538.
- [23] K. Tanaka, T. Kondo, 'Bandgap and Exciton Binding Energies in Lead-iodide-based Natural Quantum-well Crystals', *Sci. Technol. Adv. Mater.* **2003**, *4*, 599–604.
- [24] T. Ishihara, J. Takahashi, T. Goto, 'Optical Properties Due to Electronic Transitions in Two-dimensional Semiconductors (C<sub>n</sub>H<sub>2</sub>)<sub>n+1</sub>(NH<sub>3</sub>)<sub>2</sub>PbI<sub>4</sub>', *Phys. Rev. B* **1990**, *42*, 11099.
- [25] J. Rodríguez-Romero, B. C. Hames, I. Mora-Seró, E. M. Barea, 'Conjugated Organic Cations to Improve the Optoelectronic Properties of 2D/3D Perovskites', *ACS Energy Lett.* **2017**, *2*, 1969–1970.
- [26] L. Iagher, L. Etgar, 'The Effect of Cs on the Stability and Photovoltaic Performance of 2D/3D Perovskite-Based Solar Cells', *ACS Energy Lett.* **2018**, *3*, 366–372.
- [27] J. V. Milić, J.-H. Im, D. J. Kubicki, A. Ummadisingu, J.-Y. Seo, Y. Li, M. A. Ruiz-Preciado, M. I. Dar, S. M. Zakeeruddin, L. Emsley, M. Grätzel, 'Supramolecular Engineering for Formamidinium-Based Layered 2D Perovskite Solar Cells: Structural Complexity and Dynamics Revealed by Solid-State NMR Spectroscopy', *Adv. Energy Mater.* **2019**, *9*, 1900284.
- [28] F. Jahanbakhshi, M. Mladenović, E. Kneschaurek, L. C. Merten, M. Gélvez-Rueda, P. Ahlawat, Y. Li, A. Dučinskas, A. Hinderhofer, I. M. Dar, W. Tress, B. Carlsen, A. Ummadisingu, S. M. Zakeeruddin, A. Hagfeldt, F. Schreiber, F. C. Grozema, U. Rothlisberger, J. V. Milić, M. Graetzel, 'Insights

- into the Structural and Photophysical Properties of Adamantyl-based Layered Hybrid Perovskites', *J. Mater. Chem. A* **2020**, *8*, 17732–17740.
- [29] Y. Li, J. V. Milić, A. Ummadisingu, J.-Y. Seo, J.-H. Im, H.-S. Kim, Y. Liu, M. I. Dar, S. M. Zakeeruddin, P. Wang, A. Hagfeldt, M. Grätzel, 'Bifunctional Organic Spacers for Formamidinium-Based Hybrid Dion–Jacobson Two-Dimensional Perovskite Solar Cells', *Nano Lett.* **2019**, *19*, 150–157.
- [30] M. Gélvez-Rueda, P. Ahlwat, L. Merten, F. Jahanbakhshi, M. Mladenović, A. Hinderhofer, M. I. Dar, Y. Li, A. Dučinskas, B. Carlson, W. Tress, A. Ummadisingu, S. M. Zakeeruddin, F. Schreiber, A. Hagfeldt, U. Rothlisberger, F. C. Grozema, J. V. Milić, M. Graetzel, 'Formamidinium-Based Dion–Jacobson Layered Hybrid Perovskites: Structural Complexity and Optoelectronic Properties', *Adv. Funct. Mater.* **2020**, *30*, 2003428.
- [31] N. Mercier, '(HO<sub>2</sub>C(CH<sub>2</sub>)<sub>3</sub>(NH<sub>3</sub>)<sub>2</sub>CH<sub>2</sub>NH<sub>3</sub>Pb<sub>2</sub>)<sub>2</sub>: A Predicted Non-centrosymmetrical Structure Built Up from Carboxylic Acid Supramolecular Synthons and Bilayer Perovskite Sheets', *CrystEngComm* **2005**, *7*, 429–432.
- [32] A. Q. Alanazi, D. J. Kubicki, D. Prochowicz, E. A. Alharbi, M. E. F. Bouduban, F. Jahanbakhshi, M. Mladenović, J. V. Milić, F. Giordano, D. Ren, A. Y. Alyamani, H. Albrithen, A. Albadri, M. H. Alotaibi, J.-E. Moser, S. M. Zakeeruddin, U. Rothlisberger, L. Emsley, M. Grätzel, 'Atomic-Level Microstructure of Efficient Formamidinium-Based Perovskite Solar Cells Stabilized by 5-Ammonium Valeric Acid Iodide Revealed by Multinuclear and Two-Dimensional Solid-State NMR', *J. Am. Chem. Soc.* **2019**, *141*, 17659–17669.
- [33] H. Hoshi, N. Shigeeda, T. Dai, 'Improved Oxidation Stability of Tin Iodide Cubic Perovskite Treated by 5-ammonium Valeric Acid Iodide', *Mater. Lett.* **2016**, *183*, 391–393.
- [34] G. Grancini, C. Roldán-Carmona, I. Zimmermann, E. Mosconi, X. Lee, D. Martineau, S. Narbey, F. Oswald, F. De Angelis, M. Graetzel, M. K. Nazeeruddin, 'One-Year Stable Perovskite Solar Cells by 2D/3D Interface Engineering', *Nat. Commun.* **2017**, *8*, 15684.
- [35] P. Prajontat, T. Dittrich, K. Hinrichs, J. Rappich, 'Thickness of AVA<sup>+</sup> Controls the Direction of Charge Transfer at TiO<sub>2</sub>/PbI<sub>2</sub> Interfaces', *J. Phys. Chem. C* **2018**, *122*, 5020–5025.
- [36] Y. Ogomi, A. Morita, S. Tsukamoto, T. Saitho, Q. Shen, T. Toyoda, K. Yoshino, S. S. Pandey, T. Ma, S. Hayase, 'All-Solid Perovskite Solar Cells with HOCO–R(NH<sub>3</sub>)<sup>+</sup>I<sup>−</sup> Anchor-Group Inserted between Porous Titania and Perovskite', *J. Phys. Chem. C* **2014**, *118*, 16651–16659.
- [37] N. Ashari-Astani, F. Jahanbakhshi, M. Mladenović, A. Q. M. Alanazi, I. Ahmadabadi, M. R. Ejtehadi, M. I. Dar, M. Grätzel, U. Rothlisberger, 'Ruddlesden–Popper Phases of Methylammonium-Based Two-Dimensional Perovskites with 5-Ammonium Valeric Acid AVA<sub>2</sub>MA<sub>n−1</sub>Pb<sub>n</sub>I<sub>3n+1</sub> with n = 1, 2, and 3', *J. Phys. Chem. Lett.* **2019**, *10*, 3543–3549.
- [38] L. Hong, J. V. Milić, P. Ahlwat, M. Mladenović, D. J. Kubicki, F. Jahanbakhshi, D. Ren, M. C. Gélvez-Rueda, M. A. Ruiz-Preciado, A. Ummadisingu, Y. Liu, C. Tian, L. Pan, S. M. Zakeeruddin, A. Hagfeldt, F. C. Grozema, U. Rothlisberger, L. Emsley, H. Han, M. Graetzel, 'Guanine-Stabilized Formamidinium Lead Iodide Perovskites', *Angew. Chem. Int. Ed.* **2020**, *59*, 4691–4697.
- [39] S. Maheshwari, T. J. Savenije, N. Renaud, F. C. Grozema, 'Computational Design of Two-Dimensional Perovskites with Functional Organic Cations', *J. Phys. Chem. C* **2018**, *122*, 17118–17122.
- [40] A. H. Proppe, R. Quintero-Bermudez, H. Tan, O. Voznyy, S. O. Kelley, E. H. Sargent, 'Synthetic Control over Quantum Well Width Distribution and Carrier Migration in Low-Dimensional Perovskite Photovoltaics', *J. Am. Chem. Soc.* **2018**, *140*, 2890–2896.
- [41] J.-C. Blancon, H. Tsai, W. Nie, C. C. Stoumpos, L. Pedesseau, C. Katan, M. Kepenekian, C. M. M. Soe, K. Appavoo, M. Y. Sfeir, S. Tretiak, P. M. Ajayan, M. G. Kanatzidis, J. Even, J. J. Crochet, A. D. Mohite, 'Extremely Efficient Internal Exciton Dissociation Through Edge States in Layered 2D Perovskites', *Science* **2017**, *355*, 1288–1292.
- [42] J.-C. Blancon, A. V. Stier, H. Tsai, W. Nie, C. Stoumpos, B. Traoré, L. Pedesseau, M. Kepenekian, F. Katsutani, G. T. Noe, J. Kono, S. Tretiak, S. A. Crooker, C. Katan, M. G. Kanatzidis, J. J. Crochet, J. Even, A. D. Mohite, 'Scaling Law for Excitons in 2D Perovskite Quantum Wells', *Nat. Commun.* **2018**, *9*, 2254.
- [43] M. C. Gélvez-Rueda, E. M. Hutter, D. H. Cao, N. Renaud, C. C. Stoumpos, J. T. Hupp, T. J. Savenije, M. G. Kanatzidis, F. C. Grozema, 'Interconversion between Free Charges and Bound Excitons in 2D Hybrid Lead Halide Perovskites', *J. Phys. Chem. C* **2017**, *121*, 26566–26574.
- [44] N. T. P. Hartono, S. Sun, M. C. Gélvez-Rueda, P. J. Pierone, M. P. Erodici, J. Yoo, F. Wei, M. Bawendi, F. C. Grozema, M.-J. Sher, T. Buonassisi, J.-P. Corraer-Baena, 'The Effect of Structural Dimensionality on Carrier Mobility in Lead-Halide Perovskites', *J. Mater. Chem. A* **2019**, *7*, 23949–23957.
- [45] V. I. E. Queloz, M. E. F. Bouduban, I. García-Benito, A. Fedorovskiy, S. Orlandi, M. Cavazzini, G. Pozzi, H. Trivedi, D. C. Lupascu, D. Beljonne, J.-E. Moser, M. K. Nazeeruddin, C. Quarti, G. Grancini, 'Spatial Charge Separation as the Origin of Anomalous Stark Effect in Fluorous 2D Hybrid Perovskites', *Adv. Funct. Mater.* **2020**, *30*, 2000228.
- [46] J. L. Knutson, J. D. Martin, D. B. Mitzi, 'Tuning the Band Gap in Hybrid Tin Iodide Perovskite Semiconductors Using Structural Templating', *Inorg. Chem.* **2005**, *44*, 4699–4705.
- [47] F. Zhang, D. H. Kim, H. Lu, J.-S. Park, B. W. Larson, J. Hu, L. Gao, C. Xiao, O. G. Reid, X. Chen, Q. Zhao, P. F. Ndione, J. J. Berry, W. You, A. Walsh, M. C. Beard, K. Zhu, 'Enhanced Charge Transport in 2D Perovskites via Fluorination of Organic Cation', *J. Am. Chem. Soc.* **2019**, *141*, 5972–5979.
- [48] J. V. Passarelli, D. J. Fairfield, N. A. Sather, M. P. Hendricks, H. Sai, C. L. Stern, S. I. Stupp, 'Enhanced Out-of-Plane Conductivity and Photovoltaic Performance in n = 1 Layered Perovskites through Organic Cation Design', *J. Am. Chem. Soc.* **2018**, *140*, 7313–7323.
- [49] N. Zibouche, M. S. Islam, 'Structure–Electronic Property Relationships of 2D Ruddlesden–Popper Tin- and Lead-based Iodide Perovskites', *ACS Appl. Mater. Interfaces* **2020**, *12*, 15328–15337.
- [50] X. Zhang, X. Ren, B. Liu, R. Munir, X. Zhu, D. Yang, J. Li, Y. Liu, D.-M. Smilgies, R. Li, Z. Yang, T. Niu, X. Wang, A. Amassian, K. Zhao, S. F. Liu, 'Stable High Efficiency Two-dimensional Perovskite Solar Cells via Cesium Doping', *Energy Environ. Sci.* **2017**, *10*, 2095–2102.
- [51] X. Li, M. I. Dar, C. Yi, J. Luo, M. Tschumi, S. Zakeeruddin, M. K. Nazeeruddin, H. Han, M. Grätzel, 'Improved Performance and Stability of Perovskite Solar Cells by Crystal

- Crosslinking with Alkylphosphonic Acid  $\omega$ -ammonium Chlorides', *Nat. Chem.* **2015**, 7, 703–711.
- [52] B. Saporov, D. B. Mitzi, 'Organic–Inorganic Perovskites: Structural Versatility for Functional Materials Design', *Chem. Rev.* **2016**, 116, 4558–4596.
- [53] C. Katan, N. Mercier, J. Even, 'Quantum and Dielectric Confinement Effects in Lower-Dimensional Hybrid Perovskite Semiconductors', *Chem. Rev.* **2019**, 119, 3140–3192.
- [54] A. W. Götz, M. J. Williamson, D. Xu, D. Poole, S. Le Grand, R. C. Walker, 'Routine Microsecond Molecular Dynamics Simulations with AMBER on GPUs. 1. Generalized Born', *J. Chem. Theory Comput.* **2012**, 8, 1542–1555.
- [55] R. Salomon-Ferrer, A. W. Götz, D. Poole, S. Le Grand, R. C. Walker, 'Routine Microsecond Molecular Dynamics Simulations with AMBER on GPUs. 2. Explicit Solvent Particle Mesh Ewald', *J. Chem. Theory Comput.* **2013**, 9, 3878–3888.
- [56] A. Mattoni, A. Filippetti, M. I. Saba, P. Delugas, 'Methylammonium Rotational Dynamics in Lead Halide Perovskite by Classical Molecular Dynamics: the Role of Temperature', *J. Phys. Chem. C* **2015**, 119, 17421–17428.
- [57] C. Caddeo, M. I. Saba, S. Meloni, A. Filippetti, A. Mattoni, 'Collective Molecular Mechanisms in the  $\text{CH}_3\text{NH}_3\text{PbI}_3$  Dissolution by Liquid Water', *ACS Nano* **2017**, 11, 9183–9190.
- [58] S. Plimpton, 'Fast Parallel Algorithms for Short-Range Molecular Dynamics', *J. Comput. Phys.* **1995**, 117, 1–19.
- [59] P. Giannozzi, S. Baroni, N. Bonini, M. Calandra, R. Car, C. Cavazzoni, D. Ceresoli, G. L. Chiarotti, M. Cococcioni, I. Dabo, A. Dal Corso, S. de Gironcoli, S. Fabris, G. Fratesi, R. Gebauer, U. Gerstmann, C. Gougoussis, A. Kokalj, M. Lazzeri, L. Martin-Samos, N. Marzari, F. Mauri, R. Mazzarello, S. Paolini, A. Pasquarello, L. Paulatto, C. Sbraccia, S. Scandolo, G. Sclauzero, A. P. Seitsonen, A. Smogunov, P. Umari, R. M. Wentzcovitch, 'QUANTUM ESPRESSO: A Modular and Open-source Software Project for Quantum Simulations of Materials', *J. Phys. Condens. Matter* **2009**, 21, 395502.
- [60] J. P. Perdew, A. Ruzsinszky, G. I. Csonka, O. A. Vydrov, G. E. Scuseria, L. A. Constantin, X. Zhou, K. Burke, 'Restoring the Density-Gradient Expansion for Exchange in Solids and Surfaces', *Phys. Rev. Lett.* **2008**, 100, 136406.
- [61] S. Grimme, 'Semiempirical GGA-type Density Functional Constructed with a Long-range Dispersion Correction', *J. Comput. Chem.* **2006**, 27, 1787–1799.
- [62] J. Sun, A. Ruzsinszky, J. P. Perdew, 'Strongly Constrained and Appropriately Normed Semilocal Density Functional', *Phys. Rev. Lett.* **2015**, 115, 036402.
- [63] P. Umari, E. Mosconi, F. De Angelis, 'Relativistic GW Calculations on  $\text{CH}_3\text{NH}_3\text{PbI}_3$  and  $\text{CH}_3\text{NH}_3\text{SnI}_3$  Perovskites for Solar Cell Applications', *Sci. Rep.* **2014**, 4, 4467.
- [64] N. Ashari-Astani, S. Meloni, A. H. Salavati, G. Palermo, M. Grätzel, U. Rothlisberger, 'Computational Characterization of the Dependence of Halide Perovskite Effective Masses on Chemical Composition and Structure', *J. Phys. Chem. C* **2017**, 121, 23886–23895.
- [65] M. Mladenović, N. Vukmirović, 'Effects of Thermal Disorder on the Electronic Structure of Halide Perovskites: Insights from MD Simulations', *Phys. Chem. Chem. Phys.* **2018**, 20, 25693–25700.
- [66] J. M. Frost, A. Walsh, 'What is Moving in Hybrid Halide Perovskite Solar Cells?', *Acc. Chem. Res.* **2016**, 49, 528–535.
- [67] C. Vona, MSc Thesis, École Polytechnique Fédérale de Lausanne, 2018.
- [68] M. Kepenekian, B. Traore, J.-C. Blancon, L. Pedesseau, H. Tsai, W. Nie, C. C. Stoumpos, M. G. Kanatzidis, J. Even, A. D. Mohite, S. Tretiak, C. Katan, 'Concept of Lattice Mismatch and Emergence of Surface States in Two-dimensional Hybrid Perovskite Quantum Wells', *Nano Lett.* **2018**, 18, 5603–5609.
- [69] S. Meloni, G. Palermo, N. Ashari-Astani, M. Grätzel, U. Rothlisberger, 'Valence and Conduction Band Tuning in Halide Perovskites for Solar Cell Applications', *J. Mater. Chem. A* **2016**, 4, 15997–16002.
- [70] L. Mao, C. C. Stoumpos, M. G. Kanatzidis, 'Two-Dimensional Hybrid Halide Perovskites: Principles and Promises', *J. Am. Chem. Soc.* **2019**, 141, 1171–1190.

Received December 21, 2020  
Accepted February 22, 2021



# Naphthalenediimide/Formamidinium-Based Low-Dimensional Perovskites

Aditya Mishra,<sup>○</sup> Paramvir Ahlawat,<sup>○</sup> George C. Fish,<sup>○</sup> Farzaneh Jahanbakhshi,<sup>○</sup> Marko Mladenović, Masaud Almalki, Marco A. Ruiz-Preciado, María C. Gelvéz-Rueda, Dominik J. Kubicki, Pascal A. Schouwink, Vincent Dufoulon, Thomas Schneeberger, Artin Aslanzadeh, Ferdinand C. Grozema, Shaik M. Zakeeruddin, Jacques-Edouard Moser, Ursula Rothlisberger,\* Lyndon Emsley,\* Jovana V. Milić,\* and Michael Grätzel\*



Cite This: *Chem. Mater.* 2021, 33, 6412–6420



Read Online

ACCESS |



Metrics & More

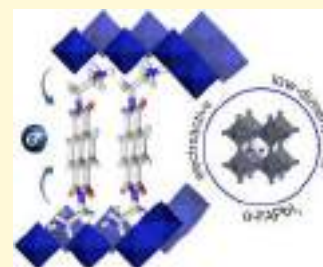


Article Recommendations



Supporting Information

**ABSTRACT:** Low-dimensional hybrid perovskites have emerged as promising materials for optoelectronic applications. Although these materials have already demonstrated enhanced stability as compared to their three-dimensional perovskite analogues, their functionality has been limited by the insulating character of the organic moieties that primarily play a structure-directing role. This is particularly the case for the layered (2D) perovskite materials based on formamidinium lead iodide (FAPbI<sub>3</sub>) that remain scarce. We demonstrate a low-dimensional hybrid perovskite material based on a SPbI<sub>4</sub> composition incorporating an electroactive naphthalenediimide (NDI) moiety as an organic spacer (S) between the perovskite slabs and evidence the propensity of the spacer to stabilize the  $\alpha$ -FAPbI<sub>3</sub> perovskite phase in hybrid low-dimensional SFA<sub>*n*-1</sub>Pb<sub>*n*</sub>I<sub>3*n*+1</sub> perovskite compositions. This has been investigated by means of solid-state nuclear magnetic resonance spectroscopy in conjunction with molecular dynamics simulations and density functional theory calculations. Theoretical calculations suggest an electronic contribution of the organic spacer to the resulting optoelectronic properties, which was confirmed by transient absorption spectroscopy. We have further analyzed these materials by time-resolved microwave conductivity measurements, revealing challenges for their application in photovoltaics.



## INTRODUCTION

Hybrid perovskites are one of the leading thin-film materials for optoelectronics.<sup>1–3</sup> They are defined by the AMX<sub>3</sub> formula, where A represents the central A cation (commonly methylammonium (MA), formamidinium (FA) or Cs<sup>+</sup>), M the divalent metal (mainly Pb<sup>2+</sup> and Sn<sup>2+</sup>), and X the halide (I<sup>-</sup>, Br<sup>-</sup>, or Cl<sup>-</sup>).<sup>1</sup> Despite their extraordinary optoelectronic properties, the challenges associated with stability hamper their commercial applications.<sup>2</sup> This obstacle stimulated the development of layered two-dimensional (2D) perovskite materials that incorporate hydrophobic organic cations between inorganic perovskite slabs.<sup>4,5</sup> They form structures that can be expressed by S'<sub>2</sub>A<sub>*n*-1</sub>Pb<sub>*n*</sub>X<sub>3*n*+1</sub> and SA<sub>*n*-1</sub>Pb<sub>*n*</sub>X<sub>3*n*+1</sub> formulas, where S' and S are either mono- or bifunctional organic spacers, respectively. Although this class of materials demonstrates enhanced stabilities against the environmental factors, the resulting performances remain inferior as compared to conventional three-dimensional (3D) hybrid perovskites.<sup>4,5</sup> One of the underlying reasons for this limitation relates to the insulating character of the organic moieties that have been employed to date,<sup>4</sup> which form natural quantum well structures with organic moieties as barriers to charge extraction (Figure 1a, top). This role can be tailored by introducing functional electroactive organic moieties as spacer units, which could

change their electronic structures (Figure 1a, bottom).<sup>5</sup> Although the potential for this approach has been demonstrated theoretically, practical realizations of functional low-dimensional perovskites remain scarce.<sup>6–9</sup> Moreover, the effort for the development of layered 2D hybrid perovskites and other low-dimensional (e.g., one-dimensional, 1D) analogues is predominantly focused on MA-based perovskite compositions, whereas FA-based analogues are underrepresented despite their higher thermal stability.<sup>10–14</sup> One of the underlying reasons is that FAPbI<sub>3</sub> exists in two forms, the room-temperature-thermodynamically-stable yellow  $\delta$ -FAPbI<sub>3</sub> and the photoactive  $\alpha$ -FAPbI<sub>3</sub> phase.<sup>10,15</sup> Stabilizing the  $\alpha$ -FAPbI<sub>3</sub> perovskite phase hence remains an ongoing challenge that could further stimulate optoelectronic applications, particularly in conjunction with electroactive spacer moieties.<sup>6</sup>

Herein, we demonstrate low-dimensional hybrid perovskite materials based on an SFA<sub>*n*-1</sub>Pb<sub>*n*</sub>I<sub>3*n*+1</sub> composition that

Received: May 12, 2021

Revised: July 21, 2021

Published: August 11, 2021



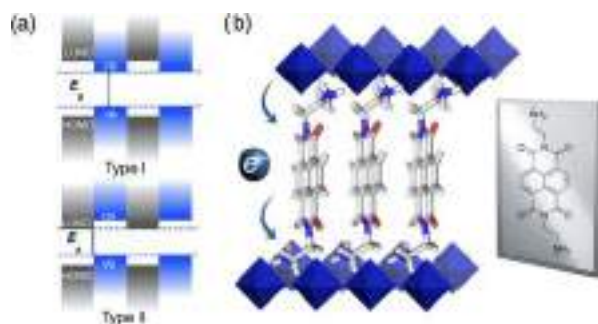


**Figure 1.** (a) Schematic representation of the electronic structure based on typical Type I (top) and Type II (bottom) quantum well structures of layered perovskites with the gray area representing the HOMO and LUMO levels of the organic spacer and blue area the band edges of the inorganic slabs. (b) Schematic representation of the layered perovskite material (left) incorporating electroactive NDIEA-based moieties (right) used in this study. NDIEA = 2,2'-(1,3,6,8-tetraoxo-1,3,6,8-tetrahydrobenzo[Imn][3,8]phenanthroline-2,7-diyl)-bis(ethylammonium); HOMO = highest occupied molecular orbital; LUMO = lowest unoccupied molecular orbital; CB = conduction band; VB = valence band.

incorporate electroactive naphthalenediimide (NDI)<sup>16–19</sup> units as spacer moieties (S) that are linked to the perovskite via ethylammonium anchoring groups (Figure 1b). A comparable system has been described by Proppe et al. based on MA and MA/FA cation compositions, suggesting low-dimensional phase formation.<sup>18</sup> We provide a comprehensive analysis of the FA-based hybrid perovskite materials by means of molecular dynamics (MD) simulations and density functional theory (DFT) calculations that reveal the capacity to form 2D perovskite structures in which spacer orbitals actively contribute to the band edge, which was complemented with the experimental characterization of the corresponding films. We demonstrate that low-dimensional perovskite phases contribute to stabilizing the  $\alpha$ -FAPbI<sub>3</sub> phase, which was evidenced by solid-state NMR spectroscopy. Moreover, we evidence electron transfer between the perovskite slabs and the organic spacer with transient absorption spectroscopy. We further probe the utility of hybrid composites by time-resolved microwave conductivity measurements, which reveal obstacles to their application due to a high level of structural disorder with respect to the low-dimensional (1D, 2D) and compositional (*n*) phase mixtures and their orientation in the material.

## EXPERIMENTAL SECTION

**Materials and Methods.** Reactions were performed in standard glassware under an ambient atmosphere unless otherwise specified. Commercially available chemicals were used without further purification. Purification was performed using dry flash chromatography on SiO<sub>2</sub> 60 (particle size 0.040–0.063 mm, 230–400 mesh) at a maximum head pressure of 0.2 bar. The procedures are detailed in the Supporting Information (SI) Sections S1 and S2.

**Synthesis of the Spacer.** *tert*-Butyl-*N*-(2-aminoethyl)carbamate (1.5 mL, 37 mmol) was added to a suspension of naphthalene-1,4,5,8-tetracarboxylic dianhydride (1.00 g, 3.73 mmol) in DMF (30 mL). The mixture was stirred for 15 h at 75 °C. The product was extracted by CH<sub>2</sub>Cl<sub>2</sub>, dried over anhydrous MgSO<sub>4</sub>, and concentrated under vacuum. Dry flash chromatography (SiO<sub>2</sub>, CH<sub>2</sub>Cl<sub>2</sub>/CH<sub>3</sub>OH 9:1) yielded a di-*tert*-butyl((1,3,6,8-tetraoxo-1,3,6,8-tetrahydrobenzo[Imn]-[3,8]phenanthroline-2,7-diyl)bis(ethane-2,1-diyl))dicarbamate intermediate (1.7 g, 83%) as an orange solid. HI (1.67 mL, 12.6 mmol, 57%) was added to its suspension (1.7 g, 3.08 mmol) in ethanol (15 mL) at 0 °C. The mixture was stirred for 12 h and the resulting

solution was concentrated, resuspended in diethyl ether (10 mL), filtered, washed with diethyl ether and isopropanol, and dried under vacuum to yield 2,2'-(1,3,6,8-Tetraoxo-1,3,6,8-tetrahydrobenzo[Imn]-[3,8]phenanthroline-2,7-diyl)bis(ethylammonium) iodide (NDIEAI<sub>2</sub>) (0.7 g, 75%) as a yellow solid. <sup>1</sup>H NMR (400 MHz, (CD<sub>3</sub>)<sub>2</sub>SO):  $\delta$  = 8.74 (s, 4H), 7.81 (s, 6H), 4.35 (t, *J* = 5.9 Hz, 4H), 3.20 (q, *J* = 5.9 Hz, 4H) ppm; <sup>13</sup>C NMR (101 MHz, (CD<sub>3</sub>)<sub>2</sub>SO):  $\delta$  = 163.73, 130.88, 127.06, 126.68, 38.35, 37.98 ppm; HRMS (ESI+/QTOF): *m/z* (%) 353.1241 (100, [M]<sup>+</sup>, calcd for C<sub>18</sub>H<sub>17</sub>N<sub>4</sub>O<sub>4</sub><sup>+</sup>: 353.1244); (ESI-/QTOF): *m/z* (%) 126.9055 (100, [M]<sup>-</sup>, calcd for I<sup>-</sup>: 126.9050).

**Synthesis of (NDIEA)PbI<sub>4</sub> and (NDIEA)FA<sub>*n*-1</sub>Pb<sub>*n*3*n*+1</sub> Thin Films.** The perovskite precursor solutions were prepared by dissolving stoichiometric amounts of PbI<sub>2</sub> (TCI), FAI (GreatCell Solar), and NDIEAI<sub>2</sub> according to the molecular formula of (NDIEA)-FA<sub>*n*-1</sub>Pb<sub>*n*3*n*+1</sub> in the dimethyl sulfoxide (DMSO)/*N,N*-dimethylformamide (DMF) mixture (1:4, v/v) at 0.4 M concentration of PbI<sub>2</sub>. The perovskite film was deposited by spin-coating at 5000 rpm for 20 s (ramp rate 2000 rpm s<sup>-1</sup>) on the glass substrates. The films were then annealed at 150 °C for 15 min. The preparation of the perovskite layer was carried out in a dry air-filled glove box with a relative humidity of <2%.

**Mechanosynthesis of Perovskite Powders.** Mechano-synthesis of perovskite powders was performed by grinding the reactants in an electric ball mill (Retsch Ball Mill MM-200) using a grinding jar (10 mL) and a ball ( $\phi$ 10 mm) for 30 min at 25 Hz. The powders were packed into 3.2 mm zirconia rotors and annealed at 150 °C for 15 min to reproduce the thin-film synthetic procedure, before transferring into the probe. The measurements were carried out under a dry nitrogen atmosphere.

**Solution NMR Spectra.** Solution NMR spectra (Figures S1–S2, SI) were recorded on a Bruker DRX 400 instrument operating at 400 MHz at 298 K. <sup>13</sup>C NMR spectra were recorded on a Bruker DRX 400 operating at 100 MHz. Multiplicities are reported as follows: bs (broad singlet), s (singlet), d (doublet), and m (multiplet). Chemical shifts  $\delta$  (ppm) were referenced to the internal solvent signals.

**X-ray Diffraction Patterns.** X-ray diffraction (XRD) patterns were recorded on an X'Pert MPD PRO (PANalytical) diffractometer equipped with a ceramic tube providing Ni-filtered (Cu anode,  $\lambda$  = 1.54060 Å) radiation and an RTMS X'Celerator (PANalytical) system. The measurements were performed in the BRAGG-BRENTANO geometry. The samples were mounted without further modification and the automatic divergence slit (10 mm) and beam mask (10 mm) were adjusted to the dimensions of the films.

**Grazing Incidence Wide-Angle X-ray Scattering.** Grazing incidence wide-angle X-ray scattering (GIWAXS) of (NDIEA)-FA<sub>*n*-1</sub>Pb<sub>*n*3*n*+1</sub> thin films on glass slides was measured at a 2° incidence angle with a D8 Discover Plus TXS (Bruker) equipped with rotating anode (Cu), a Dectris Eiger2 2D detector, and a point-collimated beam of approx. 300  $\mu$ m, at a power of 5.4 kW.

**Scanning Electron Microscopy.** Scanning electron microscopy (SEM) images were recorded using a high-resolution scanning electron microscope (Gemini-SEM 300). An electron beam accelerated to 3 kV was used with an in-lens detector. The images were measured with the perovskite infiltrated mp-TiO<sub>2</sub> films supported by FTO.

**UV–Vis Absorption Measurements.** UV–vis absorption measurements of (NDIEA)FA<sub>*n*-1</sub>Pb<sub>*n*3*n*+1</sub> films were performed using a Varian Cary5 UV–visible spectrophotometer.

**Steady-State Photoluminescence.** Steady-state photoluminescence (PL) spectra were recorded by exciting the layered perovskite films deposited onto glass slides. The emission between 460 and 830 nm was recorded with a Fluorolog 322 spectrometer (Horiba Jobin Yvon iHr320 and a CCD) within with a bandpass of 5 nm upon excitation at 420 nm with a bandpass of 5 nm. The samples were mounted at 60° and emission was recorded at 90° from the incident beam path.

**Solid-State NMR Spectroscopy.** Solid-state nuclear magnetic resonance (NMR) spectroscopy for <sup>1</sup>H (900 MHz) and <sup>13</sup>C (225 MHz) was performed at a low temperature on a Bruker Avance Neo 21.1 T spectrometer equipped with a 3.2 mm low-temperature

CPMAS probe.  $^{14}\text{N}$  (36.1 MHz) magic angle spinning (MAS) spectra were recorded on a Bruker Avance III 11.7 T spectrometer equipped with a 3.2 mm CPMAS probe.  $^1\text{H}$  and  $^{13}\text{C}$  chemical shifts were referenced to solid adamantane ( $\delta_{\text{H}} = 1.91$  ppm and  $\delta_{\text{C}} = 29.45$  (CH) and 38.48 (CH<sub>2</sub>) ppm) at 298 K.  $^{14}\text{N}$  spectra were referenced to solid  $\text{NH}_4\text{Cl}$  (0 ppm) at 298 K. A recycle delay of 0.3 s was used for the  $^{14}\text{N}$  measurements.

**Transient Absorption Spectra.** Transient absorption (TA) spectra were measured using a femtosecond (fs) pump–probe spectrometer based on an amplified Ti:sapphire laser (Clark-MXR, CPA-2001) delivering 778 nm pulses with a pulse width of 150 fs and a repetition rate of 1 kHz. For excitation at 510 nm, the pump beam was generated by passing a portion of the fundamental beam through a two-stage non-collinear optical parametric amplifier (NOPA-Plus, Clark-MXR) resulting in an excitation wavelength of 510 nm. For excitation at 390 nm, the fundamental beam was passed through a BBO ( $\beta\text{-BaB}_2\text{O}_4$ ) crystal in order to generate the second harmonic at 390 nm. The probe beam was a broadband white light continuum generated by passing part of the fundamental beam through a 5 mm thick oscillating  $\text{CaF}_2$  plate. The pump and probe beams were set at magic-angle polarization and were spatially and temporally overlapping with respect to one another using a delay stage. A chopper, set at 500 Hz, was used to modulate the frequency of the pump beam, allowing for the absorption with and without the pump to be obtained. The probe beam was split before the sample into a reference and signal beam in order to account for shot-to-shot variations. The signal and reference beams were dispersed in a grating spectrograph (SpectraPro 2500i, Princeton Instruments) and detected at 1 kHz by a  $512 \times 58$  pixel back-thinned charge-coupled device camera (Hamamatsu S07030-0906).

**Density Functional Theory Calculations of the Spacer Moiety.** Density functional theory (DFT) calculations of the spacer moiety were conducted with the Gaussian 09 Rev. D suite of programs.<sup>20,21</sup> The geometry optimizations were performed at the B3LYP/6-31G(d) level of theory (Figure 1).

**Molecular Dynamics Simulations and Density Functional Theory Calculations of Perovskite Structures.** A detailed description of the molecular dynamics (MD) simulations and DFT calculations procedure are provided in the Supporting Information Sections S3 and S4, respectively.

## RESULTS AND DISCUSSION

We investigate hybrid perovskite materials incorporating naphthalenediimide (NDI) moieties, employed to facilitate electron transport, which is functionalized with two ethylenammonium linkers as anchoring groups for inorganic perovskite slabs that form 2,2'-(1,3,6,8-tetraoxo-1,3,6,8-tetrahydrobenzo[*lmn*][3,8]phenanthroline-2,7-diyl)bis-(ethylammonium) (NDIEA; Figure 1b). This system is envisioned to form Dion–Jacobson-like ( $\text{SFA}_{n-1}\text{Pb}_n\text{I}_{3n+1}$ ) perovskite phases ( $n = 1-3$ )<sup>22-27</sup> and we thus studied these nominal compositions of the materials where  $\langle n \rangle$  refers to the stoichiometry. We have primarily focused on lower compositional representatives ( $\langle n \rangle = 1-3$ ) as  $\langle n \rangle = 1$  compositions are known to form better defined 2D phases, whereas  $\langle n \rangle > 1$  compositions commonly form mixtures of different  $\langle n \rangle$  2D/3D phases.<sup>4,5,22,23,27</sup> We analyzed the morphology, structural, and optoelectronic properties by a multi-technique approach including both theoretical and experimental analysis.

**Molecular Design and Theoretical Analysis.** We have based our investigation on NDI-based electron acceptors that are commonly used in organic electronics and supramolecular chemistry due to high electron affinity, good charge carrier mobility in the solid-state, and excellent thermal and oxidative stability.<sup>16-18</sup> Since haloplumbates based on NDI are characterized by a high degree of structural disorder (i.e., formation of both 1D and 2D phases),<sup>18,19</sup> we first assess the

possibility of NDIEA<sub>2</sub> to form layered (2D) perovskite structures by classical molecular dynamics (MD) simulations (more details are provided in Section S3 of the SI). We base the simulations on a supercell with a Dion–Jacobson structure by placing NDIEA moieties between layers of corner-sharing Pb–I octahedra of different compositions (the specific procedure is detailed in the SI).<sup>14</sup> As a result, we obtain stable and highly ordered 2D perovskite structures from classical MD (Figure S3, SI) that were subsequently relaxed at the DFT level to evidence the propensity to form a well-defined Dion–Jacobson structure. We find that the structure adopts the conformation in which the Pb–I–Pb angles are close to 180° (Figure 2). Moreover, the NDIEA spacer

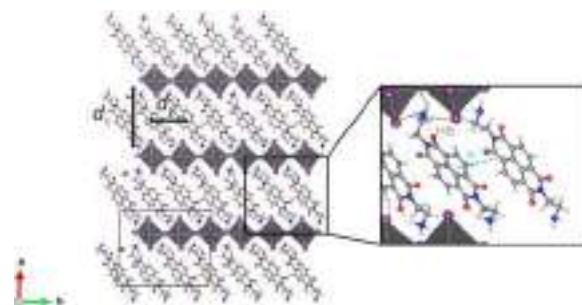


**Figure 2.** Simulated structure of (NDIEA)PbI<sub>4</sub> perovskites obtained by molecular dynamics simulations followed by DFT (PBEsol) calculations with characteristic interlayer distances ( $d_1$ ,  $d_2$ ). Experimental details and other compositions are detailed in Sections S3 and S4 of the SI.

molecules are assembled via both hydrogen bonding and  $\pi$ – $\pi$  interactions in the spacer layer (Figure 2, inset). As a result of these interactions, a rigid framework forms between the corresponding perovskite slabs (Figure 2).

To probe the templating effects of the spacer and the inorganic framework, we analyzed the average tilting angle between the octahedra (calculated as Pb–I–Pb angles), as well as the penetration depths of the spacers into the perovskite slabs by DFT calculations.<sup>14,28</sup> We found that increasing the number of inorganic layers ( $n$ ) leads to a decrease in the N $\cdots$ Pb distances and, consequently, an increase in the penetration depth.<sup>14,28-30</sup> This leads to changes in the average Pb $\cdots$ Pb distances between opposite layers ( $d_1$ ) as well as distances between the spacer moieties ( $d_2$ ) (Figure 2; Figure S4 and Table S1, SI). Similar to the behavior of other layered hybrid perovskite systems, the interlayer distance ( $d_1$ ) decreases upon deeper incorporation of the organic cation into the inorganic layer, evidencing templating effects through an interplay between the inorganic and organic layers that define the resulting structure.<sup>14,28</sup> The spacers adopt a preferred conformation that remains unchanged during 5 ps of *ab initio* MD simulations at temperatures of 200, 300, and 400 K, which points to structural stability as a result of interactions in the spacer layer. Such structural preferences stimulated further investigation of these materials and their structural and optoelectronic properties.

**Structural Properties.** NDIEA-based films of  $\text{SFA}_{n-1}\text{Pb}_n\text{I}_{3n+1}$  compositions ( $\langle n \rangle = 1-3$ ; S = NDIEA; Figure 3a) are prepared by solution-processing of stoichiometric quantities of precursor materials followed by subsequent annealing at 150 °C for 15 min (as detailed in the Experimental Section, as well as Section S1, SI). The

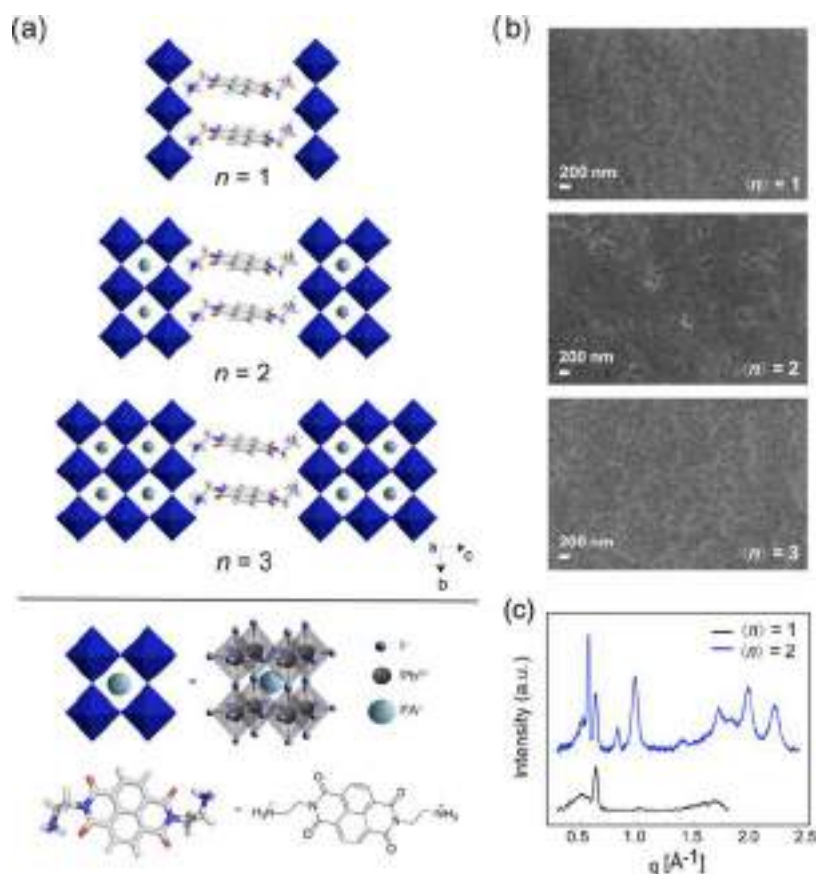


**Figure 3.** Structural representation and morphology. (a) Schematic of layered Dion–Jacobson structures based on  $(\text{NDIEA})\text{FA}_{n-1}\text{Pb}_n\text{I}_{3n+1}$  compositions ( $\langle n \rangle = 1-3$ ) with structural features of the compositional elements. The feasibility of these structures was confirmed theoretically, yet they were not experimentally evidenced since mixed low-dimensional phases form instead. (b) SEM images of perovskite films based on  $(\text{NDIEA})\text{FA}_{n-1}\text{Pb}_n\text{I}_{3n+1}$  compositions ( $\langle n \rangle = 1-3$ ). (c) Integrated diffraction patterns (from 2D GIWAXS images) for thin films of  $(\text{NDIEA})\text{FA}_{n-1}\text{Pb}_n\text{I}_{3n+1}$  ( $\langle n \rangle = 1-2$ ) compositions on microscope glass slides. Further details are provided in Section S5 and Figure S6 of the SI.

morphology of NDIEA-based films was investigated by scanning electron microscopy (SEM) of the film surface (Figure 3b). The SEM images show complete coverage of the surface of the film with relatively small nanometer-scale grain sizes that increase with increasing  $\langle n \rangle$  up to 200 nm for  $\langle n \rangle = 3$ , with improving homogeneity.

The structural properties were further investigated by X-ray diffraction (XRD) measurements of thin films. XRD patterns (Figure S6, SI) of thin films show a signal at low reflection angles  $2\theta < 10^\circ$ , which we attribute to the low-dimensional perovskite phase associated with a  $d$ -spacing of around 10 Å ( $\langle n \rangle = 1$ ) and 11–12 Å ( $\langle n \rangle = 2$ ).<sup>14,22,31</sup> However, integrated diffraction patterns of grazing incidence wide-angle X-ray scattering (GIWAXS) images (Figure S6, SI and Figure 3c) indicate a nearly complete absence of periodicity, even for  $\langle n \rangle = 1$  phases, which is related to the low crystallinity under these experimental conditions. This is in accordance with the observations by Proppe et al. who have recently shown that films of NDI-based haloplumbates are highly disordered, containing 1D and 2D phases,<sup>18</sup> although single crystals of 2D phases have also been reported.<sup>19</sup> X-ray scattering measurements suggest low-dimensional phase formation for  $\langle n \rangle = 1$  and  $\langle n \rangle > 1$  compositions revealed by the signals in the  $q_z$ -range below  $0.7 \text{ \AA}^{-1}$  ( $2\theta < 10^\circ$ ) that are commonly ascribed to the (00 $l$ ) planes (Figures 3c and S6, SI).<sup>13,14,18,19</sup> Films based on the  $\langle n \rangle = 1$  composition feature a signal at  $0.63 \text{ \AA}^{-1}$ , whereas those based on the  $\langle n \rangle = 2$  composition show signals

at  $0.56$  and  $0.52 \text{ \AA}^{-1}$  that indicate distinct low-dimensional phases (Figure S6, SI). The signals associated with the  $\langle n \rangle = 2$  composition more closely correspond to the calculated  $n = 2$  phase (Section S4, SI). We do not observe other signals for  $\langle n \rangle = 3$  compositions, which is in accordance with the previous reports suggesting that the formation of 2D FAPbI<sub>3</sub>-based  $n > 2$  phases is rather challenging.<sup>27</sup> In addition, the lack of preferential orientation in the  $\langle n \rangle = 1$  composition has been evidenced by GIWAXS (Section S5, Figure S6, SI) that display ring-shaped features with uniform angular intensity distribution that is associated with the random orientation of crystallites, whereas there is some preferential out-of-plane orientation for the distinct phase of the  $\langle n \rangle = 2$  composition. Such differences in preferential orientation between the  $n$  phases are not uncommon and have been reported previously.<sup>14,27</sup> Owing to this high degree of long-range disorder, we turn to solid-state NMR to investigate the local structure and atomic-level mixing.<sup>3,13,32–36</sup>

We have performed echo-detected <sup>14</sup>N as well as <sup>1</sup>H → <sup>13</sup>C and <sup>1</sup>H → <sup>15</sup>N cross-polarization (CP) magic-angle spinning (MAS) NMR measurements (Figure 4). We compared the corresponding spectra of bulk mechanochemical  $\alpha$ -FAPbI<sub>3</sub> as a model perovskite compound to those of the neat NDIEAl<sub>2</sub> and mechanochemical  $(\text{NDIEA})\text{FA}_{n-1}\text{Pb}_n\text{I}_{3n+1}$  perovskite compositions (experimental details are provided in the Experimental Section and Section S1, SI). The <sup>15</sup>N CP NMR resonances revealed the presence of new environments in the spectral

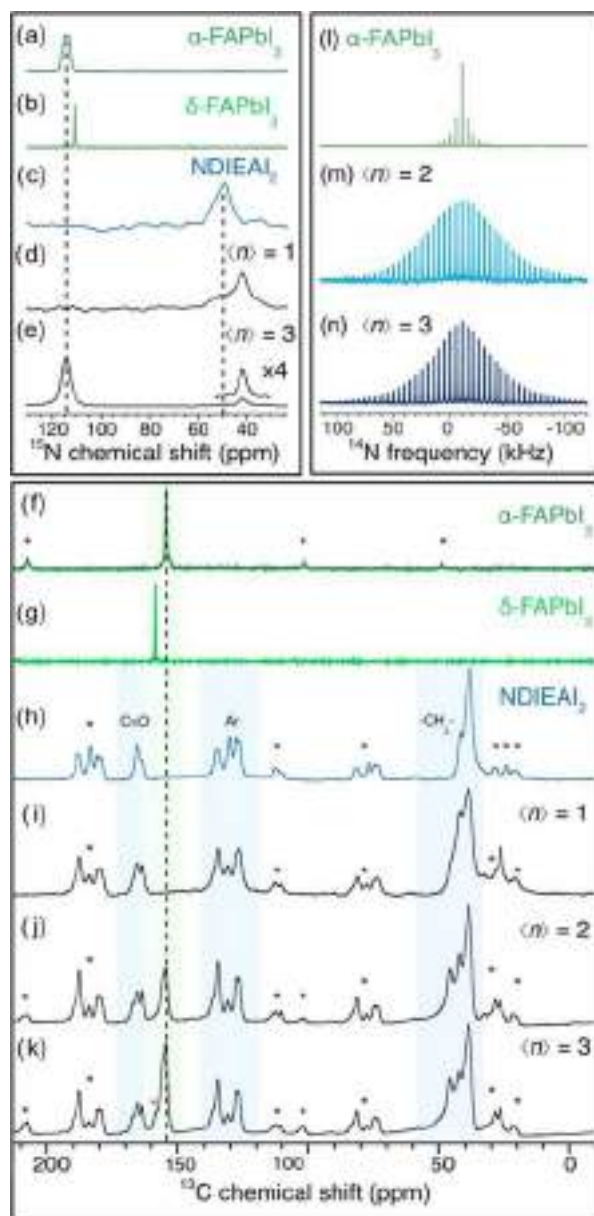


**Figure 4.** Structural properties determined by solid-state NMR spectroscopy.  $^{15}\text{N}$  MAS NMR spectra at 21.1 T, 100 K, with 12.5 kHz MAS of (a)  $\alpha\text{-FAPbI}_3$ , (b)  $\delta\text{-FAPbI}_3$ , (c) neat  $\text{NDIEAl}_2$ , and (d, e)  $(\text{NDIEA})\text{FA}_{n-1}\text{Pb}_n\text{I}_{3n+1}$  ( $\langle n \rangle = 1, 3$ ).  $^{13}\text{C}$  CP solid-state MAS NMR spectra at 21.1 T, 100 K, with 12 kHz MAS of (f)  $\alpha\text{-FAPbI}_3$ , (g)  $\delta\text{-FAPbI}_3$ , (h) neat  $\text{NDIEAl}_2$ , and (i–k)  $(\text{NDIEA})\text{FA}_{n-1}\text{Pb}_n\text{I}_{3n+1}$  ( $\langle n \rangle = 1, 2, 3$ ).  $^{14}\text{N}$  MAS NMR spectra at 21.1 T, 100 K, with 12.5 kHz MAS of bulk (l)  $\alpha\text{-FAPbI}_3$  and (m, n)  $(\text{NDIEA})\text{FA}_{n-1}\text{Pb}_n\text{I}_{3n+1}$  ( $\langle n \rangle = 2, 3$ ). Asterisks mark spinning sidebands, whereas the red asterisk in (k) indicates residual  $\delta\text{-FAPbI}_3$ .

region of both FA (100–120 ppm) and NDIEA (40–60 ppm) cations for all  $(\text{NDIEA})\text{FA}_{n-1}\text{Pb}_n\text{I}_{3n+1}$  perovskite compositions (Figure 4a–e), which are indicative of the formation of new iodoplumbate phases containing FA/NDIEA moieties formed upon the atomic-level interaction of  $-\text{NH}_3^+$  moieties and  $\text{FAPbI}_3$  perovskite lattice through hydrogen bonding. A comparison with the neat  $\text{NDIEAl}_2$  spacer precursor reveals full consumption of the spacer, as suggested by the disappearance of the spacer resonances at ca. 50 ppm (Figure 4c–e). The  $\langle n \rangle = 2$ –3 compositions further indicate the stabilization of the  $\alpha\text{-FAPbI}_3$  phase (Figure 4a,e) with the

corresponding signal at ca. 115 ppm. Similarly, the  $^{13}\text{C}$  CP NMR spectra (Figure 4f–k) of the corresponding mechanochemical mixtures reveal the formation of new phases that can be associated with the presence of the NDIEA and FA cations in new environments that are closely related to the  $\alpha\text{-FAPbI}_3$  phase, with a minor residual  $\delta\text{-FAPbI}_3$  phase in the  $\langle n \rangle = 3$  composition (Figure 4k). These environments may be ascribed to the interaction of the spacer with the surface of the  $\text{PbI}_2$  and  $\alpha\text{-FAPbI}_3$  perovskites in a low-dimensional perovskite phase, which yields  $^{13}\text{C}$  and  $^{15}\text{N}$  resonances that are not substantially shifted from the neat components, suggesting that the large NDIEA cation does not incorporate into the A-cation site of the 3D perovskite lattice and remains at the surface. As a result of this interaction, changes in the underlying crystallographic symmetry can be observed, as revealed by  $^{14}\text{N}$  NMR spectra (Figure 4l–n). The width of the  $^{14}\text{N}$  spinning sideband (SSB) manifolds is related to the local symmetry of FA reorienting inside the perovskite cavity.<sup>13,32–36</sup> In this regard, narrower  $^{14}\text{N}$  SSB manifolds indicate a higher symmetry of the local environment that is closer to the cubic one. The comparison of the  $^{14}\text{N}$  MAS NMR spectra of  $\alpha\text{-FAPbI}_3$  and  $\langle n \rangle = 2, 3$  perovskite compositions feature an SSB pattern that is broader than the neat  $\alpha\text{-FAPbI}_3$ , which suggests lowering of symmetry upon low-dimensional structure formation. In summary, solid-state NMR spectroscopy measurements confirm the formation of new structures by the interaction between  $\text{NDIEAl}_2$  and either  $\text{PbI}_2$  (for  $\langle n \rangle = 1$  compositions) or  $\alpha\text{-FAPbI}_3$  (for  $\langle n \rangle = 2, 3$  compositions) that could be ascribed to the formation of a low-dimensional phases and stabilization of the black  $\alpha\text{-FAPbI}_3$  perovskite phase, which is relevant for the optoelectronic properties.

**Optoelectronic Properties.** To further understand hybrid materials formed with NDIEA, their optoelectronic properties were assessed by means of UV–vis absorption spectroscopy. The gradual color change from dark yellow to black with the increasing number of inorganic layers  $\langle n \rangle$  is indicative of the possible effect of the spacer on the stabilization of the black  $\alpha\text{-FAPbI}_3$  perovskite phase (Figure 5a). UV–vis absorption spectra for films with  $\langle n \rangle = 1$ –3 compositions (Figure 5b) shows an excitonic peak at around 400 nm for the  $\langle n \rangle = 1$  compositions, which is typical for low-dimensional perovskites.<sup>5,14</sup> Moreover, additional absorption peaks are apparent in the region between 500 and 650 nm (Figure 5b), which might be related to the electronic exchange between the organic spacer and the inorganic slabs.<sup>18,19</sup> This further corroborates with the significant quenching of the steady-state PL spectra (Figure S8, SI), in accordance with the observations of Proppe et al.<sup>18</sup> For  $\langle n \rangle = 2$  compositions, a much broader absorption spectrum is observed with an onset above 700 nm, which is suggestive of the formation of mixed 3D perovskite phases. Possible excitonic peaks corresponding to various  $n$  phases may be visible at higher wavelengths (500–650 nm, Figure 5b, dashed lines), suggestive of potential 2D subphase formation. However, broad absorption signals are in accordance with the structural disorder that can be attributed to mixed phase formation.

To understand the optical properties, the band gaps of the DFT-optimized  $(\text{NDIEA})\text{FA}_{n-1}\text{Pb}_n\text{I}_{3n+1}$  structures were calculated (details are provided in Section S4 of the SI). The calculated band gap for  $(\text{NDIEA})\text{PbI}_4$  is found to be in a reasonable agreement with the experimental optical gap estimates of around 2.37 eV (Table S2, SI and Figure 5b). The band gap is lower as compared to other Dion–Jacobson

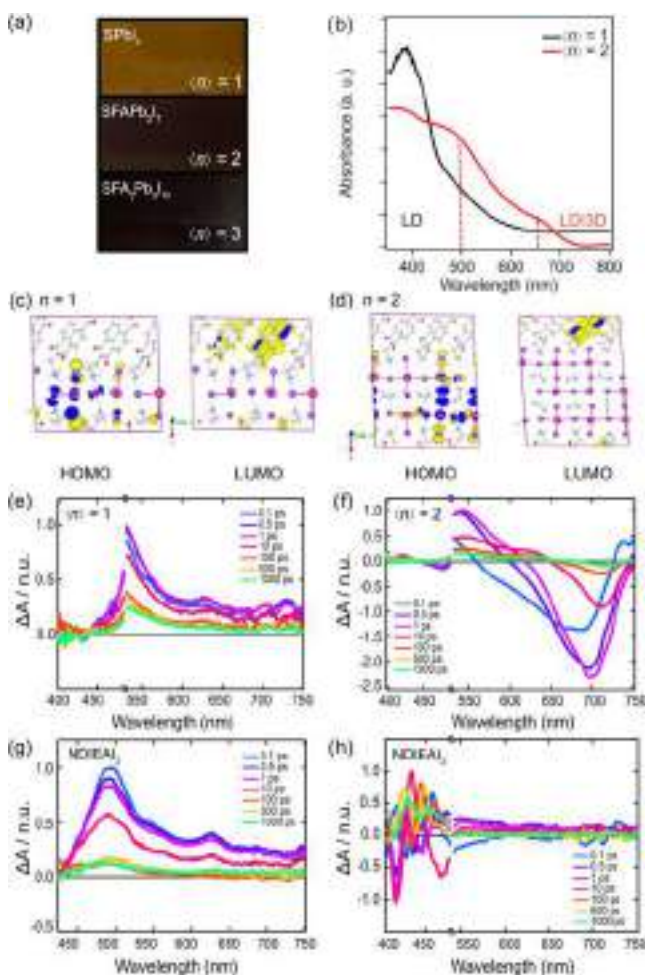


**Figure 5.** Optical properties. (a) Images of the perovskite films on microscope glass slides and (b) UV–vis absorption spectra for (NDIEA) $\text{FA}_{n-1}\text{Pb}_n\text{I}_{3n+1}$  compositions ( $\langle n \rangle = 1-2$ ). (c, d) Calculated molecular orbitals (highest occupied molecular orbital, HOMO and lowest unoccupied molecular orbitals, LUMO) for (c)  $n = 1$  and (d)  $n = 2$  phases. The partial density of states and further details are provided in the SI, Section S4. (e–h) Transient absorption spectra for thin films of the (e, f) (NDIEA) $\text{FA}_{n-1}\text{Pb}_n\text{I}_{3n+1}$  composition ( $\langle n \rangle = 1-2$ ) and (g, h) NDIEAI<sub>2</sub> upon excitation at 510 nm (e, f, h) and 400 nm (g). The spectral shape does not change over time and the generated species are long-lived.

systems, which could be the result of either the symmetry being closer to cubic that would enhance orbital overlaps or a more substantial overlap between the organic and inorganic phases. Moreover, orbitals of the organic moieties directly contribute to the bottom of the conduction band (CB) (Figures S3c,d and S5, SI), resulting in significant lowering of the CB with respect to the inorganic layer, in accordance with the Type-II quantum well structure (Figure 1b, bottom). The projected densities of states (Figure S5, SI) corroborate the contribution of the organic moieties to the band edges for all perovskite compositions. Furthermore, calculated orbitals (Figures S3c,d and S5, SI) indicate localization of the bottom of the CB as well as higher states on the NDIEA spacer moieties, while the top of the valence band (VB) is delocalized over the inorganic part. As a result, the effective masses in the in-plane directions decrease upon increasing  $n$  for both electrons and holes, while significantly higher values for electrons prevail in the perpendicular direction to the inorganic

layer (Table S2, SI). Although some of the in-plane calculated effective hole masses tend to be somewhat lower than those of 1,4-phenyldimethan ammonium (PDMA)-based Dion–Jacobson structures,<sup>14</sup> the effective masses for electrons are significantly increased with respect to other 2D perovskites<sup>37</sup> due to the localized nature of the spacer-dominated CB, which could affect charge transport in these hybrid materials.

The electronic properties and interactions between the organic spacer and the perovskite slabs were thereby probed by transient absorption (TA) spectroscopy (Figures 5e–g and S7, Section S6 SI). Upon excitation of the films with the (NDIEA) $\text{FA}_{n-1}\text{Pb}_n\text{I}_{3n+1}$  composition ( $\langle n \rangle = 1-2$ ) at 510 nm a positive feature appears within the first 100 fs between 450 and 550 nm (Figure 5e,f). The TA spectra of the neat NDIEA film at 400 nm (Figure 5g) confirm that this feature seen in the spectra of the hybrid material corresponds to the formation of NDIEA-based radical anions.<sup>16–18</sup> This is, however, not observed in the NDIEA-based films upon excitation at 510 nm (Figure 5h), confirming that it originates from the electron transfer between the organic spacer and the perovskite layers. This exchange process does not take place in systems incorporating electronically inactive spacers, such as the PDMA-based systems (Figure S7, SI), which have been previously shown to form Dion–Jacobson perovskite phases.<sup>23</sup> Although the reference PDMA-based system also involves a bleach at 520 nm characteristic for layered 2D perovskites,<sup>18</sup> we do not observe such a feature in the NDIEA-based films, which is likely covered by the signal at around 510 nm (Figures 5e,f and S7). The spectral shape does not change over time and the generated species are long-lived, in accordance with the formation of radical anions. Furthermore, the TA spectra of  $\langle n \rangle = 2$  compositions reveal an additional bleaching signal in the 625–750 nm range that is characteristic for the 3D perovskite phase (Figure 5f).<sup>38</sup>

Having evidenced a rapid charge transfer between the organic and the inorganic components of the hybrid composite, time-resolved microwave conductivity (TRMC) measurements were used to probe changes in the conductivity of hybrid perovskites by using high-frequency microwaves after the excitation by either a high energy electron pulse or a laser (Section S7, SI).<sup>7,9,14,39</sup> The generated free charge carriers absorb part of the microwave power and this fraction of the absorbed microwave power ( $\Delta G$ ) is proportional to the change in conductivity of the material ( $\Delta\sigma$ ), which, in turn, is defined as the product of charge mobility ( $\mu$ ) and quantum yield of free charge carrier formation ( $\varphi$ ).<sup>39</sup> Therefore, TRMC upon laser photoexcitation was used to analyze films of approximately 200 nm thickness with different compositions ( $\langle n \rangle = 1-3$ ; Figure S9, SI). The photoconductivity of  $\langle n \rangle = 1$  compositions was rather low, accompanied by a long lifetime on the  $\mu\text{s}$  timescale, while the photoconductivity was found to increase by 2 orders of magnitude for  $\langle n \rangle = 2$  compared to  $\langle n \rangle = 1$  compositions, and by another order of magnitude for  $\langle n \rangle = 3$  as compared to the  $\langle n \rangle = 2$  composition, with lower lifetimes than for  $\langle n \rangle > 1$  systems (below 400 ns). In contrast to the predicted theoretical structures, the photoconductivity values are found to be lower for these materials compared to conventional layered perovskite phases,<sup>7,9,14</sup> which is likely the result of the structurally disordered low-dimensional structures, as suggested by solid-state NMR and X-ray scattering measurements. The level of disorder may also be the result of stronger noncovalent interactions in the spacer layer, which could compromise its adaptability in the formation of 2D

perovskites, leading to mixed low-dimensional phases and their orientations.<sup>37</sup> In addition, the highly localized nature of the CB revealed by theoretical analysis is likely to affect the charge transport. This was further confirmed by trial tests of photovoltaic performances in conventional solar cell devices (detailed in Section S8, SI) that suggest lower performances under several conditions as compared to other 2D and 2D/3D perovskites (Tables S3–S5, Figure S10, SI). These limitations stimulate further investigations towards minimizing the level of disorder in the compositions with enhanced phase purity, which could enable the effective incorporation of such functional materials into other optoelectronic devices in the future.

## CONCLUSIONS

We have investigated hybrid FA-based perovskites incorporating 2,2'-(1,3,6,8-tetraoxo-1,3,6,8-tetrahydrobenzo[*lmn*][3,8]-phenanthroline-2,7-diyl)bis(ethylammonium) (NDIEA) moieties to assess the possibility to develop low-dimensional perovskite materials with enhanced charge transport. Molecular dynamics simulations complemented by density functional theory calculations suggested the existence of well-defined Dion–Jacobson perovskite phases based on (NDIEA)-FA<sub>*n*-1</sub>Pb<sub>*n*</sub>I<sub>3*n*+1</sub> (*n* = 1–3) compositions, which were analyzed experimentally in powders and thin films. X-ray scattering measurements and solid-state NMR spectroscopy confirmed the formation of low-dimensional phases and the stabilization of the black  $\alpha$ -FAPbI<sub>3</sub> perovskite phase, yet with a higher level of structural disorder without exhibiting well-defined layered perovskites. Furthermore, DFT calculations predicted the formation of Type II quantum well structures in layered perovskites, which is assumed to contribute to the narrowing of the band gaps and facilitate charge transfer. However, the calculated effective masses for electron transport turn out to be significantly increased due to a highly localized nature of the spacer-centered bottom of the CB. Accordingly, transient absorption spectroscopy confirms the electronic exchange between the organic moieties and hybrid perovskite slabs that corroborates with the significant quenching of the steady-state PL spectra, whereas time-resolved microwave conductivity measurements reveal lower photoconductivity that is attributed to structural disorder in the mixed low-dimensional phases and highly localized nature of the bottom of the CB, which affect optoelectronic properties. This study thereby unravels critical features of these low-dimensional electron-transporting perovskites, stimulating further investigations to enable their utility in optoelectronics.

## ASSOCIATED CONTENT

### Supporting Information

The Supporting Information is available free of charge at <https://pubs.acs.org/doi/10.1021/acs.chemmater.1c01635>. Data presented here can be accessed at DOI:10.5281/zenodo.5172265 and it is available under the license CC-BY-4.0 (Creative Commons Attribution-ShareAlike 4.0 International) or from the corresponding authors upon request.

Materials and methods, structural data, molecular dynamics simulations, DFT calculations, X-ray scattering measurements, transient absorption spectroscopy, time-resolved microwave conductivity measurements, and photovoltaic performance (PDF)

## AUTHOR INFORMATION

### Corresponding Authors

**Ursula Rothlisberger** – Laboratory of Computational Chemistry and Biochemistry, École Polytechnique Fédérale de Lausanne, 1015 Lausanne, Switzerland; [orcid.org/0000-0002-1704-8591](https://orcid.org/0000-0002-1704-8591); Email: [ursula.roethlisberger@epfl.ch](mailto:ursula.roethlisberger@epfl.ch)

**Lyndon Emsley** – Laboratory of Magnetic Resonance, École Polytechnique Fédérale de Lausanne, 1015 Lausanne, Switzerland; [orcid.org/0000-0003-1360-2572](https://orcid.org/0000-0003-1360-2572); Email: [lyndon.emsley@epfl.ch](mailto:lyndon.emsley@epfl.ch)

**Jovana V. Milić** – Laboratory of Photonics and Interfaces, École Polytechnique Fédérale de Lausanne, 1015 Lausanne, Switzerland; Adolphe Merkle Institute, University of Fribourg, 1700 Fribourg, Switzerland; [orcid.org/0000-0002-9965-3460](https://orcid.org/0000-0002-9965-3460); Email: [jovana.milic@unifr.ch](mailto:jovana.milic@unifr.ch)

**Michael Grätzel** – Laboratory of Photonics and Interfaces, École Polytechnique Fédérale de Lausanne, 1015 Lausanne, Switzerland; [orcid.org/0000-0002-0068-0195](https://orcid.org/0000-0002-0068-0195); Email: [michael.graetzel@epfl.ch](mailto:michael.graetzel@epfl.ch)

### Authors

**Aditya Mishra** – Laboratory of Magnetic Resonance, École Polytechnique Fédérale de Lausanne, 1015 Lausanne, Switzerland

**Paramvir Ahlawat** – Laboratory of Computational Chemistry and Biochemistry, École Polytechnique Fédérale de Lausanne, 1015 Lausanne, Switzerland; [orcid.org/0000-0003-2355-3663](https://orcid.org/0000-0003-2355-3663)

**George C. Fish** – Photochemical Dynamics Group, École Polytechnique Fédérale de Lausanne, 1015 Lausanne, Switzerland

**Farzaneh Jahanbakhshi** – Laboratory of Computational Chemistry and Biochemistry, École Polytechnique Fédérale de Lausanne, 1015 Lausanne, Switzerland; [orcid.org/0000-0001-7113-2746](https://orcid.org/0000-0001-7113-2746)

**Marko Mladenović** – Laboratory of Computational Chemistry and Biochemistry, École Polytechnique Fédérale de Lausanne, 1015 Lausanne, Switzerland

**Masaud Almalki** – Laboratory of Photonics and Interfaces, École Polytechnique Fédérale de Lausanne, 1015 Lausanne, Switzerland

**Marco A. Ruiz-Preciado** – Laboratory of Photonics and Interfaces, École Polytechnique Fédérale de Lausanne, 1015 Lausanne, Switzerland

**María C. Gelvéz-Rueda** – Department of Chemical Engineering, Delft University of Technology, 2629 Delft, The Netherlands

**Dominik J. Kubicki** – Laboratory of Magnetic Resonance, École Polytechnique Fédérale de Lausanne, 1015 Lausanne, Switzerland; Laboratory of Photonics and Interfaces, École Polytechnique Fédérale de Lausanne, 1015 Lausanne, Switzerland; [orcid.org/0000-0002-9231-6779](https://orcid.org/0000-0002-9231-6779)

**Pascal A. Schouwink** – X-ray Diffraction and Surface Analytics, École Polytechnique Fédérale de Lausanne, 1951 Sion, Switzerland

**Vincent Dufoulon** – Laboratory of Photonics and Interfaces, École Polytechnique Fédérale de Lausanne, 1015 Lausanne, Switzerland

**Thomas Schneeberger** – Laboratory of Photonics and Interfaces, École Polytechnique Fédérale de Lausanne, 1015 Lausanne, Switzerland; X-ray Diffraction and Surface Analytics, École Polytechnique Fédérale de Lausanne, 1951 Sion, Switzerland

**Artin Aslanzadeh** – *Adolphe Merkle Institute, University of Fribourg, 1700 Fribourg, Switzerland*

**Ferdinand C. Grozema** – *Department of Chemical Engineering, Delft University of Technology, 2629 Delft, The Netherlands*; [orcid.org/0000-0002-4375-799X](https://orcid.org/0000-0002-4375-799X)

**Shaik M. Zakeeruddin** – *Laboratory of Photonics and Interfaces, École Polytechnique Fédérale de Lausanne, 1015 Lausanne, Switzerland*

**Jacques-Edouard Moser** – *Photochemical Dynamics Group, École Polytechnique Fédérale de Lausanne, 1015 Lausanne, Switzerland*; [orcid.org/0000-0003-0747-4666](https://orcid.org/0000-0003-0747-4666)

Complete contact information is available at:

<https://pubs.acs.org/10.1021/acs.chemmater.1c01635>

### Author Contributions

○A.M., P.A., G.C.F., and F.J. contributed equally to this work. The manuscript was written by A.M. and J.V.M. through contributions of all authors. The research was conceptualized and coordinated by J.V.M., who performed the preliminary study and supervised the investigation. A.M. performed the solid-state NMR spectroscopy and data analysis with the support of D.J.K., whereas P.A. conducted molecular dynamics simulations. F.J. and M.M. performed the DFT calculations. M.A.R.-P. performed the photovoltaic device fabrication and characterization with the support of M.A., who performed additional film characterization. M.A. and P.A.S. performed the GIWAXS measurements and analysis. V.D. prepared thin films and performed their characterization by UV–vis absorption and PL spectroscopy. T.S. and A.A. synthesized and characterized the spacer and T.S. performed the mechanosynthesis, while G.C.F. and J.-E.M. performed transient absorption spectroscopy measurements and analysis. S.M.Z. was involved in the discussions. U.R., L.E., and M.G. directed the study. All authors have contributed to the manuscript and given approval to the final version.

### Funding

This work is supported by the Swiss National Science Foundation Grants No. 193174, 200020 178860, 200021\_175729, 200020\_165863, NCCR-MUST, NRP70, and the SINERGIA interdisciplinary research program EPISODE, as well as the GRAPHENE Flagship Core 2 project of the European Commission H2020 Programme under contract 785219.

### Notes

The authors declare no competing financial interest.

### ACKNOWLEDGMENTS

J.V.M. acknowledges support from the Swiss National Science Foundation (SNSF) Grant No. 193174. M.G. is grateful for the financial support from the European Union's H2020 programme under grant agreement no. 785219. A.M., D.J.K., and L.E. are grateful for support from SNSF Grant No. 200020\_178860. G.C.F. and J.-E.M. thank the SNSF (grant no. 200021\_175729) and NCCR-MUST for financial support. U.R. acknowledges SNSF Grant No. 200020 165863, NCCR-MUST, NRP70, and the SINERGIA interdisciplinary research program EPISODE for funding, as well as the computing time from the Swiss National Supercomputing Centre (CSCS). The authors are grateful to Dr. Amita Ummadisingu (EPFL) for insightful discussions and Dr. Renana Gershoni-Poranne (ETH Zurich) for electrostatic potential surface mapping.

### ABBREVIATIONS

CB, conduction band; DFT, density functional theory; GIWAXS, grazing incidence wide-angle X-ray scattering; HOMO, highest occupied molecular orbital; LUMO, lowest unoccupied molecular orbital; MD, molecular dynamics; NDI, naphthalenediimide; NDIEA, 2,2'-(1,3,6,8-tetraoxo-1,3,6,8-tetrahydrobenzo[*lmn*][3,8]phenanthroline-2,7-diyl)bis(ethanol-1-aminium); NMR, nuclear magnetic resonance; PDMA, 1,4-phenyldimethan ammonium; PL, photoluminescence spectroscopy; TAS, transient absorption spectroscopy; TRMC, time-resolved microwave conductivity; XRD, X-ray diffraction

### REFERENCES

- (1) Grätzel, M. The Light and Shade of Perovskite Solar Cells. *Nat. Mater.* **2014**, *13*, 838–842.
- (2) Rong, Y.; Hu, Y.; Mei, A.; Tan, H.; Saidaminov, M. I.; Seok, S. I.; McGehee, M. D.; Sargent, E. H.; Han, H. Challenges for Commercializing Perovskite Solar Cells. *Science* **2018**, *361*, No. eaat8235.
- (3) Milić, J. V.; Kubicki, D. J.; Emsley, L.; Grätzel, M. Multifunctional Molecular Modulation for Efficient and Stable Hybrid Perovskite Solar Cells. *Chimia* **2019**, *73*, 317–323.
- (4) Saparov, B.; Mitzi, D. B. Organic–Inorganic Perovskites: Structural Versatility for Functional Materials Design. *Chem. Rev.* **2016**, *116*, 4558–4596.
- (5) Mao, L.; Stoumpos, C. C.; Kanatzidis, M. G. Two-Dimensional Hybrid Halide Perovskites: Principles and Promises. *J. Am. Chem. Soc.* **2019**, *141*, 1171–1190.
- (6) Maheshwari, S.; Savenije, T. J.; Renaud, N.; Grozema, F. C. Computational Design of Two-Dimensional Perovskites with Functional Organic Cations. *J. Phys. Chem. C* **2018**, *122*, 17118–17122.
- (7) Gélvez-Rueda, M. C.; Hutter, E. M.; Cao, D. H.; Renaud, N.; Stoumpos, C. C.; Hupp, J. T.; Savenije, T. J.; Kanatzidis, M. G.; Grozema, F. C. Interconversion between Free Charges and Bound Excitons in 2D Hybrid Lead Halide Perovskites. *J. Phys. Chem. C* **2017**, *121*, 26566–26574.
- (8) Passarelli, J. V.; Fairfield, D. J.; Sather, N. A.; Hendricks, M. P.; Sai, H.; Stern, C. L.; Stupp, S. I. Enhanced Out-of-Plane Conductivity and Photovoltaic Performance in *n* = 1 Layered Perovskites through Organic Cation Design. *J. Am. Chem. Soc.* **2018**, *140*, 7313–7323.
- (9) Herckens, R.; Van Gompel, W. T. M.; Song, W.; Gélvez-Rueda, M. C.; Maufort, A.; Ruttens, B.; D'Haen, J.; Grozema, F. C.; Aernouts, T.; Lutsen, L.; Vanderzande, D. Multi-Layered Hybrid Perovskites Templated with Carbazole Derivatives: Optical Properties, Enhanced Moisture Stability and Solar Cell Characteristics. *J. Mater. Chem. A* **2018**, *6*, 22899–22908.
- (10) Weller, M. T.; Weber, O. J.; Frost, J. M.; Walsh, A. Cubic Perovskite Structure of Black Formamidinium Lead Iodide,  $\alpha$ -[HC(NH<sub>2</sub>)<sub>2</sub>]PbI<sub>3</sub>, at 298 K. *J. Phys. Chem. Lett.* **2015**, *6*, 3209–3212.
- (11) Yan, J.; Fu, W.; Zhang, X.; Chen, J.; Yang, W.; Qiu, W.; Wu, G.; Liu, F.; Heremans, P.; Chen, H. Highly Oriented Two-Dimensional Formamidinium Lead Iodide Perovskites with a Small Bandgap of 1.51 eV. *Mater. Chem. Front.* **2018**, *2*, 121–128.
- (12) Wang, Z.; Lin, Q.; Chmiel, F. P.; Sakai, N.; Herz, L. M.; Snaith, H. J. Efficient Ambient-Air-Stable Solar Cells with 2D–3D Heterostructured Butylammonium-Caesium-Formamidinium Lead Halide Perovskites. *Nat. Energy* **2017**, *2*, No. 17135.
- (13) Milić, J. V.; Im, J.-H.; Kubicki, D. J.; Ummadisingu, A.; Seo, J.-Y.; Li, Y.; Ruiz Preciado, M. A.; Dar, M. I.; Zakeeruddin, S. M.; Emsley, L.; Grätzel, M. Supramolecular Engineering for Formamidinium-Based Layered 2D Perovskite Solar Cells: Structural Complexity and Dynamics Revealed by Solid-State NMR Spectroscopy. *Adv. Energy Mater.* **2019**, *9*, No. 1900284.
- (14) Gélvez-Rueda, M. C.; Ahlawat, P.; Merten, L.; Jahanbakhshi, F.; Mladenović, M.; Hinderhofer, A.; Dar, M. I.; Li, Y.; Dučinskas, A.; Carlsen, B.; Tress, W.; Ummadisingu, A.; Zakeeruddin, S. M.; Schreiber, F.; Hagfeldt, A.; Rothlisberger, U.; Grozema, F. C.; Milić, J.



V.; Graetzel, M. Formamidinium-Based Dion-Jacobson Layered Hybrid Perovskites: Structural Complexity and Optoelectronic Properties. *Adv. Funct. Mater.* **2020**, *30*, No. 2003428.

(15) Binek, A.; Hanusch, F. C.; Docampo, P.; Bein, T. Stabilization of the Trigonal High-Temperature Phase of Formamidinium Lead Iodide. *J. Phys. Chem. Lett.* **2015**, *6*, 1249–1253.

(16) Bhosale, S. V.; Jani, C. H.; Langford, S. Chemistry of Naphthalene Diimides. *Chem. Soc. Rev.* **2008**, *37*, 331–342.

(17) Al Kobaisi, M.; Bhosale, S. V.; Latham, K.; Raynor, A. M.; Bhosale, S. V. Functional Naphthalene Diimides: Synthesis, Properties, and Applications. *Chem. Rev.* **2016**, *116*, 11685–11796.

(18) Proppe, A. H.; Tremblay, M.-H.; Zhang, Y.; Yang, Z.; Quintero-Bermudez, R.; Kelley, S. O.; Barlow, S.; Marder, S. R.; Sargent, E. H. Naphthalenediimide Cations Inhibit 2D Perovskite Formation and Facilitate Subpicosecond Electron Transfer. *J. Phys. Chem. C* **2020**, *124*, 24379–24390.

(19) Li, X.; Yang, J.; Song, Z.; Chen, R.; Ma, L.; Li, H.; Jia, J.; Meng, J.; Li, X.; Yi, M.; Sun, X. Naphthalene Diimide Ammonium Directed Single-Crystalline Perovskites with “Atypical” Ambipolar Charge Transport Signatures in Two-Dimensional Limit. *ACS Appl. Energy Mater.* **2018**, *1*, 4467–4472.

(20) Foresman, J. B.; Frisch, A. *Exploring Chemistry with Electronic Structure Methods*, 2nd ed.; Gaussian, Inc., 1995; pp 1–335.

(21) Frisch, M. J.; Trucks, G. W.; Schlegel, G. W.; Scuseria, H. B.; Robb, G. E.; Cheeseman, M. A.; Scalmani, J. R.; Barone, G.; Mennucci, V.; Petersson, B.; Nakatsuji, G. A.; Caricato, H.; Li, M.; Hratchian, X.; Izmaylov, H. P.; Bloino, A. F.; Zheng, J.; Sonnenberg, G.; Hada, J. L.; Ehara, M.; Toyota, M.; Fukuda, K.; Hasegawa, R.; Ishida, J.; Nakajima, M.; Honda, T.; Kitao, Y.; Nakai, O.; Vreven, H.; Montgomery, T., Jr.; Peralta, J. A.; Ogliaro, J. E.; Bearpark, F.; Heyd, M.; Brothers, J. J.; Kudin, E.; Staroverov, K. N.; Kobayashi, V. N.; Normand, R.; Raghavachari, J.; Rendell, K.; Burant, A.; Iyengar, J. C.; Tomasi, S. S.; Cossi, J.; Rega, M.; Millam, N.; Klene, J. M.; Knox, M.; Cross, J. E.; Bakken, J. B.; Adamo, V.; Jaramillo, C.; Gomperts, J.; Stratmann, R.; Yazyev, R. E.; Austin, O.; Cammi, A. J.; Pomelli, R.; Ochterski, C.; Martin, J. W.; Morokuma, R. L.; Zakrzewski, K.; Voth, V. G.; Salvador, G. A.; Dannenberg, P.; Dapprich, J. J.; Daniels, S.; Farkas, A. D.; Foresman, O.; Ortiz, J. B.; Cioslowski, J. V.; Fox, D. J. *Gaussian D09*; Gaussian, Inc., 2009.

(22) Mao, L.; Ke, W.; Pedesseau, L.; Wu, Y.; Katan, C.; Even, J.; Wasielewski, M. R.; Stoumpos, C. C.; Kanatzidis, M. G. Hybrid Dion–Jacobson 2D Lead Iodide Perovskites. *J. Am. Chem. Soc.* **2018**, *140*, 3775–3783.

(23) Li, Y.; Milić, J. V.; Ummadisingu, A.; Seo, J.-Y.; Im, J.-H.; Kim, H.-S.; Liu, Y.; Dar, M. I.; Zakeeruddin, S. M.; Wang, P.; Hagfeldt, A.; Grätzel, M. Bifunctional Organic Spacers for Formamidinium-Based Hybrid Dion–Jacobson Two-Dimensional Perovskite Solar Cells. *Nano Lett.* **2019**, *19*, 150–157.

(24) Cohen, B.-E.; Li, Y.; Meng, Q.; Etgar, L. Dion–Jacobson Two-Dimensional Perovskite Solar Cells Based on Benzene Dimethan ammonium Cation. *Nano Lett.* **2019**, *19*, 2588–2597.

(25) Li, X.; Ke, W.; Traore, B.; Guo, P.; Hadar, I.; Kepenekian, M.; Even, J.; Katan, C.; Stoumpos, C. C.; Schaller, R. D.; Kanatzidis, M. G. Two-Dimensional Dion–Jacobson Hybrid Lead Iodide Perovskites with Aromatic Diammonium Cations. *J. Am. Chem. Soc.* **2019**, *141*, 12880–12890.

(26) Xu, Z.; Chen, M.; Liu, S. F. First-Principles Study of Enhanced Out-of-Plane Transport Properties and Stability in Dion–Jacobson Two-Dimensional Perovskite Semiconductors for High-Performance Solar Cell Applications. *J. Phys. Chem. Lett.* **2019**, *10*, 3670–3675.

(27) Milić, J. V.; Zakeeruddin, S. M.; Grätzel, M. Layered Hybrid Formamidinium Lead Iodide Perovskites: Challenges and Opportunities. *Acc. Chem. Res.* **2021**, *54*, 2729–2740.

(28) Ashari-Astani, N.; Jahanbakhshi, F.; Mladenović, M.; Alanazi, A. Q. M.; Ahmadabadi, I.; Ejtehadi, M. R.; Dar, M. I.; Grätzel, M.; Rothlisberger, U. J. Ruddlesden–Popper Phases of Methylammonium-Based Two-Dimensional Perovskites with 5-Ammonium Valeric Acid  $\text{AVA}_2\text{MA}_{n-1}\text{Pb}_n\text{I}_{3n+1}$  with  $n = 1, 2$ , and  $3$ . *J. Phys. Chem. Lett.* **2019**, *10*, 3543–3549.

(29) Alanazi, A. Q.; Kubicki, D. J.; Prochowicz, D.; Alharbi, E. A.; Bouduban, M. E. F.; Jahanbakhshi, F.; Mladenović, M.; Milić, J. V.; Giordano, F.; Ren, D.; Alyamani, A. Y.; Albrithen, H.; Albadri, A.; Alotaibi, M. H.; Moser, J.-E.; Zakeeruddin, S. M.; Rothlisberger, U.; Emsley, L.; Grätzel, M. Atomic-Level Microstructure of Efficient Formamidinium-Based Perovskite Solar Cells Stabilized by 5-Ammonium Valeric Acid Iodide Revealed by Multi-Nuclear and Two-Dimensional Solid-State NMR. *J. Am. Chem. Soc.* **2019**, *141*, 17659–17669.

(30) Ahmad, S.; Fu, P.; Yu, S.; Yang, Q.; Liu, X.; Wang, X.; Wang, X.; Guo, X.; Li, C. Dion–Jacobson Phase 2D Layered Perovskites for Solar Cells with Ultrathin Stability. *Joule* **2019**, *3*, 794–806.

(31) Cao, D. H.; Stoumpos, C. C.; Farha, O. K.; Hupp, J. T.; Kanatzidis, M. G. 2D Homologous Perovskites as Light-Absorbing Materials for Solar Cell Applications. *J. Am. Chem. Soc.* **2015**, *137*, 7843–7850.

(32) Kubicki, D. J.; Prochowicz, D.; Hofstetter, A.; Pěchy, P.; Zakeeruddin, S. M.; Grätzel, M.; Emsley, L. Cation Dynamics in Mixed-Cation  $(\text{MA})_x(\text{FA})_{1-x}\text{PbI}_3$  Hybrid Perovskites from Solid-State NMR. *J. Am. Chem. Soc.* **2017**, *139*, 10055–10061.

(33) Kubicki, D. J.; Prochowicz, D.; Hofstetter, A.; Zakeeruddin, S. M.; Grätzel, M.; Emsley, L. Phase Segregation in Cs-, Rb- and K-Doped Mixed-Cation  $(\text{MA})_x(\text{FA})_{1-x}\text{PbI}_3$  Hybrid Perovskites from Solid-State NMR. *J. Am. Chem. Soc.* **2017**, *139*, 14173–14180.

(34) Kubicki, D. J.; Prochowicz, D.; Hofstetter, A.; Sasaki, M.; Yadav, P.; Bi, D.; Pellet, N.; Lewiński, J.; Zakeeruddin, S. M.; Grätzel, M.; Emsley, L. Formation of Stable Mixed Guanidinium–Methylammonium Phases with Exceptionally Long Carrier Lifetimes for High-Efficiency Lead Iodide-Based Perovskite Photovoltaics. *J. Am. Chem. Soc.* **2018**, *140*, 3345–3351.

(35) Bi, D.; Li, X.; Milić, J. V.; Kubicki, D. J.; Pellet, N.; Luo, J.; LaGrange, T.; Mettraux, P.; Emsley, L.; Zakeeruddin, S. M.; Grätzel, M. Multifunctional Molecular Modulators for Perovskite Solar Cells with over 20% Efficiency and High Operational Stability. *Nat. Commun.* **2018**, *9*, No. 4482.

(36) Hope, M. A.; Nakamura, T.; Ahlawat, P.; Mishra, A.; Cordova, M.; Jahanbakhshi, F.; Mladenović, M.; Runjhun, R.; Merten, L.; Hinderhofer, A.; Carlsen, B. I.; Kubicki, D. J.; Gershoni-Poranne, R.; Schneeberger, T.; Carbone, L. C.; Liu, Y.; Zakeeruddin, S. M.; Lewiński, J.; Hagfeldt, A.; Schreiber, F.; Rothlisberger, U.; Grätzel, M.; Milić, J. V.; Emsley, L. Nanoscale Phase Segregation in Supramolecular  $\pi$ -Templating for Hybrid Perovskite Photovoltaics from NMR Crystallography. *J. Am. Chem. Soc.* **2021**, *143*, 1529–1538.

(37) Jahanbakhshi, F.; Mladenović, M.; Dankl, M.; Boziki, A.; Ahlawat, P.; Rothlisberger, U. Organic Spacers in 2D Perovskites: General Trends and Structure-Property Relationships from Computational Studies. *Helv. Chim. Acta* **2021**, *104*, No. e2000232.

(38) Franco, C. V.; Mahler, B.; Cornaggia, C.; Gustavsson, T.; Cassette, E. Charge Carrier Relaxation in Colloidal  $\text{FAPbI}_3$  Nanostructures Using Global Analysis. *Nanomaterials* **2020**, *10*, No. 1897.

(39) Gélvez-Rueda, M. C.; Fridriksson, M. B.; Dubey, R. K.; Jäger, W. F.; van der Stam, W.; Grozema, F. C. Overcoming the Exciton Binding Energy in Two-Dimensional Perovskite Nanoplatelets by Attachment of Conjugated Organic Chromophores. *Nat. Commun.* **2020**, *11*, No. 1901.



## VI International School and Conference on Photonics

Belgrade, Serbia, August 28<sup>th</sup> – September 1<sup>st</sup>, 2017

Institute of Physics Belgrade, Pregrevica 118, 11080 Belgrade, Serbia  
Phone: +381 11 3713 000; Fax: +381 11 3162 190, E-mail: [photonica2017@ipb.ac.rs](mailto:photonica2017@ipb.ac.rs), [www.photonica.ac.rs](http://www.photonica.ac.rs)

---

Dr. Marko Mladenović,  
Institute of Physics, University of Belgrade, Serbia

Belgrade, April 11<sup>th</sup>, 2017

Dear Dr. Mladenović,

On behalf of the Organizing Committee of the International School and Conference on Photonics, we are pleased to invite you to the **PHOTONICA2017** conference scheduled from **August 28<sup>th</sup>** till **September 1<sup>st</sup> 2017** in **Belgrade, Serbia**. This conference will be organized by the Institute of Physics Belgrade, Belgrade, Serbia, Optical Society of Serbia and Serbian Academy of Sciences and Arts.

It is our special pleasure to invite you to attend the meeting and present a **progress report lecture (20 min)**. The lecture is expected to contain a review and up-to-date progress in the specific field.

We would be honored if you could accept this invitation and accordingly send us a title of your lecture by April 30<sup>th</sup>, to be included in the Conference Announcement. The abstract of the lecture, 1 page in length, should be submitted at the conference website by May, 31<sup>st</sup>.

Kindly, as a progress report speaker, the Organizers will cover a half of your conference fee.

Should you have any question please don't hesitate to contact us by e-mail, telephone, mail or fax.

Yours sincerely

Aleksandar Krmpot  
(Chair of the Organizing Committee)

phone: +381 11 3713 012

fax: +381 11 3162 190

cell: +381 64 202 65 62

e-mail: [krmpot@ipb.ac.rs](mailto:krmpot@ipb.ac.rs)

[photonica2017@ipb.ac.rs](mailto:photonica2017@ipb.ac.rs)

**PHOTONICA 2017 Timetable (Serbian Academy of Sciences and Arts - Main Hall)**

Monday, August 28 <sup>th</sup>	Tuesday, August 29 <sup>th</sup>	Wednesday, August 30 <sup>th</sup>	Thursday, August 31 <sup>st</sup>	Friday, September 1 <sup>st</sup>
08.00-17.00 Registration	08.00-17.00 Registration	08.00-12.00 Registration	08.00-12.00 Registration	
<b>08.30-09.00 Opening</b>				
09.00-09.35 Krolikowski	09.00-09.35 Chichkov	09.00-09.35 Zalevsky	09.00-09.35 Weis	09.00 – 09.45 Pernice
09.35-09.45 Discussion break	09.35-09.45 Discussion break	09.35-09.45 Discussion break	09.35-09.45 Discussion break	
09.45-10.20 Krolikowski	09.45-10.20 Chichkov	09.45-10.20 Zalevsky	09.45-10.20 Weis	09.45– 10.30 Belić
<b>10.20-10.40 Coffee break</b>	<b>10.20-10.40 Coffee break</b>	<b>10.20-10.40 Coffee break</b>	<b>10.20-10.40 Coffee break</b>	<b>10.30 – 10.50 Coffee break</b>
10.40-11.25 Hingerl	10.40-11.25 Jerker	10.40-11.25 Kralj	10.40-11.25 Adhikari	10.50 – 11.35 Barry
11.25-11.35 Discussion break	11.25-11.35 Discussion break	11.25-11.35 Discussion break	11.25-11.35 Discussion break	
11.35-12.05 Pasiskevicius	11.35-12.05 Jakovcevski	11.35-12.05 Artemyev	11.35-12.05 Pelster	11.35-11.45 Discussion break
12.05-12.35 Fratalochi	12.05-12.35 Štrancar	12.05-12.35 Teichert	12.05-12.35 Salasnich	11.45 - 12.15 Leisher
<b>12.35-14.30 LUNCH BREAK</b>	<b>12.35-14.30 LUNCH BREAK</b>	<b>12.35-14.30 LUNCH BREAK</b>	<b>12.35-14.30 LUNCH BREAK</b>	12.15 - 12.45 Gerharth
				<b>12.45-14.30 LUNCH BREAK</b>
14.30-15.05 Radić	14.30-15.00 Luning	14.30-15.00 Rakich	14.30-15.00 Loew	14.30-15.00 van Oosten
15.05-15.10 Discussion break	15.00-15.30 Dučić	15.00-15.30 Baronio	15.00-15.30 Affolderbach	15.00-15.30 Zamfiresku
15.10-15.45 Radić				
15.45-16.00 CT1	15.30-15.45 CT3	15.30-16.00 Setzpfandt	15.30-15.45 CT6	15.30-15.45 CT8
<b>16.00-16.20 Coffee break</b>	15.45-16.00 CT4		15.45-16.00 CT7	15.45-16.00 CT9
16.20-16.50 Slavik	16.20-16.50 Borzsonyi	<b>18.00 – 20.00 Excursion (boat trip and sightseeing from Belgrade rivers)</b>	<b>16.30 – 18.30 Posters &amp; Industrial talks</b>	16.20-16.50 Longo
16.50-17.10 Tarasov	16.50-17.10 Krešić			16.50-17.10 Stupar
17.10-17.30 Chernysheva	17.10-17.30 Mladenović			17.10-17.30 Bajić
17.30-17.50 Popovic	17.30-17.50 Ralević			17.30-17.50 Obradov
17.50-18.05 CT2	17.50-18.05 CT5			17.50 -18.05 CT10
<b>18.30 -20.00 Cocktail</b>	<b>18.15 – 20.00 Posters &amp;Industrial talks</b>			18.05-18.20 CT11
			<b>20.00 ---- Conference dinner (bohemian quarter Skadarlija)</b>	<b>18.20 Closing</b>

Tutorial lecture	2x35 min	Keynote lecture	45 min	Invited lecture	30 min	Special invited lecture	30 min	Progress report	20 min	Contributed talk -CT	15 min
---------------------	-------------	--------------------	-----------	--------------------	-----------	-------------------------------	-----------	--------------------	-----------	-------------------------	-----------

# International Conference on Hybrid and Organic Photovoltaics (HOPV18)

**Benidorm, Spain, 2018 May 28th - 31st**

**Conference Chairs: Emilio Palomares and Rene Janssen**

## Conference Program

<b>May 28th - Day 1 (Monday)</b>	
16:30 - 17:30	<b>Registration</b>
17:30 - 19:00	<b>welcome reception</b>
<b>May 29th - Day 2 (Tuesday)</b>	
08:00 - 08:45	<b>Registration</b>
08:45 - 08:50	<b>Announcement of the day</b>
08:50 - 09:00	<b>Opening</b>
<b>Session G1.1</b> Chair: Rene Janssen	
09:00 - 09:45	<u>Harald Ade</u> ( <i>North Carolina State University</i> )
G1.1-K1	Nonfullerene Organic Solar Cells: Importance of Molecular Interaction and Vitrification
09:45 - 10:15	<u>Juan Bisquert</u> ( <i>Institute of Advanced Materials (INAM), Universitat Jaume I</i> )
G1.1-I1	10 years of Hybrid and Organic Photovoltaics
10:15 - 10:45	<u>Tsutomu Miyasaka</u> ( <i>Toin University of Yokohama</i> )
G1.1-I2	Metal oxide-based perovskite solar cells and their superior tolerance in the space environment
10:45 - 11:15	<b>Coffee Break</b>
<b>Session G1.2</b> Chair: Rene Janssen	
11:15 - 11:45	<u>Laura Herz</u> ( <i>Department of Physics of University of Oxford</i> )
G1.2-I1	Fundamental charge conduction and recombination mechanisms in hybrid perovskites operating near the intrinsic limit
11:45 - 12:15	<u>Vincent Artero</u> ( <i>Université Grenoble Alpes</i> )
G1.2-I2	Molecular-based H <sub>2</sub> -evolving photocathodes
12:15 - 12:45	<u>Mohammad Nazeeruddin</u> ( <i>Group for Molecular Engineering of Functional Materials, École Polytechnique Fédérale de Lausanne, Valais Wallis, CH-1951 Sion, Switzerland</i> ), Kyung Taek Cho, Giulia Grancini, Yonghui Lee, Manuel Yonghui, Sanghyun Paek
G1.2-I3	Growth of layered perovskites for stable and efficient photovoltaics
12:45 - 13:00	<u>Luca Sorbello</u> ( <i>Greatcell Solar S.A.</i> )
G1.2-S1	GreatCell Solar S.A.
13:00 - 14:30	<b>Lunch</b>
<b>Session A1</b> Chair: Henk Bolink Room: New Perovskite Materials	
14:30 - 15:00	<u>Carolin Sutter-Fella</u> ( <i>Lawrence Berkeley National Laboratory</i> )
A1-IS1	Optoelectronic Properties and Halide Demixing in Br-Containing Metal Halide Perovskites

15:00 - 15:15 A1-O1	<p><u>Sagar Jain</u> (<i>SPECIFIC IKC, College of Engineering, University of Swansea, Swansea, U.K.</i>), Gerrit Boschloo, James Durrant</p> <p>Vapour assisted morphological tailoring by reducing metal defect sites in lead-free, (CH<sub>3</sub>NH<sub>3</sub>)<sub>3</sub>Bi<sub>2</sub>I<sub>9</sub> perovskite solar cells for improved performance and long-term stability</p>
15:15 - 15:30 A1-O2	<p><u>Pavao Andricevic</u> (<i>Laboratory of Physics of Complex Matter (LPMC), Ecole Polytechnique Fédérale de Lausanne</i>), Xavier Mettan, Márton Kollár, Bálint Náfrádi, Andrzej Sienkiewicz, Tonko Garma, László Forró, Endre Horváth</p> <p>Vertically Aligned Carbon Nanotubes as Electrodes in Perovskite Single Crystal Light Emitting Electrochemical Cells</p>
15:30 - 15:45 A1-O3	<p><u>Shuzi Hayase</u> (<i>Kyushu Institute of Technology, Japan</i>), Nozomi Ito, Muhammad Akmal Kamarudin, Qing Shen, Yuhei Ogomi, Satoshi Iikubo, Kenji Yoshino, Takashi Minemoto, Taro Toyoda</p> <p>Pb free perovskite-SnGe mixed metal perovskite solar cell with 7.5 % efficiency and enhanced solar cell stability at air without encapsulation</p>
15:45 - 16:00 A1-O6	<p><u>Giulia Longo</u> (<i>Department of Physics, Oxford University</i>), Henry J. Snaith</p> <p>Vapour deposited lead free double perovskite for photovoltaic applications</p>
16:00 - 16:30	<b>Coffee Break</b>
16:30 - 16:45 A1-O4	<p><u>Lissa Eyre</u> (<i>Cavendish Laboratory, University of Cambridge, JJ Thomson Avenue, Cambridge CB3 0HE, United Kingdom</i>), Robert Hoyer, Pablo Docampo, Hannah Joyce, Felix Deschler</p> <p>Ultrafast spectroscopy of lattice-charge carrier interactions in bismuth-based perovskites</p>
16:45 - 17:00 A1-O5	<p><u>Aslihan Babayigit</u> (<i>Institute for Materials Research (IMO-IMOMECE), Hasselt University, Wetenschapspark 1, 3590 Diepenbeek, BE</i>), Melissa Van Landeghem, Bert Conings, Nobuya Sakai, Etienne Goovaerts, Hans-Gerd Boyen, Henry Snaith</p> <p>Estimating oxidised Sn<sup>4+</sup> species at the precursor stage: on the effect of reducing agents in Sn-based perovskites.</p>
17:00 - 17:15 A1-O7	<p><u>Lukas Kinner</u> (<i>AIT Austrian Institute of Technology, Center for Energy, Photovoltaic Systems, Gleifinggasse 4, 1210 Wien</i>), Neha Bansal, Martin Bauch, Felix Hermerschmidt, Emil List-Kratochvil, Theodoros Dimopoulos</p> <p>Highly transparent and conductive embedded silver nanowire electrode for use in flexible solar cells</p>
17:15 - 17:30 A1-O8	<p><u>Sascha Feldmann</u> (<i>University of Cambridge</i>), Jasmine PH Rivett, Tudor H Thomas, Mojtaba Abdi Jalebi, Stuart Macpherson, Sam D Stranks, Michael Saliba, Felix Deschler</p> <p>Cation substitution reduces non-radiative losses in hybrid lead-halide perovskites</p>
<b>Session B1</b> Chair: Annamaria Petrozza Room: Spectroscopy of Perovskite Materials	
14:30 - 15:00 B1-IS1	<p><u>Felix Deschler</u> (<i>Cavendish Laboratory, University of Cambridge, JJ Thomson Avenue, Cambridge CB3 0HE, United Kingdom</i>)</p> <p>Understanding carrier recombination and luminescent yields in metal-halide perovskites</p>
15:00 - 15:15 B1-O1	<p>Ramón Arcas, Elena Mas-Marzá, Alberto García-Fernández, <u>Francisco Fabregat-Santiago</u> (<i>Institute of Advanced Materials (INAM), Universitat Jaume I</i>)</p> <p>Photoluminescence of dual ion perovskite monocrystals</p>
15:15 - 15:30 B1-O2	<p><u>Arvydas Ruseckas</u> (<i>Organic Semiconductor Centre, SUPA, School of Physics and Astronomy, University of St Andrews, St Andrews, U.K.</i>), Oskar Blaszczyk, Jonathan R. Harwell, Lethy Krishnan Jagadamma, Ifor D. W. Samuel</p> <p>Charge recombination in methylammonium lead triiodide at low temperatures</p>
15:30 - 15:45 B1-O3	<p><u>Xiaofeng Tang</u> (<i>Institute of Materials for Electronics and Energy Technology (i-MEET), Department of Materials Science and Engineering, Friedrich-Alexander-Universität Erlangen-Nürnberg, Erlangen, 91058, Germany.</i>), Gebhard Matt, Christoph Brabec</p> <p>Topography-dependent phase-segregation in mixed-halide perovskite</p>
15:45 - 16:00 B1-O6	<p>Dengyang Guo, Roberto Brenes, Zahra Andaji Garmaroudi, Eline Hutter, Samuel Stranks, <u>Tom Savenije</u> (<i>Department of Chemical Engineering, Delft University of Technology, 2629 HZ Delft, The Netherlands.</i>)</p> <p>How Charge Carrier Dynamics are Affected by Light Soaking in (Mixed) Halide Perovskites</p>

- 16:00 - 16:30 **Coffee Break**
- 16:30 - 16:45 Hernan Miguez (*Instituto de Ciencia de Materiales de Sevilla (ICMS-CSIC)*), Miguel Anaya, Mauricio Calvo, Juan Galisteo, Juan Pedro Espinos  
B1-O4 Origin of Light Induced Ion Migration in Organic Metal Halide Perovskites in the Presence of Oxygen
- 16:45 - 17:00 Robert Westbrook (*Imperial College London, Department of Chemistry and Centre for Plastic Electronics*), Jose Marin-Beloqui, Irene Sanchez-Molina, Hugo Bronstein, Saif Haque  
B1-O5 Illuminating Charge-Transfer at the Absorber/Hole Transport Material Interface in Perovskite Solar Cells
- 17:00 - 17:15
- 17:15 - 17:30

**Session C1**

Chair: Dieter Neher  
Room: Theory

- 14:30 - 15:00 Ardalan Armin (*Department of Physics, Swansea University, Single Park, Swansea SA2 8PP, United Kingdoms*)  
C1-IS1 Shockley-type versus Transport-limited Organic Solar Cell
- 15:00 - 15:15 Eline Hutter (*Department of Chemical Engineering, Delft University of Technology, 2629 HZ Delft, The Netherlands.*), Rebecca Sutton, Yinghong Hu, Michiel Petrus, Pablo Docampo, Samuel Stranks, Henry Snaith, Tom Savenije  
C1-O1 The Role of the Monovalent Cation on the Recombination Kinetics in Lead Iodide Perovskites
- 15:15 - 15:30 Juan A. Anta, Jesus Idígoras, Lidia Contreras-Bernal (*Departamento de Sistemas Físicos, Químicos y Naturales, A&#769;rea de Química Física, Universidad Pablo de Olavide*), Antonio Riquelme, Susana Ramos-Terrón  
C1-O2 Small perturbation analysis of perovskite solar cells: feature extraction and modelling
- 15:30 - 15:45 Alessio Gagliardi, Ajay Singh, Waldemar Kaiser (*Technische Universitaet Muenchen*)  
C1-O3 Simulation of ion migration in perovskite solar cells using a kinetic Monte Carlo/drift diffusion numerical model and analysis of the impact on device performance
- 15:45 - 16:00 Gregory Kozyreff (*Université libre de Bruxelles*), Marina Mariano-Juste, Jorge Bravo-Abad, Guillermo Martinez-Denegri, Jordi Martorell  
C1-O4 Light trapping by intermittent chaos in a Photonic Fiber Plate
- 16:00 - 16:30 **Coffee Break**
- 16:30 - 16:45 Sebastian Müller (*School of Mathematics, University of Bristol, Bristol BS8 1TW, UK*)  
C1-O5 Continuum limit of the Gaussian disorder model for organic solar cells
- 16:45 - 17:00 Juan F. Galisteo-López (*Instituto de Ciencia de Materiales de Sevilla (ICMS-CSIC)*), Alberto Jiménez-Solano, Hernán Míguez  
C1-O6 Absorption and emission of light in optoelectronic nanomaterials: the role of the local optical environment
- 17:00 - 17:15 Pascal Kaienburg (*IEK5-Photovoltaics, Forschungszentrum Jülich, 52425 Jülich, Germany*), Paula Hartnagel, Bart E. Pieters, David Grabowski, Jiaoxian Yu, Thomas Kirchartz  
C1-O7 Impact of Non-linear Shunts from Pinholes on Device Performance
- 17:15 - 17:30 Marko Mladenovic (*Laboratory of Computational Chemistry and Biochemistry, Dept. of Chemistry, Ecole Polytechnique Fédérale de Lausanne*), Ursula Roethlisberger  
C1-O8 First-principles calculations of halide perovskites

**Session D1**

Chair: Jianhui Hou  
Room: Organic Photovoltaics

- 14:30 - 15:00 Monica Lira-Cantu (*Catalan Institute of Nanoscience and Nanotechnology (ICN2), CSIC and The Barcelona Institute of Science and Technology, Campus UAB, Bellaterra, 08193 Barcelona, Spain*)  
D1-IS1 Novel Metal Oxides as Transport Layers in Halide Perovskite Solar Cells
- 15:00 - 15:15 Chang He (*Institute of Chemistry, Chinese Academy of Sciences*)  
D1-O1 Optimized molecular orientation and domain size enables efficient non-fullerene small-molecule organic solar cells

15:15 - 15:30 D1-O2	<u>Z.J.W.A. Leijten</u> ( <i>Laboratory of Materials and Interface Chemistry, Department of Chemical Engineering and Chemistry, Eindhoven University of Technology, Groene Loper 5, 5612 AE Eindhoven</i> ), G. de With, H. Friedrich Mapping of oxygen and water related degradation across P3HT:PCBM interfaces
15:30 - 15:45 D1-O3	<u>Wenchao Zhao</u> ( <i>Institute of Chemistry, Chinese Academy of Sciences</i> ), Sunsun Li, Yun Zhang, Shaoqing Zhang, Jianhui Hou Over 13% Efficiency in Blade-coated Organic Solar Cells
15:45 - 16:00 D1-O4	<u>Huifeng Yao</u> ( <i>Institute of Chemistry, Chinese Academy of Sciences</i> ) Modulation of Intramolecular Charge Transfer Effect in Highly Efficient Non-fullerene Acceptor
16:00 - 16:30	<b>Coffee Break</b>
16:30 - 16:45 D1-O5	<u>Fallon Colberts</u> ( <i>Molecular Materials and Nanosystems, Eindhoven University of Technology, Netherlands</i> ), Martijn Wienk, Vincent Le Corre, Lambertus Koster, Rene Janssen Processing of polymer solar cells on a water substrate
16:45 - 17:00 D1-O6	<u>Vikas Negi</u> ( <i>Molecular Materials and Nanosystems, Eindhoven University of Technology, Netherlands</i> ), Olga Wodo, Jacobus Franeker, Rene Janssen, Peter Bobbert Full 3D simulation of phase separation in solution-processed organic solar cells
17:00 - 17:15 D1-O7	<u>Mengmeng Li</u> ( <i>Molecular Materials and Nanosystems, Institute for Complex Molecular Systems, Eindhoven University of Technology, P.O. Box 513, 5600 MB Eindhoven, The Netherlands</i> ), Martijn Wienk, Rene Janssen Impact of Device Polarity on the Photovoltaic Performance of Polymer Solar Cells
17:15 - 17:30 D1-O8	<u>Jiaying Wu</u> ( <i>Imperial College London, Department of Chemistry and Centre for Plastic Electronics</i> ), James Durrant Towards OPV devices scaling up: understand the loss mechanisms for thick devices

17:30 - 19:00 **Poster session**

### May 30th - Day 3 (Wednesday)

08:55 - 09:00 **Announcement of the day**

#### Session G2.1

Chair: Emilio Palomares

09:00 - 09:45 G2.1-K1	<u>Michael Graetzel</u> ( <i>Laboratory of Photonics and Interfaces, Ecole Polytechnique Fédérale de Lausanne, Switzerland</i> ) Molecular Photovoltaics and Perovskite Solar Cells
09:45 - 10:15 G2.1-I1	<u>Jenny Nelson</u> ( <i>Department of Physics and Centre for Plastic Electronics, Imperial College London, London, SW7 2AZ, UK.</i> ) The impact of chemical and physical structure on charge pair generation and solar energy conversion in molecular photovoltaic materials
10:15 - 10:45 G2.1-I2	<u>Jianhui Hou</u> ( <i>Beijing National Research Center for Molecular Sciences, Institute of Chemistry, Chinese Academy of Sciences, Beijing 100190, China</i> ) Material Design for Fullerene-free Polymer Solar Cells with Over 14% Efficiency

10:45 - 11:15 **Coffee Break**

#### Session G2.2

Chair: Sagar Motilal Jain

11:15 - 11:45 G2.2-I1	<u>Maria Antonietta Loj</u> ( <i>Photophysics and OptoElectronics, Zernike Institute for Advanced Materials, University of Groningen, Nijenborgh 4, 9747 AG, The Netherlands</i> ) Sn-based Hybrid Perovskites: from solar cells to hot electrons
11:45 - 12:15 G2.2-I2	<u>Iain McCulloch</u> ( <i>Imperial College London, Department of Chemistry and Centre for Plastic Electronics</i> ) Non-fullerene acceptors for high performance organic photovoltaics
12:15 - 12:45 G2.2-I3	<u>Gerasimos Konstantatos</u> ( <i>ICFO-Institut de Ciències Fotoniques, The Barcelona Institute of Science and Technology</i> ) Near and Short-wave Infrared Colloidal Quantum Dot Solar Cells

12:45 - 13:00	<u>Taro Tanabe</u> ( <i>TCI Europe NV</i> )
G2.2-S1	TCI Chemicals
13:00 - 14:30	<b>Lunch</b>
	<b>Session A2</b> Chair: Trystan Watson Room: Large Area Processing of Perovskites
14:30 - 15:00	Xiongfeng Lin, <u>Udo Bach</u> ( <i>ARC Centre of Excellence in Exciton Science, Monash University</i> )
A2-IS1	Back-Contact Perovskite Solar Cells
15:00 - 15:15	<u>Ilker Dogan</u> ( <i>Holst Centre/TNO – Solliance</i> ), Francesco Di Giacomo, Santosh Shanmuham, Valerio Zardetto,
A2-O1	Henri Fledderus, Harrie Gorter, Gerwin Kirschner, Ike de Vries, Weiming Qiu, Wiljan Verhees, Robert Gehlhaar, Yulia Galagan, Herbert Lifka, Tom Aernouts, Sjoerd Veenstra, Pim Groen, Ronn Andriessen Towards roll-to-roll production of perovskite solar cells: sheet-to-sheet slot-die processing of high efficiency cells and modules
15:15 - 15:30	Florian Mathies, Gerardo Hernandez Sosa, Fabian Schackmar, Bryce S. Richards, Ulrich Lemmer, <u>Ulrich W. Paetzold</u> ( <i>Light Technology Institute, Karlsruhe Institute of Technology, Engesserstr. 13, 76131, Germany</i> )
A2-O2	Inkjet Printed Perovskite Photovoltaics
15:30 - 15:45	<u>Wallace Choy</u> ( <i>Department of Electrical and Electronic Engineering, The University of Hong Kong, Pok Fu Lam Road, Hong Kong SAR, China</i> ), Jian Mao
A2-O3	Solution-based and Microfabrication-free Approach to Form Ordered Nanostructured Perovskites for Photovoltaic and LED Applications
15:45 - 16:00	Daniel Perez-del-Rey, <u>Pablo P. Boix</u> ( <i>Universidad de Valencia - ICMol (Institute of Molecular Science)</i> ), Benedikt Dänekamp, Jorge Ávila, Cristina Momblona, Michele Sessolo, Henk Bolink
A2-O4	Working mechanisms of vacuum-deposited perovskite solar cells
16:00 - 16:30	<b>Coffee Break</b>
16:30 - 16:45	<u>James Blakesley</u> ( <i>National Physical Laboratory</i> )
A2-O5	Introducing energy rating standards and their implication for Perovskite modules
16:45 - 17:00	<u>Trystan Watson</u> ( <i>1SPECIFIC, College of Engineering, Swansea University Bay Campus, Fabian Way, SA1 8EN Swansea, United Kingdom</i> ), Francesca De Rossi, Jenny Baker, David Beynon, Katherine Hooper, Simone Meroni, Zhengfei Wei, Dave Worsley, Daniel Williams
A2-O6	Design and development of all printable perovskite solar modules with 198 cm <sup>2</sup> active area
17:00 - 17:15	Clara Aranda, Juan Bisquert, <u>Antonio Guerrero</u> ( <i>Institute of Advanced Materials (INAM), Universitat Jaume I</i> ), Wei Peng, Osman Bakr, Germa Garcia-Belmonte
A2-O7	Ionic Diffusion Quantification in Lead Halide Perovskite Single Crystals
17:15 - 17:30	<u>Juliane Borchert</u> ( <i>Clarendon Laboratory, Department of Physics, University of Oxford, Parks Road, Oxford, OX1 3PU, United Kingdom</i> ), Rebecca L Milot, Jay B Patel, Christopher L Davies, Adam D Wright, Laura Martínez Maestro, Henry J Snaith, Laura M Herz, Michael B Johnston
A2-O8	Co-evaporated Formamidinium Lead Iodide Solar Cells
	<b>Session B2</b> Chair: Maria Antonietta Loi Room: Spectroscopy of Organic Materials
14:30 - 15:00	<u>Tracey Clarke</u> ( <i>Department of Chemistry, University College London</i> ), Kealan Fallon, Michelle Vezie, Jenny Nelson, Artem Bakulin, Hugo Bronstein
B2-IS1	Ultra-low band gap polymers for organic electronic applications
15:00 - 15:15	<u>DOUGLAS YEBOAH</u> ( <i>Charles Darwin University</i> ), Jai Singh
B2-O1	Correlative Influence of Charge Carrier Recombination and Extraction Processes on the Fill Factor in Bulk Heterojunction Organic solar Cells
15:15 - 15:30	<u>Mohammed Azzouzi</u> ( <i>Department of Physics and Centre for Plastic Electronics, Imperial College London, London, SW7 2AZ, UK.</i> ), Jun Yan, Thomas Kirchartz, Jenny Nelson
B2-O2	Non-Radiative Energy Losses in Bulk-Heterojunction Organic Photovoltaics



- 15:30 - 15:45 Yanting Yin (*Chemical Physics and Nanotechnology Research Leader Flinders Centre for NanoScale Science and Technology School of Chemical and Physical Sciences, Flinders University*)  
B2-O3 Within few Nanometres-the Way to Characterise Dipoles and Reconstruct Energy Bands at Metal Oxide/Organic Interface
- 15:45 - 16:00 Michael Price (*Optoelectronics Group, University of Cambridge*), Xu-hui Jin, George Whittell, Richard Friend, Ian  
B2-O4 Manners  
Efficient exciton transport in conjugated polyfluorene nanofibers
- 16:00 - 16:30 **Coffee Break**
- 16:30 - 16:45 Adam Pockett (*SPECIFIC, Swansea University*), Harrison Lee, Wing Chung Tsoi, Matthew Carnie  
B2-O5 Studying degradation in OPV devices using a combination of frequency and time domain optoelectronic techniques
- 16:45 - 17:00 Mustapha Abdu-Aguye (*Photophysics and Optoelectronics, Zernike Institute for Advanced Materials, University of Groningen, The Netherlands*), Nutifafa Doumon, Ivan Terzic, Vincent Voet, Katya Loos, Jan Anton Koster,  
B2-O6 Maria Antonietta Loi  
Photophysical properties of semiconducting-ferroelectric block copolymers for organic photovoltaics
- 17:00 - 17:15 Jose Manuel Marin-Beloqui (*Department of Chemistry, University College London*), Kealan Fallon, Hugo  
B2-O7 Bronstein, Tracey Clarke  
Donor and Acceptor Character in a Cross-Conjugated Polymer: a Transient Absorption Spectroscopy Study
- 17:15 - 17:30 Blaise Godefroid (*Université libre de Bruxelles*), Gregory Kozyreff  
B2-O8 Organic solar cell design as a function of internal luminescence quantum efficiency

**Session C2**

Chair: Gerasimos Konstantatos  
Room: Perovskite Nanocrystals

- 14:30 - 15:00 David Tilley (*Department of Chemistry, University of Zurich*)  
C2-IS1 Earth-Abundant Materials for Solar Water Splitting
- 15:00 - 15:15 Iván Mora-Seró (*Institute of Advanced Materials (INAM), Universitat Jaume I*)  
C2-O1 The next step forward: Halide Perovskite Nanocrystals
- 15:15 - 15:30 Junsheng Chen (*Chemical Physics and NanoLund, Lund University, P.O. Box 124, 22100 Lund, Sweden*), Pavel  
C2-O2 Chábera, Maria E. Messing, Kaibo Zheng, Tonu Pullerits  
Photophysics of two-photon absorption in CsPbBr<sub>3</sub> perovskite quantum dots
- 15:30 - 15:45 Marina Gerhard (*Chemical Physics and NanoLund, Lund University, P.O. Box 124, 22100 Lund, Sweden*), Boris  
C2-O3 Louis, Rafael Camacho, Aboma Merdasa, Jun Li, Alexander Dobrovolsky, Johan Hofkens, Ivan Scheblykin  
Non-radiative recombination in organo-metal halide perovskites: Seeing beyond the ensemble-averaged picture with temperature-dependent photoluminescence microscopy
- 15:45 - 16:00 Satoshi Uchida (*Research Center for Advanced Science and Technology (RCAST) The University of Tokyo*),  
C2-O4 Tae Woon Kim, Ludmila Cojocar, Tomonori Matsushita, Takashi Kondo, Hiroshi Segawa  
Superlattice inside the perovskite solar cells
- 16:00 - 16:30 **Coffee Break**
- 16:30 - 16:45 Mauricio Calvo (*Multifunctional Optical Materials Group, Instituto de Ciencia de Materiales de Sevilla, Consejo Superior de Investigaciones Científicas-Universidad de Sevilla*), Andrea Rubino, Miguel Anaya, Juan Francisco  
C2-O5 Galisteo, Hernan Miguez  
ABX<sub>3</sub> perovskite nanocrystals templated in porous matrices
- 16:45 - 17:00 Zahra Zolfaghari, Seog Joon Yoon (*Institute of Advanced Materials (INAM), Universitat Jaume I*), Iván Mora Seró  
C2-O6 Photoinduced Charge Transfer Processes of Cesium Lead Halide Perovskite Quantum Dots in Optoelectronic Devices
- 17:00 - 17:15 Meltem F. Ayguler (*Department of Chemistry and Center for Nanoscience (CENS), Ludwig-Maximilians Universität (LMU)*), Bianka M. D. Puscher, Thomas Bein, Ruben D. Costa, Pablo Docampo  
C2-O7 Light-emitting Electrochemical Cells based on Inorganic Metal Halide Perovskite Nanocrystals
- 17:15 - 17:30 Erik M.J Johansson (*Uppsala University, Sweden*)  
C2-O8 Efficient, low-weight and semitransparent quantum dot solar cells

**Session D2**

Chair: Gerrit Boschloo

Room: Dye Sensitized Solar Cells and Water Splitting

- 14:30 - 15:00 **Kevin Sivula (EPFL)**  
D2-IS1 Engineering semiconductor materials for robust photoelectrochemical solar fuel production
- 15:00 - 15:15 Yan Hao, Wenxing Yang, **Gerrit Boschloo (Department of Chemistry- Ångström Laboratory, Uppsala University)**  
D2-O1 Fine-tuning of redox intermediates for highly efficient dye-sensitized solar cells
- 15:15 - 15:30 **Marina Freitag (Uppsala University, Sweden)**  
D2-O2 Copper Complexes for Dye-sensitized Solar Cells
- 15:30 - 15:45 **Qingqing Miao (Institute of Process Engineering, Chinese Academy of Sciences)**, Suojian Zhang  
D2-O3 Hybrid/Tandem Strategy for High-efficient Solar Cell Systems
- 15:45 - 16:00 **Hannes Michaels (Uppsala University, Sweden)**  
D2-O4 Highly-stable Cu(I)/(II) oxazoline-bipyridine complexes
- 16:00 - 16:30 **Coffee Break**
- 16:30 - 16:45 **Antonio Alfano (Center for Nano Science and Tecnology, Istituto Italiano di Tecnologia)**, Alessandro Mezzetti,  
D2-O5 Francesco Fumagalli, Chen Tao, Maria Rosa Antognazza, Emilio Palomares, Annamaria Petrozza, Fabio Di Fonzo  
Tandem Hybrid Organic-Inorganic Photocathode-Perovskite Solar Cell For Unassisted Water Splitting
- 16:45 - 17:00 Ingrid Rodríguez-Gutiérrez, Manuel Rodríguez-Pérez, Rodrigo García-Rodríguez, Alberto Vega-Poot, Geonel  
D2-O6 Rodríguez-Gattorno, Bruce A. Parkinson, **Gerko Oskam (Departamento de Física Aplicada, CINVESTAV-IPN Mérida)**  
CuBi<sub>2</sub>O<sub>4</sub> for solar water reduction: an IMPS analysis
- 17:00 - 17:15 **Roger Jiang (Department of Chemistry- Ångström Laboratory, Uppsala University)**, Gerrit Boschloo  
D2-O7 Overcoming The Mass Transport Limitations of Dye-Sensitised Solar Cells
- 17:15 - 17:30 **Bo Xu (Physical Chemistry, Department of Chemistry-Ångström Laboratory, Uppsala University, Box 523, SE-751 20 Uppsala, Sweden)**, Haining Tian  
D2-O8 High Performance All-Solid-State Dye-Sensitized Solar Cells

19:00 - 22:00 **Social Dinner and party****May 31st - Day 4 (Thursday)**08:55 - 09:00 **Announcement of the day****Session G3.1**

Chair: Iain McCulloch

- 09:00 - 09:45 **Antoni Llobet (ICIQ-BIST. Avda. Països Catalans, 16. Tarragona. E-43007. Spain)**  
G3.1-K1 Hybrid molecular photoanodes for water splitting
- 09:45 - 10:15 **Koen Vandewal (Institute for Materials Research (IMO-IMOMECE), Hasselt University, Wetenschapspark 1, 3590 Diepenbeek, BE)**  
G3.1-I1 The open-circuit voltage of organic photovoltaics
- 10:15 - 10:45 **He Yan (Department of Chemistry, The Hong Kong University of Science and Technology, Clear Water Bay, Kowloon, Hong Kong)**  
G3.1-I2 Temperature dependent aggregation enables efficient fullerene and non-fullerene organic solar cells -- A new path toward next generation organic solar cells

10:45 - 11:15 **Coffee Break****Session G3.2**

Chair: Kevin Sivula

- 11:15 - 11:45 **Neil Greenham (Cavendish Laboratory, University of Cambridge, JJ Thomson Avenue, Cambridge CB3 0HE, United Kingdom)**  
G3.2-I1 Singlet Fission to Enhance Photovoltaic Efficiency

11:45 - 12:15 G3.2-I2	<u>Annamaria Petrozza</u> ( <i>Center for Nano Science and Technology @Polimi, Istituto Italiano di Tecnologia, via Giovanni Pascoli 70/3, 20133, Milan, Italy.</i> ) Defect Physics and (In)Stability in Metal-halide Perovskite Semiconductors
12:15 - 12:45 G3.2-I3	<u>Filippo De Angelis</u> ( <i>CNR-ISTM Perugia</i> ) Origin of high open circuit voltage in lead-halide perovskite solar cells
12:45 - 13:00 G3.2-S1	<u>Filippo De Angelis</u> ( <i>Istituto di Scienze e Tecnologie Molecolari del CNR (CNR-ISTM)</i> ) Introducing next HOPV edition in Rome, Italy
13:00 - 14:30	<b>Lunch</b>
	<b>Session A3</b> Chair: Monica Lira-Cantu Room: Stability of Perovskite Solar Cells
14:30 - 15:00 A3-IS1	<u>Antonio Abate</u> ( <i>Helmholtz-Center Berlin for Materials and Energy Kekuléstraße 5 12489 Berlin Germany</i> ) Active materials for stable perovskite solar cells
15:00 - 15:15 A3-O1	<u>Alessandro Senocrate</u> ( <i>Max Planck Institut for Solid State Research</i> ), Tolga Acartürk, Gee Yeong Kim, Rotraut Merkle, Ulrich Starke, Michael Grätzel, Joachim Maier Mechanism of oxygen interaction with halide perovskites
15:15 - 15:30 A3-O2	<u>Amjad Farooq</u> ( <i>Institute of Microstructure Technology, Karlsruhe Institute of Technology, Hermann-von-Helmholtz-Platz 1, 76344 Eggenstein-Leopoldshafen, Germany</i> ), Ihtez Hossain, Jonas Schwenzler, Bryce Richards, Efthymios Klampaftis, Ulrich Paetzold Ultra-Violet Light Driven Degradation in Perovskite Solar Cells
15:30 - 15:45 A3-O3	<u>Dechan Angmo</u> ( <i>Commonwealth Scientific and Industrial Research Organisation, Australia</i> ), Xiaojin Peng, Chuantian Zuo, Youn-Jung Heo, Mei Gao, Doojin Vak Translating gas/solvent-assisted perovskite film formation from spin-coating in the glovebox to scalable manufacturing methods under ambient conditions
15:45 - 16:00 A3-O4	<u>Bardo Bruijners</u> ( <i>Molecular Materials and Nanosystems, Eindhoven University of Technology, Netherlands</i> ), Eric Schiepers, Christ Weijtens, Stefan Meskers, Martijn Wienk, René Janssen The importance of oxygen exposure of perovskite solar cells with a PEDOT:PSS hole transport layer
16:00 - 16:30	<b>Coffee Break</b>
16:30 - 16:45 A3-O5	<u>Ute Cappel</u> ( <i>Applied Physical Chemistry, Dept. of Chemistry, Royal Inst. of Technology (KTH)</i> ), Sebastian Svanström, Håkan Rensmo Composition dependence of photo-induced chemical changes in mixed-ion perovskite materials
16:45 - 17:00 A3-O6	<u>Francesca De Rossi</u> ( <i>Swansea University - SPECIFIC</i> ), Jenny Baker, James McGettrick, Trystan Watson The influence of 5-AVAI content on the stability of all printed perovskite solar cells and modules
17:00 - 17:15 A3-O7	<u>Ajay Jena</u> ( <i>1Toin Univeristy of Yokohama, Kanagawa, Japan</i> ), Youhei Numata, Masashi Ikegami, Tsutomu Miyasaka Strategic Compositional Changes at MAPbI <sub>3</sub> /spiro-OMeTAD Junction to Improve Thermal Stability of The Solar Cells
17:15 - 17:30 A3-O8	<u>Emilio J. Juarez-Perez</u> ( <i>Energy Materials and Surface Sciences Unit (EMSS), Okinawa Institute of Science and Technology Graduate University (OIST), 1919-1 Tancha, Onna-son, Okinawa 904-0495, Japan</i> ) Mitigation of photodecomposition processes in lead halide based solar cells to improve operational stability
	<b>Session B3</b> Chair: Carolin Sutter-Fella Room: Perovskite Solar Cells
14:30 - 15:00 B3-IS1	<u>Gustavo de Miquel</u> ( <i>Departamento de Química Física y Termodinámica Aplicada, Instituto Universitario de Investigación en Química Fina y Nanoquímica IUQFN, Universidad de Córdoba, Campus de Rabanales, Edificio Marie Curie, Córdoba, Spain</i> ), Alexander Davis Jodlowski, Cristina Roldán-Carmona, Luis Camacho Delgado, Mohammad Khaja Nazeeruddin Guanidinium/Methylammonium Lead Iodide Perovskite: An Unexplored Avenue for Stable and 20% Efficient Solar Cells

- 15:00 - 15:15 B3-O1 Yongyoon Cho (*UNSW School of Photovoltaic & Renewable Energy Engineering*), Arman Mahboubi Soufiani, Jae Sung Yun, Jincheol Kim, Da Seul Lee, Jan Seidel, Xiaofan Deng, Martin A. Green, Shujuan Huang, Anita W.Y. Ho-Baillie  
Mixed 3D-2D passivation treatment for mixed-cation lead mixed-halide perovskite solar cells for higher efficiency and better stability
- 15:15 - 15:30 B3-O2 Matthieu Manceau, Muriel Matheron, Ibrahim Bulut, Noëlla Lemaitre (*Univ. Grenoble Alpes, INES, CEA, LITEN, DTS*), Solenn Berson  
From Perovskite-based Solar Cells to Large area Modules for Indoor Applications
- 15:30 - 15:45 B3-O3 Yinghong Hu (*Department of Chemistry and Center for NanoScience (CeNS), LMU Munich, Butenandtstr. 11, 81377 Munich, Germany*), Eline M. Hutter, Philipp Rieder, Irene Grill, Jonas Hanisch, Meltem F. Aygüler, Alexander G. Hufnagel, Matthias Handloser, Thomas Bein, Achim Hartschuh, Kristofer Tvingstedt, Vladimir Dyakonov, Andreas Baumann, Tom J. Savenije, Michiel L. Petrus, Pablo Docampo  
Understanding the Role of Cesium and Rubidium Additives in Perovskite Solar Cells: Trap States and Charge Carrier Mobility
- 15:45 - 16:00 B3-O4 Endre Horváth (*EPFL SB IPHYS LPMC, station 3, 1015, Lausanne*), Massimo Spina, Bálint Náfrádi, Eric Bonvin, Márton Kollár, Andrzej Sienkiewicz, Anastasiia Glushkova, Alla Arakcheeva, Zsolt Szekrényes, Hajnalka Tóháti, Katalin Kamarás, Richard Gaal, László Forró  
Organic-inorganic lead halide perovskite nanowires: formation mechanism and optoelectronic applications
- 16:00 - 16:30 **Coffee Break**
- 16:30 - 16:45 B3-O5 Riva Alkarsifi (*Aix-Marseille University, Centre Interdisciplinaire de Nanosciences de Marseille CINaM, UMR CNRS 7325, Marseille, France*), Florent Pourcin, Pavlo Perkhun, Mats Fahlman, Christine Vidélot-Ackermann, Olivier Margeat, Jörg Ackermann  
Doped Metal Oxide Nanocrystals for Solution-Processed Hole Extraction Layers in High Efficient Organic Solar Cells
- 16:45 - 17:00 B3-O6 Petra Cameron (*Department of Chemistry, University of Bath*), Dominic Ferdani, Samuel Pering, Isabella Poli, Peter Baker  
Understanding the Changes Introduced by Cation Substitution in Perovskite Solar Cells
- 17:00 - 17:15 B3-O7 Luis Pazos-Outon (*University of California, Berkeley, US*), T. Patrick Xiao, Eli Yablonovitch  
Fundamental efficiency limit of lead iodide perovskite solar cells
- 17:15 - 17:30 B3-O8 Fabio Matteocci (*C.H.O.S.E-Univ. Tor Vergata*), Emanuele Calabrò, Luigi Vesce, Alessandro Lorenzo Palma, Valentina Mirruzzo, Enrico Lamanna, Aldo Di carlo  
Perovskite solar modules: a new era for thin film PV technology
- Session C3**  
Chair: Udo Bach  
Room: Multi-junction Solar Cells
- 14:30 - 15:00 C3-IS1 Henk Bolink (*Instituto de Ciencia Molecular, Universidad de Valencia, C/ Catedrático J. Beltrán 2, 46980 Paterna, Spain*), Lidon Gil-Escrig, Pablo P. Boix, Cristina Momblona, Jorge Avila, Daniel Perez del Rey, Michele Sessolo, Benedikt Daenekamp  
Fully Evaporated High Efficiency Single Junction and Tandem Perovskite based Solar Cells.
- 15:00 - 15:15 C3-O1 Mehrdad Najafi (*ECN – Solliance, High Tech Campus 21, 5656 AE, Eindhoven, The Netherlands*), Valerio Zardetto, Dong Zhang, Maarten Dorenkamper, Francesco Di Giacomo, Ilker Dogan, Wiljan Verhees, Herbert Lifka, Alessia Senes, Paul Poodt, Bart Geerligs, Tom Aernouts, Sjoerd Veenstra, Ronn Andriessen  
Stable semi-transparent perovskite solar cells for 26.1%-Efficiency Perovskite/c-Si 4-Terminal tandem cell
- 15:15 - 15:30 C3-O2 César Omar Ramírez Quiroz (*Friedrich-Alexander University Erlangen-Nürnberg, Institute of Materials for Electronics and Energy Technology (I-MEET), Department of Materials Science and Engineering, Erlangen, Germany.*), Pierre J. Verlinden, Xueling Zhang, Martin A. Green, Anita Ho-Baillie, Loïc M. Roch, Michael Salvador, Steve Albrecht, Tobias Unruh, Andreas Hirsch, Alán Aspuru-Guzik, Christoph J. Brabec, George D. Spyropoulos, Bernd Rech  
From 4T to 2T solution processed silicon/perovskite tandems solar cells

15:30 - 15:45 C3-O3	<u>Dario Di Carlo Rasi</u> ( <i>Molecular Materials and Nanosystems, Eindhoven University of Technology, Netherlands</i> ), Martijn Wienk, Rene' Janssen Quadruple-junction polymer solar cells with four different complementary absorber layers
15:45 - 16:00 C3-O4	<u>F. Javier Ramos</u> ( <i>IPVF, Institut Photovoltaïque d'Île-de-France, 30 RD 128, 91120 Palaiseau, France</i> ), Sebastien Jutteau, Jorge Posada, Adrien Bercegol, Amelle Rebai, Thomas Guillemot, Romain Bodeux, Nathanaelle Schneider, Nicolas Loones, Daniel Ory, Cedric Broussillou, Gilles Goer, Laurent Lombez, Jean Rousset Efficient MoOx-Free Semitransparent Perovskite Solar Cell for a 22.4% 4-T Tandem with a 3% Boost over Commercially-Available Al-BSF Si Cell
16:00 - 16:30	<b>Coffee Break</b>
16:30 - 16:45 C3-O5	<u>Peter Fiala</u> ( <i>Ecole Polytechnique Fédérale de Lausanne (EPFL), Institute of Microengineering (IMT) Photovoltaics and Thin-Film Electronics Laboratory (PV-Lab), Rue de la Maladière 71b, 2002 Neuchâtel, Switzerland.</i> ), Terry Chien-Jen Yang, Jérémie Werner, Florent Sahlí, Matthias Bräuninger, Brett A. Kamino, Gizem Nogay, Fan Fu, Raphaël Monnard, Arnaud Walter, Soo-Jin Moon, Loris Barraud, Bertrand Paviet- Salomon, Laura Ding, Juan J. Diaz Leon, Mathieu Boccard, Matthieu Despeisse, Sylvain Nicolay, Bjoern Niesen, Quentin Jeangros, Christophe Ballif Hybrid Fabrication Method for High Efficiency Monolithic Perovskite/Silicon Tandem Solar Cells
16:45 - 17:00 C3-O6	<u>Miguel Anaya</u> ( <i>Institute of Materials Science of Seville, CSIC-US</i> ), Gabriel Lozano, Mauricio Calvo, Hernán Míguez Optical design to boost the performance of perovskite based tandem solar cells
17:00 - 17:15 C3-O7	<u>Benjamin Smith</u> ( <i>SPECIFIC / Swansea University</i> ), Trystan Watson Semi Transparent Perovskite Solar Cells with Transparent Back Contacts
17:15 - 17:30 C3-O8	<u>Tobias Abzieher</u> ( <i>Karlsruhe Institute of Technology, Light Technology Institute (LTI), Engesserstrasse 13, 76131 Karlsruhe, Germany</i> ), Jonas A. Schwenzler, Florian Sutterlüti, Michael Pfau, Erwin Lotter, Michael Hetterich, Uli Lemmer, Michael Powalla, Ulrich W. Paetzold Upscalable All-Evaporated Perovskite Solar Cells Based on Inorganic Hole Transport Layers
<b>Session D3</b> Chair: Koen Vandewal Room: Electrical Characterization of Perovskites	
14:30 - 15:00 D3-IS1	<u>Dieter Neher</u> ( <i>nstitute of Physics and Astronomy, University of Potsdam</i> ), Christian Wolff, Martin Stollerfoht Hybrid Multilayer Design for Efficient Perovskite-based Solar Cells
15:00 - 15:15 D3-O1	<u>Tereza Schönfeldová</u> ( <i>Laboratory of Nanostructures and Nanomaterials, Institute of Physics, Academy of Sciences of the Czech Republic, v. v. i., Cukrovarnická 10, 162 00 Prague, Czech Republic</i> ), Jakub Holovský, Zdeňka Hájková, Lucie Abelová, Neda Neykova, Ha Stuchlíková, Jan Kočka, Stefaan De Wolf, Antonín Fejfar, Martin Ledinský Study of Static and Dynamic Disorder in Organic-Inorganic Halide Perovskites
15:15 - 15:30 D3-O2	<u>Andreas Baumann</u> ( <i>Bavarian Center for Applied Energy Research, Magdalene-Schoch-Str. 3, 97074 Würzburg, Germany</i> ), Mathias Fischer, Kristofer Tvingstedt, Vladimir Dyakonov Doping profile in planar perovskite solar cells
15:30 - 15:45 D3-O3	David Kiermasch, Andreas Baumann, Mathias Fischer, Vladimir Dyakonov, <u>Kristofer Tvingstedt</u> ( <i>Experimental Physics VI, Julius Maximilian University of Würzburg, 97074 Würzburg, Germany</i> ) On the assignment of carrier lifetimes in high absorption coefficient thin film solar cells via electrical transient methods
15:45 - 16:00 D3-O4	<u>Anna Todinova</u> ( <i>Molecular Materials and Nanosystems, Eindhoven University of Technology, Netherlands</i> ), Lidia Contreras-Bernal, Manuel Salado, Shahzada Ahmad, Neftali Morillo, Jesus Idigoras, Juan Antonio Anta Choice of equivalent circuit for impedance spectra of perovskite cells: Universal approach and empirical analysis.
16:00 - 16:30	<b>Coffee Break</b>
16:30 - 16:45 D3-O5	<u>Matt Carnie</u> ( <i>1SPECIFIC, College of Engineering, Swansea University Bay Campus, Fabian Way, SA1 8EN Swansea, United Kingdom</i> ), Adam Pockett, Jenny Baker, Francesca De Rossi, Trystan Watson Recombination and Ion Migration in Triple Mesoporous Perovskite Solar Cells

16:45 - 17:00 D3-O6	<u>Tian Du</u> ( <i>Department of materials, Imperial College London</i> ), Weidong Xu, Jinhyun Kim, Matyas Daboczi, Ji-seon Kim, James Durrant, Martyn McLachlan Charge extraction limits open-circuit voltage in inverted planar perovskite solar cells
17:00 - 17:15 D3-O7	<u>Meltem F. Ayguler</u> ( <i>Department of Chemistry and Center for Nanoscience (CeNS) University of Munich (LMU)</i> ), Alexander G. Hufnagel, Philipp Rieder, Michael Wussler, Wolfram Jaegermann, Thomas Bein, Vladimir Dyakonov, Michiel L. Petrus, Andreas Baumann, Pablo Docampo The Influence of Fermi Level Alignment with Tin Oxide on the Hysteresis of Perovskite Solar Cells
17:15 - 17:30 D3-O8	<u>Philipp Rieder</u> ( <i>Experimental Physics VI, Julius Maximilian University of Würzburg, 97074 Würzburg, Germany</i> ), Yinghong Hu, Meltem F. Aygüler, Alexander G. Hufnagel, Michiel L. Petrus, Pablo Docampo, Kristofer Tvingstedt, Andreas Baumann, Thomas Bein, Vladimir Dyakonov Reduced defect density in triple and quadruple cation perovskite solar cells by incorporation of Cesium
17:30 - 18:00	<b>Closing ceremony</b>

## Poster Contribution

003	<u>Saeid Rafizadeh</u> ( <i>Fraunhofer Institute for Solar Energy Systems ISE</i> ), Karl Wienands, Laura E. Mundt, Alexander J. Bett, Patricia S.C. Schulze, Ludmila Cojocar, Lucio Claudio Andreani, Martin Hermle, Stefan Glunz, Jan Christoph Goldschmidt Record Stabilized Efficiencies Exceeding 18% for Hybrid Evaporation-Spincoating Planar Perovskite Solar Cells
005	<u>Haining Tian</u> ( <i>Physical Chemistry, Department of Chemistry-Ångström Laboratory, Uppsala University, Box 523, SE-751 20 Uppsala, Sweden</i> ), Lei Tian, Jens Föhlinger Solid State p-Type Dye Sensitized Core-Shell Solar Cells
006	<u>Yue Hu</u> ( <i>Michael Grätzel Center for Mesoscopic Solar Cells, Wuhan National Laboratory for Optoelectronics</i> ), Yaoguang Rong, Hongwei Han Improved Performance of Printable Perovskite Solar Cells with Bifunctional Conjugated Organic Molecule
007	<u>Yaoguang Rong</u> ( <i>Michael Grazel Center for Mesoscopic Solar Cells, Wuhan National Laboratory for Optoelectronics, Huazhong University of Science and Technology</i> ), Yue Hu, Xiaomeng Hou, Mi Xu, Hongwei Han Ambient-processed efficient and stable printable mesoscopic perovskite solar cells
008	<u>Cho Fai Jonathan Lau</u> ( <i>Australian Centre for Advanced Photovoltaics, School of Photovoltaic and Renewable Energy Engineering, University of New South Wales, Sydney 2052, Australia</i> ), Xiaofan Deng, Jianghui Zheng, Jincheol Kim, Zhilong Zhang, Meng Zhang, Jueming Bing, Benjamin Wilkinson, Long Hu, Robert Patterson, Shujuan Huang, Anita Ho-Baillie Enhanced Performance via Partial Pb Replacement with Ca for CsPbI <sub>3</sub> Perovskite Solar Cell exceeding 13% Power Conversion Efficiency
010	<u>Isabella Poli</u> ( <i>Centre for Sustainable Chemical Technologies, University of Bath</i> ), Salvador Eslava, Petra Cameron Simple solution-processing strategy for halide perovskite solar cells with enhanced stability towards moisture
030	<u>Lidia Contreras-Bernal</u> ( <i>Área de Química Física, Universidad Pablo de Olavide, E-41013, Sevilla, Spain</i> ), Clara Aranda, Marta Valles-Pelarda, Thi Tuyen Ngo, Susana Ramos-Terrón, Juan Jesús Gallardo, Javier Navas, Antonio Guerrero, Iván Mora-Seró, Jesús Idígoras, Juan A Anta Homeopathic Perovskite Solar Cells: Effect of Humidity During Fabrication on the Performance and Stability of the Device
036	<u>Alejandra Maria Castro Chong</u> ( <i>Departamento de Física Aplicada, CINVESTAV-IPN Mérida</i> ), Tom Aernouts, Gerko Oskam, Weiming Qiu, Joao Bastos Influence of the Presence of a Mesoporous Electron Extraction Layer on the Stability of Hybrid Perovskite Solar Cells.
045	<u>Markus Kohlstädt</u> ( <i>University of Freiburg, Freiburg Materials Research Center (FMF)</i> ), Mohammed A. Yakoob, Jan P. Herterich, Laura E. Mundt, Uli Würfel From cell to mini-module – blade coating and controlled drying for planar inverted perovskite solar cells
046	<u>Bart Roose</u> ( <i>Cavendish Laboratory, University of Cambridge, JJ Thomson Avenue, Cambridge CB3 0HE, United Kingdom</i> ) Engineering metal oxides for UV-stable perovskite solar cells

050	<u>Dominic Ferdani</u> ( <i>Centre for Sustainable Chemical Technologies, University of Bath</i> ), Andrew Johnson, Simon Lewis, Peter Baker, Petra Cameron Investigating Mixed Cation Perovskites with Muon Spin Relaxation
051	<u>Samuel Pering</u> ( <i>Department of Chemistry, University of Bath</i> ), Petra Cameron A-site Cationic Additives: What Do They Do?
053	<u>Joel Smith</u> ( <i>The University of Sheffield</i> ), Onkar Game, Michael Wong-Stringer, Melissa McCarthy, Benjamin Freestone, Claire Greenland, Thomas Routledge, Ian Povey, David Lidzey Electron beam evaporation of tin oxide layer for planar perovskite solar cells
054	<u>Sunsun Li</u> ( <i>Institute of Chemistry, Chinese Academy of Sciences</i> ), Wenchao Zhao, Long Ye, Harald Ade, Jianhui Hou Rational Molecular Design of Non-fullerene Acceptor towards High-efficiency Polymer Solar Cells
055	<u>Dong Ding</u> ( <i>Imperial College London, Department of Chemistry and Centre for Plastic Electronics</i> ) Recent Advances in Solution-Processed Hybrid Nanostructured Tin Monosulfide Solar Cells
069	<u>Luis Lanzetta</u> ( <i>Imperial College London, Department of Chemistry and Centre for Plastic Electronics</i> ), Sozos Michael, Chloe Wong, Saif A. Haque Layered Organic Tin Halide Perovskite: Interfacial Charge Carrier Dynamics and Device Applications
073	<u>Karen L. Valadez-Villalobos</u> ( <i>Department of Applied Physics, CINVESTAV-IPN, Mérida, Yuc. 97310, México</i> ), Jesús Idígoras, Lilian Pérez, Juan A. Anta, Gerko Oskam Effect of Different Materials as Electron Selective Contacts in the Performance of Perovskite Solar Cells
078	Su Htike Aung, Lichen Zhao, Kazuteru Nonomura, Shaik M. Zakeeruddin, <u>Nick Vlachopoulos</u> ( <i>Laboratory of Photomolecular Science, Department of Chemical Science and Engineering, Swiss Federal Institute of Technology in Lausanne, EPFL--ISIC-FSB-LSPM, Station 6, CH-1015 Lausanne, Switzerland</i> ), Anders Hagfeldt, Michael Grätzel Electrochemically deposited blocking underlayers in efficient n-p-i perovskite solar cells
082	<u>Yi-Bing Cheng</u> ( <i>Monash University, Department of Materials Science and Engineering</i> ), Jinbao Zhang, Quentin Daniel, Tian Zhang, Xiaoming Wen, Bo Xu, Licheng Sun, Udo Bach Effects of dopants in hole transport material (HTM) for perovskite solar cells
084	<u>Yinghong Hu</u> ( <i>Department of Chemistry and Center for NanoScience (CeNS), LMU Munich, Butenandtstr. 11, 81377 Munich, Germany</i> ), Meltem F. Aygüler, Michiel L. Petrus, Thomas Bein, Pablo Docampo Impact of Rubidium and Cesium Cations on the Moisture Stability of Multiple-Cation Mixed-Halide Perovskites
086	<u>Sandy Sanchez</u> ( <i>University of Fribourg, Adolphe Merkle Institute</i> ) Flash infrared annealing for perovskite solar cells
090	<u>Lei Tian</u> ( <i>Uppsala University, Sweden</i> ) Charge transfer kinetics in a Core-Shell NiO-Dye-TiO <sub>2</sub> Mesoporous Film
094	<u>Liang Wang</u> ( <i>National Center for Nanoscience and Technology</i> ), Fengjing Liu, Xiaoyong Cai, Chao Jiang A New Strategy of Methylamine Iodide Solution Assisted Repair for Pinhole-Free Perovskite Films in High-Efficiency Photovoltaics under Ambient Conditions
097	<u>Bart Saes</u> ( <i>Molecular Materials and Nanosystems, Eindhoven University of Technology, Netherlands</i> ), Michael Pätzel, Martin Herder, Martijn Wienk, Rene Janssen, Stefan Hecht Photochromism in Bulk Heterojunction Organic Solar Cells
098	<u>Bowon Yoo</u> ( <i>Department of Chemistry, Imperial College London, South Kensington Campus, London SW7 2AZ, United Kingdom</i> ), Dong Ding, Luis Lanzetta, Jose Marin-Beloqui, Xiangnan Bu, Saif Haque Thin layer for efficient charge separation of bismuth iodide thin films for improved carrier transportation for photovoltaic application
103	<u>Sebastian Svanström</u> ( <i>Uppsala University, Sweden</i> ), Jesper Jacobsson, Håkan Rensmo, Ute Cappel In-situ chemical characterisation of perovskite interfaces using XPS
105	<u>Konstantins Mantulnikovs</u> ( <i>Laboratory of Physics of Complex Matter, École Polytechnique Fédérale de Lausanne, CH-1015 Lausanne, Switzerland</i> ), Anastasiia Glushkova, Péter Matus, Luka Ćirić, Márton Kollár, László Forró, Endre Horváth, Andrzej Sienkiewicz Morphology and photoluminescence of CH <sub>3</sub> NH <sub>3</sub> PbI <sub>3</sub> deposits on non-planar, strongly curved substrates

- 111 Artiom Magomedov (*Department of Organic Chemistry, Kaunas University of Technology*), Ernestas Kasparavičius, Kasparas Rakstys, Sanghyun Paek, Natalia Gasilova, Kristijonas Genevičius, Gytis Juška, Tadas Malinauskas, Mohammad Khaja Nazeeruddin, Vytautas Getautis  
Pyridination of Hole Transporting Materials in Perovskite Solar Cells
- 115 Wanning Li (*Institute of Chemistry, Chinese Academy of Sciences*), Long Ye, Sunsun Li, Huifeng Yao, Harald Ade, Jianhui Hou  
A High Efficiency Organic Solar Cell Enabled by Strong Intramolecular Electron Push-Pull Effect of Non-Fullerene Acceptor
- 118 Jan-Henrik Smått (*Laboratory of Physical Chemistry, Åbo Akademi University*), Muhammad Talha Masood, Syeda Qudsia, Simon Sandén, Oskar J. Sandberg, Mathias Nyman, Paola Vivo, Peter D. Lund, Ronald Österbacka  
Utilizing the Dip Coating Method to Prepare Uniform Contact Materials for Perovskite Solar Cells
- 121 Runnan Yu (*Institute of Chemistry, Chinese Academy of Sciences (ICCAS)*), Jianhui Hou  
Two Well-miscible Acceptors Work as One for Efficient Fullerene-free Organic Solar Cells
- 123 Wallace Choy (*Department of Electrical and Electronic Engineering, The University of Hong Kong, Pok Fu Lam Road, Hong Kong SAR, China*)  
New Class of Green Low-Temperature Solution-Processed Metal Oxides for High Performance Organic Solar Cells
- 126 Blaise Godefroid (*Université libre de Bruxelles*), Gregory Kozyreff  
Multi-resonance tandem geometry for an improved light trapping at long-wavelength in thin-film solar cells
- 127 Sebastian F. Hoefler (*Institute for Chemistry and Technology of Materials (ICTM), Graz University of Technology, Stremayrgasse 9, 8010 Graz, Austria*), Thomas Rath, Mathias Hobisch, Nadiia Pastukhova, Egon Pavlica, Guido Bratina, Dorothea Scheunemann, Sebastian Wilken, Gregor Trimmel  
Assessing the Role of Polymer Molecular Weight for High-Performance Indacenodithiophene-Based Fullerene-Free Organic Solar Cells
- 135 Waldemar Kaiser (*Technical University of Munich*), Alessio Gagliardi  
Enhanced thermodynamic efficiency study of excitonic solar cells
- 144 Atanas Katerski (*Department of Materials and Environmental Technology, Tallinn University of Technology, Ehitajate tee 5, 19086, Tallinn, Estonia.*), Jako Siim Eensalu, Erki Kärber, Ilona Oja Acik, Arvo Mere, Malle Krunks  
TiO<sub>2</sub>/Sb<sub>2</sub>S<sub>3</sub> by ultrasonic spray method for rapid fabrication of a hybrid solar cell
- 145 Catherine Suenne De Castro (*Applied Photochemistry Group, SPECIFIC, Materials Research Centre, College of Engineering, Swansea University, Bay Campus, Fabian Way, Swansea SA1 8EN, United Kingdom*)  
Photophysical Characterisation of Perovskites
- 150 Viresh Dutta (*Indian Institute of Technology Delhi, New Delhi-India*)  
Synthesis of Bismuth Iodide Perovskite Thin film by Spray Technique for Solar Cell Applications
- 155 Yuriy Luponosov (*Enikolopov Institute of Synthetic Polymer Materials of Russian Academy of Sciences, Moscow, Russia*), Alexander Solodukhin, Sergei Ponomarenko  
Alkyl-free D-A small molecules based on triphenylamine and phenyldicyanovinyl blocks as promising class of stable materials for organic solar cells
- 160 Denys Shevchenko (*Solomya*)  
Mass Spectrometry Analysis of Hybrid and Organic Solar Cells
- 166 Robert Baker (*Centre for Sustainable Chemical Technologies and Department of Chemistry, University of Bath*), Xinxing Liang, Petra Cameron  
Controllable Synthesis of Perovskite Quantum Dots using Flow Chemistry
- 177 Pedro Rodríguez-Cantó (*INTENANOMAT S.L, C/ Catedrático José Beltrán 2, 46980 Paterna, Spain.*), Eduardo Aznar, Juan P. Martínez-Pastor, Rafael Abargues  
Novel transparent conducting polymeric materials suitable for hole transport in perovskite-based devices
- 178 Sixto Gimenez (*Institute of Advanced Materials (INAM), Universitat Jaume I*), Drialys Cardenas-Morcoso, Miguel Garcia-Tecedor, Roser Fernandez-Climent  
Solar fuels production with metal oxide semiconductor materials



183	<u>Enrico Lamanna</u> ( <i>CHOSE (Centre for Hybrid and Organic Solar Energy), Department of Electronic Engineering, University of Rome - Tor Vergata</i> ), Emanuele Calabrò, Fabio Matteocci, Aldo Di Carlo, Luca Serenelli, Mario Tucci, Paola Delli Veneri, Vera La Ferrara, Antonella De Maria Enhancing IR transmittance of Perovskite Solar Cells for 2-terminal Silicon/Perovskite tandem devices
185	<u>Emanuele Calabrò</u> ( <i>Centre for Hybrid and Organic Solar Energy (CHOSE), Department of Electronic Engineering, University of Rome TOR Centre for Hybrid and Organic Solar Energy (CHOSE), Department of Electronic Engineering, University of Rome TOR VERGATA</i> ), Fabio Matteocci, Enrico Lamanna, Aldo Di Carlo Improving the efficiency of Low temperature planar MAPbI <sub>3</sub> Perovskite Solar Cells using a Cesium doped SnO <sub>2</sub>
189	<u>Sigalit Aharon</u> ( <i>The Hebrew University of Jerusalem, The Institute of Chemistry, Casali Center for Applied Chemistry, Jerusalem, Israel</i> ), Lioz Etgar The effect of the alkylammonium cation on the optical and physical properties of organic-inorganic perovskite nanoparticles
196	<u>Narges Yaghoobi Nia</u> ( <i>CHOSE. (Centre for Hybrid and Organic Solar Energy), University of Rome "Tor Vergata", via del Politecnico 1, Rome 00133, Italy.</i> ), Fabrizio Giordano, Mahmoud Zendeheel, Alessandro Lorenzo Palma, Lucio Cinà, Fabio Matteocci, Shaik Mohammed Zakeeruddin, Michael Graetzel, Aldo Di Carlo A Scalable Crystal Engineering Approach for Fabrication of Efficient and Stable Multi Cation/Anion Perovskite Solar Cells and Modules Via Sequential Deposition in Ambient Condition
198	<u>Neeti Tripathi</u> ( <i>Department of Physics, School of Physical Sciences, Doon University, Kedarpur, Dehardun, Uttarakhand 24800, INDIA</i> ), Masatoshi Yanagida, Yasuhiro Shirai, Kenjiro Miyano Reduced recombination losses in planar perovskite devices via amine based polymer
201	<u>Petra Matunová</u> ( <i>Institute of Physics ASCR</i> ), Vít Jirásek, Bohuslav Rezek Effects of different nanodiamond surface terminations on HOMO/LUMO separation in complexes with polypyrrole: a DFT study.
207	<u>Marius Franckevičius</u> ( <i>Center for Physical Sciences and Technology, Saulėtekio Av. 3, LT-10257 Vilnius, Lithuania</i> ), Rokas Gegevičius, Marius Treideris, Vidmantas Gulbinas The Role of Oxide Layer on the Gain Enhancement in Hybrid Perovskite Photodetectors
208	<u>Jimmy Mangalam</u> ( <i>Institute for Chemistry and Technology of Materials (ICTM), Graz University of Technology, Stremayrgasse 9, 8010 Graz, Austria</i> ), Thomas Rath, Stefan Weber, Birgit Kunert, Gregor Trimmel Functionalized benzylphosphonic acid SAMs for modification of nickel oxide hole transport layers in lead halide perovskite solar cells
210	<u>Ningning Liang</u> ( <i>Institute of Chemistry, Chinese Academy of Science, Beijing 100190, PR China</i> ), Kai Sun, Jianhui Hou, Zhaohui Wang Near-Infrared Non-Fullerene Electron Acceptors Based on Terrylene Diimides for Organic Solar Cells
211	<u>Simone Meroni</u> ( <i>SPECIFIC, Swansea University</i> ), Katherine Hooper, Francesca De Rossi, Jennifer Baker, Trystan Watson Design and Optimisation of Fully Printable Perovskite Solar Modules by Scribing Method
213	<u>Osbel Almora</u> ( <i>Institute of Materials for Electronics and Energy Technology (i-MEET), Friedrich-Alexander Universität Erlangen-Nürnberg, Martensstr. 7, 91058 Erlangen, Germany</i> ), Kyung Taek Cho, Sadig Aghazada, Iwan Zimmermann, Gebhard J. Matt, Christoph J. Brabec, Nazeeruddin Mohammad Khaja, Germà Garcia-Belmonte Discerning Recombination Mechanisms in Perovskite Solar Cells including 2D/3D Interfaces and Mixed Anions/Cations Absorbers
214	<u>Ariadni Boziki</u> ( <i>Swiss Federal Institute of Technology, EPFL, ISIC, LCBC, CH-1015, Lausanne, Switzerland</i> ), José A Flores-Livas, Daniele Tomerini, Sandip De, Michele Ceriotti, Stefan Goedecker, Ursula Röthlisberger Structure discovery of organic-inorganic halide perovskites
216	<u>Dibyajyoti Ghosh</u> ( <i>Department of Chemistry, University of Bath</i> ) Good Vibrations: Locking of Octahedral Tilting in Mixed-Cation Iodide Perovskites for Solar Cells
217	<u>Renan Escalante</u> ( <i>Centro de Investigación y de Estudios Avanzados del IPN</i> ), Dena Pourjafari, Alberto Vega-Poot, Juan Anta, Gerko Oskam Dye-sensitized solar cells: comparison between different TiO <sub>2</sub> phases and scale-up

218	<u>Masatoshi Yanagida</u> ( <i>Global Research Center for Environment and Energy based on Nanomaterials Science (GREEN), National Institute for Materials Science (NIMS)</i> ), Md Bodiul Islam, Namrata Pant, Yasuhiro Shirai, Kenjiro Miyano PbI perovskite solar cells consisted of RF sputtered NiOx as hole transport layer
220	Jian Qing, <u>Xiao-Ke Liu</u> ( <i>Department of Physics Chemistry and Biology Linköping University 58183 Linköping , Sweden</i> ), Mingjie Li, Chun-Sing Lee, Tze Chien Sum, Feng Gao Aligned and Graded Type-II Ruddlesden-Popper Perovskite Films for Efficient Solar Cells
221	<u>Mahdi Alqahtani</u> ( <i>Electronic &amp; Electrical Engineering - University College London</i> ), Fan Cui, Jiang Wu Protective nanostructure for an efficient and stable water-splitting GaAs photoanode
223	<u>Andrea Rubino</u> ( <i>Multifunctional Optical Materials Group, Instituto de Ciencia de Materiales de Sevilla, Consejo Superior de Investigaciones Científicas-Universidad de Sevilla</i> ), Miguel Anaya, Mauricio Calvo, Juan Galisteo, Hernan Miguez Highly emissive hybrid MAPbX3 perovskite nanocrystals flexible films
224	<u>David Tiede</u> ( <i>Instituto de Ciencia de Materiales de Sevilla (ICMS-CSIC)</i> ), Juan F. Galisteo-López, Miguel Anaya, Mauricio E. Calvo, Hernán Míguez Post-fabrication halide treatment in CH <sub>3</sub> NH <sub>3</sub> PbBr <sub>3</sub> single crystals as a means to improve its photoluminescence
225	<u>Claire Greenland</u> ( <i>Department of Physics and Astronomy, University Of Sheffield</i> ), Sai Rajendran, Onkar Game, David Lidzey Temperature-dependent charge carrier dynamics in (FAPbI <sub>3</sub> ) <sub>0.85</sub> (MABr) <sub>0.15</sub> thin films
226	<u>Arvydas Ruseckas</u> ( <i>School of Physics and Astronomy, University of St. Andrews</i> ), Scott J. Pearson, Gordon J. Hedley, Ifor D.W. Samuel Charge recombination via polymer triplet state in PTB7:fullerene blends
227	<u>Anastasiia Glushkova</u> ( <i>EPFL SB IPHYS LPMC, Lausanne, CH-1015, Switzerland</i> ), Alla Arakcheeva, Phil Pattison, Marton Kollar, Pavao Andricevic, Balint Nafradi, Laszlo Forro, Endre Horvath Influence of the organic cation disorder on photoconductivity in ethylenediammonium lead iodide, NH <sub>3</sub> CH <sub>2</sub> NH <sub>2</sub> NH <sub>3</sub> PbI <sub>4</sub>
228	<u>Alberto Viñas</u> ( <i>University of Copenhagen</i> ), Jonas Lissau, Henrik Gotfredsen, Martyn Jevric, Mogens Brønsted Nielsen, Theis Sølling Irreversible Energy Transfer in Fullerene Derivatives: through-Space Energy Transfer for Triplet Harvesting
229	<u>Mincheol Park</u> ( <i>Center for Multiscale Energy Systems</i> ), Woohyung Cho, Mansoo Choi Highly reproducible large-scale perovskite solar cells fabricated via megasonic spray system
230	<u>Yoshiyuki Nakajima</u> ( <i>Riken Keiki Co. Ltd</i> ), Satoshi Uchida, Hiroshi Segawa Electronic properties of raw materials of Perovskite and Quantum dots Solar Cell Estimated with "Photoemission Yield Spectroscopy in Air (PYSA)"
231	<u>Man Gu Kang</u> ( <i>ICT Materials Research Group, ICT Materials &amp; Components Research Laboratory, Electronics and Telecommunications Research Institute</i> ), Seong Hyun Lee Optimum Design in series connected DSCs and PSCs Modules
232	<u>Laurence Lutsen</u> ( <i>imec-department imomec</i> ) Solid-state Nuclear Magnetic Resonance Spectroscopy applied to formamidinium-methylammonium mixed hybrid perovskites
233	<u>Huimin Zhu</u> ( <i>Physical Chemistry, Department of Chemistry-Ångström Laboratory, Uppsala University, Box 523, SE-751 20 Uppsala, Sweden</i> ) The Effect of Dopant-Free Hole Transport Polymers P3HT, P3TI and TQ1 on Charge Generation and Recombination in Cesium-Bismuth-Iodide Solar Cells
236	Gee Yeong Kim, <u>Alessandro Senocrate</u> ( <i>Max Planck Institute for Solid State Research</i> ), Tae-Youl Yang, Giuliano Gregori, Michael Graetzel, Joachim Maier Huge photo-enhancement of ion conduction in methylammonium lead iodide
238	<u>Ming-Chun Tang</u> ( <i>KAUST Solar Center (KSC) and Physical Science and Engineering Division (PSE), King Abdullah University of Science and Technology (KAUST), Thuwal 23955-6900, Saudi Arabia</i> ), Kai Wang, Hoang X. Dang, Dounya Barrit, Rahim Munir, Detlef-M. Smilgies, Stefaan De Wolf, Aram Amassian In situ investigation of mixed-cation and mixed-halide hybrid perovskite films achieving 20% PCE

239	<u>Rodrigo García-Rodríguez</u> ( <i>Bath University</i> ), Sam Pering, Adam Pockett, Petra Cameron INFLUENCE OF IODIDE AND BROMIDE CONTENT ON IONIC MOVEMENT IN MIXED-HALIDE PEROVSKITE SOLAR CELLS
240	<u>Nuria Vicente Agut</u> ( <i>Institute of Advanced Materials (INAM), Universitat Jaume I</i> ), Germà Garcia-Belmonte High Li-ion Concentration and Diffusion in Methylammonium Lead Bromide Perovskite Battery Anodes
241	<u>Aaron Bayles</u> ( <i>Instituto de Ciencia de Materiales de Sevilla (ICMS-CSIC)</i> ), Mauricio E. Calvo, Sol Carretero Palacios, Hernán Míguez Plasmonic Enhancement of Perovskite Thin Film Absorption
243	Alba Mingorance, Haibing Xie, Hui-Seon Kim, Jose Carlos Pereira, Amador Perez-Tomas, Zaiwei Wang, Marc Balsells, Anna Morales-Malgares, Wolfgang Tress, Neus Domingo, Anders Hagfeldt, <u>Monica Lira-Cantu</u> ( <i>Catalan Institute of Nanoscience and Nanotechnology (ICN2), CSIC and The Barcelona Institute of Science and Technology, Campus UAB, Bellaterra, 08193 Barcelona, Spain</i> ) Binary, Doped and Complex Oxides as Transport Layers in Halide Perovskite Solar Cells
244	Junke Jiang, Chidozie K. Onwudinanti, Ross A. Hatton, <u>Peter A. Bobbert</u> ( <i>Center for Computational Energy Research, Department of Applied Physics, Eindhoven University of Technology, P.O. Box 513, 5600 MB Eindhoven, The Netherlands</i> ), Shuxia Tao Stabilizing Lead-Free All-Inorganic Tin Halide Perovskites by Ion Exchange
245	<u>Chiara Carbonera</u> ( <i>Research Center for Renewable Energies &amp; Environment - Solar Department - Eni S.p.A., Novara, Italy</i> ), Alessandra Cominetti, Riccardo Po', Mario Salvalaggio, Alberto Savoini, Stefano Zanardi Study of alternative printable interlayers for organic photovoltaic devices
246	<u>Haralds Āboliņš</u> ( <i>Cavendish Laboratory, University of Cambridge, JJ Thomson Avenue, Cambridge CB3 0HE, United Kingdom</i> ), Felix Deschler Understanding and Tuning the Energetic Landscape for Mixed Dimensionality Perovskites
249	<u>Yan Hao</u> ( <i>Royal Institute of Technology (KTH)</i> ), Lars Kloo, Gerrit Boschloo, Wenxing Yang Exploring Tris(4-alkoxyphenyl)amines Intermediates in Cobalt Complex based Tandem Electrolytes for High Voltage and High Performance Dye-sensitized Solar Cells
250	<u>Amalraj Peter Amalathas</u> ( <i>Centre for Advanced Photovoltaics, Faculty of Electrical Engineering, Czech Technical University in Prague, Technická 2, 166 27 Prague, Czech Republic</i> ), Lucie Abelová, Brianna Conrad, Branislav Dzurňák, Martin Ledinský, Jakub Holovský Interface charge dynamics in heterogeneous CH <sub>3</sub> NH <sub>3</sub> PbI <sub>3</sub> perovskite structures studied by Kelvin Probe and Photoluminescence techniques
251	<u>Lukas Wagner</u> ( <i>Fraunhofer-Institut für Solare Energiesysteme ISE, Heidenhofstraße 2, D-79110 Freiburg, Germany</i> ), Gayathri Mathiazhagan, Simone Mastroianni, Andreas Hinsch Certified Printed Perovskite Photovoltaics by a Molten Salt Approach
252	<u>Thi Tuyen Ngo</u> ( <i>Institute of Advanced Materials (INAM), University Jaume I, Avenida de Vicent Sos Baynat, s/n, 12006 Castelló de la Plana, Castellón (Spain)</i> ), Ramon Tena-Zaera, Iván Mora-Seró ZnO Spray-Pyrolyzed as Electron Selective Contact for Long Term Stable Planar CH <sub>3</sub> NH <sub>3</sub> PbI <sub>3</sub> Perovskite Solar Cells
253	<u>Carlos Echeverría-Arondo</u> ( <i>Institute of Advanced Materials (INAM), Universitat Jaume I</i> ) Perovskite Solar Cells: Photovoltage Formation Unveiled from First Principles
254	<u>Ramón Arcas</u> ( <i>Institute of Advanced Materials (INAM), University Jaume I, Avenida de Vicent Sos Baynat, s/n, 12006 Castelló de la Plana, Castellón (Spain)</i> ), Elena Mas-Marzá, Francisco Fabregat-Santiago Moisture effect on the hysteresis of perovskite solar cells
255	<u>Ehsan Hassanabadi</u> ( <i>Institute of Advanced Materials (INAM), University Jaume I, Avenida de Vicent Sos Baynat, s/n, 12006 Castelló de la Plana, Castellón (Spain)</i> ), Isaac Suárez, Alberto Maulu, Niccolò Carlino, Cecilia Ada Maestri, Masoud Latifi, Paolo Bettotti, Iván Mora-Seró, Juan P. Martínez-Pastor Integration of Optical Amplifier and Photodetector on flexible Nanocellulose Substrate

- 256 Gonzalo García-Espejo (*Departamento de Química Física y Termodinámica Aplicada, Instituto Universitario de Investigación en Química Fina y Nanoquímica IUQFN, Universidad de Córdoba, Campus de Rabanales, Edificio Marie Curie, Córdoba, Spain*), Daily Rodríguez-Padrón, Marta Pérez-Morales, Rafael Luque, Gustavo de Miguel, Luis Camacho  
One-dimensional (1D) hybrid perovskites incorporating polycyclic aromatic cations obtained via mechanosynthesis
- 257 Jegadesan Subbiah (*School of Chemistry, Bio21 Institute, University of Melbourne, , Parkville, VIC 3010, Australia.*), Paul Geraghty, David Jones  
Highly efficient small molecule organic solar cells using halogen-free solvent
- 258 Robin Willems (*Molecular Materials and Nanosystems, Institute for Complex Molecular Systems, Eindhoven University of Technology, P. O. Box 513, 5600 MB Eindhoven, The Netherlands*), Christ Weijtens, Xander de Vries, Reinder Coehoorn, René Janssen  
Accurate determination of HOMO energies in conjugated diketopyrrolopyrrole-based polymers for predicting the open-circuit voltage of organic photovoltaic devices
- 259 Christian Ahläng (*Physics, Faculty of Science and Engineering and Center for Functional Materials, Åbo Akademi University*), Oskar Sandberg, Ronald Österbacka  
2D drift-diffusion study of interfacial effects in thin-film solar cells
- 260 Ludmila Cojocaru (*Freiburg Center for Interactive Materials and Bioinspired Technologies (FIT), Laboratory for Photovoltaic Energy Conversion, Department of Sustainable Systems Engineering (INATECH), University of Freiburg, Georges-Köhler-Allee 105, 79110 Freiburg, Germany*), Karl Wienands, Saeid Rafizadeh, Jan Christoph Goldschmidt, Stefan W. Glunz  
High crystalline CH<sub>3</sub>NH<sub>3</sub>PbI<sub>3</sub> structure prepared by evaporation method for efficient perovskite solar cells
- 261 Namrata Pant (*Interdisciplinary Graduate School of Medicine and Engineering, University of Yamanashi*), James Ryan, Masatoshi Yanagida, Yasuhiro Shirai, Kenjiro Miyano  
Influence of Hole Transport Layers : Nickel Oxide and PEDOT:PSS in Lead Iodide perovskite Solar Cells
- 262 Sandheep Ravishankar (*Institute of Advanced Materials (INAM), University Jaume I, Avenida de Vicent Sos Baynat, s/n, 12006 Castelló de la Plana, Castellón (Spain)*), Pablo P. Boix, Clara Aranda-Alonso, Juan A. Anta, Germà Garcia-Belmonte, Juan Bisquert  
Kinetic Influences on the Measured External Quantum Efficiency of Perovskite Solar Cells
- 263 Bruno Clasen Hames (*Institute of Advanced Materials (INAM), Universitat Jaume I*), Jesús Rodríguez-Romero, Eva M. Barea, Iván Mora-Sero  
Anilinium cation for 2D/3D perovskite with enhanced properties.
- 264 Wei Zhang (*Applied Physical Chemistry, Dept. of Chemistry, Royal Inst. of Technology (KTH)*), Yong Hua, Lars Kloo  
Metal Complexes as Hole Transport Materials in Perovskite Solar Cells
- 266 Marta Vallés-Pelarda (*Institute of Advanced Materials (INAM), University Jaume I, Avenida de Vicent Sos Baynat, s/n, 12006 Castelló de la Plana, Castellón (Spain)*), Sebastian F. Völker, Jorge Pascual, Silvia Collavini, Fernando Ruiperez, Elisabetta Zuccatti, Luis E. Hueso, Ramón Tena-Zaera, Iván Mora-Seró, Juan Luis Delgado  
Fullerene-Based Materials as Hole-Transporting/Electron Blocking Layers. Applications in Perovskite Solar Cells
- 267 Junke Wang (*Molecular Materials and Nanosystems, Institute for Complex Molecular Systems, Eindhoven University of Technology, P. O. Box 513, 5600 MB Eindhoven, The Netherlands*), Martijn Wienk, René Janssen  
Surface modification of tin oxide transport layer with fullerenes for efficient perovskite solar cells
- 268 Miguel García-Tecedor (*Institute of Advanced Materials (INAM), Universitat Jaume I*), Sacha Corby, Sven Tengeler, Drialys Cárdenas, Roser Fernández, Laia Francas, Bernhard Kaiser, Wolfram Jaegermann, James R. Durrant, Juan Bisquert, Sixto Giménez  
Mechanistic insights on NiOx electrocatalysts for water splitting
- 269 Pieter Leenaers (*Molecular Materials and Nanosystems, Institute for Complex Molecular Systems, Eindhoven University of Technology, P. O. Box 513, 5600 MB Eindhoven, The Netherlands*), Martijn Wienk, René Janssen  
Influence of regioregularity on the photovoltaic performance of asymmetric DPP polymers
- 270 Haijun Bin (*Molecular Materials and Nanosystems, Institute for Complex Molecular Systems, Eindhoven University of Technology, P. O. Box 513, 5600 MB Eindhoven, The Netherlands*), Martijn M. Wienk, Rene A. J. Janssen  
Effect of Alkylsilyl Side-Chain Structure on Photovoltaic Properties of Medium Bandgap Conjugated Polymer Donor

- 271 Manuel Garcia-Rosell, Agustín Bou (*Institute of Advanced Materials (INAM), Universitat Jaume I*), Juan A Jiménez-Tejada, Juan Bisquert, Pilar Lopez-Varo  
Analysis of the Influence of Selective Contact Heterojunctions on the Performance of Perovskite Solar Cells
- 272 Laurent Le Brizoual (*Institute of Electronics and Telecommunications of Rennes (IETR), UMR CNRS 6164, University of Rennes 1, 35042 Rennes, France*), Régis Rogel, Noelia Devesa Canicoba  
Comparison of perovskite solar cells processed in different atmospheres
- 273 Benjamin Feleki (*Molecular Materials and Nanosystems, Department of Applied Physics, Eindhoven University of Technology, P.O. Box 513, 5600 MB Eindhoven, The Netherlands*), Ricardo Bouwer, Sanjana Chandrashekar, Martijn M. Wienk, René A.J. Janssen  
Perovskite solar cells on steel substrates: Optimization of a dielectric/metal/dielectric transparent top electrode
- 274 Golnaz Sadoughi (*Merck Performance Materials Ltd.*), Luca Lucera, Graham Morse  
Organic Photovoltaics: state of the art at Merck
- 275 Jesús Rodríguez Romero (*Institute of Advanced Materials (INAM), Universitat Jaume I*), Bruno Clasen-Hames, Iván Mora-Seró, Eva María Barea  
Anilinium iodide as bulky cation in 2D/3D perovskite
- 276 Cordula Wessendorf (*Zentrum für Sonnenenergie- und Wasserstoff-Forschung (ZSW) Baden-Württemberg, Meitnerstr. 1, 70563 Stuttgart, Germany*), Jonas Hanisch, Erik Ahlswede  
Optimization of solution-processed Bi-based lead-free solar cells
- 277 Farzaneh Jahanbakhshi (*Swiss Federal Institute of Technology, EPFL, ISIC, LCBC, CH-1015, Lausanne, Switzerland*), Marko Mladenovic, Ursula Rothlisberger  
Investigating the Interfacial Effects on the Performance of Perovskite Solar Cells
- 278 Melissa Van Landeghem (*Department of Physics, University of Antwerp, 2610 Wilrijk, BE*), Julija Kudrjasova, Wouter Maes, Etienne Goovaerts  
Understanding low efficiencies: triplet-mediated recombination in fullerene-free MDMO-PPV:diCN-DTTzTz solar cells
- 279 Drialys Cardenas-Morcoso (*Institute of Advanced Materials (INAM), Universitat Jaume I*), Maged N. Shaddad, Prabhakarn Arunachalam, Miguel García-Tecedor, Mohamed A. Ghanem, Juan Bisquert, Abdullah Al-Mayouf, Sixto Gimenez  
Enhancing the Optical Absorbance and Interfacial Properties of BiVO<sub>4</sub> with Ag<sub>3</sub>PO<sub>4</sub> Nanoparticles for Efficient Water Splitting
- 280 Ivan Sudakov (*Department of Physics, University of Antwerpen, B-2610 Wilrijk, Belgium*), Biniam Zerai Tedlla, Feng Zhu, Matthijs Cox, Bert Koopmans, Victoria L. Whittle, J.A. Gareth Williams, Etienne Goovaerts  
Parasitic interactions in upconversion via triplet-triplet fusion in triplet-sensitized super-yellow PPV
- 281 Ruurd Heuvel (*Molecular Materials and Nanosystems, Institute for Complex Molecular Systems, Eindhoven University of Technology, P. O. Box 513, 5600 MB Eindhoven, The Netherlands*), Martijn Wienk, René Janssen  
Aggregation behaviour and solar cell performance of a carboxylic ester substituted polythiophene with linear side chains
- 282 Gayathri Mathiazhagan (*Fraunhofer Institute for Solar Energy Systems (ISE), Heidenhofstraße 2, 79110 Freiburg, Germany*), Kübra Yasaroglu, Shankar Bogati, Lukas Wagner, Simone Mastroianni, Andreas Hensch  
Ultrathin space layer for graphite based perovskite solar cells
- 283 Gaël Heintges (*Molecular Materials and Nanosystems & Institute for Complex Molecular Systems, Eindhoven University of Technology*), Koen Hendriks, Mengmeng Li, Fallon Colberts, René Janssen  
The effects of siloxane bearing side-chains on the photovoltaic performance of conjugated polymers
- 284 Jonas Hanisch (*Zentrum für Sonnenenergie- und Wasserstoff-Forschung Baden-Württemberg (ZSW), Meitnerstrasse 1, 70563 Stuttgart, Germany*), Tina Wahl, Moritz Schultes, Erik Ahlswede  
Detailed analysis of various types of perovskite solar cells with ToF-SIMS using different sputter sources
- 285 Ece Aktas (*Institute of Chemical Research of Catalonia—the Barcelona Institute of Science and Technology (ICIQ-BIST), Avda. Països Catalans 16, E-43007 Tarragona, Spain.*), Jesús Jiménez-López, Cristina Rodríguez-Seco, Rajesh Pudi, Emilio Palomares  
The Effect of Passivation Layer in Perovskite Solar Cells by 3-Fluoropyridine-Substituted Truxene Derivative Based Small Molecule

- 286 Lingjin Wang (*Organic Chemistry, Department of Chemistry, KTH Royal Institute of Technology, SE-10044 Stockholm, Sweden*), Jinbao Zhang, Bo Xu, Licheng Sun  
Synthesis of spiro[dibenzo[c,h]xanthene-7,9'-fluorene]-based dopant-free hole transport materials for perovskite solar cells
- 287 Malgorzata Czichy (*Faculty of Chemistry, Silesian University of Technology, M. Strzody 9, 44-100 Gliwice, Poland*), Pawel Zassowski, Aleksandra Wolinska-Grabczyk, Mieczyslaw Lapkowski  
Phthalimides and naphthalimides fused with diamionaphthalene as novel blocks building conjugated polymers for optoelectronics applications
- 288 Hye min Oh (*Department of Energy Science, Sungkyunkwan University, Suwon 16419, Republic of Korea*), Hobeom Jeon, Ngoc Thanh Duong, Chulho Park, Dae Young Park, Mun Seok Jeong  
2-D perovskite material based metal-insulator-semiconductor light-emitting devices
- 289 Yong Cui, Jianhui Hou (*Institute of Chemistry, Chinese Academy of Sciences*)  
Organic Solar Cells with an Efficiency Approaching 15%
- 290 Su Htiike Aung (*Laboratory of Photomolecular Science, Department of Chemical Science and Engineering, Swiss Federal Institute of Technology in Lausanne, EPFL--ISIC-FSB-LSPM, Station 6, CH-1015 Lausanne, Switzerland*), Kazuteru Nonomura, Than Zaw Oo, Shaik M. Zakeeruddin, Nick Vlachopoulos, Anders Hagfeldt, Michael Grätzel  
Poly(3,4-ethylenedioxyppyrrrole), PEDOP Counter Electrode For Copper Complex Redox Shuttles Based Dye Sensitized Solar Cells
- 291 Ashish Kulkarni (*Graduate School of Engineering, Toin University of Yokohama, 1614, Kuroganecho, Aoba, Yokohama 225-8503, Japan.*), Ajay Jena, Masashi Ikegami, Tsutomu Miyasaka  
Solvent Engineering Technique to Enhance the Efficiency and Stability of Silver-Bismuth Halide Materials for Lead- Free Perovskite Solar Cells
- 292 Antonio Alfano (*Center for Nano Science and Technology @Polimi, Istituto Italiano di Tecnologia, via Giovanni Pascoli 70/3, 20133, Milan, Italy.*), Alessandro Mezzetti, Francesco Fumagalli, Fabio Di Fonzo  
In Search of Stable and Efficient Hole Selective Contacts for Hybrid Organic Photoelectrochemical Water Splitting
- 293 Kunal Datta (*Molecular Materials and Nanosystems, Eindhoven University of Technology, Netherlands*), Martijn M. Wienk, René A. J. Janssen  
Bandgap tuning of mixed-cation lead halide perovskites for tandem applications
- 294 Didac Pitarch Tena (*Institute of Advanced Materials (INAM), Universitat Jaume I*)  
Band-Offset Effect on PbS Quantum Dots in Perovskite Matrix
- 295 Alba Mingorance (*Catalan Institute of Nanoscience and Nanotechnology (ICN2), CSIC and The Barcelona Institute of Science and Technology, Campus UAB, Bellaterra, 08193 Barcelona, Spain*), Francesca di Rossi, Haibing Xie, Jose Carlos Pereyra, Marc Balsells, Anna Morales, David Tanenbaum, Trsytan Watson, Jordi Fraxedas, Rodolfo Lopez, Anders Hagfeldt, Monica Lira-Cantu  
Printable Carbon-based Perovskite Solar Cells Employing functionalized Oxide Interlayers
- 296 Somayeh Moghadamzadeh (*Light Technology Institute, Karlsruhe Institute of Technology, Engesserstr. 13, 76131 Karlsruhe, Germany*), Ihtez M. Hossain, Diana Rueda-Delgado, Bryce S. Richards, Uli Lemmer, Ulrich W. Paetzold  
Enhancement of Stabilized Power Conversion Efficiency in Triple Cation Perovskite Solar Cells
- 298 Tim van de Goor (*University of Cambridge, UK*), Felix Deschler, Sián Dutton  
Towards understanding light induced phase transitions in mixed halide hybrid perovskites
- 299 Sean Bourelle (*Optoelectronics Group, University of Cambridge*), Ravichandran Shivanna, Felix Deschler  
Towards Circularly Polarised Two Dimensional Hybrid Perovskite LEDs
- 301 Haibing Xie (*Catalan Institute of Nanoscience and Nanotechnology (ICN2), CSIC and the Barcelona Institute of Science and Technology (BIST). Building ICN2, Campus UAB E-08193, Bellaterra, Barcelona, Spain.*), Zaiwei Wang, Kubicki Dominik Józef, Agarwalla Anand, Hui-Seon Kim, Prochowicz Daniel, Alba Mingorance, Neus Domingo, Shaik Mohammed Zakeeruddin, Michael Grätzel, Anders Hagfeldt, Monica Lira-Cantu  
Interfacial and doping engineering for stable perovskite solar cells

- 302 Pascal Kaienburg (*IEK5-Photovoltaics, Forschungszentrum Jülich, 52425 Jülich, Germany*), Shuo Wang, Benjamin Klingebiel, Thomas Kirchartz  
Prospects of Spin-coated Planar Antimony Sulfide Solar Cells
- 304 Pavlo Perkhun (*Aix-Marseille University, Centre Interdisciplinaire de Nanosciences de Marseille CINaM, UMR CNRS 7325, Marseille, France*), Riva Karsifi, Birger Zimmermann, Uli Würfel, Christine Videlot-Ackermann, Olivier Margeat, Jean-Jacques Simon, Jörg Ackermann  
Impact of device structure and interfacial layers on the performance of Polymer Solar Cells using ITIC/derivatives as non-Fullerene Acceptor
- 307 Elena Barulina (*Aix-Marseille University, Centre Interdisciplinaire de Nanosciences de Marseille CINaM, UMR CNRS 7325, Marseille, France*), Sadok Ben Dkhil, Pavlo Perkhun, Jean-Jacques Simon, Olivier Margeat, Jörg Ackermann, Christine Videlot-Ackermann  
Investigation of stability of highly efficient polymer solar cells as a function of device structure and interfacial layers
- 308 Sarune Daskeviciute (*Department of Organic Chemistry, Kaunas University of Technology*), Nobuya Sakai, Marius Franckevicius, Maryte Daskeviciene, Artiom Magomedov, Vygintas Jankauskas, Henry Snaith, Vytautas Getautis  
Amorphous, Fluorene-Based Hole Transporting Materials for Efficient and Stable Perovskite Solar Cells
- 309 Ruo Xi Yang (*Department of Chemistry, University of Bath*), Jonathan M. Skelton, Estelina Lora da Silva, Jarvist M. Frost, Aron Walsh  
Spontaneous octahedral tilting in cubic inorganic cesium halide perovskites
- 310 Sergio Castro-Hermosa (*CHOSE (Centre for Hybrid and Organic Solar Energy), Department of Electronic Engineering, University of Rome Tor Vergata, Via del Politecnico 1, 00133 Rome, Italy.*), Janardan Dagar, Andrea Marsella, Giulia Lucarelli, Thomas M. Brown  
Perovskite Solar Cells on Paper Substrates
- 311 Namyoung Ahn (*Global Frontier Center for Multiscale Energy Systems*), Il Jeon, Jungjin Yoon, Esko Kauppinen, Yutaka Matsuo, Shigeo Maruyama, Mansoo Choi  
Carbon-sandwiched perovskite solar cells as the solutions of cost and stability
- 314 Silver-Hamill Turren-Cruz (*École Polytechnique Fédérale de Lausanne, Station 6, CH-1015-Lausanne, Switzerland*), Michael Saliba, Matthew T. Mayer, Hector Juárez-Santiesteban, Xavier Mathew, Lea Nienhaus, Wolfgang Tress, Mounqi G. Bawendi, Michael Grätzel, Antonio Abate, Anders Hagfeldt, Juan-Pablo Correa-Baena  
Enhanced charge carrier mobility and lifetime suppress hysteresis and improve efficiency in planar perovskite solar cells

## Symposia &amp; program

[Plenary sessions](#)
[Exhibition](#)
[E-MRS tv](#)
[Satellite events](#)
[Practical Information](#)

## 2019 Spring Meeting

## MATERIALS FOR ENERGY

**G**

Halide perovskites: low dimensions for devices

INFORMATION

PROGRAM

[May 27, 2019](#) [May 28, 2019](#) **[May 29, 2019](#)** [May 30, 2019](#) [May 31, 2019](#)

START AT	SUBJECT	View All	NUM.
----------	---------	----------	------

[Lead free halide perovskites](#) : Paulina PLOCHOCKA

09:00	Computational design of novel double perovskites	⌵	G.6.1
-------	--	---	-------

09:30	Novel low-dimensional tin and antimony halide compounds: structures, properties and perspective applications	⌵	G.6.2
-------	--	---	-------

09:45	Lead-free materials for solar cell applications	⌵	G.6.3
-------	---	---	-------

Authors : Marko Mladenovic Ursula Roethlisberger  
 Affiliations : École polytechnique fédérale de Lausanne Laboratory of Computational Chemistry and Biochemistry

Resume : Halide perovskite have attracted enormous interest during the last decade due to their outstanding electronic properties. However, there are still unsolved issues that keep halide perovskites out of large-scale market: their instability and lead toxicity. To tackle the second issue, we have investigated halide perovskites based on Ge and Sn and silver bismuth iodides. We identified few lead-free halide perovskite compounds that can replace Pb-based ones and we discuss their stability with respect to decomposition and oxidation. We have additionally found that silver bismuth iodides, despite having band gaps suitable for solar cell application, have few intrinsic drawbacks which limit their solar cell efficiency.

 10:00 *COFFEE break*
[Joint session with symposium B: Strategies for More Stable Perovskite Solar Cells](#) : Maksym KOVALENKO

10:30	Tailoring phase purity, crystallinity and orientation in 2D perovskites for high-efficiency optoelectronic devices	⌵	G.7.1
-------	--	---	-------

11:00	Defect Physics and (In)Stability in Metal-halide Perovskite Semiconductors	⌵	G.7.2
-------	--	---	-------

11:30	From Multifunctional Molecular Modulation to Layered Two-Dimensional Architectures for Stable Hybrid Perovskite Solar Cells	⌵	G.7.4
-------	---	---	-------

11:45	Ultra-high open circuit voltage beyond the 90% Shockley-Queisser limit in high efficiency wide bandgap perovskite solar cells	⌵	G.7.5
-------	---	---	-------

 12:30 *LUNCH*
[Extended and localized states: excitons, polarons,...](#) : Harald HILLEBRECHT

14:00	Polaron signatures in 2D layered hybrid perovskites from spectroscopy modeling	⌵	G.8.1
-------	--	---	-------

14:30	Optical properties and exciton recombination in Metal Halide Perovskites	⌵	G.8.2
-------	--	---	-------

14:45	Observation of an important exciton dissociation in confined multi-layered Ruddlesden-Popper Perovskites	⌵	G.8.3
-------	--	---	-------

15:00	Optical spectroscopy od 2D perovskites in high magnetic fields	⌵	G.8.4
-------	--	---	-------

15:15	Light emission form stoichiometrically tuned quasi two-dimensional perovskites	⌵	G.8.5
-------	--	---	-------

 15:30 *COFFEE break*
[Growth and Upscaling](#) : Aditya D. MOHITE

16:00	Photovoltaic lead halide perovskite nanowires: quest for epitaxial growth condition?	⌵	G.9.1
-------	--	---	-------

16:30	Perovskite module characterization using dark lock-in thermography and luminescence imaging	⌵	G.9.2
-------	---	---	-------

16:45	Continuous mass production of green-emitting Cs4PbBr6 perovskite luminescence materials for display application	⌵	G.9.3
-------	---	---	-------

17:00	Ultra-lightweight, Flexible and Semitransparent Colloidal Quantum Dot Solar Cells	⌵	G.9.4
-------	---	---	-------

 19:00 *Graduate Student Award ceremony followed by the social event*

## Symposium organizers

**Claudine KATAN**  
 ISCR - Institut des Sciences Chimiques  
 Campus de Beaulieu, Bât. 10B, Case 1009, F-35042 Rennes, France  
 Phone : +33682580335  
 Mail : [claudine.katan@univ-rennes1.fr](mailto:claudine.katan@univ-rennes1.fr)

**Constantinos C. STOUMPOS**  
 University of Crete  
 Department of Materials Science and Technology, Heraklion, Crete, Greece  
 Mail : [cstoumpos@materials.uoc.gr](mailto:cstoumpos@materials.uoc.gr)

**Samuel STRANKS**  
 University of Cambridge  
 JJ Thomson Avenue, Cambridge CB3 0HE, UK  
 Phone : +44 1223 337288  
 Mail : [sds65@cam.ac.uk](mailto:sds65@cam.ac.uk)

print 4

Share 3

[Home](#)
[Contact us](#)
[Legal notices](#)
[Awards](#)
[Publications](#)
[News & Events](#)
[Membership](#)
[Become a member](#)
[Contact us](#)

+33.3 88 10 63 72  
 23 Rue du Loess  
 BP 20 - 67037  
 Strasbourg Cedex 02  
 France  
[emrs@european-mrs.com](mailto:emrs@european-mrs.com)

[Follow us](#)
[Newsletter](#)
 [Subscribe](#)



## Symposia &amp; program

[Plenary sessions](#)
[Exhibition](#)
[E-MRS tv](#)
[Satellite events](#)
[Practical Information](#)

## 2019 Spring Meeting

## MATERIALS FOR ENERGY

Halide perovskites: low dimensions for devices

## INFORMATION

## PROGRAM

[May 27, 2019](#) [May 28, 2019](#) [May 29, 2019](#) [May 30, 2019](#) [May 31, 2019](#)

START AT	SUBJECT	View All	NUM.
<a href="#">Toward logic design with perovskites</a> : Stefaan DE WOLF			
09:00	Bismuth-doped 2D Cesium Lead Iodide Perovskite with Enhanced Air-Stability for Resistive Switching Memory and Artificial Synapse	⌵	G.13.1
09:15	High-Performance Cross-Point Resistive Memory Devices Based on Solution-Processed Organo-Metal Halide Perovskite	⌵	G.13.2
09:30	2D Hybrid Organic-Perovskite Blends for Resistive Switching Memory Devices	⌵	G.13.3
09:45	Photolithographically patterned solution processed perovskite transistor towards circuit application	⌵	G.13.4
10:00	<i>COFFEE break</i>		
<a href="#">Versatility of 2D Halide Perovskites</a> : Jacky EVEN			
10:30	2D Halide Perovskites: Unrivaled Versatility for Semiconductor Design and Fabrication	⌵	G.14.1
11:00	Control of Quantum Well Orientation and Distribution in Quasi-2D Perovskite Films	⌵	G.14.2
11:15	Crystallization of Reduced Dimensional Perovskites: An in situ Viewpoint	⌵	G.14.3
11:30	Low-dimensional Hybrid Perovskites Containing an Organic Cation with an Extended Conjugated System	⌵	G.14.4
11:45	"The role of spacer molecules in designing 2D Ruddlesden-Popper perovskites"  Authors : F.Jahanbakhshi, M.Mladenovic, N.Ashari Astani and U.Roethlisberger Affiliations : Laboratory of Computational Chemistry and Biochemistry, Ecole polytechnique fédérale de Lausanne (EPFL) Laboratory of Computational Chemistry and Biochemistry, Ecole polytechnique fédérale de Lausanne (EPFL) Physics Department, Sharif University of Technology Laboratory of Computational Chemistry and Biochemistry, Ecole polytechnique fédérale de Lausanne (EPFL)  Resume : "The role of spacer molecules in designing 2D Ruddlesden-Popper perovskites" F.Jahanbakhshi, M.Mladenovic, N.AshariAstani and U.Roethlisberger Ruddlesden-Popper (RP) 2D perovskites have the generic chemical formula $(RNH_3)_2MA_n-1MnX_{3n+1}$ where $RNH_3$ is an organic ammonium ion that acts as spacer between the 3D perovskite layers and methyl ammonium (MA) mostly serves as a monovalent cation, with M being a bivalent cation (e.g. Pb, Sn, ...), and X representing a halogen. Basically, any aliphatic ammonium salt with a larger organic part can be used as spacer, however, butyl ammonium (BA), phenethylammonium (PEA), hexylammonium (Hex), 5-ammonium valeric acid (5-AVA), anilinium (Anyl), and benzyl ammonium have so far been incorporated. Despite the general agreement on the positive effect of the spacers on either the efficiency or the stability, it is not yet clear, whether the overall success is due to the formation of RP phases regardless of the type of spacer, or the spacer chemical composition also matters in cross-linking and determining RP phase properties. We have performed a comparative study to characterise structural and electronic properties of 2D RP phases with 5-AVA spacer and to compare them to analogous structures of other ligands such as BA. We have found that aliphatic spacers affect electronic properties of the 2D perovskites by distortions imposed on the perovskite frame, while the chemical composition of such spacer molecules is not as important as their geometrical arrangement in the isolating layer.	⌶	G.14.5
12:00	<i>CLOSING REMARKS AND AWARDS CEREMONY</i>		

## Symposium organizers

**Claudine KATAN**

 ISCR - Institut des Sciences Chimiques  
 Campus de Beaulieu, Bât. 10B,  
 Case 1009, F-35042 Rennes,  
 France

 Phone : +33682580335  
 Mail : [claudine.katan@univ-rennes1.fr](mailto:claudine.katan@univ-rennes1.fr)
**Constantinos C. STOUMPOS**

 University of Crete  
 Department of Materials Science  
 and Technology, Heraklion, Crete,  
 Greece

 Mail :  
[cstoumpos@materials.uoc.gr](mailto:cstoumpos@materials.uoc.gr)
**Samuel STRANKS**

 University of Cambridge  
 JJ Thomson Avenue, Cambridge  
 CB3 0HE, UK

 Phone : +44 1223 337288  
 Mail : [sds65@cam.ac.uk](mailto:sds65@cam.ac.uk)

print 4

Share 3

[Home](#)
[Contact us](#)
[Legal notices](#)
[Awards](#)
[Publications](#)
[News & Events](#)
[Membership](#)
[Become a member](#)
[Contact us](#)

 +33 3 88 10 63 72  
 23 Rue du Loess  
 BP 20 - 67037  
 Strasbourg Cedex 02  
 France  
[emrs@european-mrs.com](mailto:emrs@european-mrs.com)
[Follow us](#)

[Newsletter](#)
[Subscribe](#)

## Atomistic origins of the preferential stabilization of perovskite over non-perovskite phases of mixed cation lead halide perovskites

Ariadni Boziki<sup>a</sup>, Simone Meloni<sup>a,§</sup>, Marko Mladenović<sup>a</sup> and Ursula Rothlisberger<sup>a</sup>

<sup>a</sup> *Laboratory of Computational Chemistry and Biochemistry, Institute of Chemical Sciences and Engineering, École Polytechnique Fédérale de Lausanne, § Present address: Dipartimento di Scienze Chimiche e Farmaceutiche (DipSCF), Università degli Studi di Ferrara – Unife*  
ursula.roethlisberger@epfl.ch

Mixed cation lead halide perovskites have attracted wide attention due to the possibility of preferentially stabilizing the perovskite phase with respect to photovoltaically less suitable competing phases.[1-2] In this work, through a theoretical analysis, we study the phase stability of binary  $\text{HC}(\text{NH}_2)_2^+$  ( $\text{FA}^+$ )-rich[1] and  $\text{Cs}^+$ -rich  $\text{FA}/\text{Cs}$  and  $\text{CH}_6\text{N}_3^+$  ( $\text{GUA}$ )/ $\text{FA}$  mixtures as well as ternary  $\text{Cs}/\text{GUA}/\text{FA}$  mixtures. Our study yields a series of design principles for the fabrication of stable lead halide perovskites with mixtures of monovalent cations.

Calculations of  $\text{FA}^+$ -rich  $\text{Cs}_x\text{FA}_{(1-x)}\text{PbI}_3$  ( $0 < x < 0.5$ ),[1] suggest that if the structural characteristics of the non-perovskite  $\delta$  phases of the pure compounds differ significantly, mixing is energetically favoring the perovskite over the non-perovskite phase. However, despite the significant differences in the  $\delta$  phases of  $\text{FAPbI}_3$  and  $\text{CsPbI}_3$ , in  $\text{Cs}^+$ -rich  $\text{FA}_x\text{Cs}_{(1-x)}\text{PbI}_3$  ( $0 < x < 0.5$ ) mixtures, stable perovskite phases cannot be formed. This contrasting finding leads us to consider not only the structural differences between the non-perovskite phases of the pure compounds but also the volume difference between their perovskite phases. Indeed, mixing in the perovskite phase is getting unfavorable upon incorporation of a large cation into a relatively small lattice.

Although mixing of  $\text{FA}/\text{GUA}$  is possible, it is not sufficient to stabilize the perovskite phase at room temperature. Probing the possible stabilization in ternary  $\text{Cs}/\text{GUA}/\text{FA}$  mixtures, instead we conclude that stable mixtures that contain 17% of  $\text{Cs}^+$  and  $\text{GUA}$  up to 33% can be formed. This finding reveals a third design principle, according to which mixing monovalent cations that would be per se outside the stability range with other cations that can compensate the size, so that the average radii of the mixed cations lies within the suitable Goldschmidt tolerance range[3] can lead to the formation of ternary perovskite mixtures with enhanced stability.

Our investigations on the potential preferential stabilization of the perovskite phase upon mixing is complemented by band gap calculations of the mixtures that show that the stable perovskite phases of binary  $\text{FA}^+$ -rich  $\text{FA}/\text{Cs}$  and of the ternary  $\text{Cs}/\text{GUA}/\text{FA}$  mixtures can be potential candidates for single-junction solar cell applications. In addition, if the perovskite phase of  $\text{Cs}^+$ -rich  $\text{Cs}/\text{FA}$  mixtures could be kinetically trapped it would be a potential candidate for tandem solar cell applications. In such a way, our suggested design principles pave the way for the preparation of mixed cation lead halide perovskites with enhanced stability and optical properties.

### References

1. C. Yi, J. Luo, S. Meloni, A. Boziki, N. Ashari-Astani, C. Grätzel, S. M. Zakeeruddin, U. Rothlisberger and M. Grätzel, *Energy Environ. Sci.* **9** (2016), 656.
2. M. Saliba, T. Matsui, K. Domanski, J.-Y. Seo, A. Ummadisingu, S. M. Zakeeruddin, J.-P. Correa-Baena, W. R. Tress, A. Abate, A. Hagfeldt and Michael Grätzel, *Science* **354** (2016), 206.
3. V. M. Goldschmidt, *Sci. Nat.* **14** (1926), 477.

# Ruddlesden-Popper phases of 2D halide perovskites

Marko Mladenović<sup>a,b</sup>, Farzaneh Jahanbakhshi<sup>a</sup> and Ursula Röthlisberger<sup>a</sup>

<sup>a</sup>Laboratory of Computational Chemistry and Biochemistry, École Polytechnique Fédérale de Lausanne

<sup>b</sup>Scientific Computing Laboratory, Center for the Study of Complex Systems, Institute of Physics Belgrade, University of Belgrade

**Abstract.** Halide perovskites are promising candidates for solar cell applications due to their outstanding electronic and transport properties. However, their instability at finite temperature presents an unsolved issue that keeps them out of large-scale market. Addition of large organic spacers and reducing dimensionality of halide perovskites have been shown to have beneficial effects on their stability. In this work, we study electronic and structural properties of Ruddlesden-Popper phases 2D halide perovskites based on 5-ammonium valeric acid (AVA)<sup>1,2</sup>. In contrast to aromatic and aliphatic spacers without additional functional groups, the RP phases of AVA are characterized by the formation of a regular and stable H-bonding network between the carbonyl head groups of adjacent AVA molecules in opposite layers (Fig. 1), which may lead to an enhanced thermal stability. Additionally, we have developed a theoretical framework that can predict and correlate electronic and structural properties of any 2D halide perovskite system, which may serve as a guideline to design new compounds.

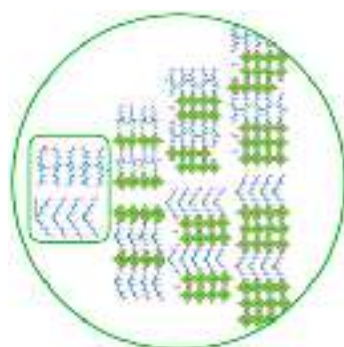


**FIGURE 1.** Structural model of Ruddlesden-Popper (RP) phases of  $\text{AVA}_2(\text{CH}_3\text{NH}_3)_{n-1}\text{Pb}_n\text{I}_{3n+1}$  for  $n = 1, 2$ , and  $3$ .

## REFERENCES

1. N. Ashari-Astani, F. Jahanbakhshi, M. Mladenović, A. Q. M. Alanazi, I. Ahmadabadi, M. R. Ejtehadi, I. Dar, M. Grätzel, and U. Röthlisberger, Ruddlesden-Popper phases of methylammonium-based 2D perovskites with 5-ammonium valeric acid  $\text{AVA}_2\text{MA}_{n-1}\text{Pb}_n\text{I}_{3n+1}$  with  $n = 1, 2$  and  $3$ , *Journal of Physical Chemistry Letters*. **10** (13), 3543-3549 (2019)
2. Anwar Q. Alanazi, Dominik J. Kubicki, Daniel Prochowicz, Essa A. Alharbi, Marine E. F. Bouduban, Farzaneh Jahanbakhshi, Marko Mladenović, Jovana V. Milić, Fabrizio Giordano, et al, Atomic-Level Microstructure of Efficient Formamidinium-Based Perovskite Solar Cells Stabilized by 5-Ammonium Valeric Acid Iodide Revealed by Multi-Nuclear and Two-Dimensional Solid-State NMR, *submitted*

# Citation overview

The citation overview has been downloaded as a comma separated file (.csv).

[Back to document results](#)

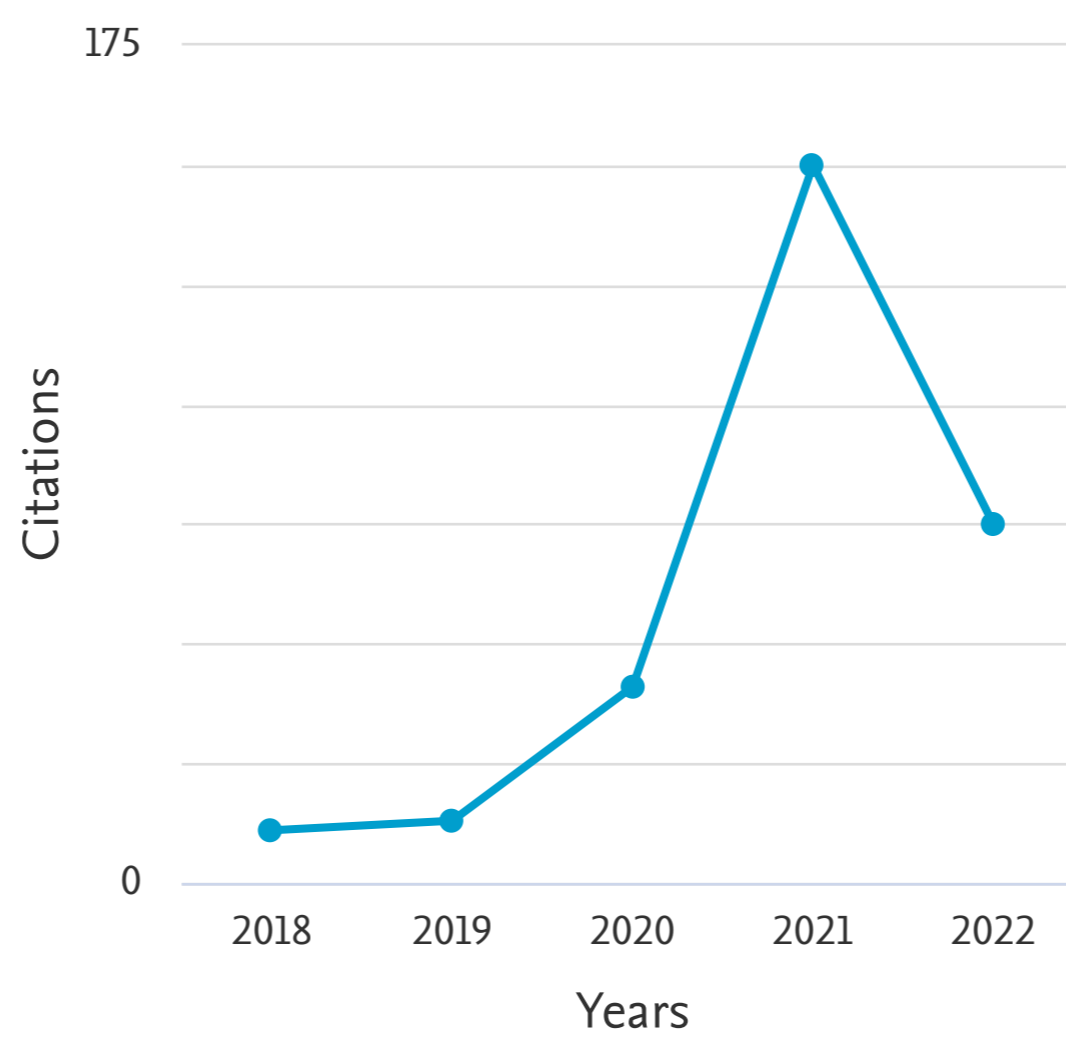
[Export](#) [Print](#)

This is an overview of citations for the documents you've selected.

Document *h*-index : 10 [View \*h\*-graph](#)

18 cited documents [+ Add to list](#)

Date range:  to   Exclude self citations of all authors  Exclude citations from books [Update](#)



Sort on: [Date \(newest\)](#)

Page [Remove](#)

Documents	Citations	<2018	2018	2019	2020	2021	2022	Subtotal	>2022	Total
<input type="checkbox"/> 1 Multimodal host–guest complexation for efficient and stable ...	2021					2	7	9		9
<input type="checkbox"/> 2 Naphthalenediimide/Formamidinium-Based Low-Dimensional Perov...	2021							0		0
<input type="checkbox"/> 3 Organic Spacers in 2D Perovskites: General Trends and Struct...	2021					3		3		3
<input type="checkbox"/> 4 Nanoscale Phase Segregation in Supramolecular $\pi$ -Templating f...	2021					14	8	22		22
<input type="checkbox"/> 5 Crown Ether Modulation Enables over 23% Efficient Formamidin...	2020					35	16	51		51
<input type="checkbox"/> 6 Why choosing the right partner is important: stabilization o...	2020					1		1		1
<input type="checkbox"/> 7 Unravelling the structural complexity and photophysical prop...	2020					5	1	6		6
<input type="checkbox"/> 8 Formamidinium-Based Dion-Jacobson Layered Hybrid Perovskites...	2020				1	20	6	27		27
<input type="checkbox"/> 9 Guanine-Stabilized Formamidinium Lead Iodide Perovskites	2020				9	17	12	38		38
<input type="checkbox"/> 10 Atomic-Level Microstructure of Efficient Formamidinium-Based...	2019				15	25	16	56		56
<input type="checkbox"/> 11 Ruddlesden-Popper Phases of Methylammonium-Based Two-Dimensi...	2019			1	9	14	3	27		27
<input type="checkbox"/> 12 Effects of thermal disorder on the electronic structure of h...	2018			4	3	3	2	12		12
<input type="checkbox"/> 13 Spontaneous Polarization Induced by Side Chains in Ordered P...	2016		1			2		3		3
<input type="checkbox"/> 14 Electronic States at the Interface between Crystalline and A...	2015	2	1	1		2		4		6
<input type="checkbox"/> 15 Charge Carrier Localization and Transport in Organic Semicon...	2015	17	5	4	2	4	3	18		35
<input type="checkbox"/> 16 Effects of thermal disorder on the electronic properties of ...	2014	8	3	2	1		1	7		15
<input type="checkbox"/> 17 Atomic and electronic structure of grain boundaries in cryst...	2013	1						0		1
<input type="checkbox"/> 18 Electronic states at low-angle grain boundaries in polycryst...	2013	12	1	1	1	3		6		18

Display:  results per page

[1](#)

[Top of page](#)

## About Scopus

- [What is Scopus](#)
- [Content coverage](#)
- [Scopus blog](#)
- [Scopus API](#)
- [Privacy matters](#)

## Language

- [日本語に切り替える](#)
- [切换到简体中文](#)
- [切换到繁體中文](#)
- [Русский язык](#)

## Customer Service

- [Help](#)
- [Tutorials](#)
- [Contact us](#)

< BACK TO SEARCH RESULTS

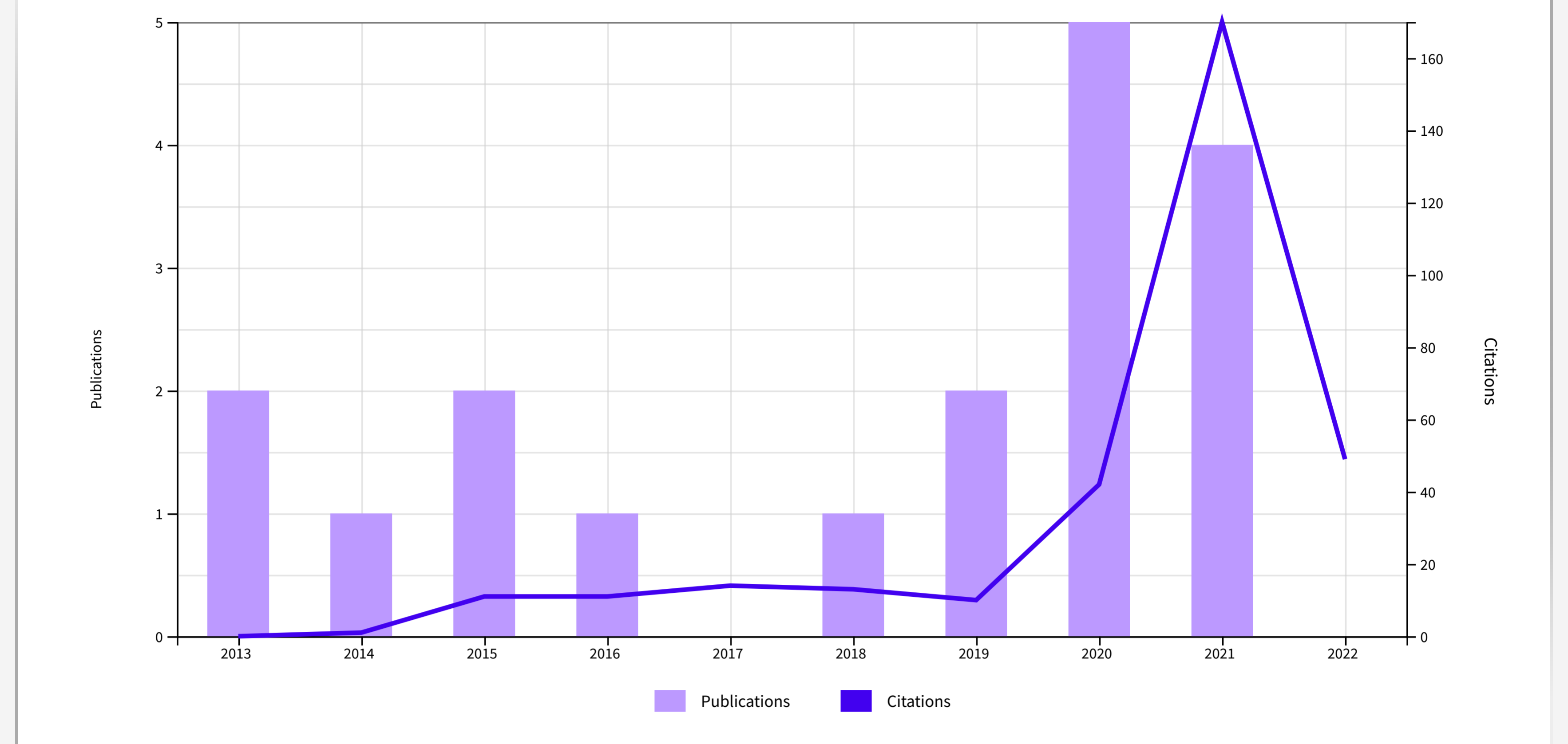
Citation Report  Analyze Results Create Alert

- Refined By:
- NOT Radulovic, NS et al. (2013)
  - NOT Mitrovic, T et al. (2014)
  - NOT Radulovic, NS et al. (2015)
  - NOT Todosijevic, R et al. (2016)
  - NOT Todosijevic, R et al. (2017)
  - NOT Stojanovic, NM et al. (2019)
  - NOT Djenic, A et al. (2016)
  - NOT Radulovic, NS et al. (2019)
  - NOT Radulovic, NS et al. (2014)
  - NOT Radulovic, NS et al. (2014)
  - NOT Radulovic, NS et al. (2012)
  - NOT Mladenovic, D et al. (2014)
  - NOT Radulovic, NS et al. (2013)
  - NOT Radulovic, NS et al. (2014)
  - NOT Mladenovic, M et al. (2020)
  - NOT Mladenovic, MZ and Radulovic, NS (2017)
  - NOT Dekic, BR et al. (2019)
  - NOT Gencic, MS et al. (2022)
  - NOT Andjelkovic, Z et al. (2014)
  - NOT Mladenovic, M et al. (2021)
  - NOT Banic, M et al. (2022)
  - NOT Radulovic, NS et al. (2017)
  - NOT Radulovic, NS et al. (2021)
  - NOT Radulovic, NS et al. (2020)
  - NOT Radulovic, NS et al. (2022)
  - NOT Mladenovic, M et al. (2017)
  - NOT Stojiljkovic, P et al. (2017)
  - NOT Mladenovic, M et al. (2019)
  - NOT Mladenovic, MZ and Radulovic, NS (2019)
  - NOT Radulovic, NS et al. (2020)
  - NOT Leinberger-Jabari, A et al. (2021)
  - NOT Stojanovic, NM et al. (2022)
  - NOT Milovanovic, J et al. (2021)
  - NOT Mladenovic, M et al. (2015)
  - NOT Mladenovic, D et al. (2015)
  - NOT Mladenovic, M et al. (2015)
  - NOT Jiang, L et al. (2018)
  - NOT Grcic, N et al. (2018)
- Clear all

Export Full Report

<b>Publications</b> <b>18</b> Total From 1900 to 2022	<b>Citing Articles</b> <b>259</b> Analyze Total <b>248</b> Analyze Without self-citations	<b>Times Cited</b> <b>321</b> Total <b>289</b> Without self-citations	<b>10</b> H-Index <b>17.83</b> Average per item
--	---	---	--

Times Cited and Publications Over Time DOWNLOAD



18 Publications	Sort by: Citations: highest first	Citations						
		Previous year		Next year			Average per year	Total
		2018	2019	2020	2021	2022		
<b>Total</b>		13	10	42	170	49	35.67	321
1 <a href="#">Atomic-Level Microstructure of Efficient Formamidinium-Based Perovskite Solar Cells Stabilized by 5-Ammonium Valeric Acid Iodide Revealed by Multinuclear and Two-Dimensional Solid-State NMR</a> <i>Alanazi, AQ; Kubicki, DJ; (...); Gratzel, M</i> Nov 6 2019   JOURNAL OF THE AMERICAN CHEMICAL SOCIETY 141 (44), pp.17659-17669		0	0	15	28	12	13.75	55
2 <a href="#">Crown Ether Modulation Enables over 23% Efficient Formamidinium-Based Perovskite Solar Cells</a> <i>Su, TS; Eickemeyer, FT; (...); Gratzel, M</i> Nov 25 2020   JOURNAL OF THE AMERICAN CHEMICAL SOCIETY 142 (47), pp.19980-19991		0	0	0	43	10	17.67	53
3 <a href="#">Guanine-Stabilized Formamidinium Lead Iodide Perovskites</a> <i>Hong, L; Milic, JV; (...); Gratzel, M</i> Mar 16 2020   Feb 2020 (Early Access)   ANGEWANDTE CHEMIE-INTERNATIONAL EDITION 59 (12), pp.4691-4697		0	0	9	19	7	11.67	35
4 <a href="#">Charge Carrier Localization and Transport in Organic Semiconductors: Insights from Atomistic Multiscale Simulations</a> <i>Mladenovic, M and Vukmirovic, N</i> Apr 1 2015   ADVANCED FUNCTIONAL MATERIALS 25 (13), pp.1915-1932		6	4	2	4	2	4.13	33
5 <a href="#">Formamidinium-Based Dion-Jacobson Layered Hybrid Perovskites: Structural Complexity and Optoelectronic Properties</a> <i>Gelvez-Rueda, MC; Ahlawat, P; (...); Gratzel, M</i> Sep 2020   Jul 2020 (Early Access)   ADVANCED FUNCTIONAL MATERIALS 30 (38)		0	0	1	22	7	10	30
6 <a href="#">Ruddlesden Popper Phases of Methylammonium-Based Two-Dimensional Perovskites with 5-Ammonium Valeric Acid AVA(2)MA(n-1)Pb(n)(3n+1) with n=1, 2, and 3</a> <i>Ashari-Astani, N; Jahanbakhshi, F; (...); Rothlisberger, U</i> Jul 4 2019   JOURNAL OF PHYSICAL CHEMISTRY LETTERS 10 (13), pp.3543-3549		0	0	10	13	2	6.25	25
7 <a href="#">Nanoscale Phase Segregation in Supramolecular pi-Templating for Hybrid Perovskite Photovoltaics from NMR Crystallography</a> <i>Hope, MA; Nakamura, T; (...); Emsley, L</i> Jan 27 2021   Jan 2021 (Early Access)   JOURNAL OF THE AMERICAN CHEMICAL SOCIETY 143 (3), pp.1529-1538		0	0	0	18	3	10.5	21
8 <a href="#">Electronic States at Low-Angle Grain Boundaries in Polycrystalline Naphthalene</a> <i>Mladenovic, M; Vukmirovic, N and Stankovic, I</i> Aug 1 2013   JOURNAL OF PHYSICAL CHEMISTRY C 117 (30), pp.15741-15748		1	1	1	3	0	1.7	17
9 <a href="#">Effects of thermal disorder on the electronic properties of ordered polymers</a> <i>Mladenovic, M and Vukmirovic, N</i> 2014   PHYSICAL CHEMISTRY CHEMICAL PHYSICS 16 (47), pp.25950-25958		3	2	1	1	0	1.67	15
10 <a href="#">Effects of thermal disorder on the electronic structure of halide perovskites: insights from MD simulations</a> <i>Mladenovic, M and Vukmirovic, N</i> Oct 28 2018   PHYSICAL CHEMISTRY CHEMICAL PHYSICS 20 (40), pp.25693-25700		0	2	3	3	2	2	10
11 <a href="#">Multimodal host-guest complexation for efficient and stable perovskite photovoltaics</a> <i>Zhang, H; Eickemeyer, FT; (...); Mladenovic, M</i> Jun 7 2021   NATURE COMMUNICATIONS 12 (1)		0	0	0	4	4	4	8
12 <a href="#">Unravelling the structural complexity and photophysical properties of adamantyl-based layered hybrid perovskites</a> <i>Jahanbakhshi, F; Mladenovic, M; (...); Gratzel, M</i> Sep 14 2020   JOURNAL OF MATERIALS CHEMISTRY A 8 (34), pp.17732-17740		0	0	0	6	0	2	6
13 <a href="#">Electronic States at the Interface between Crystalline and Amorphous Domains in Conjugated Polymers</a> <i>Mladenovic, M and Vukmirovic, N</i> Oct 15 2015   JOURNAL OF PHYSICAL CHEMISTRY C 119 (41), pp.23329-23333		2	1	0	1	0	0.75	6
14 <a href="#">Spontaneous Polarization Induced by Side Chains in Ordered Poly(3-hexylthiophene)</a> <i>Mladenovic, M and Vukmirovic, N</i> Aug 25 2016   JOURNAL OF PHYSICAL CHEMISTRY C 120 (33), pp.18895-18900		1	0	0	2	0	0.43	3
15 <a href="#">Organic Spacers in 2D Perovskites: General Trends and Structure-Property Relationships from Computational Studies</a> <i>Jahanbakhshi, F; Mladenovic, M; (...); Rothlisberger, U</i> Apr 2021   Apr 2021 (Early Access)   HELVETICA CHIMICA ACTA 104 (4)		0	0	0	2	0	1	2
16 <a href="#">Why choosing the right partner is important: stabilization of ternary Cs(y)GUA(x)FA((1-y-x))PbI(3) perovskites</a> <i>Boziki, A; Mladenovic, M; (...); Rothlisberger, U</i> Sep 28 2020   PHYSICAL CHEMISTRY CHEMICAL PHYSICS 22 (36), pp.20880-20890		0	0	0	1	0	0.33	1
17 <a href="#">Atomic and electronic structure of grain boundaries in crystalline organic semiconductors</a> <i>Mladenovic, ML; Vukmirovic, N and Stankovic, I</i> 3rd International Conference on the Physics of Optical Materials and Devices Nov 2013   PHYSICA SCRIPTA T157		0	0	0	0	0	0.1	1
18 <a href="#">Naphthalenediimide/Formamidinium-Based Low-Dimensional Perovskites</a> <i>Mishra, A; Ahlawat, P; (...); Gratzel, M</i> Aug 24 2021   Aug 2021 (Early Access)   CHEMISTRY OF MATERIALS 33 (16), pp.6412-6420		0	0	0	0	0	0	0

Citation Report Publications Table

# Acknowledgements

*This is an end to five indispensable years  
Filled with invaluable gains and irreplaceable losses,  
Bursting with screams of joy and tears of sorrow,  
This very moment,  
Is where I shall start again  
...for this is the end*

First and foremost, I would like to express my sincerest appreciation to my advisor, *Prof. Ursula Röthlisberger*. Her unconditional support since day one, not only throughout my research but also in my personal well being, has set the bar so high that words fall short to do her justice. I might as well abide by saying "Thank you for the genuine human being that you are and for all you have done for me". I would also like to especially thank the esteemed jury members of my doctoral oral exam, Prof. Berend Smit, Prof. Giulia Galli, Prof. Constantinos Stoumpos and Prof. Raffaella Buonsanti who I am deeply honored to have in my thesis defense session.

Dozens of people have paved my way throughout this journey without whom this very day would not have come. Five years at LCBC gave me the opportunity to witness tens of individuals joining, befriending, making carriers and leaving, which requires a trip down memory lane to name them all. I remain humbly appreciative to every single person who I have come in contact with during my stay at LCBC, particularly, the one and only Karin who will always be near and dear to my heart and my fellow nerd *Marko* with whom I shared tons of memories, uphill and downhill, and I could not be more blessed that our co-workship has turned into an authentic friendship. I would also like to express my especial thanks to all the collaborators in the group of Prof. Michael Grätzel. Outside the LCBC members, I had few genuine friends who I spent the least yet the most quality time with, from my first ever trip to Lausanne to this very day. *Ali and Vahid*, you belong in the brightest spots of my memory. Five years ago, I left my home town to fulfil the mutual dream of mine and my Dad's, my biggest cheer leader, my everlasting soul mate, whose last words whispered into my ears were "I believe in you more

## Acknowledgements

---

than I believe in myself." before he lost an unfair year-long battle to cancer. This very moment, I cannot say for certain he has left us in immense shock and is no longer with us, embraced by all his vivid memories and all his inspiring words heard deep in the stillness. *I forever, cherish all you gave me Dad and will always love you to the moon and back.*

*Mom and Ali*, my only family members and relatives, I remain endlessly beholden for having you, even thousands of miles away. I could not have been more blessed and indebted to all the sacrifices you made, my adored Mom, and I pray that you live long and blissfully. And you, my beloved brother, my partner in crime, I am forever filled with gratitude that you have always been there for me and that you are the living memory of Dad.

*May tomorrow be a better day..*

Lausanne, May 2021

EJB



ИНСТИТУТ ЗА ФИЗИКУ			
ПРИМЛЕНО: 24.04.2018			
Рад јед.	Б р о ј	Арх.шифра	Прилог
0801	598/1		

Научном већу Института за физику у Београду

### Извештај жирија за доделу Годишње награде за научни рад и Студентске награде Института за физику у Београду

#### 1) Годишња награда за научни рад

За Годишњу награду за научни рад Института за физику у Београду за 2018. годину предложена су три кандидата:

1. **др Ненад Врањеш**, виши научни сарадник - предлагачи: др Лидија Живковић, научни саветник, академик Ђорђе Шијачки, научни саветник у пензији;
2. **др Жељка Никитовић**, научни саветник - предлагачи: др Душан Арсенивић, научни саветник, др Владимир Стојановић, виши научни сарадник, др Зоран Распоповић, виши научни сарадник;
3. **др Невена Пуач**, научни саветник - предлагачи: академик Зоран Петровић, научни саветник, др Вељко Дмитрашиновић, научни саветник.

Након детаљне квалитативне и квантитативне анализе научног доприноса кандидата током претходне две календарске године, а посебно узимајући у обзир квалитет објављених радова и њихов импакт на научну област, односно проблематику којој припадају, стваралачки удео кандидата у оствареним резултатима, удео Института у оствареним резултатима, као и број радова и њихове категорије у смислу Правилника о поступку и начину вредновања, и квантитативном исказивању научноистраживачких резултата Министарства надлежног за науку, **жири је донео једногласну одлуку да се Годишња награда за научни рад Института за физику у Београду за 2018. годину додели**

#### **др Ненаду Врањешу**

за значајан допринос мерењу масе  $W$  бозона на АТЛАС експерименту

#### Образложење:

Сви предложени кандидати имају импресиван научни опус и током претходне две календарске године су објавили нове и значајне резултате у међународним научним часописима и представили их на међународним конференцијама.





**Др Ненад Врањеш** се бавио мерењем параметара Стандардног модела на АТЛАС експерименту на Великом сударачу хадрона (LHC) у Церну. Као члан АТЛАС колаборације, др Врањеш је аутор на свим радовима колаборације, док је кључан допринос имао на четири рада M21 категорије, а сами резултати његовог рада су изузетно допринели објављивању још четири рада M21 категорије. Главна тема истраживања др Врањеша је било прецизно мерење масе  $W$  бозона. Ова мерења су кључна за проверу конзистентности Стандардног модела, а веће одступање од предвиђених вредности може да укаже на физику ван Стандардног модела. Теорија Стандардног модела предвиђа масу  $W$  бозона са прецизношћу од 8 MeV, а да би експериментални резултати били упоредиви потребно је достићи релативну прецизност од 0.01%. Др Врањеш је кључно допринео у неколико битних аспеката овог мерења: i) имплементирао је иновативне алгоритме и технике који су омогућили бољу калибрацију импулса миона, што је најкритичнија компонента овог истраживања, ii) имао је кључну улогу у мерењу ефикасности и тригровања миона, калибрацији хадронског узмака, одабиру интересантних догађаја, као и у целокупној анализи података у мионском каналу. Постигнута неодређеност од 19 MeV је најпрецизније мерење на експериментима у физици честица, а добијени резултат је у складу са најновијим теоријским предвиђањима. Др Ненад Врањеш био је коресподентни аутор на датом раду, а сам резултат је приказан на посебном семинару у Церну, свим конференцијама из области, а био је и предмет Церновог саопштења за медије које је пренесено у више других медија из различитих земаља. Иначе ово је прво и, за сада, једино објављено мерење масе  $W$  бозона на експериментима LHC-а. Додатно, др Врањеш је имао значајну улогу у објављивању резултата прецизног мерења топ кварка, као и у мерењу и калибрацији луминозности, где се резултати користе у већини радова АТЛАС експеримената. Због свог изузетног рада и доприноса, др Врањеш је међународно препознат и именован за руководиоца АТЛАС групе за анализу података са  $W$  и  $Z$  бозонима. Резултати др Врањеша у претходне две године представљају, не само значајан допринос најактуелнијим истраживањима у физици елементарних честица, већ и до сада вероватно најзначајнији допринос истраживача из наше земље у активностима Церн-ових колаборација.

**Др Желјка Никитовић** се бавила транспортом наелектрисаних честица у смешама основног гаса са радикалима, сударним процесима на високим  $E/N$ , као и прорачунима транспортних и брзинских коефицијената јона у неутралном гасу који су од интереса за моделовање ниско-температурских плазми које се користе у биомедицини. Потреба за базама података које би служиле за моделовање плазми за производњу интегрисаних кола и наноструктура нужно укључује позитивне јоне. Међутим, за позитивне јоне са великим рекомбинационим потенцијалом ситуација је потпуно различита. Егзотермне реакције, које уједно врше и промену идентитета посматраних јона, драстично мењају транспортне особине ових јона, а тиме и утичу на особине неравнотежних плазми којима доминирају судари у гасу. По први пут је у литератури приказано одређивање транспортних параметара јона у индукваном поларизационом потенцијалу, уз учешће егзотермних реакција асоцијације и реакција промене идентитета јона. У овим истраживањима др Никитовић је користила Монте Карло рачунарске симулације. Поред наведеног, предлагачи истичу допринос кандидаткиње везан за теоријску



анализу појаве *four wave mixing-a* у врућим парама калијума у пулсном режиму ласера при чему се користи модел заснован на Bloch-Maxwell једначинама уз узимање у обзир Доплеровог ефекта. У периоду од претходне две године кандидаткиња је објавила девет радова (M13:1, M21a:1, M21:2, M22: 2, M23:3, M24:1)

Др Невена Пуач се бави пројектовањем и дијагностиком неравнотежних плазми и њиховом применама у биологији, медицини и пољопривреди. Она је учествовала у развоју високо-напонских извора и појачавача неопходних за одржавање неравнотежних плазми на високом притиску. У дијагностици неравнотежне плазме, др Пуач је постигла значајне резултате, укључујући мерење снаге деривативним сондама, мерење параметара плазме Лангмуровим и каталитичким сондама и оптичком емисионом спектроскопијом. Током претходне две календарске године, др Невена Пуач је објавила укупно 9 радова у међународним часописима (M21a:1, M21:6, M23:2). Посебно се издвајају два рада из области примена неравнотежних плазми у пољопривреди и процесирању хране. Један од ових радова је написан по позиву и представља тзв. мишљење експерта (енгл. *expert opinion article*). Овај рад је привукао велику пажњу у заједници истраживача који се баве овом тематиком, јер је дефинисао будуће правце истраживања. Ово јасно показује да је др Невена Пуач један од лидера у својој области истраживачког рада чиме је значајно допринела порасту угледа Института за физику у свету. Други рад представља кулминацију вишегодишњег рада др Невене Пуач на разумевању механизма интеракције плазме и семена са циљем бржег клијања и раста биљака. У овом раду су анализрани ефекти третмана плазмом на физиологију семена на основу испитивања ензима одговорног за уклањање сигналног молекула  $H_2O_2$ . Научна активност др Невене Пуач је пример квалитетног и успешног мултидисциплинарног рада како са колегама у земљи тако и са колегама у иностранству. Она је остварила веома успешну сарадњу са Институтом за биолошка истраживања Синиша Станковић, Стоматолошким факултетом и Медицинским факултетом Универзитета у Београду, као и са колегама из Португалије, Словеније, Мађарске, Италије и Чешке.

#### Закључак:

На основу свега наведеног, иако су сва три кандидата дала значајне научне доприносе у свом раду током претходне две календарске године, два кандидата др Пуач и др Вранеш се посебно истичу у погледу квалитета постигнутих резултата и свом доприносу повећања међународног угледа Института за физику. Међутим, резултати др Вранеша у претходне две године представљају, не само значајан допринос најактуелнијим истраживањима у физици елементарних честица, већ и до сада вероватно најзначајнији допринос истраживача из наше земље у активностима Цериових колаборација. Имајући ово у виду **сматрамо да се научни резултати др Ненада Вранеша посебно истичу по свом изузетном квалитету и значају, да доприносе повећању међународног угледа Института за физику, и да због тога Годишњу награду за научни рад Института за физику за 2018. годину треба доделити др Ненаду Вранешу.**



## II) Студентска награда

За Студентску награду Института за физику у Београду за 2017. годину предложено је седам кандидата:

1. **др Маријана Гавриловић Божовић**, истраживач сарадник - предлагач: др Соња Јовићевић, научни саветник у пензији;
2. **др Владимир Лончар**, истраживач сарадник - предлагач: др Антун Балаж, научни саветник;
3. **др Срђан Марјановић**, истраживач сарадник - предлагач: академик Зоран Петровић, научни саветник;
4. **др Марко Младеновић**, научни сарадник - предлагач: др Ненад Вукмировић, научни саветник;
5. **др Јелена Пешић**, истраживач сарадник - предлагач: др Радош Гајић, научни саветник;
6. **др Урош Ралевић**, истраживач сарадник - предлагач: др Горан Исић, научни сарадник;
7. **др Јелена Смиљанић**, истраживач сарадник - предлагач: др Марија Митровић Данкулов, научни сарадник.

Након детаљне анализе докторских дисертација и научних доприноса кандидата, а посебно узимајући у обзир квалитет дисертација и објављених радова и њихов импакт на научну област, односно проблематику којој припадају, стваралачки удео кандидата у оствареним резултатима, удео Института у оствареним резултатима, као и број радова и њихове категорије у смислу Правилника о поступку и начину вредновања, и квантитативном исказивању научноистраживачких резултата Министарства надлежног за науку, жири је донео једногласну одлуку да се Студентска награда Института за физику у Београду за 2017. годину додели

### **др Марку Младеновићу**

за докторску дисертацију под називом *"Електронска својства органских полупроводника на границама домена"*.

#### Образложење:

Жири констатује да су докторске дисертације свих предложених кандидата изузетно високог квалитета. Сви кандидати имају значајан број објављених радова у квалитетним међународним часописима, а своје резултате су представили на бројним међународним и домаћим конференцијама.

**Др Маријана Гавриловић Божовић** је докторску дисертацију под називом *Узајамно дејство кавитационог мехура и зрачења плазме код пробоја индукованог једним*



ласерским импулсом на мети у течности одбранила на Електротехничком факултету Универзитета у Београду, под руководством проф. др Јована Цветића. Она је у својој дисертацији проучавала развој кавитационог мехура, појаву ударних таласа и зрачење ласерски индуковане плазме у течној средини. У истраживању плазме је коришћена техника брзе фотографије и оптичка емисиона спектроскопија, ударни таласи су анализирани помоћу шлирен методе, а еволуција кавитационог мехура је проучавана шадографијом и техником пробног снопа. У току израде докторске дисертације је објавила 9 радова у међународним часописима (M21a:1, M21:5, M23:3).

Др Владимир Лончар је докторску дисертацију под називом *Hybrid Parallel Algorithms for Solving Nonlinear Schrodinger Equation* одбранио на Природно-математичком факултету Универзитета у Новом Саду, под руководством др Антуна Балажа. У својој дисертацији он се бавио развојем паралелних алгоритама за решавање једног облика Грос-Питаевски једначина који се извршавају на графичком процесору, на вишејезгарним процесорима, као и на системима са дистрибуираном меморијом односно рачунарским кластерима. У току израде докторске дисертације др Лончар је објавио четири рада у међународним часописима (M13: 1, M21a:3).

Др Срђан Марјановић је докторску дисертацију под називом *Monte Carlo симулација транспорта позитрона у реалним системима испуњеним гасом* одбранио на Електротехничком факултету Универзитета у Београду, под руководством академика др Зорана Љ. Петровића. Др Срђан Марјановић је у својој дисертацији у Монте Карло симулацијама разматрао реалне системе и уређаје испуњене гасом који своју функцију базирају на елементарним сударним и транспортним процесима позитрона. Највећу пажњу је посветио разматрању позитронског трапа, компресије снопа позитрона ротирајућим електричним пољем и термализације позитрона у биолошки релевантним срединама. У току израде докторске дисертације, др Срђан Марјановић је објавио 15 радова у међународним часописима (M21a:3, M21:7, M22:4, M23:1).

Др Марко Младеновић је докторску дисертацију под називом *Electronic Properties of Interfaces between Domains in Organic Superconductors* (Електронска својства органских полупроводника на границама домена) одбранио на Електротехничком факултету Универзитета у Београду, под руководством др Ненада Вукмировића. У својој дисертацији, он се бавио проучавањем проблема граница између домена у органским полупроводницима, т.ј. материјалима који су због своје лаке и једноставне производње од великог значаја за примене у индустрији, а са друге стране слабо проучени због њихове комплексне структуре. У току израде докторске дисертације, која је трајала четири године, и која је представљала једно од првих теоријских истраживања која разматрају овај проблем, др Марко Младеновић је (као први аутор) објавио 7 радова у међународним часописима (M21a:2, M21:3, M22:1, M24:1).

Др Јелена Пешић је докторску дисертацију под називом *Investigation of Superconductivity in Graphene and Related Materials Based on Ab-initio Methods* (Истраживање суперпроводности у графену и сличним материјалима коришћењем ab-



*initio* метода) која је рађена под менторством др Радоша Гајића. Фокус истраживања је на електрон-фононској интеракцији у овим материјалима и појави суперпроводности. У току израде докторске дисертације Др Пешић је објавила 8 радова у међународним часописима (M21a:2, M21:3, M22:3).

**Др Урош Ралевић** је докторску дисертацију под називом Наноскопија и примене дводимензионалних и квази дводимензионалних система (енг. "*Nanoscopy and applications of two-dimensional and quasi-two-dimensional systems*") одбранио на Електротехничком факултету Универзитета у Београду, под менторством др Горана Исића. Кандидат се бавио испитивањем електронских и оптичких особина дводимензионалних материјала попут графена и монослојева молибден дисулфида, слојевитих материјала попут церијум трителурида и металних наночестица и њихових кластера. У току израде докторске дисертације Др Ралевић је објавио 16 радова у међународним часописима.

**Др Јелена Смиљанић** је докторску дисертацију под називом *Испитивање својстава комплексних мрежа са дискретном динамиком* одбранила на Електротехничком факултету Универзитета у Београду, под менторством др Марије Митровић Данкулов. Фокус истраживања је био на анализи динамичких процеса, структуре мреже интеракција, као и њиховог међусобног утицаја у социјалним системима који подразумевају непосредну комуникацију. У току израде докторске дисертације Др Смиљанић је објавила 5 радова у међународним часописима (M21a:1, M21:2, M22:1, M13:1).

#### **Закључак:**

Имајући у виду разноликост истраживачких тема и области, разнородност доприноса кандидата, као и квалитет докторских дисертација и радова проистеклих из њих, било је изузетно тешко одабрати добитника овогодишње Студентске награде. Ипак, **жири је одлучио да награду додели др Марку Младеновићу**, због изузетно квалитетног истраживања које омогућава разумевање електронских особина граница између домена у огранским полупроводницима, а које је урадио у изузетно кратком временском року. Поред тога, посебно желимо да истакнемо и дисертацију др Срђана Марјановића која је урађена у нешто дужем року року, али представља систематичан и изузетно значајан допринос моделовању и даљем развоју позитронских трагова испуњених гасом.

На крају бисмо поново желели да истакнемо да су све овогодишње докторске дисертације високог квалитета и да то видимо као велики успех предложених кандидата, њихових ментора, као и Института за физику у Београду.

Надамо се још јачој и бројнијој конкуренцији следеће године и свим кандидатима честитамо на извршним научним резултатима, а добитницима на освојеним наградама.

УНИВЕРЗИТЕТ У БЕОГРАДУ  
ИНСТИТУТ ЗА ФИЗИКУ БЕОГРАД

Прегревица 118, 11080 Земун - Београд, Србија  
Телефон: +381 11 3713000, Факс: +381 11 3162190, www.ipb.ac.rs  
ПИБ: 100105980, Матични број: 07018029, Текући рачун: 205-66984-23



Београд, 24. април 2018. год.

A handwritten signature in blue ink, appearing to read 'Borjević M.'.

др Магдалена Ђорђевић  
научни саветник, Институт за физику у Београду

A handwritten signature in blue ink, appearing to read 'Sasa Dujko'.

др Саша Дујко  
научни саветник, Институт за физику у Београду

A handwritten signature in blue ink, appearing to read 'Milovan Šuvačok'.

др Милован Шуваков  
виши научни сарадник, Институт за физику у Београду

22-Jun-2016

Dear Mr Mladenovic:

TITLE: [REDACTED]

AUTHORS: [REDACTED]

(See below for abstract and previous reviewer reports)

I invite you to re-review this revised manuscript, which has been submitted for publication in Physical Chemistry Chemical Physics (PCCP). Based on the previous reviewer reports the authors were asked to revise their manuscript and have now submitted a new version for publication in PCCP, published by the Royal Society of Chemistry.

Please advise whether your original concerns, and those of the other reviewers (reports copied below), have been satisfactorily addressed and whether this work is now suitable for publication in PCCP. Thank you in advance for taking the time to look at this work again.

At PCCP we aim to provide a rapid service for our authors. Therefore, please respond to this invitation by clicking on the appropriate link below within 3 days of receiving this email, and provide your report within 10 days of agreeing (7 days for communications and 14 days for reviews). If you need longer to provide your report please let me know. If you are unable to review at this time, I would be grateful if you could recommend another expert reviewer.

Once you accept the invitation to review this manuscript, you will receive a second email giving you access to the manuscript and our reviewer guidelines.

-----  
Please note that:

- your anonymity as a reviewer will be strictly preserved;
- you have the responsibility to treat the manuscript and any communications on the manuscript as confidential;
- the manuscript (or its existence) should not be shown to, disclosed to, or discussed with others, except in special cases, where specific scientific advice may be sought. In this event, please contact me with the names of those you have consulted;
- you should contact me immediately to report any conflict of interest, or suspicion of duplicate publication, fabrication of data or plagiarism.

Thank you for your support as a reviewer for the Royal Society of Chemistry. By providing a review for Physical Chemistry Chemical Physics you are part of the world's leading chemistry community.

Yours sincerely,

Prof. Gaoquan Shi  
Associate Editor  
Physical Chemistry Chemical Physics

Република Србија  
МИНИСТАРСТВО ПРОСВЕТЕ,  
НАУКЕ И ТЕХНОЛОШКОГ РАЗВОЈА  
Комисија за стицање научних звања

Број: 660-01-00006/211  
29.11.2017. године  
Београд

МИНИСТАРСТВО ЗА ФИЗИКУ			
ПРИМЉЕНО: 27-12-2017			
Рад.јед.	б р о ј	Арх.шифра	Прилог
офр/	1848/1		

На основу члана 22. став 2. члана 70. став 4. Закона о научноистраживачкој делатности ("Службени гласник Републике Србије", број 110/05, 50/06 – исправка, 18/10 и 112/15), члана 3. ст. 1. и 3. и члана 40. Правилника о поступку, начину вредновања и квантитативном исказивању научноистраживачких резултата истраживача ("Службени гласник Републике Србије", број 24/16, 21/17 и 38/17) и захтева који је поднео

*Институт за физику у Београду*

Комисија за стицање научних звања на седници одржаној 29.11.2017. године, донела је

**ОДЛУКУ  
О СТИЦАЊУ НАУЧНОГ ЗВАЊА**

**Др Марко Младеновић**

стиче научно звање

**Научни сарадник**

у области природно-математичких наука - физика

**О Б Р А З Л О Ж Е Њ Е**

*Институт за физику у Београду*

утврдио је предлог број 381/1 од 21.03.2017. године на седници Научног већа Института и поднео захтев Комисији за стицање научних звања број 406/1 од 28.03.2017. године за доношење одлуке о испуњености услова за стицање научног звања **Научни сарадник**.

Комисија за стицање научних звања је по претходно прибављеном позитивном мишљењу Матичног научног одбора за физику на седници одржаној 29.11.2017. године разматрала захтев и утврдила да именовани испуњава услове из члана 70. став 4. Закона о научноистраживачкој делатности ("Службени гласник Републике Србије", број 110/05, 50/06 – исправка, 18/10 и 112/15), члана 3. ст. 1. и 3. и члана 40. Правилника о поступку, начину вредновања и квантитативном исказивању научноистраживачких резултата истраживача ("Службени гласник Републике Србије", број 24/16, 21/17 и 38/17) за стицање научног звања **Научни сарадник**, па је одлучила као у изреци ове одлуке.

Доношењем ове одлуке именовани стиче сва права која му на основу ње по закону припадају.

Одлуку доставити подносиоцу захтева, именованом и архиви Министарства просвете, науке и технолошког развоја у Београду.

ПРЕДСЕДНИК КОМИСИЈЕ

*Др Станислава Стојић-Грујић*  
Др Станислава Стојић-Грујић,  
научни саветник

МИНИСТАР

*Младен Шарчевић*  
Младен Шарчевић







0801 Број 478/1  
Датум 04. 05. 2022

## ПОТВРДА О РУКОВОЂЕЊУ ПРОЈЕКТНИМ ЗАДАТКОМ

Овим потврђујем да је научни сарадник др **Марко Младеновић**, за кога се покреће избор у звање виши научни сарадник, у оквиру пројекта основних истраживања „Моделирање и нумеричке симулације сложених вишечестичних система“ (ОН171017), руководио пројектним задатком: „Испитивање ефекта термалног неуређења на електронске особине перовскита на бази халогених елемената“ од августа 2016. до јуна 2017. године. На поменутом задатку су били ангажовани следећи истраживачи: др Марко Младеновић, др Ненад Вукмировић, Милан Јоцић.

др Антун Балаж  
научни саветник  
руководилац пројекта ОН171017